2 Accelerator

2.1 Accelerator physics

2.1.1 Introduction

Energy Recovery Linacs (ERLs), proposed already in [1], have received much attention during the last decade because they have the potential to accelerate currents much larger than those of non-recovering Linacs and to provide emittances smaller than those in x-ray storage rings at similar energies and for similar beam currents. The first potential is due to the fact that the current in Linacs is limited by the available electric power if the energy of the accelerated particles is not recovered. In that case, accelerating a 100 mA beam to 5 GeV would require a beam power of 0.5 GW, which is technically not feasible. We therefore propose to use an ERL for these large currents of Linac quality beams. The second potential is due to the fact that the emittances in an ERL are those of the electron source if emittance increase during acceleration can be avoided. Once high-current, ultra-low-emittance electron sources become available, beams accelerated in an ERL will have a brigthness significantly larger than that of high-energy storage rings.

Energy Recovery Linacs for x-ray light sources have particular challenges that are related to four properties of the beam they are to deliver: small transverse emittances, low energy spread, short bunches, and large currents. In this chapter, the design of the proposed ERL is explained and how it meets these particular challenges is discussed. It is shown that computer models of the accelerator indicate that the design parameters are suitably chosen, limiting emittance growth from Incoherent Synchrotron Radiation (ISR), Coherent Synchrotron Radiation (CSR) and other sources. The design also limits emittance growth from beam-breakup (BBU) and ion instabilities as well as keeping energy spread from short-range wakefields tolerable, collimating beam halo, and holding other detrimental effects in check.

Small transverse emittances

The design of an injector that would produce the required small emittances by overcoming destructive effects of the space-charge forces that dominate beam motion at low energy and high beam density is described, along with how the beam is to be accelerated to high energies with little emittance growth. At higher energy, space charge becomes less important, but deviations from a cylindrically-symmetric accelerating fields in a Linac, e.g. due to cavity misalignments and coupler kicks, can continue to increase the emittance and must therefore be limited. The accelerated beam is then sent through bends of the accelerator until it reaches the x-ray users. In these bends, emittance excitation from incoherent synchrotron radiation occurs, just as in storage rings, and we show how linear and nonlinear low-emittance-growth optics can limit this excitation. In storage rings, this leads to an equilibrium emittance after a few damping times, typically during several hundred revolutions. In an ERL, the horizontal

emittance can consequently be several hundred times smaller than in rings. In fact, it can become so small and the electron beam so narrow that it is nearly indistinguishable from a point source for hard x-rays, producing waves that are coherent in both transverse directions. The vertical emittance in a storage ring can already be made very small, sometimes even smaller than in an ERL. However, often this emittance is then smaller than required for a coherent hard x-ray beam so that the advantage of reducing the horizontal emittance in an ERL is much larger than that of further reduction in the vertical emittance.

Low energy spread

Bunches that are accelerated in a Linac can have a very low energy spread compared to a storage ring. The energy spread in a ring is due to the stochastic nature of synchrotron-radiation emission accumulated over hundreds of turns, as discussed for the horizontal emittance. In an ERL, however, the energy spread is determined by the bunch length because the accelerating field in a Linac changes with time over the duration of the bunch. An ERL's short bunch length produces low energy spread, and therefore low x-ray frequency spread, which allows longer undulators to be used more efficiently in an ERL than typical for a storage ring. However, short bunch length also increases wakefields and coherent synchrotron radiation. The presented design takes these effects into account.

Short bunches

The electron source of an ERL can produce bunches that are much shorter than those in storage rings. While this allows for time-resolved x-ray experiments, it also poses challenges for the beam dynamics; and those were taken into account for the presented design. For example, the strong wakefields that short bunches create can lead to an energy spread after deceleration too large for simple beam transport into the beam stop. A bunch compressor can further reduce the bunch length in an ERL significantly, and we therefore present a bunch compression at high energy that takes effects like CSR and nonlinear time-of-flight into account.

Large currents

Large currents of short bunches produce significant wakefield heating in all beam pipe components and excite Higher-Order Modes (HOMs) in the superconducting RF cavities. The ERL's cavities are designed with cooled HOM absorbers that reduce the quality factor of these modes sufficiently to avoid recirculative beam-breakup instabilities up to the desired current of 100 mA. Because large beam currents can produce large radiation background rates from beam-halo scraping or from component failures, a beam-abort and beam-collimation system is part of the presented ERL design.

State of the art

In Fig. 1.3.3 the spectral brightness and coherent fraction of the ERL have been compared to ring-based light sources, and in Tab. 1.3.1 the primary operating modes A) High Flux B) High Coherence and C) Short Pulse have been defined. Comparisons with state of the art storage rings are shown in Tab. 2.1.1.

Table 2.1.1: Electron beam parameters in the ERL's high-brightness and high-current modes as compared to leading storage rings for each parameter. The ERL furthermore has a mode for bunch durations as short as 100 fs described in Tab. 1.3.1.

Parameter	ERL	Ring	Ring name
Horizontal emittance ϵ_x	8 pm/30 pm	1 nm	PETRA-3
Vertical emittance ϵ_y	8 pm/30 pm	1.2 pm	Australian LS
Bunch duration σ_t	2 ps	16 ps	ESRF
Energy spread σ_δ	2×10^{-4}	1×10^{-3}	typical
Current I	25 mA/100 mA	500 mA	SPring-8

The fact that several of the ERL's critical beam parameters are comparable to those of the leading storage rings shows that many diagnostic techniques can be adopted from these rings, e.g. for high-precision transverse beam position stabilization, ultra-low emittance measurements, bunch length measurements, beam-loss measurements, etc. Other diagnostics techniques can be adopted from Linacs or from the JLAB-FEL, the only operating SRF ERL. At that accelerator, 9.2 mA have been accelerated in ERL mode and its Beam-Breakup (BBU) diagnostics, bunch-charge stabilization, electric field and amplitude stabilization can be adopted to Cornell's hard x-ray ERL.

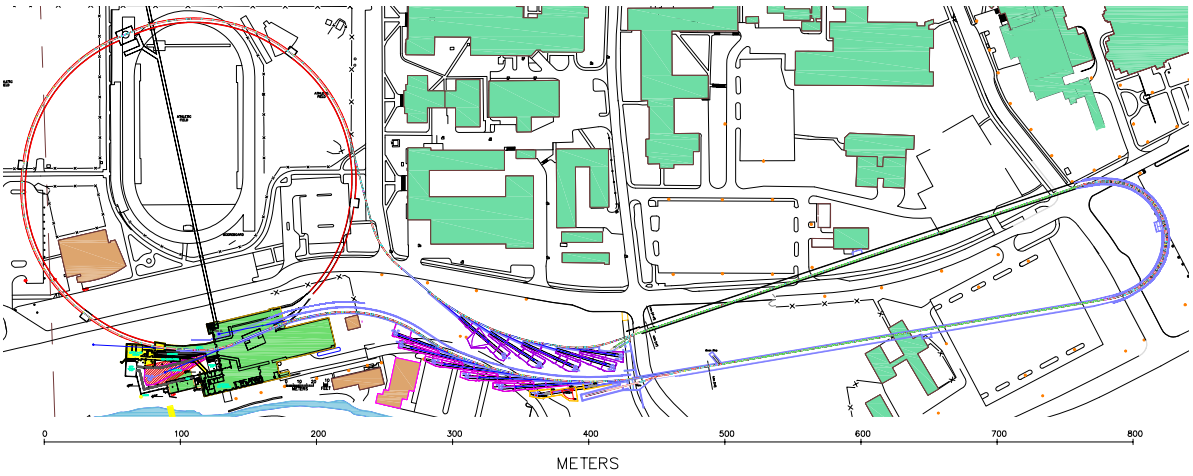

Figure 2.1.1: The Cornell ERL on the campus map

2.1.2 Layout

The development of an ERL at Cornell presents unique opportunities. Cornell has significant infrastructure and an existing 5 GeV particle accelerator. Therefore, the ERL example makes as much use as possible of the existing facilities at the Wilson Synchrotron Laboratory, which include CESR, the CHESS G-line beamline, and the Wilson Lab building. Because the CESR components were designed to sustain 8 GeV electrons, this section can comprise part of the 5 GeV return arc of the ERL.

The location of Wilson Lab lies on a hillside between the Cornell campus and Cascadilla creek. The CESR tunnel is approximately 15 m below the athletic field to the north of this hillside. This terrain is used in the ERL design by having the accelerator housed mostly in an underground tunnel, while the x-ray beamline section is located outside the hill where a new x-ray science building is to be located.

The current design is shown in Fig. 2.1.1. The logic in choosing this design is discussed in the following section. The layout is divided into nine discrete sections, shown in Fig. 2.1.2, roughly in accordance with their function: The injector (IN) delivers a 15 MeV beam into Linac A (LA), which accelerates the beam 2.7 GeV. This beam feeds into Turnaround A (TA), which bends it around to connect to Linac B (LB). The beam is accelerated through LB to 5 GeV into the South Arc (SA) containing nine undulators, which connects to part of CESR (CE), which connects to the North Arc (NA) containing five more undulators. The NA connects back into LA, which decelerates the beam to 2.3 GeV, recovering 2.7 GeV. A demerging dipole separates this beam from the 2.7 GeV accelerating beam into TB. Thereafter a merging dipole combines this decelerating beam with the accelerating beam from TA and directs it into LB, where it is decelerated to 10 MeV, recovering 2.3 GeV. Finally the beam is sent to the Beam Stop (BS).

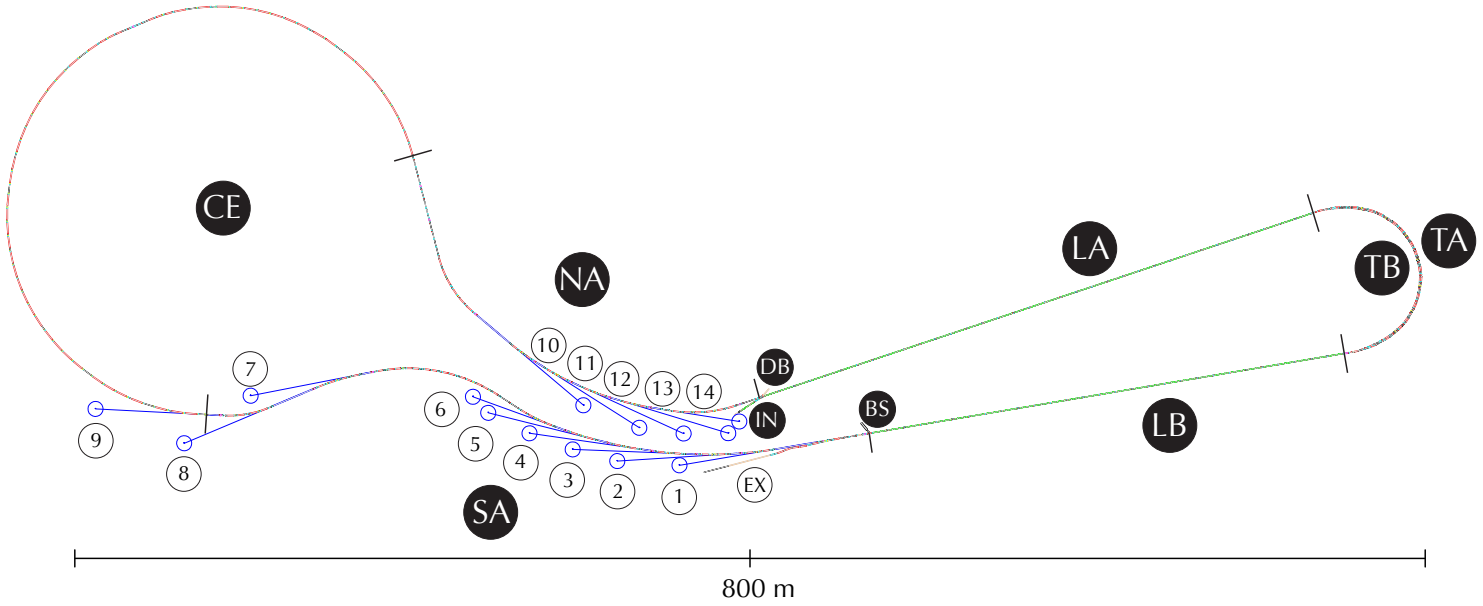

Figure 2.1.2: The ERL layout with section labels. A bunch is accelerated to 15 MeV in the injector (IN), and merged into the beginning of Linac A (LA), which accelerates it to 2.7 GeV. The bunch traverses Turnaround A (TA), and gains another 2.3 GeV through Linac B (LB). Now at 5 GeV, the bunch travels through undulators in the South Arc (SA), the CESR tunnel (CE), and undulators in the North Arc (NA). It then reenters LA off phase, which decelerates it to 2.3 GeV, enters Turnaround B (TB), and is decelerated to 10 MeV through LB. Finally it is extracted and sent to the beam stop (BS). To optimize the emittance out of the injector, a diagnostic beamline (DB) is used before the main Linac.

In order to be a competitive and cost-effective light source, the ERL must

- Utilize as much of CESR as possible.
- Provide at least 14 x-ray beamlines with easy access.
- Have a single building to house all x-ray beamlines outside of Wilson Lab, as well as the the injector.
- Accommodate at least two 25 m long undulators.
- Include the CHESS G-line beamline.

As mentioned, the natural extension of the ERL from CESR is to the east. Taking advantage of the curved hillside in this direction, the South Arc and the North Arc are shaped to conform to the terrain. The curvature is suitable for housing 70 m long x-ray beamlines with reasonably large experimental hutches. In this manner, beamlines from both arcs are housed in a single new x-ray science building. Furthermore, space has been allotted for three x-ray beamlines in Wilson lab, including G-line and one from a 25 m long undulator. The new building alone will contain up to eleven beamlines. Of these beamlines, up to six are from the South Arc and up to five from the North Arc, with each Arc containing one 25 m long undulator. The ERL design thus accommodates three 25 m undulators and eleven 5 m undulators.

The radius of curvature of the tunnel housing TA and TB is fixed at 40 m to limit the linear synchrotron-radiation-power density on the vacuum-chamber wall to not much above 1 kW/m. The bends and the beginning of the SA and the end of the NA are adjusted so that the two Linacs connect tangentially to the circular arc of the turnaround loop. The Linacs then have a relative angle of approximately 9°, and therefore TA and TB bend the beam by approximately 189°. The high-energy sections SA, CE, and NA bend the beam by approximately 125°, 253°, and 100° respectively, for a total of approximately $2.6\,\pi$ rad.

In the following, the design process is described using scaling laws for 9 critical performance values. If a preliminary design produces unreasonable values, it can be improved following the scaling laws. These are written with design parameters normalized to values of the ERL so that setting all fractions in parentheses to 1 leads to its critical performance values. It will be seen that these 9 values are all reasonable for the presented design.

In order to transport the beam through this geometry, the dipole magnets need to be of reasonable strength. Their fields scale as

$$B \approxeq 0.6\,\mathrm{T}\left(\frac{28\,\mathrm{m}}{\rho}\right)\left(\frac{\mathcal{E}}{5\,\mathrm{GeV}}\right) \tag{2.1.1}$$

for a bending radius ρ and particle energy $\mathcal{E}$. This design has a reasonable field strength ofno more than 0.6 T.

$$\Delta\mathcal{E}_{\mathrm{ISR}} \approx -2.6\,\mathrm{MeV}\left(\frac{\theta}{2.6\,\pi}\right)\left(\frac{28\,\mathrm{m}}{\rho}\right)\left(\frac{\mathcal{E}}{5\,\mathrm{GeV}}\right)^4 \quad \text{and} \tag{2.1.2}$$

$$\Delta\mathcal{E}_{\mathrm{u}} \approx -2.1\,\mathrm{MeV}\left(\frac{L_{\mathrm{u}}}{130\,\mathrm{m}}\right)\left(\frac{B_{\max}}{1\,\mathrm{T}}\right)^2\left(\frac{\mathcal{E}}{5\,\mathrm{GeV}}\right)^2 \tag{2.1.3}$$

show that for the total length L_u of undulators in the ERL, the energy loss during one pass is about 5 MeV when all undulators are turned on. With an energy of 15 MeV after the injector, the beam is stopped at 10 MeV, which we show to be a reasonable value.

Additionally, it has to be checked that coherent synchrotron radiation does not add a significant loss for a bunch charge Q and bunch duration σ_t. This loss is given by [2]

$$\Delta\mathcal{E}_\mathrm{CSR} \approx -119\,\mathrm{keV}\left(\frac{Q}{77\,\mathrm{pC}}\right)^3\left(\frac{\rho}{28\,\mathrm{m}}\right)^{1/3}\left(\frac{2\,\mathrm{ps}}{\sigma_t}\right)^{4/3}\left(\frac{\theta}{2.6\,\pi}\right) \tag{2.1.4}$$

and with approximately 0.1 MeV per electron it clearly does not.

Furthermore, it has to be checked that the power deposition on the vacuum-chamber wall by ISR near dipole magnets is not too large,

$$\frac{dP}{dL} \approx 1.1\,\mathrm{kW/m}\left(\frac{I}{100\,\mathrm{mA}}\right)\left(\frac{28\,\mathrm{m}}{\rho}\right)^2\left(\frac{\mathcal{E}}{5\,\mathrm{GeV}}\right)^4 . \tag{2.1.5}$$

A linear power density of 1.1 kW/m is large but not untypical for storage rings.

Further, taking into account the vertical beam size, the maximum power per unit area on the vacuum-chamber wall near dipole magnets should be limited for a typical vertical beta function β_y and normalized vertical emittance $\epsilon_{N,y}$,

$$\frac{dP}{dA} \approx 37\,\mathrm{W/mm^2}\left(\frac{I}{100\,\mathrm{mA}}\right)\left(\frac{28\,\mathrm{m}}{\rho}\right)^2\left(\frac{\mathcal{E}}{5\,\mathrm{GeV}}\right)^{9/2}\sqrt{\frac{30\,\mathrm{m}}{\beta_y}\frac{0.3\,\mu\mathrm{m}\cdot\mathrm{rad}}{\epsilon_{N,y}}} , \tag{2.1.6}$$

and $37\,\mathrm{W/mm^2}$ is a manageable value.

Preserving the low emittance of the injected bunches is of prime importance in the ERL. One source of emitance growth is emission of ISR, and the normalized emittance growth scales as

$$\Delta\epsilon_N \approx 0.034\,\mu\mathrm{m}\cdot\mathrm{rad}\left(\frac{16}{N_\mathrm{b}}\right)^3\left(\frac{\theta_\mathrm{tot}}{\pi}\right)^4\left(\frac{28\,\mathrm{m}}{\rho}\right)\left(\frac{\mathcal{E}}{5\,\mathrm{GeV}}\right)^6 \tag{2.1.7}$$

where N_b is the number of bends in an arc with total angle θ_tot. This formula assumes close to ideal beam optics [3], and shows that the emittance growth during a full pass around the ERL can be less than the small emittance of the high-spectral-brightness mode B.

This ISR also increases the energy spread in the bunch, scaling as

$$\frac{\Delta\sigma_\mathcal{E}}{\mathcal{E}} \approx 3.7\cdot 10^{-5}\left(\frac{\theta_\mathrm{tot}}{2.6\,\pi}\right)^{1/2}\left(\frac{28\,\mathrm{m}}{\rho}\right)\left(\frac{\mathcal{E}}{5\,\mathrm{GeV}}\right)^{5/2} \tag{2.1.8}$$

which is reasonably small for the ERL's design, and the beam's total energy spread of 2×10^{-4}. Note again that the 5 GeV sections SA, CE, and NA together bend the beam by an angle $2.6\,\pi$.

However, the relative energy spread increases during deceleration but has to remain small enough to steer the full beam into the beam stop (BS). There, the ISR energy spread

$$\frac{\Delta\sigma_\mathcal{E}}{\mathcal{E}_{BS}} \approx 1.8\cdot 10^{-2}\left(\frac{10\,\mathrm{MeV}}{\mathcal{E}_{BS}}\right)\left(\frac{\theta_\mathrm{tot}}{2.6\,\pi}\right)^{1/2}\left(\frac{28\,\mathrm{m}}{\rho}\right)\left(\frac{\mathcal{E}}{5\,\mathrm{GeV}}\right)^{7/2} \tag{2.1.9}$$

is still only 1.8% and therefore reasonably small.

2.1.3 Optics overview

Linear optics-design criteria

In order to deliver a high-quality beam to the undulators and perform energy recovery, the optics in the ERL must overall

- Accommodate simultaneously accelerating and decelerating beams in the LA and LB sections.
- Accommodate one high-energy beam in the SA, CE, and NA sections.
- Limit radiative emittance growth as much as possible prior to undulators.

Since TA and TB maneuver the accelerating and decelerating beams separately, and the SA, CE, and NA sections only manage the high-energy beam, the only sections that must handle both beams are LA and LB, and the demerger and merger sections at the entrances and exits of the turnarounds. The optimization of these sections is challenging. Emittance growth occurs in every bending magnet due to the quantum nature of synchrotron radiation. It must be controlled everywhere, especially in TA and between the SA undulators. Unfortunately, the CESR magnet arrangement reused in CE does not admit a low-emittance solution, and therefore the emittance in the NA is relatively large compared to SA. For this reason, an upgrade option to CE is also given.

In order to provide the desired transverse beam size and length to undulators, the linear optics must provide

- Flexible time of flight terms r_{56} for each turnaround loop.
- $r_{56} = 0$ for the return arc (SA, CE, NA).
- Tunable r_{56} within some subsections.
- Flexible beta functions and zero dispersion in all undulators.
- Beta functions less than 200 m almost everywhere.

In general, the time of flight terms r_{56} for different sections and the phases of the accelerating cavities are used to manipulate the longitudinal phase space. In particular, r_{56} must be zero from the end of LB to the beginning in LA in order for the energy spread profile to correctly match the decelerating RF voltage and therefore allow full energy recovery. The beta functions in all undulators are flexible in order to satisfy the requirements of individual users of these devices. The dispersion is zero in undulators to avoid an apparent increase in beam size. As a rule of thumb, the beta functions are also kept below 200 m as much as possible to limit sensitivity to field errors in magnets, and it is generally advantageous to keep them small in dipoles in order to limit emittance growth from ISR.

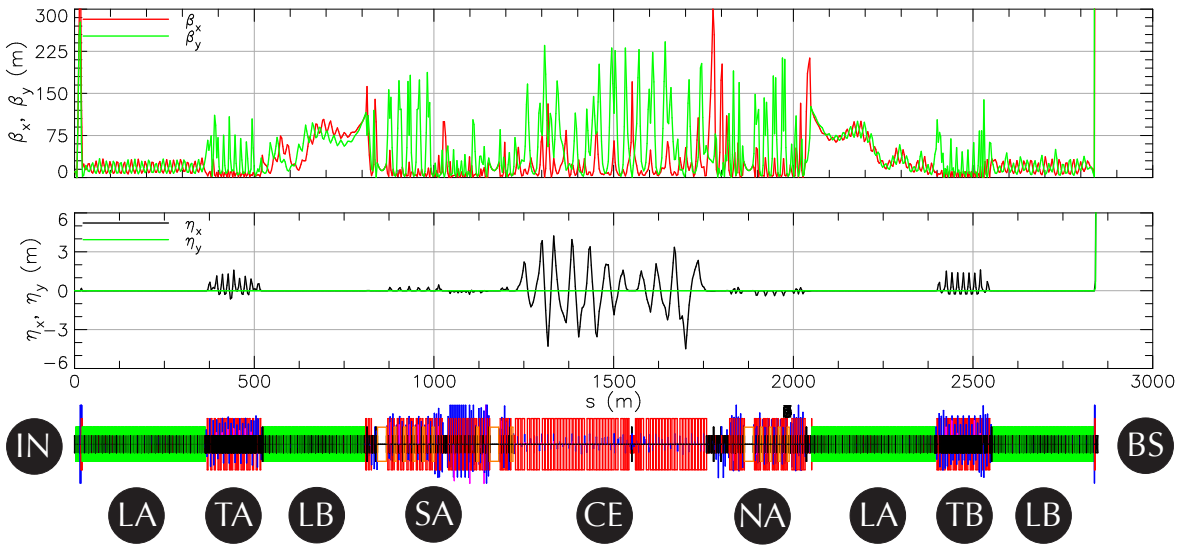

Figure 2.1.3: Linear optics for the full ERL, including the energy recovery pass.

Second-order optics-design criteria

For further refinement of the transverse beam size and of the bunch duration, the nonlinear optics must provide

- Zero second-order dispersion t_{566} in all undulators.
- Second-order achromatic sections, i.e. $t_{166} = 0$ and $t_{266} = 0$ from the beginning to end of each section.
- Flexible second-order time of flight term t_{566} in all sections (typically close to zero).

Similar to the first-order dispersion, the zero second-order dispersion in undulators avoids an apparent increase in beam size. As a rule of thumb, it is often easiest to control second-order dispersion when $t_{166} = 0$ and $t_{266} = 0$ for every subsection.

System optimization

The design and optimization of the ERL lattice is detailed through the following sections. Nearly all of the beam optics, with the notable exception of the injector in §2.1.4, are designed, simulated, and optimized using the Bmad and Tao software tools developed at Cornell [4]. The injector modeling has been performed using state-of-the-art 3D space-charge codes experimentally benchmarked as a part of Cornell ERL Phase 1a project [5].

The general strategy is to design first-order optics, including dispersion and time-of-flight, by optimizing the placement and strengths of dipole and quadrupole magnets section by section. Adjacent sections are spliced together by relaxing and matching Twiss parameters and dispersion functions. Second-order optics are manipulated by strategic placement of sextupole magnets, and further optimizing their fields.

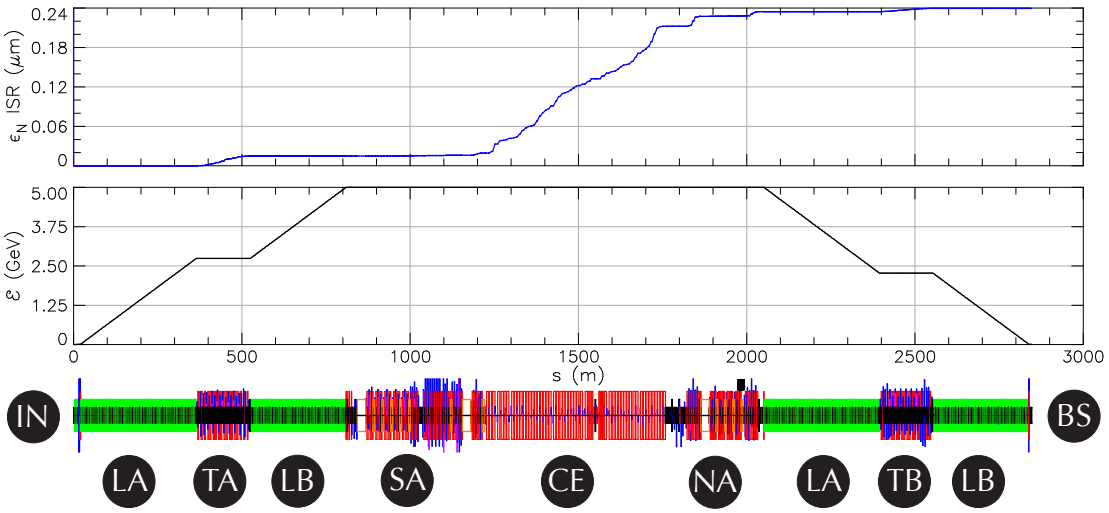

Figure 2.1.4: Emittance growth due to ISR, and the design energy $\mathcal{E}$, through the entire ERL.

The full linear optics for the ERL, including the second pass through the Linacs, are shown in Fig. 2.1.3. Emittance growth due to ISR, as well as the beam energy, are shown in Fig. 2.1.4. The relative energy spread is dominated by the accelerating RF curvature and remains at approximately 2×10^{-4} in the 5 GeV region.

2.1.4 Injector and merger (IN)

Design criteria

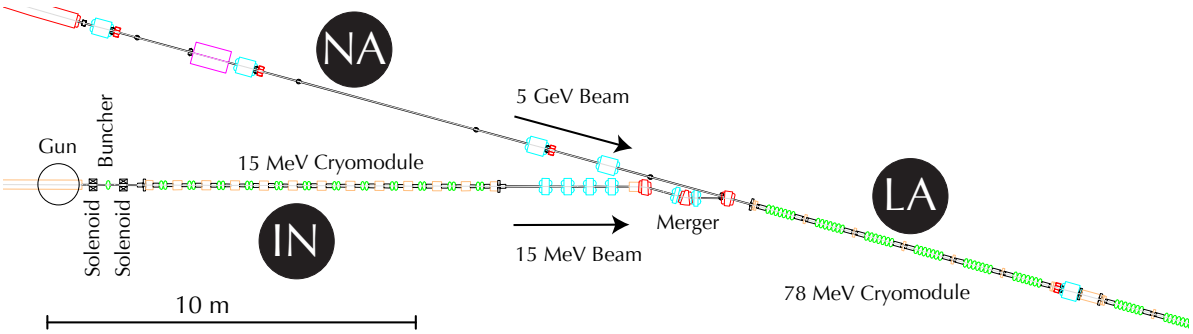

Figure 2.1.5: Layout for the injector section IN. The diagnostic beamline section DB, which mirrors the merger section, is not shown.

The injector section IN, described in technical details in §2.3, is a critical part of the ERL. It must

- Provide beams for all of the operating modes listed in Tab. 1.3.1.
- Have a layout that completely fits in the new building.
- Merge its 15 MeV beam with the returning 5 GeV beam.

The layout for IN is shown in Fig. 2.1.5.

Beam brightness from photoinjectors

In order to achieve high-brightness x rays, an injector of very low emittances is critical. Given the importance of the low-emittance beams, a considerable research and development effort in the accelerator community is presently devoted to the development and demonstration of both high average current (100 mA) and ultra-low emittance beams from the electron sources, photoinjectors in particular. Here we present the current understanding of the limiting factors to beam emittance and supporting simulations showing how the parameters suitable for the ERL x-ray source can be achieved using the photoinjector based on a high-voltage DC gun.

On a fundamental level, the maximum beam brightness and hence the smallest electron beam emittance is determined by the maximum accelerating field at the photocathode during the laser pulse illumination and the mean transverse energy (MTE) of the electrons leaving the surface of the cathode. In particular, for a laser pulse that assumes a pancake shape near the cathode, the minimum normalized rms emittance is given by [6]

$$\epsilon_n = \sqrt{\frac{3q \cdot \mathrm{MTE}}{10\pi\epsilon_0 mc^2 E_{\mathrm{cath}}}}, \text{ or } \epsilon_n(\mu\mathrm{m}) = 0.145\sqrt{\frac{q(\mathrm{pC}) \cdot \mathrm{MTE(eV)}}{E_{\mathrm{cath}}(\mathrm{MV/m})}} \tag{2.1.10}$$

relating the charge per bunch q, cathode field E_{cath}, and mean transverse energy MTE of the photocathode (e.g. , MTE ~ 1 eV for metal and ~ 0.1 eV for semiconductor negative electron affinity photocathodes). Using $E_{\mathrm{cath}} = 5\,\mathrm{MV/m}$ as typical for high-voltage DC guns, and MTE $= 0.12$ eV as measured for GaAs illuminated with 520 nm laser light [7], one finds that 0.2 μm rms normalized emittance should be achievable in principle for 77 pC/bunch operation.

Many practical matters must be addressed before the emittance can approach the limit given by Eq. (2.1.10). A very high degree of emittance space charge compensation needs to be realized [8], something which is achieved though a combination of appropriate electron beam optics and laser pulse shaping; geometric and chromatic aberrations need to be kept in check, particularly in the DC gun vicinity where the beam tends to occupy a large volume; time dependent effects of RF-focusing and RF input coupler kicks in accelerating structures need to be considered and their degrading effect on the beam emittance addressed. Much of the beam physics phenomena under consideration can be properly accounted for in detailed beam dynamics simulations using state-of-the-art space-charge codes. e.g. several 3D space-charge codes have been benchmarked with experimental data in the ERL photoinjector prototype and found to be in excellent agreement with the measurements [5]. We use the same numerical tools for the design of the ERL photoinjector.

To better understand the mechanisms of emittance growth, the problem has been divided into two largely independent parts:

- optimization of the high-voltage DC photoemission gun geometry followed by the straight section accelerating the beam to about 15 MeV.
- study of various merger design options and their evaluation for transport of an ultra-low emittance beam that is matched to the main Linac.

Presented below are 3D space-charge simulations of the baseline injector design as depicted in Fig. 2.1.5, taking the beam through one full cryomodule section of the main Linac to high enough energy (about 100 MeV), where the effects of the space charge on beam emittance become negligible.

Gun and injector optimizations

In this section, the results of multi-objective genetic algorithm optimizations are presented for the purpose of studying the optimal performance in a photoinjector that could be used for the ERL. The general layout of the accelerator under investigation is tested by Cornell's prototype ERL injector shown in Fig. 2.1.6 (up to the merger section). The injector layout for the full ERL is essentially that of the ERL prototype photoinjector, with 12 instead of 5 two-cell cavities: a DC photoemission gun followed by an RF buncher cavity positioned between the two solenoids; the SRF cryomodule hosting 12 2-cell SRF cavities, each capable of delivering up to 1.25 MeV of energy gain to the beam. Since the beam stays axially symmetric throughout the entire beamline (9.5 m), a faster 2D routine is used in this numerical study [9]. Some 24 parameters were varied in the multi-objective optimizer to map out the optimal front of injector performance following the work that introduced this method [10]. The parameters varied represent the strengths of magnetostatic elements and those of the RF cavities, their phases, as well as the shape of the laser pulse. One important innovation

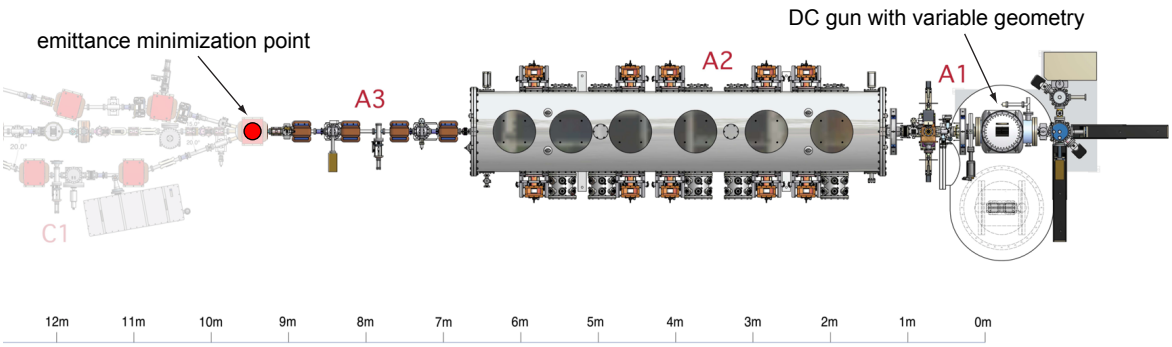

Figure 2.1.6: The layout of the straight section of the injector being optimized. The emittance minimization point is at 9.5m from the photocathode just prior to the entry into the merger. The quadrupoles magnets in A3 section are off. When the merger is included, these quadrupole magnets are used to match the beam through the dipole magnets into the main Linac.

is the introduction of the ability to adjust the DC gun geometry in the genetic algorithm optimizer, e.g. vary the electrode angle that introduces electrostatic focusing at the cathode or change the cathode-anode gap, see Fig. 2.1.7a. A realistic constraint on the maximum voltage vs. the shortest high-voltage gap distance in the gun is imposed following the empirical data obtained from a collection of measurements for large area electrodes as summarized in [11] and depicted in Fig. 2.1.7b. The salient feature of this empirical voltage breakdown condition is that there exists a trade-off between the largest achievable cathode gradient and the maximum gun voltage, both of which would ideally be present for low-emittance generation and preservation. Constraining the gun voltage to be below the empirical breakdown condition allows determination of an optimal and at the same time realistic operating gun point and geometry.

The emittance at the end of the beamline (9.5 m from the cathode) is presented in Fig. 2.1.8, which shows the smallest normalized rms emittance obtained vs. charge per bunch. Here the beamline is straight and the beam dynamics are cylindrically symmetric, so a 2D simulation is sufficient. The typical final energy is 13 MeV, and the final bunch is 3 ps rms (the initial laser pulse duration varies between 20 and 30 ps). Also, Fig. 2.1.8b shows the electric field inside the gun that corresponds to the optimum performance under the voltage breakdown condition (the corresponding gun voltage is about 500 kV). The importance of the photocathode mean transverse energy (MTE) is demonstrated in Fig. 2.1.8a: MTE = 500, 120, and 25 meV cases are plotted for comparison. Here we note that while the values of MTE = 120 meV have been measured for GaAs illuminated with a 520 nm laser [7], and a corresponding prompt response of less than 1 ps [7, 12], more recent advances in the understanding of thermal emittance formation mechanisms from Negative Electron Affinity (NEA) photocathodes have opened up the possibility of achieving sub-thermal MTE values together with a prompt photoemission response (as required for effective laser shaping) [13].

In summary, a realistic high-voltage DC gun in combination with a low thermal emittance photocathode is an excellent choice for delivering an ultralow emittance beam as required for

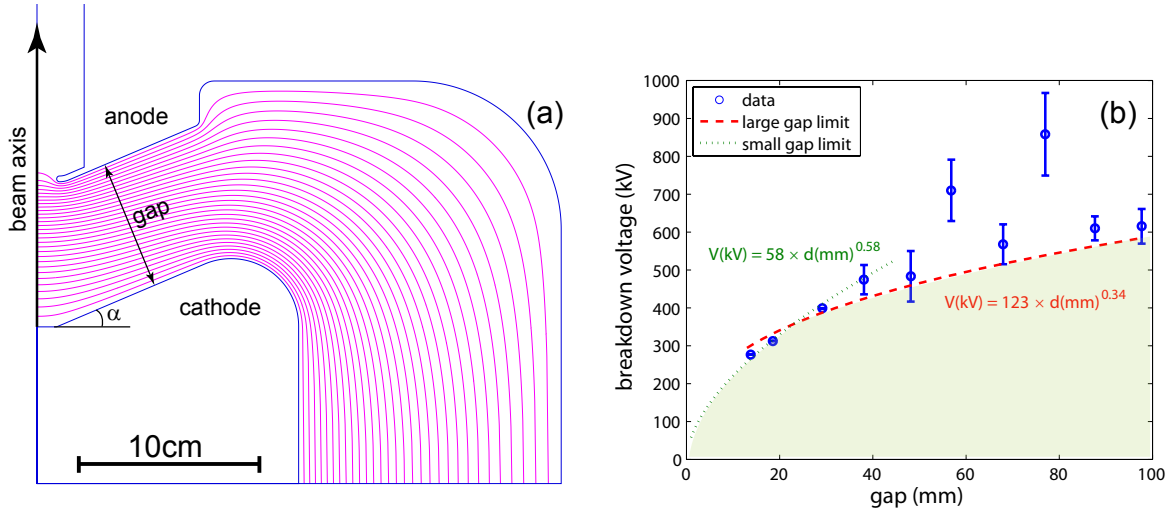

Figure 2.1.7: (a) Parameterized DC gun geometry with variable angle and gap. (b) Empirical voltage breakdown condition (adopted after [11]) used to constrain the gun voltage (the filled area under the curves designates the allowed values).

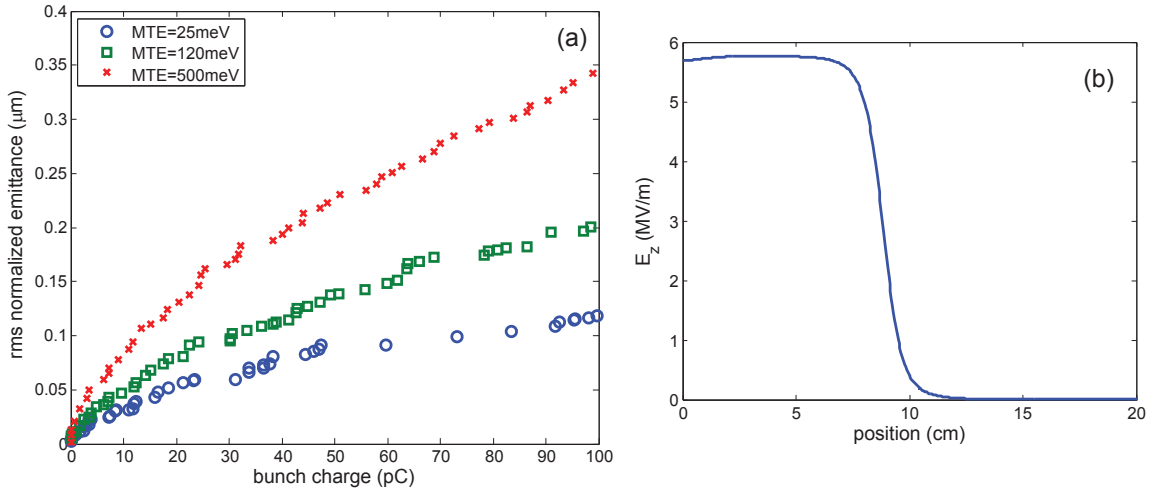

Figure 2.1.8: (a) Optimized 2D simulation results for beam emittance at the end of the straight section (9.5m from the photocathode) of the injector vs. the charge per bunch. The final beam energy is about 12 MeV and the rms bunch length is 3 ps. (b) Electric field inside the gun corresponding to these results. The gun voltage is 508 kV.

the ERL x-ray source. A new DC gun adopting the optimized geometry as well as a variable cathode-anode gap design to allow experimental exploration of the trade-off between gun voltage and electric field at the photocathode is now being constructed at Cornell University. We also remark that the emittance scaling with the bunch charge obtained in the simulations follows closely that of Eq. (2.1.10), deviating slightly mainly due to using of a longer laser

pulse at the photocathode. Fitting the results of Fig. 2.1.8a gives an emittance scaling with charge as $\propto q^{\alpha}$ where α is $0.5 - 0.6$.

Merger studies

This section presents a comparison of different merger designs along with the evaluation of their performance. The importance of the merger section is due to the fact that the beam is not yet ultrarelativistic at this section, and therefore the space-charge forces inside this chromatic section can lead to emittance growth and thereby degrade the performance of the facility. Two merger cases have been considered: a 3-bend achromat similar to the one used in the Cornell ERL photoinjector prototype, and a 'zig-zag' merger [14]. Each merger employs 15° bends (with two 30° inside bends as required for the zig-zag design), see Fig. 2.1.9. For the purpose of direct comparison, the two merger types are made of equal length (2.55 m). A drift of the same length is included in the comparison to provide a baseline of the smallest emittance. The overall beamline consists of the merger followed by 5 SRF cavities of the main Linac taking the beam energy to about 80 MeV.

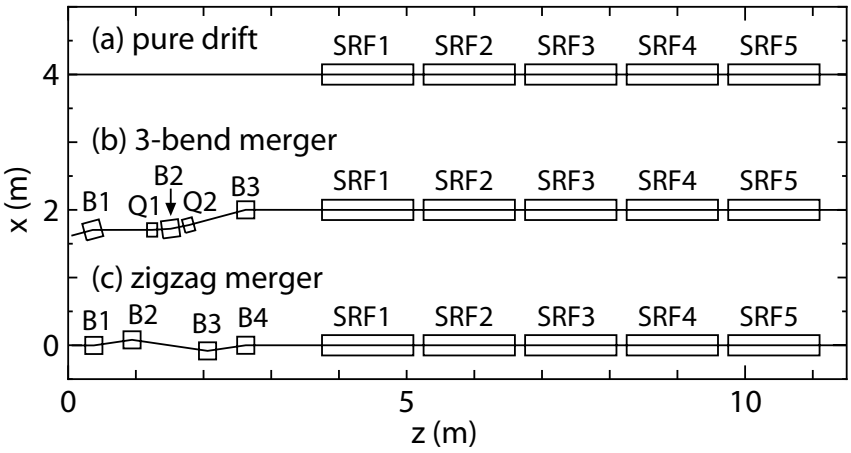

Figure 2.1.9: Merger types compared in simulations. Baseline case (a) with a simple drirft, (b) 3-bend merger, and (c) zig-zag merger. The length of each merger is 2.55 m, followed by 5 SRF accelerating cavities.

The initial electron bunch is taken to be of a uniform cylindrical shape, with a given bunch length duration σ_t, energy spread $\sigma_\delta = 10^{-3}$, variable spot size, and divergence in both planes. The initial transverse emittance is set to zero (i.e. all divergence is correlated) to emphasize emittance growth caused by the merger proper.

Fig. 2.1.10a shows the effect of the space charge (80 pC/bunch) induced emittance growth for the case of the two mergers and the drift of identical length. The General Particle Tracer (GPT) code with improvements to the 3D space-charge routine [15] have been used for these simulations. Furthermore, the 3-bend merger case includes two options: quadrupole magnets set to the achromat condition that corresponds to the no-space-charge case, and adjustable quadrupoles that are used to minimize the emittance due to the space-charge induced beam

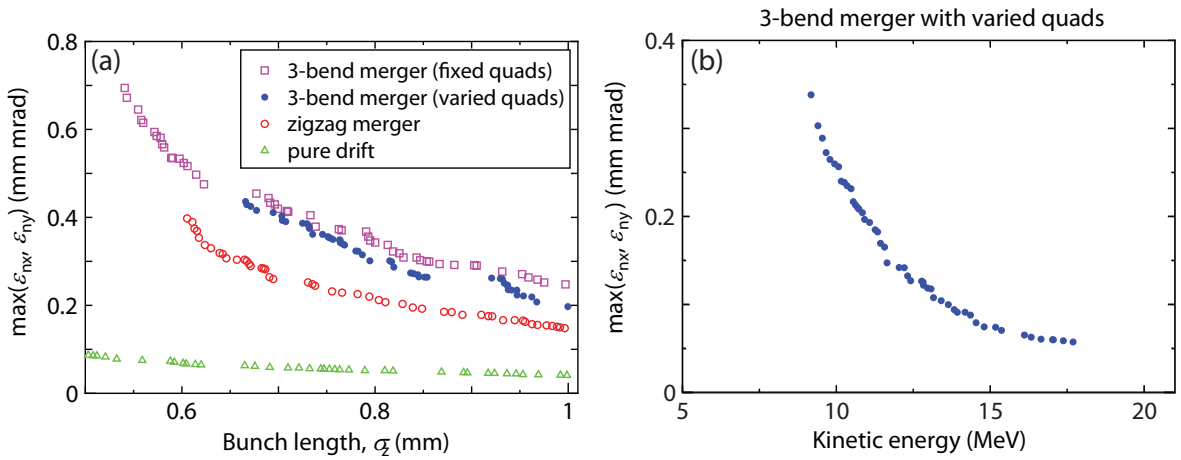

Figure 2.1.10: Merger performance in a 3D simulation with 80 pC bunch charge for (a) varied bunch length and fixed 10 MeV kinetic energy; (b) varied kinetic energy and fixed 0.9 mm rms bunch length.

envelope dispersion [16]. As anticipated, the zig-zag merger shows better emittance preservation characteristics. However, the 3-bend achromat is simplest to implement to merge very high-energy (5 GeV) beam with the injector low energy beamline, and as a result is more appealing from a practical point of view.

Whereas Fig. 2.1.10a shows the emittance growth for a fixed beam (kinetic) energy of 10 MeV going into the merger, Fig. 2.1.10b shows the 3-bend merger performance for different initial kinetic energy while the bunch length stays fixed (0.9 mm rms). It is seen that the emittance growth from the merger is less than 0.1 μm at 3 ps rms for 15 MeV beam and about twice that much for a 2 ps rms 80 pC bunch. This fact, along with the anticipated energy loss and induced energy spread in the 5 GeV ERL transport beamline, determined the choice of 15 MeV injector energy.

Another potential emittance-degrading mechanism in the merger is CSR. A new routine has been implemented in GPT to allow simulations of this effect [15] along with the 3D space charge. It was found, however, that the combination of charge per bunch, bunch duration, and beam energy in the ERL merger results in negligible CSR-induced emittance growth [17].

Simulated performance of the baseline design

To deliver 15 MeV energy to the beam, twelve 2-cell SRF cavities were chosen, each delivering (with some overhead) up to 150 kW to the beam. The baseline design includes a 4-quadrupole-telescope section following the injector cryomodule for matching the beam into the merger and the main Linac. Six 7-cell SRF cavities of the main Linac are included in the simulations (done with GPT) to account for the entire region of relevance for beam-emittance growth due to space-charge forces. See Fig. 2.1.5 for the baseline photoinjector layout.

The results of the transverse beam emittance at around 100 MeV beam energy are shown in Fig. 2.1.11 for 77 pC (100 mA average current) and 19 pC (25 mA average current). Gaps in the plots are due to the stochastic nature of the optimizer and limited number of generations.

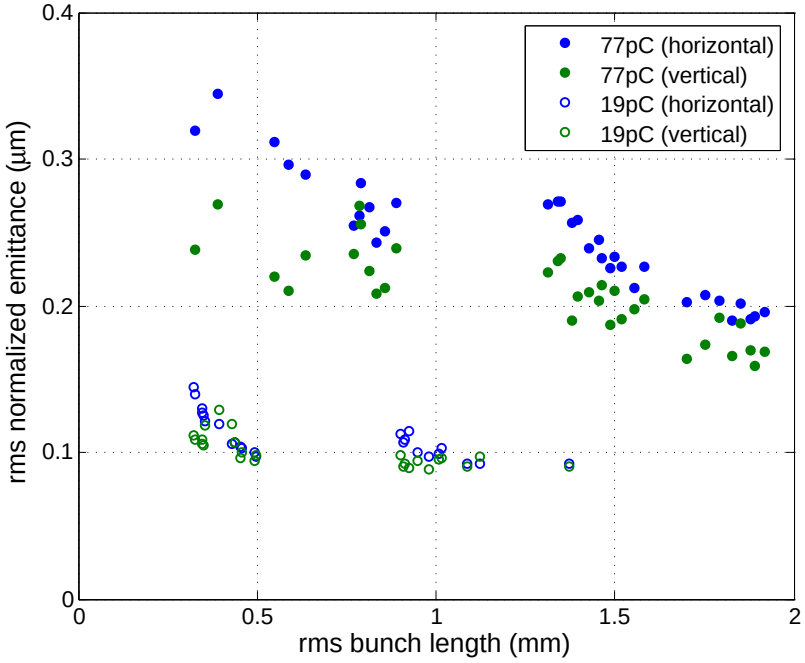

Figure 2.1.11: ERL baseline injector performance: rms normalized emittance at the end of the first cryomodule in the main Linac LA vs. the bunch length for two different bunch charges.

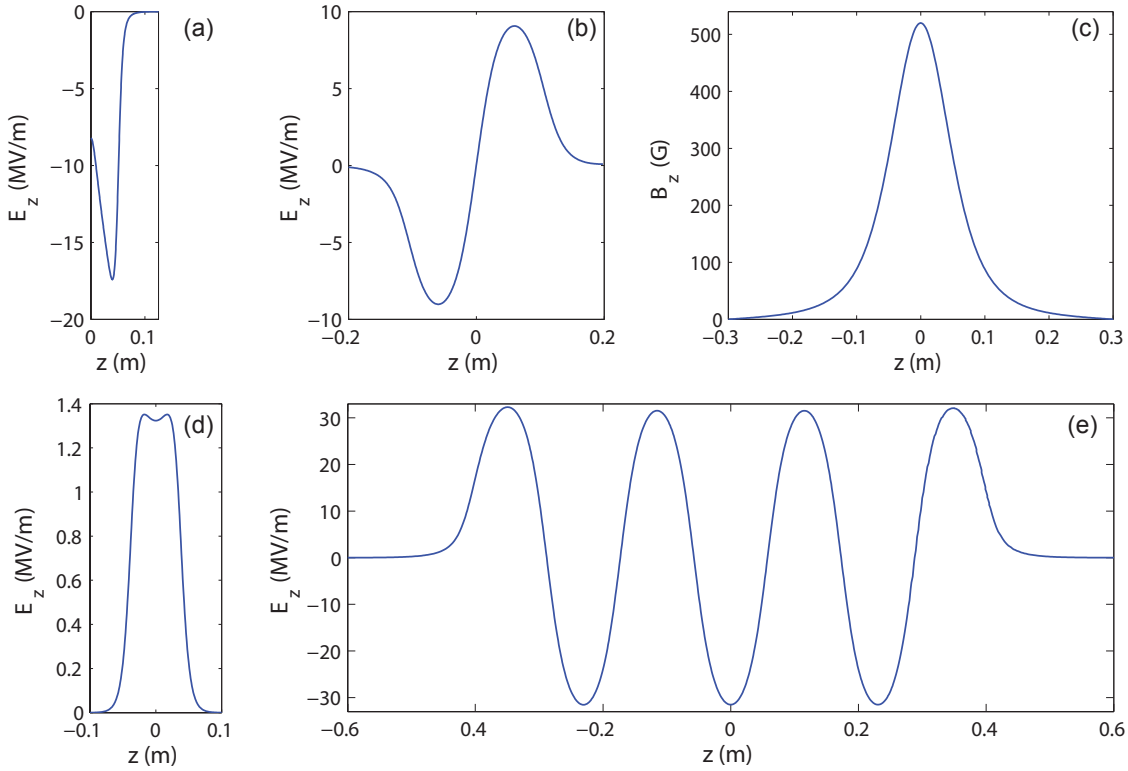

Figure 2.1.12: Typical on-axis fields from the field maps used to model the injector and first LA cryomodule: (a) high-voltage DC gun, (b) 2-cell SRF cavity, (c) solenoid, (d) RF bunching cavity, (e) 7-cell SRF cavity. The longitudinal scale is the same for all the field maps.

The simulations were done with 200,000 macroparticles using 3D field-maps for all elements in the injector section (IN). These injector simulations used a photocathode MTE of 25 meV [13].

Fig. 2.1.12 shows the field maps used in the simulation of the injector. The gun geometry used in these simulations corresponds to the presently operating Cornell gun, and the gun voltage is set at 750 kV. The more recent results presented in a previous §2.1.4 have not yet been included in the optimization of the baseline design, although the cathode field, which is the primary reason for the smallest possible laser spot size (and beam emittance), is comparable in the two cases. (The stronger electrode focusing in the present Cornell gun design leads to about a factor of 2 smaller field at the photocathode than the maximum on-axis electric field in the cathode-anode gap). The newly optimized gun geometry in Fig. 2.1.8b has a field on the cathode for 500 kV that is similar to the field in today's gun for 750 kV. The new gun should therefore perform similar to simulations of today's gun at 750 kV.

Fig. 2.1.14 demonstrates the beam envelopes that corresponds to the 77 pC/bunch case with 2.1 ps rms final bunch duration. The transverse phase space at about 90 MeV is shown in Fig. 2.1.13. Overall, we observe that the final minimum emittance is consistent with the

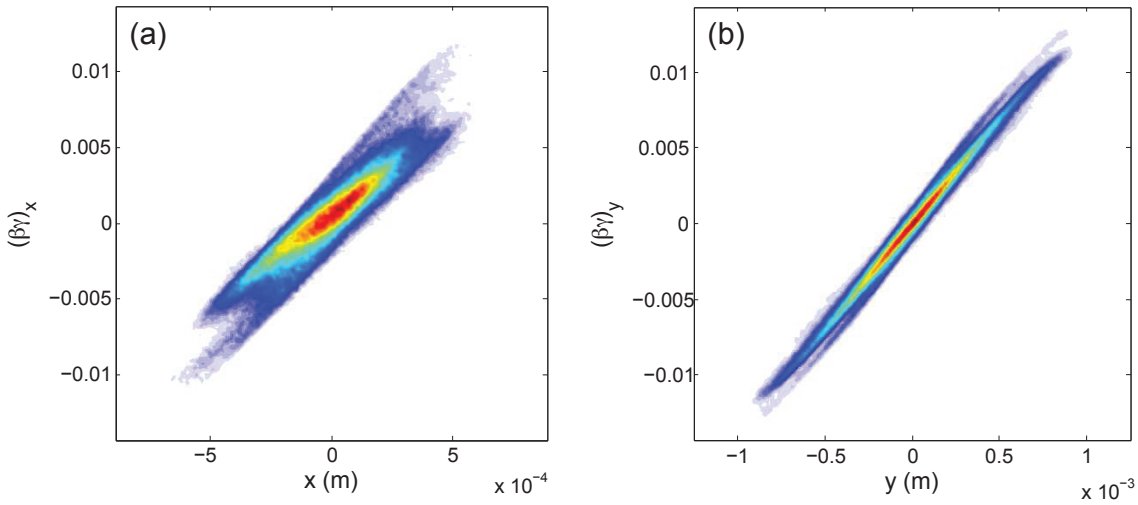

Figure 2.1.13: Computed (a) horizontal and (b) vertical phase space of the beam. Beam emittances are as following: 100% beam $\epsilon_{nx,y}(100\%) = 0.28, 24$ μm, 90% beam $\epsilon_{nx,y}(90\%) = 0.19, 0.16$ μm, beam core fraction $\xi_{x,y} \approx 70\%$ and core emittance $\epsilon_{nx,y,\text{core}} = 0.12, 0.09$ μm [6].

contributions described in the previous two subsections.

The baseline design of the photoinjector continues to evolve towards obtaining lower beam emittances. Several obvious extensions to the present work are:

- use a higher energy out of the photoinjector to minimize the emittance growth in the merger section. This is particularly relevant for 25 mA operation since the cavity gradients and the RF power in the injector cryomodule are moderate in this case.
- explore an option of using a slightly longer bunch with lower transverse emittance out of the injector and perform energy spread compression [18] in the split Linac and the 2.7 GeV turn-around arc.
- develop a new merger of practical layout configuration and superior emittance preservation characteristics to the present 3-bend merger.

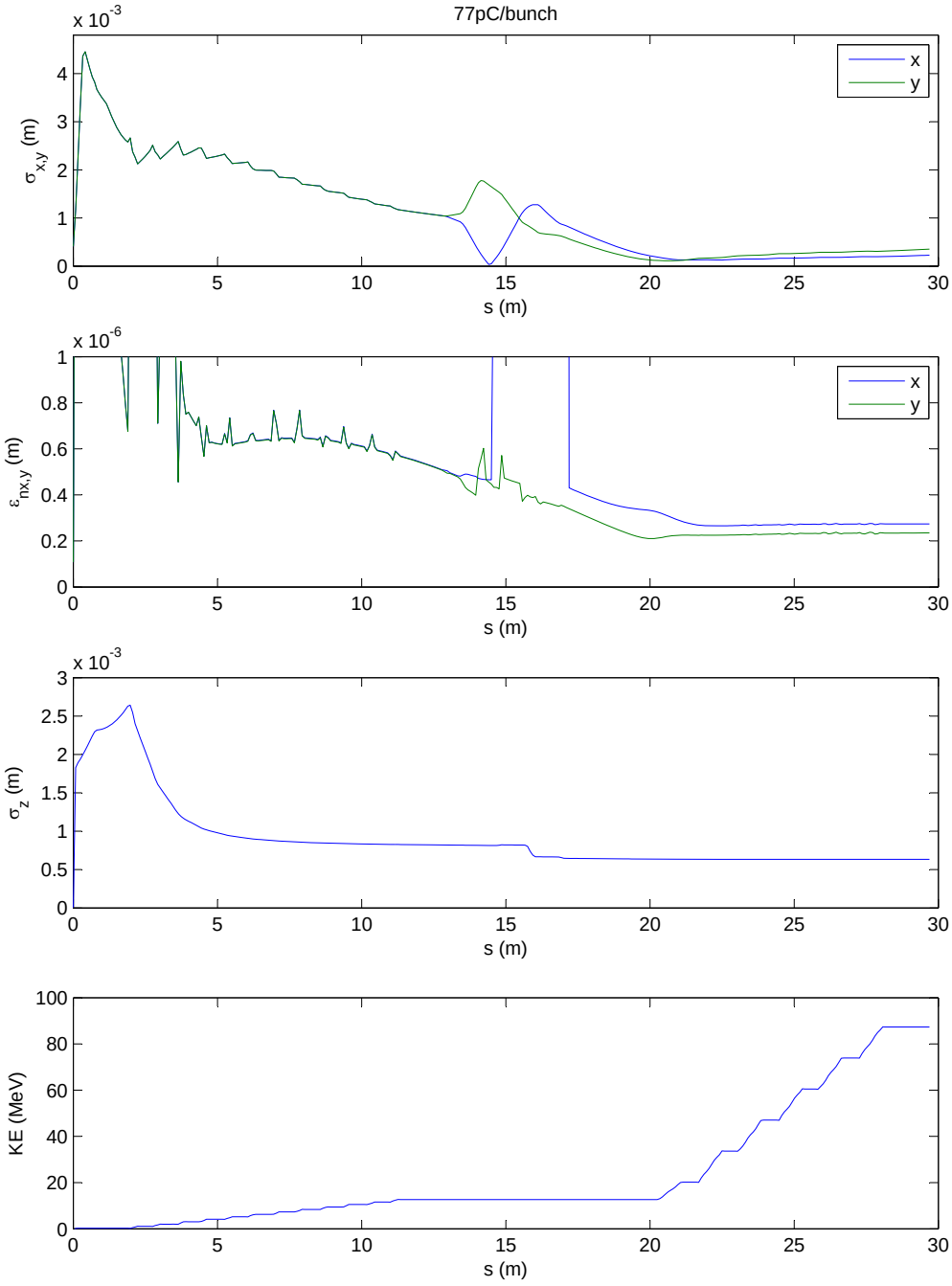

Figure 2.1.14: Rms beam sizes, emittances, bunch length, and kinetic energy in the injector section (IN) through the first cryomodule of the main Linac (LA). The final rms bunch duration $\sigma_t = 2.1\,\text{ps}$, transverse rms normalized emittances $\epsilon_{nx,y} = 0.28, 0.24\ \mu\text{m}$, and longitudinal rms emittance $\epsilon_{nz} = 31$ keV-ps.

2.1.5 Main Linac (LA & LB)

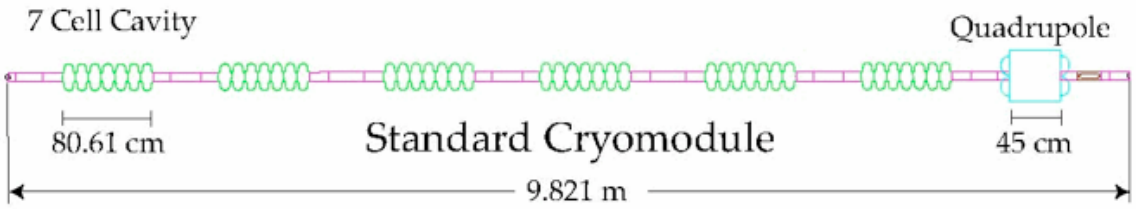

Figure 2.1.15: Layout of the ERL cryomodule with 6 SRF cavities, each having 7 cells, and a superconducting quadruple and corrector package.

The ERL Linacs consist of 64 identical cryomodule cells divided among LA and LB, with the layout for the standard ERL cryomodule shown in Fig. 2.1.15 Each cryomodule contains six superconducting accelerating cavities and a superconducting-magnet package with a quadrupole and two steering coils, along with other elements, e.g. higher-order mode absorbers, gate valves, and beam position monitors, which can be considered to be drifts for purposes of the beam optics. Using the dimensions in the standard ERL cryomodule, in order to bring a 15 MeV beam to 5 GeV, each cavity must provide an average energy gradient of 16.1 MeV/m and therefore a single cryomodule can give or take 78 MeV to or from a beam.

Because the ERL has two turnaround loops TA and TB operating at different energies, one Linac needs to be longer than the other. In general, for N_{A} and N_{B} standard cryomodules in LA and LB, respectively, the changes in energy of the beam in these Linacs are

$$\Delta\mathcal{E}_{\mathrm{LA}} = \frac{N_{\mathrm{A}}}{N_{\mathrm{A}} + N_{\mathrm{B}}} \left(\mathcal{E}_{\mathrm{max}} - \mathcal{E}_{\mathrm{min}}\right) \tag{2.1.11}$$

$$\Delta\mathcal{E}_{\mathrm{LB}} = \mathcal{E}_{\mathrm{max}} - \mathcal{E}_{\mathrm{min}} - \Delta\mathcal{E}_{\mathrm{LA}} \tag{2.1.12}$$

where $\mathcal{E}_{\mathrm{min}}$ is the injection energy and $\mathcal{E}_{\mathrm{max}}$ is the full operating energy. For $N_{\mathrm{A}} = 35$ and $N_{\mathrm{B}} = 29$, with energies $\mathcal{E}_{\mathrm{min}} = 15\,\mathrm{MeV}$ and $\mathcal{E}_{\mathrm{max}} = 5\,\mathrm{GeV}$, we get $\Delta\mathcal{E}_{\mathrm{LA}} = 2726.17\,\mathrm{MeV}$ and $\Delta\mathcal{E}_{\mathrm{LB}} = 2258.83\,\mathrm{MeV}$. The beam in TA therefore has an energy of 2741.17 MeV and the beam in TB has an energy of 2268.82 MeV (accounting for a 5 MeV loss in the return arc due to ISR). These will often be abbreviated as 2.7 GeV and 2.3 GeV, respectively.

The beam optics in the Linacs must

- Have zero dispersion.
- Keep beta functions as small as possible for both accelerating and decelerating beams.
- Accept Twiss parameters from the IN for LA.
- Provide the correct Twiss parameters for the BS from LB.

The adjacent sections provide zero dispersion to LA and LB, and because there are no bends (other than corrector coils) within the Linacs there is no creation of dispersion. The beta functions are manipulated by the 35 and 29 quadrupole magnets in LA and LB, respectively.

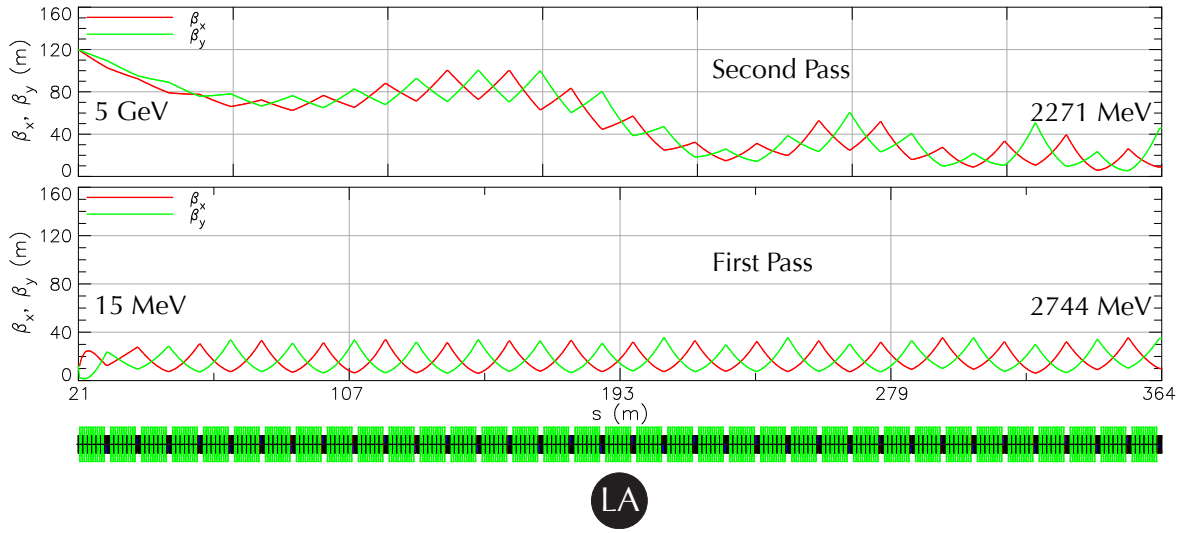

Figure 2.1.16: Beta functions for the first pass (accelerating) beam and energy recovery (decelerating) beam in LA. The optimization criteria are to keep the beta functions as small as possible and to match the low energy beam at $s = 0$ to the Twiss parameters from the IN. It has been found to be efficient to optimize by propagating the beta functions 'backwards' from the end of LA by varying β_x and β_y there along with the 35 quadrupole fields.

System optimization

Some optics guidelines for ERL Linacs are discussed in [19] and [20]. The main difficulty in optimization of the beta functions in the Linacs is due to the presence of two beams of different energies. The quadrupole strengths k seen by the two beams are inversely proportional to their reference momenta P, as in

$$k_a = \frac{P_a}{P_d} k_d, \tag{2.1.13}$$

in which the subscripts a and d denote the decelerating and accelerating beams, respectively. For example, in the first quadrupole magnet in the first cryomodule of LA, where the accelerating beam is at $(15 + 78)$ MeV and the decelerating beam is at $(4995 - 78)$ MeV, we have the quadrupole strengths $k_d \approx k_a/53$. Cryomodules are arranged in the opposite orientation in LB, so the quadrupole strength immediately prior to the BS section has the same ratio. Both beams have nearly equal energies around the 32$^{\text{nd}}$ quadrupole of LA. Because quadrupole gradients at the beginning of LA and end of LB must be weak enough so as to not over-focus the low energy beam, it becomes difficult for them to focus the high-energy beam.

The results of optimizing the beta functions for the first pass (accelerating) beam and energy recovery (decelerating) beam in LA are shown in Fig. 2.1.16 There it is seen that as the beams approach similar energies, the beta functions become more similar. Likewise, where the beam energies are the most different, so are the beta functions. There is no known rule for finding good solutions in this situation, though in practice it has been found that alternating positive and negative quadrupole strengths similar to a FODO lattice gives a good starting point.

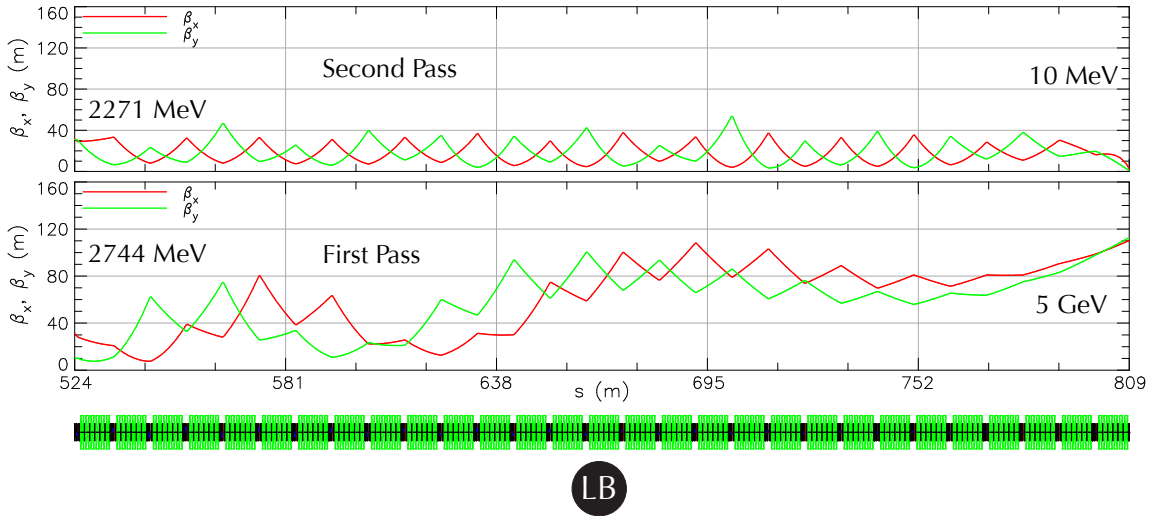

Figure 2.1.17: Beta functions for the first pass (accelerating) beam and energy recovery (decelerating) beam in LB. Optimization is similar to that in LA described in Fig. 2.1.16.

In this solution, we see that the beginning of LA for the first pass beam has very regularly focusing and defocusing beta functions, while the beta functions for the high-energy beam behave similarly to those in a long drift. The optics for LB are shown in Fig. 2.1.17. It is optimized in the same way as LA.

The relative effectiveness of quadrupole magnets on the different beams happens to be a virtue for matching from the IN and to the BS, because quadrupole fields near those sections can be tuned for the low energy beam with little effect on the high-energy beam. Therefore matching from the IN and to the BS is relatively simple compared to the overall optimization. In particular, the Twiss parameters for the first pass beam are matched near the end of the first cyromodule, because space-charge calculations in the IN include the first few cavities in

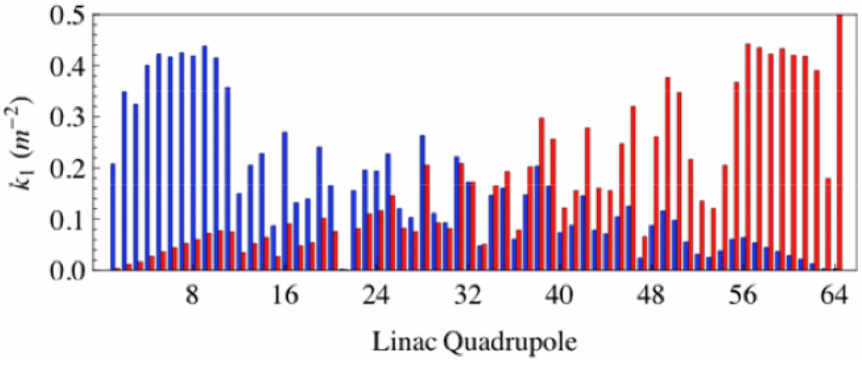

Figure 2.1.18: Quadrupole k_1 strengths seen by the accelerating beam (blue bars) and decelerating beam (red bars) in the Linacs.

LA and fix those values. The resulting quadrupole strengths seen by each beam are shown in Fig. 2.1.18.

2.1.6 Turn-Around loops (TA & TB)

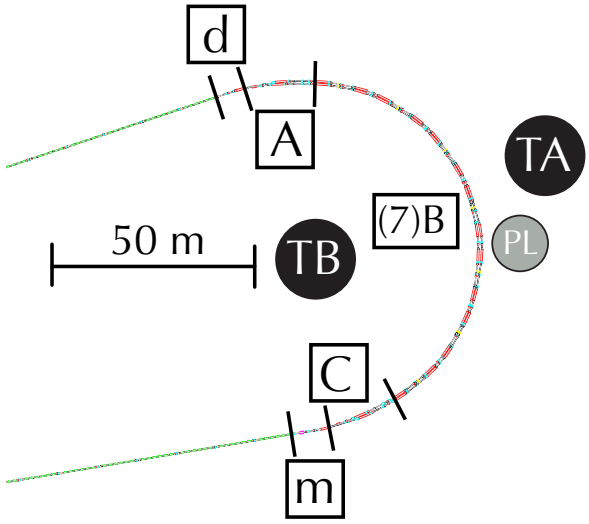

Figure 2.1.19: Layout for TA and TB with cell divisions. PL indicates the path length adjuster section. The demerger and merger section are indicated as d and m, respectively.

Design criteria

Two turnaround arcs provide an additional level of flexibility in the optics relative to single turnarounds in previous designs. In particular, having two turnarounds allows for the compensation of wakefields by tuning time of flight terms, a scheme that reduces the energy spread by up to 80% as described in [21]. This is important because the correlated relative energy spread from wakes at high energy becomes 500 times larger after deceleration and can potentially lead to particle loss before the beam stop.

First pass particles exit LA at 2.7 GeV, and follow TA. The second pass particles exit LA at 2.3 GeV, and follow TB. These sections must

- Demerge first and second pass beams from LA into TA and TB, respectively.
- Have variable r_{56}, close to 0, for both TA and TB.
- Have variable t_{566}, close to 0, for both TA and TB.
- Have the lowest possible radiative emittance growth for TA. Emittance growth is less critical for TB.
- Incorporate a path length adjustment section in TA.
- Keep beta functions as small as possible everywhere.
- Merge TA and TB beams for transport into LB.

Because the accelerating (first pass) and decelerating (second pass) beams enter the turnaround region at different energies, they can be separated by a dipole magnet. The radiative emittance growth must be limited so as not to spoil the excellent emittance bunches prior to acceleration by LB. In order to have the first and second pass bunches arrive in synchrony with LB, the path lengths of TA and TB must differ by an integer number of wavelengths λ_{rf}. Like many sections, the beta functions are kept as small as possible to minimize the effects of alignment errors. Finally, the beams must be rejoined for entry into LB.

System optimization

To achieve these criteria, both TA and TB are divided into five types:

Demerger Separates the first and second pass beams exiting LA. Contains two quadrupole magnets seen by both beams, and a demerging dipole magnet

Cell A Matches Twiss parameters from the demerger section into the appropriate cell B section

Cell B Roughly periodic section containing two dipole magnets and four quadrupole magnets – occurs seven times

Cell C Matches Twiss parameters from the last cell B into the merging section

Merger Joins the beams in TA and TB to enter LB. Similar to the demerger section in reverse

These sections are shown in Fig. 2.1.19. In the demerging section, the demerging dipole has a 0.6 T magnetic field and is 2 m long. This separates the beams by 26 mm at the magnet's exit end with a relative angle of 27 mrad. Some detail of this section is shown in Fig. 2.1.20. A septum bend aids in the separation of the TB beam.

The bulk of TA (and similarly TB) is built out of cell B sections. For an initial optics solution, a single cell B is highly optimized to provide small periodic beta functions, small radiation integral, and zero r_{56} by varying the four quadrupole strengths. The demerging section, of cell A type for both turnarounds, and the first sections of cell B type for both turnarounds are optimized simultaneously to match into these periodic optics. The cell C and merger sections are similarly optimized.

The resulting linear optics of TA and TB are shown in Fig. 2.1.21 and Fig. 2.1.22. Here the TB optics are very periodic, but the TA optics are slightly irregular. This is because the path length adjustment section, detailed in Fig. 2.1.23, is extended by approximately 10 cm from its normal position, which breaks the symmetry in the optics.

The radiative emittance growth and time of flight terms for TA are shown in Fig. 2.1.24. Here it is seen that the first and second-order dispersion have been manipulated to make both arcs isochronous and achromatic to second-order with the aid of seven sextupole magnets in each arc. This emittance growth for TA accounts for roughly 13% of the mode B emittance in Tab. 1.3.1. The plot for TB is similar, and not shown.

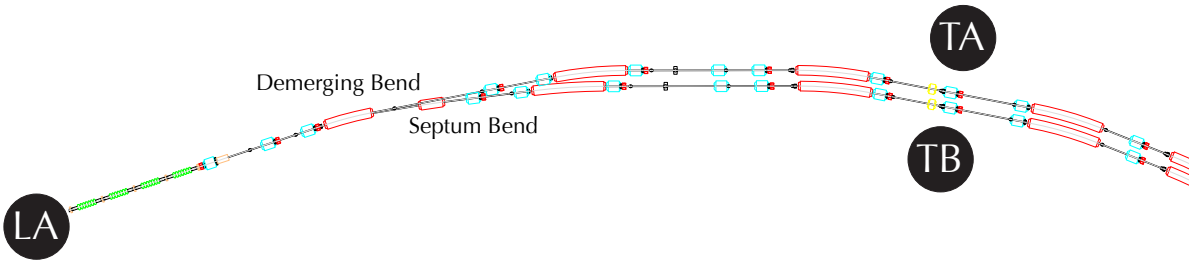

Figure 2.1.20: Demerger section for TA and TB. The merger section downstream is similar.

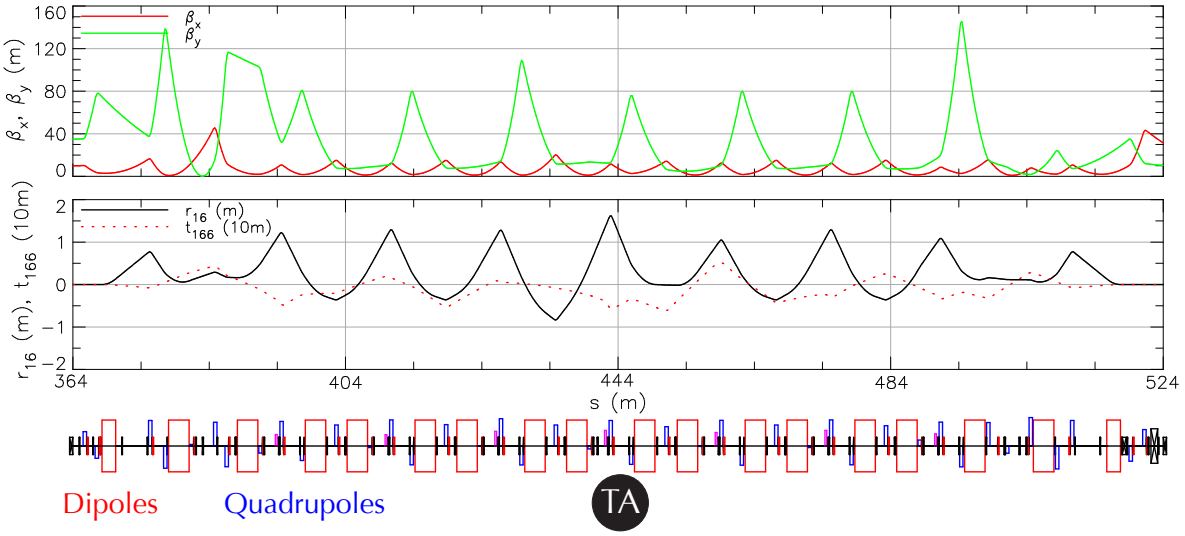

Figure 2.1.21: Linear optics for TA, with second-order dispersion.

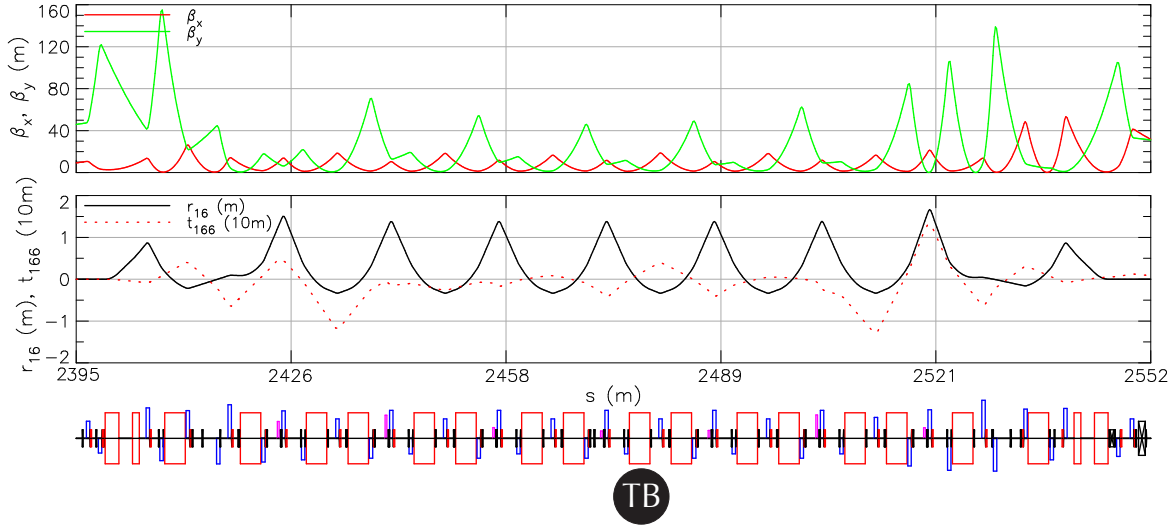

Figure 2.1.22: Linear optics for TB, with second-order dispersion.

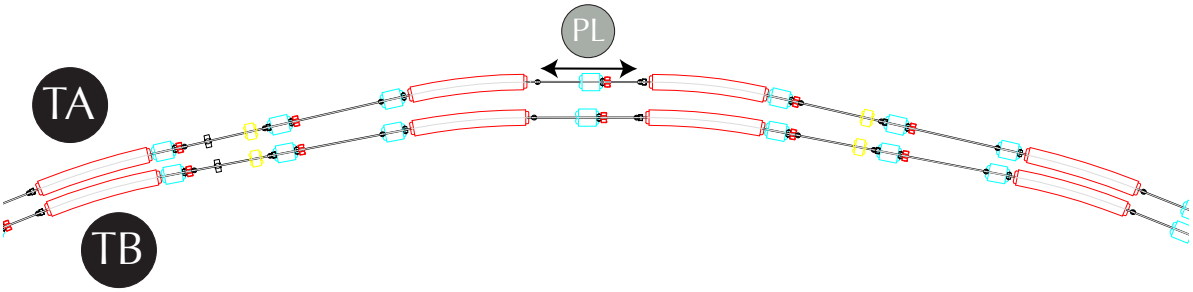

Figure 2.1.23: Path Length adjuster subsection of TA. These four dipoles have variable strength to be able to extend or contract the arrowed section by 10 cm.

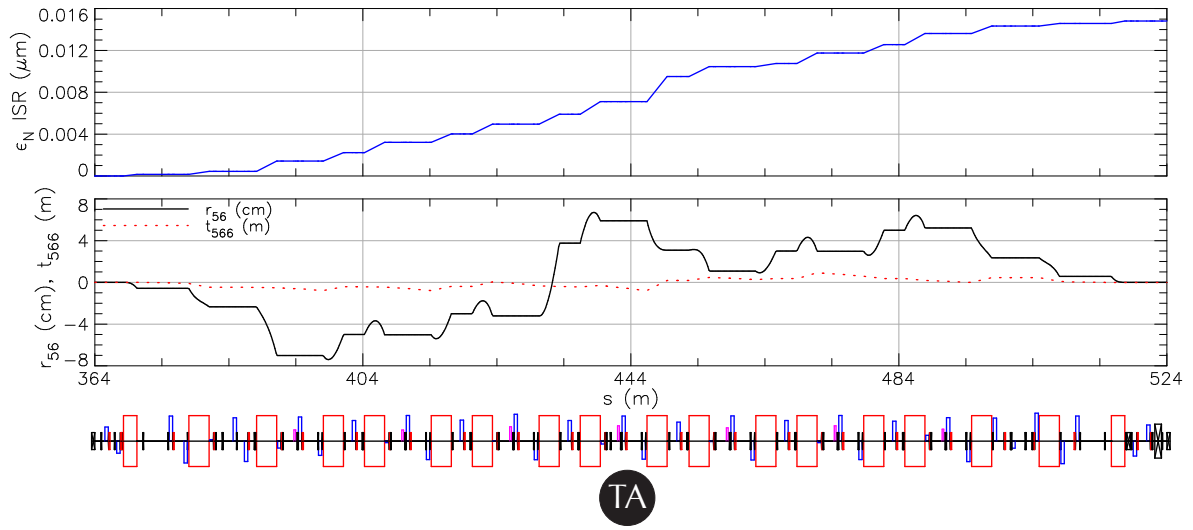

Figure 2.1.24: Normalized emittance growth due to incoherent synchrotron radiation, and time of flight terms r_{56} and t_{566} for TA.

2.1.7 South Arc (SA)

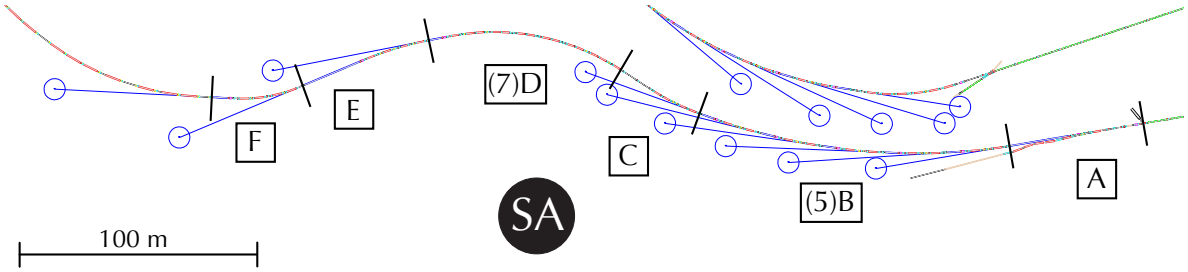

Figure 2.1.25: Layout showing the SA section. The different cell sections are labeled in boxes. For example, (5)B indicates five instances of cell B sections in a row.

Design criteria

The SA contains the first undulators in the ERL that receive the 5 GeV beam. This section must

- Receive the 5 GeV beam from the exit of LB.
- Contain six undulators in the new building, including one that is 25 m long.
- Provide two new undulators in Wilson Laboratory, as well as the G-line undulator.
- Allow for the extraction of the beam to the EX section.
- Collimate the beam halo prior to the first undulator.
- Minimize emittance growth throughout.
- Provide customized beam sizes with zero dispersion in all undulators.
- Control first and second-order time of flight terms r_{56} and t_{566}.

This section lies partially in a new building, and partially in the existing Wilson Laboratory. The new building will also house an extracted beamline EX for accelerator physics studies, and the SA section must provide space for such extraction. Because there are undulators throughout the entire section, emittance growth must be controlled everywhere. Additionally, in order to limit the amount of time of flight term r_{56} contributed by CE and NA in order to make the return arc (SA, CE, NA) isochronous, the r_{56} term for the SA must also be kept as small as possible. Finally, the t_{566} term must be controlled for the bunch compression mode.

System optimization

The SA section, shown in Fig. 2.1.25, is approximately 410 m long and contains the majority of undulators in the ERL. It is the first section after the beam has been accelerated to 5 GeV by LB, and therefore receives bunches with the lowest possible emittance. It is divided into six section types:

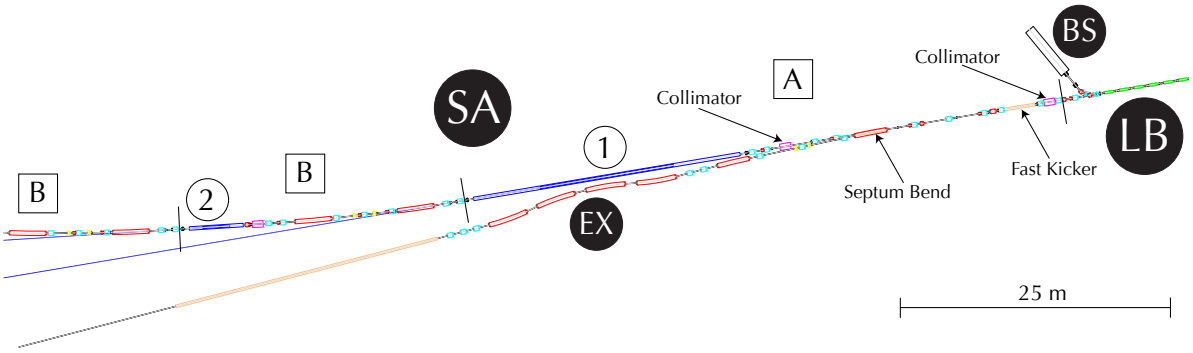

Figure 2.1.26: The layout for the beginning of the SA section, showing cell A with the long undulator and the first cell B sections. Undulator numbers 1 and 2 are indicated in circles. The beam moves from the right at LB to the left. The EX section is described in §2.1.12.

Cell A Matches Twiss parameters from LB into the first 25 m long undulator.

Cell B Periodic section containing a 5 m undulator and a two-bend achromatic section – occurs five times.

Cell C Matches Twiss parameters from the last cell B into the first cell D.

Cell D Periodic section consisting of a two-bend achromat for beam transport, with the last cell containing a 5 m long undulator – occurs seven times.

Cell E Matches Twiss parameters from the last cell D into a 25 m long undulator.

Cell F Matches Twiss parameters from cell E into the G-line undulator just prior to the CE section.

The layout for the beginning of the SA is shown in Fig. 2.1.26 with cell A and the first two cell B sections. There are three bends following the BS demerger magnet that compensate for dispersion and provide a net angle of approximately 1 mrad to protect users of the first undulator from bremsstrahlung originating in LA. A fast kicker, which can create an additional 1 mrad horizontal deflection, can be used in conjunction with a septum bend downstream to extract high-charge bunches for the EX section, which is described in §2.1.12. Two collimators also serve to eliminate the beam halo. The beam halo from Touschek scattering has been simulated in detail in §2.1.17 and has been used to dimension the collimators in §2.1.17. Other halo sources still have to be added to the simulation. The first 25 m undulator follows, and is followed by the first cell B.

The linear optics for cell A are shown in Fig. 2.1.27. Eleven quadrupole magnets manipulate the beam from the end of LA to match $\alpha_x = \alpha_y = 0$ and $\beta_x = \beta_y = 12.5\,\mathrm{m}$ at the center of the 25 m undulator. To use definite values in the optics design, we adjust the beta functions in each undulator to half its length. However, the optics design is very flexible and other beta functions can be employed. Additionally, they provide high β_x in the collimators, which

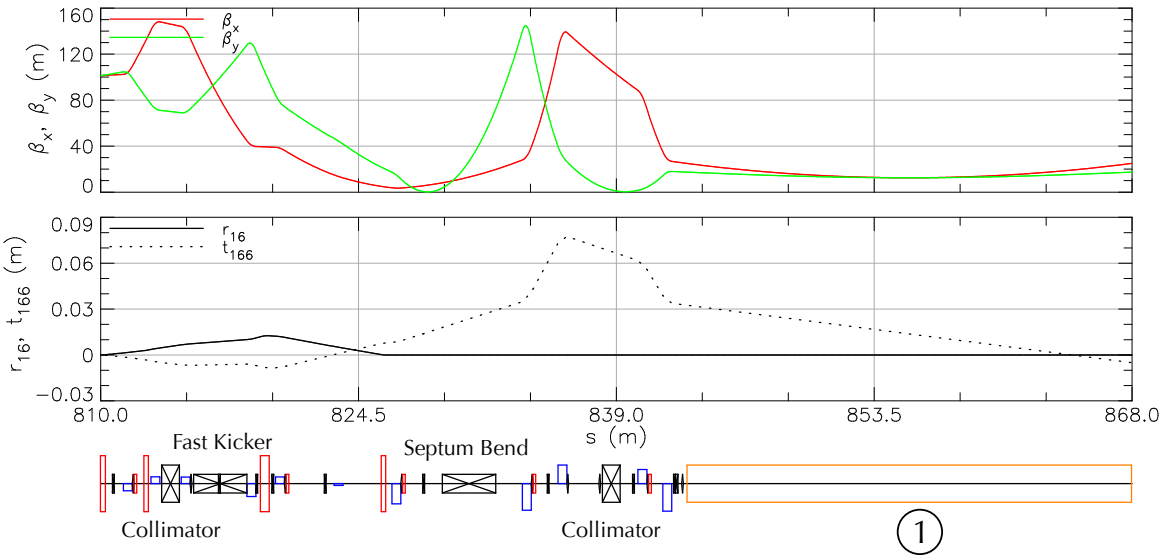

Figure 2.1.27: The optics for cell A in the SA section.

are separated by a 90° horizontal phase advance. The second-order dispersion created here is brought to zero at the end of the following cell B.

The linear optics for the first cell B are shown in Fig. 2.1.28. The cell consists of a two-bend achromat followed by a 5 m undulator. The optics within the undulator are flexible, with this example having $\alpha_x = \alpha_y = 0$ and $\beta_x = \beta_y = 2.5\,\mathrm{m}$ at the center of the undulator. The dispersion and its slope are brought to zero prior to the undulator. Two sextupole magnets placed symmetrically about the center of the achromat provide $t_{166} = 0$ and $t_{266} = 0$ from the prior cell A to the beginning of the undulator. Emittance growth due to ISR is reduced as much as possible while maintaining the Twiss parameter and dispersion requirements in undulators. Additionally, in order to reduce IBS losses, the trajectories of particles scattered in regions of large dispersion are manuipulated to pass through insertion devices and undulator protectors. A soft 0.5 mrad bend and a taper protect the undulator from trailing synchrotron radiation from the second bend. This undulator is also protected from beam halo losses by a protector collimator. Four corrector magnets and five BPMs allow for orbit correction.

There are five such cell B sections, with the last containing undulator number 6. The following cell C and the seven cell Ds serve as beam transport lines to undulator number 7, and therefore must primarily limit emittance growth and control the time of flight. The optics for these sections are shown in Fig. 2.1.29. There one can see that linear optics are well contained. The second-order dispersion, while seemingly erratic, is actually optimized to zero at the beginning of undulator number 8, as seen in Fig. 2.1.30.

Cells E and F are shown in this figure. Because the spacings between undulators 7, 8, and 9 are larger than in the previous sections of type cell B, more dipole and quadrupole magnets can be used to make achromatic sections. The 25 m undulator in cell E is very similar to those at the beginning of cell A, so the quadrupole strengths are optimized in the same way to provide $\alpha_x = \alpha_y = 0$ and $\beta_x = \beta_y = 12.5\,\mathrm{m}$ at the center of this undulator. The final four-

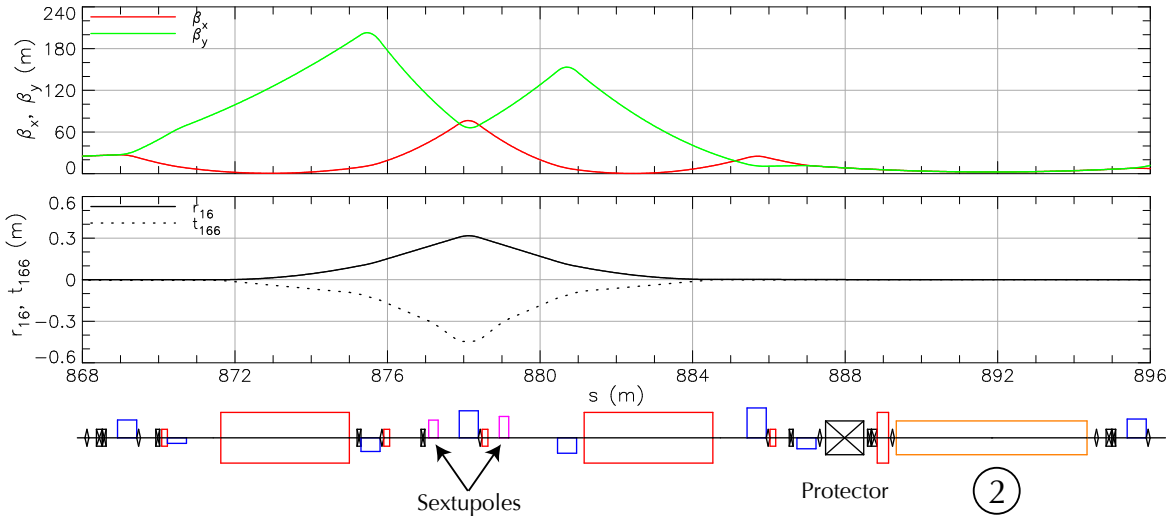

Figure 2.1.28: Optics for the first SA cell B section, which consists of a two-bend achromat followed by a 5 m undulator.

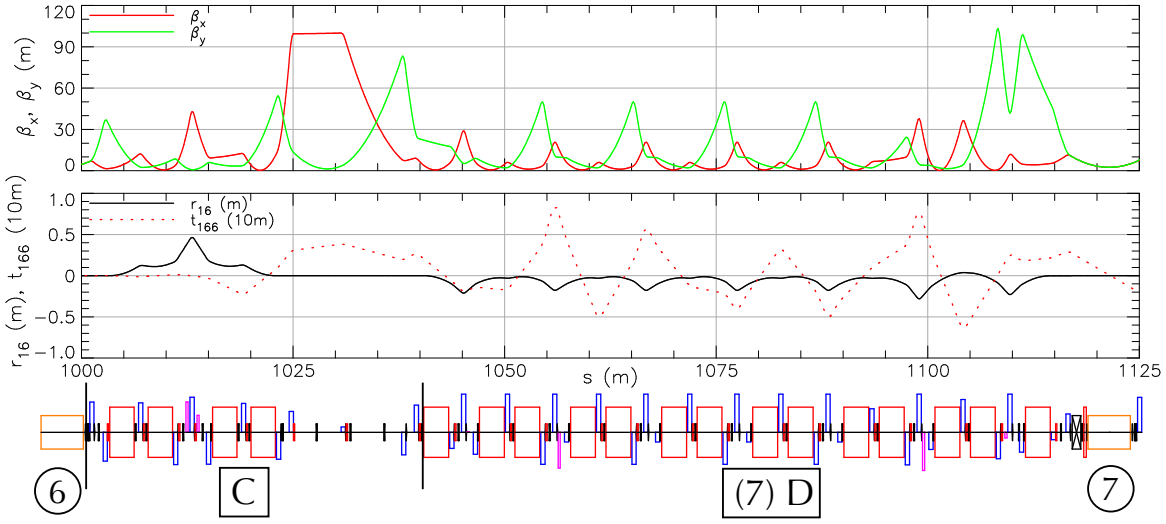

Figure 2.1.29: Optics for the SA cell C and the seven cell D sections.

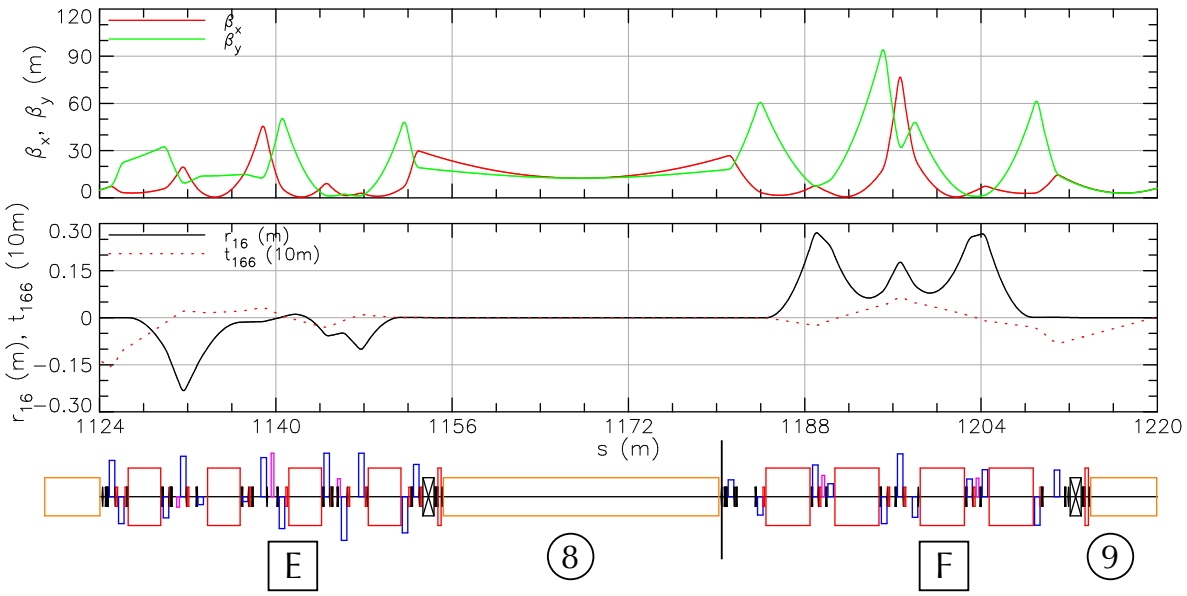

Figure 2.1.30: Optics for the SA cell E and F sections. The quadrupole strengths between the first two undulators are optimized similarly to cell B.

bend achromat focus the beam into the 6 m G-line undulator. The second-order dispersion is controlled by sextupole magnets in the same way as portions of cells A and B.

The optics for the entire SA section are shown in Fig. 2.1.31. Radiative emittance growth and time of flight terms r_{56} and t_{566} are shown in Fig. 2.1.32. One sees that the emittance growth is dominated by portions of cell F. This is due to the relatively strong bends needed to place the undulators in Wilson lab. These bends are among the strongest in the high-energy part of the machine, with bending radii of 36 m and fields of approximately 0.46 T. Note that the total ISR emittance growth at the end of SA amounts to approximately 15% of the mode B emittance in Tab. 1.3.1.

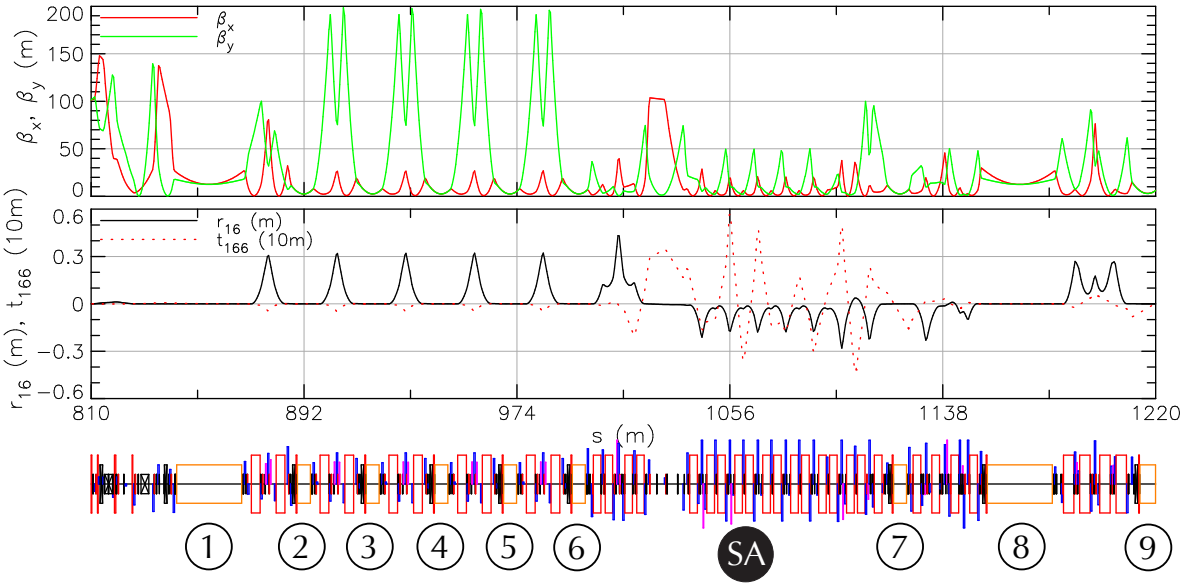

Figure 2.1.31: Optics for the entire SA section.

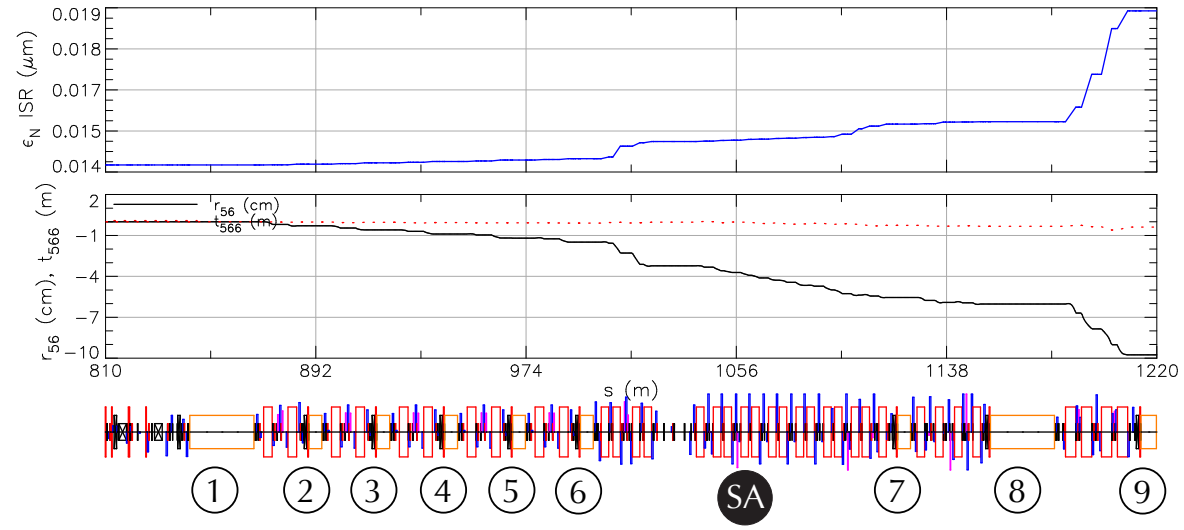

Figure 2.1.32: Normalized radiative emittance growth ϵ_N and time of flight terms r_{56} and t_{566} for the SA. Emittance growth in this section is dominated by relatively strong bends in cell E.

2.1.8 CESR (CE)

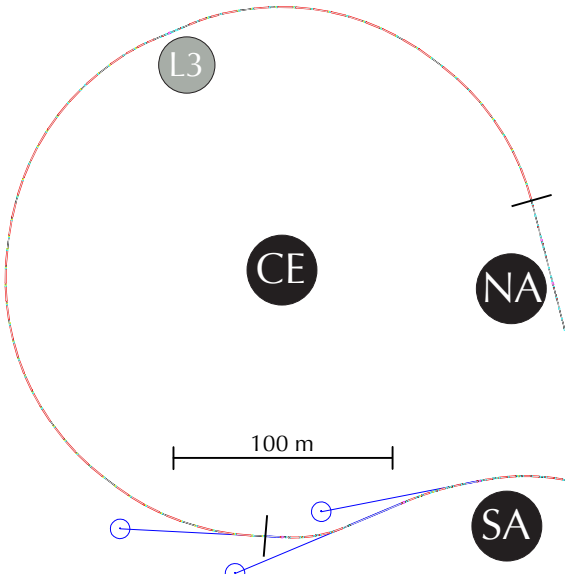

Figure 2.1.33: Layout for the CE section.

Design criteria

The CE section is the only part of the Cornell ERL lattice that already exists. It must

- Accept the SA beam and transport it to the NA section.
- Limit emittance growth.
- Control time of flight terms r_{56} and t_{566}.
- Limit beta functions.
- Be achromatic to second order.
- Provide a collimator for the beam halo.

This section is primarily used for beam transport, but in the bunch-compression mode C it also provides some of the time of flight terms r_{56} and t_{566} needed for compression in the NA section. In order to easily tune the optics of this section with other sections, CE must be have $r_{16} = 0$, $r_{26} = 0$, $t_{166} = 0$, and $t_{266} = 0$ as a whole. Finally, it must contain a collimator to remove the beam halo.

System optimization

The CE layout, shown in Fig. 2.1.33, is essentially the current existing layout for a large potion of CESR. The only noteworthy changes are the addition of a collimator in the L3 region around $s = 1550\,\mathrm{m}$ and three additional corrector magnets and BPMs.

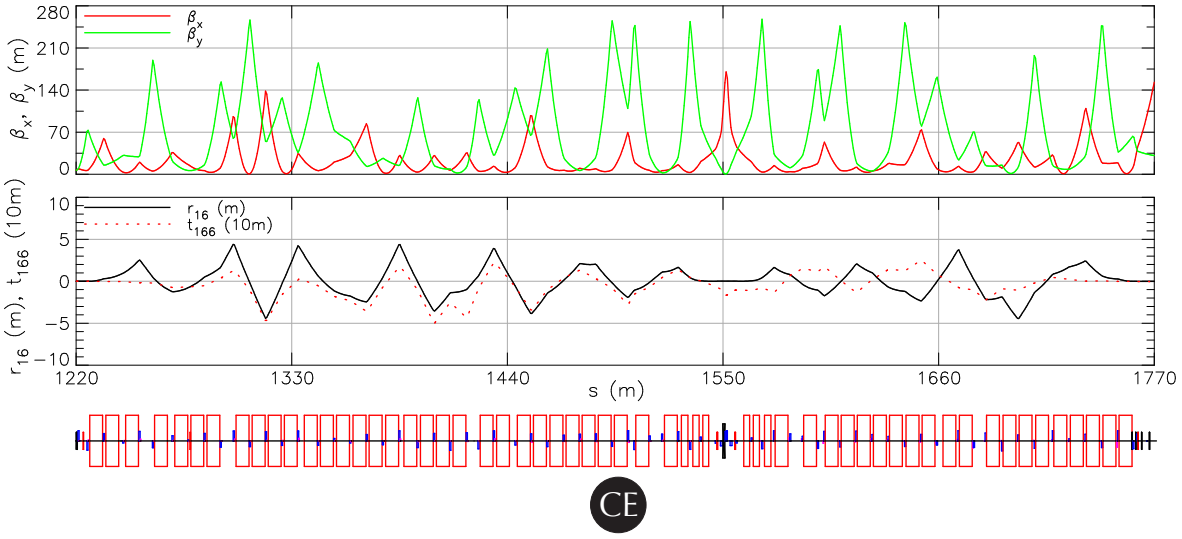

Figure 2.1.34: Optics for the CE section.

The bulk of this section is roughly made up of FODO cells, and therefore does not have the same degree of optics flexibility as the other arcs in the machine. Unfortunately, this configuration is not completely regular, and it does not lend itself to periodic cells as do the other sections. Therefore it is optimized as a whole for controlled beta functions and emittance growth, as well as controlled time of flight terms, by varying all quadrupole strengths for the linear optics and all sextupole strengths for the second-order optics. Special care is also taken that the r_{56} term does not vary too wildly, so that in the bunch compression mode the bunches do not get over-compressed. The resulting optimized optics are shown in Fig. 2.1.34. The radiative emittance grown and time of flight terms are shown in Fig. 2.1.35.

Upgrade optics

The CESR magnets can effectively transport the beam from the SA to the NA, but they contribute to most of the emittance growth in the ERL. Here an upgrade option for the CE section is presented that provides very low emittance growth. It uses the same 6.57 m long dipole magnets as in the CESR as well as the same sextuple magnets, and with about 80 additional quadrupole magnets. The dipoles will produce more bend angle, which their original 8 GeV design can provide. This upgrade therefore only requires new quadrupole magnets, power supplies, vacuum chambers, girders, and stands. In an effort of quality engineering, the baseline ERL design does not contain this upgrade, and therefore the NA x-ray beam lines have significantly larger emittance.

The CESR tunnel is a mixture of pure arcs connected by straight sections. In this upgrade, the CESR dipole magnets are rearranged to span the arcs by periodic cells containing two bends. The straight sections are drifts with three quadrupole magnets. For optimization, CE is divided into seven cell types:

Cell P Periodic cell with two bends – occurs twenty times.

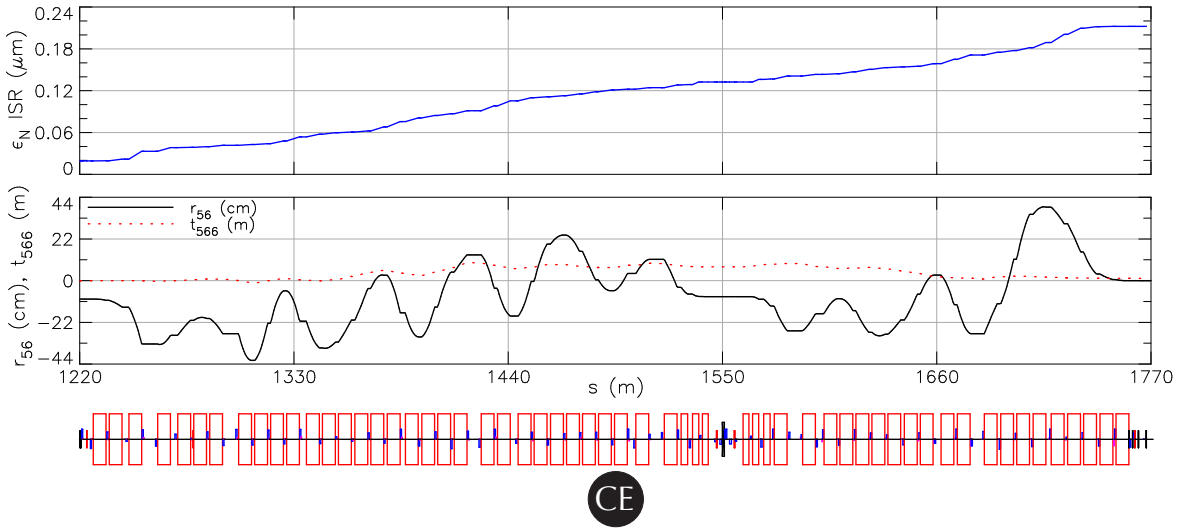

Figure 2.1.35: Normalized radiative emittance growth and time of flight terms for CE for modes A and B. Note that the emittance growth in this section dominates that in the entire 5 GeV arc.

Cell A Matches optics from the SA into the first cell P.

Cell B, C, D, E Matches optics from a cell P to a cell P.

Cell F Matches optics from the last cell P into the NA.

The positions of these cells are shown in Fig. 2.1.38. Essentially multiple cell P sections comprise most of CE, with matching cells A and F for connecting to the SA and the NA, respectively. Cells B, C, D, and E account for the straight sections in the tunnel. Each is similar to two cell P sections, with an extended drift and extra quadrupole magnets between the third and fourth bends.

In a cell P, the four quadrupole strengths are optimized to produce periodic beta functions and first-order dispersion that yield a specified value for the r_{56} contribution and low radiative emittance growth. Next the two sextupole strengths are optimized to produce a specified value for the t_{566} contribution.

The optics for cell B are shown in Fig. 2.1.37. Due to symmetry, it is sufficient to optimize the section by setting the Twiss parameters and dispersion at the entrance to those of the end of cell P, and vary quadrupole strengths symmetrically about the center quadrupole magnet in the straight section to produce $\alpha_x(s_c) = 0$, $\alpha_y(s_c) = 0$, and $D'(s_c) = 0$, with $s = s_c$ at the center of that magnet. The value of $D(s_c)$ can be chosen freely, and therefore the r_{56} contribution by the section is adjustable. The two sextupole strengths are optimized symmetrically to match $t_{266}(s_c) = 0$.

Cells C and E are practically identical to cell B, all having a 6.3 m straight section. Cell D has a longer straight section of 12.2 m, but the optimization strategy is the same as that of cell B. Finally, there are enough quadrupole and sextupole magnets in cell A and cell F to match Twiss parameters between the adjacent sections, and to fine tune the total r_{56} and t_{566}

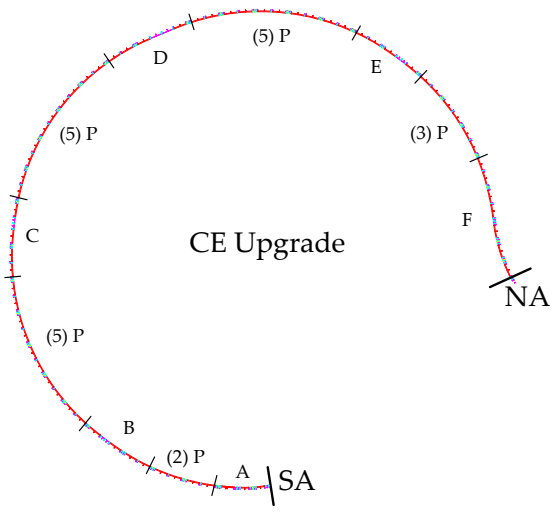

Figure 2.1.36: Layout for an upgrade to the CE section

contributions by CE. The resulting emittance growth and dispersion functions for all of CE are shown in Fig. 2.1.38. There it is seen that, due to the similarity of all the cells, both the emittance growth and dispersion functions are very regular and relatively small in the bulk CE.

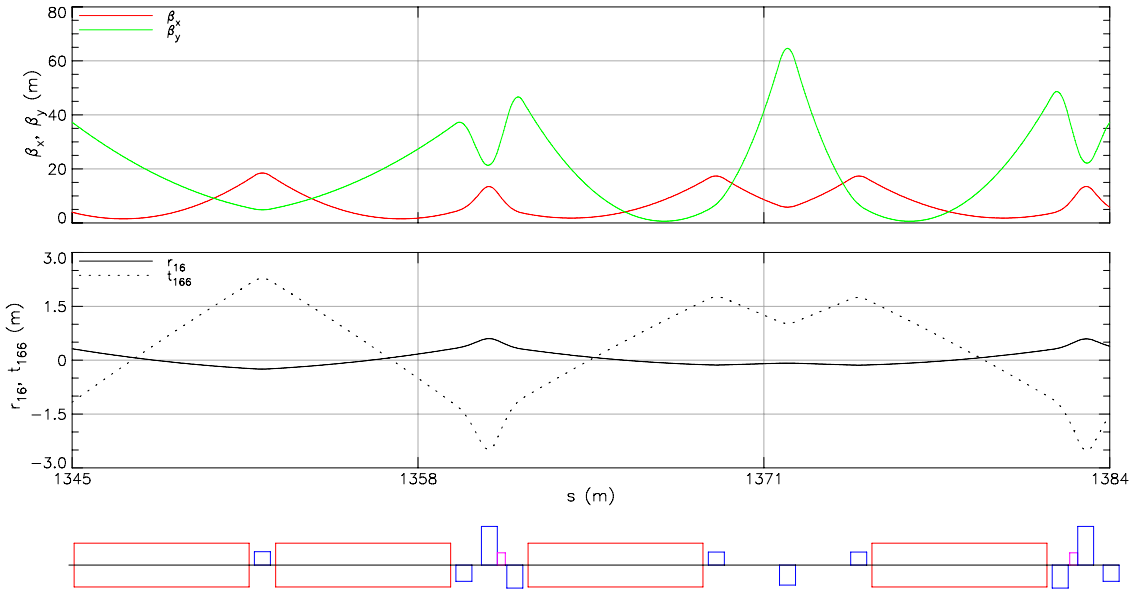

Figure 2.1.37: Optics for the upgrade CE cell B

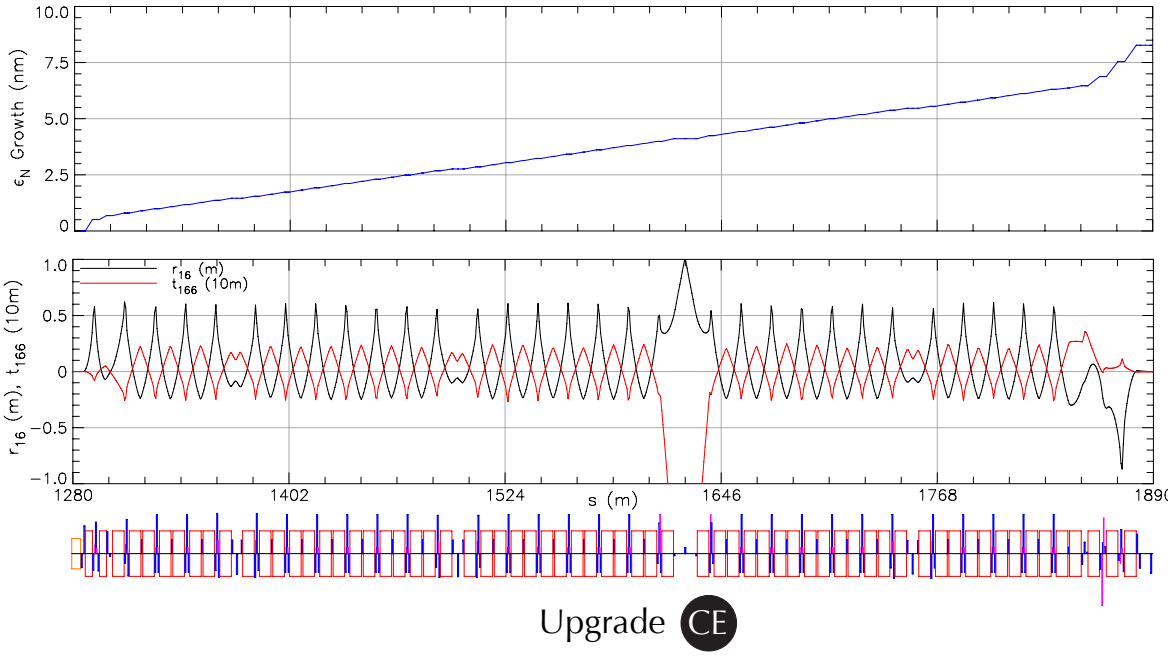

Figure 2.1.38: Optics for the CE upgrade section.

2.1.9 North Arc (NA)

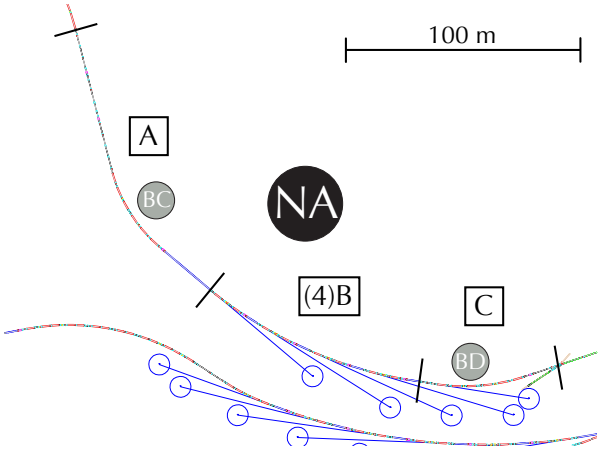

Figure 2.1.39: B.1 26: Layout for the NA section. Part of the SA is shown for reference.

Design criteria

The NA contains the last five undulators in the ERL. This section must

- Receive the beam from CE.
- Contain five undulators in the new building, including one that is 25 m long.
- Collimate the beam halo prior to the first undulator.
- Provide customized beam sizes with zero dispersion in all NA undulators.
- Include a bunch compression section, and be able to maintain short bunches through all undulators.
- Include a bunch decompression section after all undulators, at the end of the NA.
- Merge the high-energy beam into LA for energy recovery.

These criteria are similar to those for the SA described in §2.1.7. Notably the NA contains bunch compression and decompression sections, which are further detailed in §2.1.10.

System optimization

The NA is approximately 290 m long. It is divided into four cell types:

Cell A Matches optics from CE into undulator number 10, and contains a bunch compression subsection BC.

Cell B Periodic section containing a three-bend isochronous achromat and a 5 m undulator – occurs four times.

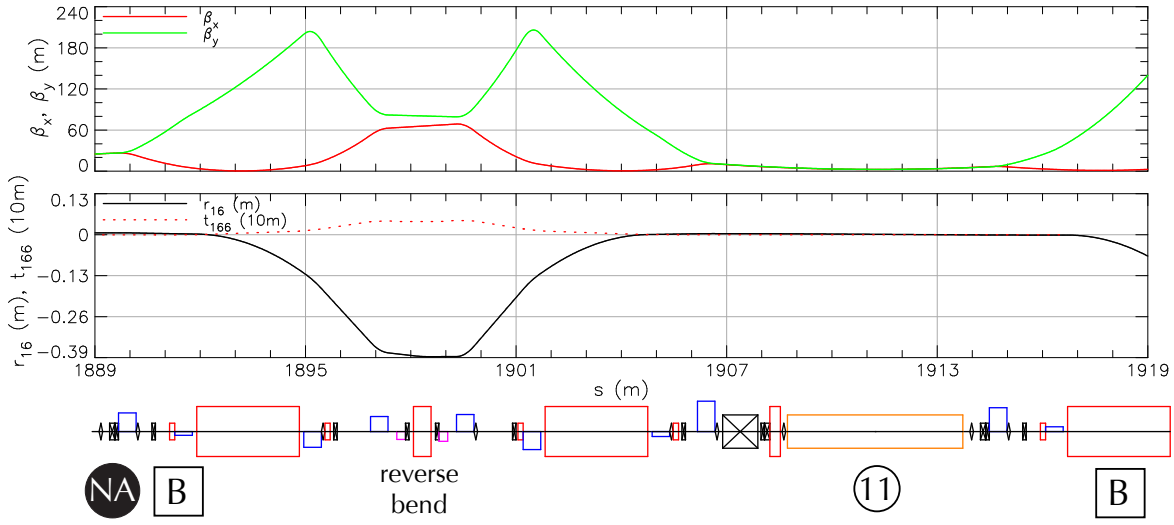

Figure 2.1.40: B.1 27: Optics for the first NA cell B section.

Cell C Matches optics from the last cell B into LB for energy recovery, and contains a bunch decompression subsection BD.

The layout for these cells is shown in Fig. 2.1.39.

In the bunch compression modes, where the BC subsection compresses the bunch, it is necessary to keep the bunch short in all undulators. Therefore, in addition to being achromatic, the arcs between all undulators are also isochronous. This is achieved by adding a short 'negative' bend between the two long bends in an achromat, which can be seen in all cell B sections. Besides this short bend, all NA cell B sections are similar to the layout of the SA cell B sections. Cell C is similar to a cell B section, except with a longer 25 m undulator.

Optimization for these cells is therefore similar to the method described in §2.1.7 for the SA cell B, with the additional constraint that $r_{56} = 0$ through a cell. Two sextupole magnets make the section achromatic to second order. The resulting optics for cell B are shown in Fig. 2.1.40.

The NA cell A section matches Twiss parameters and dispersion from CE into undulator number 10. The optics for this cell are shown in Fig. 2.1.41. These optics are for mode A (non-compression), so the bunch compressor section is just an isochronous achromat. The first and second-order dispersion are fine tuned to give the desired r_{56} and t_{566} terms from the beginning of CE to the beginning of the first NA undulator.

This section accepts Twiss parameters and dispersion from the end of CE, and matches them to the first NA cell B section. Additionally, the time of flight terms r_{56} and t_{566} are fine tuned when the ERL is operating in bunch compression mode. All quadrupole and sextupole strengths are varied independently to satisfy these constraints.

After the last 5 m undulator, the NA ends with cell C, containing an arc with 6 bends that connects the beam back into LA for energy recovery. In the mode where the bunch arrives compressed, this section serves to decompress the bunch by providing rather large dispersion through the central bends and a correspondingly large r_{56} compensation. It also contains a

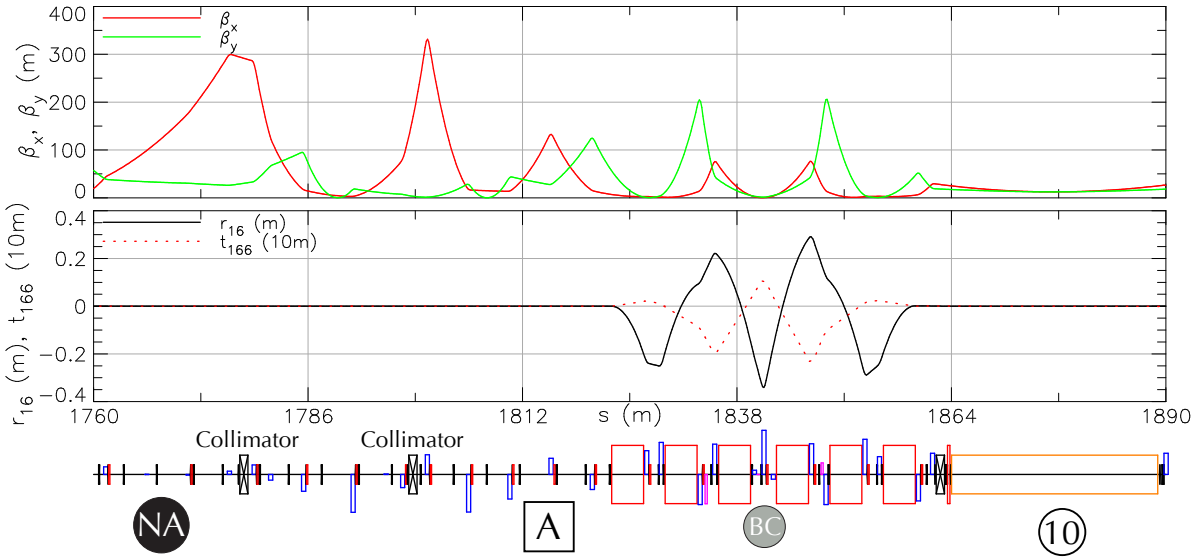

Figure 2.1.41: Optics for the NA cell A section, for mode A.

collimator for the beam halo.

Optics for the entire NA section are shown in Fig. 2.1.42, with radiative emittance growth and time of flight terms shown in Fig. 2.1.43. Because the time of flight terms are calculated starting at the beginning of the SA, one sees that they indeed go to zero at the end of the NA and thus the SA-CE-NA sections together are achromatic and isochronous to second order.

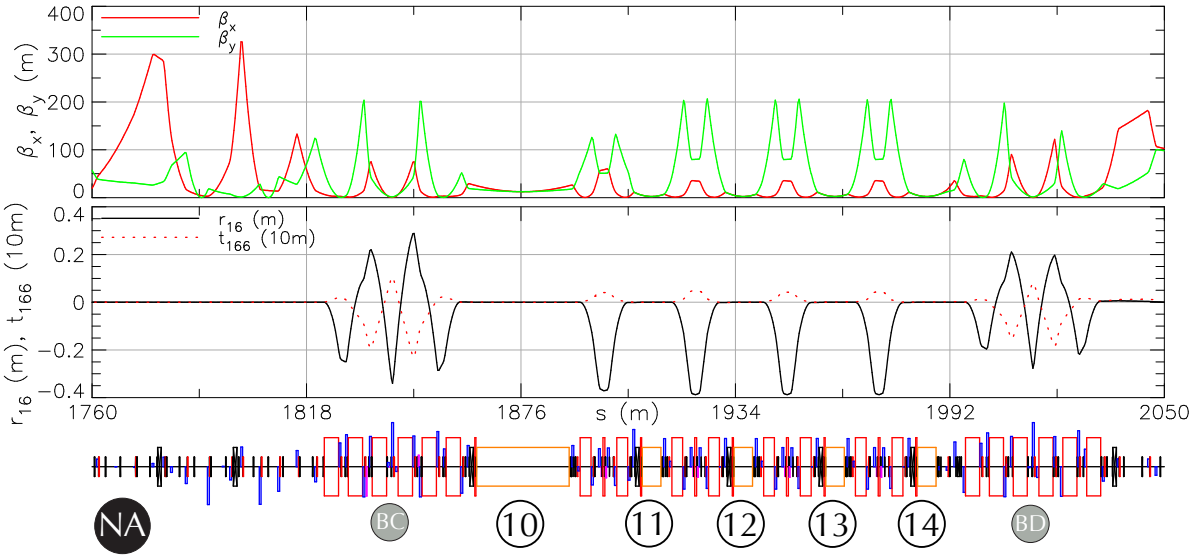

Figure 2.1.42: Optics for the entire NA section.

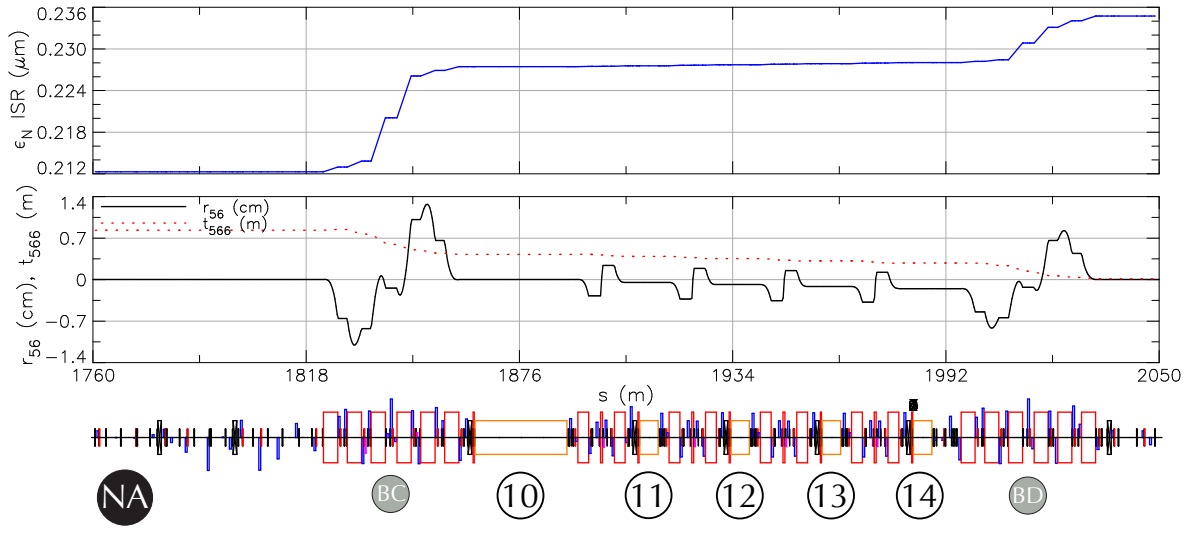

Figure 2.1.43: Normalized radiative emittance growth ϵ_N and time of flight terms r_{56} and t_{566} for the NA.

2.1.10 Bunch-compression optics in the ERL

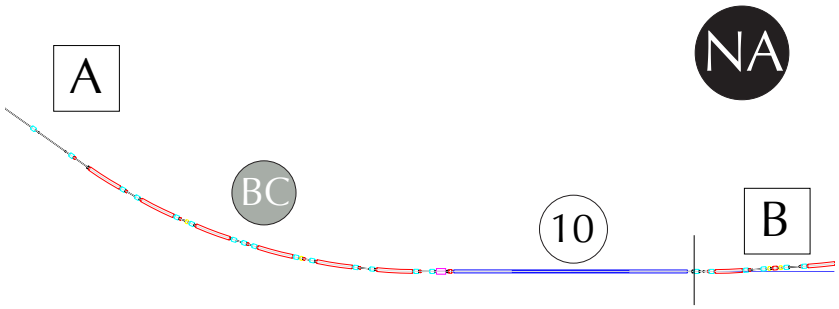

Figure 2.1.44: Layout for the bunch compressor BC in the NA.

Design criteria

The operation mode C in Tab. 1.3.1 calls for compressed bunches in the NA section. The bunch compression scheme for this mode must

- compress bunches to 100 fs prior to all NA undulators. Shorter bunches are possible, but require larger energy spread as shown in Fig. 2.1.45.
- ensure that all undulators see these short bunches.
- decompress these bunches for energy recovery.

In particular, the bunches should undergo final compression in the BC section shown in Fig. 2.1.44. This mode utilizes off-crest acceleration to perfrom this compression, which greatly increases the full energy spread of the bunch, and can potentially lead to beam losses in regions with large dispersion. Therefore, the initial bunch duration from the injector is chosen to be 1 ps instead of the 2 ps duration of mode A. This leads to relatively higher HOM powers in the Linacs, so mode C operates with a reduced bunch charge of 19 pC, leading to 25 mA average current at 1.3 GHz. This lower bunch charge also reduces the detrimental effect of CSR.

System optimization

Manipulation of the first- and second-order time-of-flight terms r_{56} and t_{566} in the CE and NA sections, combined with off-crest acceleration in LA and LB at phase ϕ, allow bunches to be compressed in the BC section just prior to undulators 10–14. This works as follows: bunches with 1 ps durations are accelerated with $\phi \approx 6.6^\circ$ through LA and LB and enter SA at 5 GeV. The time-of-flight terms r_{56} and t_{566} are controlled throughout the CE region, which partially compresses these bunches, and the six-dipole arc, just prior to undulator 10, performs the final compression to 100 fs. The achromatic arcs between the subsequent undulators each incorporate a 'reverse' bend to make them isochronous, and thereby maintain this short bunch length for each undulator. Following the final undulator 14, the bunches are decompressed in

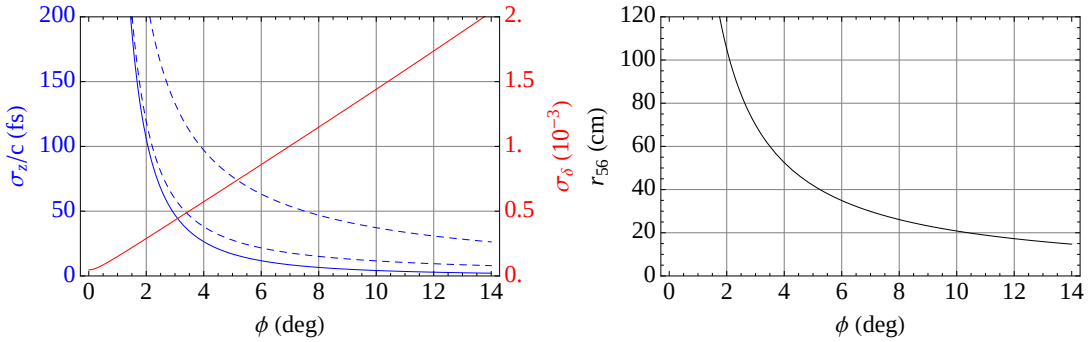

(a) (b)

Figure 2.1.45: Estimates of the minimum bunch length from second-order bunch compression at high energy. The blue curve in Fig. 2.1.45a assumes an initial bunch length of 1 ps. The upper dashed line incorporates the expected slice energy spread increase due to ISR in dipole and undulator magnets by $\Delta\sigma_\delta = 5.33 \times 10^{-5}$. If undulator magnets are turned off in the SA section this becomes $\Delta\sigma_\delta = 1.56 \times 10^{-5}$, shown in the lower dashed line. The red line shows the correlated rms energy spread. Figure 2.1.45b shows the required r_{56} term to provide this compression.

a similar six-dipole arc to 1 ps, after which their energy is recovered in a second pass through LA and LB.

There is some freedom in choosing r_{56}, t_{566}, and ϕ to produce the 100 fs bunches. Roughly speaking, using a larger ϕ implies that a smaller r_{56} term is needed to fully compress the bunch, at the cost of a larger relative energy spread σ_δ. In addition, the bunch must be decompressed in a relatively short section at the end of NA, with an r_{56} of approximately the same value and opposite sign as that from the beginning of SA through the BC section. Generally, in order to accommodate all of the other linear optics constraints, it is easiest to make the necessary $|r_{56}|$ as small as possible. With all of these considerations, the baseline mode C lattice has been designed to provide $r_{56} \approx 30$ cm and $t_{566} \approx -1$ m from the beginning of SA through the end of the bunch compressor BC using $\phi \approx -6.6°$.

To estimate what is further possible with second-order compression in the system, the minimum bunch length, along with the energy spread, as a function of accelerating phase ϕ are shown in Fig. 2.1.45a, calculated with formulas that can be found in, for example, [18]. The corresponding r_{56} needed are shown in Fig. 2.1.45b. An important consideration is the energy spread induced by ISR in dipole and undulator magnets, which limits the compression process.

To simulate this bunch compression process, it is also important to consider CSR, which is described in §2.1.14. Depending on the bunch charge and length, CSR can be a limiting factor in the compression process. Fortunately, the bunch parameters in mode C are such that CSR does not hinder our compression or decompression, as shown by particle tracking simulations in Fig. 2.1.46.

Figure 2.1.46 shows that the time-of-flight term r_{56} varies wildly through CE. This is due

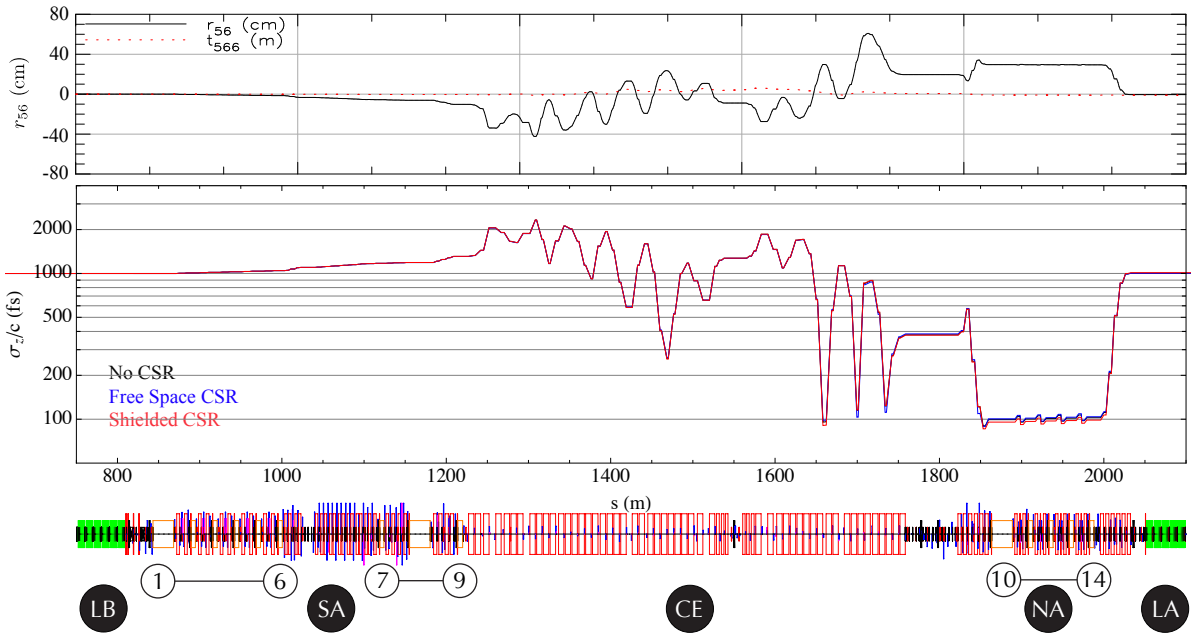

Figure 2.1.46: Bunch length and time-of-flight terms for the bunch-compression mode C through the high-energy arc SA-CE-NA. These simulations track 100,000 particles. Simulations with and without CSR show that our design limits this effect, as described in §2.1.14.

to the relatively fewer quadrupoles in CE compared to other sections, which makes it more difficult to control both the dispersion (the integral of which affects r_{56}) and the beta functions simultaneously. Care is taken, however, to limit the number of times that r_{56} crosses the 30 cm mark, which highly compresses the bunch.

2.1.11 Demerger and Beam Stop (BS)

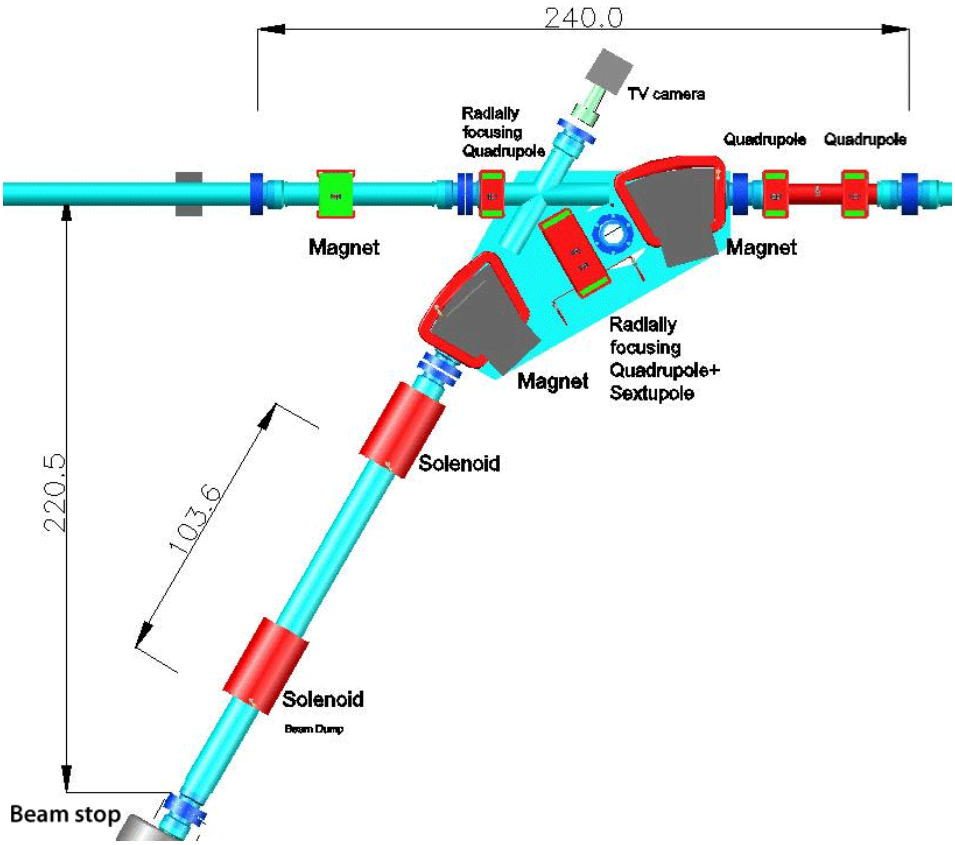

Figure 2.1.47: The achromatic section of bends used to separate high- and low-energy beams. It uses two bending magnets and a quadrupole in between. This quadrupole is equipped with a sextupole corrector. Dimensions are given in cm.

Design criteria

The demerger and beam stop are located directly after LB, the south string of SRF structures. Together these sections must

- demerge the second-pass 10 MeV beam from the first-pass 5 GeV beam.
- have an energy acceptance of $\pm 2.5\,\mathrm{MeV}$.
- expand the low energy beam as much as possible for absorption at the beam stop.

The demerger serves to separate the low-energy from the high-energy beams. It is located directly after LB, the south string of SRF structures. The high-energy beam has an average energy of $\langle \mathcal{E} \rangle \approx 5\,\mathrm{GeV}$ and a small rms energy spread $\sigma_\delta = \delta\mathcal{E}/\mathcal{E} \approx 2 \times 10^{-4}$. The low-energy beam, which has already been used for x-ray production, has an average energy $\langle \mathcal{E} \rangle \approx 10\,\mathrm{MeV}$

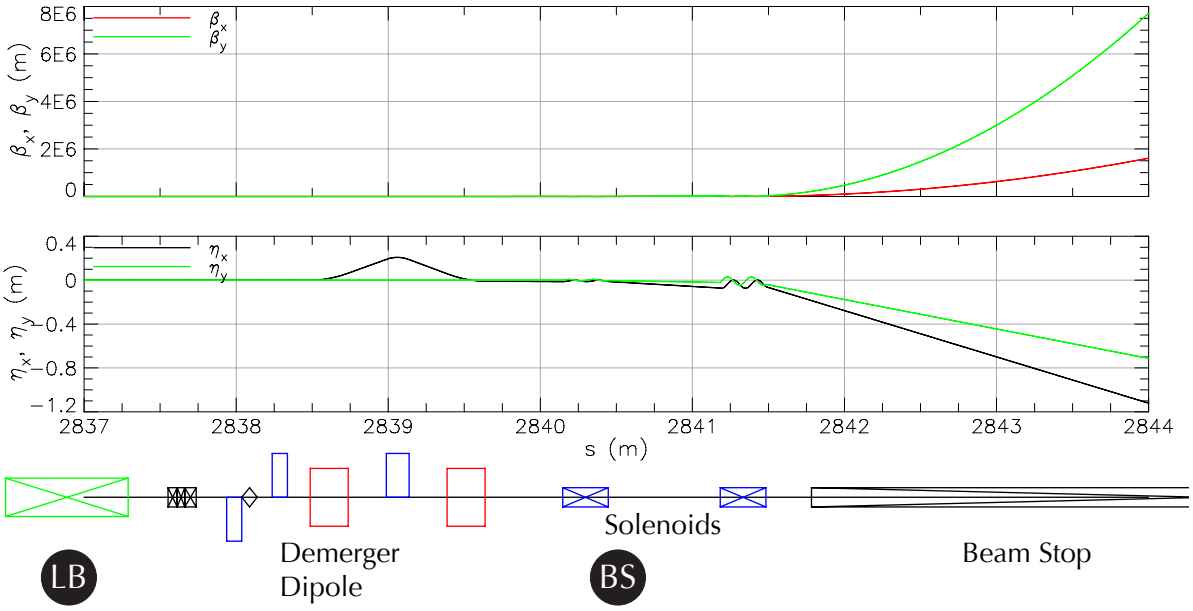

Figure 2.1.48: Envelope functions and dispersion in the beam-stop line. Dipoles are shown as red boxes, quadrupoles as blue boxes and solenoids by blue boxes with a cross. The beam is coming from the left.

and an full energy spread of $\Delta\mathcal{E} \approx \pm 1\,\text{MeV}$, which can be seen later in Fig. 2.1.62. The line that transfers this beam to the beam stop therefore needs to have very large energy acceptance, and has to be able to accept significant beam loss. Finally, it is crucial to have a large beam size to lower the power density in the beam-stop system.

System optimization

Each dipole magnet in the BS section bends the low-energy beam by $\phi \approx 30°$, with a bending radius of $\rho \approx 0.5\,\text{m}$. The 5 GeV beam only passes through the first magnet and is bent by only approximately 1 mrad.

To compensate the dispersion generated after the separation magnet, the demerger is equipped with a radially focusing quadrupole and a complementary bending magnet, so that the total BS section bend becomes achromatic. Because the energy of the beam is low, this quadrupole lens can be constructed as a Hand-Panofsky quadrupole. This lens is equipped with sextupole correction windings to compensate the quadrupole's chromaticity contribution. The windings in the rectangular frame are generated by a linear current variation at the top and bottom poles, and by a parabolic current distribution at the side walls of the quadrupole. Another possible solution for the magnets might be a permanent magnet, with a coil for field control. This would provide beam stop protection in the case of power supply failure, a practice that is typical for high-power systems.

The beam in between the two large aperture bends is allowed to be approximately $\pm 6\,\text{cm}$ wide. The wide walls of the chamber are covered in the graphite absorbers to protect against beam loss by energy fluctuations.

In the optics model presented here, a solenoid installed in front of the beam-stop is used as a simplifying model to control the beam size. In reality, an over-focusing quadrupole will be used. This magnet produces horizontal and vertical crossovers near its exit, to allow for rapid expansion of beam dimensions as shown in Fig. 2.1.48. The next magnet provides three corrector coils arranged in form of a sextupole, powered with three-phase 60 Hz AC. These coils will sweep the electron beam in the transverse direction to create a circular sweep with 60 Hz.

2.1.12 Extraction line (EX)

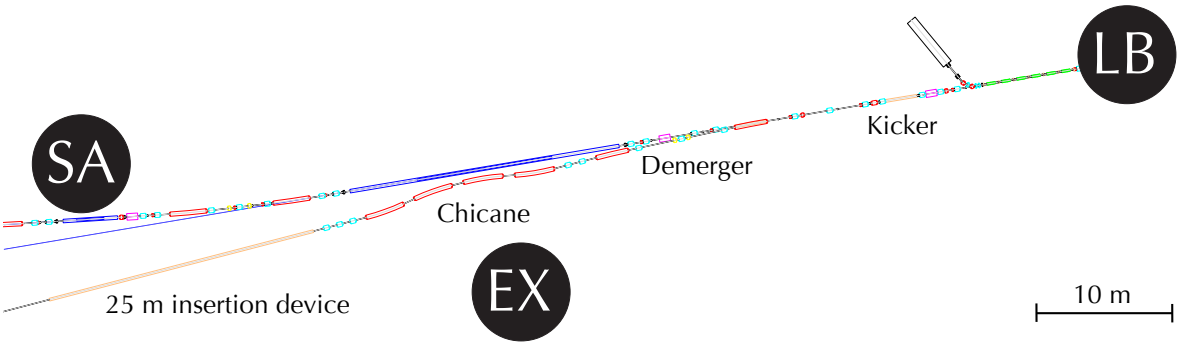

Figure 2.1.49: Layout for the EX section.

Design criteria

The relatively low bunch charge in the bunch compression scheme described in §2.1.10 leads to compression that is not limited by CSR. However, a bunch with a much higher charge of 1 nC would be significantly damaged in this compression process, and it would be difficult to recapture its energy in deceleration. In order to study the use of such bunches, an extraction beamline section EX has been designed that

- extracts high-charge (1 nC) bunches from the exit of LB at a rate of below 100 kHz.
- compresses these bunches to 100 fs duration or less.
- provides space for a 25 m long insertion device.

In order to avoid the detrimental effects of CSR for 1 nC bunches in the TA, this high-charge bunch must remain relatively long (2 ps), and be compressed at high energy (5 GeV). An appropriate bunch compressor must take second-order effects into account, which adds complications to the large energy spread associated with compression to 100 fs or less. We have therefore designed a very simple four dipole bunch compressor without sextuples at high energy that uses second-order time-of-flight terms in the turnaround arc rather than in the bunch compressor. This design was tested using particle tracking simulations that incorporate CSR.

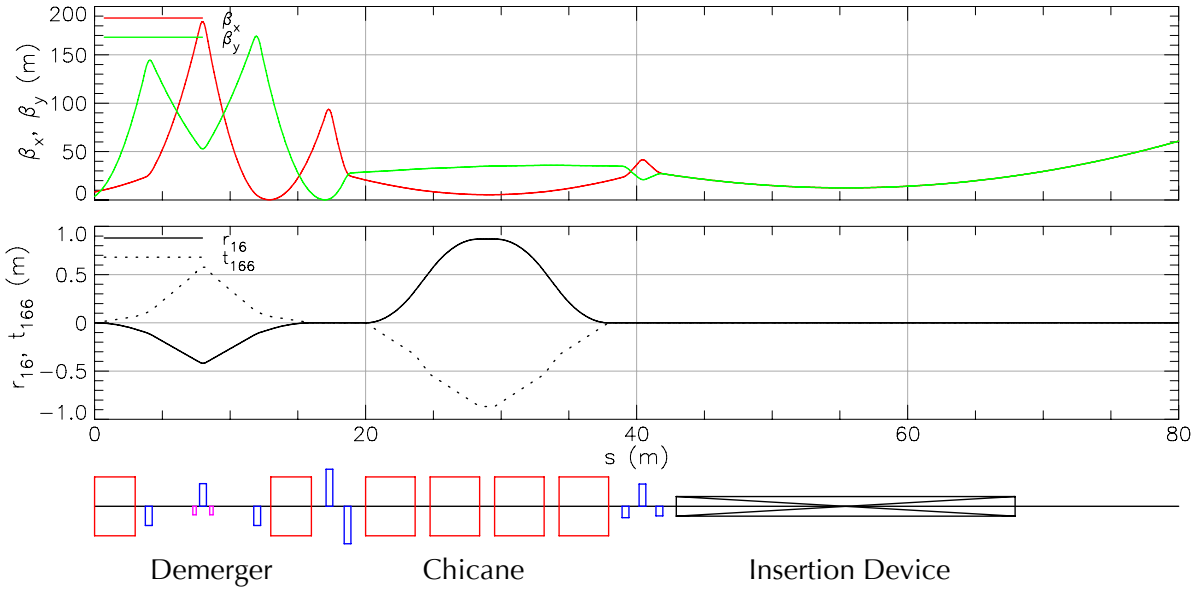

Figure 2.1.50: Optics for the EX section. The chicane and demerger together provide a time-of-flight term $r_{56} = 23.5\,\text{cm}$ to compress the bunch for the 25 m long insertion device.

Table 2.1.2: Beam parameters after the extraction line EX

	77 pC	1 nC	Unit
ϵ_x	280	2300	pm
ϵ_y	33	33	pm
σ_δ	2.6	2.6	10^{-3}

System optimization

The EX compressor lattice consists of three parts: an achromatic demerger section, the chicane compressor, and finally an undulator. Because energy is not recovered in compression, the beam must be extracted from the main line. Extraction is done by kicking the beam by 1 mrad, then demerging the beam with two bending magnets, then bending the beam 2.5° each from the main line. Between these two magnets, a quadrupole triplet with field strengths of approximately 10 T/m is optimized to cancel the dispersion introduced by the demerging bends. Also the aberrations t_{166} and t_{266} are canceled.

Following the demerger, a quadrupole doublet is placed to control the beta functions entering the compressor and undulator. The compressor itself is a simple chicane achromat consisting of four equal and opposite dipoles each bending by 10.5° with a 20 m radius. The optics for the EX section are shown in Fig. 2.1.50.

The demerger lattice in Fig. 2.1.49 is very close to the main line it bends away from, so to avoid overlapping elements the positions of the magnets in this section are limited to the open spaces between the structures in the main line.

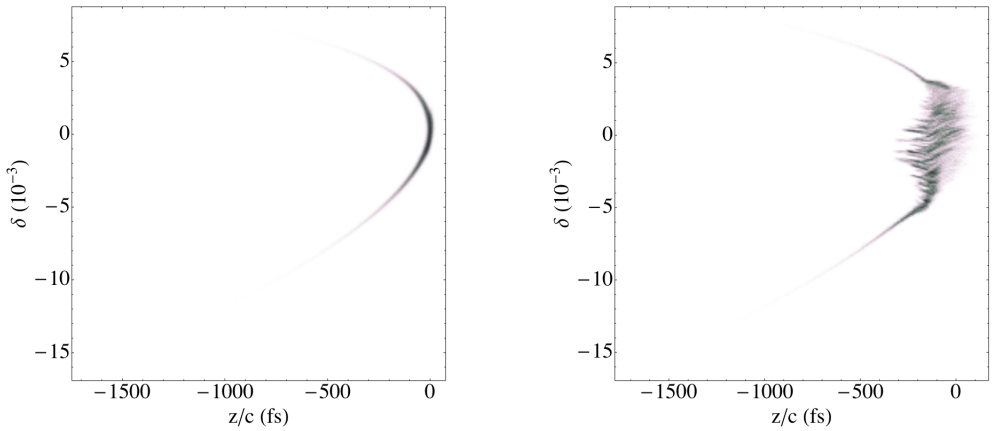

(a) 77 pC (b) 1 nC

Figure 2.1.51: The longitudinal phase space for particles at the end of the chicane shown in Fig. 2.1.50 for bunches of different charge. These simulations tracked 200,000 particles and used the 1-D shielded CSR method in Bmad [22]. The bunch durations for both situations is approximately 100 fs.

Examples of the CSR damage to bunches in this compressor are shown in Fig. 2.1.51. These simulations were done using the 1-D shielded CSR method in Bmad [22]. Both the 77 pC and 1 nC bunches achieve the desired 100 fs duration, but the 1 nC bunch suffers significantly more emittance growth. Beam parameters after the extraction line for both bunch charges is shown in Tab. 2.1.2. Radiation characteristics from FELs using this extraction line are currently being considered [23].

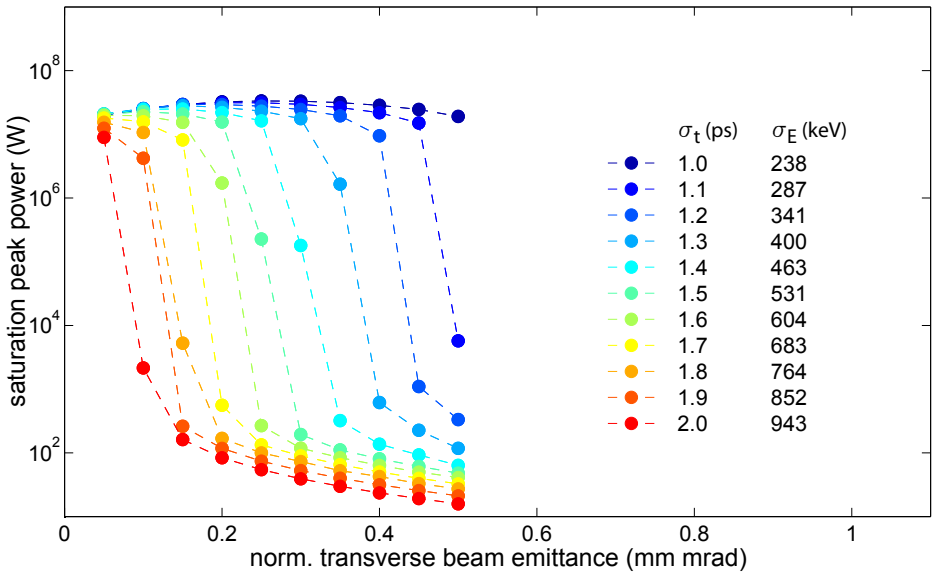

Figure 2.1.52: Simulated intra-cavity power of an XFEL-O driven by the Cornell ERL. Shown is the peak power at saturation as a function of transverse beam emittance and bunch duration generated in the injector. A bunch charge of 25 pC was assumed, as well as an undulator with 3000 periods of $\lambda_U = 15\,\text{mm}$. The radiation wavelength is 0.103 nm.

2.1.13 Electrons for an XFEL-O

The CW operation of the accelerator, its high repetition rate, as well as the very small beam emittance make the Cornell ERL an superb machine to test and operate future accelerator technologies. A very promising scheme is an FEL oscillator operating in the hard x-ray regime (XFEL-O), which was proposed and analyzed in various references [24–27]. More detailed studies are underway. Here we only show a feasibility study for driving such a light source with beam parameters similar to the ERL high coherence Mode B. The resonator of such an FEL would be composed of high-reflectivity, narrow-bandwidth Bragg mirrors of sapphire or diamond crystals and reasonable resonator dimensions to yield pulse round-trip rates of $\sim 1\,\text{MHz}$. Such a device is expected to produce transform limited picosecond x-ray pulses with megawatts of beam power and a resulting narrow bandwidth as small as $\Delta\omega/\omega \sim 10^{-7}$. Due to the very narrow bandwidth, this would be a complementary source of x-rays compared to SASE x-ray FELs, both of which provide comparable peak spectral brightnesses.

We present an initial analysis of the feasibility for an XFEL-O within the Cornell ERL by following up on the work presented in [27]. In that work, a 1D code was developed to simulate the evolution of the light field in the optical resonator and its interaction with the driving electron beam. Comparisons of this 1D code with the 2D code `GINGER` give very good agreement, which is why the studies presented here are based on the faster 1D code. The simulations assume an undulator with 3000 periods of $\lambda_U = 15\,\text{mm}$, tuned to a fundamental

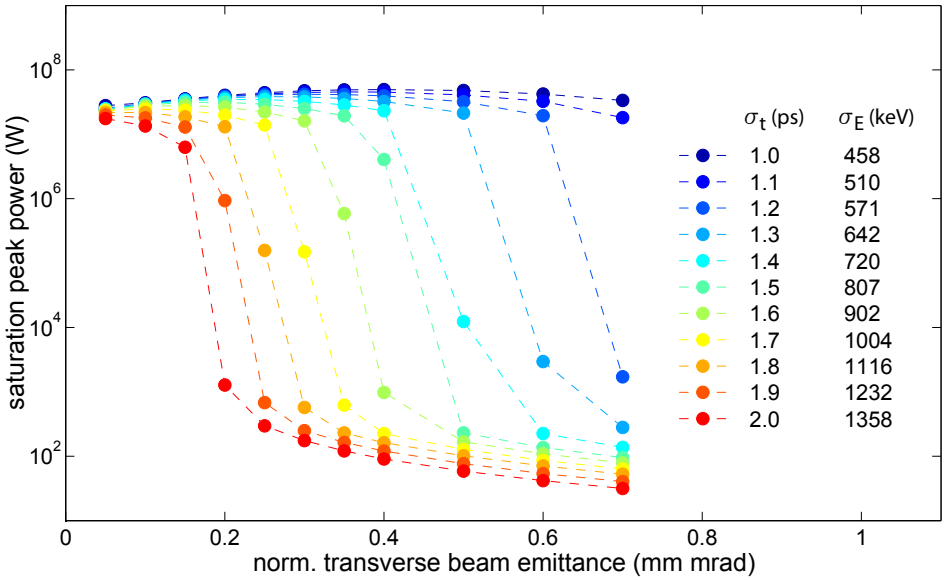

Figure 2.1.53: Simulated intra-cavity power of an XFEL-O driven by the Cornell ERL if operated at 7 GeV, provided by accelerating (rather than decelerating) the beam in the second pass through Linac A. Shown is the peak power at saturation as a function of the transverse beam emittance and the bunch duration generated in the injector. A bunch charge of 25 pC was assumed as well as an undulator with 3000 periods of $\lambda_U = 15\,\mathrm{mm}$. The radiation wavelength is 0.103 nm.

radiation wavelength of $\lambda_{ph} = 0.103\,\mathrm{nm}$ for a 5 GeV electron beam. The (spectral) losses in the resonator are the same as in [27] (15% per roundtrip including 4% of the power which is coupled out by a thin Bragg mirror). The radiation is focussed with grazing incidence mirrors to provide a waist within the undulator. The Rayleigh length was used to optimize the linear FEL gain and the electron beam optics was matched to the light beam.

A small transverse beam emittance and a small energy spread are of greatest importance to achieve a sufficiently high FEL gain. Simulations of the expected intra-cavity peak power have been performed for various transverse beam emittances and various bunch durations generated in the injector. As an example, we have adopted a bunch charge of 25 pC in all cases, and a beam energy spread assumed to be normally-distributed and composed of two contributions: curvature of the accelerating fields and incoherent synchrotron radiation. Figure 2.1.52 summarizes the simulation results and indicates that a shorter bunch duration of around 1 ps or less would be favorable, since this relaxes significantly the requirements on the normalized transverse beam emittance. The results also indicate that the expected beam emittances will likely be small enough to allow the operation of an XFEL-O. A higher beam energy would relax the requirements on the beam emittance, which is indicated in Figure 2.1.53 and would relax requirements on the undulator period.

While in principle an XFEL-O could be driven by an electron beam the repetition rate of which is an integer multiple of the fundamental XFEL-O resonator frequency, the thermal load might be a limiting factor.

2.1.14 Wakefield effects

Impedance budget

Wakefields from vacuum-chamber discontinuities can cause (a) component heating, (b) instabilities, (c) correlated energy spread. Component heating and instabilities tend to be the dominant effects in storage rings, whereas the correlated energy spread is the dominant concern in an ERL, where the relative energy spread is amplified by the high- to low-energy ratio during deceleration [28], about a factor of 500 in the Cornell ERL. Care has to be taken that this energy spread is not too large to transport the beam into the beam stop. The total energy loss and component heating also has to be considered. The power loss in a vacuum component with loss parameter $k_{\rm loss}$ for an average circulating current $I_{\rm av}$ at a repetition frequency $f_{\rm rep}$ is

$$P_{\rm loss} = \frac{I_{\rm av}^2 \cdot k_{\rm loss}}{f_{\rm rep}} = 7.69\,{\rm W}\left(\frac{k_{\rm loss}}{1\,{\rm V/pC}}\right)\ , \tag{2.1.14}$$

where the second equality gives the proportionality constant for this ERL design in regions with a single beam for operation mode A. The constant is doubled when two beams pass through the same chamber.

The correlated energy spread is caused by the induced wakevoltage seen by a reference particle traveling with the bunch a distance s behind the bunch center. For a bunch charge q_b, the induced voltage for one traversal of the ERL is

$$V_\parallel(s)\big|_{\rm ERL} = q_b \cdot W_\parallel(s)\big|_{\rm ERL} \tag{2.1.15}$$

where $W_\parallel(s)$ is the longitudinal wake at the particle's position s. The maximum energy acceptance of the beam stop $\Delta\mathcal{E}_{\rm acc}$ limits the allowable energy spread of the beam and if the wakefields alone are only permitted to produce 50% of the energy acceptance, the maximum permissible wakefield for $q_b = 77\,{\rm pC}$ is

$$\max\left\{ W_\parallel(s)\big|_{\rm ERL}\right\} \le 0.5\frac{1}{q_b}\Delta\mathcal{E}_{\rm acc} = 0.5\cdot\frac{5\,{\rm MeV}}{77\,{\rm pC}} = 32\,{\rm kV/pC} \tag{2.1.16}$$

where the beam stop has an energy acceptance of ± 2.5 MeV. This places an impedance budget limit on the total ERL wakefield of 32 kV/pC.

The wakefields and loss parameters have been estimated for models of the ERLs vacuum-chamber components with the simulation programs ABCI [29], NOVO [30], MAFIA [31], and with analytic models for surface-roughness and resistive-wall wakefields. The RF accelerator structures were modeled by scaling the wakefield for the TESLA RF structure [32]. Results are summarized in Tab. 2.1.3 for a Gaussian-shaped bunch of length $\sigma_z = 0.6\,{\rm mm}$ for the most significant vacuum-chamber components. Accounting for the change in beam-pipe cross-section, calculations for the HOM-load chambers, neglecting ferrite absorber tiles, were undertaken using NOVO. The following vacuum-chamber components were approximated by cylinder-symmetric models using ABCI: 1) The expansion joint is a 4 mm thick tube sliding inside a 35 mm diameter tube with spring-finger contacts breaching the 1 mm gap between the sliding surfaces and 30° tapers at each end, 9 mm apart. 2) The BPM button was modeled as a 15 mm square plate attached to a 1 mm stem with a 1 mm gap between the electrode and the wall. 3) The stripline was modeled as a 2.3 mm thick conducting shell with a 4 mm radial step to

Table 2.1.3: Wakefield and loss-parameter contributions for the total number (or length) of each component in the ERL. If unspecified, the radius of the beam pipe r_{pipe} is 12.7 mm.

Component	Number or length	Neg. Wake (kV/pC)	Pos.Wake (kV/pC)	k_{loss} (kV/pC)
7-cell RF cavity	2×384	-6.47	0	5.81
HOM load ($r_{\text{pipe}} = 110\,\text{mm}$)	384	-0.50	0	0.36
Expansion Joint	356	-0.74	0.10	0.53
BPM (Button)	664	-0.35	0	0.24
BPM (Stripline)	20	-0.01	0	0.01
Flange joint	356	-0.90	0	0.64
Clearing electrode	150	-0.18	0.14	0.04
Gate valve	68	-0.71	0.69	0.42
Resistive wall ($r_{\text{pipe}} = 12.7\,\text{mm}$)	2500 m	-4.00	0	2.75
Surf. rough. 3μm ($r_{\text{pipe}} = 12.7\,\text{mm}$)	2500 m	-14.00	0.50	8.75
Undulator taper ($r_{\text{pipe}} = 3\,\text{mm}$)	18	-0.61	0.37	0.36
Resistive wall ($r_{\text{pipe}} = 3\,\text{mm}$)	144 m	-0.98	0	0.69
Surf. rough. 0.5μm ($r_{\text{pipe}} = 3\,\text{mm}$)	144 m	-3.60	0.12	2.52

the outer wall and a 1 mm gap at its end. 4) The vacuum-chamber flange is an approximation of a Varian flange with a 2.5 mm outward radial step, a 10 mm long and a 2 mm thick gasket extends 2 mm radially inward from the larger diameter. 5) The gate valve was approximated by a 12 mm diameter tube 5 mm long connected to the beam pipe with 40° tapers. 6) The tapered undulator chambers were simulated by a radially-inward taper to 5 mm radius pipe with the taper length of 25 mm. MAFIA was used to calculate the ion-clearing electrodes as two opposite diamond-shaped plates, 25 mm long and with a 30° taper at their ends. Each undulator is preceded by a protector collimator with a 5 mm aperture. Because this is larger than the 3 mm undulator apertures, the protectors have been neglected in Tab. 2.1.3.

For the full beam traversal, Tab. 2.1.3 gives the number or total length of the components, the maximum excursions of the wakefield within 3σ of the center of the bunch, and the loss parameter. It shows that along with the 7-cell RF Cavity structures, the surface-roughness and resistive-wall wakefield in the standard beam pipes (12.7 mm radius) and surface roughness of the undulator beam pipes (3 mm were used here) are the most important contributors to the ERL wakefield. The surface-roughness parameters for the standard beam pipe and undulator beam pipe were 3 μm and 0.5 μm, respectively.

Since in general the maxima and minima of the wakefields for different components do not occur at the same position s, the individual wake functions must be summed to compute the total ERL wakefield, which is seen in Fig. 2.1.54. The peak-to-peak variation of the wakefield over the bunch distribution is 30 kV/pC, just below the impedance limit. The calculations give a value of 24 kV/pC for the ERL loss parameter k_{loss} and a predicted power loss of 180 kW distributed fairly uniformly around the ERL for the 100 mA circulating beam. Note that as our design evolves, these wake estimates will evolve accordingly.

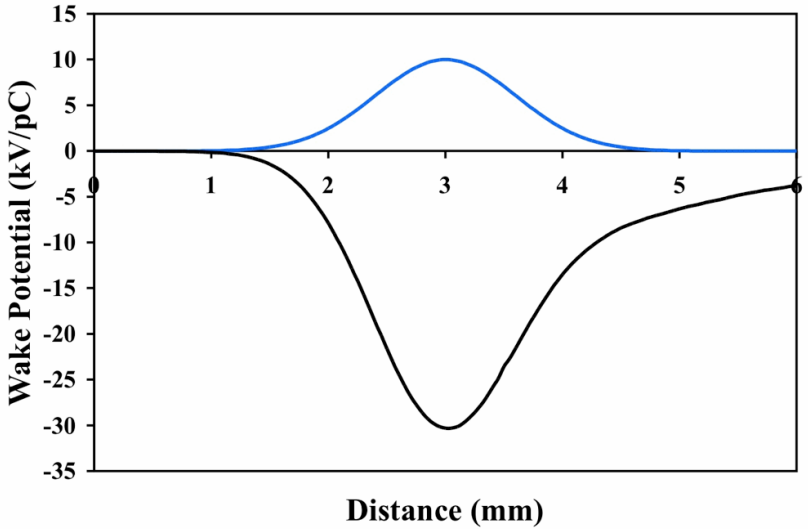

Figure 2.1.54: Total wakefield (lower trace) of the components in Tab. 2.1.3 for a Gaussian-shaped bunch (upper trace.) The peak-to-peak variation of the wakefield is 30 kV/pC.

CSR wakes

When a charged particle is transversely accelerated in a bending magnet, it produces radiation according to the well-known synchrotron radiation spectrum. When N such particles are bunched on a scale of length σ, the power spectrum per particle at frequencies smaller than c/σ in this spectrum is enhanced by roughly a factor N. This results in increased radiation, and hence increased energy losses from the individual particles. This coherent synchrotron radiation was first calculated in a seminal paper by Schwinger [33].

Here the CSR wake $W_{\mathrm{CSR}}(z)$ is the energy change per unit length of a particle with longitudinal position z in a bunch, and it can be shown that for ultra-relativistic particles this $W_{\mathrm{CSR}}(z)$ scales with the factor

$$W_0 = N r_c m c^2 \left(\frac{\kappa}{\sigma^2}\right)^{2/3} \tag{2.1.17}$$

where m is the mass of a single particle, r_c is its classical electromagnetic radius, and κ is the trajectory curvature (e.g. see [2]).

Additionally, the low frequencies of the radiation spectrum are 'shielded' when the particles travel inside a conducting structure. In [33], Schwinger calculated the radiation spectrum for particles traveling in a circle between two infinite conducting parallel plates, and concluded that the lowest frequencies are suppressed depending on the plate separation h, as well as κ and σ. His formulas, however, are difficult to evaluate numerically due to the presence of very high-order Bessel functions, but fortunately an excellent approximation for ultra-relativistic particles can be found in the appendix of [34]. Some manipulation reveals that this suppression depends entirely on the shielding parameter

$$b_s = h \left(\frac{\kappa}{\sigma^2}\right)^{1/3} \tag{2.1.18}$$

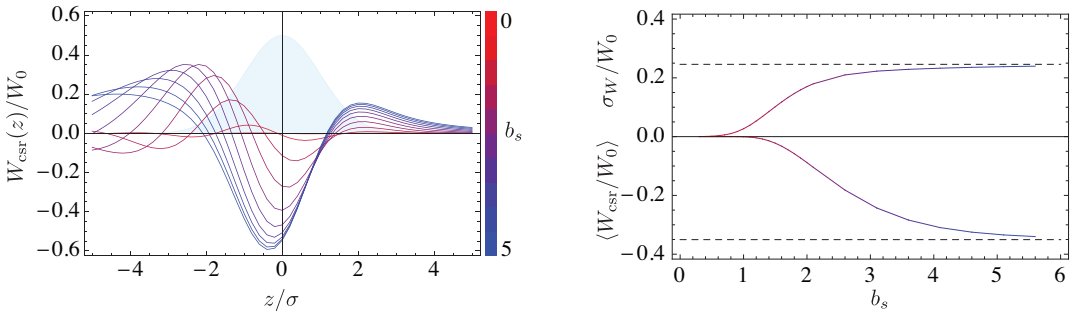

Figure 2.1.55: Normalized shielded steady-state CSR wakes $W_{\rm CSR}$ for a Gaussian bunch of length σ, along with average energy loss and energy spread from these curves for various shielding parameters b_s.

and the longitudinal bunch density (see section 5.2.2 in [35] and a heuristic argument in [22]).

To visualize this suppression, Fig. 2.1.55a shows the CSR wakes for a bunch with Gaussian longitudinal density for various b_s. The averages and standard deviations of these wakes over the distribution are shown in Fig. 2.1.55b and reveal that shielding plays a significant role when $b_s \lesssim 3$. The dashed lines are drawn at the limiting values of these curves, and are approximately -0.35 and 0.25. This is the 'free-space' regime.

Using the design bunch lengths, Fig. 2.1.56a show b_s for operating modes A, B, and C in all of the bends in the ERL. This plot suggests that CSR in modes A and B will be strongly shielded, but that mode C will not be, especially in the short pulse region. For a more accurate CSR calculation we use Bmad, which simulates shielding using the image charge method, and is able to calculate all of the entrance and exit transient effects that are not seen in curves like Fig. 2.1.55a. This code has been benchmarked against other codes as well as analytical formulas in [22].

Figure 2.1.56b shows the cumulative energy losses due to CSR by tracking particles through the ERL lattice, along with estimates from the values in Fig. 2.1.56a. As expected, modes A and B are well shielded, but mode C suffers energy loss in the short pulse region. Nevertheless, CSR does not limit the bunch compression process, as shown in Fig. 2.1.57a (also previously suggested in Fig. 2.1.46) with the CSR calculation turned on and off.

Finally, even though CSR does not limit the compressed bunch length, we must check that this bunch can still be decompressed for energy recovery. The relative energy distribution after deceleration to 10 MeV for mode C is shown in Fig. 2.1.57b.

Compensation of wakefield effects

As seen in §2.1.14, the energy spread within the bunch caused by wakefields from the vacuum chamber structures places an important limitation on both the vacuum chamber design via the impedance budget for the ERL and the design of the accelerator in the vicinity of the beam stop. Several methods have been explored for partially compensating the effects of the wakefields in order to relax some of the design constraints and to allow for larger operational

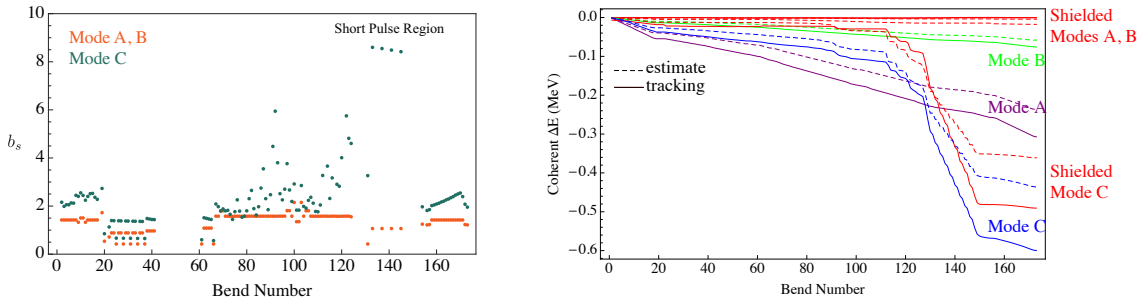

Figure 2.1.56: The shielding parameter b_s at all bends in the Cornell ERL for the different bunch operation modes is shown in Fig. 2.1.56a. Modes A and B use the same optics, and bunches in this mode have durations of $\sigma_z/c \simeq 2\,\text{ps}$, and mode C compresses the bunches to 100 fs. Figure 2.1.56b shows an estimate for the cumulative coherent energy losses through these bends using the bottom curve in Fig. 2.1.55b, along with particle tracking results from Bmad that take into account all entrance and exit transients for the CSR wake.

margin.

The correlated energy spread of the bunches may be reduced by decreasing its slope and curvature in the time-energy phase space. One class of possible solutions utilizes the acceleration of the bunch off-crest in the Linacs, an energy-dependent time-of-flight transport followed by acceleration of the bunch off-crest in the Linacs. Three options for the location of the time-of-flight transport for this method were explored, 1) in CE, 2) in a single turn-around arc for both accelerated and decelerated beams and 3) two turn-around arcs TA and TB, one for each of the beams [36].

When the necessary time-of-flight transport is added to 1) the CE arc, the beam must be accelerated off-crest and admitted into CE with a first-order phase-space energy correlation, which produces a large energy spread that will broaden the x-ray spectrum undesirably in the experimental regions, making this possibility unfeasible. For solution 2) with the common turn-around loop, it is necessary to operate the two Linacs off the RF field crest by $\Delta\phi$. However, the curvature correlation added to the time-energy phase space in the first pass through the common turn-around arc is removed in the beam's second pass through the arc. This method does not permit the compensation of even-order time-energy correlations.

However, method 3) with two turn-around loops permits different time-energy correlations to be created in the each arc thereby allowing independent reduction of the beam energy spread in the CESR arc and at the beam stop. Simply using the independent phasing of the two Linac sections reduces the energy spread by about a factor of 3 [36]. From these considerations it was concluded that two separate turn-around arcs are necessary to accommodate a reduction in the beam energy spread.

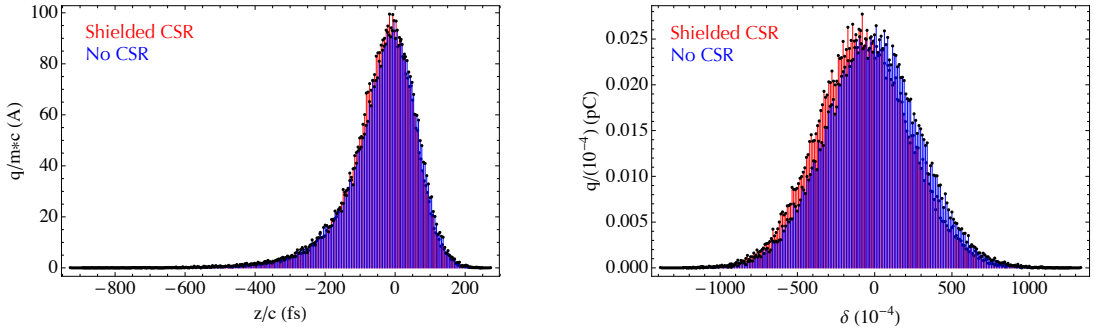

(a) Fully compressed longitudinal current distribution, at 5 GeV

(b) Relative energy distribution after deceleration to 10 MeV

Figure 2.1.57: The longtudinal current distribution in the final undulator for the compressed mode C, as well as the relative energy distribution just prior to the beam stop demerger, from particle tracking in Bmad (with and without the CSR calculation).

2.1.15 Start-to-end simulation

Overview

The ERL lattice is designed assuming perfect alignment and field qualities of all components. Electron bunches injected with the design phase-space distributions will still experience some distortions due to, for example, incoherent synchrotron radiation and geometric optical aberrations, but will do so in predictable ways. Unfortunately the actual machine built will not have such perfect qualities, and furthermore, many of the errors in this machine will not be known *ab initio*. Particles injected into this realistic machine should be kept near the design orbit, and to that end a set of beam position monitors (BPMs) and orbit corrector coils are installed in the lattice. This scheme is described below, along with an analysis of allowable tolerances in the ERL.

Additionally, the collective effects of space charge and CSR influence the bunch distributions in ways that require computationally intensive particle simulations in order to obtain reasonable estimates. Fortunately space charge is only a dominant effect at low energies, and has already been taken into account in large multi-objective optimizations described in §2.1.4 using the code GPT.

Start to end simulations must therefore first deal with errors in the model and their compensation by orbit correction, and then proceed to particle tracking.

Orbit correction

To understand the capabilities of modern orbit correction schemes, consider the following achievements at existing facilities. At the Advanced Photon Source (APS), extensive incremental improvements to orbit stabilization systems have been made since the machine went in operation in 1996. The strategy for achieving true sub-micron orbit stability at the APS has been to study and compensate for multiple systematic effects and noise sources, enhance orbit correction feedback systems, and employ feed-forward methodology where applicable [37]. At the European Synchrotron Radiation Facility (ESRF), in addition to a slow orbit correction (every 5 minutes), a fast global feedback system (4.4 kHz) is implemented to correct, in the vertical direction, the fast orbit distortion caused by quadrupole magnet vibrations [38]. Similarly, a slow correction procedure is used at ELETTRA to counteract slow orbit motions and drifts due to thermal effects, while a number of local fast orbit feedback systems are installed to correct faster orbit disturbances generated by ID gap changes, by vibrations of the quadrupole magnets and by ripple of the magnet power supplies [39]. At SPring-8, sub-micron orbit stability is achieved not by the feedback systems alone, but by thorough source suppression as a first step and some proper feedback correction to push the stability up to the sub-micron level as a second step [40]. In the Swiss Light Source (SLS), long and short term orbit stability of the electron beam is achieved by dynamic alignment systems and by fast closed orbit feedback [41]. The SLS reproduces and stabilizes a previously established reference orbit within $1/10^{\text{th}}$ of the vertical beam size corresponding to $\approx 1\,\mu$m at the insertion devices (IDs) [42, 43]. Required and achieved orbit stability for these machines are listed in Tab. 2.1.4.

Orbit stabilization requires the maintenance of two different tolerances: uncorrected (jitters) and slower orbit changes that can be compensated by feedback. Here we show a detailed

Table 2.1.4: Orbit stability of third generation synchrotron light sources

Machine	Horizontal Orbit (μm)		Vertical Orbit (μm)	
	Requirement	Achieved	Requirement	Achieved
APS	14.0	12.6	0.45	0.59
ESRF	N/A	1.0	N/A	0.6
ALS	10.3	2	1.2	0.5
ELETTRA	5.0	0.85	5	0.47
Spring-8	28.0	4	0.4	1
SLS	N/A	1.0	0.7	0.6

Table 2.1.5: Counts for BPMs and correctors for all of the sections in the ERL.

	LA	LB	TA	TB	SA	CE	NA	Total
BPM	35	31	38	33	81	70	52	340
Corrector Pair	35	29	30	26	54	1	37	212
Horizontal Correctors	0	0	0	0	6	39	2	47
Vertical Correctors	0	0	0	0	4	37	3	44

analysis of the latter. The former is still under investigation.

An orbit correction scheme based on singular value decomposition (SVD) has been implemented in the Bmad and Tao simulation environments. This scheme minimizes the deviation of the orbit from the design reference, with monitors located at critical locations (such as undulators and collimators) receiving extra emphasis. Additionally, the strengths of the corrector coils are added to this minimization algorithm, so that unreasonably strong fields are not required. Finally, the dispersion is corrected at critical locations. An example of this correction is shown in Fig. 2.1.58. Note that the physical orbit correction system is described in §2.10.2 and §2.10.3.

The number of and placement of monitors and correctors has also been optimized using SVD decomposition techniques on the generalized response matrices from correctors and errors to monitors. See, for example, [44]. Counts of these devices, per section, are shown in Tab. 2.1.5.

Many errors are simulated for the ERL, and are listed in Tab. 2.1.6. For example, magnetic field errors caused by power supply fluctuations can affect both the particle orbit and the optics [45]. Magnetic field fluctuations can cause wrong beam steering that leads to emittance growth and thus increase the beam size at the ID sections. Similarly, quadrupole field errors can affect the beta function and phase advance in both vertical and horizontal directions. Furthermore, a combination of dipole field errors and quadrupole field errors, although a second-order effect, can have a significant impact on the particle's orbit in the insertion devices. In addition to power supply fluctuations, the misalignment of accelerator components can lead to orbit distortions and beam-emittance dilution. A misaligned quadrupole magnet can create, in addition to the quadrupole field for beam focusing, an effective dipole field that will introduce unwanted dispersion. An RF cavity with a pitch angle can accelerate the beam in off-axis directions, and thus produce time-varying transverse deflections that lead to emittance growth.

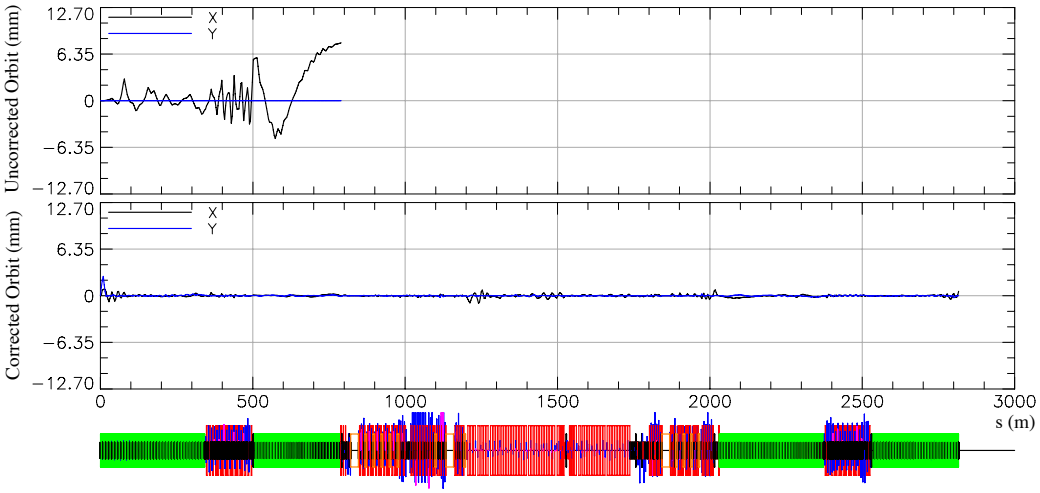

Figure 2.1.58: Examples of the beam orbit before and after correction.

The baseline values listed in Tab. 2.1.6 represent what we estimate is achievable in alignment and field quality of elements in the machine. To further analyze the tolerances of these various errors, we use the procedure in Tab. 2.1.7, which leads to the allowable errors in Tab. 2.1.6. These rms limits are determined by allowing a 10% increase in the projected emittance or beam size, or allowing a 10% of the correctors to have more than 0.5 mrad maximum angles.

For example, we find that *in addition to all of the baseline errors*, if we further misalign all quadrupole horizontal positions by 300 μm, then the horizontal corrector strenghts C_x needed to correct such errors is unacceptably large. Because the baseline quadrupole horizontal offset was already 120 μm, this means that this unacceptably misaligned machine actually has rms quadrupole offsets of about $\sqrt{120^2 + 300^2}\,\mu\text{m} \approx 323\,\mu\text{m}$.

Statistics for emittance and beam size at all undulators for mode B, from $N = 100$ randomly misaligned ERLs, are shown in Fig. 2.1.59. These values should also apply to mode A, because mode B uses the same optics but has a smaller initial emittance. Note that the jump in horizontal emittance from undulator 9 to undulator 10 is almost entirely due to ISR in the CE section, as previously suggested in Fig. 2.1.35. Analysis of mode C is still in progress.

Table 2.1.6: Errors considered in ERL simulations for the low emittance mode B. Baseline numbers are rms values with a cutoff at 3 times his value. The symbols C_x and C_y deonote horizontal and vertical corrector strengths, respectively. The symbol+ indicates the maximum rms error simulated, without significant effect. OC indicates the failure of the orbit correction algorithm.

Error	Unit	Baseline (1σ)	Allowable (1σ)	Primary effect
Quadrupole x offset	μm	120	300	C_x
Quadrupole y offset	μm	100	250	C_y & OC
Sextupole x offset	μm	120	300	σ_y
Sextupole y offset	μm	100	200	ϵ_y & σ_y
Cryomodule quad x & y offset	μm	300	1600	C_x & C_y
Dipole roll	μrad	80	1000	ϵ_y
Quadrupole roll	μrad	80	200	ϵ_y
Dipole x & y pitch	μrad	80	5000+	ϵ_y
Quadrupole x & y pitch	μrad	80	1000+	ϵ_y
Acc cavity x & y offsets	μm	500	2000	σ_y & OC
Acc cavity x & y pitch	μrad	1000	1500	ϵ_x & ϵ_y & OC
Acc cavity gradient	relative	10^{-4}	60×10^{-4}	σ_y
Acc cavity ϕ_{rf}	degree	0.1	1.0+	σ_y
Dipole chain field	relative	10^{-4}	10×10^{-4}+	
Quadrupole k_1	relative	10^{-4}	5×10^{-4}	σ_y
Sextupole k_2	relative	10^{-4}	10^{-3}+	

Table 2.1.7: Tolerance analysis procedure. Typically this procedure is iterated for $N = 100$ times.

Step	Procedure
1	Initialize design lattice
2	Calculate orbit and dispersion response matrices
3	Enable synchrotron radiation losses and fluctuations
4	Perturb the lattice with all of the baseline errors listed in Tab. 2.1.6
5	Additionally perturb the property to be analyzed
6	Apply the SVD orbit correction algorithm
7	Save this perturbed lattice
8	Track particles through, and save statistics at all undulators
9	Reset the lattice
10	Repeat steps 4-9 N times

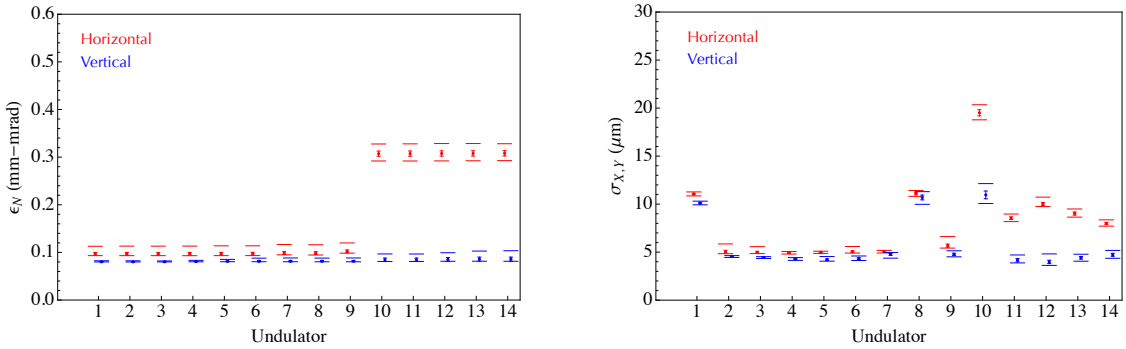

(a) Mode B emittance

(b) Mode B beam size

Figure 2.1.59: Statistics for $N = 100$ randomly misaligned ERL lattices, after orbit correction, at all of the undulators. Mean values are shown as dots, with attached error bars at one standard deviation. The maximum and minimum values encountered are shown as separated long bars. It is apparent that the standard errors hardly damage the emittance.

Full simulation

Table 2.1.8: Relevant start to end simulation parameters.

Parameter	mode A	mode B	mode C	unit
$\epsilon_{N,x}$ injected	0.29	0.11	0.19	mm mrad
$\epsilon_{N,y}$ injected	0.24	0.10	0.14	mm mrad
σ_z/c injected	2.11	1.52	1.00	ps
σ_δ injected	1.66	0.66	1.17	10^{-4}
$\phi_{\rm rf}$ for LA and LB	0	0	6.6	degree

To perform full simulations for the ERL, favorable particle distributions are chosen from Fig. 2.1.11 to represent realistic bunches at the end of the first cryomodule in LA. Some relevant properties of these bunches are listed in Tab. 2.1.8. Note that these properties deviate somewhat from the design values in Tab. 1.3.1.

For modes A and B, articles are then tracked through the remainder of the machine with Bmad using a misaligned (and orbit and dispersion corrected) lattice, according to the baseline errors in Tab. 2.1.6. Mode C is tracked using an unperurbed lattice, because the full error analysis for this mode is not yet complete. The resulting emittance and bunch durations at all undulators are shown in Fig. 2.1.60.

In particular, the plot in Fig. 2.1.60a is consistent with Fig. 2.1.59, and shows that the emittance growth is well controlled everywhere except for the CE section between undulators 9 and 10. For modes A and B, the usage of the more 'realistic' bunches from GPT incur no additional effects over the more simple Gaussian bunches used in the orbit correction and tolerance simulations. The compressed bunch duration of mode C particles in Fig. 2.1.60b is approximately 120 fs, but this is likely can be shortened to 100 fs by minor changes in r_{56} and/or the accelerating phase, as suggested in §2.1.10. Figure 2.1.61 shows the transverse phase space at the center of the first undulator for the emittance sensitive modes A and B.

Finally, it must be checked that these particles have an acceptable energy spread after deceleration, just prior to the demerger before the beam stop. Figure 2.1.62 shows δ distributions for all three modes, all of which have an rms energy spread of $\sigma_\delta \approx 3\%$. All particles similated lie completely within $\delta = \pm 15\%$.

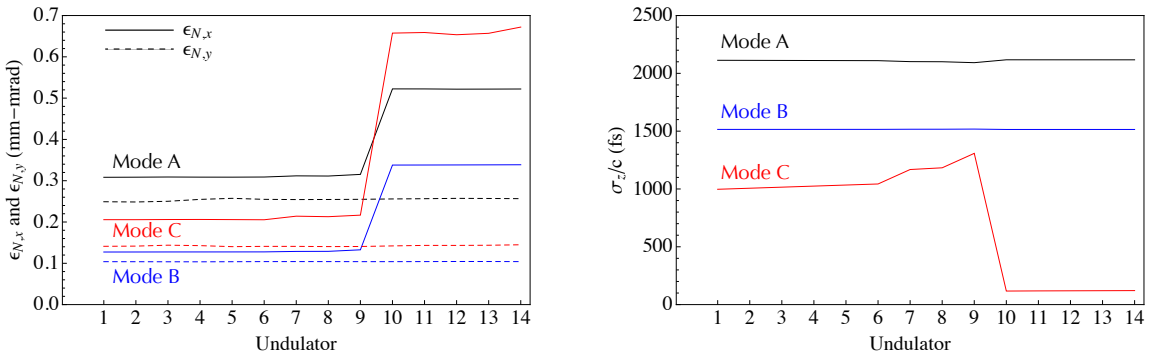

Figure 2.1.60: Emittances and bunch durations for all of the ERL operating modes. Particles are generated from the laser pulse on the cathode, and simulated through the end of the first LA cryomodule using the code GPT (see §2.1.4). These particles are then imported into Bmad, with properties listed in Tab. 2.1.8, and tracked through a lattice that has been misaligned (and orbit and dispersion corrected) according to the baseline errors in Tab. 2.1.6.

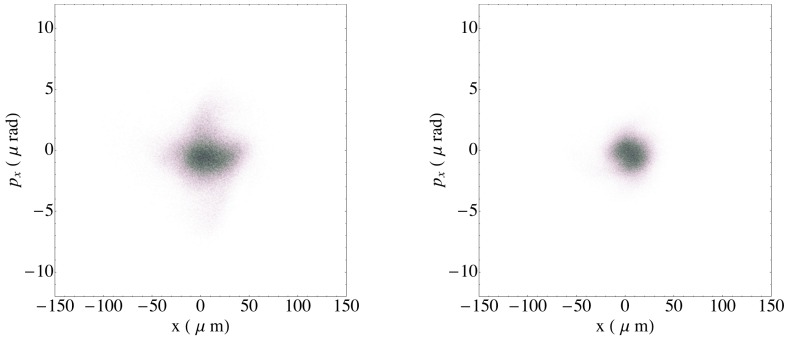

(a) Mode A, $\gamma\epsilon_x = 0.31\,\text{mm mrad}$

(b) Mode B, $\gamma\epsilon_x = 0.13\,\text{mm mrad}$

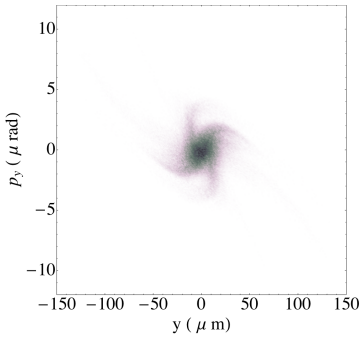

(c) Mode A, $\gamma\epsilon_y = 0.25\,\text{mm mrad}$

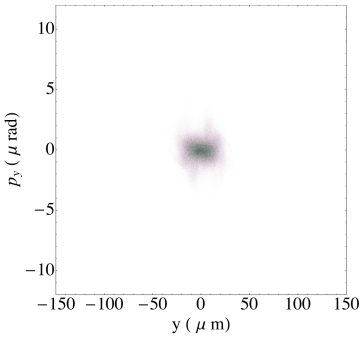

(d) Mode B, $\gamma\epsilon_y = 0.10\,\text{mm mrad}$

Figure 2.1.61: Transverse phase-space distributions at the center of undulator 1 for modes A and B. These plots are are the result of splicing the 200,000 particle output of GPT (with parameters listed in Tab. 2.1.8) with a misaligned and orbit corrected Bmad lattice.

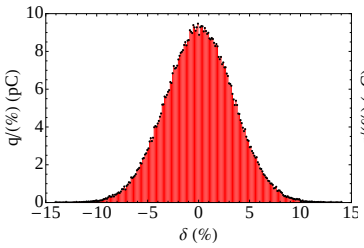

(a) Mode A

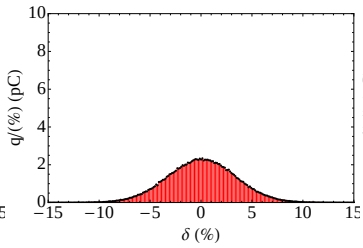

(b) Mode B

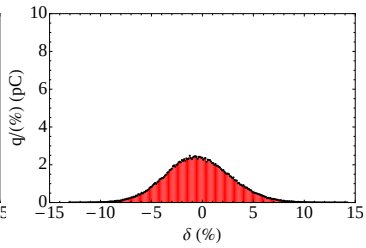

(c) Mode C

Figure 2.1.62: Final relative energy distributions just prior to demerger before the beam stop. The reference energy is 10 MeV. The standard deviation of δ for all modes is approximately 3%.

2.1.16 Beam instabilities

Introduction

Beam-breakup (BBU) instabilities of several varieties impose operational current limitations on energy recovery Linacs and other types of recirculating linear accelerators. In recent years the continuous-wave theory for recirculating Linacs [46] has been extended to energy-recovery Linacs and quantitative studies of mitigating effects have been published [47].

Transverse dipole BBU

Transverse dipole BBU instabilities arise from the one-turn T_{12} term coupling beam displacement and kick in the RF cavities. Like the longitudinal and quadrupole instabilities described below, the transverse dipole instability thresholds have been calculated using the detailed lattice analysis and design software package Bmad developed at Cornell for CESR and other projects. An approximation to the threshold current in the case of a single HOM in a single cavity is given by

$$I_{\rm th} = -\frac{\omega_\lambda}{e\left(\frac{R}{Q}\right)_\lambda Q_\lambda}\frac{1}{T_{12}^* \sin\omega_\lambda t_r} T_{12}^* = T_{12}\cos^2\theta_\lambda + \frac{T_{14}+T_{32}}{2}\sin 2\theta_\lambda + T_{34}\sin^2\theta_\lambda \qquad (2.1.19)$$

where $(R/Q)_\lambda$ is the shunt impedance, Q_λ is the quality factor, θ_λ is the polarization angle from the x direction, ω_λ is the HOM frequency, t_r is the bunch return time, e is the elementary charge and the matrix $\mathbf{T}$ describes how transverse momentum is transported to a transverse displacement after one turn.

A validation of the Bmad tracking calculation for a simplified case of the ERL optics is described in [48] . The Bmad tracking code is used to compute the BBU threshold current for the HOMs of a preliminary cavity design, shown in Tab. 2.1.9. The frequency spread for HOMs of different cavities must be made as large as $\sigma_f = 10$ Mhz to obtain the large threshold currents shown in Fig. 2.1.63. To obtain a trustworthy estimate of the threshold current, we compute it for 120 random seeds for the HOM frequency spread and use the average and rms values of the results as judgement criteria. The average single-turn instability threshold is $I_{\rm th} =$ 1083 mA with an rms spread of $\sigma_{I_{\rm th}} = 127$ mA. The worst case of 700 mA provides a factor of seven margin over the ERL design current. Subsequently we varied the cavity geometry to further increase a) the threshold current and b) the insensitivity to cavity production errors.

Table 2.1.9: Higher-order-mode parameters from the optimized cavity design, used in the BBU threshold modeling

HOM	f_λ (MHz)	Q_λ	R/Q (Ω/ cm^2)
1	1708.4	826	5.7932
2	1856.3	2781	2.8852
3	1870.8	3539	4.0064
4	2552.3	1579	7.7736
5	3078.9	93360	0.3617

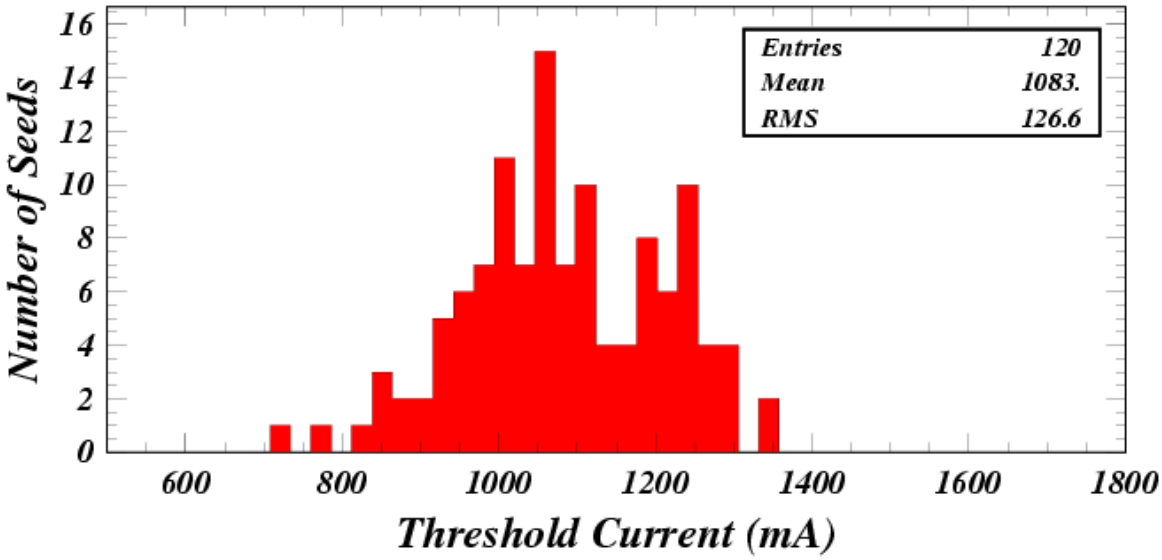

Figure 2.1.63: Modeled BBU instability thresholds for the case of the five HOMs in Tab. 2.1.9 excited in each cavity of the full ERL 7.4 optics. A HOM frequency spread of 0.33% was introduced, re-randomized for each of the calculations.

The resulting optimized cavity shape is shown in §2.4. With realistic, cylindrically-symmetric construction errors of up to 1/8 mm, this cavity design shows a threshold current of 450 mA. For these simulations, the HOM parameters are implemented in all cavities, and a randomized HOM frequency spread of 0.33% of the HOM frequency is applied to each calculation.

One means of mitigating the beam breakup effect even further is to introduce an X-Y coupling in the optics and to polarize the HOMs in the cavities. To calculate the degree of improvement which can be obtained, a coupling element was introduced between the Linacs and polarized HOMs were implemented in each cavity. For the cavities used in this study, X-Y coupling increased the threshold current from about 400 mA to 2200 mA [47]. This means of BBU instability mitigation can provide an additional margin of about a factor of five. No specific plan to implement such a mitigation technique is being developed, since the BBU instability limit is sufficient without it, polarized cavities are more difficult to produce, and there is little operational experience with such cavity designs.

Transverse quadrupole BBU

Quadrupole HOMs can be excited by beams with a nonzero quadrupole moment. Their effect is to distort the linear optics by providing additional focusing. The threshold current due to a quadrupole kick at position 1 acting at position 2 for a single HOM with frequency ω_λ, shunt impedance $\frac{R}{Q}_\lambda$ and quality factor Q_λ in a single cavity can be approximated by

$$I_{th} = -\frac{\omega_\lambda \gamma E_e}{2\frac{ec}{r_0^4}\left(\frac{R}{Q}\right)_\lambda Q_\lambda \varepsilon_n} \frac{1}{(\beta_{x1}\beta_{x2}\sin 2\Delta\psi_x + \beta_{y1}\beta_{y2}\sin 2\Delta\psi_y)} \frac{1}{\sin \omega_\lambda t_r} \tag{2.1.20}$$

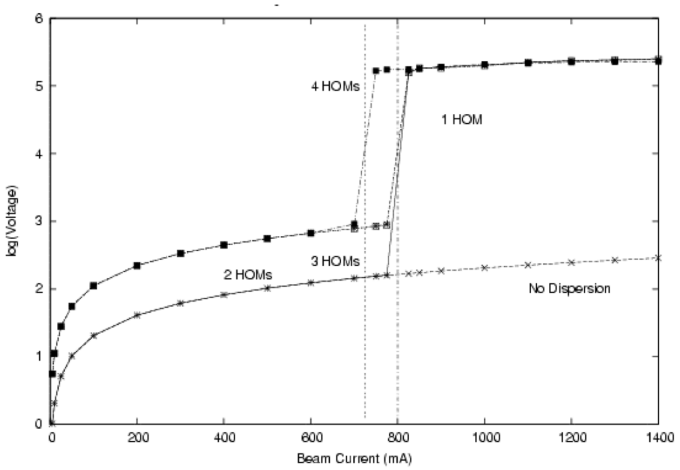

Figure 2.1.64: B.1 49: Longitudinal higher-order mode excitation voltage versus beam current as calculated in [50]

.

where E_e is the beam energy, ε_n is the normalized emittance, and r_0 is the radius where $\left(\frac{R}{Q}\right)_\lambda$ is measured. The $\Delta\psi$ values are the differences in betatron phase and t_r is the time difference between positions 1 and 2.

Such instabilities have been studied in [49] for typical HOM parameters and for the beam quadrupole moment derived from the difference of horizontal and vertical beta functions in the ERL linear optics. The instability threshold current was found to be above 200 mA as long as the HOM Q_λ is less than about half of the cavity Q_0 for the fundamental mode.

Longitudinal BBU

Longitudinal instabilities can be caused by excitation of longitudinal higher-order modes (HOMs) in the RF cavities by the beam bunches. The time-of-flight term r_{56} plays an important role in the excitation of such instabilities, since the main effect of the longitudinal HOM is to change the bunch energy. These instabilities have been studied in [50]. Figure 2.1.64 shows the limits obtained for various HOM configurations in an ERL lattice model. The conclusion of this study is that instability threshold level will far exceed the ERL design operating current of 100 mA as long as the magnitude of r_{56} is well below 10 m. The threshold current is inversely proportional to r_{56} and increases with HOM frequency spread in the cavities as well. For nominally isochronous lattice of the recirculating arc ($r_{56} \approx 0$ for all operating modes), the longitudinal BBU poses no threat.

2.1.17 Collimation

During operation of any high-energy accelerator, particles are lost along the beam transport. There are several processes that produce beam halo and electron loss in the Cornell ERL. Two dominant and unavoidable mechanisms are Touschek scattering and electron scattering off residual gas nuclei. Of the two, Touschek scattering is by far the dominant process but rest-gas scattering dominates losses in the vertical plane. Although the fraction of electrons lost is typically less than 5×10^{-6}, this loss has non-trivial consequences.

The beam loss due to these mechanism has been simulated to place collimators effectively to perform two essential functions. One is to protect areas occupied by personnel or sensitive equipment, and the other is to protect insertion devices. The 5 GeV electrons intercepted by the collimators generate an electron-photon cascade, and the energetic neutrons and photons produced in the cascade create a radiation hazard. Accordingly, the design of collimators is such as to reduce the resulting radiation field as much as possible in the vicinity of the lost particles. This in turn ensures that shielding walls of a reasonable thickness can be used to reduce radiation exposure in areas occupied by personnel to safe workplace levels. Based on 2000 hours of occupancy per year, these are 100 mrem/y for visitors, and 500 mrem/y for radiation workers (see §4.6.4).

Protection criteria for insertion devices are based on 5000 hours of operation per year, and are discussed in more detail below. The design of the various collimators was evaluated using the extended many particle Monte Carlo code MCNPX v.27d [51] and further details are discussed in [52].

Touschek scattering

Collisions among particles within a bunch can change their trajectories so much that they are transported to large amplitudes and constitute a beam halo, or are lost at the vacuum pipe. This loss mechanism is referred to as Touschek scattering. Bremsstrahlung is produced when the particles collide with the beam pipe, and collimators have therefore been designed to avoid radiation hazards to hardware and personnel. These collimators are placed in the tunnel and away from x-ray user regions. Relatively small losses can damage the permanent magnets of undulators and a protector device is therefore placed in front of every undulator.

To determine where collimators are to be placed, Touschek scattering has been simulated and the trajectories of scattered particles were followed to their loss point. These simulations are based on [53] and [54], which has been validated in storage-ring-lifetime measurements [55]. Following scattered particles shows where a collimator will intercept most particles which would otherwise be lost in sensitive regions, and it was also studied where these particles have scattered so that the beam optics in these regions can be changed to minimize Touschek scattering.

2.1.18 Gas scattering

Residual-Gas Scattering (RGS) refers to a beam-loss process resulting from electron collisions with residual gas molecules in the beam pipe. To avoid that resulting loss of beam particles along the chamber walls pose a hazard to hardware or personnel, it has been studied whether the ERL's collimators manage these losses adequately. It is found that RGS contributes about

Table 2.1.10: Touschek losses for protectors P and collimators M shown in Fig. 2.1.65

Protector	P2	P3	P4	P5	P6	P7	P8	P9	P10	P11	P12	P13	P14
I(pA)	0	0	0.01	0.37	0.18	46	147	58	1360	0.01	0.04	0.09	0.14

Collimator	M1	M2	M3	M4	M5	M6
I(nA)	31.7	7.85	110	163	136	2.17

0.2% of the total flux of lost particles, while Touschek-losses contribute 99.8% [56] for ERL parameters. However, while Touschek scattering leads to particle losses in the horizontal plane, rest-gas scattering produces losses in every direction. This is due to the fact that rest-gas scattering changes the electron trajectory with equal likelihood in any direction, whereas Touschek scattering mostly changes the energy of scattered particles, and particles with change energy are bent incorrectly in the horizontal plane by subsequent magnets.

RGS is well-understood and experimental observations in storage rings are documented at [57, 58]. Equations for the scattering cross-section are available at [59]. These show that even at the very low pressures of the ERL beam pipe, the rate of collisions between beam particles and gas particles will be high enough to require detailed studies. A simulation was used that generated scattered particles according to the rest-gas scattering cross section at every step along the accelerator and follows these particles to where they are lost. This shows whether collimators are suitably placed and whether protectors shield undulators adequately.

It is worth noting that the simulation methods and collimation techniques applied to RGS have much in common with those used for Touschek losses. Both RGS and Touschek losses are due to single-event scattering processes that change the phase-space coordinate of the colliding particles, resulting in particle loss downstream of the scattering event. Both processes can be succinctly described by distribution functions that give the rate at which particles with perturbed phase-space coordinated are generated. Finally, the primary method for mitigating the detrimental effects of each process is the strategic placement of collimators. We therefore employ a unified method to model halo production and collimation that can be extended to further processes that add to the beam halo.

Another method for mitigating RGS would be a lowering of the gas pressure to below the average rate of 1 nTorr that has been used for this report. Additional vacuum pumps would have to be installed in regions where the scattering rate is high.

Collimator layout

The overall layout of the collimators in the ERL as determined by simulation is shown in Fig. 2.1.65. The Touschek-current intercepted by each of these collimators is given in Tab. 2.1.10. The 'P' collimators protect undulators, while the 'M' collimators remove larger currents. The two types of collimators are discussed separately. A typical probability distribution of Touschek particles as a function of position incident on a protector/collimator is shown in Fig. 2.1.66

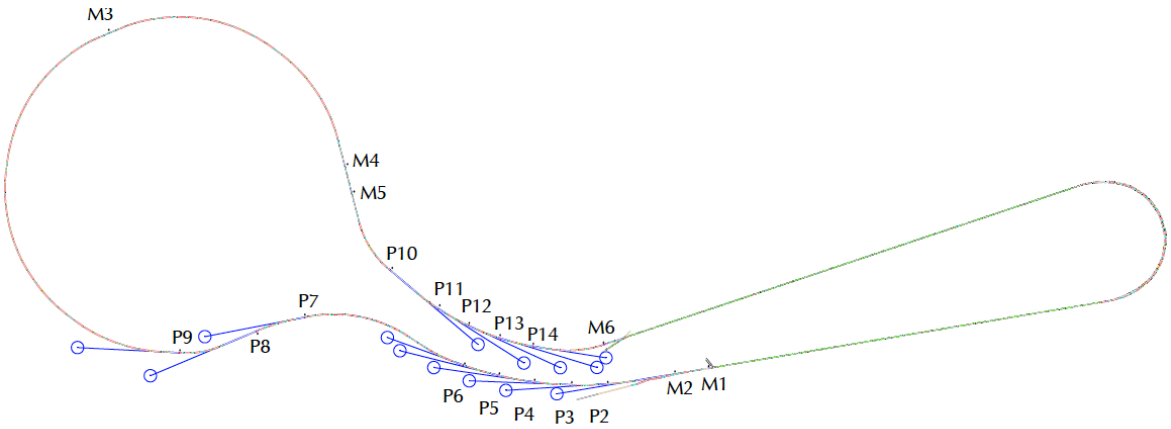

Figure 2.1.65: ERL protector and collimator layout

Undulator protectors

Undulator protectors P2 through P6 are in the south arc, while P11 through P14 are in the north arc. (See Fig. 2.1.65.) In the south arc the protectors are located in the space bounded by shielding walls, while in the north arc (NA), the space is bounded by a shielding wall and the hillside to the north. The maximum current loss in this region is less than 0.37 pA. Undulator protectors P7 and P9 are located within a space bounded by shielding walls inside the Wilson Lab experimental hall. Undulator protector P9 is located within the CESR tunnel, and P10 is located in the underground tunnel joining CESR and the north arc.

Undulator protector design

The radiation field in the vicinity of the protector is dominated by bremsstrahlung. Accordingly, the general design criteria for the undulator protectors (and collimators) are based on the following. In passing through matter, electrons lose energy by radiation in collisions with atomic nuclei and electrons, and by ionizing collisions with atoms. At energies greater than the critical energy, E_c, energy loss by radiation dominates. E_c is approximately given by [60]

$$E_c = \frac{800}{Z + 1.24}\,\mathrm{MeV} \tag{2.1.21}$$

where Z is the pertinent atomic number. In the high energy limit, where the initial electron energy E_o is very much greater than the electron rest mass, $m_e c^2$, the electron energy is reduced by a factor of $1/e$ in a distance X_o, called the radiation length, and given by [60]

$$X_o = \frac{716\,A}{Z(Z+1)\log\left(287\,Z^{1/3}\right)}\,\mathrm{g/cm^2} \tag{2.1.22}$$

and where Z and A are the atomic number and weight. Most of the energy is carried away by energetic photons. These have large pair production cross-sections, and the photon energy is shared equally by the electron and positron produced. The electrons and positrons in turn

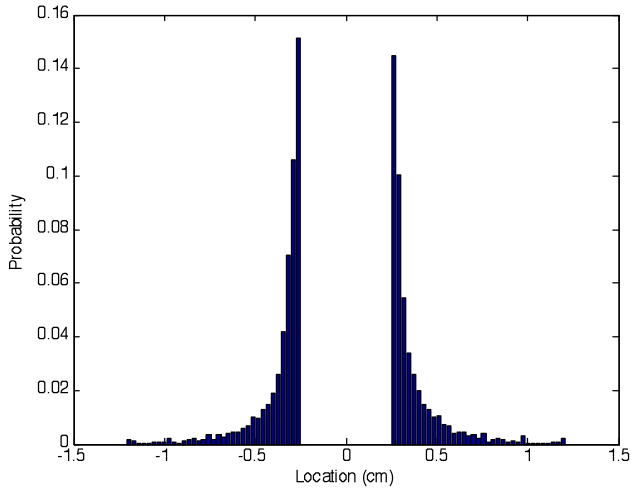

Figure 2.1.66: Typical probability distribution of Touschek particles as a function of position incident on a protector/ collimator

create more photons, which again produce electron positron pairs, and the process keeps on cascading until emission of energetic photons and pair creation can no longer take place.

The cascade process takes place in the same way in all materials if the thickness is measured in units of the radiation length X_o. For an initial electron energy E_o, the shower reaches a maximum at X_{max} where [61]

$$X_{max} = 1.01 \left[\log \left(\frac{E_o}{E_c} \right) - 1 \right] X_o. \tag{2.1.23}$$

The angular spread of the cascade shower is not large since at high energies both photon emission and pair production are directed forward, along the direction of the incident electron. The Moliere radius X_M characterizes the radial distribution of the cascade shower. X_M is given by[60]

$$X_M = \sqrt{\frac{4\pi}{\alpha}} \left(\frac{m_e c^2}{E_c} \right) X_o \tag{2.1.24}$$

where α is the fine structure constant.

In a given material characterized by radiation length X_o, 99% of the electron energy is deposited in a cylinder that is infinitely long, and $7X_M$ in diameter. [62] Accordingly, the diameter of the basic collimator is taken as $7X_M$. The collimator length depends on several factors. For 5 GeV electrons, the shower maximum ranges from $3.6X_o$ to $5.4X_o$ for the materials listed in Tab. 2.1.11. The distance traversed by an electron in order to reduce its energy from 5 GeV to E_c ranges from $4.6X_o$ to $6.3X_o$ for the same materials . Finally, the most penetrating photon shower component has energies near the Compton minimum ($E_{\mathrm{Compt.min}}$) in the photo-absorption cross section. Again, for the materials listed in Tab. 2.1.11, the mean free path for these energetic photons ranges from $1.9X_o$ to $3.8X_o$. Based on these considerations one would expect a collimator length of 10–$15X_o$ to be reasonable.

Table 2.1.11: General properties of possible shielding materials. Note that X_o and $X_{\text{showermax}}$ are measured here in cm.

Property	Element						Unit
	Al	Fe	Cu	Ta	W	Pb	
Density	2.70	7.87	8.96	16.65	19.3	11.35	g/cm^3
E_c	51.0	27.4	24.9	10.4	10.2	9.51	MeV
X_o	8.9	1.76	1.44	0.41	0.35	0.56	cm
$X_{\text{showermax}}$	32	7.5	6.2	2.1	1.8	3.0	cm
$\left(\frac{\mu}{\rho}\right)_{\text{Compt.min}}$	0.0215	0.0296	0.0304	0.0399	0.0403	0.0419	g/cm^2
$E_{\text{Compt.min}}$	22	9.0	8.4	3.7	3.7	3.6	MeV

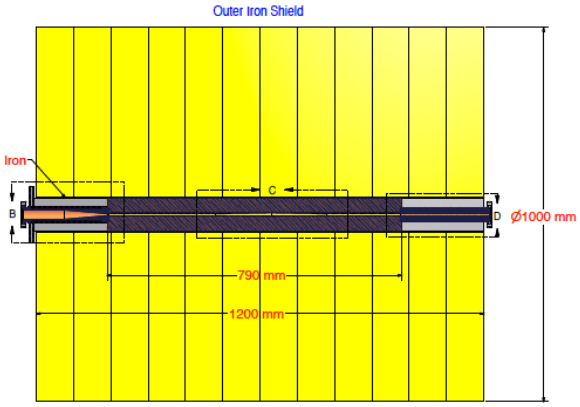

Figure 2.1.67: Cross section of protector

However, attenuation of photons is not the only concern. Energetic bremsstrahlung photons interacting with matter can also produce neutrons, protons, $\mu^{\pm}$, and $\pi^{\pm}$ mesons. Of particular shielding concern are photo-neutrons produced by 10–20 MeV photons via the giant dipole resonance mechanism.

The choice of collimator material thus depends not only on how well it attenuates photons and neutrons, but also on its activation tendency by neutrons, determined by the pertinent neutron reaction energy thresholds, neutron cross sections and resulting radionuclide half-lives. Attenuation of both photons and neutrons adds considerable mass to the basic collimator design. General properties of various possible shielding materials are shown in Tab. 2.1.11

A number of undulator protector designs were investigated. The undulator protectors are of the general form shown in Fig. 2.1.67.

Neutron and gamma shielding properties of the protector were investigated using MCNPX. The input geometry is cylindrically symmetric, of crossections and dimensions shown in Fig. 2.1.68. 5 GeV electrons with the probability distribution shown in Fig. 2.1.66 and directed along the x-axis of the collimator specified the incident particle source. In the calculations, particle tracks were terminated at 4.7 MeV for electrons, and 1.0 MeV for photons.

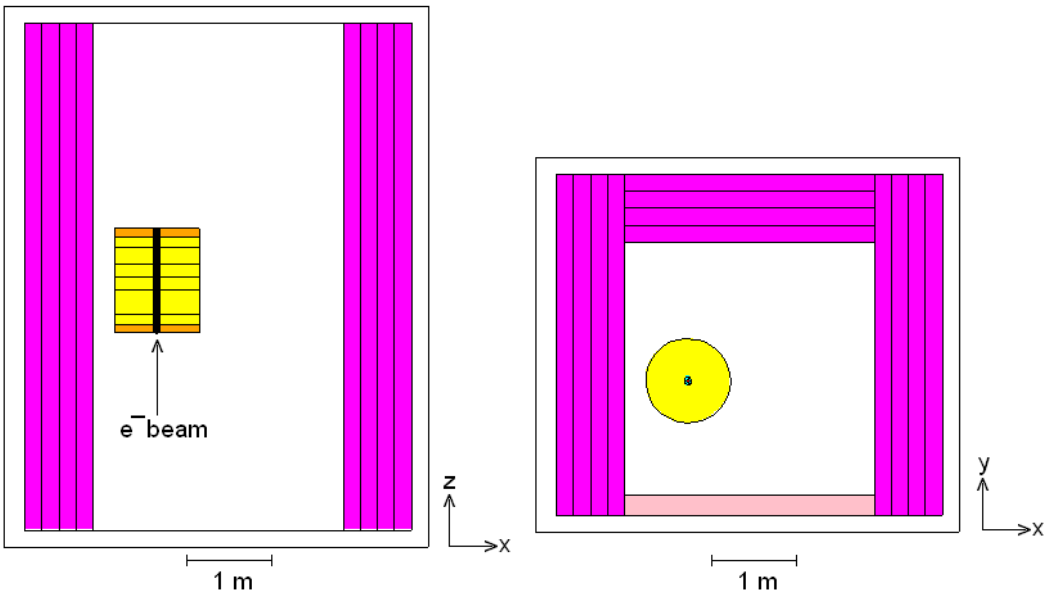

(a) Cut through the xz–plane at $y = 0$.

(b) Cut through the xy–plane at $z = 0$.

Figure 2.1.68: MCNPX input geometry to calculate neutron and photon dose rates. The center of the protector is at $(x, y, z) = (0, 0, 0)$. The electron beam propagates in the +z-direction. Yellow is iron, orange is lead, purple is heavy concrete, and pink is ordinary concrete.

Neutrons were followed down to 0.001 MeV. Typically, 5×10^5 particles were run to provide a relative tally error of less than 0.10. Standard flux and mesh tally data (normalized per starting particle) provided the required information. In MCNPX, the standard F2 tally records the number of particles of all energies (either photons, neutrons, or electrons) that cross a given surface, and tallies the average fluence (particles/ cm^2/incident particle). Similarly, the F6 tally records the energy deposited by particles averaged over a cell (MeV/g/incident particle).

In addition to the standard tallies, the mesh tally capability of MCNPX provides a means for graphically displaying particle flux, dose or other quantities on a rectangular, cylindrical or spherical mesh overlaid on the protector/collimator geometry. (To get the dose, the flux is modified by an energy dependent dose function.) The dose functions used for neutrons and photons in these calculations are the ICRP-21 1977 values. A more detailed comparison of the different and more recent AMSI/ANS standard dose functions will be carried out later.

Personnel protection

Figure 2.1.68 shows outlines of the MCNPX input geometry. Figure 2.1.69 and Fig. 2.1.70 show the neutron dose rate contours (rem/h)/(el/s) in the xz– and xy– planes through the center of the protector at $(x, y, z) = (0, 0, 0)$. From the figure, the contour at the outer surface of the 80 cm thick, heavy concrete shielding wall is 1.0×10^{-14} (rem/h)/(el/s), and similarly for the photon dose rate, Fig. 2.1.71 and Fig. 2.1.72 . The largest current, 0.37 pA, lost in

the north and south arc areas is on protector P5. For 2000 hours/year occupancy in the immediate vicinity of the shielding wall, this corresponds to a total annual dose of 0.1 mrem due to neutrons and gammas.

Protector P8 intercepts 147 pA, and for 2000 hours/year occupancy gives a total annual dose of 37 mrem due to neutrons and gammas. Protectors P7 and P8 give a total annual dose of 12 and 15 mrem due to neutrons and gammas. Protector P10 which intercepts the largest current, 1360 pA, is located in the tunnel between CESR and the north arc, and as such does not pose a hazard to personnel.

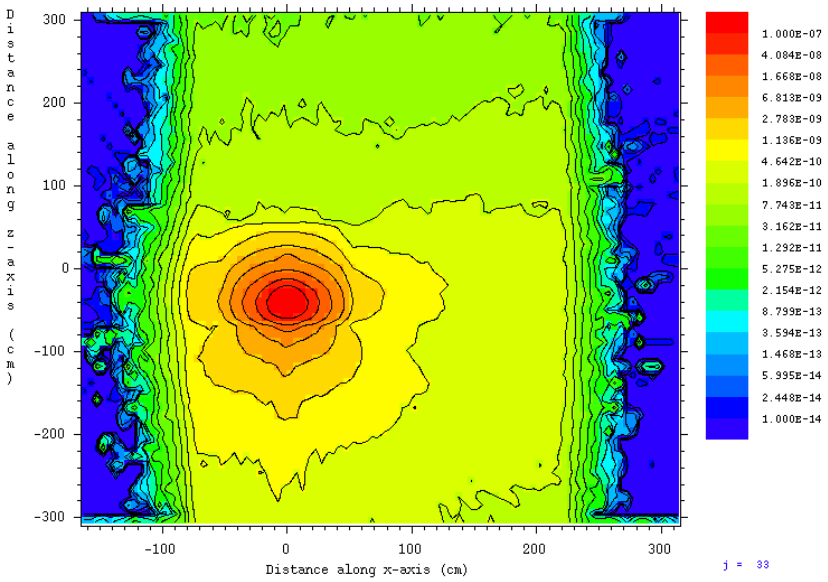

Figure 2.1.69: Neutron dose rate contours in (rem/h)/(el/s) in the xz–plane at $y = 0$, (electron beam line), through the undulator protector. Electron beam enters from the bottom of the figure.

Undulator protection

The undulators (described in §2.7) are located 0.72 m downstream from each protector. The dose rates in the xy-plane at 0.72 m are 3×10^{-11} (rem/h)/(el/s) for neutrons, and 10^{-12} (rem/h)/(el/s) for photons (except for the intense central plume ≈ 20 cm wide which has a peak value of 3×10^{-10} (rem/h)/(el/s)) (see Fig. 2.1.71). All attempts to reduce this plume by various collimator designs proved unsuccesful (the plume is due to small angle electron and photon scattering in the vicinity of the 5 mm diameter collimator hole).

Protector P10 intercepts 1360 pA. Assuming 5000 h of operation per year, this corresponds to a neutron dose of 1300 rem/y. Outside the plume the gamma dose is 43 rem/y, however, in the vicinity of the beam line it is 13,000 rem/y.

The intervening space between the protector and undulator contains drift regions, a gate valve, slits, and a weak dipole magnet. The effect of the forward gamma radiation 'plume' on the NdFeB magnets in the undulator was modeled as shown in Fig. 2.1.73 A section of the delta undulator NdFeB permanent magnet assembly is represented by a 1 m long cylinder,

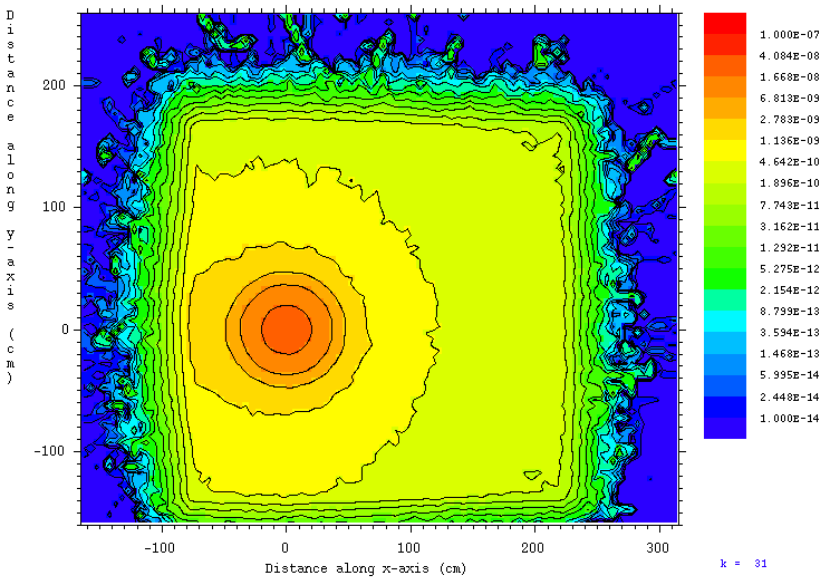

Figure 2.1.70: Neutron dose rate contours in (rem/h)/(el/s) in the xy–plane at $z = 0$ through the undulator protector.

2.54 cm in diameter with a 0.5 cm diameter hole through it. The cylinder is broken up into 10 cells, each 10 cm long, and MCNPX tally 6 is used to calculate the MeV/g/electron deposited by neutrons and photons in each cell.

An average value of 7.6×10^{-6} MeV/g is deposited by photons in the first 20 cm long section of the undulator magnets, and the energy deposited decreases by a factor of ten in each subsequent 10 cm section. The largest current intercepted by protector P10 is 1360 pA. This corresponds to 6.45×10^{4} Mev/g/s, or 1.03×10^{-5} J/kg/s. In 5000 hours of operation, to 186 J/kg or, an annual dose of 1.86×10^{4} rad in the first 10 cm of the NdFeB magnet assembly. The neutron dose is a factor of 2400 times smaller.

Demagnetization of NdFeB permanent magnet material by radiation is of concern in the design of insertion devices. However, the change in the magnetic moment of the material as a function of dose depends very much on the quality of the material. For example, [63] has measured only 1% demagnetization dose of 11.3 Mrad in V block type, N40SH NdFeB permanent magnet material. Thus, assuming a 20 year lifetime of the insertion device and an annual dose of 18.6 krad, the total dose over the first 20 cm or so of the device over the lifetime is well within the 1% demagnetization limit.

M type collimators

Collimators M1 through M6 remove larger Touschek losses. M1 and M2 are located in the tunnel near the entrance to the south arc, M3 is located in CESR, M4 and M5 are in the tunnel joining CESR to the north arc and M6 is in the tunnel near the injector. Due to their location, these collimators do not present a direct hazard to personnel; however, the intense radiation fields pose a problem to electronics in the vicinity, and appropriate steps

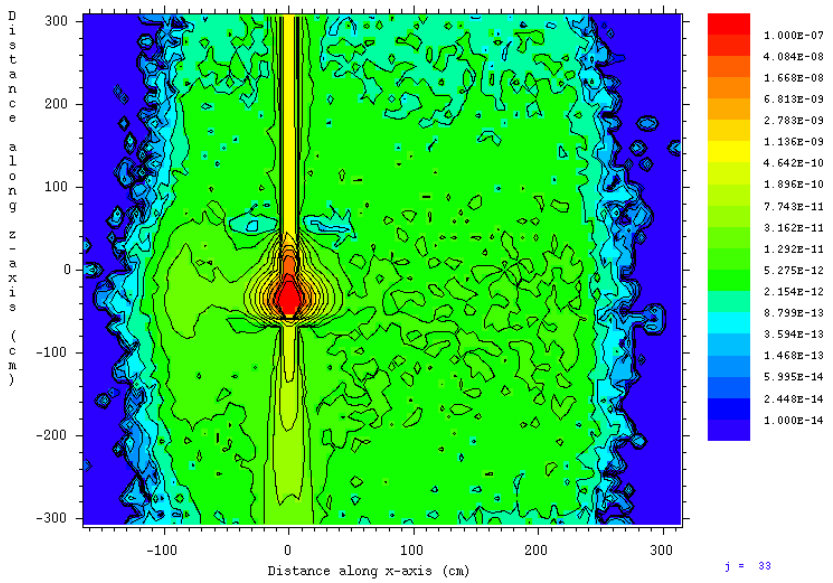

Figure 2.1.71: Photon dose rate contours in (rem/h)/(el/s) in the xz–plane at $y = 0$, (electron beam line), through the undulator protector. Electron beam enters from the bottom of the figure.

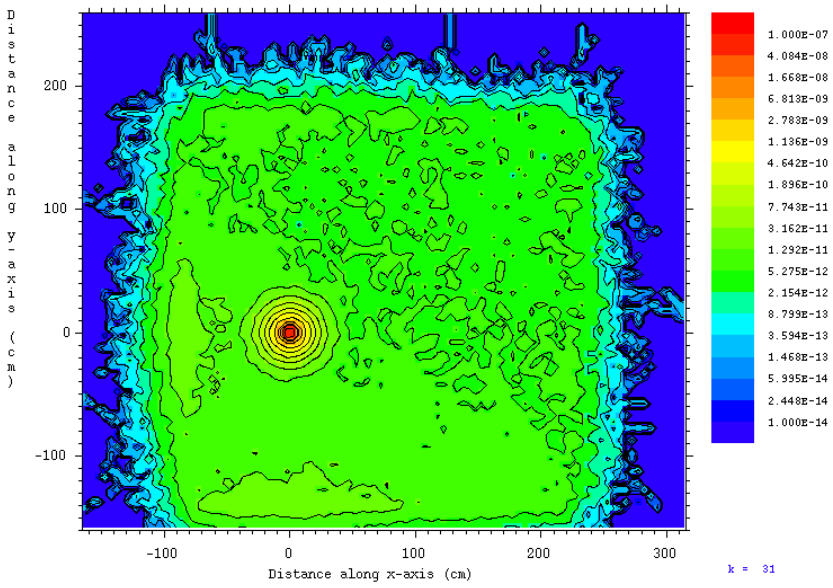

Figure 2.1.72: Photon dose rate contours in (rem/h)/(el/s) in the xy–plane at $z = 0$ through the undulator protector.

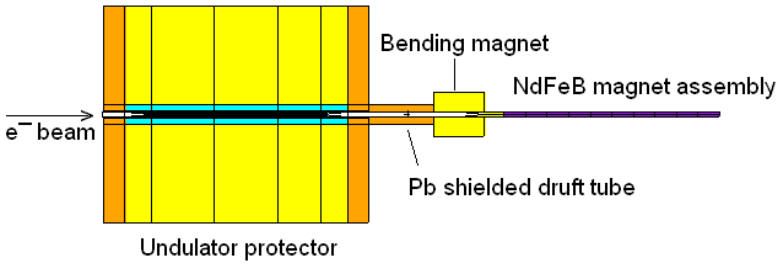

Figure 2.1.73: MCNPX input geometry to calculate the dose to NbBFe permanent magnets in the undulator. The beam pipe between the protector and the the weak solenoid is shielded with lead. an iron cylinder repereents the weak bend magnet in front of the undulator magnet assembly

to shield the electronics will be taken. The collimator design is shown in Fig. 2.1.74 (see also §2.2.4 for details). The neutron and photon dose rates were calculated using MCNPX as described above for undulator protectors. The collimator in the tunnel input geometry is shown in Fig. 2.1.75 and the resulting dose rate contours are similar to those shown in Fig. 2.1.69 through Fig. 2.1.72. The calculated neutron dose rate 1 m downstream from

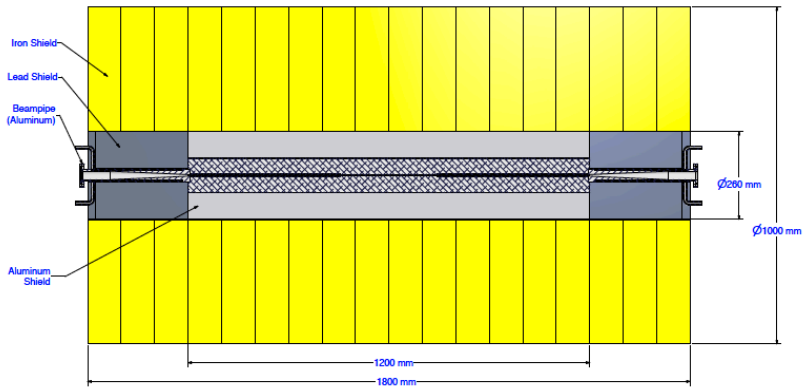

Figure 2.1.74: M type collimator. The top picture shows the overall collimator with iron shield (yellow),

the M collimator in the xy–plane is 7×10^{-12} (rem/h)/(el/s). Collimator M4 intercepts the largest current, 163 nA. Assuming 5000 h of operation per year, this corresponds to a total annual dose of 36,000 rem. Similarly the average photon dose rate 1 m downstream from the M collimator in the xy–plane is 4×10^{-13} (rem/h)/(el/s), and 2.5×10^{-10} (rem/h)/(el/s) in the central, 20 cm wide plume. Again, assuming 5000 hours of operation per year, the total annual dose is 2040 rem outside the plume and 1.3×10^{6} rem in the plume.

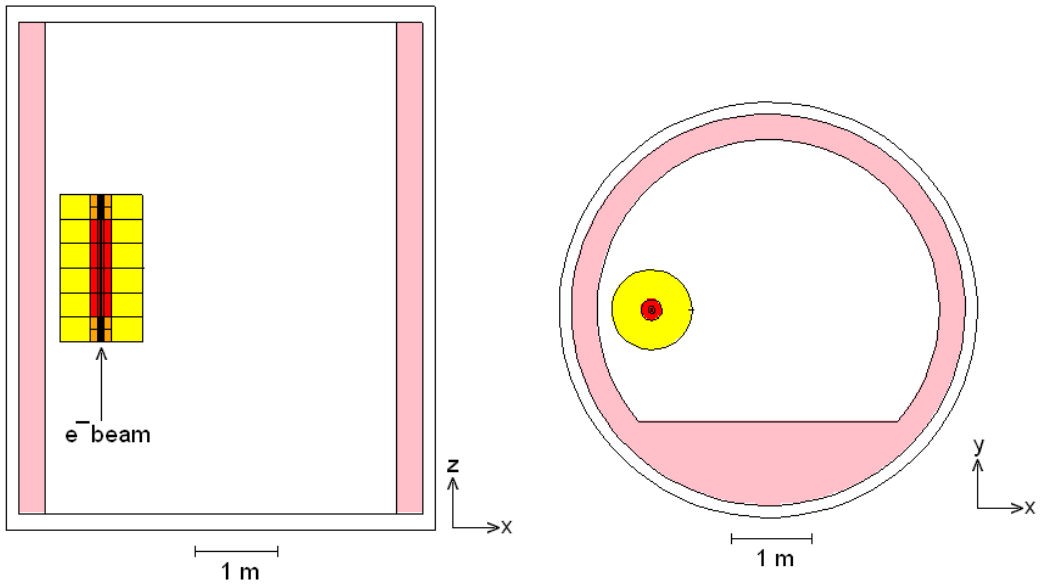

(a) Cut through the xz–plane at $y = 0$.

(b) Cut through the xy–plane at $z = 0$.

Figure 2.1.75: MCNPX input geometry to calculate neutron and photon dose rates for the M-type collimators. The center of the collimator is at $(x, y, z) = (0, 0, 0)$. The electron beam propagates in the $+z-$ direction. Yellow is iron, red is aluminum, orange is lead, and pink ordinary concrete.

Activation of collimators

Activation of collimators and collimator shielding materials is mostly due to neutrons produced in photonuclear reactions. Possible neutron reactions that can produce radioisotopes in collimator materials of interest are (n,γ), $(n,2n)$, $(n,^3\mathrm{He})$, (n,α) and (n,d) reactions. The bulk of the collimator is made from aluminum, copper, and iron. Most of the radioisotopes produced have half-lives in the minute, hour, and day range. A few have half-lives in the 0.5-5 year range. Possible long-lived radio-isotopes that can be produced include ^{26}Al, $T_{1/2} = 7.2 \times 10^5$ y, ^{54}Mn, $T_{1/2} = 312$ y, and ^{63}Ni, $T_{1/2} = 100$ y. The radio-nuclides decay by $\beta^{\pm}$ emission and electron capture either to excited states followed by γ emission, or to the ground state. The thick iron shell used in both the protector and collimator designs to slow down energetic neutrons is also an effective shield against the radiations emitted by the decaying radionuclides produced in the inner $7X_M$ diameter cylinder.

Bremsstrahlung produced in the 25 m long undulator

A preliminary estimate of bremsstrahlung produced by residual gas in the 25 m long undulator was obtained as follows: A 25 m long column of air at atmospheric pressure, irradiated at one end by 5 GeV electrons, was contained in a 0.866" ID, 1.0" OD aluminum tube, surrounded by a 30 cm diameter, 52.5 m long evacuated space. This represents the inner 25 m long undulator space plus a 27.5 m beam line from the end of the undulator to the experimental hutch shielding wall (A more realistic calculation using a 25 m long 5 mm diameter residual gas column surrounded by NdFeB material will be carried out). At 1.0 nTorr, there is a very low probability of electrons interacting with the gas. Accordingly, the calculation was done at atmospheric pressure, and the results scaled linearly to 1 nTorr [64]. That is, the calculated contours have to be multiplied by 1.0×10^{-9} Torr/760 Torr=1.316×10^{-12}.

The cylindrically symmetric photon dose rate (rem/h)/(el/s) as a function of x (or y) perpendicular to the electron beam at 27.5 m downstream from the end of the 25 m long beam pipe containing air at 1 nTorr is shown in Fig. 2.1.76. For a peak value of 10^{-18} (rem/h)/(el/s), over a 1 cm diameter hole, 100 mA corresponds to a dose rate of 0.62 rem/h.

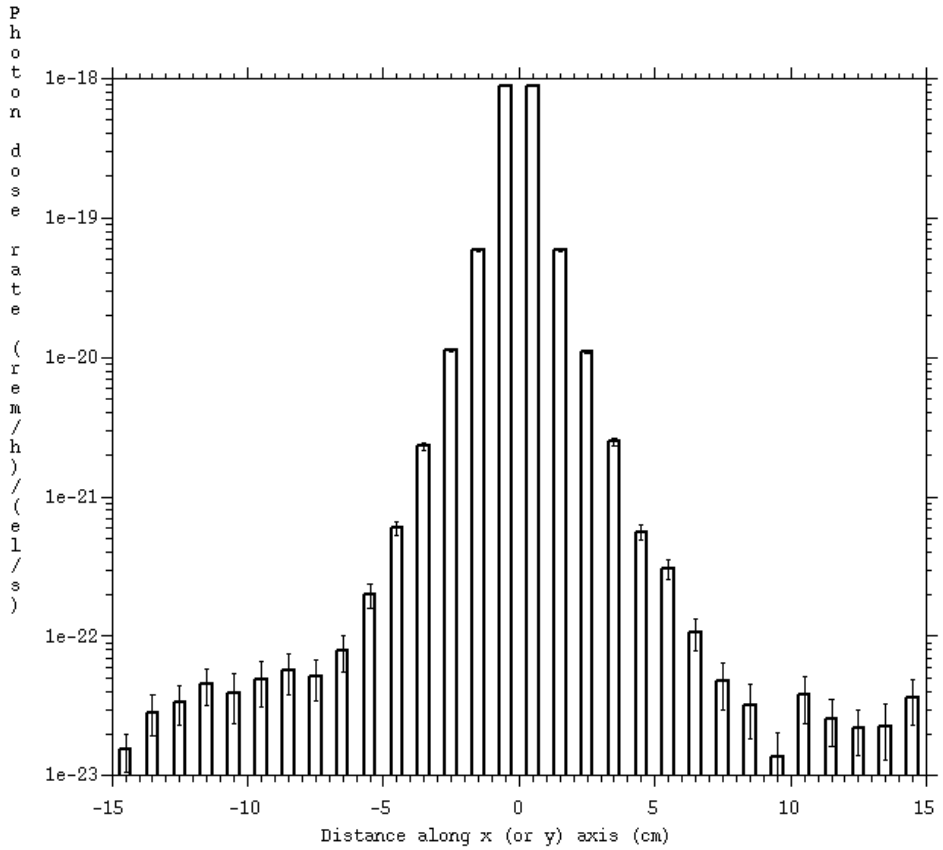

Figure 2.1.76: Photon dose rate (rem/h)/(el/s) as a function of x (or y) 27.5 m downstream from the end of the 25 m long undulator containing air at 1 nTorr

2.1.19 Ion effects

Residual gas in the beam pipe is ionized by the passage of the electron beam. The resulting positive ions can become trapped by the negative potential well of the electron beam. These trapped ions form a charged column along the beam path. This ion column can perturb the motion of the beam by exerting a nonlinear focusing force, and coupled oscillations between the column and the beam can blow-up the effective size of the beam.

Ion phenomena are routinely observed in storage rings, where they manifest as an increase in beam size along the bunch train. Ions are typically dealt with in a storage by using a clearing gap. A clearing gap is a periodic gap that allows accumulated ions to drift out of the beam path. Because of the energy-recovery mechanism in an ERL, a sufficiently long clearing gap is not easily produced [65], reduces the average current, and limits flexibility of the operation.

Other rings eliminate ions by clearing electrodes where their effectiveness as mitigating ion effects has been proven [66]. It has therefore been decided to employ ion-clearing electrodes approximately every 20 m along the electron-beam transport, based on simulations of the equilibrium ion density that is established between ion production by scattering and ion propagation toward clearing electrodes [67].

Section 2.2.4 describes the design for ion-clearing electrodes for the ERL. These counteract the production of ion beams, which are dominated by H_2 and have an ion build-up time on the order of several seconds. To overcome the steep potential of the ERL's ultra-low emittance beams, 1.9 kV across a 2.5 cm aperture is needed. To avoid component heating by image charges, those electrodes are designed to have very low impedances.

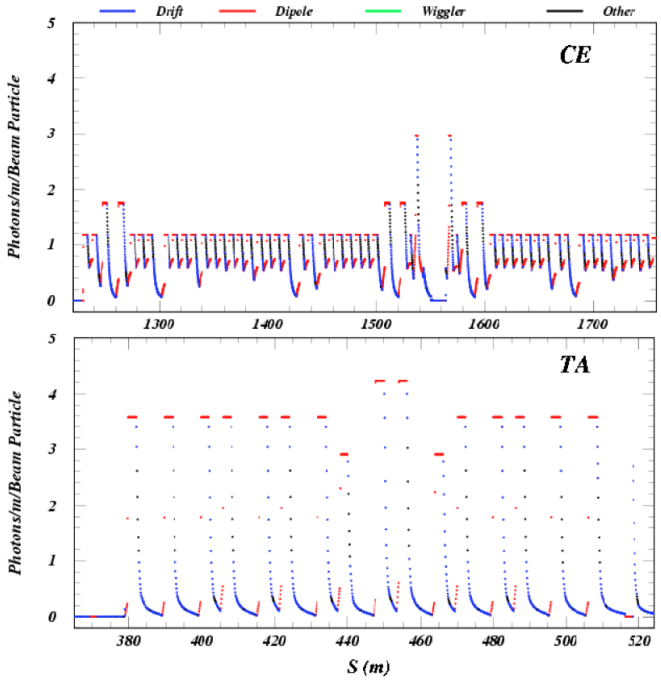

Figure 2.1.77: Synchrotron radiation patterns in the ERL sections CE and TA as calculated for the ERL 8.1 lattice using the Bmad SYNRAD utility.

2.1.20 Electron-cloud effects

The production of low-energy electron clouds via synchrotron-radiation-induced photoeffect on the vacuum chamber walls in synchrotrons has been under active study since the 1990's, when it was determined to be a limiting factor at KEKB [6].

Among various cloud-related instabilities are single-bunch head-tail instabilities, multibunch instabilities associated with the wakes of disturbed clouds, resonant effects relating vacuum chamber transit times and bunch spacing. In addition, the transverse cloud shape, density and time development can distort the linear optics via its space-charge field. While many of these effects are of concern primarily for positively-charged beams, since they attract the cloud electrons, intense clouds can build up in electron accelerators as well. In this section we summarize calculations of electron cloud development in the Cornell ERL, obtaining estimates of the equilibrium density, transverse shape, space-charge field gradients, and address the consequences of gaps in the cloud-repelling bunch train.

This study consists of two calculation steps. First, the ERL 8.1 lattice is analyzed with the SYNRAD utility in Bmad to determine the rate of photons from synchrotron radiation in the various beamline element types in each of the sections of the ERL. Second, the 2D particle-in-cell simulation code ECLOUD employs the beam parameters and photon rates determined in the first step to calculate the time development of the cloud in the ERL sections and element types in which the cloud effects are strongest.

Figure 2.1.77 shows the radiation pattern in 1-cm steps for the CE section, color-coding the radiation in the drift and dipole regions, as well as for the section with the highest av-

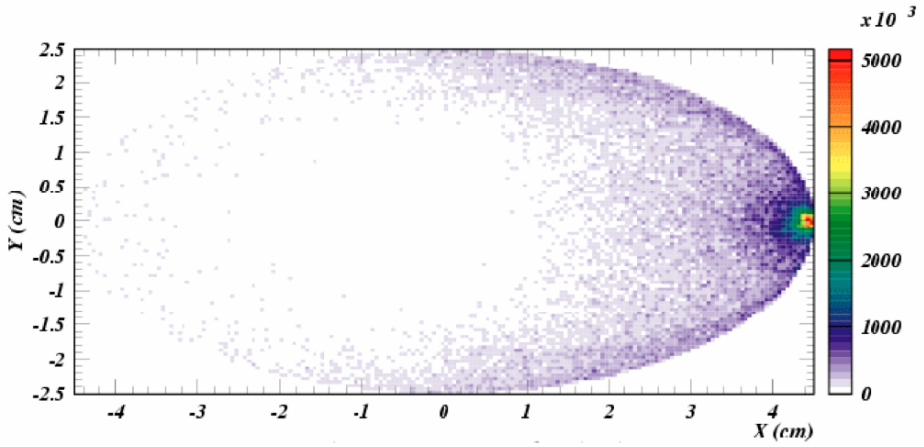

Figure 2.1.78: Snapshot of the cloud profile in a field-free region of the CE section two bunch spacings following the 150th bunch. The vacuum chamber surface is aluminum.

erage photon rate, TA. While the average photon rate is higher in the TA due to its smaller bending radius, the electron cloud simulation accounts for a large suppression due to the effectiveness of the antechamber in absorbing the direct synchrotron radiation and trapping the photoelectrons.

The input parameters for the ECLOUD calculation can be categorized in four types: numerical parameters, beam characteristics, photoelectron production, and the secondary yield model for cloud electrons. Many of the parameters used here have been developed in the context of the CESR Test Accelerator project (CesrTA) [68], for which measurements of coherent tune shifts were successfully modeled for electron and positron beam energies ranging from 1.9 to 5.3 GeV and bunch populations between 6.4×10^9 and 1.9×10^{10} [69, 70].

The secondary yield model is made up three contributions, varying with the energy and angle of the cloud electron incident on the beampipe wall. At low energy, the predominant production mechanism is an elastic reflection off the wall with an average charge yield factor of about 0.5. This value largely determines the cloud decay rate in the absence of beam and agrees well with the CesrTA tune shift measurements. The "true secondary" component is the main source of runaway cloud development, since its yield value peaks at 1.8 at an incident energy of 310 eV, so if such high incident energies are present, as can be caused by the beam kicks, exponential growth is possible. It can be generally stated that the beam kicks to be expected from the ERL bunch population are well below this threshold. These true secondaries are produced with only a few eV of energy, independent of the incident energy. Finally, the third contribution to the secondary yield is comprised of "rediffused" electrons, which can carry a substantial fraction of the incident energy, but with a charge yield of only 0.2, independent of the incident energy. These parameters for the secondary yield model were found to accurately reproduce the CesrTA (aluminum vacuum chamber) coherent tune shift measurements. The ECLOUD results were also thoroughly cross-checked using independent calculations with the POSINST software package.

For reasonable parameters, the electron-cloud buildup is simulated following the start of an electron beam. Figure 2.1.78 shows a snapshot of the cloud profile in the CE beampipe two

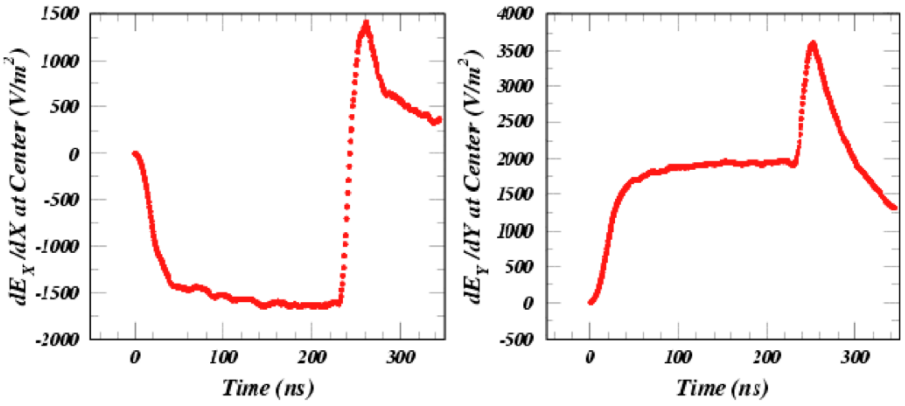

Figure 2.1.79: ECLOUD calculations of the horizontal and vertical space-charge field gradients at the center of the vacuum chamber during the cloud buildup in the field-free regions of the CE section.

bunch spacings following the 150^{th} filled bunch. The cloud model consists of 123k macroparticles each carrying 1.8×10^9 electrons. The buildup curve shows the cloud after production and decay have largely equilibrated. No relevant cloud density has reached the center of the beam pipe. This fact can also be seen in the field-gradient time dependence shown in Fig. 2.1.79 if one considers that Gauss's law for a charge free region requires that the horizontal and vertical field gradients must add to zero. Figure 2.1.79 shows that the increase in magnitude of the field gradients stops after about 50 ns at a value less than 2000 V/m^2. The equivalent focusing strength of a quadrupole magnet is about 7×10^{-6} T/m. Since the total length of the quadrupoles in the CE is 43.6 m, compared to the total length of field-free regions of 117 m, we can conclude that the relative distortion of the linear optics due to the electron cloud will not exceed 2×10^{-6}. In the case of a gap in the bunch train, the vertical field gradient will begin to increase, as shown in Fig. 2.1.79, but the cloud decay time of less than 100 ns will prevent any appreciable distortion of the linear optics. Figure 2.1.79 also shows that if there is a gap in the bunch train, the vertical field gradient will increase by about a factor of two as the cloud collapses, but will decay away over a time period of about 50 ns.

References

[1] Tigner, M. *A Possible Apparatus for Electron Clashing-Beam Experiments.* Nuovo Cimento, **37**, pages 1228–1231 (1965).

[2] Mayes, C. and G. Hoffstaetter. *Exact 1D model for coherent synchrotron radiation with shielding and bunch compression.* Phys. Rev. ST Accel. Beams, **12** (2), page 024401 (Feb 2009). doi:10.1103/PhysRevSTAB.12.024401.

[3] Wiedemann, H. *Particle Accelerator Physics I.* Springer Verlag, Berlin, second edition (1999).

[4] Sagan, D. *Bmad: A relativistic charged particle simulation library.* Nucl. Instrum. Methods Phys. Res., Sect. A, **558**, pages 356–359 (2006).

[5] Bazarov, I. V., *et al. Benchmarking of 3D space charge codes using direct phase space measurements from photoemission high voltage dc gun.* Phys. Rev. ST AB, **11** (100703) (2008).

[6] Bazarov, I. V., B. M. Dunham, and C. K. Sinclair. *Maximum Acheivable Beam Brightness from Photoinjectors.* Phys. Rev. Lett., **102** (104801) (2009).

[7] Bazarov, I. V., *et al. Thermal emittance and response time measurements of negative electron affinity photocathodes.* Journal of Applied Physics, **103** (5) (2008).

[8] Carlsten, B. *New Photoelectric injector design for the Los Alamos National Laboratory XUV FEL accelerator.* Nucl. Instr. and Meth. A, **285** (1-2), pages 313–319 (1989).

[9] Flottman, K. *ASTRA: a space charge tracking algorithm.* DESY (2000).

[10] Bazarov, I. V. and C. K. Sinclair. *Multivariate optimization of a high brightness dc gun photoinjector.* Phys. Rev. ST AB, **8** (2005).

[11] Slade, P. G. *The vacuum interrupter: theory, design, and application.* CRC Press (2008).

[12] Bazarov, I. V., *et al. Efficient temporal shaping of electron distribution for high-brightness photoemission electron guns.* Phys. Rev. ST AB, **11** (4) (2008).

[13] Karkare, S. and I. Bazarov. *Effect of nano-scale surface roughness on transverse energy spread from GaAs photocathodes.* Applied Physics Letters, **98** (2011).

[14] Litvinenko, V., R. Hajima, and D. Kayran. *Reduction of field emission dark current for high-field gradient electron gun by using a molybdenum cathode and titanium anode.* Nucl. Instr. and Meth. A, **557** (1), pages 165–175 (2006).

[15] Bazarov, I. and T. Miyajima. *Calculation of Coherent Synchrotron Radiation in General Particle Tracer.* In *Eleventh European Particle Accelerator Conference, EPAĆ08*, pages 118–120. EPAC08, Genoa, Italy (2008).

[16] Venturini, M. and M. Reiser. *rms Envelope Equations in the Presence of Space Charge and Dispersion.* Phys. Rev. Lett., **81** (1), pages 96–99 (1998).

[17] Miyajima, T. and I. V. Bazarov. *Simulation study of Cornell L0 beamline.* Report ERL 11-02, Cornell (2011).

[18] Bazarov, I. and G. Hoffstaetter. *Lattice options for a 5 GeV light source at Cornell.* In *PAC03*. Portland/OR (2003).

[19] Bazarov, I., G. Krafft, and L. Merminga. *Linac Optics for Energy Recovery Linac.* In *PAC01*. Chicago/IL (2001).

[20] Douglas, D. *Design Considerations for Recirculating and Energy Recovering Linacs.* Report JL-TN 00-0027, Jefferson Lab (2000).

[21] Hoffstaetter, G. H. and Y. H. Lau. *Compensation of wakefield-driven energy spread in energy recovery linacs.* PRST, **11**, page 070701 (2008).

[22] Sagan, D., *et al. Extended one-dimensional method for coherent synchrotron radiation including shielding.* Phys. Rev. ST Accel. Beams, **12** (4), page 040703 (Apr 2009). doi: 10.1103/PhysRevSTAB.12.040703.

[23] Meseck, A., *et al. FELs as x-ray sources in ERL facilities.* In *Proceedings of PAC11* (2011).

[24] Colella, R. and A. Luccio. Opt. Commun., **50**, page 41 (1984).

[25] *A proposal for an x-ray free-electron laser oscillator with and energy recovery linac.* Phys. Rev. Lett., **100**, page 244802 (2008).

[26] *Tunable optical cavity for an x-ray free-electron-laser oscillator.* Phys. Rev. ST Accel. Beams, **12**, page 030703 (2009).

[27] Lindberg, R. R. and K.-J. Kim. *Mode growth and competition in the x-ray free-electron laser oscillator start-up from noise.* Phys. Rev. ST Accel. Beams, **12**, page 070702 (2009).

[28] Billing, M. *et al. Effect of wakefields in an energy recovery linac.* In *Particle Accelerator Conference PAC2009, Vancouver, Canada* (2009).

[29] Chin, H. *User's Guide for ABCI Version 9.4.* Technical Report KEK Report 2005-06, KEK (2005).

[30] Novokhatski, S. *The Computer Code NOVO for the Calculation of Wake Potentials of Very Short ultra-relativistic bunches.* Technical Report SLAC-PUB-11556, SLAC (2005).

[31] MAFIA Collaboration. *MAFIA manual.* Technical report, CST GmbH, Darmstadt (1997).

[32] Novokhaski, A. *et al. Single Bunch Energy Spread in the TESLA Cryomodule.* Technical Report DEST-TESLA-1999-16, DESY (1999).

[33] Schwinger, J. *On Radiation by Electrons in a Betatron.* In K. A. Milton, editor, *A Quantum Legacy: Seminal Papers of Julian Schwinger*, pages 307–331. World Scientific, Singapore (1945). Also in Report LBNL-39088.

[34] Agoh, T. and K. Yokoya. *Calculation of coherent synchrotron radiation using mesh*. Phys. Rev. ST Accel. Beams, **7** (5), page 054403 (May 2004). doi:10.1103/PhysRevSTAB.7.054403.

[35] Mayes, C. *Energy Recovery Linear Accelerator Lattice Design & Coherent Synchrotron Radiation*. Ph.D. thesis, Cornell University, Ithaca, NY (May 2009). http://hdl.handle.net/1813/13477.

[36] Hoffstaetter, G., M. Billing, and Y. Lau. *Wake-field compensation in Energy Recovery Linacs*. In *Proceedings EPAC08*. Genoa/IT (2008).

[37] Singh, O. and G. Decker. *Beam Stability at the Advanced Photon Source*. In *Proceedings of PAC05, Knoxville* (2005).

[38] Zhang, L., L. Farvacque, *et al. Electron Beam Stabilization Experiences at the ESRF*. Presentation, Advanced ICFA Beam Dynamics Workshop on Nanometre-Size Colliding Beams, Lausanne (2002).

[39] Bulfone, D., R. D. Monte, *et al. Status of the ELETTRA Global Orbit Feedback Project*. In *Proceedings of EPAC06*. Edinburgh (2006).

[40] Tanaka, H., H. Aoyagi, *et al. Beam Orbit Stabilization at the SPring-8 Storage Ring*. In *Proceedings of the 7th International Workshop on Accelerator Alignment*. SPring-8 (2002).

[41] Streun, A., M. Boege, *et al. Beam Stability and Dynamic Alignment at SLS*. In *SSILS01*. Shanghai (2001).

[42] Boege, M., B. Keil, *et al. Orbit Stability at the SLS*. Technical report (2003). PSI Scientific Report 2003, Vol. VI.

[43] Schilcher, T., *et al. Global Orbit Feedback System for the SLS Storage Ring*. In *Proceedings of ICALEPCS99*. Trieste (1999).

[44] Chao, Y.-C. and V. Mertens. *Analysis and Optimisation of Orbit Correction Configurations Using Generalised Response Matrices and its Application to the LHC Injection Transfer Lines TI 2 and TI 8*. Technical report (2001). LHC Project Report 470.

[45] Song, C. and G. Hoffstaetter. *Magnetic Field Error Sensitivity in an Energy Recovery Linac*. Technical report, Cornell (2007). Report ERL-07-03.

[46] Hoffstaetter, G. H. and I. Bazarov. *Beam-Breakup Instability Theory for Energy Recovery Linacs*. PRST, **7**, page 54401 (2004).

[47] Hoffstaetter, G., I. Bazarov, and C. Song. *Recirculating Beam-Breakup Thresholds for Polarized Higher-Order Modes with Optical Coupling*. Phys. Rev. ST-AB, **10** (044401) (2007).

[48] Crittenden, J. *Recent Progress on Beam-Breakup Calculation for the Cornell X-Ray ERL*. In *Proceedings of ERL09*. Ithaca, NY (2009).

[49] Song, C. and G. Hoffstaetter. *Cornell Report ERL-07-10*. Technical report, Cornell (2007).

[50] Song, C. and G. Hoffstaetter. *Cornell Report ERL-06-04*. Technical report, Cornell (2007).

[51] Pelowitz, D. B., *et al. MCNPX 2.7.D Extensions*. Technical Report LA-UR-10-07031, Los Alamos National Laboratory, Los Alamos National Laboratory, Los Alamos, NM (October 2010).

[52] Kostroun, V. *ERL Collimator Design*. CLASSE Technical Report ERL-RN-11-02, Cornell University (2011). In Preparation.

[53] Piwinski, A. *The Touschek effect in strong focusing storage rings*. Technical Report DESY 98-179, DESY (1998).

[54] Hoffsaetter, G. and M. Ehrlichman. *Touschek Losses in Linear Accelerators* (2011). In preparation.

[55] Xiao, A. and M. Borland. *Touschek effect calculation and its application to a transport line*. In *twenty-second Particle Accelerator Conference*, pages 3453–3455. Albuquerque, New Mexico (2007).

[56] Temnykh, A. B., M. P. Ehrlichman, and G. Hoffstaetter. *Beam losses due to intra-beam and residual gas scattering for Cornell's energy recovery linacs*. In *eleventh European Particle Accelerator Conference, EPAC'08*, pages 214–216. Genoa,Italy (2008).

[57] Bizek, H. M. *Some results of the Advanced Photon Source beam lifetime studies*. In *Poroceedings of the 1997 Particle Accelerator Conference*, pages 1493–1495. Vancouver, B.C., Canada (1997).

[58] Spencer, M., *et al. Lifetime contribution measurements at the Australian synchrotron*. In *twenty-second Particle Accelerator Conference*, pages 914–916. Albuquerque, New Mexico (2007).

[59] Chao, A. W. and M. Tigner. *Handbook of Accelerator Physics and Engineering (3rd printing)* (2006).

[60] Nakamura, K. and P. D. Group). *Review of Particle Physics*. Journal of Physics G: Nuclear and Particle Physics, **37**, page 075021 (2010). Chapter 27, Passage of particles through matter.

[61] *Radiation Protection for Particle Accelerator Facilities*, volume NCRP Report No. 144. National Council on Radiation Protection and Measurements, National Council on Radiation Protection and Measurements, 7910 Woodmont Avenue, Suite 400/Bethesda, Maryland 20814-3095, 2005 edition (2003).

[62] Neal, R. B., editor. *The Stanford Two-Mile Accelerator*. Benjamin, New York (1968). Chapter 26 Shielding and Radiation by H. De Staebler, T. M. Jenkins and W.R. Nelson.

[63] Temnykh, A. B. *Measurement of NdFeB permanent magnets demagnetization induced by high energy electron radiation.* Nucl. Instrum. Methods Phys. Res., Sect. A, **587**, pages 13–19 (2008).

[64] Ferrari, A., M. Pelliccioni, and P. Sala. *Estimation of fluence rate and absorbed dose rate due to gas bremsstrahlung from electron storage rings.* Nucl. Instr. and Meth. B, **83**, pages 518 – 524 (1993).

[65] Hoffstaetter, G. H. and M. Liepe. *Ion clearing in an ERL.* Nuclear Instruments and Methods in Physics Research Section A: Accelerators, Spectrometers, Detectors and Associated Equipment, **557** (1), pages 205 – 212 (2006). ISSN 0168-9002. doi: DOI:10.1016/j.nima.2005.10.069. Energy Recovering Linacs 2005 - Proceedings of the 32nd Advanced ICFA Beam Dynamics Workshop on Energy Recovering Linacs.

[66] Feikes, J. *et al. Commissioning and operation of the metrology light source.* In *Eleventh European Particle Accelerator Conference, EPAC08*, pages 2010–2012. EPAC08, Genoa, Italy (2008).

[67] Hoffstaetter, G. H. and C. Spethmann. *Equilibrium ion distribution in the presence of clearing electrodes and its influence on electron dynamics.* Phys. Rev. ST Accel. Beams, **11** (1), page 014001 (Jan 2008). doi:10.1103/PhysRevSTAB.11.014001.

[68] Palmer, M. *et al. The Conversion and Operation of the Cornell Electron Storage Ring as a Test Accelerator for Damping Rings Research and Development.* In *Proceedins of PAC09* (2009).

[69] Crittenden, J. A. *et al. Studies of the Effects of Electron Cloud Formation on Beam Dynamics at CesrTA.* In *Proceedings of PAC09* (2009).

[70] Calvey, J. R. *et al. Electron Cloud Modeling Considerations at the CESR Test Accelerator.* In *Proceedings of PAC09* (2009).

2.2 Vacuum

2.2.1 Introduction

Overview

This section describes the vacuum system that is part of the electron-beam transport system, including the turn-around arcs (TA and TB detailed in §2.1) connecting the two main superconducting Linacs – the north and south arcs that host the insertion devices and x-ray user beamlines – and the large turn-around arc in the existing CESR tunnel. The vacuum system includes all the chambers, pumps, gauges, valves, vacuum instrumentation and control, and vacuum facilities. The existing vacuum system of the CESR accelerator will be re-used with minimum modifications.

The vacuum chambers constitute the electron-beam delivery system that provides adequate beam aperture with low impedances for the electron beams. Adequate vacuum pumping must be installed to ensure low enough pressure so that beam loss from the residual gas scattering is not an issue for beam lifetime, accelerator component radiation damage, and radiation background to x-ray beamline user areas. From considerations of ion accumulation in the beam, gas-scattering-engendered radiation damage in the undulators, and control of beam-gas Bremsstrahlung therein, an average pressure goal of low 10^{-9} Torr range has been set.

The scope of this section is limited to the vacuum components that form the basic building blocks of the vacuum system for beam transport. There are many accelerator components that are parts of the vacuum system but serve specific functions, including beam instrumentation and control (such as beam-position monitors, beam-current monitors, x-ray-generating IDs, etc). These functional components will be described in their respective sections.

Beampipe aperture and material

In most of the beam-transport vacuum chambers, the beampipe aperture is 25 mm in the vertical and somewhat larger in the horizontal direction. In the arcs, aluminum extrusions with built-in cooling and pumping channels will be used. Efforts must be made to minimize beam impedance of the vacuum chambers, including adequate inner-surface smoothness, gentle transitions with angles less than 10° between different chamber cross-section shapes and proper RF shielding or bridging of vacuum flange joints.

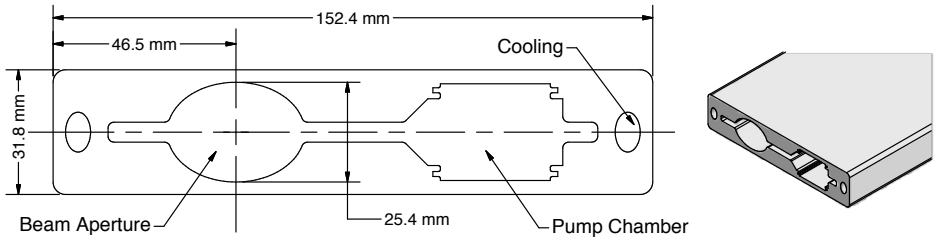

Figure 2.2.1: Extruded aluminum chambers comprise the beam aperture and the ante chamber for pumping and cooling channels.

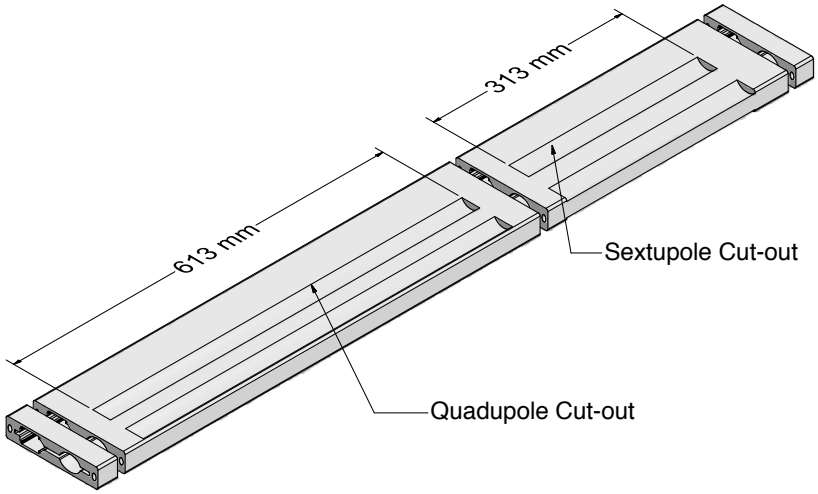

Figure 2.2.2: The extrusion with pole-tip grooves for both quadrupole and sextupole magnets

To achieve the low-thermal outgassing and the photon-induced desorption, all vacuum chambers and appendage-vacuum components will be fabricated with UHV-compatible practices, which have been well established through many years of CESR operations.

Vacuum pumping

Sufficient ultra-high vacuum-compatible pumps, both localized (lumped) and distributed, will be installed in the vacuum system to maintain the required average gas pressure (low 10^{-9} Torr range) at a beam current of 100 mA. The installed pumping system must have enough pumping speed and capacity to allow vacuum-system conditioning of reasonably short duration during the initial accelerator commissioning, and after installation of new vacuum components for upgrades and/or repairs. Typical pumps are sputter-ion pumps (noble-diode style), Non-Evaporable Getters (NEGs) and titanium-sublimation pumps (TiSPs).

Vacuum instrumentation and control

The vacuum system will be divided into sectors by RF-shielded gate valves to facilitate staged vacuum-system installations, vacuum-system upgrades, maintenance, and repairs. A typical length of a vacuum sector is 30 m.

Cold-cathode ion gauges (CCGs) will be installed periodically throughout the vacuum system to monitor vacuum-system performance and for vacuum-system trouble-shooting. Each vacuum sector will be equipped with at least one residual gas analyzer (RGA). Numerous thermocouples will monitor local temperatures of vacuum components. Monitoring and interlock functions will be integrated into the central control system.

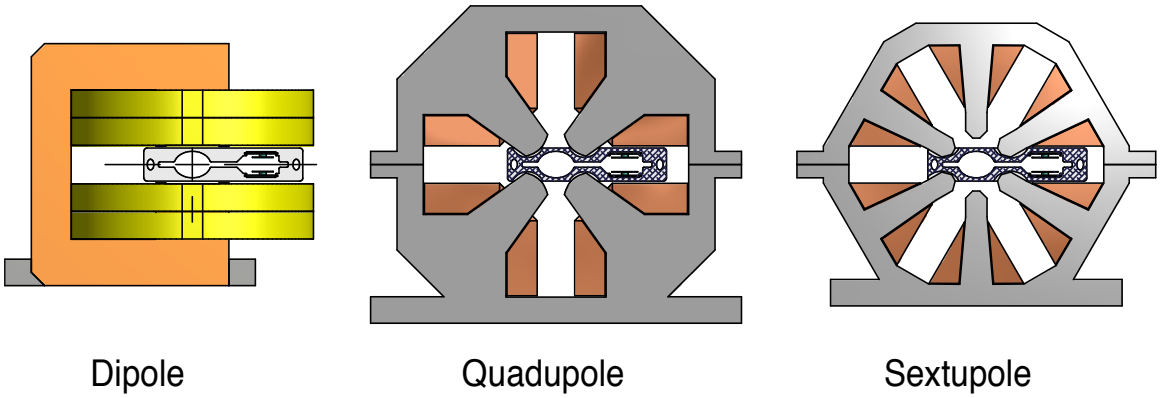

Figure 2.2.3: Cross sections of the beampipe extrusions and magnets at dipole, quadrupole and sextupole magnets.

2.2.2 Electron beam lines

Aluminum beampipe extrusions

Aluminum extrusions made of Type 6063-T4 or -T6 alloy will be employed owing to their good electrical and thermal properties, excellent machinability, and welding qualities.

The extrusion consists of a beam aperture and an ante-chamber for distributed pumps and cooling channels, as shown in Fig. 2.2.1. The pumping ante-chamber is located radially outward in the bending magnets so that synchrotron radiation generated from the bending magnets is intercepted by the water cooled walls close to the distributed pumps. This arrangement has two obvious advantages. First, it brings the distributed pumping close to the gas load from SR-induced desorption. Secondly, it significantly limits scattered photons (and photo-electrons) from entering the beam space.

Due to the short electron beam-bunch length, it is important to have the best interior surface finish possible within the beam aperture. One of the challenging requirements is to reduce surface roughness of less than 3μm rms, at least in the longitudinal dimension of the beam bore. Recent experience at LCLS proved that sub-μm rms-surface finishes are achievable [1] with a combination of high quality aluminum extrusions and further surface polishing via a technique called abrasive-flow machining [2]. The highly polished interior surfaces bring additional benefit to the vacuum system, as it reduces effective surface area, thus lowering the static thermal-outgassing rate. Such finishes have been achieved during careful extrusion [3].

Aluminum beampipe extrusions in magnets

The aluminum extrusion shown in Fig. 2.2.2 will be used for most of the vacuum chambers passing through magnets. In the dipoles, the extrusion will be bent to the required radius. In quadrupole and sextupole magnets, grooving, as illustrated in Fig. 2.2.2, will be done to bring the magnet pole tips as close to the electron beam as possible, while maintaining sufficiently strong structure for withstanding atmospheric pressure. Figure 2.2.3 shows cross-section views of the extrusion in magnets.

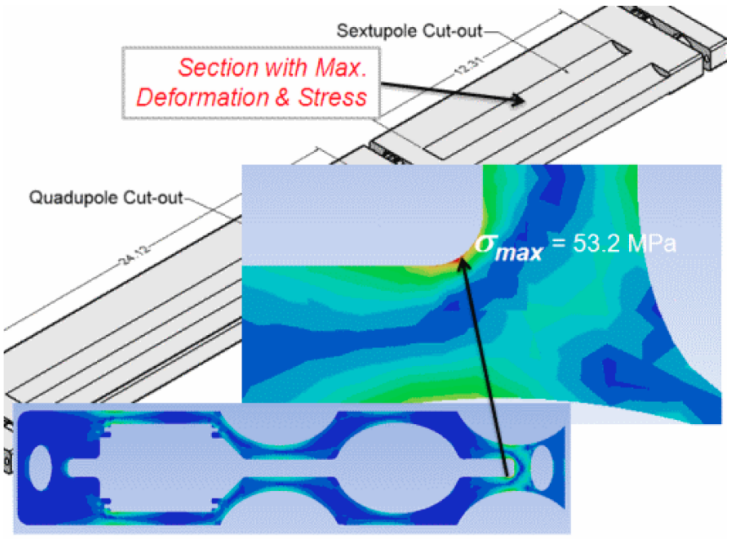

Figure 2.2.4: Calculated deformation of the chamber extrusion after pole-tip grooving. Maximum deformation is ≈ 0.1 mm in the middle of a sextupole magnet, and maximum stress at the corner is ≈ 53.2 MPa, well below material yield stress of 240 MPa for 6063-T6 aluminum alloy

The mechanical stress and deformation caused by atmospheric pressure on the extrusions was evaluated using the commercially available mechanical-design and simulation code ANSYS®. As expected, maximum deformation and stress occurs at locations where the maximum amount of material is removed, in the center of a sextupole magnet. The calculated maximum deformation and stress are 0.10 mm and 53 MPa, respectively, (as shown in Fig. 2.2.4). The calculated maximum stress is well below the yield stress (≈ 240 MPa) of Type 6063-T6 aluminum alloy.

Conceptual vacuum chamber design

Building blocks are attached to the aluminum extrusions, via TIG welding, to form various functional vacuum chambers. The building blocks must be fabricated with UHV-compatible materials. Due to the nature of very short electron-bunch length, it is important to avoid steps and gaps on the interior wall in the vicinity of the electron beam with dimensions comparable to the bunch length. When a beam aperture cross-section change is necessary, a smooth transition must be used, keeping the inclination angle less than 10° with respect to the electron beam.

Some conceptual vacuum chambers with functional components are shown in Fig. 2.2.5 to Fig. 2.2.9. As depicted in Fig. 2.2.5, NEG strips mounted on hangers are inserted in the ante-chamber to provide distributed-vacuum pumping. The NEG strips are electrically insulated from the chambers, so they may be resistively heated during activation. For initial pumpdown and NEG activation, localized pumps, typically sputter-ion pumps, are connected to pump ports, as illustrated in Fig. 2.2.6. To facilitate fabrication and installation, UHV

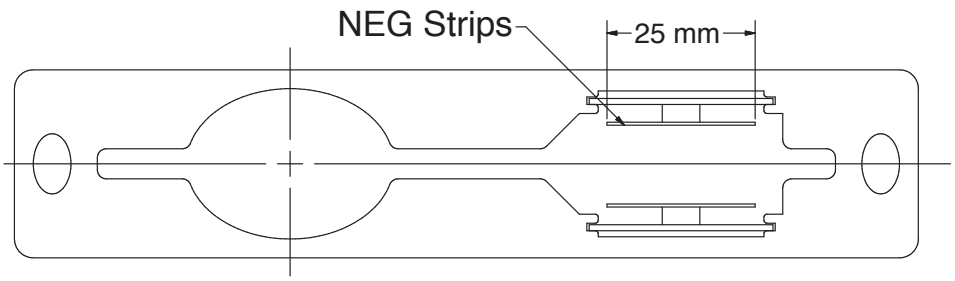

Figure 2.2.5: NEG strips are mounted in the ante-chamber, located on the radial outside of a bending magnet, close to the SR-induced gas load.

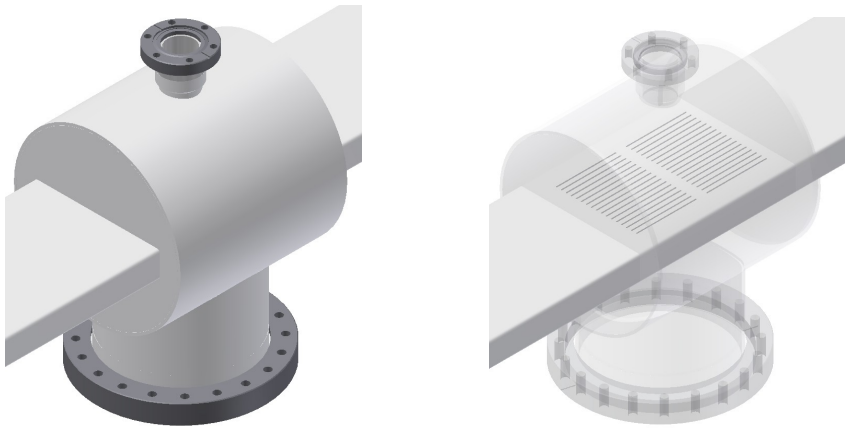

(a) (b)

Figure 2.2.6: Lumped pumps are installed at pump ports comprising a shroud (Fig. 2.2.6a) welded around the extrusion with pumping slots and (Fig. 2.2.6b) cutting through both top and bottom.

flanges (ConFlat®-type) with metallic seals are attached to the ends of vacuum chambers, with an example shown in Fig. 2.2.7. Explosion-bonded aluminum to stainless-steel-transition blocks are used not only to facilitate welding, but also to provide a smooth cross-section transition from the complex extrusion cross section to a simple rectangular one. The rectangular cross sections at the flanges are desirable for joining the chamber to many essential vacuum components, such as RF shielded bellows and RF-shielded UHV gate valves.

A conceptual vacuum chamber is shown in Fig. 2.2.8 with integrated components. Integration of the chamber into an accelerator period in the south arc is given in Fig. 2.2.9.

Synchrotron radiation power

To assess vacuum-chamber cooling requirements, synchrotron-radiation (SR) power density on the vacuum chambers was calculated for 100 mA electron beam at 5 GeV. SR radiation only from bending magnets is considered as SR from the insertion devices will be extracted to the user beamlines. For simplicity, the SR calculation was done for a uniform beampipe of

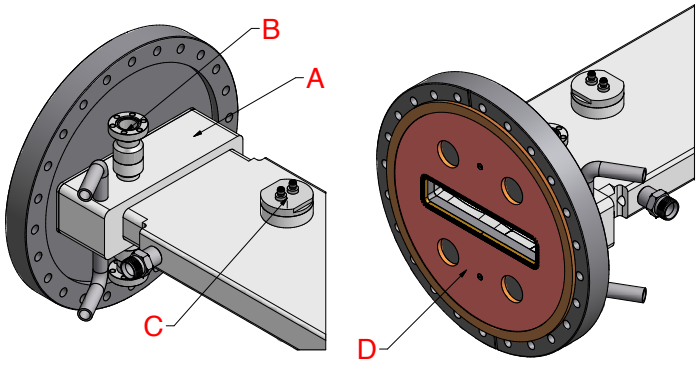

Figure 2.2.7: Conceptual vacuum chamber design. Stainless-steel (SST) UHV flanges are welded to the Al extrusions via explosion bonded SST/Al transitions (A). The transition also hosts a pair of ports (B) for electrical connections to the NEG strips. An RF-insert gasket with beryllium-copper finger contacts (D), is used to bridge the gap in the flange joint. The beam-position monitor (BPM) assembly, (C), is directly welded to the extrusion.

25.4 mm inner diameter (ID) throughout the electron-beam line. In practice, the beampipe IDs that intercept SR are always equal or larger than 25.4 mm, thus the actual SR power-area density will be generally lower than calculated here.

The calculated SR linear-power and area-power densities on the vacuum chamber walls are shown in Fig. 2.2.10. On average, the SR power deposited on the vacuum-chamber walls is $\approx 100\,\mathrm{W/m}$. With a typical chamber cooling loop of $\lesssim 10$ m in length, a cooling-water flow rate of 0.5 GPM is sufficient to keep the average chamber temperature rise less than 10° C. The thermal stress of the aluminum chamber, induced by the vertically narrow SR strip, is calculated for a maximum power density of $3\,\mathrm{W/mm^2}$. The result, shown in Fig. 2.2.11, indicates the thermal stress is well below the yield stress of the material with adequate cooling.

Vacuum pumping and pressure distributions

The pressure profiles are calculated in the electron beamlines, using a 1D finite-element method developed at CESR, in which the electron-beam transfer lines are divided into 10 cm segments. The purpose of the calculation is to provide a general assessment of the conceptual vacuum design. Many special beamline components (such as in-vacuum insertion devices and electron-beam collimators) are not considered.

Two sources of gas load are included in the calculations: the thermal desorption and the SR-induced desorption from the vacuum chamber walls. A thermal outgassing rate of 10^{-11} Torr $\times$ liter/s/cm^2 (at room temperature) is used to calculate the thermal gas-load. The SR-induced gas-load is calculated using the SR photon flux (F_{SR}, see Fig. 2.2.12),

$$\dot{Q} = \eta_{\mathrm{ph}} \cdot F_{\mathrm{SR}} \tag{2.2.1}$$

with a photon desorption yield η_{ph} (molecules/photon). With properly cleaned vacuum cham-

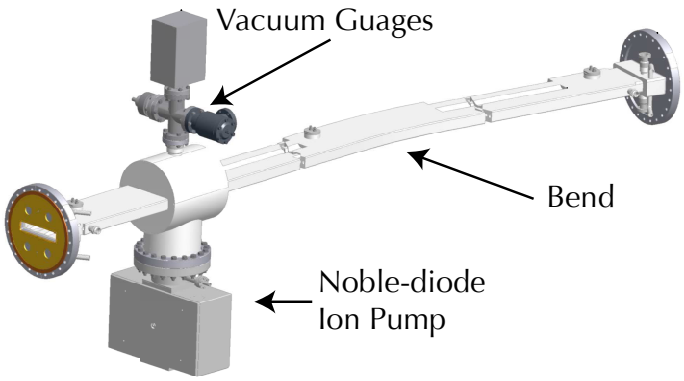

Figure 2.2.8: A vacuum chamber with integrated vacuum pumps, gauges, BPMs and features to accommodate dipole, quadrupole and sextupole magnets.

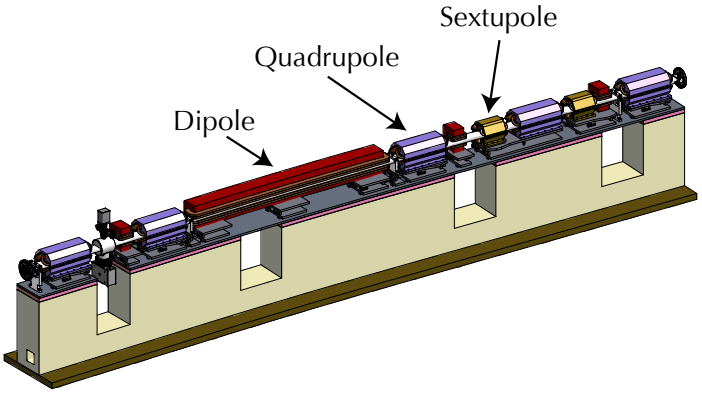

Figure 2.2.9: A typical period in the South Arc.

bers, the SR desorption yield decreases with beam dose, typically following

$$\eta_{\rm ph} \propto D^{-\alpha} \tag{2.2.2}$$

where D is the accumulated electron-beam dose (in Ampere-hour), and $\alpha = 0.6 \sim 1.0$. Operational experiences showed that the SR-desorption yield drops below 10^{-6} molecule/photon after accumulation of a few 100 Ampere-hour, as demonstrated from CESR operational experience (see Fig. 2.2.13).

Adequate vacuum pumping needs to be installed to achieve the required vacuum level, that is, with average pressure in the low 10^{-9} Torr range. Though the final vacuum-pumping configuration is yet to be developed, a model of evenly spaced pumps is used for this calculation, with an exception in the CESR portion of the electron-beam line, where existing lumped and distributed-ion pumps are used in the calculations. Two categories of vacuum pumps are used: localized pumps (or lumped pumps, LPs) and distributed pumps (DPs). The LPs are mounted on pumping ports (see, for example, Fig. 2.2.6), and they may be noble diode sputter-ion pumps, cartridge NEGs or TiSPs. The LPs will be the primary pumps for the initial vacuum-system pump-down and beam conditioning. The DPs are mounted in the ante-

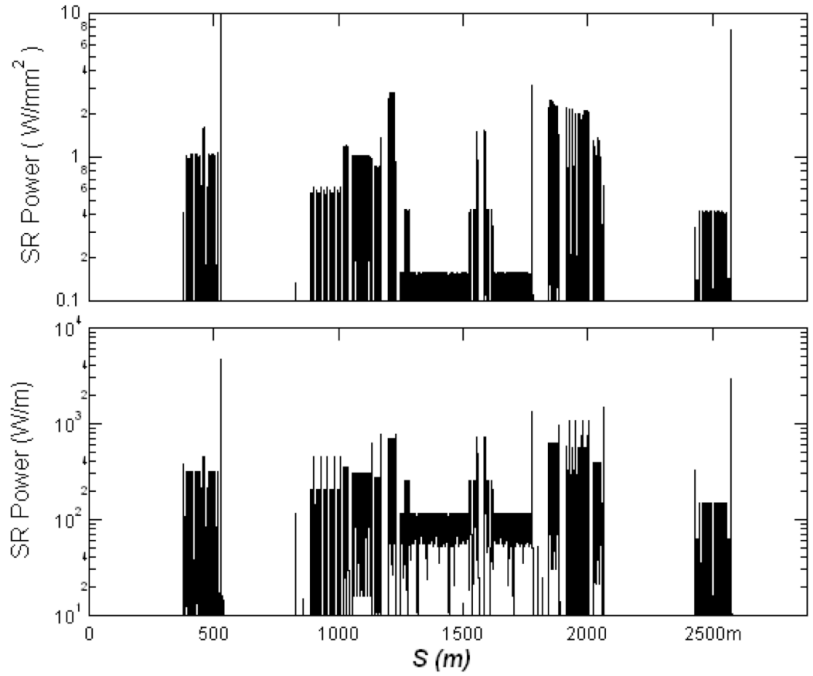

Figure 2.2.10: Calculated synchrotron radiation (SR) linear-power and area-power densities on the walls of the vacuum chambers, for 100 mA electron-beam current at 5 GeV. All calculations are done with uniform beam pipes of 25.4 mm inner diameter. (The exceptions are at the entrance of the Linacs, located at ≈ 500 m and ≈ 2500 m, where actual beampipe-aperture changes are taken into account. These result in spikes in the calculated power level at these locations.)

chambers of the beam chambers. In the CESR section, existing distributed-ion pumps will be re-used. In the other sections, NEG strips (st707 type by SAES Getters Inc.) will be used (see, Fig. 2.2.5). The typical pumping speed for the LPs and DPs are listed in Tab. 2.2.1 for all sections, excluding the superconducting Linacs. The pumping speed of the NEG strips may decrease due to saturation [4]. The calculated pressure profiles at various NEG conditions are shown in Fig. 2.2.14. The results clearly indicate that the proposed vacuum-pumping installation is able to maintain the average pressure well, even with partially saturated NEG strips in the accelerator parts TA, NA, SA and TB that have been designed in §2.1.

To maintain effective pumping, the distributed NEG strips need to be re-activated before significant saturation. However, the NEG activation process requires significant downtime (on the order of eight hours or longer) due to hydrogen outgassing during the activation and the pressure recovery following the activation. In Tab. 2.2.2, the NEG-strip-time duration between activations is estimated for TA, NA, SA and TB sections. For well-conditioned vacuum chambers, the residual gas is usually composed >90% of H_2, and <10% of CO, CH_4, H_2O, CO_2 in combination. It is well-known that NEG has extremely high pumping capacity for H_2 so the NEG saturation is normally due to adsorption of carbon- and oxygen-containing molecules. Correspondingly, the gas-load listed in the Tab. 2.2.2 represents 10% of the amount

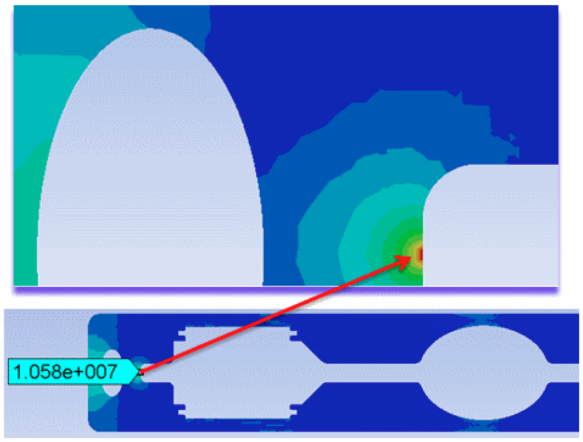

Figure 2.2.11: ANSYS calculation shows the thermal stress at locations with maximum SR power density ($3\,\mathrm{W/mm^2}$) is $\approx 10.6\,\mathrm{MPa}$, well below the yield stress (240 MPa) of 6063-T6 aluminum alloy. A film coefficient of $1000\,\mathrm{W/m^2/K}$ at the cooling surface was used for the calculation.

of SR-induced gas-load as calculated by Eq. (2.2.1), using data reported in [4]. The calculations clearly indicate that the installed NEG-pumping capacity is sufficient, and the activations may easily fit in the scheduled accelerator maintenance downtime.

2.2.3 X-ray frontend and transport

X-ray frontend design

Insertion devices in the North and South Arcs generate high-brilliance SR radiation for the x-ray users. Special vacuum components, referred to as the x-ray frontend, are used to safely separate the x-ray beams from the electron beam. The x-ray frontend allows operational independence between the accelerator and the x-ray user systems. The frontends are gener-

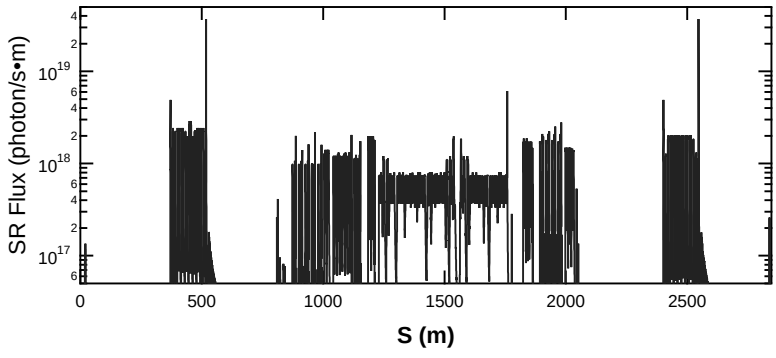

Figure 2.2.12: Calculated total SR photon flux impinging on both inner and outer walls of the beam pipes with uniform 25.4 mm aperture.

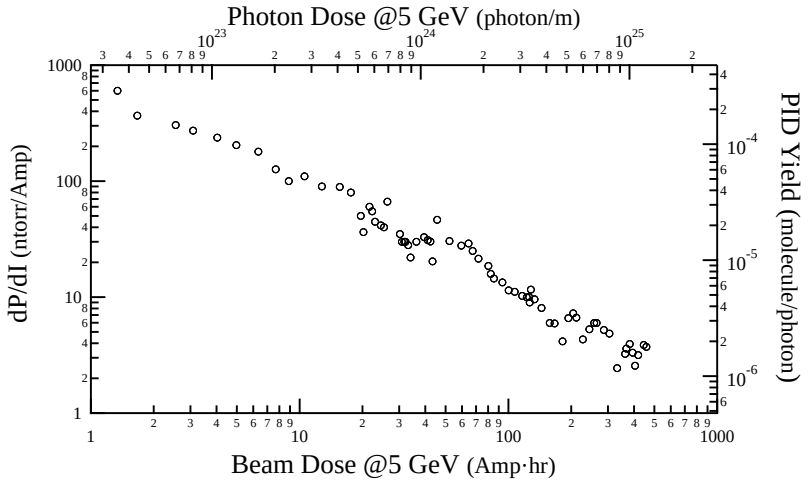

Figure 2.2.13: A typical vacuum-beam conditioning trend of a newly installed aluminum chamber in a CESR dipole magnet.

Table 2.2.1: Installed pumping speed along electron-beam transfer lines. Notes: A) NEG pumping speed for N_2 at full activation, see [4], B) Distributed ion pump in CESR was measured for N_2

section	LP speed (l/s), every 3 m	DP speed (l/s/m)	Note
TA	40	350	A
SA	40	350	A
CE	100	100	B
NA	40	350	A
TB	40	350	A

ally located on the accelerator side of the facility (as defined by radiation shield wall). The frontends are installed at the same time as the electron beam line components, allowing later development of the x-ray lines as needed.

Figure 2.2.15 shows the beam line frontend of G-line at CHESS, which may serve as a model for ERL beamlines. A 'crotch' provides a safe branch off of the electron beam and the photon beam. A pair of UHV-gate valves and a pair of photon shutters allow independent operations of the accelerator and the beamline-user facility.

Crotch

The power density of the SR (primarily originating from an adjacent bending magnet) striking the crotch, or junction between the x-ray beamline and the main electron beamline, can be very high. Careful design of the vacuum surface and cooling channels is required. Two types of design are presented here.

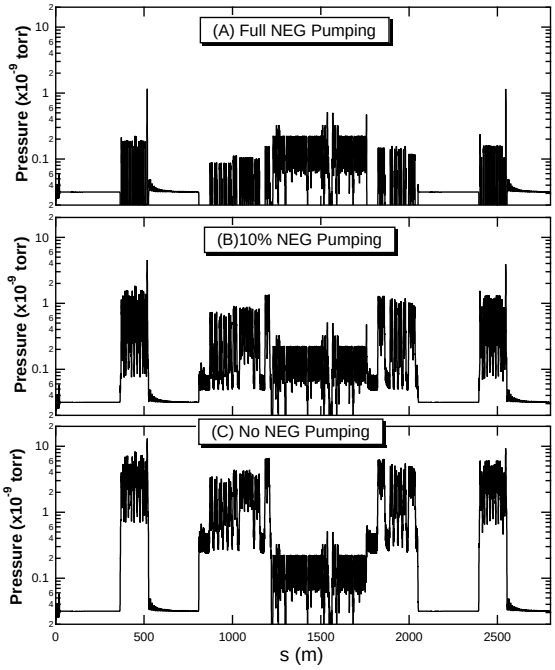

Figure 2.2.14: Calculated pressure profiles along the beam pipe for a 100 mA electron beam at 5 GeV, with desorption yield $\eta_{\rm ph} = 10^{-6}$ molecule/photon, at various NEG pumping speeds.

Figure 2.2.16 shows a crotch used at the CHESS G-line. This is a fully flanged chamber that is directly inserted into the main accelerator beamline. The crotch assembly is constructed from OFHC copper, with a gently inclined surface intercepting the SR fan from a bending magnet (of 87 m bending radius). The water-cooled inclined surface was designed for a 500 mA electron beam at 5 GeV, significantly above the total power requirement for the ERL beamlines. Thus a scaled-down design may be suitable.

Figure 2.2.17 shows a more compact crotch design, which is used at APS and NSLS II. The compact design allows the absorber to be inserted in a side port on a dipole chamber where an x-ray beamline branches off. To handle a much higher power density, the absorbers are made of Glidcop®(copper-based metal-matrix composite alloys mixed primarily with aluminum-oxide ceramic particles).

Photon shutter

As seen in Fig. 2.2.18, photon shutters are used to stop the intense SR beam generated by the IDs, allowing radiation isolation between the main accelerator vacuum and the x-ray beamline users. Adequate thermal design must be implemented to handle very high power density. Figure 2.2.18 shows a model design of a photon shutter used in the CHESS G-line frontend. An engineering design is needed for the Cornell ERL, as the x-ray beam power density of the ERL IDs will be significantly higher than that of the CHESS G-line. Normally, a pair of photon shutters is installed in a series for additional operational safety.

Table 2.2.2: NEG Duration with continuous 100 mA Operation

Section	Average SR Flux (Photon/s/m)	SR Gas-load (CO-equivalent) (Torr×l/s/m)	Time before losing 50% pumping speed (Days at 100mA)
TA	7.80×10^{16}	2.21×10^{-10}	89
SA	3.42×10^{16}	9.68×10^{-11}	203
NA	3.91×10^{16}	1.11×10^{-10}	178
TB	6.49×10^{16}	1.84×10^{-10}	107

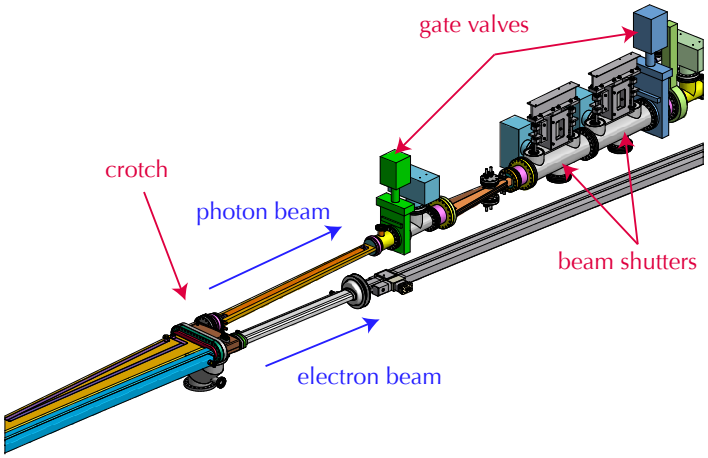

Figure 2.2.15: CHESS G-line frontend as a design model. The x-ray beamline physically separates from the electron-beam line at the crotch. In normal operation, the x-rays generated from an ID may reach the users with the gate valves and the photon beam stops open. When not needed, the photon shutters safely absorb the x-rays while not affecting the operation of the accelerator.

2.2.4 Special vacuum components

In-vacuum IDs

In-vacuum insertion devices (IV-IDs) are used to produce the high quality x-ray beams. As a complex system, an IV-ID should be designed as a self-contained device, with its own vacuum pumping and instrumentation. The detailed description of the IV-IDs is given in §2.7.

Protector for IDs

For the longevity of small-bore IV-IDs, an electron-beam collimator or protector is used at the entrance of every IV-ID to protect it from synchrotron radiation and particles lost through IBS and gas scattering. A conceptual protector design is presented in Fig. 2.2.19, comprising a copper vacuum beampipe and an iron-radiation shield. For optimal radiation shielding, a high-Z material (tantalum) lining is inserted in the copper beampipe. The radiation-shielding

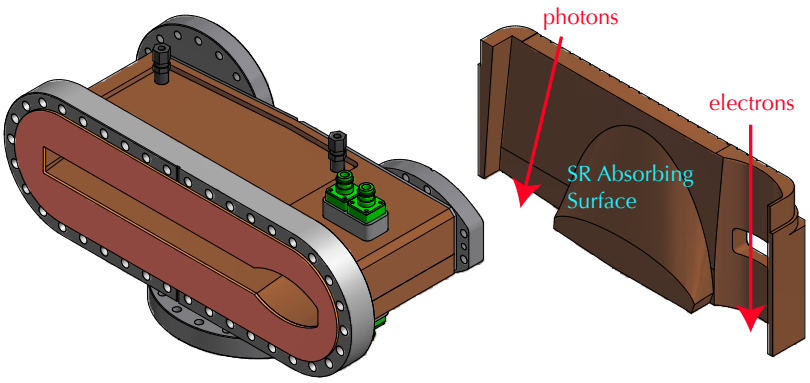

Figure 2.2.16: Crotch design for CHESS G-line (left) with a water-cooled top half (right). The inclined-vacuum surface on the top half stops SR fan from the upstream bending magnet.

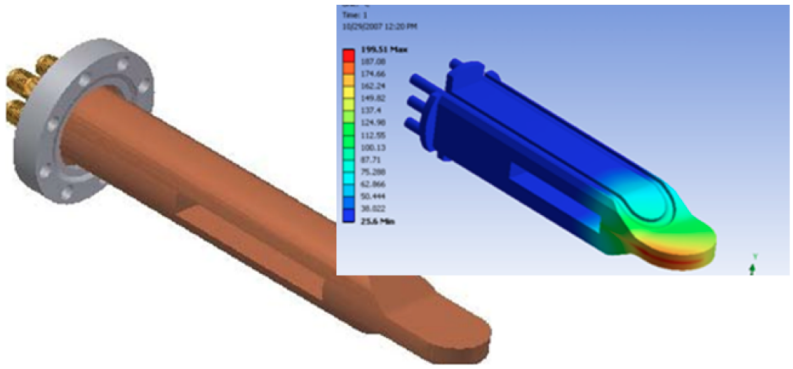

Figure 2.2.17: NSLS II insertable crotch design. To handle very high SR power density, the heat absorber is made of Glidcop®.

considerations of the protector design is described in §2.1.17. Vacuum aspects of the protector are presented here.

Copper is chosen as the beampipe material, to provide better a radiation-shielding effect in the forward direction as compared to aluminum. A taper at the entrance of the collimator, with full opening angle of 10°, provides a beam-aperture transition from a 25 mm to 5 mm diameter, the aperture of a typical IV-ID. The water-cooled taper will shield the IV-ID from any SR, up to a few hundred watts. The expected electron-beam loss along the beampipe is well below 10^{-10} A, with a power deposition of less than 1 W; thus additional cooling for the center portion of the beam pipe is not needed. The taper is welded to a 1 m-long copper tube with a thick wall (25.4 mm OD, 5.0 mm ID), going through the radiation shields of the collimator.

A water-cooled aluminum taper assembly is used to provide smooth transition in the horizontal walls between an extruded-aluminum chamber and the protector. A concept for such a taper assembly is given in Fig. 2.2.20.

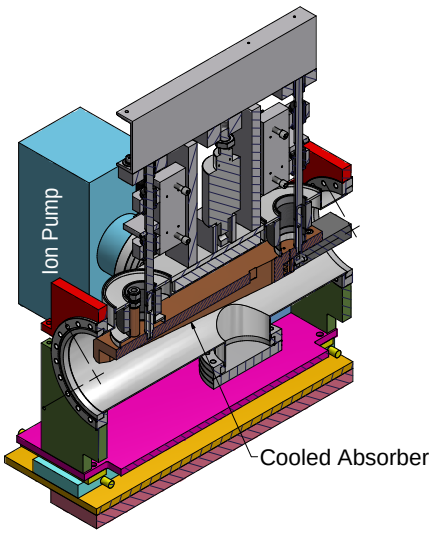

Figure 2.2.18: Beam shutter used at CHESS G-line. It is capable of absorbing a full photon beam generated from a G-line wiggler with 500 mA electron-beam current at 5 GeV.

Electron beam collimators

There are electron-beam losses along the electron-beam lines due to IBS. Electron-beam collimators are installed in the electron-beam transport lines at strategic locations (based on beam-lattice design and the accelerator's physical layout, see §2.1.17) to 'clean' up the electron beam. A concept for the collimator is given in Fig. 2.2.21. At some locations, the collimator may intercept up to a 163 nA beam-loss current, dumping 800 W power onto the first half of the center aluminum-beam pipe. Thus water cooling is also needed for the center aluminum-beam pipe.

Unlike the ID protectors, it is required to transition the beam-pipe aperture between the 5 mm ID and the extruded beampipe down stream. A pair of transition tapers, as shown in Fig. 2.2.20, will be used on both ends of the collimator.

Beam position monitors

Beam position monitors (BPMs) are essential for the electron-beam transport lines. Two types of BPMs will be considered, as depicted in the conceptual designs of Fig. 2.2.22. An engineering design will have to consider detailed issues like impedance matching and fabrication. Pickup buttons are the most commonly used and can be readily deployed directly on the aluminum extrusion with minimum space requirement. In the button-type design, the BPM assembly may be 'mass-produced' economically. The pickup buttons are welded to the coaxial vacuum feedthroughs (SMA-type), which are in turn welded onto housing blocks made of explosion-bonded aluminum-to-stainless-steel transitions. The stripline BPMs are more sensitive, as compared to the pickup buttons. Stripline BPMs, as shown in Fig. 2.2.22b, were successfully fabricated at Cornell and installed at the prototype ERL injector. However, the stripline

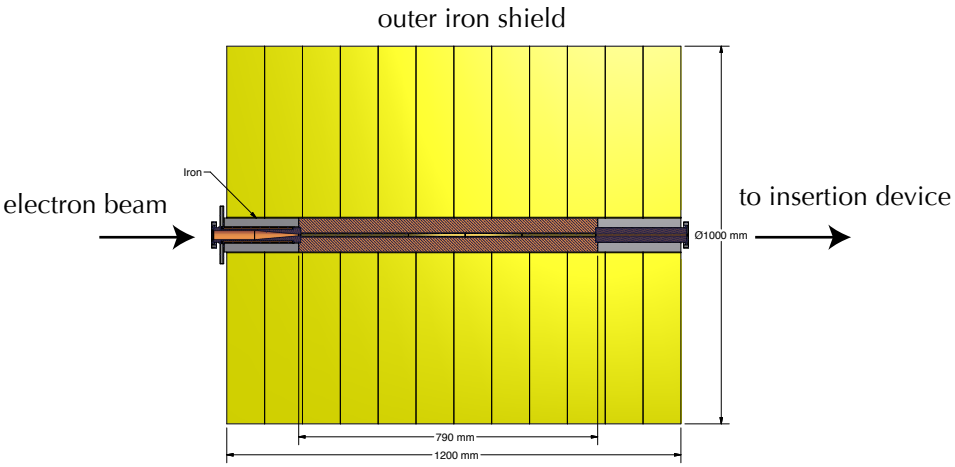

(a)

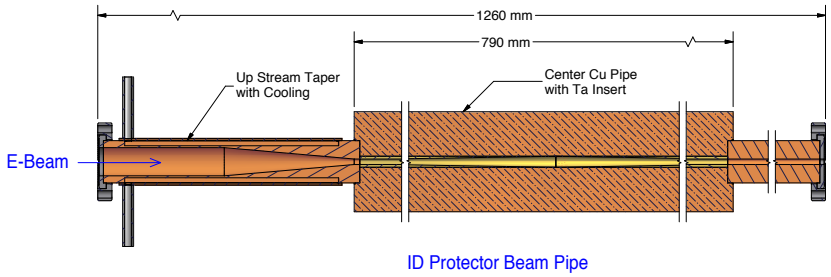

(b)

Figure 2.2.19: A conceptual design of the protector for small-bore in-vacuum ID. Figure 2.2.19a shows a protector with a copper vacuum beampipe and iron radiation shield; Figure 2.2.19b shows the copper vacuum beampipe with water-cooled up-stream taper from 25 mm to 5 mm beam aperture, and tantalum inserts.

BPMs are much more costly and more difficult in fabrication. These BPMs normally need to be fully flanged (due to the required tuning procedure) and also require beam-aperture transitions; thus they demand significantly more space.

Ion-clearing electrodes

Residual gas in the beampipe is readily ionized, predominantly by collisions with the high-energy electron beam. Positive ions are attracted to electron beams and create a nonlinear potential in the vicinity of the beam, which can lead to beam halo, particle loss, optical errors, or transverse and longitudinal instabilities. The ion-trapping and its impact to the electron beam in the ERL was analyzed in [5]. As discussed in that paper, the neutralization time for a residual gas by electron-beam collision can be calculated as

$$\tau_{\mathrm{col}} = (\sigma_{\mathrm{col}} \cdot \rho_{\mathrm{gas}} \cdot c)^{-1} \tag{2.2.3}$$

where σ_{col} is the collision-ionization cross section, ρ_{gas} is the gas density, and c the speed of light in vacuum. The neutralization times are calculated for a pressure of 10^{-9} Torr, with a gas

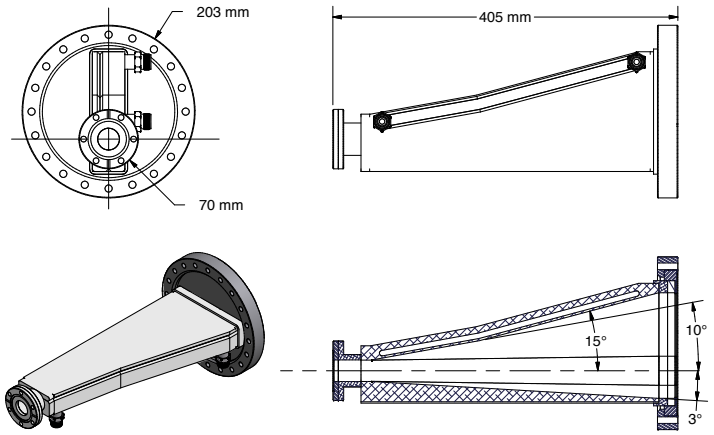

Figure 2.2.20: Transition taper is used to connect an aluminum vacuum chamber to a collimator.

Table 2.2.3: Neutralization time for dominant gases in ERL

Gas	$\sigma_{\rm col}$ ($\rm m^2$)	$\rho_{\rm gas}$ ($\rm m^{-3}$)	$\tau_{\rm col}$ (s)
H_2	3.1×10^{-23}	3.0×10^{13}	3.6
CO	1.9×10^{-22}	3.5×10^{12}	5.0
CH_4	2.0×10^{-22}	1.8×10^{12}	9.5

composition of 85% H_2, 10% CO and 5% CH_4, as listed in Tab. 2.2.3, which clearly indicate that the ions can be readily trapped in the ERL beam.

In many electron accelerators (such as electron storage rings), the trapped ions may be cleared simply with a sufficiently long gap between electron bunches. However, the clearing gap can introduce an undesirable transient in the superconducting-RF Linac. Therefore, ions have to be cleared from the electron-beam region by some other means. The only tested approaches are electro-static clearing electrodes. The clearing electrode must create an electric field at the center of the electron beam that is stronger than the beam field exerted on the ions. The calculation [5] shows that the required clearing field may be as high as 150 kV/m. With a pair of DC electrodes on top and bottom of the beampipe of a 25 mm vertical aperture, a clearing DC-voltage of ±1.9 kV is needed. To enhance the effectiveness of the clearing, the electrodes are placed at the locations of beam-potential minima.

In the clearing electrode design, it is critically important to minimize beam impedance introduced by the electrodes and to avoid significant RF excitations in the gaps behind the electrodes (that are necessary for withstanding required DC voltages). In a recent development for the large storage rings of the KEK B-factory[6] and at Cornell's CesrTA accelerator project [7, 8], low-profile clearing electrodes are developed as a electron-cloud suppression technique. These electrodes are directly deposited onto the vacuum-chamber wall via thermal-spray technology. Figure 2.2.23 depicts such an electrode implemented at the bottom of vacuum beampipe in a superconducting wiggler of CesrTA. The thickness of both the dielectric coating (Al_2O_3) and the metallic coating (tungsten) is ≈ 0.20 mm, which is proven to

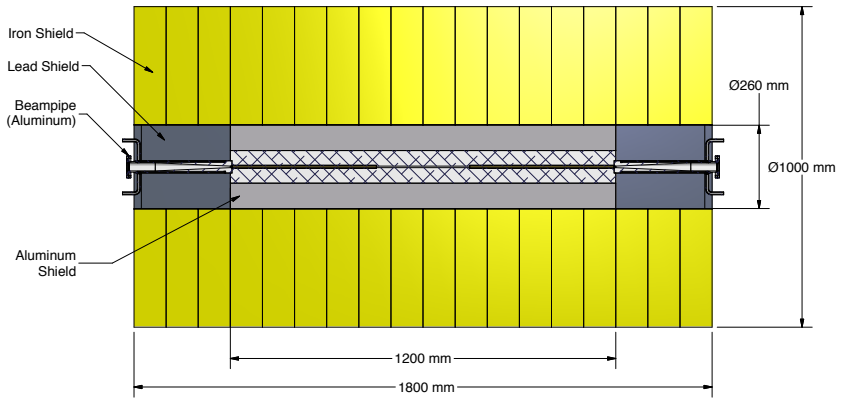

(a)

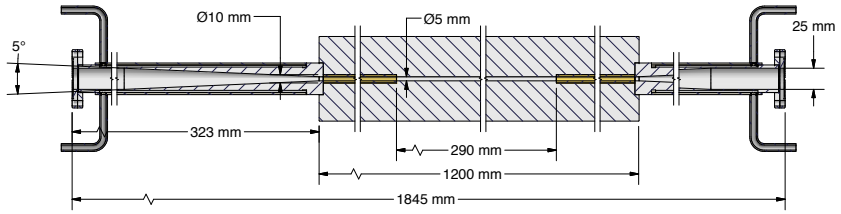

(b)

Figure 2.2.21: A conceptual design of electron beam collimator. Figure 2.2.21a shows a collimator with a aluminum vacuum beampipe and iron radiation shield; Figure 2.2.21b shows the aluminum vacuum beampipe with water-cooled up-stream taper from 25 mm to 5 mm beam aperture and tantalum inserts. Tantalum sleeves are inserted in the center aluminum beampipe for more effective radiation shielding.

withstand DC voltages up to 2 kV, meeting the required ion-clearing voltage for ERL. Means for absorbing the deposited beam-wake energy need to be devised.

RF shielded bellows

Flexible bellows with proper RF shielding are required periodically in the electron-transport beamline to allow for thermal expansion and contraction during accelerator operations and to facilitate beamline component installation and replacement. Two conceptual designs are considered here, as shown in Fig. 2.2.24. Design A is similar to the RF-shielded bellows currently used in the CESR, with beryllium copper contact springs travelling with the 'male' sliding flange. Design B is derived from a DAΦNE design [9], with 'floating' RF contacts. The pros and cons of these two designs are compared in Tab. 2.2.4. The designs shown here are fully flanged. In practice, the sliding joint assembly may be directly welded to the beampipe without flange(s), not only to minimize required space, but also to reduce beam impedance associated with flange joint(s).

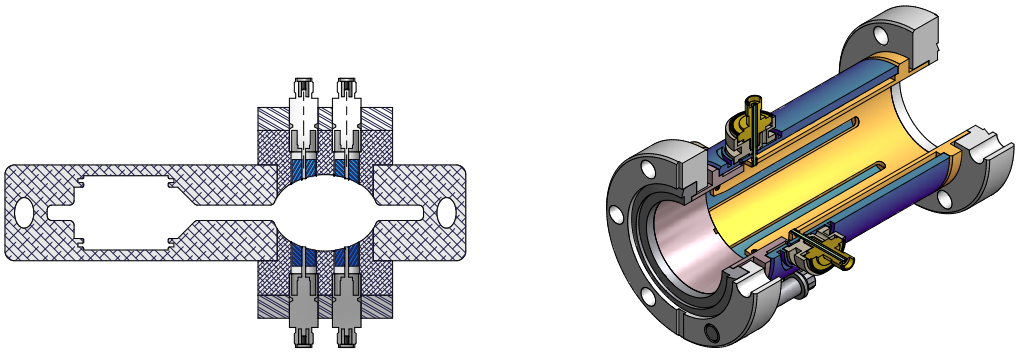

(a) BPM design A (b) BPM design B

Figure 2.2.22: Two types of BPM designs are to be considered: (A) pickup buttons and (B) striplines.

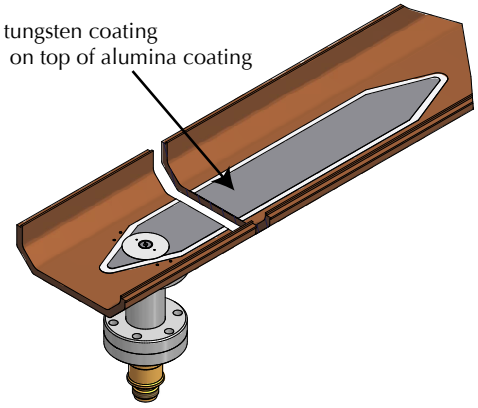

Figure 2.2.23: Electrode deposited on the vacuum chamber via thermal-spray technology. The electrode has already been used for electron clearing in a superconducting wiggler as a part of CesrTA project.

2.2.5 Vacuum system procurement

Procurement for the vacuum system is discussed in the Project Execution Plan [10]. Some vacuum chambers and components will be built in house; most however will be fabricated by qualified vendors, using CLASSE designs. These include dipole- and multipole-extruded aluminum chambers, IDs (both in-vacuum and ex-vacuum), UHV-pumping chambers and pumps, RF-shielded bellows, RF-shielded gate valves, BPMs and crotches. CLASSE personnel will work closely with the vendors in drafting fabrication specifications and procedures.

On-site vacuum facilities and associated personnel are described in [10] and are necessary to perform the following tasks:

- Acceptance of all vacuum chambers and components
- Final cleaning (particulates)

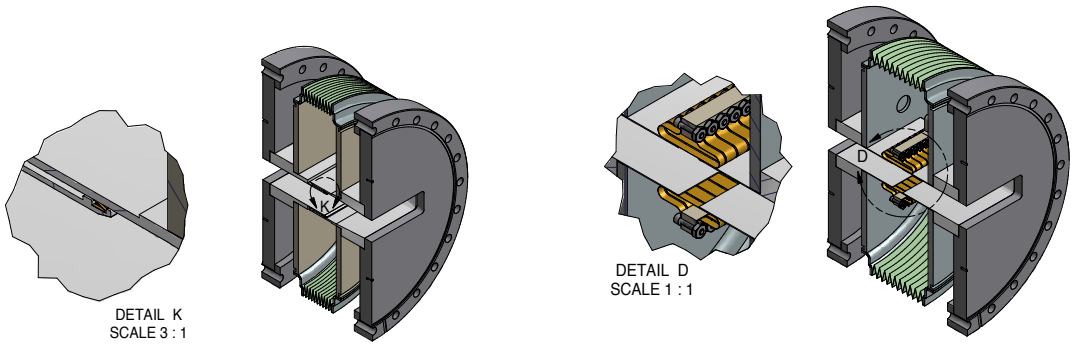

(a) Design A (b) Design B

Figure 2.2.24: Conceptual designs for RF-shielded bellows.

Table 2.2.4: Comparison of two RF-shielded bellows

Style	Pros	Cons
CESR	Simple design Unlimited stroke Local experience	Larger vertical step ($\lesssim 2\,\mathrm{mm}$)
DAΦNE	Low impedance Angular flexibility	Many small parts Limited stroke

- Final assembly onto girders and alignment
- Vacuum bakeout prior to installation
- On-site repair and modification
- Fabrication (including proto-type) of unique vacuum components
- Vacuum equipment staging and maintenance

Space for these facilities is housed in the existing Wilson laboratory, in close-by rented areas, or designed into the architectural plans developed by ARUP [11].

References

[1] Trakhtenberg, E., *et al.* *LCLS Extruded Aluminum Chamber - New Approaches.* In *Proceeding of MEDSI/Pan-American SRI2008 Workshop.* Saskatoon, Saskatchewan, Canada (2008). http://www.lightsource.ca/medsi-sri2008/pdf/PPT-LCLS_extruded_aluminum_vacuum_chambers.pdf.

[2] Benedict, G. F. *Nontraditional manufacturing processes.* CRC Press (1987).

[3] *Budgetary Estimate for ERL Beamline Components.* Technical Report report 3086-BP-8384-0, Research Intruments (2010). Report is on file at Cornell.

[4] Benvenuti, C. and P. Chiggiato. *Pumping characteristics of the St707 nonevaporable getter (Zr 70 V 24.6-Fe 5.4 wt %).* Journal of Vacuum Science & Technology A: Vacuum, Surfaces, and Films, **14** (6), pages 3278–3282 (1996). doi:10.1116/1.580226.

[5] Hoffstaetter, G. H. and M. Liepe. *Ion clearing in an ERL.* Nucl. Instr. and Meth. A, **557** (1), pages 205–212 (2006).

[6] Suetsugu, Y., *et al.* *Demonstration of electron slearing effect by means of a clearing electrode in high-intensity position ring.* Nucl. Instr. and Meth. A, **598** (2), pages 372–378 (2009).

[7] Palmer, M. A. *et al.* *Electron Cloud at Low Emmittance in CesrTA.* In *Proceedings of the first International Particle Accelerator Conference*, pages 1251–1255. Kyoto, Japan (2010). http://accelconf.web.cern.ch/AccelConf/IPAC10/papers/tuymh02.pdf.

[8] Calvey, J. R., *et al.* *CesrTA Retarding Field Analyzer Measurements in Drifts, Dipoles, Quadrupoles and Wigglers.* pages 1970–1972 (2010).

[9] Tomassini, S., *et al.* *A New RF Shielded Bellows for DAΦNE Upgrade.* Eleventh European Particle Accelerator Conference Proceedings, pages 1706–1708 (2008).

[10] ERL@CESR. *Project Execution Plan* (2011). To Be Completed.

[11] ARUP. *Energy Recovery Project Definition Design, Volume I Report.* Technical report (2010).

2.3 Injector

2.3.1 Introduction

Overview

The injector is a key element of the ERL. This is simply because the electron beam quality at the full ERL energy is no better than that exiting the injector. The properties of the final x-ray beams are thus directly related to the beam quality generated in the injector. In particular, generating a fully coherent x-ray beam at 1 Å wavelength with a 5 GeV electron beam requires a normalized transverse emittance of the order of 0.1 mm-mrad. For the ERL, this beam must be generated as a train of short duration bunches at a repetition rate of 1.3 GHz. The ERL will have two primary operating modes – one delivering 100 mA average beam current with the lowest possible normalized emittance, and a second delivering a reduced average current – initially expected to be around 25 mA – with normalized emittance of 0.1 mm-mrad. No electron injector constructed to date has delivered beams approaching these challenging parameters.

Photoemission cathodes are essential to generate the low emittance beams. This is because emission from these cathodes follows the transverse and temporal profiles of the illuminating light to very small distance and time scales, allowing one to create electron bunches optimally shaped in three dimensions to minimize the uncorrelated emittance growth, and because they can support very high instantaneous current densities. Certain photocathodes offer the additional advantage of a very small thermal emittance. For the high average currents of the ERL, high quantum efficiency photocathodes are necessary.

Selection of the type of gun and the photocathode are the most important issues in the design of a high brightness, high average current injector. The gun is followed by a conventional NC RF bunching cavity, steering and focusing magnets, precision beam diagnostics, and a heavily beam loaded SRF accelerator to reach the final injector energy.

CW operation: To deliver CW electron beams, one must use either a DC gun, or a CW RF gun – the latter employing either normal conducting (NC) or superconducting (SRF) technology. Each type of electron gun – DC, NCRF, and SRF – has its own technical challenges. It is necessary to assess the technical issues and present state-of-the-art with each gun type in making a selection.

DC guns: DC guns, particularly at very high voltages and electric field strengths, are limited by field emission (FE) and ultimately breakdown across the cathode-anode gap. Long before breakdown is reached, field emission can result in the release of gases chemically harmful to the photocathode. Ceramic insulators for these guns become problematic at higher voltages, and in the presence of field emission currents which may cause charging and punch through failures. On the other hand, it is relatively straightforward to achieve excellent vacuum conditions in a DC gun. Such vacuums are required for long photocathode operational lifetimes.

NCRF guns: CW NCRF guns suffer from significant Ohmic heating of the cavity walls, even at modest accelerating gradients. Hundreds of kW of average RF power, dissipated as heat in the cavity walls, are required to establish even modest gradients. Photoemission cathodes are degraded at the elevated cavity operating temperature, and there is increased outgassing, which can further degrade the cathode through ion back bombardment or chemical

poisoning. Furthermore, the need for precise azimuthal symmetry of the cavity to minimize emittance growth, along with the choice of operating frequency, severely restricts the size and location of ports in the cavity, making vacuum pumping problematic. Mounting a high quantum efficiency photocathode in the cavity wall also presents a number of problems. Many groups are working on low frequency, high power NCRF guns now, but extending those designs to work at 100 mA and 1.3 GHz is not deemed possible.

SRF guns: The obvious solution to the problems of a CW RF gun is to use SRF. Gradients well above those possible in CW NC structures are routinely achieved in SRF cavities. A high average current, such as the 100 mA of our ERL, requires coupling a very large RF power into the gun cavity. Presently, couplers delivering over 50 kW CW at 1.3 GHz have been demonstrated at Cornell, but higher average power delivery would be required for a gun operating at reasonable gradients. While all three gun types require that the cathode be inserted and removed through a vacuum load lock, the vacuum, mechanical, and thermal issues associated with accomplishing this are most challenging with an SRF gun.

On examining the technical issues and demonstrated performance of each gun type, we have chosen to develop a very high voltage DC gun for our application. DC gun technology is the most mature for CW applications. While an SRF gun may ultimately prove to be the best choice for a high average current CW gun, the technology is in its infancy, and much remains to be learned or demonstrated. A recent issue of the ICFA Beam Dynamics Newsletter reviewed current low emittance electron source activities world wide [1]. While not a refereed journal, this review is a broad survey of the present day efforts in the field. There are SRF gun projects underway at Rossendorf, BNL, and NPS, NCRF gun projects at Los Alamos and LBNL, and HVDC gun activities at a number of laboratories.

Photocathodes: The high average current of the ERL requires the use of a high quantum efficiency (QE) photocathode. The photoemission current from a linear photoemitter is given by:

$$I(\mathrm{mA}) = \frac{\lambda(\mathrm{nm})}{124} P_{\mathrm{laser}}(\mathrm{W}) \times \mathrm{QE}(\%), \tag{2.3.1}$$

showing that delivery of the 100 mA ERL beam from a 5% QE photocathode requires about 5 W of light at 520 nm. As the photocathode QE degrades with use, a significantly higher average power laser is required. There are three families of high quantum efficiency photocathodes – alkali tellurides, alkali antimonides, and negative electron affinity (NEA) semiconductors. NEA GaAs offers high quantum efficiency in the visible and near infrared, while the antimonides require near ultraviolet to green illumination, and the tellurides have high QE only in the ultraviolet. The final emittance from an electron injector results from the thermal emittance of the photocathode and the effects of nonlinear fields from space charge and accelerator elements. A computational optimization of an electron injector with a DC gun photoemission has demonstrated that for the single bunch charges of our ERL, it is possible to have the final emittance dominated by the thermal emittance of the photocathode [2]. This makes a strong case for using cathodes with the smallest practical thermal emittance – the NEA semiconductors – which also operate at the most accessible wavelengths. The thermal emittance of the antimonide and telluride cathodes has not been broadly studied, but the few measurements reported give values significantly larger than those of the NEA photocathodes. Though the NEA semiconductors have a number of challenging aspects to their use, we have selected NEA GaAs for our application for the moment, for its demonstrated very low thermal emittance

and convenient operating wavelength. NEA GaAs is by far the most thoroughly studied photocathode in terms of its thermal emittance and temporal response [3]. Other photoemissive materials are being evaluated for the ERL application, both at Cornell and in the accelerator community in general [4], and we anticipate further progress in this important area.

In practice, the quantum efficiency of a photocathode declines with use. There are several physical mechanisms that can degrade a photocathode, with the ultimate limit set by ion back bombardment. This fact places a premium on achieving exceptionally low vacuum pressures in the gun. At the 100 mA average current of our application, the photocathode must provide 360 Coulombs/hour. The time interval between replacing or restoring a photocathode must be on the order of 100 hours to limit accelerator down time, and thus the cathode must deliver $\approx$ 36,000 Coulombs before intervention. No photocathode has approached this level of charge delivery. Furthermore, the maximum optical power on the photocathode will be of the order of 20 W. Since a fraction of this optical power is absorbed in the cathode, it is necessary to incorporate a means to cool the cathode during operation.

Our solutions to the technical issues with HVDC electron guns and NEA photoemission cathodes are given below.

State of the art

Thermionic DC guns: Very high voltage DC photoemission electron guns are in operation or under development in a number of laboratories [1]. In addition, two thermionic guns are in operation at or above 500 kV [5, 6]. These latter guns have ungridded thermionic cathodes, pulsed high voltage, and oil insulation. They deliver relatively long duration beam pulses at low repetition rate, have only moderate beam brightness, and are unsuitable for our application.

Photoemission DC guns: The best performing DC photoemission guns are the FEL gun at JLab [7], several polarized electron sources at JLab [8], and the ERL gun under development at Cornell [9]. The JLab FEL gun has operated for several years at 350 kV, and typically delivers several hundred Coulombs from an NEA GaAs photocathode before intervention is necessary. The JLab polarized electron sources operate at 100 kV, and are mentioned only because they have convincingly shown very good cathode operational lifetimes that are limited only by ion back bombardment. With very good vacuum in these guns, they have reported cathode dark lifetimes over 22,000 hours, and charge density lifetimes of 2×10^6 C/cm^2 [10].

The developmental gun at Cornell has been HV processed to 440 kV, where field emission problems were encountered. Operation to date has been primarily at 350 kV, to allow progress without dealing with the FE problems. As of May 2013, the maximum current delivered from this gun is 75 mA, with 65 mA sustained for 8 hours, which exceeds the previous record from a photoemission gun by more than a factor of 2 (unpublished, see Ref. [11]). Additionally, about a thousand of Coulombs at 25 mA has been extracted from a single spot on the photocathode without any measurable QE degradation. At 60 mA, the measured QE decay implies over 30 hours of $1/e$ lifetime which, with the demonstrated laser power overhead [12], should allow on the order of a few days of uninterrupted running before the photocathode would have to be changed.

Small emittances: Recently, low emittance measurements were performed in the merger section of the Cornell injector. The settings of the machine for these measurements were determined using a multi-objective genetic algorithm and a complete model of the injector

with the 3D space charge code GPT [13]. Two optimized settings were eventually generated corresponding to 19 and 77 pC per bunch. Loading these settings into the machine, and using a 50 MHz laser system to limit the beam power hitting the interceptive emittance measurement systems, the normalized horizontal and vertical projected phase spaces were directly measured at both bunch charges, and the normalized emittances computed. In addition, the time-resolved horizontal phase space was measured. From this the bunch current profile and rms bunch length were measured. All measurements were taken at 8 MeV.

In the horizontal plane, the measured projected normalized emittance at 19 (77) pC per bunch was 0.23 (0.51) mm-mrad for 90% beam fraction and 0.14 (0.28) for the core beam fraction, in this case 67 (64)%. In the vertical direction, the corresponding values were 0.14 (0.29) mm-mrad for 90% beam fraction, and 0.09 (0.19) mm-mrad for the core fraction, in this case 70 (70)%. These values should be compared to the measured values of the thermal emittance in each plane. In both planes, the thermal emittance was for these settings was 0.12 (0.24) mm-mrad. The quoted core emittances in the horizontal plane are thus dominated by the thermal emittance. In the vertical plane, both the 90% and core emittances are dominated by the thermal emittance value. All of these emittances were measured with an rms bunch length of ≤ 3 ps, and with an rms energy spread on the order of 10^{-3} [14].

If accelerated to 5 GeV, the normalized horizontal emittances would give a corresponding geometric emittance of 24 (52) pm and 14 (29) pm for 90% and core beam fractions at 19 (77) pC per bunch, respectively. In the vertical plane, the corresponding geometric emittances would be 14 (30) pm and 9.2 (19) pm for the 90% and core beam fractions at 19 (77) pC per bunch. These values should be compared with the horizontal emittance found in third generation light sources such as APS: 3 nm (effective) at 7 GeV, [15], and PETRA III: 1 nm at 6 GeV, 100 mA [16].

Detailed simulations show that improvements to the photoinjector can reduce the emittances even further by roughly a factor of 3, resulting in about 10 times higher beam brightness [17].

Field Emission: Field emission from the cathode electrode structure is a major limitation on the operating voltage of very high voltage guns. Field emitted electrons striking the ceramic insulator of the gun result in charging and localized melting, release of gas, ion formation, and ultimately a punch through failure of the ceramic. This phenomenon currently limits the maximum operating voltage of both the JLab FEL and Cornell guns. Various techniques to reduce field emission from the electrode surfaces, to prevent field emitted electrons from striking the ceramic insulator, and to drain away charge accumulated in the ceramic insulator, are actively being pursued at several laboratories.

The voltage holdoff of a vacuum gap increases more slowly than linearly with the gap dimension, as shown in Fig. 2.3.1 [18]. This figure shows the best values reported for the holdoff voltage of a vacuum gap, independent of the electrode materials, their area, and their surface treatment. This behavior indicates that the anode plays a significant role. Different combinations of molybdenum, titanium, and high quality stainless steel have been studied as cathode and anode electrode materials at Nagoya University, with the conclusion that a molybdenum cathode and a titanium anode gives the best high voltage performance of the various pairs of these metals [19]. At Cornell, it was reasoned that the ideal anode would have a very good thermal conductivity, to rapidly diffuse the heat deposited by field emitted electrons, and a very low Z, to maximize the depth to which field emitted electrons penetrate the material and minimize the x-ray yield. Accordingly, the anode of the Cornell gun is Be.

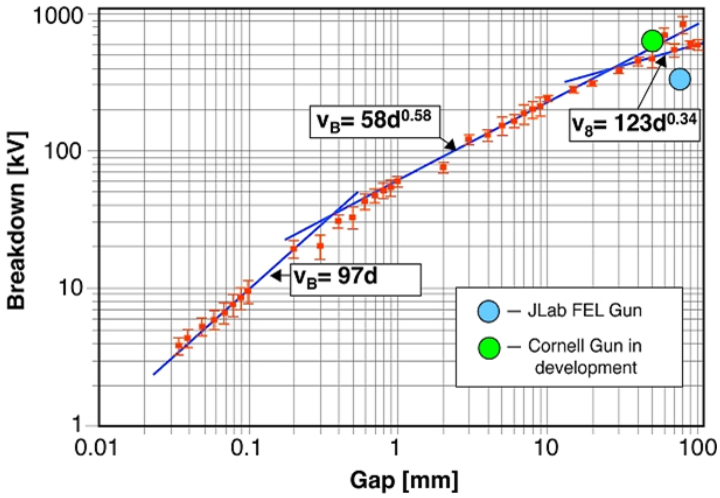

Figure 2.3.1: The voltage holdoff of a vacuum gap as a function of the gap dimension [18]. Also shown are the operating points of two photoemission guns: the JLab FEL gun at 350 kV and an 8 cm gap, and the Cornell gun at 625 kV with a 5 cm gap.

Cathode electrodes of both 316LN stainless steel and the titanium alloy Ti4V6Al are available.

The Cornell gun has been used to extensively study the thermal emittance and temporal response of NEA GaAs photocathodes [3]. Detailed measurements of the transverse emittance of highly space charge dominated bunches from this gun have been used to benchmark two codes widely used to model the performance of electron injectors – GPT and Parmela3D [20]. This latter work also led to an understanding of the minimum possible emittance of a short duration bunch from a photoemission cathode in a high voltage gun [21]. These benchmarked codes have been used to design and predict the performance of the ERL injector as detailed in beam dynamics §2.1.4.

ERL performance parameters

The ERL light source will operate in two primary modes – a high flux mode from a 100 mA average current beam of 77 pC bunches at a repetition rate of 1.3 GHz, with the lowest emittance possible with this bunch charge, and a high coherence mode formed from the highest average current 1.3 GHz bunch train with 19 pC bunches with reduced emittance. The bunch length in either of these two modes is significantly shorter than in present day light sources – about 2 ps rms through the Linac and most undulators, and as short as 100 fs at dedicated undulators. In addition to these two 'workhorse' modes, it is possible to prepare a beam of significantly higher charge bunches, at repetition rates in the range of 0.1 to 1 MHz, with the bunches temporally compressed to less than 100 fs after the 5 GeV Linac. Such a beam would be used for experiments involving very fast time resolution, such as pump-probe measurements. Finally, this running mode can be suitable for driving a SASE or HGHG FEL, though this application will not be implemented initially. This specialized operation mode would involve no more than partial, if any, energy recovery, depending on the total beam power for the mode. A dedicated electron source would be used to deliver the smallest transverse emittance, were

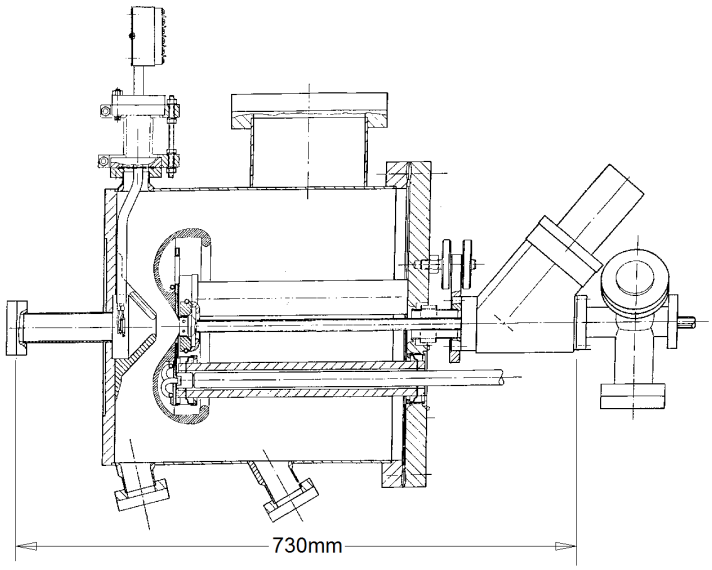

Figure 2.3.2: The 200 kV inverted gun developed at SLAC. The large cathode electrode is supported by three hollow ceramic rods inside a grounded vacuum chamber. The Cathode is inserted from a load-lock system mounted to the right of the 45° angle valve on the right, and the HV connection is through one of the ceramic rods.

that an important aspect. The full beam requirements for these various modes are presented in Tab. 1.3.1 along with detailed 3D space charge calculations of the photoinjector performance in §2.1.4.

2.3.2 Gun design

Baseline design

In the simplest photoemission electron gun, the thermionic cathode of a conventional gun is replaced with a photoemission cathode, and the necessary devices to form or activate the photocathode *in situ* are added to the gun. While this approach has been used successfully for a number of polarized sources and the JLab FEL gun, it is unsuited to the ERL application due to the high average current, which will require that the cathode be reformed or replaced with some regularity. High quantum efficiency photocathodes cannot be exposed to even very tiny quantities of many gases, such as oxygen, water, and carbon dioxide, leading to a general requirement that they be formed in ultrahigh vacuum. The ERL injector will require a load lock system attached to the gun to allow the cathode to be formed external to the gun, and translated into the cathode electrode structure under ultrahigh vacuum conditions.

A load lock system is reasonably complex, and is physically large due to the need to transfer cathodes over significant distances. Attaching the system directly to the cathode terminal would imply having the entire load lock at cathode potential, which is highly undesirable at the very high voltages of an ERL gun. Three designs have been developed to allow the load

lock system to be operated at ground potential. The first of these, shown in Fig. 2.3.2, is the so-called 'inverted' gun [22]. In this scheme, the cathode electrode is supported inside the gun vacuum chamber by relatively small ceramic insulators. The load lock is attached to the gun chamber at ground potential. This design has much appeal, but only two relatively low voltage examples have been constructed to date. The higher voltage version showed significant field emission and very short cathode lifetimes, even without photoemission, at its 200 kV design voltage, limiting its operating voltage to 120 kV. The cathode high voltage was delivered through one of the ceramic insulator rods. Reaching the much higher voltages desired for an ERL gun would require significant changes to this basic design.

A different scheme to place the load lock at ground potential uses a second ceramic insulator, with the load lock at the ground end of this second ceramic. This design was adopted for the 100 kV polarized source at NIKHEF [23], and for a 200 kV gun being developed as a polarized source for the ILC at Nagoya University [24]. As there is nothing inside the second ceramic during gun operation, this ceramic may be simpler than the one containing the cathode electrode.

Finally, one can make the cathode electrode a hollow cylinder supported by a tube perpendicular to the axis the cylinder. The photocathode is moved through the cylinder and secured into its operating position at one end. This design was originally developed for a 100 kV polarized electron source at JLab [25], and has been adopted for the Cornell ERL injector development program. The Cornell version, designed to operate up to 750 kV, is shown in Fig. 2.3.3 [9]. The photocathode is held in position by an array of spring fingers.

As described below, the photocathode is a GaAs wafer mounted on a molybdenum 'puck'. This puck is seated in a massive copper cylinder, which in turn is connected to the external environment by a large copper rod. This provides a path for cathode cooling during high power illumination. There are two arrays of non-evaporable getter (NEG) pumps mounted parallel to the cathode electrode axis close to the chamber walls, and a 400 l/s DI pump with a NEG array is mounted on the bottom flange. After careful measurement, our final estimate is that the system base pressure with all gauging unpowered was likely in the range of 5×10^{-12} to 1×10^{-11} Torr. This result is very similar to one obtained in a similar measurement with the JLab polarized guns [8]. This gun design has the disadvantage of having a very large electrode area at high field strength. The gun as initially assembled with a test beam line is shown in Fig. 2.3.4. In use the gun ceramic and HVDC power supply are located in a common pressure vessel, and insulated with pressurized SF6 gas, as shown in Fig. 2.3.5.

The load lock system attached to this gun is shown in Fig. 2.3.6. Both the load lock and the gun are built up on thermally insulating tables. Thermally insulating walls are assembled around these systems for vacuum bakeouts. Cathode wafers are cleaned by exposure to atomic hydrogen, heating to high temperature (ca. 550°C), or both. The activation chamber has storage for a second fully activated cathode, allowing a used cathode to be removed and replaced relatively quickly. The translation mechanisms are motor driven for speed and reproducibility.

The gun HV power supply – 750 kV at 100 mA – is based on proprietary insulating core transformer technology. It is comprised of a stack of circuit boards insulated from each other. Each board contains two ferrite cores which couple a high frequency magnetic field from one board to the next. Each board can deliver up to 12.5 kV at 100 mA, and is only 5mm thick, leading to a very compact supply. 62 boards are used in the full stack, which is shown in

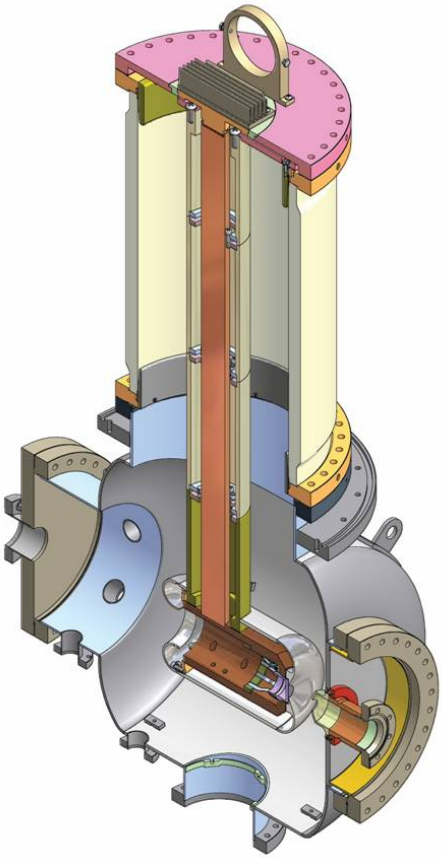

Figure 2.3.3: A cutaway view of the 750 kV gun under development at Cornell. Photocathodes are prepared in a load lock system mounted on the large flange at the left, and transported through the cathode cylinder to the operating position in the Pierce electrode shape on the right. The beam exits through the small flange to the right.

Fig. 2.3.7. The primary of the ferrite insulating core transformer is powered by an external high frequency driver. The HV terminal of the power supply is attached to the cathode terminal of the gun by a 4 inch diameter tube. During initial HV conditioning of the gun, a HV series resistor is used to limit the current to the gun. A battery powered picoammeter is mounted between the power supply and gun, with its signal delivered to ground potential by fiber optic cables. This HV power supply technology is believed to be capable of reaching 1.5 to 2 MV in a practical supply [26], giving an obvious upgrade path if field emission can be controlled.

The two primary technical issues for a photoemission gun of this design are achieving ultrahigh (UHV) or extreme high vacuum (XHV), and reduction of field emission (FE) and mitigation of its effects. We treat these in order.

There is nothing inherent in the photoemission process that degrades the QE of a photocathode. NEA photocathodes are degraded by exposure to certain chemically active gases, such as

Figure 2.3.4: The developmental gun at Cornell, without its HV power supply and SF_6 tank, followed by the initial test beamline. The load-lock system is on the right rear of the gun.

O_2, H_2O, and CO_2, and by ion back bombardment. Gases such as H_2, N_2, CH_4, and Ar are not chemically harmful, and CO is only very minimally so, while ion back bombardment damage occurs with all gas species. In the course of achieving the necessary UHV or XHV vacuum pressures, the chemically active gases are effectively eliminated from the gun, leaving H_2 as the predominant residual gas species [27]. The mechanism of ion back bombardment damage is believed to be removal of the Cs-F activation layer by sputtering. Calculations based on the code SRIM have indicated that sputtering by hydrogen ions, even with their very low sputter yield, may account for all of the measured QE degradation within the uncertainties [28].

Ion back bombardment damage to the cathode QE can be characterized by the number of Coulombs delivered per unit illuminated area. This is an imperfect characterization as the ions can damage the cathode outside of the illuminated area. However, in a very high voltage gun, the great majority of the ions are produced close to the cathode and thus strike the illuminated area typically chosen to be off center with respect to the electrostatic axis of the gun, and we will use this parameter to characterize the QE damage. If the delivery of a given charge per unit area $(Q/A)\,(\mathrm{C/cm^2})$ results in a $1/e$ reduction of the QE, then a cathode will be able to deliver a constant average current I for a time T given by

$$T(\mathrm{hours}) = 0.278\frac{(Q/A)A(\mathrm{C})}{I(\mathrm{mA})}\ln\left(\frac{P_{\max}(\mathrm{W})\,\lambda(\mathrm{nm})\,\mathrm{QE}_0(\%)}{124\,I_0(\mathrm{mA})}\right) \tag{2.3.2}$$

where A is the illuminated area in units of $\mathrm{cm^2}$, QE_0 is the initial QE, λ is the illumination wavelength, and $P_{\max}$ is the maximum laser power. (Q/A) values greater than $10^6\,\mathrm{C/cm^2}$ have been reported from several 100 kV polarized guns at Jefferson Lab [8, 10]. If this performance is duplicated in the ERL gun, than a 20 W maximum laser power at 520 nm should be able to deliver 100 mA average current for over 50 hours from a 2 mm diameter illuminated spot on a cathode with an initial QE of 5%. In our experience, these numbers are all achievabele. Our laser has already produced 60 W, and our quantum efficiencies can be higher. Operational lifetimes of several days at 100 mA average current should therefore be possible. In fact, we

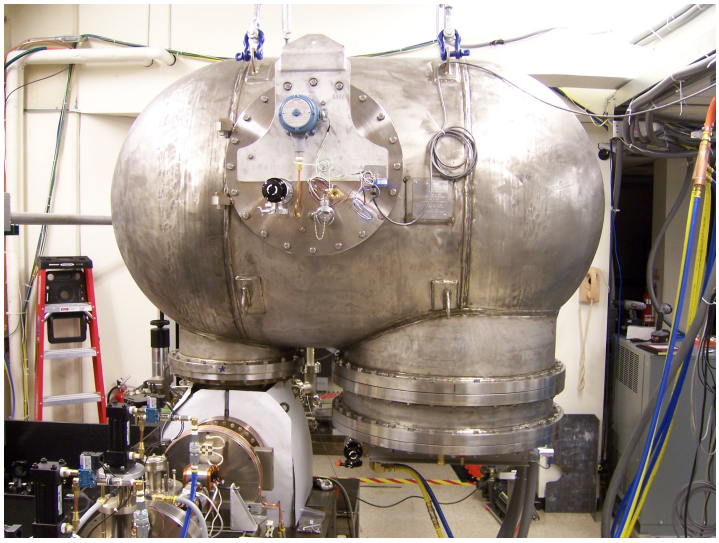

Figure 2.3.5: The Cornell gun with its SF_6 pressure vessel mounted. The HV power supply is mounted in the port to the right of the gun.

have already operated for over 8 hours at 20 mA with no recognizable loss in quantum efficiency. Overall, we conclude that while achieving the necessary vacuum conditions is challenging, and improvements are desirable (and possible), achieving a low emittance, high average current beam from an NEA photoemission cathode for useful periods of time is well within reach. It should be noted that in the case of ion back bombardment damage, only the QE in the vicinity of the illuminated area is damaged. Since the active cathode area is much larger than the illuminated area, it is possible to operate from multiple illuminated areas before it is necessary to replace the photocathode. This has been clearly demonstrated with the JLab polarized guns, and allows longer operating times before a cathode change is required.

Field emission is a very challenging issue. It is detrimental to the operation of a very high voltage gun for two separate reasons. First, FE electrons striking the ceramic insulator can lead to localized charging and melting, and ultimately a punch through failure of the ceramic. While the tiny vacuum leak resulting from punch through is easily repaired, the problem will recur until the source of FE is eliminated, presumably by HV processing. Although HV processing a gun results in a very tiny FE current at the operating field strengths, FE can be very dramatically higher during the processing, and the ceramic may not survive this processing. Secondly, FE electrons striking low thermal conductivity metallic areas results in sharply elevated temperatures, sometimes to the point of localized melting, and an associated release of gas from the metal. This gas may be ionized by the incoming electrons. These ions increase the local field near the metal, and are accelerated back to the cathode, providing an anode-cathode feedback mechanism that may ultimately lead to breakdown across the gap. Furthermore, gases released from the heated volume may chemically poison the photocathode. Several guns have observed short cathode lifetimes with full voltage applied even with no photoemission, causing them to be operated at much reduced HV, or with very low duty factor pulsed HV [22, 23, 29]. Thus, the challenge of dealing with FE is both to reduce the FE current to very low levels even during processing, and to develop a gun insulator that will

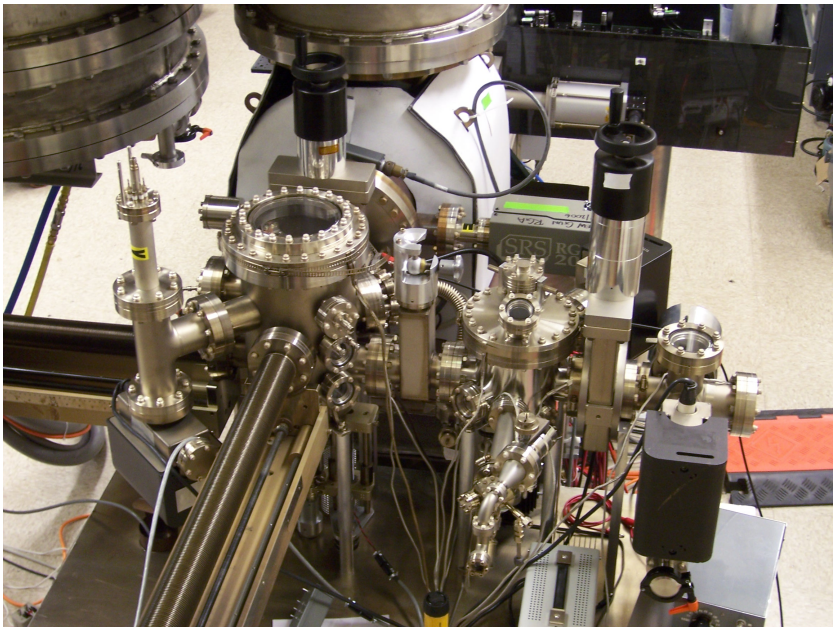

Figure 2.3.6: The load-lock system of the Cornell gun. GaAs cathode wafers, mounted on molybdenum pucks, are introduced into the small vacuum cross on the right while the remainder of the system is isolated by the vacuum valve on the left of the cross. Cathode cleaning is done in the chamber to the left of this valve, and cathode activation and storage is in the leftmost chamber. A conductance restriction valve is between the cleaning and activation chambers, to limit the pressure rise in the activation chamber during cleaning operations. Two 90 cm bellows translation mechanisms, visible at the lower left, move the pucks from chamber to chamber, and from the activation and storage chamber into the gun.

survive HV processing and operation at full field strength without punch through failure.

It is well known from studies of field emission in superconducting RF cavities that particulate contamination is a prominent source of field emission. The technique of high pressure water rinsing (HPR), developed for the removal of particulates from SRF cavities, has resulted in a very significant and reproducible advance in achievable cavity accelerating gradients. Accordingly, the HPR treatment was evaluated in the DC case in a test system. An example of the field emission reduction obtained with a 116 cm^2 test electrode is given in Fig. 2.3.8, showing an onset of field emission well above 20 MV/m at a given gap. The most recent electrode set for the gun has been HPR treated, and the gun assembled in a class 10 clean room. We anticipate pursuing HPR treatment for the gun electrodes to generate reproducible FE reduction.

Guns for different operation modes

The baseline gun design described above will support both primary operational modes, and is capable of delivering higher bunch charges with larger emittances. The gun is anticipated to perform well with charges up to 200 pC [17]. However, to deliver significantly higher bunch

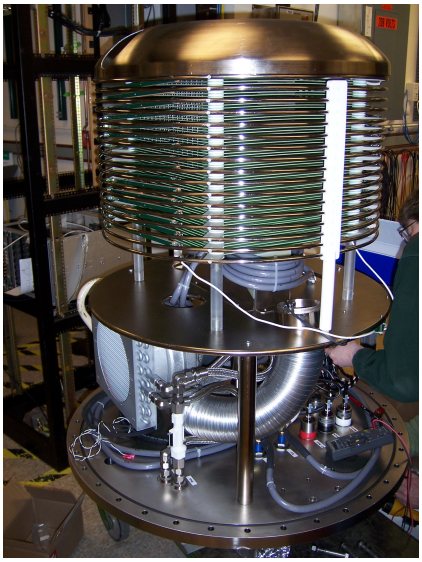

Figure 2.3.7: The HV section of the 750kV power supply. Individual circuit boards are visible inside the potential grading rings. The primary winding of the insulating core transformer is the large diameter gray-insulated wire below the circuit boards. The HV section is mounted in the pressurized SF_6 tank with its axis parallel to the axis of the gun ceramic.

charge – 1 nC or more – at low duty factor and without emphasis on the lowest possible emittance would use a larger illuminated cathode area and a much longer duration pulse. Alternatively, a CW NCRF gun can be employed operating at a subharmonic of 1.3 GHz to deliver lower repetition rate high-charge bunches [30, 31]. Such options will be pursued along with a possible extensions to the DC gun for the low repetition high-charge mode in the ERL.

Gun improvement options

The most immediate issue with the present gun is to develop an insulator that is not susceptible to punch through failure during HV processing and full voltage operation. The best solution appears to be the development of a segmented insulator, comprised of a stack of ceramic rings separated by metal leaves, with the leaves shaped to prevent FE electrons from the cathode support tube from striking the ceramic surface. Such insulators have been developed in the past for several very high voltage thermionic guns [32]. Freedom from punch through failure would allow processing of the gun to its design voltage, and may very well permit the development of a gun operating at even higher voltage. The new Cornell gun under construction employs the segmented ceramic as well as a variable cathode-anode gap to maximize the electric field in the 'physics region' at the photocathode for the highest voltage that will be achieved in the gun.

FE reduction is highly desirable, to permit operation at the highest field strengths, and to reduce HV processing time. An active program of FE studies using the existing test system, and possibly a higher voltage system using an available 300 kV supply, will be pursued. It

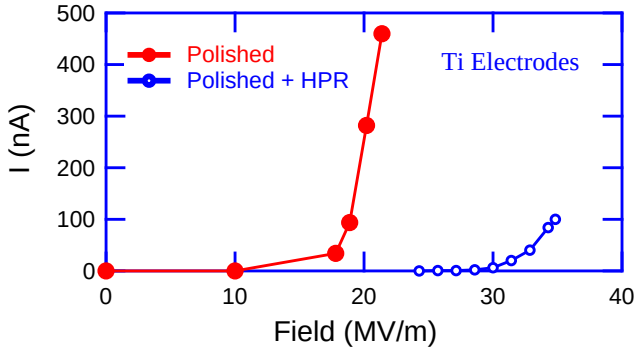

Figure 2.3.8: The reduction in field emission obtained by HPR treatment of a 116 cm^2 mechanically polished titanium electrode. The anode was also polished, but untreated, titanium, and the gap was 3.5mm.

seems very likely that a careful program of HPR treatment of the electrodes will dramatically reduce FE in the existing gun. Electropolishing may also be advantageous.

Reduction of the base vacuum pressure in the gun is desirable to reduce QE degradation from ion back bombardment. It appears that the present base pressure is dominated by hydrogen outgassing from the thick metal parts of the system [33]. A reengineered gun would minimize all thick metal pieces, since it is not practical to deplete the hydrogen from very thick pieces by high temperature bakeout. Hybrid chambers, with a fully hydrogen depleted thin wall chamber contained within a thicker walled, vacuum isolated chamber to support the external pressure have been suggested, and may be feasible in our application [34, 35].

The only gas other than hydrogen present in the gun is methane. The source of methane is unclear, but is widely believed to arise from the carbon present in the titanium plates of the sputter-ion pump [36]. It may be possible to eliminate or greatly reduce this source of methane by the use of highly pure titanium plates. While the hydrogen in the gun is predominantly pumped by the NEGs, methane is pumped only by the DI ion pump. Such crossed field pumps are known to have a greatly reduced pumping speed at very low pressures. It may be possible to develop an ion pump with much improved pumping speed at low pressures [36]. Alternatively, a different pumping scheme, such as a clean turbo pump backed by a small ion pump, might be adopted. Measurements are necessary to decide on the best way to reduce methane. The reduction of methane is likely to be quite important, as the ion back bombardment damage from a CH_4 ion, or a fragment of that ion, is considerably greater than that from an H_2 or H ion.

An inverted gun design offers potentially attractive characteristics, such as a greatly reduced probability for FE electrons to strike the ceramic insulators, a very large reduction in the electrode surface area at high field strength, and elimination of many of the thick metal pieces that are a source of hydrogen outgassing. Relatively small commercial ceramic feedthroughs operational to 225 kV are available, and could be adapted to deliver HV to the cathode electrode [37]. Although the maximum practical operating voltage for an inverted gun design is not clear, it appears possible to develop an inverted gun operating at $\approx 500\,kV$. Such a gun

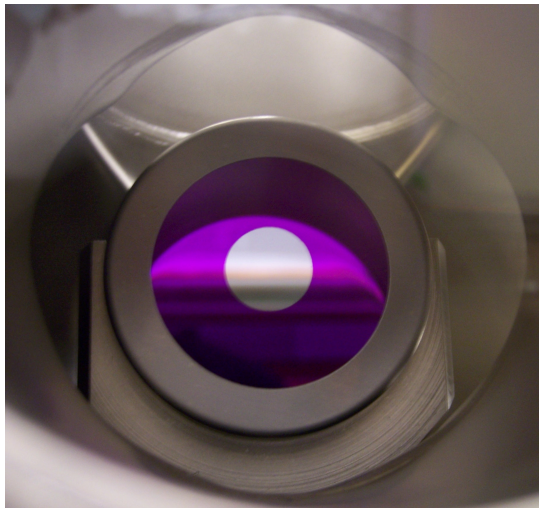

Figure 2.3.9: An end on view of a GaAs wafer mounted on its molybdenum puck. The puck is sitting in a U-shaped cradle in the entry chamber of the load lock system. The outer diameter gray annular ring is the tantalum retaining ring. The blue-violet annular region is an anodically grown oxide layer. This region has zero quantum efficiency. The active photocathode is the central gray circular area.

will be investigated as an alternative to the present design.

No doubt other options for gun improvements will appear in time. These will be pursued as resources permit, as the performance of the gun is a very central issue for the performance of an ERL-based synchrotron light source.

2.3.3 The photocathode

Baseline photocathode

The baseline cathode is bulk (as opposed to epitaxial) p-type GaAs activated to negative electron affinity with cesium and nitrogen trifluoride. Such a photocathode reliably provides an initial quantum efficiency of 10% or greater when illuminated by the baseline green light at $\approx 520\,\mathrm{nm}$. The GaAs is a commercial, substrate quality wafer cut a nominal 2° off the 100 face, and p-doped, typically with zinc, to about $5 \times 10^{18}\,\mathrm{cm}^{-3}$. The GaAs wafer is mounted on a molybdenum carrier (the so-called 'puck') by indium soldering, and is backed by a tantalum retaining ring. The GaAs is mounted on the puck prior to introduction into the load-lock system. A puck with a GaAs wafer mounted, sitting in the entry cradle of the load lock system, is shown in Fig. 2.3.9.

Atomically clean GaAs is necessary to obtain good quantum efficiency. Great care is taken to assure that the commercial GaAs wafers are kept clean during mounting on the puck. Once inside the load lock system, the GaAs may be cleaned by exposure to atomic hydrogen, which has been demonstrated to effectively clean GaAs [38–40]. During atomic hydrogen cleaning, the GaAs wafer becomes loaded with hydrogen, which is detrimental to good cathode lifetime. The hydrogen is removed by a heat treatment to $\approx 450°\mathrm{C}$ for about 1 hour. It is also possible

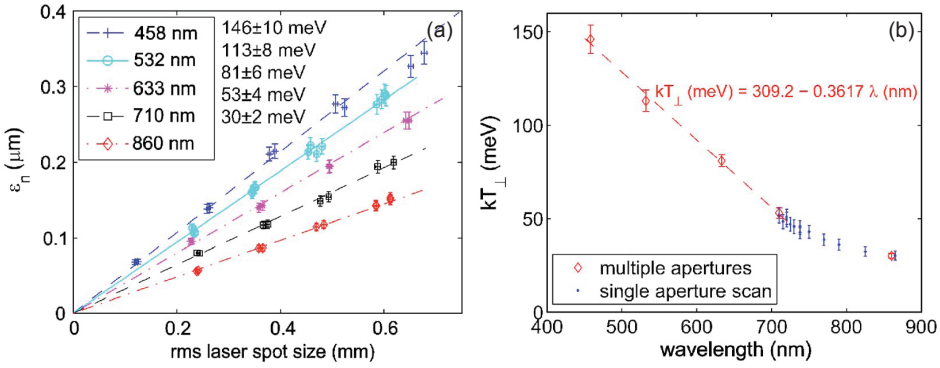

Figure 2.3.10: The thermal emittance of a GaAs photocathode as a function of the illuminated spot size, for various illumination wavelengths.

to simply clean the GaAs wafer by a heating cycle without the atomic hydrogen treatment.

Electrons photoemitted from the region of the cathode close to the cathode electrode receive a large transverse kick, and subsequently strike the beam line vacuum chamber walls, releasing gas and thus shortening the cathode lifetime through ion back bombardment. To prevent this, the cathode is activated only in the central region, away from the cathode electrode. This is accomplished by either growing an anodic oxide over an annular region at large radius on the cathode wafer, as shown in Fig. 2.3.9, prior to its mounting on the puck, or by masking the cathode wafer during its activation, so that cesium is applied only in the central area of the wafer. Both methods have been shown to work well.

The thermal emittance and temporal response of GaAs photocathodes as a function of illumination wavelength has been well characterized by our studies at Cornell [3]. Figure 2.3.10 show the measured thermal emittance and effective transverse energy for NEA GaAs photocathodes. Table 2.3.1 gives values of the temporal response for different illumination wavelengths and gun voltages. The temporal response times presented in [3] and Tab. 2.3.1 have been independently verified using a transverse deflection cavity [41]. These results show that at the baseline 520 nm wavelength, GaAs is a prompt (sub-ps) photoemitter with an effective transverse thermal energy of 120 meV. At longer illumination wavelengths, the temporal response becomes slower, and the effective transverse thermal energy decreases. Significant progress has been made recently in understanding the effects of nanoscale roughness that develops at the surface of GaAs and its implications for the prospects of a prompt (sub-ps) and sub-thermal transverse energy photocathodes [42].

Photocathode improvement options

The importance of photocathodes for high brightness photoinjectors have been recognized recently in a number of workshops, meetings, and reports [4, 43, 44]. A considerable research effort is underway to understand the physics of the photocathodes and their relevant properties for accelerator applications at several national laboratories and universities, including Cornell.

Several photocathode improvement options present themselves. Here, we only remark on the two most pressing and promising directions. At the moment, it appears essential to use

Table 2.3.1: The temporal response time of a GaAs photocathode for different illumination wavelengths and gun voltages.

Wavelength (nm)	τ (ps)	Comment
860	76 ± 26	$V_{\rm gun} = 200\,{\rm kV}$
860	69 ± 22	$V_{\rm gun} = 250\,{\rm kV}$
785	11.5 ± 1.2	$V_{\rm gun} = 200\,{\rm kV}$
785	9.3 ± 1.1	$V_{\rm gun} = 250\,{\rm kV}$
710	5.8 ± 0.5	$V_{\rm gun} = 200\,{\rm kV}$
710	5.2 ± 0.5	$V_{\rm gun} = 250\,{\rm kV}$
520	< 1	upper estimate placed
460	< 0.14	upper estimate placed

NEA photocathodes to achieve the lowest thermal emittance. The use of epitaxial material may improve the QE somewhat near the bandgap, due to an improved diffusion length, but at somewhat shorter wavelengths, this improvement quickly disappears. To the extent that the operational lifetime is limited by ion back bombardment, vacuum improvements are the solution, rather than cathode changes. As shown recently in [42], surface roughness that develops on GaAs surface as a part of high temperature cleaning can account for most of the measured thermal emittance. Much lower emittances are anticipated with a proper control of the surface condition. The effect is due to the fact that the effective mass of electron inside GaAs in the Γ-valley is very small leading to an analog of Snell's law for electrons emitted from the bulk into vacuum, resulting in a narrow cone emission [45]. Thus, by achieving the proper surface condition it should be possible to achieve mean transverse energy of the photoelectrons no greater than 25 meV even for laser illumination with 520 nm wavelength where the response of the GaAs is known to be prompt for efficient temporal shaping of the laser pulse [41]. Fig. 2.3.11a shows theoretical calculations explaining the experimental data of thermal emittance for measured surface roughness of GaAs samples activated for use in the gun. Fig. 2.3.11b shows predictions of the mean transverse energy for two typical surface roughnesses: that of the samples heat treated to ∼600°C and atomically polished GaAs prior to the activation. Thus, we anticipate a significant reduction in the thermal emittance for properly prepared GaAs wafers in accordance with the theory [42] and measurements [45] reported recently.

For applications where the emittance is not a key parameter, such as the high bunch charge modes, a different cathode — K_2CsSb, for example — may prove superior. These cathodes have been reproducibly demonstrated to have very high QE (ca. 17%) under green illumination [46]. The Cornell group has been able to achieve 6% QE in the green for this material. Initial beam experiments indicate that K_2CsSb shows fifty times lower quantum efficiency degradation than GaAs under identical operating conditions. That can be understood if one considers the sputtering from ion back bombardment as the main lifetime limiting phenomenon: a bulk stoichiometric compound like K_2CsSb behaves differently than NEA GaAs, where the essential CsF activation layer is only a monolayer thick.

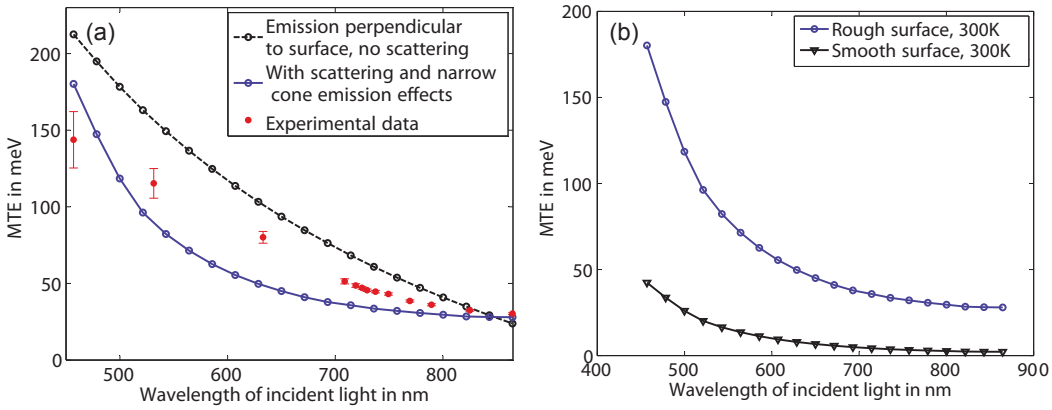

Figure 2.3.11: Effect of GaAs nano-roughness on thermal emittance: (a) theoretical predictions vs. experimental data for mean transverse energy (MTE) from GaAs used in the HVDC gun (6 nm rms surface roughness); (b) anticipated thermal emittance for 'smooth' (0.5 nm rms) vs. 'rough' (6 nm rms) GaAs photocathodes as a function of laser wavelength [42].

2.3.4 The laser system

Laser requirements

The key design parameters of the initial implementation of the ERL photoinjector laser system are given in Tab. 2.3.2. A brief justification for these parameter choices follows. The wavelength chosen for the laser is 515–530 nm – corresponding to the frequency of doubled Neodymium or Ytterbium fiber lasers. This wavelength is a reasonable match to the desirable properties of GaAs-like photocathodes, and it is relatively easy to generate significant average optical powers. Nd and Yb lasers allow the generation of a high frequency comb of pulses with a range of optical pulse widths. It is also relatively easy to shape these visible optical pulses transversely and longitudinally, and to control the light reaching the photocathode with fast electro-optic devices. These characteristics make this wavelength range near ideal for the initial beam studies to be conducted with the ERL injector. These requirements will be investigated during the ERL injector studies, and an optimal laser and cathode choice made for the final ERL.

As noted earlier, it is realistic to deliver 100 mA average beam current for >50 hours from a small illuminated spot on a GaAs photocathode provided that 20 W of optical power can be delivered to the photocathode. Between the exit of the laser and the photocathode, a large number of optical and electro-optical devices are necessary, to transversely and longitudinally shape the optical pulses, transport them from the laser exit to the photocathode, focus them on the photocathode, provide a suitable means to start up beam delivery for both tuning and full power operation, and finally to rapidly terminate beam delivery in the case of a fault. The large number of optical elements means that even with antireflection coatings on all surfaces, there will be a very significant optical power loss, from both reflection and absorption, between the laser and the photocathode. A factor of two loss is not exceptional, and indeed, requires

Table 2.3.2: Key design parameters for the ERL photoinjector laser system

Wavelength	515–530 nm
Average power at laser exit	50 Watts
Repetition rate	1.3 GHz to match Linac frequency
Synchronization to external an RF signal	Better than 1 ps rms
Pulse duration (rms)	10-30 ps
Pulse temporal shape	Flat top, < 2 ps rise and fall
Transverse shape	Elliptical
Power stability	Better than 2%
Position stability	10 microns rms

care to achieve. Accordingly, we require that the laser system provide at least 50 W of average optical power at its exit, which has already been achieved. An even larger value may be required to provide additional headroom for optical losses, laser beam shaping, and feedback overhead.

The synchronization of the laser output pulses with the RF signal from the Master Oscillator affects the timing jitter of the beam bunches with the accelerator RF. This timing jitter is compressed during the bunching that takes place in the injector by a factor of 10–20. The present laser system has already achieved < 1 ps rms jitter.

The 10–30 ps optical pulse duration requirement is based on simulations showing that this pulse width range gives the smallest final beam emittance from the injector (the actual value is not very critical due to the presence of RF buncher). It is unlikely this pulse width range will be generated directly in the laser – rather it will be obtained by external optical pulse shaping. These simulations also show that the rise and fall times of the individual optical pulses must be no more than a few percent of the total pulse width, and that the smallest emittance is obtained with a transverse beam profile approaching elliptical shape (which can be well approximated with a truncated Gaussian beam). Small variations from the elliptical transverse and flat-top longitudinal profiles may be required to obtain the very smallest emittance. Such topics are being explored during the injector beam studies.

A power stability of 2% is typically the best such a high power laser can produce without feedback. The sources of instability are thermal drift in mechanical components, vibrations in gain fibers or crystals, and noise in the pump lasers. For Yb-fiber lasers, the inversion time is on the order of milliseconds, producing noise at kHz rates, but the pulse-to-pulse stability at 1.3 GHz will be very good as the time between pulses (770 ps) is much shorter than this. Pump lasers can generate noise at many frequencies, from typical line frequencies to 100+ kHz for those using switching supplies. The electron beam current stability will need to be better than 1%, thus requiring a series of slow and fast feedback systems between the beam and the laser. We are currently testing such fast feedback systems with good success.

Poor pointing stability leads to a smearing out of the electron beam size (and shape), leading to emittance growth. Beam simulations show that a 10 μm rms position jitter is acceptable from the point of beam centroid jitter, which generally responds differently to the accelerator optics than the beam envelope in the space charge dominated regime of the photoinjector. Based on our experience, the laser can achieve 10 μm rms jitter directly after second harmonic

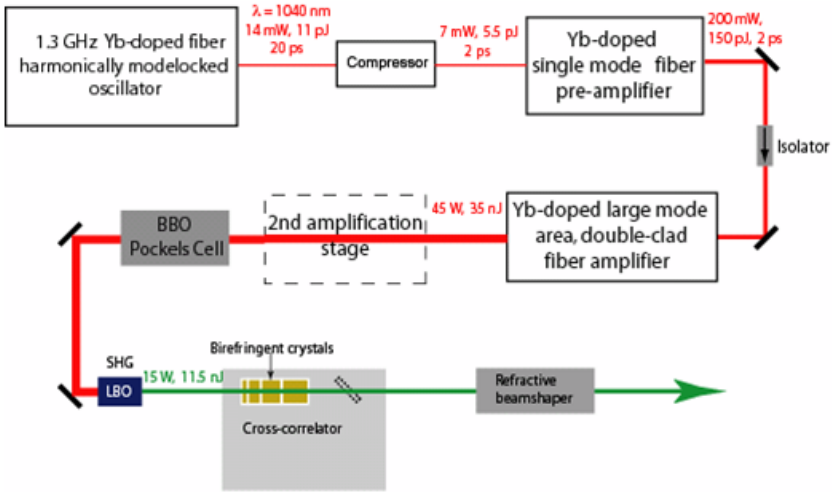

Figure 2.3.12: Drive laser system schematic.

generation (SHG) crystal, at the position of a beam waist. Using a series of 1:1 imaging telescopes to transport the beam to the photocathode, the low jitter after the laser can be maintained. For cases when the position jitter specification cannot be met, feedback systems exist which promise positional stability at these levels. We have purchased such a system and initial tests proved it to work well.

Laser system design and characterization

The generation of a high charge, low emittance electron beam from a photoemission electron gun imposes challenging requirements on the laser illuminating the photocathode, and on the characteristics and mounting of the optical and electro-optical elements between the laser and the photocathode. The necessary lasers are state-of-the-art, producing optical pulse trains at GHz repetition rates. The individual micropulses must have high energies, and be precisely synchronized to an external master clock. Following the laser, the micropulses are shaped both transversely and temporally to achieve the smallest possible electron beam emittance. We have developed a high average power, frequency doubled ytterbium (Yb) fiber based oscillator-amplifier laser system to meet these demanding requirements [47].

The 1.3 GHz laser system is shown schematically in Fig. 2.3.12. The oscillator is a commercially built- harmonically mode-locked fiber laser [48]. It provides a 1.3 GHz train of 20 ps-long pulses synchronized to an external clock. These pulses are fed to a single mode fiber pre-amplifier where the pulse energy is boosted to 150 pJ (200 mW average power). This pulse energy is small enough to avoid nonlinear effects in the fiber. The required pulse energy of 100 nJ is achieved through amplification in a double-clad large-mode-area fiber amplifier built to work in a nearly single mode regime. The pulses are compressed to 2 ps after the amplifier using a pair of gratings. The amplified IR pulses are frequency doubled in a LBO crystal to produce pulses centered at 520 nm. Currently, with one high power amplification stage we have achieved 110 W average IR power and 60W average green power with good stability. This is the highest average power achieved with a fiber laser at this frequency.

Longitudinal and transverse shaping

As is well known, generating low emittance beams from a photocathode gun depends strongly on the laser shape incident on the cathode. We have developed a technique to shape the pulses longitudinally by stacking 2^n short pulses in n birefringent crystals [41]. This technique produces a nearly flat-top laser pulse, has low optical losses, is easy to implement, and is currently being used for the Phase 1a injector studies. Depending on the results from Phase 1a, more powerful longitudinal shaping techniques may need to be developed in the future.

In the transverse plane, either a top-hat or an elliptical distribution is desirable for generating low emittance. We have tried a number of commercial devices with only moderate success. The old-fashioned method of expanding the laser before it passes through a pin-hole, then imaging the pinhole to the cathode is still the most reliable method. However, it wastes considerable beam power, leading to a rather high requirement for power at the laser exit. In our experience, the commercial devices are similarly inefficient in practical use. Some groups have experimented with transverse shaping using deformable mirrors, which may be the best solution in the future.

ERL startup

The complete details of machine startup are discussed in §2.9, only the details relevant to laser requirements are discussed here. There are two possible ways to ramp up the laser power. In the first of these modes, the amplitude of the 1.3 GHz CW optical pulse train will be ramped from zero to a value that produces an average beam current of 100 mA over a time no shorter than 16 ms, the cavity fill time. This latter time is the minimum necessary to assure that beam loading effects in the RF cavities are tolerable and controllable. A second mode will involve the generation of macropulses of variable duration and repetition rate with the optical pulse amplitude stable during the macropulse at a value corresponding to the desired average current during the macropulse.

For the first mode, one simply needs to quickly rotate a waveplate between crossed polarizers. The only difficulty is finding a device to move quickly enough to meet the requirements of the accelerator. There is at least one commercial product that can rotate fast enough for this mode (Aerotech model ADRH100). This mode is not particularly desirable, though, as the electron optics will need to be altered in step to match the changing space charge forces in the bunch versus time.

The macropulse mode can be accomplished only with an electro-optical switch – a Pockels cell (PC). The PC must be able to turn on/off fast enough so as not to cut off part of a micropulse, which are spaced 770 ps apart. Also, some PC exhibit ringing effects when they turn off, letting portions of trailing pulses through. The extinction ratio – a measure of the amount of light transmitted between macropulses – is a key requirement, as any of this extraneous light can lead to beam halo and background problems.

Typically, the PC is placed after the amplifier but before the SHG crystal. A good PC has an extinction ratio of 1000:1, which improves to 10^6:1 after passing through the SHG crystal due to its non-linear properties. This is an adequate amount of attenuation between macropulses for operations. When placed after the amplifier, the PC must also be able to withstand high average powers (as much as 100 W). Presently the only materials that come close to meeting

these requirements are BBO and RTP. RTP unfortunately gives a low contrast ratio, while BBO requires very high driving voltages. Producing a very high voltage drive pulse with fast rise and fall times is technically challenging. We currently use a 7 mm aperture BBO PC with half-wavelength voltage of $\approx 9\,\mathrm{kV}$ and rise time of $\approx 5\,\mathrm{ns}$. There is literature data [8] for a Pockels cell switch that can achieve a switching time of 240 ps at 4 kV. It thus appears that switching technology is able to provide the switch we need for a BBO Pockels cell. One limitation on the BBO cell we currently use is that the duty factor cannot exceed 5% without reducing the crystal lifetime substantially. Thus, at the present time there is not a straightforward solution using a PC after the amplifier.

A new electro-optic modulator (EOSpace Inc.) with bandwidths above 30 GHz is easily fast enough to modulate our laser accurately and at any frequency or duty factor desired. It can only operate at low powers, however, and therefore must be used directly after the oscillator. This introduces new problems, as the pre-amplifier/amplifier chain cannot remain unseeded while the pump laser is on to avoid the amplifier damage. The only way around this is to set up a feed-forward system to modulate the pump lasers to turn them down when the EO modulator is off. We have recently purchased such a modulator and are testing its performance to determine whether the feedforward control is practical.

2.3.5 RF systems

Energy choice

The energy choice for the injector is a tradeoff between several competing requirements. Higher energy benefits low emittance transport of space charge dominated beam from the injector cryomodule to the main Linac, minimizes unwanted beam degradation in the merger and facilitates a simpler merger design. Overall maximum synchrotron radiation losses in the ERL from beam transport and insertion devices are estimated to be around 5 MeV, the energy best supplied to the beam during injection as it benefits the machine performance by providing lower emittance beams and the injector RF system is already designed for efficient RF power transfer to the beam. On the other hand, a smaller injection and beam stop energies mean lower power consumption for the entire ERL.

Based on the injector performance discussed in §2.1.4 and a number of factors, mainly, the emittance growth after the full photoinjector including the merger and the energy spread after the energy recovery, it was decided that the injector energy will be 15 MeV with twelve 2-cell SRF cavities delivering most of the energy to the beam. The number of the cavities is largely decided by the maximum power that can be reliably delivered through the 'twin' RF input couplers at this frequency.

RF systems overview

Two types of 1.3 GHz cavities are used in the ERL injector: a normal conducting buncher cavity [49] and twelve 2-cell superconducting cavities in two injector cryomodules [50, 51]. As RF power requirements differ significantly between these two cavity types, two distinct RF systems were developed [52].

Three types of the high CW RF power generating devices are used in Linacs operating in the L frequency band: solid state amplifiers, inductive output tubes, and klystrons. Klystrons

Table 2.3.3: Buncher RF system specifications

Operating frequency	1.3 GHz
Cavity shunt impedance, Rsh = $V_{acc}^2/2P$	1.7 MΩ
Cavity quality factor	20,000
Nominal accelerating voltage	120 kV
Cavity detuning by beam current at nominal voltage	46.0 kHz
Cavity wall dissipation power at nominal voltage	4.24 kW
Maximum accelerating voltage	200 kV
Cavity detuning by beam current at maximum voltage	27.6 kHz
Cavity wall dissipation power at maximum voltage	11.8 kW
Maximum IOT output power	16 kW
Amplitude stability	8×10^{-3} rms
Phase stability	0.1° rms

have traditionally been used as high power amplifiers for accelerator's RF systems operating in UHF and L frequency bands. At high power levels (approximately 30 kW and higher) klystrons are still the technology of choice. Inductive Output Tubes (IOTs) are competing with klystrons at medium power levels. The main advantages of IOTs over klystrons are: higher efficiency, absence of saturation, higher linearity, smaller size, and a lower cost. The disadvantages are the lower gain and limited output power. An IOT based high-power RF amplifier fits well to the buncher cavity requirements (see Table 2.3.3). While solid state amplifier technology makes rapid advances, the demonstrated output power and efficiency are still lower than those of the other two technologies.

Each superconducting injector cavity requires 120 kW of RF power to provide the energy to accelerate the 100 mA beam. A scheme of one klystron per cavity is used, resulting in 12 RF power stations for two injector cryomodules. As a rather moderate RF power is required to maintain voltage on the buncher cavity, an IOT based high power RF amplifier is employed.

Buncher cavity and RF power station

To reduce emittance dilution due to space charge effects in the beam line between the gun and the first superconducting cavity, the electron bunches are created at the photocathode with the rms duration of 10-30 ps or 5-14° at 1.3 GHz. On the other hand, to minimize a nonlinear energy spread due to RF waveform in the main superconducting Linac, a much shorter bunch duration of about 2 ps rms is desirable. Hence, the bunch length has to be compressed after the gun. The first stage of the bunch compression happens in the beam line between the gun and the injector superconducting Linac. As the beam is still non-relativistic at this point, the simplest method of bunch compression is the velocity bunching, a well-known technique used, for example, in klystrons. Rather moderate requirements for the buncher cavity voltage (up to 200 kV) make it possible to use a normal conducting structure. Table 2.3.3 summarizes buncher cavity and RF system specifications.

In order to maximize the energy variation along the bunch at a given cavity accelerating voltage $V_{\rm acc}$, the beam passes the buncher cavity $-90°$ off crest, i.e. at its zero-crossing. The

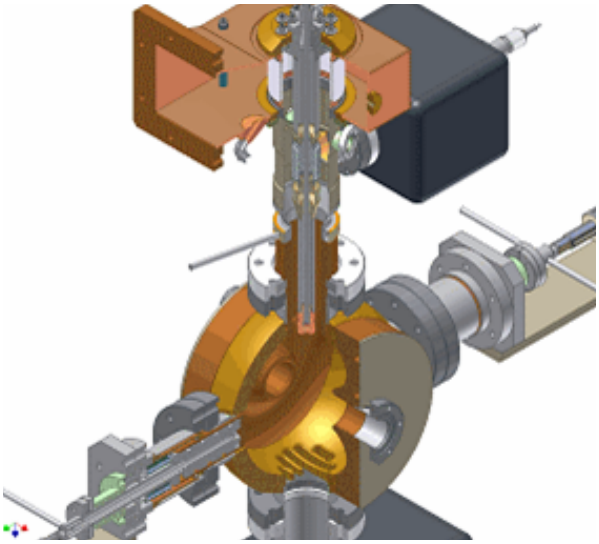

Figure 2.3.13: 3D view of the buncher cavity showing input coupler, plunger-type frequency tuner, pumping slots.

RF power required to maintain a constant field in the cavity is then given by

$$P_{\text{forw}} = \frac{V_{\text{acc}}^2}{R/Q \cdot Q_{\text{ext}}} \frac{(1+\beta)^2}{4\beta^2} \left[1 + \frac{Q_0^2}{(1+\beta)^2} \left(2\frac{\Delta\omega}{\omega} - \frac{I_b\, R/Q}{V_{\text{acc}}} \right)^2 \right] \tag{2.3.3}$$

where $\beta = Q_0/Q_{\text{ext}}$ is the coupling factor of the input coupler, ω_c is the cavity resonant frequency, $\Delta\omega = \omega_c - \omega$, and ω is the RF frequency. It is desirable to minimize the required RF power with and without beam passing through the cavity. The minimum power of 5.8 kW is required at nominal accelerating voltage, if the cavity frequency is tuned to 1300.000 + 0.023 MHz and if the coupling factor is $\beta = 1.7$. Amplitude fluctuations of the buncher cavity voltage will affect the resulting bunch length. If the bunch length fluctuation should not be more than 0.1 ps rms, the amplitude stability requirement is only 8×10^{-3} rms. The phase stability is derived from the required energy error and is 0.1° rms.

The buncher cavity [49] is a copper single-cell cavity that has an optimized spherical reentrant shape. A 3D view is shown in Fig. 2.3.13. The cavity input coupler is of a water-cooled coaxial loop type. Its coaxial part is short and ends with a coax-to-waveguide transition, which incorporates a ceramic window similar to the warm window of the TTF III coupler [53]. The coupling can be adjusted during installation by rotation of the coupling loop. Coupling loop, inner conductor and part of the outer conductor of coaxial line are water cooled. The cavity has two tuners with water-cooled 40 mm pistons. Pistons are moved by linear motion actuators with stepper motors. Two tuners provide a better field symmetry on the beam axis. Only one tuner is used for routine operation, the other one is used for preliminary frequency adjustment. During operation, the tuner has to compensate thermal effects (roughly 400 kHz from cold cavity to maximum voltage) and beam detuning. That corresponds to plunger travel of 2 mm. The full 15 mm stroke of one tuner gives a tuning range of 2.5 MHz.

The buncher RF power station in the prototype injector [52] comprises low level RF (LLRF)

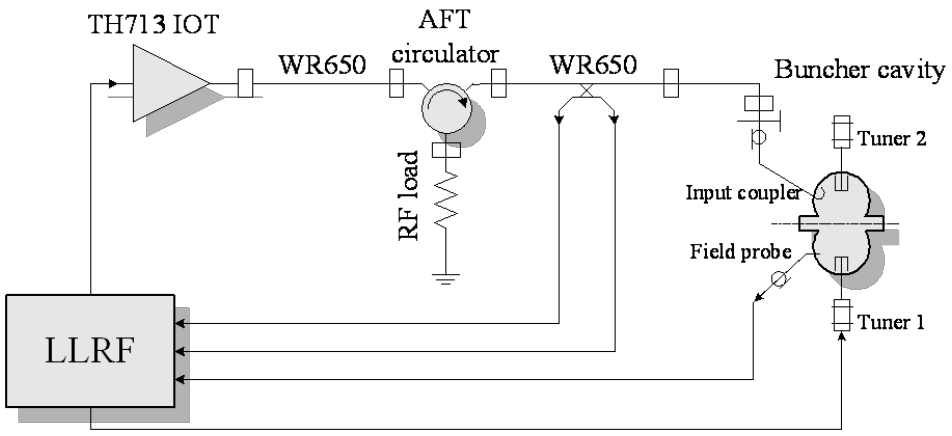

Figure 2.3.14: Block diagram of the buncher cavity RF system.

electronics, a high power amplifier (HPA), and waveguide transmission line components connecting the HPA to the cavity. It is anticipated that the injector described here will be of construction similar to that of the prototype. The block diagram of the buncher RF is shown in Fig. 2.3.14. An IOT based HPA was used in the prototype. It incorporated a 16 kW tube in a commercial broadcast unit a photo of which is shown in Fig. 2.3.15. The HPA efficiency is 60% with a gain of 21 dB at maximum power output [54]. The amplitude and phase ripple noise without the LLRF feedback are 0.13% and 0.5° respectively.

Injector cryomodule high power RF system

Two injector cryomodules house twelve 2-cell SC cavities, each delivering 120 kW to the beam. Because the cavities operate independently, the system consists of twelve identical channels. Each channel includes a set of LLRF electronics and RF interlocks, a klystron based HPA, and a waveguide distribution network. RF power is delivered to the cavities via twin input couplers [55] each carrying 60 kW. The main parameters of the system are given in Tab. 2.3.4 and a block diagram is presented in Fig. 2.3.16. A motorized, adjustable short-slot hybrid power splitter and a two stub phase shifter in one of the waveguide arms are used to are used to tune relative amplitude and phase between the two couplers [56]. A 170 kW ferrite circulator is used for klystron protection.

In the injector prototype 7 cavity klystrons with 165 kW saturated power output were used. Similar tubes are anticipated for the 12 cavity injector complement. To provide stable regulation of the cavity field the klystron must have finite gain and thus cannot run in saturation. The maximum power output for the prototype tube was defined as 0.5 dB/dB of drive and specified to be no less than 120 kW. At this level the efficiency of the prototype tubes is at least 50% and the bandwidth not less than ±2.5 MHz at -1 dB level and not less than ±3 MHz at -3 dB level. Six of these tubes have been in operation since 2008.

Figure 2.3.15: IOT inside the transmitter.

Table 2.3.4: Main parameters of the injector cryomodule RF system and power source

Number of RF channels	12
RF power per cavity	120 kW
Maximum useful klystron output power with incremental gain of 0.5 dB/dB	$\geq$ 120 kW
Klystron efficiency at maximum useful power	$>$ 50%
Tube bandwidth at -1 dB	$\pm$2 MHz
Tube bandwidth at -3 dB	$\pm$3 MHz
Klystron gain at nominal operating conditions	$>$ 45 dB
Klystron beam high voltage	45 kV
Typical klystron current	5.87 A
Maximum klystron CW output power	135 kW
Klystron saturated output power (pulsed)	165 kW
Tube efficiency at saturated power	$>$ 60%
Cavity field amplitude stability	9.5×10^{-4} rms
Cavity field phase stability	0.1° rms

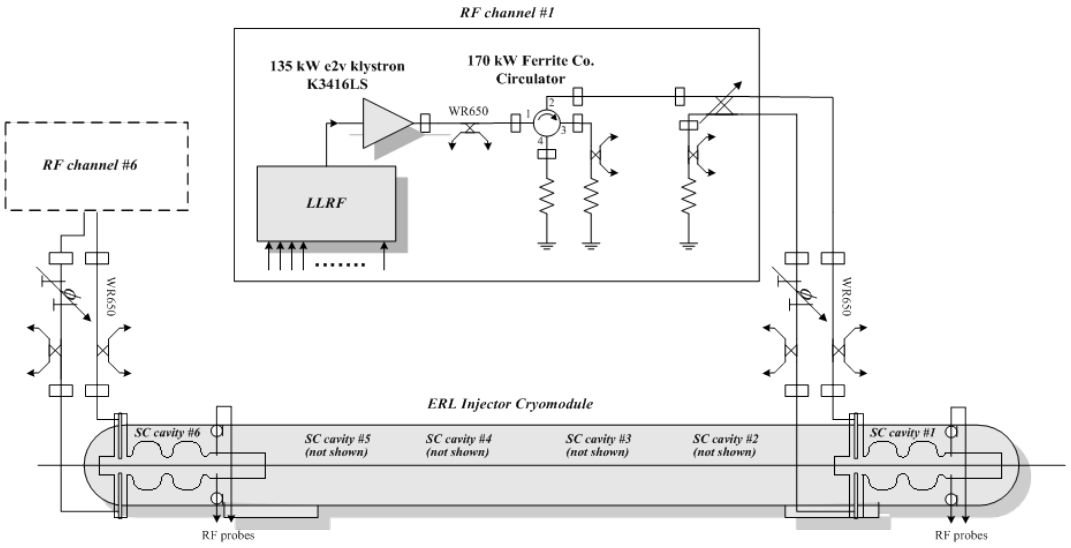

Figure 2.3.16: Block diagram of the ERL injector RF system (one cryomodule is shown).

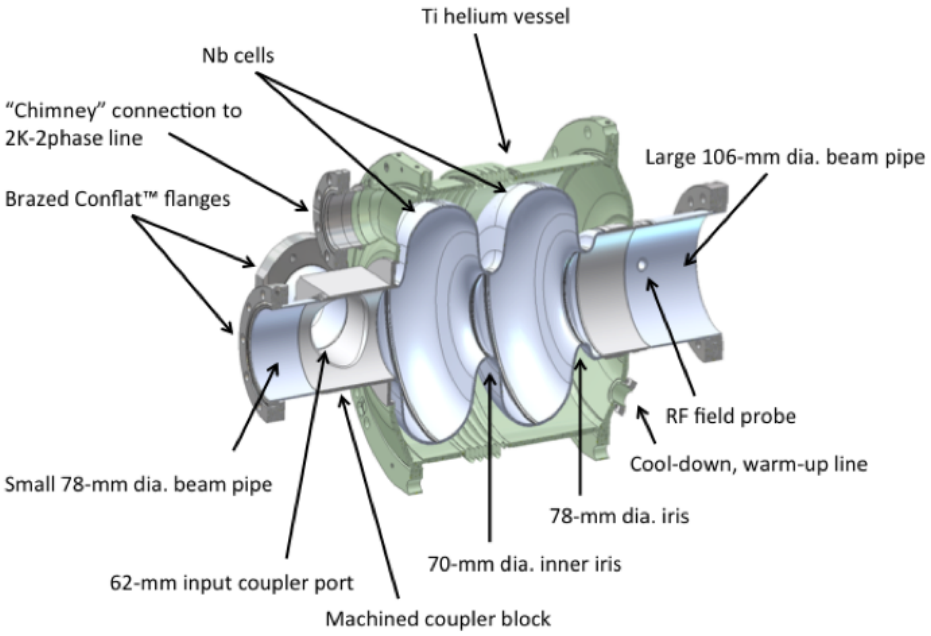

Figure 2.3.17: ERL injector cavity.

2.3.6 Injector Linac design

Introduction

The ERL injector cryomodule contains twelve 2-cell superconducting RF cavities, each providing an energy gain of up to 1.2 MeV at 100 mA beam current (including the gun energy, this totals to 15 MeV). RF power is transferred to each cavity via two input couplers, 'twin couplers', up to 120 kW per cavity. Efficient absorption of the Higher Order Mode (HOM) power is achieved by placing broadband HOM absorbers in the beam tube sections between the cavities. The cryomodule design is based on the TTF-III technology with modifications for CW operation.

A five-cavity prototype injector cryomodule has been designed and fabricated as part of the Cornell ERL Phase 1a effort with the goal of demonstrating a high quality ERL beam source [57]. This prototype has provided very valuable experience and is the basis for the design for the full twelve-cavity ERL injector cryomodule. In the following sections, the designs of the 2-cell SRF cavity, input coupler, HOM absorbers, LLRF system, and cryomodule are discussed in detail.

Injector cavities

Two-cell 1.3 GHz superconducting cavities were developed for the ERL injector prototype. The cavity design (Fig. 2.3.17) was optimized for handling high-current, low-emittance CW beams [50]. The cavity parameters are listed in Tab. 2.3.5. Efficient damping of the HOMs is essential to reduce resonant heating due to monopole HOMs and to avoid beam breakup instabilities due to dipole HOMs. Since the TTF-III technology was chosen as the baseline

Table 2.3.5: Parameters of the injector cavity

Resonant frequency (π mode)	1.3 GHz
Accelerating voltage	1.2 MV
Accelerating gradient, $E_{\rm acc}$	5.5 MV/m
Cells per cavity	2
R/Q	222 Ω
Geometry factor, G	261 Ω
Cavity quality factor, Q_0	$> 1 \times 10^{10}$
Nominal external quality factor, $Q_{\rm ext}$	5.4×10^4
Cell-to-cell coupling	0.7%
$E_{\rm pk}/E_{\rm acc}$	1.94
$H_{\rm pk}/E_{\rm acc}$	42.8 Oe/(MV/m)
Small beam pipe diameter	78 mm
Large beam pipe diameter	106 mm
Inner iris diameter	70 mm
Active cavity length	0.218 m
Cavity length flange to flange	0.536 m

for the injector design, the inner iris diameter (70 mm) and the beam pipe diameter (78 mm) are identical to those of the TESLA cavity [58]. However, in this geometry the lowest dipole HOM (TE11-like) is trapped. To facilitate propagation of this mode toward a beamline HOM absorber, the diameter of one of the cavity beam pipes was increased to 106 mm. A 78 mm diameter iris at this end of the cavity keeps the electromagnetic fields of fundamental mode from leaking out of the cell and is similar to the KEKB cavity [59]. The cell shapes were optimized for a maximum value of $G \cdot R/Q$ to minimize the cryogenic load while ensuring that the frequency of the lowest TE11-like mode stays at least 10 MHz above the large beam pipe cut-off frequency.

To support a 100 mA CW beam, the input coupler has to be strongly coupled to the cavity and this induces a strong, non-symmetric local perturbation of the otherwise axially symmetric cavity fields. This produces a transverse kick to the beam even if it traverses the cavity on axis. To compensate for this kick, the injector cavity uses two identical symmetrically placed antenna type couplers (twin couplers) that are described below. An additional benefit of using twin couplers is a 50% reduction in the RF power per coupler. Optimization of the coupler antenna tip was part of the cavity design process. The result is a bent elliptic disc, which conforms to the radius of the beam pipe [57] and is shown in Fig. 2.3.18. Bending of the disc increased the coupling by 20%. Since one of the goals for the ERL injector prototype was to explore a range of beam energies from 5 to 15 MeV, the input coupler was designed to be adjustable. Whether the final injector input couplers will also be adjustable has yet to be determined.

The TE11-like mode can have two polarizations resulting in two degenerate modes with identical resonant frequencies. The geometric perturbation introduced by the input couplers resolves the degeneracy and splits the modes into an 'in-plane' mode and a 'perpendicular' mode with respect to input couplers as shown in Fig. 2.3.19. The frequencies of the modes are

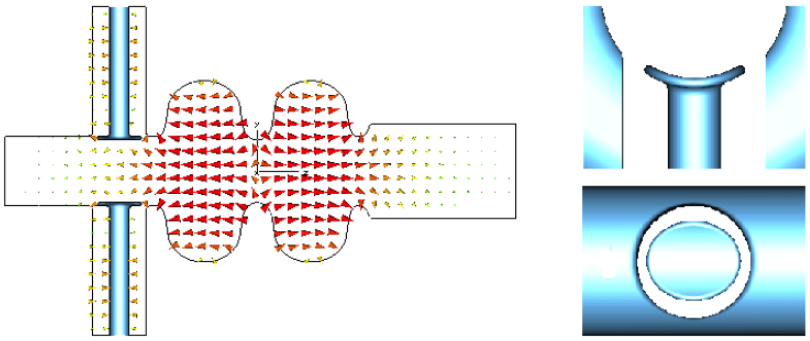

Figure 2.3.18: Geometry of the cavity and details of the coupler antenna with the electric field lines of the fundamental mode indicated

different from the original one but stay high enough above the cut-off frequency. The in-plane mode is strongly coupled not only to the beam pipe but also to the input couplers resulting in an external Q of 250, compared to the Q_{ext} of 1000 for the perpendicular mode.

High-purity, RRR = 250-300, 1/8"-thick niobium sheets are used for the cavity cell fabrication. The very modest accelerating gradient needed does not justify post-purification of the niobium at 1400° C. There is no stiffening ring between the cavity cells as the Lorentz force detuning is not as important for CW operation as it is for the pulsed mode operation. The strong coupling required to deliver high-average RF power to the beam requires a small separation between the coupler port and adjacent cell. This and the tight tolerances needed to achieve precise symmetry between the twin couplers led to the selection of the fabrication method for coupler ports. The coupler block is machined from a 4 inch thick solid high-purity niobium (RRR=200). Reactor grade niobium tubes are used for the cavity beam pipes to reduce the static heat load to the 2 K liquid helium. All cavity flanges are of a modified ConFlat® design. The regular ConFlat® joint has small gaps with extended depth between mating flanges and short bunches could excite dangerous wakefields in the gap space of beamline flange joints. A modified ConFlat® flange was designed [60] with reduced diameter and tapered flange surface to limit the risk of overheating and arcing. The knife edge was machined after a 316LN stainless-steel ring was furnace brazed onto a niobium tube. Each cavity has six brazed flanges plus one more on the liquid helium vessel. The helium vessel dishes were fabricated from titanium and electron beam welded to the niobium cavity. The helium vessel (flanges, tank and bellows) was also made from titanium and was entirely manufactured with electron-beam welding. Figure 2.3.20 shows a picture of the 2-cell cavity before and after the helium vessel was welded.

Six cavities, one prototype and five production cavities, were fabricated for the ERL injector prototype. The inner surface of each completed cavity was etched to remove 120 μm with BCP 1:1:2 at a temperature below 15° C maintained by water-cooling the exterior of the cavity. Because of the vertical orientation during etching, the cavity needed to be flipped to eliminate asymmetric removal across the cells. Brazed joints and knife edges at the ConFlat® flanges were protected with Teflon plugs to shield them from being attacked by the acid. After chemical etching, the cavity was rinsed with a closed-loop DI water system overnight followed by a four-hour session of high-pressure water rinsing in a clean room. All cavities reached the

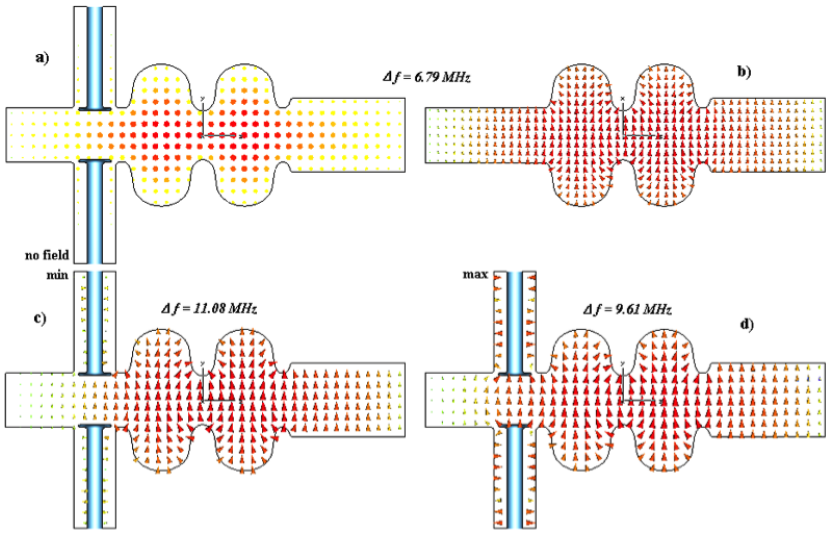

Figure 2.3.19: Electric field of the two dipole modes: a) and b) the 'perpendicular' mode; c) and d) the 'in-plane' mode with electric and magnetic walls at the ends of coaxial lines, respectively

performance goal during vertical RF tests [51].

Injector input coupler

The input coupler is one of the key components of the injector Linac due to strict requirements such as a high CW power transferred to the beam (up to 120 kW per cavity), strong coupling, wide range of coupling adjustment, and small distortion of transverse beam motion. Each injector cavity is equipped with two identical antenna type couplers symmetrically attached to a beam pipe of the cavity. This is a remedy to reduce RF power per single coupler, coupling to the cavity, and the transverse kick to the beam.

The coupler was developed at Cornell in collaboration with MEPhI (Moscow Engineering Physics Institute, Russia) for the ERL injector prototype [55, 61]. The design of the ERL injector couplers is based on the design of TTF III input coupler [53], consisting of a cold section mounted on the cavity in the clean-room and sealed by a 'cold' ceramic window, and a warm section incorporating a transition from the evacuated coaxial line to the air-filled waveguide. The warm coaxial line is sealed by a 'warm' ceramic window. Both windows are made of alumina ceramics and have anti-multipacting titanium nitride coating. Bellows in the inner and outer conductors of the coaxial line of the coupler allow a few mm of motion between the cryomodule cold mass and the vacuum vessel when the cavities are cooled from room temperature to 2 K. A low thermal conductivity is achieved by using stainless steel pipes and bellows with a 10–30 μm copper plating at the radio frequency conducting surfaces. Also, the bellows allow 16 mm of center conductor movement for coupling adjustment.

The ERL injector coupler design has, however, significant modifications necessary to handle much higher average RF power [55]:

- The cold part was completely redesigned using a 62 mm, 60 Ω coaxial line (instead of a

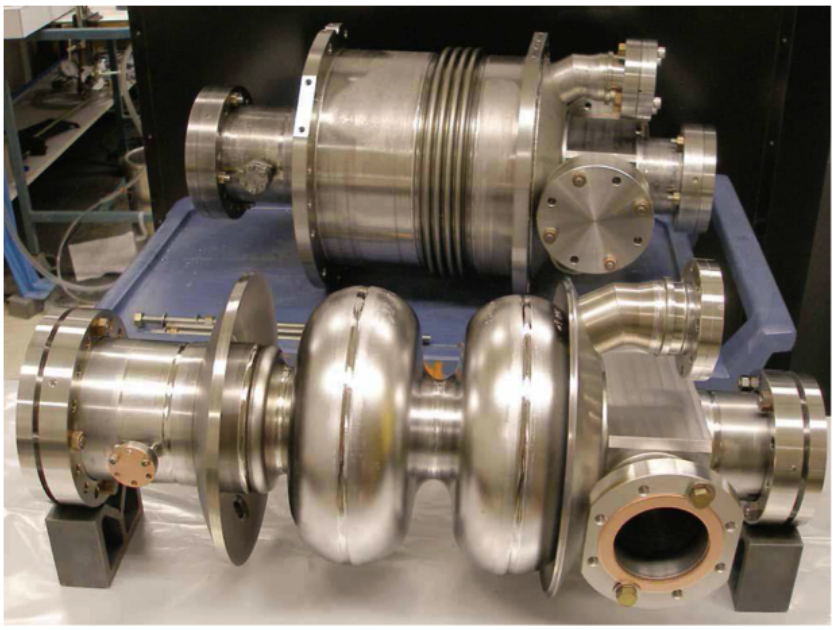

Figure 2.3.20: 2-cell cavity before and after welding the helium vessel

40 mm, 70 Ω) for stronger coupling, better power handling, and alleviating multipacting.

- The antenna tip was enlarged and shaped for stronger coupling.
- The 'cold' window was enlarged to the size of the 'warm' window.
- The outer conductor bellows design (both in warm and cold coaxial lines) was improved forbetter cooling (heat intercepts were added).
- Forced air cooling of the warm inner conductor bellows and warm ceramic window was added.

The parameters of couplers for the injector cavities are summarized in Tab. 2.3.6. The general design of the coupler is shown in Fig. 2.3.21.

Two prototype and ten production couplers were commercially produced for the Phase 1a ERL injector cryomodule. The prototype units and two production couplers were tested to verify their performance at high RF power [62]. A traditional scheme was used for coupler tests: two couplers connected in series, with a coupling device included between them. A cavity with very strong coupling was used as the coupling device. The cold portion of the couplers is designed to operate at cryogenic temperatures and relies on higher electric and thermal conductivities of copper and lower dielectric losses in the cold ceramic window at these temperatures for efficient heat transfer and reduced heat generation. Therefore to test the couplers to full power, it is absolutely necessary to keep their cold assemblies at low temperatures (around 80 K). Special liquid nitrogen cooled Coupler Test Cryostat (CTC) with a copper coupling cavity inside has been designed and built. The whole cold portion of couplers is cooled to 80 K. Figure 2.3.22 shows the assembly of CTC with a coupling cavity and

Table 2.3.6: Parameters if the injector input power couplers

Central frequency	1.3 GHz
Bandwidth	±10 MHz
Maximum RF power transferred to matched load	60 kW
Number of ceramic windows	2
Qext range	9.2×10^4 to 8.2×10^5
Cold coaxial line impedance	60 Ω
Warm coaxial line impedance	46 Ω
Coaxial line OD	62 mm
Antenna stroke	16 mm
Heat leak to 2 K	< 0.2 W
Heat leak to 5 K	< 3 W
Heat leak to 80 K	< 75 W

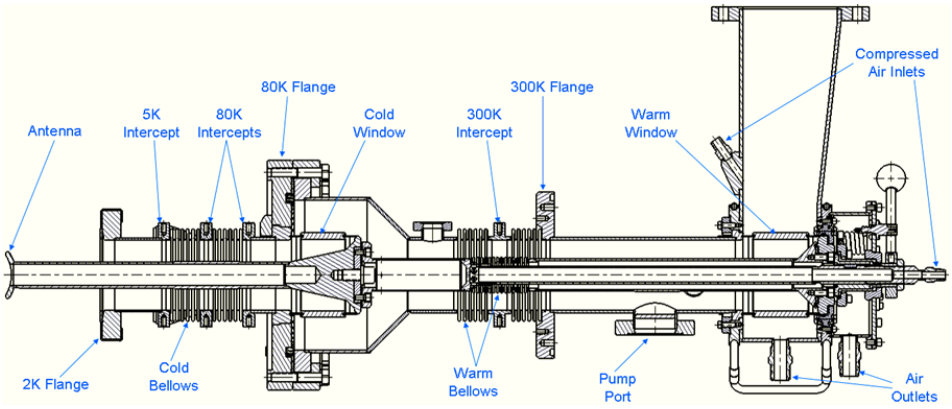

Figure 2.3.21: 2D section view of the injector input coupler.

two couplers. The production couplers showed stable operation during the test. The heating was in a reasonable agreement with predictions from thermal simulations. A maximum CW power of 61 kW was reached after approximately 15 hours of processing time.

Installed in a cryomodule, high power input couplers require conditioning at high RF power, especially if they were not pre-conditioned before installation. However, *in situ* conditioning is not as flexible as that in a dedicated set up: it is limited to only standing wave (full reflection) mode of operation. In the Phase 1a injector all input couplers were processed in pulsed mode up to 25 kW per coupler (50 kW klystron power) at full reflection. All couplers conditioned well, reaching these power levels within 25 to 75 hours (RF on time) of processing multipacting. If the conventional RF processing of multipacting is a limiting factor, two additional built-in measures of alleviate this phenomenon can be employed. First, the warm couplers can be baked *in situ* using special heating elements install on them. Second, a special capacitor assembly can be installed, isolating the center conductor from ground and allowing use of DC bias for multipactor suppression.

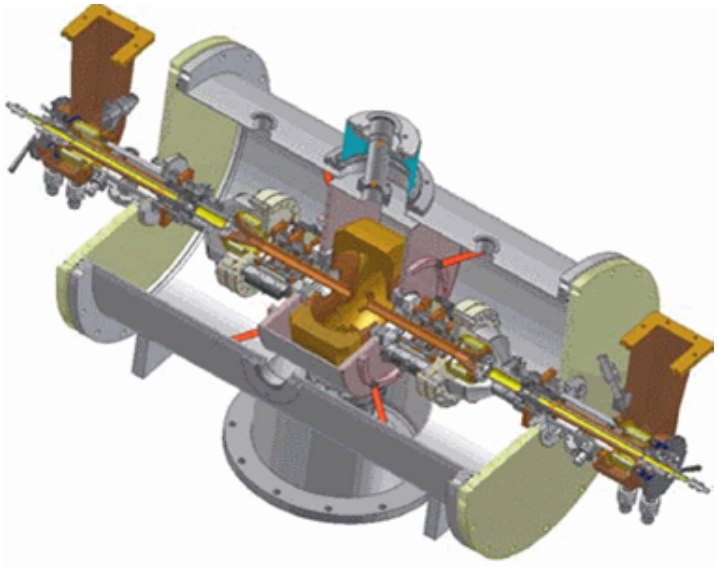

Figure 2.3.22: Coupler test cryostat assembled with coupling cavity and two couplers.

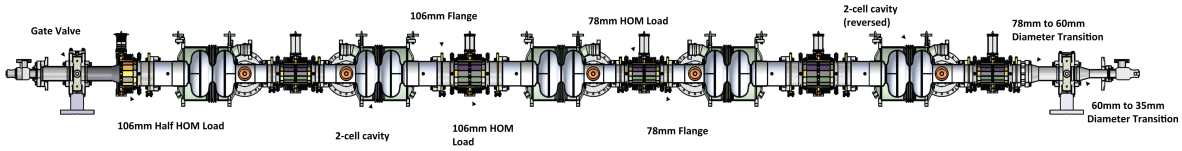

Figure 2.3.23: CAD model view of the Cornell ERL prototype injector cryomodule beam line with five 2-cell cavities. Note that the full ERL injector will have 12 2-cell cavities. Beam line components from left (beam entrance) to right (beam exit): gate valve; 106 mm half HOM load; first SRF cavity; 78 mm HOM load; second SRF cavity; 106 mm HOM load; third SRF cavity; 78 mm HOM load; fourth SRF cavity; 106 mm HOM load; fifth SRF cavity; 78 mm HOM load; 78 mm to 60 mm diameter transition; gate valve; 60 mm to 35 mm diameter transition.

Wakefield and HOM calculations

When the 100 mA beam current passes though the 12 cavity beam line in the injector cryomodule, the electron bunches will leave behind significant electromagnetic fields. The power transferred to these wakefields needs to be intercepted in the Higher-Order-Mode (HOM) absorbers located in the beam pipe sections between the individual cavities. In addition, these HOM absorbers need to damp monopole and dipole modes sufficiently to avoid excessive HOM power in case of resonant excitation of a monopole mode and to guarantee beam stability.

The longitudinal loss factor $k_{||}$ of a beam line section can be used to estimate the average power transferred from the beam to electromagnetic fields excited by the beam:

$$P_{\text{average}} = k_{||} \cdot q \cdot I \,, \tag{2.3.4}$$

where q is the bunch charge and I is the average beam current. The total longitudinal loss factor of the beam line section with five 2-cell injector cavities as shown in Fig. 2.3.23 was

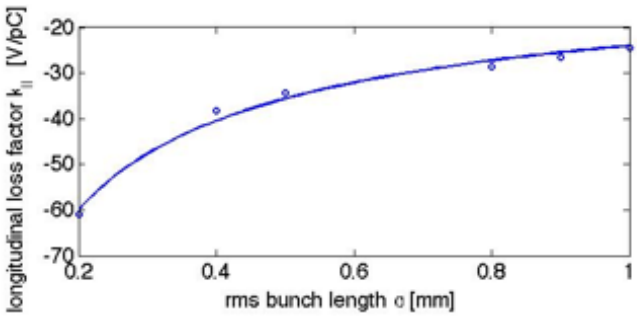

Figure 2.3.24: Total loss factor in the prototype injector cryomodule beam line with 5 2-cell cavities as a function of bunch length.

calculated [63]. The result is a longitudinal loss factor of 6.4 V/pC per one-cavity section (32 V/pC for 5 cavities) at the design bunch length of $\sigma = 0.6$ mm, see Fig. 2.3.24. Accordingly, the average monopole mode HOM power excited by the 100 mA, 77 pC beam is found to be ≈ 50 W per cavity section, i.e. per HOM absorber.

To verify the effectiveness of the HOM damping scheme with HOM beam pipe absorbers located between the cavities as shown in Fig. 2.3.23, the resulting HOM damping was studied both numerically and experimentally. Figure 2.3.25 shows simulation results for the quality factors of monopole modes between 1.5 GHz and 5.5 GHz, as well as the product of $(R/Q)Q$, which is the figure of merit in case of resonant excitation of an HOM by the beam. The quality factors of the modes are reduced strongly to very low values of typically 100 to a few 1000. Only the modes of the accelerating TM010 passband at 1.3 GHz remain unaffected by the HOM dampers because their frequencies are below the cut-off frequency of the beam pipes at the cavity ends. Even in the unlikely event of resonant mode excitation, the power transferred to any of these strongly damped modes would be modest and well below the maximum power handling specifications of the HOM dampers. HOM measurements at the Cornell ERL injector prototype cryomodule have confirmed these simulation results [64].

Injector HOM dampers

The requirements on the beam pipe HOM absorbers in the ERL injector are similar to the HOM damping requirements in the ERL main Linac. The only differences are (1) a factor of ≈ 4 smaller average power to be intercepted per load and (2) slightly different beam pipe radii (39 mm and 53 mm instead of 55 mm in the main Linac). Therefore, the HOM dampers in the ERL injectors will be a modified version of the beampipe HOM dampers developed for the ERL main Linac. Refer to §2.4.4 for a detailed discussion of the main Linac HOM dampers.

Cryogenic HOM beampipe absorber prototypes have been tested successfully in the Cornell ERL injector prototype. Figure 2.3.26 shows one of the prototype HOM loads prior to installation in the ERL prototype injector beam line. The damping of HOMs in the injector cavities by these beamline absorbers was investigated using a vector network analyzer to excite modes via pick-up antennas located at the cavity beam tubes and at the HOM loads (see Fig. 2.3.27). Preliminary results confirm very strong suppression of monopole and dipole modes with typical quality factors of only a few 1000 as predicted by simulations. Heater

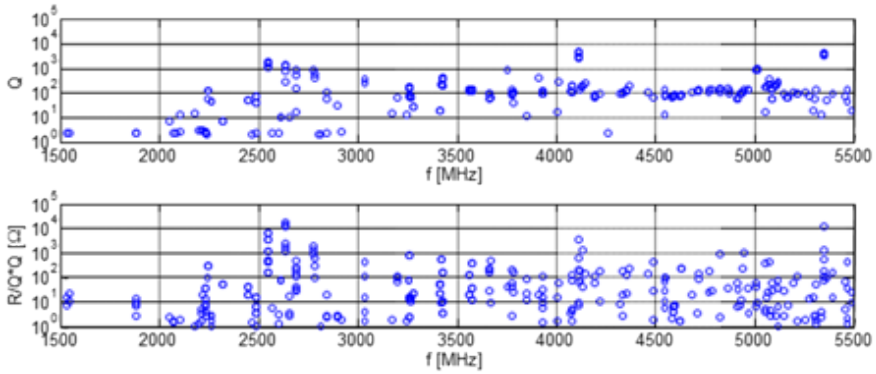

Figure 2.3.25: Simulated monopole mode damping in the full ERL injector (CLANS results). Top: Quality factor of all monopole modes between 1.5 GHz and 5.5 GHz. Bottom: $R/Q \cdot Q$ of these modes. Realistic complex dielectric properties where used in these simulations for the RF absorbing materials in the HOM dampers.

elements on the HOM absorber load bodies were used to verify the effective heat exchange to the high pressure cooling gas up to the maximum design heat load of 200 W; see Fig. 2.3.27. The measured temperature increase of the HOM load body was found to be in good agreement with simulation results.

The injector prototype HOM designs suffered from several problems which will be addressed in the final design for the injector. The RF tile soldering was not robust, and several tiles detached and fell, generating dust and particles. In addition, two of the three tile types became insulating enough at 80 K that any charge accumulated on their surfaces would not bleed off. This charge could be from electrons scattered during beam tuneup, or from x-rays and UV light generated during cavity processing. The electrostatic fields generated from the charge buildup severely distorted the beam passing through the cryomodule, making the beam unusable. For the prototype, the tiles facing the beam were removed, and the solder joints improved on the others to eliminate these problems.

Injector RF stability requirements and LLRF

The intra-bunch energy spread after the injector is about $\sigma_{\mathrm{inj}} = 15\,\mathrm{keV}$. It is desirable for the bunch-to-bunch energy fluctuation (bunch centroid energy) at the end of the injector to be below the intra-beam energy spread so that the total energy spread of the beam is dominated by the intra-bunch energy spread. The gun laser timing jitter, the buncher cavity as well as the 12 superconducting injector cavities each contribute to a bunch-to-bunch energy variation in the injector. We have to distinguish between uncorrelated and correlated (from cavity to cavity) errors. For the ERL injector cavities, small fluctuations in the 100 mA beam loading will be the dominating source of field perturbation, which will cause correlated field errors. Accordingly, we shall assume here correlated field errors in the injector cavities. We will require that the bunch-to-bunch energy fluctuation caused by the injector SRF cavities increases the total energy spread at the end of injector by no more than 20%, i.e. to a total of 18 keV rms. Accordingly, the maximum allowable bunch-to-bunch centroid energy gain

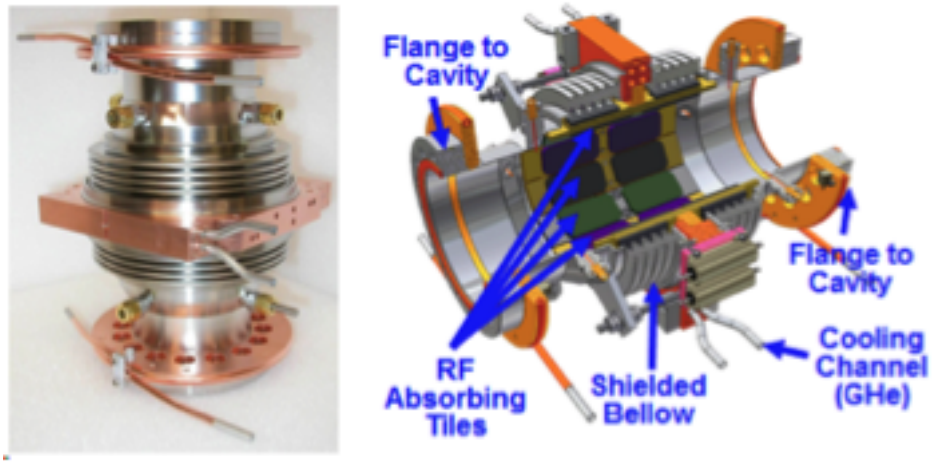

Figure 2.3.26: Cornell ERL injector prototype HOM load. Left: Finished load. Right: Cut-open CAD model of the prototype load showing the RF absorber tiles.

fluctuation is 10 keV, assuming no correlation between the intra-bunch energy spread and the bunch-to-bunch gain fluctuation. We will allow for 5 keV energy spread contribution from each phase errors and amplitude errors in the 12 injector cavities. This simple estimate results in a requirement for the relative amplitude stability of $\sigma_A/A = 5\,\mathrm{keV}/15\,\mathrm{MeV} = 3.3 \times 10^{-4}$. Assuming acceleration with a phase within 5 deg of on-crest then gives a requirement for the phase stability of $\sigma_p = 0.2°$.

A digital LLRF control system will be used to stabilize the RF fields in the injector cavities in amplitude and phase to these stability levels. A combination of feedforward and feedback control will be used to stabilize the cavity fields in the presence of strong beam loading and other perturbations of the RF fields. Sensors will be used to monitor all relevant signals, including the cavity fields, the incident and reflected RF power, and the beam current. Any disturbances due to klystron noise and ripple can be handled using feedforward. Extremely reliable hardware, a high degree of automation, and sophisticated built-in diagnostics will ensure a high degree of operability, availability and maintainability of the LLRF system.

The novel LLRF control system developed for the Cornell ERL Phase 1a injector is a prototype for the final injector LLRF system, and has been tested extensively, showing excellent performance (see Fig. 2.3.28). This LLRF system is an improved generation of the LLRF system previously developed for CESR [65], with lower loop latency ($< 1\mu$s), reduced noise, and increased sample rates and ADC resolution (16 bits). The integral and proportional gains of the fast feedback loop used to stabilize the RF fields in the cavities were optimized, as shown in Fig. 2.3.28. At optimal gains, exceptional field stabilities of $\sigma_A/A < 2 \times 10^{-5}$ in relative amplitude and $\sigma_p < 0.01°$ in phase (in-loop measurements) have been achieved, far exceeding the ERL injector and ERL main Linac requirements. In addition to the fast feedback loop, the system employs feedforward control to compensate beam loading and fluctuations in the high voltage of the klystrons, a state machine for automatic start-up and trip recovery, trip detection, and cavity frequency control.

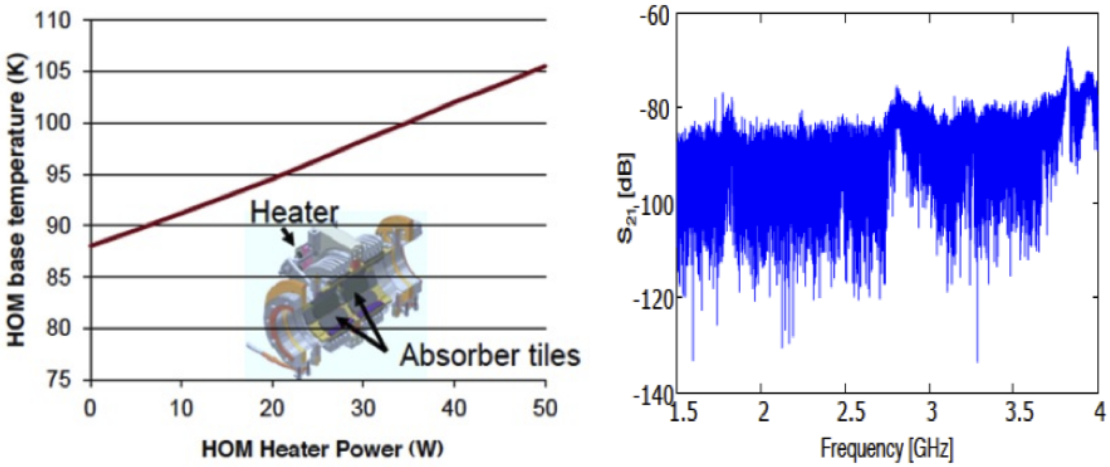

Figure 2.3.27: Left: Temperature of the HOM load temperature as function of power intercepted. The test was done at a relatively low cooling gas flow speed. Right: Vector network analyzer scan for HOMs between 1.5 GHz to 4 GHz. Shown is the transmission amplitude vs. scan frequency. Pick-up antennas on the cavities and HOM loads were used to couple to the HOMs.

Injector cryomodule

The ERL injector cryomodule design is based on TTF III technology with modifications for CW operation. This builds upon the considerable development work performed for this Linac technology over the past 15 years. TTF III technology is at the forefront of SRF Linac performance in regard to cavity gradient, Q, power coupled to the beam, cavity tuning, minimal cryogenic heat load, industrial fabrication, and operational reliability. A prototype injector cryomodule has been designed and fabricated as part of the Cornell ERL Phase 1a effort with the goal of demonstrating a sufficiently high quality ERL beam source [66]. A great deal of insight has been gained from this effort, allowing for high confidence in a design for the full ERL injector cryomodule.

The modifications to TTF III technology for CW operation of an injector cryomodule are structurally subtle, but have significant operational differences. Among the modifications to the TTF III cryomodule are the following:

- Use 2 coax RF input couplers per cavity, where one 120 kWCW klystron feeds a cavity coupler pair, each coupler rated at 60 kW CW.
- The coax RF input couplers have outer conductors with 62 mm diameter and increased cooling for high average power.
- The SRF cavities have only 2 cells per cavity with a 0.2 m active length, operated at a nominal gradient of 6 MV/m (1.2 MeV) to deliver the 120 kW klystron power to the beam.
- 12 SRF cavities in the injector cryomodule for 14.4 MeV total energy gain.

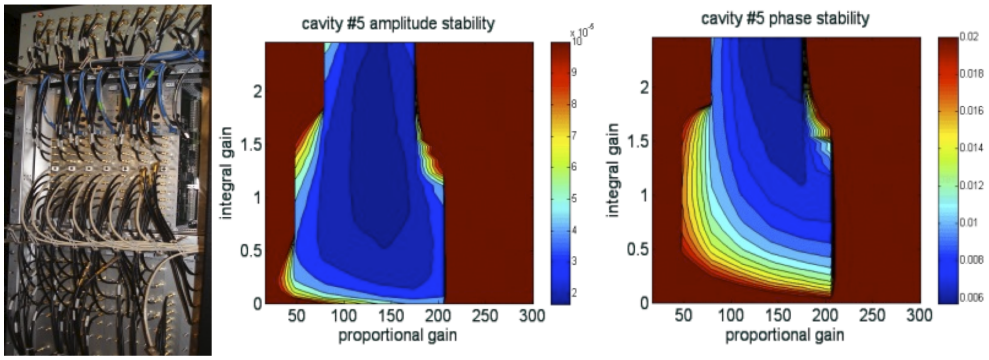

Figure 2.3.28: Left: LLRF control system used to stabilize the RF fields in the superconducting RF cavities in the Cornell ERL prototype injector. Middle: Measured accelerating field amplitude stability as function of proportional and integral gains used in the feedback controller. At optimal gains $\sigma_A/A < 2 \times 10^{-5}$ was achieved (in-loop measurement). Right: Measured accelerating phase stability as function of proportional and integral gains used in the feedback controller. At optimal gains $\sigma_p < 0.01^\circ$ was achieved (in-loop measurement).

- One side of the SRF cavity has a larger beam tube diameter, 106 mm, to allow better propagation and damping of Higher Order Modes (HOMs).
- Implement beamline HOM Loads for strong broadband damping of HOMs generated by the high current and short bunches.
- Cooling of thermal intercepts is provided by small 'jumper' tubes with flowing He gas, such as to the HOM loads and the RF couplers, as opposed to copper straps.
- Use the INFN blade tuner with the addition of piezos for fast tuning.
- Locate access ports in the vacuum vessel to allow the tuner stepper motor to be accessible for replacement while the string is in cryomodule.
- Use precision fixed surfaces between the beamline components and the Gas Return Pipe(GRP) for easy 'self' alignment of the beamline.
- Use rails mounted on the inside of the vacuum vessel and rollers on the composite support posts to insert the cold mass into the vacuum vessel, as opposed to Big Bertha.
- Increase the magnetic shielding so that the cavity Q is limited only by the BCS resistance.
- Do not include a 5 K shield.
- Increase the diameter of the cavity helium vessel port to 10 cm for the high CW heat load.
- Increase the diameter of the 2-phase 2 K He pipe to 10 cm for the high CW gas load.
- Use a module end-cap and cryogenic feed-cap with reduced length.

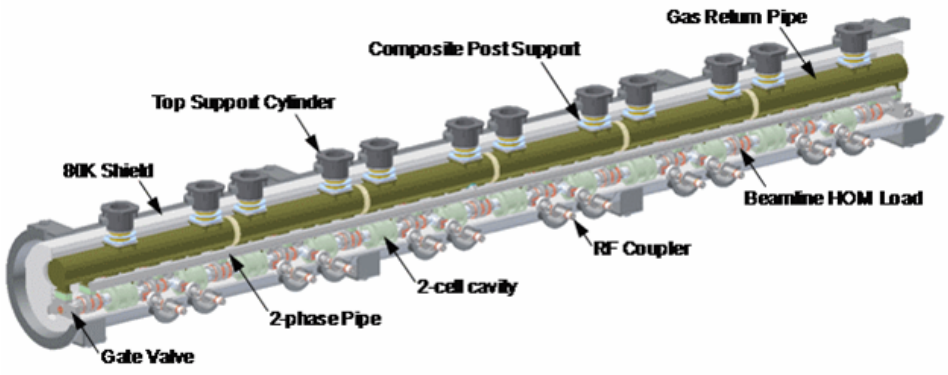

Figure 2.3.29: A cut-away CAD model showing the main features of the 12-cavity injector cryomodule.

A cut-away CAD model of the 12-cavity injector cryomodule is shown in Fig. 2.3.29, which includes only the main features of the module, with a closer view shown in Fig. 2.3.30. The design incorporates twelve 2-cell SRF cavities, beamline HOM loads, two coax RF couplers per cavity, a segmented GRP with fixed and sliding supports, gate valves at each end, and is 10 m long. As a point of reference, Tab. 2.3.7 lists the beamline components of the injector cryomodule and their lengths. In the sections that follow, the details of many of the ERL injector cryomodule components and its assembly will be described.

The ERL injector cryomodule shown in Fig. 2.3.29 is based on the TTF III module structure. All of the cavity helium vessels are pumped to 1.8 K (12 Torr) through a common 25 cm inside diameter Gas Return Pipe (GRP) which also serves as the mechanical support from which the beamline components are suspended. To minimize the heat load to the refrigeration plant, all of the 1.8 K cryomodule components are surrounded by 5 K intercepts to minimize the heat leak to 1.8 K, and the 5 K intercepts are likewise surrounded by 100 K intercepts, which absorb the heat load from the 293 K vacuum vessel. The GRP is suspended from composite support posts that are constructed from low-thermal conductivity G-10 fiberglass. The composite posts have integral metal stiffening disks and rings that also serve as thermal intercepts at 5 K and 100 K between the 1.8 K face that attaches to the GRP and the 293 K face that attaches to the vacuum vessel bosses that support the cold mass. There are stainless steel manifolds of smaller diameter than the GRP running the length of the module that transport the supply of liquid helium and the supply and return of 5 K and 100 K helium gas for the thermal intercepts. Jumper tubes with 5 mm inner diameter are connected between the 5 K and 100 K supply and return manifolds to the various thermal intercepts within a module. A shell of 6 mm thick, grade 1100 aluminum sheet surrounds the beamline and the GRP and is linked to the 100 K manifold to serve as a thermal radiation shield between the 293 K vacuum vessel and the cold mass. The aluminum 100 K shield has apertures through which the RF couplers pass and also has panels with instrumentation feedthroughs. The 100 K shield is mechanically suspended from one of the integral metal stiffeners in the composite support posts. Multi-layer insulation is wrapped around the exterior of the 100 K shield as well as all of the 1.8 K and 5 K cold mass components.

The magnetic shielding in the cryomodule must keep the field in the region of the SRF

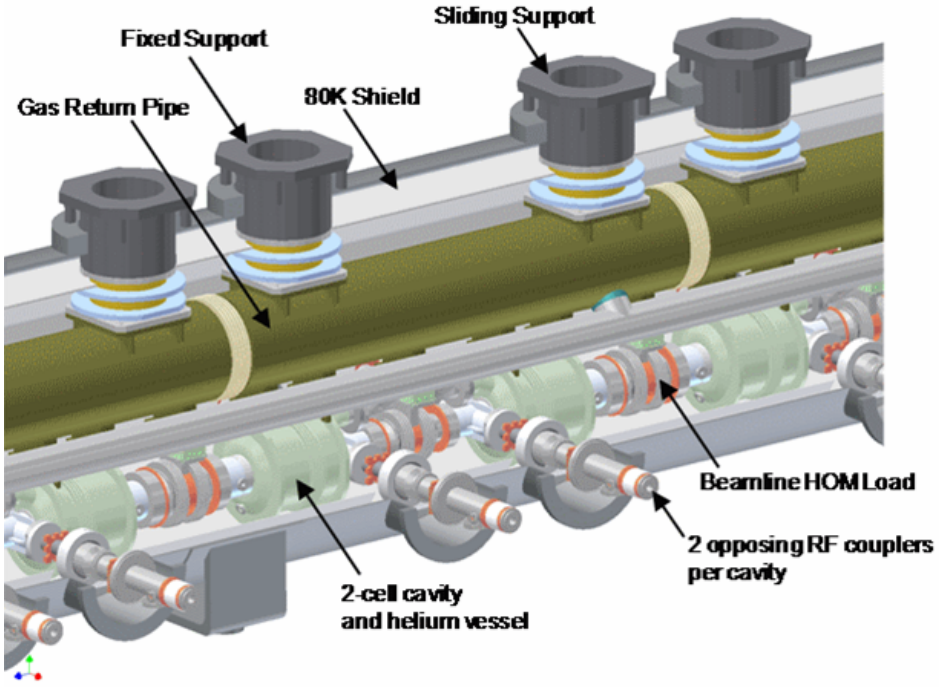

Figure 2.3.30: A closer view of the main features of the injector cryomodule.

cavity to < 2 mG to have negligible residual SRF wall loss and provide a good safety margin for the goal of cavity $Q_0 = 2 \times 10^{10}$. Such a low field is accomplished by de-gaussing the carbon-steel vacuum vessel, lining it with co-netic mu-metal shielding that will be at 293 K, and then wrapping each cavity's 1.8 K helium vessel with a magnetic shield that is formulated to have maximal shielding at the low temperatures around 4 K [67].

Many of the modifications made to the TTF III technology are necessitated by the CW high current ERL beam, as opposed to the 1% duty operation for which standard TTF technology has evolved. However, a few additional changes unrelated to CW operation have been implemented for the injector design as a result of experience gained from fabrication and operation of TTF modules. These modifications have proven to be successful in the Cornell injector prototype. Most of these modifications have also been implemented in the design of the ERL Linac cryomodule.

The injector cryomodule delivers high average power to the injected beam. Even with a modest cavity gradient of 6 MV/m and only 2 cells per cavity, the input RF power of 120 kWCW per cavity to the 100 mA beam is pushing the limits of input couplers, as described in §2.3.6. Having two RF couplers per cavity requires the vacuum vessel RF ports to be symmetrically located on each side of the cryomodule, as opposed to one coupler per cavity with ports along only one side of the module. Having only two cells per cavity makes the cavity much shorter than 7-cell or 9-cell cavities, and the cryomodule structure in the vicinity of the cavities more congested. The blade tuner is then slightly longer than the cavity helium vessel and the helium pumping port must be located on the end cone rather than on the OD of the helium vessel.

Table 2.3.7: Beamline components and lengths of the injector cryomodule.

	Component	Length (m)
	Entrance Spool & Steering	0.1500
	Gate Valve	0.0750
	1/2 HOM Load	0.2000
	106 mm Nb beam tube	0.1689
	Cavity active length	0.2186
	78 mm Nb beam tube	0.1509
Repeat 5 times	78 mm HOM load	0.2460
	78 mm Nb beam tube	0.1509
	Cavity active length	0.2186
	106 mm Nb beam tube	0.1689
	106 mm HOM load	0.2460
	106 mm Nb beam tube	0.1689
	Cavity 11 active length	0.2186
	78 mm Nb beam tube	0.1509
	78 mm HOM load	0.2460
	78 mm Nb beam tube	0.1509
	Cavity 12 active length	0.2186
	106 mm Nb beam tube	0.1689
	1/2 HOM Load	0.2000
	Gate Valve	0.0750
	Exit Spool & Steering	0.1500
	Module Length	10.0168
	Fill Factor	0.26

The short bunch and high average current of the ERL beam require beamline HOM loads for strong broadband damping of HOMs, as described in §2.3.6. There are numerous implications to the cryomodule due to the use of beamline HOM loads. The beamline loads will operate at 100 K to reduce the cryoplant load, and thus necessitate thermal gradients along the beamline between cavities by way of cooled intercepts. The expected 100 W HOM heat load to the RF absorber requires rigorous helium gas cooling via small jumper tubes from the 100 K manifolds, rather than high thermal conductivity straps. The 5 K intercepts at the ends of each HOM load will also require helium gas cooling. Even though the heat load to each intercept is only about 3 W, the temperature drop along a typical RRR=100 copper strap would be about 2 K, raising the intercept temperature to 7 K. Such a modest increase in the temperature of this intercept would unfortunately increase the heat load to the 1.8 K SRF cavity and unacceptably reduce the safety factor of keeping the niobium beam tube in a superconducting state.

The beamline HOM loads will also require low thermal conductivity mechanical supports from the GRP to suspend the HOM loads, which are not present in standard TTF technology. The cryomodule length will be greater than that of an equivalent TTF module since the length of a beamline HOM load is greater than that of a HOM loop coupler.

In standard TTF technology, alignment of the beamline within a module is accomplished during module assembly by surveying and adjustment of suspensions between beamline components and the GRP. A simplification to module assembly is to use accurately machined support blocks between the GRP and the beamline in conjunction with accurately machined mounting surfaces on the GRP and on the beamline components. The heights of the support blocks take into account the thermal contraction of all of the components upon cooldown. Simple bolting together of these components then yields an alignment accuracy of $< \pm 0.2$ mm with no adjustment operation required. This accuracy is more than sufficient for the beamline alignment tolerance of large-aperture SRF cavities, which is a relatively loose ± 1.0 mm.

The sag of the GRP under load will detract from the beamline alignment tolerance. A related consideration is the axial thermal contraction of the cold components. Though the effect of thermal contraction on vertical alignment can be accounted for by varying the support heights, the RF couplers can accommodate only modest axial contraction between the beamline cavity RF coupler port and the vacuum vessel RF coupler port. The injector GRP must then be segmented with a bellows and fixed/sliding support pair every 2 cavities, as shown in Fig. 2.3.29. Having numerous supports improves the sag of the GRP, and analysis shows that the maximum vertical deflection under load is only 0.1 mm for a 10.75" OD schedule 40 (wall thickness of 0.365") titanium grade 2 pipe.

The added cost of the precise machining of the alignment components can be small given a fabrication sequence where the precise trimming occurs only as a final skim cut, and the final tolerances are well within the capabilities of a modern machine shop. Since the GRP is nominally 9.5 m long with about 40 component mounting surfaces, precise trimming is best performed at a machine shop with a sufficiently long mill bed. Numerous shops throughout the country are tooled for such jobs, and their infra-structure and familiarity with large components often allows them to produce parts at lower cost than could smaller shops meeting much coarser tolerances, even at low quantities. Fabrication of the Cornell ERL injector prototype cryomodule utilized one such shop to mill a surface on a beamline assembly fixture that was 6 m long with a planarity tolerance of ± 0.05 mm (± 0.002"). The cost was quite reasonable and the vendor can accommodate parts that are 10 m long [68].

Experience from the Cornell ERL injector showed that the minor additional cost of precision-machined mounting surfaces was justified by the simple and robust cold mass assembly. Direct survey measurements of the injector beamline alignment showed an accuracy of $< \pm 0.2$ mm while at room temperature prior to insertion into the vacuum vessel. Monuments mounted to the top of the composite posts then provided an external alignment reference after insertion of the cold mass into the vacuum vessel. Measurement of beamline component motion during cooldown from room temperature to 1.8 K using a Wire Position Monitor (WPM) system showed that the accumulated errors in beamline alignment due to variations in thermal contraction were $< \pm 0.2$ mm. This yielded a net alignment accuracy of $< \pm 0.4$ mm, which is well within ERL Linac requirements.

Inserting the cold mass into the vacuum vessel is critical operation near the end of cryomodule assembly. The cold mass is built up on a fixture that holds the composite posts in similar fashion to their support in the vacuum vessel. Attached to the composite posts are the GRP, the beamline, cooling gas manifolds, the 100 K shield, instrumentation, and so on. In standard TTF technology, rigid cylinders are inserted into the ends of the GRP and the cold mass is lifted by the cylinders using large cantilevered supports, a.k.a. Big Bertha, and

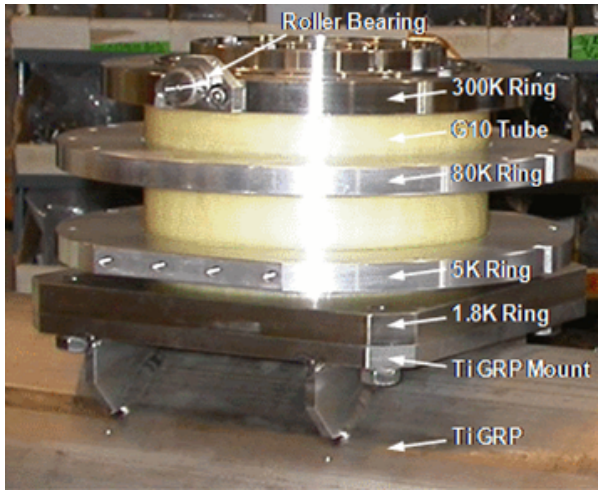

Figure 2.3.31: Roller bearings on the composite posts of the Cornell ERL injector prototype.

then inserted into the vacuum vessel. Using Big Bertha, additional floor space is required in the assembly area to manipulate the cold mass onto and off of Big Bertha. An alternate method of cold mass insertion as used for the ERL injector prototype is to place small (25 mm diameter) roller bearings on the sides of the composite post 293 K rings and place rails on the cold mass assembly fixture and inside of the vacuum vessel, as shown in Fig. 2.3.31. Cold mass insertion is then accomplished by aligning the rails on the assembly fixture with the rails inside of the vacuum vessel and simply pushing the cold mass into the vacuum vessel, as shown in Fig. 2.3.32 and Fig. 2.3.33.

The cold mass insertion rail system proved to be fast, easy, and gentle on the cold mass for the Cornell ERL injector prototype. The rail technique also saves on assembly hall floor space since the vacuum vessel need only be aligned end-to-end with the cold mass for the insertion process. Including rails in each vacuum vessel adds a small amount to their cost, but is comparable to the cost of Big Bertha amortized over the 64 modules of the ERL main Linac.

A 5 K thermal shield has not been included in the 12-cavity injector cryomodule design, nor was one utilized in the 5-cavity injector prototype. An analysis of the additional cryogenic heat load due to omitting the 5 K shield has been performed, as described in §2.4.8. This analysis shows that it would take over a decade of cryoplant electricity savings obtained by including a 5 K shield to recover the structural costs to a cryomodule of the 5 K shield. This cost recovery timescale does not justify the complications of a 5 K shield to a cryomodule, especially considering that the 100 K beamline loads in the ERL cryomodules would require segmenting the 5 K shield around each cavity.

Cryomodule assembly starts with the beamline and proceeds as a layered growth out to the vacuum vessel and warm coupler attachment. The specific choices for configuration of many of the components also impacts the configuration of other components. For example, the choice between using a blade tuner vs. a Saclay tuner dictates the type of bellows and support flanges on the cavity helium vessel, as well as the magnetic shield around the helium vessel. Described in the following is the assembly sequence of the baseline choices for the principle

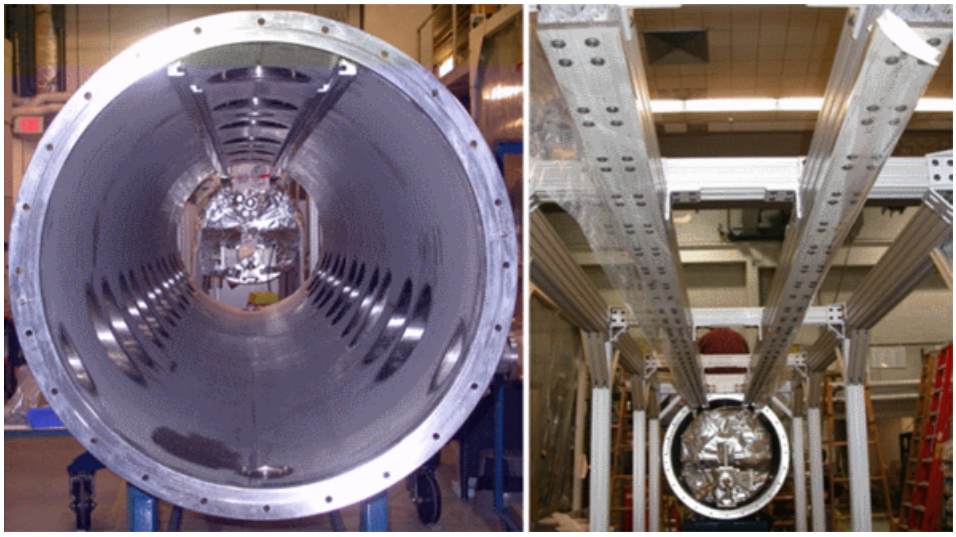

Figure 2.3.32: The Cornell ERL injector prototype cold mass before and after being inserted into the vacuum vessel by a rail system.

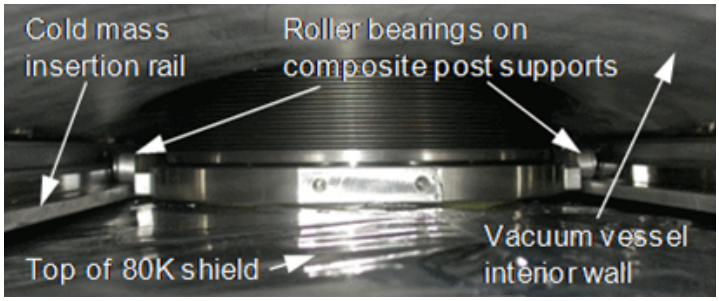

Figure 2.3.33: Internal view of the Cornell ERL injector prototype cold mass inserted into the vacuum vessel by a rail system.

injector cryomodule components, along with descriptions of the components not discussed in previous sections.

The beamline consisting of the cavities, HOM loads, cold couplers, tapers, and gate valves (Tab. 2.3.7) is assembled in a class 100 or better clean room. All components are flushed with filtered water or alcohol and individually receive a mild vacuum bake at 120° C for 24 hours. The components are mounted on an assembly fixture one by one in the clean room. Each added component is aligned to the other components with the only critical alignment being the azimuthal position about the beam axis. The azimuthal alignment is needed so that the flat precision mounting surface at their tops will mate to the planar precision surfaces on the GRP. This alignment can be accomplished with a simple accurate spirit level. Any longitudinal spacing or planar shift errors of the mounting surfaces are accommodated by the flex in the HOM load bellows. The component mating vacuum flanges are then bolted together. A photograph of the assembled ERL injector prototype beamline string in the clean room is shown in Fig. 2.3.34. After all components are assembled, the beamline string is vacuum leak

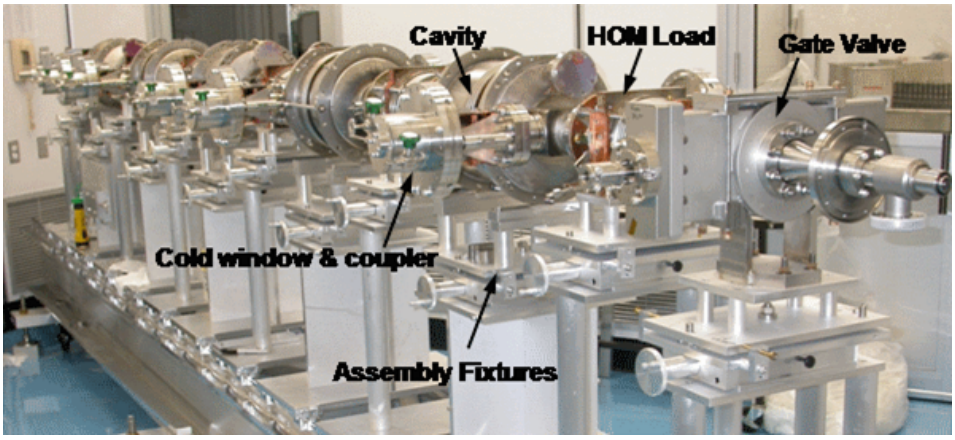

Figure 2.3.34: Assembled ERL injector prototype beamline string in the clean room.

tested while still in the clean room so that only filtered particulate-free air will pass through any potential leak. The pumping and purging during the leak test is performed at a slow rate of 1–2 Torr/minute through the viscous flow range of 760 Torr–1 Torr to minimize propagation of any particulate contamination throughout the beamline.

As a parallel operation to the beamline string assembly in a clean room, the cold mass assembly fixture can be set up in a high-bay area with overhead crane access. The composite support posts are attached to the GRP and the GRP is hung from the assembly fixture by the composite posts. The 2-phase pipe is then mounted to one side of the GRP and its exhaust is welded into the GRP. The choice of the number of composite posts supporting the GRP and the GRP wall thickness was determined by analyses of the static deformation of the titanium GRP due to the estimated 5443 kg (12000 lb) weight of the cold mass.

After the beamline string passes the vacuum leak test, it is removed from the clean room and positioned underneath the cold mass assembly fixture. The string is raised and the precision mounting surfaces on the string and the GRP are brought together with integral alignment pins being engaged. The mating surfaces are then bolted together. A photograph of the injector prototype beamline hung from the GRP is shown in Fig. 2.3.35. String attachment to the GRP in this manner proved to be quick and easy for the ERL injector prototype, the entire procedure taking about 1 hour.

After the beamline is hung from the GRP, magnetic shielding layer I is attached to the helium tanks of the cavities. This shielding will reside at 1.8 K. Traditional co-netic 'mu-metal' shielding derates at cryogenic temperatures to about 15% of its 300 K shielding capacity, so the magnetic shield I material is formulated to have maximal shielding at low temperatures [67].

The cavity blade tuners are attached after the magnetic shielding. The stepping motors of the tuners have to be wrapped in a copper sleeve that is tied to 5 K to prevent the motor heat from propagating to the helium vessel. The stepping motors are also wrapped with low temperature magnetic shielding since they can have stray fields of a few hundred mG, which would otherwise be present in close proximity to apertures in magnetic shield I.

After the tuner is mounted, its force on the cavity must be to pre-biased to compensate

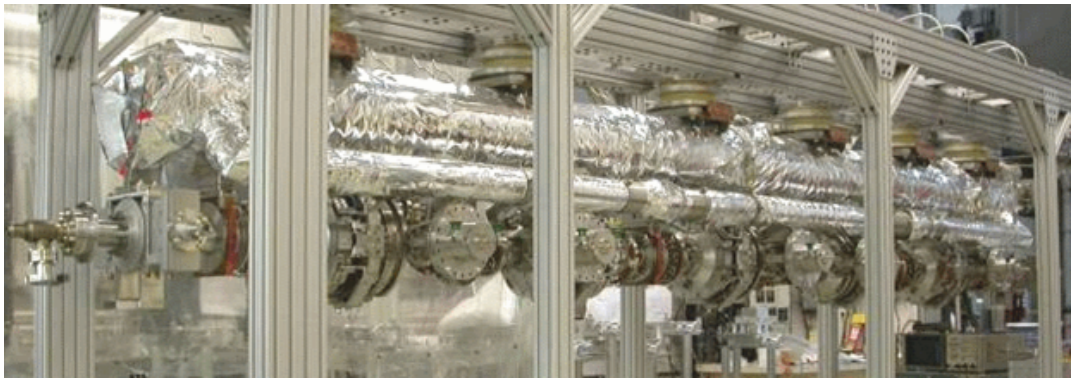

Figure 2.3.35: Beamline string hung from the GRP for the ERL injector prototype.

for stresses developed during cooldown due to thermal contraction differences between the cavity materials and the tuner materials. Without this pre-bias force, it is possible that the tuner piezos could crack or become loose, and that the cavity could plastically deform. The best measure of the tuner bias is the frequency of the room-temperature cavity. The cavity frequency can be measured using SMA feedthroughs on the cold coupler protective caps that have a spring-loaded contact to the center conductor. The tuner is initially attached with the cavity in its relaxed position, and Belleville washers in the piezo support mechanism are compressed with adjustment nuts until the cavity is at its target room-temperature frequency.

Several cryogen manifolds run the length of the cryomodule. These manifolds include a 1.8 K liquid helium supply to the 'fill' ports located at the bottom of each of the cavity helium vessels, the supply and return of 5 K helium gas, and the supply and return of 100 K helium gas.

The liquid helium and 5 K gas manifolds are mounted close to the GRP using G-10 standoffs, thus keeping similar temperatures in close proximity to each other with low thermal conductivity connections between them. These manifolds are the next components mounted on the cold mass. Jumper tubes with 6 mm ID are then routed from the liquid helium manifold to the helium vessel fill ports. Jumper tubes from the 5 K gas manifolds are then connected to thermal intercepts on the HOM loads and RF couplers. This final joining of the stainless steel jumper tubes from the manifold to the thermal intercepts is performed by orbital welding. In standard TTF technology, the connections between the manifolds and the thermal intercepts are accomplished by copper straps. For the ERL injector with CW operation, both the 5 K and 100 K heat loads are large enough to require gas flow from the manifolds to the intercepts through jumper tubes.

The 100 K manifolds are mounted outboard of the 5 K manifolds and are attached to the 100 K thermal radiation shield. One of the 100 K supply lines cools the shield, and the return lines are hung from low thermal conductivity hangars. The material of the 100 K shield is grade 1100 aluminum, chosen for its high thermal conductivity and light weight. The shield is fabricated from standard flat panels that are cut and formed to shape. The top portion of the shield is attached to the 100 K ring of the composite support post and is 6 mm thick to support the weight of the cryogen manifolds and the lower portion of the shield.

The 100 K shield was modeled for heat loads as described in §2.4.8. A key to the 100 K shield

Figure 2.3.36: Photograph of the completed ERL injector prototype 100 K shield being wrapped with MLI.

performance is that the connections to the 100 K manifolds must have low thermal impedance. In the ERL injector prototype, the manifolds were made from grade 316 stainless steel pipe and were thermally connected to the shield by copper braid. ANSYS thermal models show that the temperature increase along the braid can be 17 K, with further temperature increase due to contact impedance at the clamped ends. Thus the shield will reside at a substantially elevated temperature, as confirmed by measurements in the ERL injector prototype. The remedy for maintaining the thermal shield at 100 K is to simply duplicate the technique used in standard TTF technology. There, the manifolds are made of aluminum and contain an integral flat panel to intimately attach to the thermal shield plate. The thermal model of this manifold configuration as applied to the heat load in the ERL Linacs shows that the shield will reside only 2 K above the manifold temperature.

After the cryogen manifolds and intercept jumpers are attached to the cold mass, low thermal conductivity coax cable is routed from the cavity RF field probes with thermal anchoring to the 5 K manifold, along with cabling from temperature sensors, helium level sticks, and other instrumentation. The lower half of the 100 K shield is attached and the instrumentation cabling is thermally anchored at this point to a 100 K instrumentation feed-through panel on the shield. The 100 K shield is then wrapped with 30 layers of Multi Layer Insulation (MLI) and the cold mass is ready for insertion into the vacuum vessel. A photograph of the completed ERL injector prototype 100 K shield being wrapped with MLI is shown in Fig. 2.3.36.

The injector vacuum vessel cylinder has top ports to support the weight of the cold mass hung from the composite posts, has side ports for the RF couplers and instrumentation, side ports for the gate valve actuators, bottom pads to mount the vessel in the Linac tunnel, lifting points for transport, and has end flanges to accommodate beam entrance and exit and cryogen feed lines. The locations of the various ports on the vacuum vessel are dictated by the cold mass components. The vacuum vessel mounting and lifting points have some freedom of location, though the vessel deformation under loading must not exceed acceptable limits. An ANSYS model of the injector vacuum vessel with eight mounting points, vacuum loading, gravitational loading, and cold mass loading of 12,000 lbs (53379 N) is shown in Fig. 2.3.37.

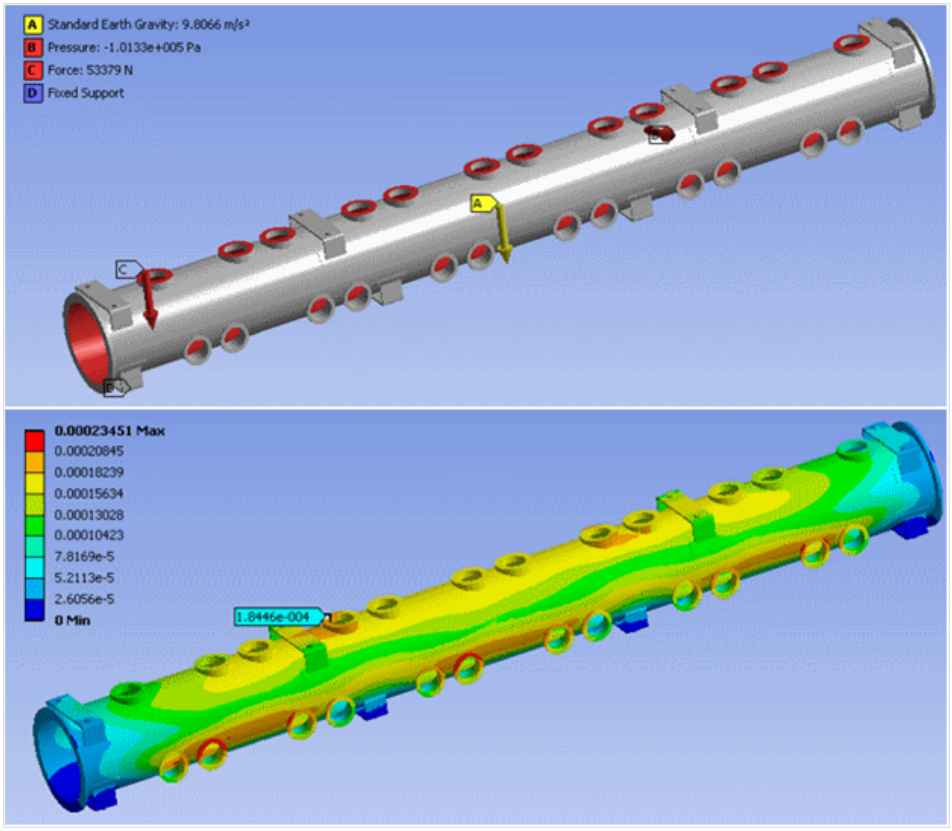

Figure 2.3.37: ANSYS model of the injector vacuum vessel with eight mounting points, vacuum loading, gravitational loading, and cold mass loading of 12,000 lbs (53379 N).

The deformation of the top ports that bear the load of the cold mass is seen to be a maximum of 0.19 mm. This deformation is an acceptable portion of the alignment budget for maintaining the beamline alignment within ±1.0 mm.

The vacuum vessel cylinder is made of carbon steel and will contribute to the magnetic shielding after being de-magnetized. After abrasive cleaning of any corrosion on the carbon steel, the vessel interior will be painted with low volatile polyurethane paint and the exterior painted with a marine epoxy for ferrous materials. The ports, which include o-ring sealing surfaces, are made of stainless steel. Rails are welded to the interior of the vacuum vessel for cold mass insertion. The interior of the vacuum vessel is then lined with a layer of mu-metal magnetic shielding that will remain at 293 K after module cooldown to retain its full shielding performance without cold temperature degradation.

The cold mass that is wrapped with MLI is pushed into the vacuum vessel and then leveled and aligned inside of the vacuum vessel using jack screws connected to the composite support posts at the top ports. The warm portions of the RF couplers are attached to the cold portions through side ports on the vacuum vessel while under small portable clean rooms, as shown in Fig. 2.3.38 for the ERL injector prototype. The vessel end plates are attached to the vacuum vessel and it is pumped out and vacuum leak tested. The injector cryomodule is then complete

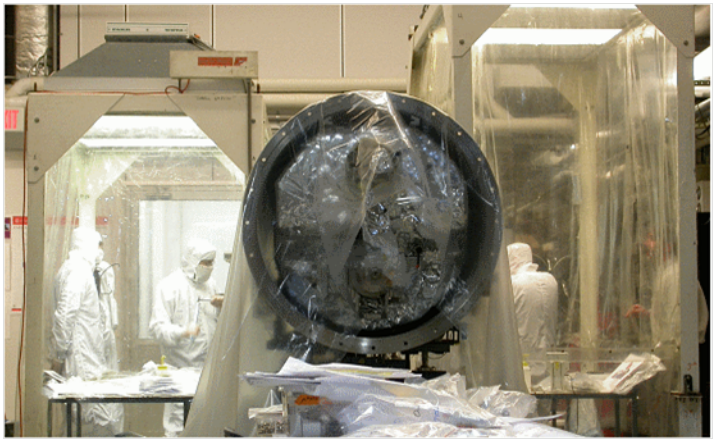

Figure 2.3.38: ERL injector prototype warm couplers being attached to the cold couplers through side ports on the vacuum vessel while under small portable clean rooms.

and ready for transport to the Linac tunnel as shown in Fig. 2.3.39.

Figure 2.3.39: Transport of the completed ERL injector prototype cryomodule from the Cornell Newman Lab assembly area to the Wilson Lab test area.

References

[1] *ICFA Beam Dynamics Newsletters*. Technical report. Available from: http://www-bd.fnal.gov/icfabd/news.html.

[2] Bazarov, I. V. and C. K. Sinclair. *Multivariate optimization of a high brightness dc gun photoinjector*. Phys. Rev. ST AB, **8** (2005).

[3] Bazarov, I. V., *et al.* *Thermal emittance and response time measurements of negative electron affinity photocathodes*. Journal of Applied Physics, **103** (5) (2008).

[4] *Photocathode Physics for Photoinjectors Workshop* (October 2010). https://indico.bnl.gov/conferenceDisplay.py?confId=290.

[5] Haimson, J., B. M. G. Stowell, and E. L. Wright. *A fully demountable 550 kV electron gun for low emittance beam experiments with a 17 GHz linac*. In *Proceedings of the 1997 Particle Accelerator conference 3*, pages 2808–2810. Vancouver, B.C., Canada (1997).

[6] Togawa, K., *et al.* *CeB6 electron gun for low emittance injector*. Phys. Rev. ST AB, **10** (2) (2007).

[7] Siggins, T., *et al.* *Performance of a DC GaAs photocathode gun for the Jefferson lab FEL*. Nucl. Instr. and Meth. A, **475** (1-3), page 549 (2001).

[8] Sinclair, C. K., *et al.* *Development of a high average current polarized electron source with long cathode operational lifetime*. Phys. Rev. ST AB, **10** (023501) (2007).

[9] Dunham, B. M., *et al.* *Performance of a Very high Voltage Photoemission Electron Gun for a High Brightness, High Average Current ERL Injector*. In *Proceedings of the 2007 Particle Accelerator Conference*, pages 1224–1226. Albuquerque,New Mexico (2007).

[10] Grames, J., *et al.* *Measurements of Photocathode Operational Lifetime at Beam Currents up to 10 mA using an Improved DC High Voltage GaAs Photogun*. In *Proceedings of the* 17^{th} *International Spin Physics Symposium and Workshop*, volume 915, page 1037. Kyoto, Japan (2007). http://www.jlab.org/accel/inj_group/docs/2007/SPIN06paper_grames.pdf.

[11] Dunham, B., *et al.* *Record high-average current from a high-brightness photoinjector*. Applied Physics Letters, **102** (3), 034105 (2013). doi:10.1063/1.4789395.

[12] Zhao, Z., *et al.* *Generation of 110 W infrared and 65 W green power from a 1.3-GHz sub-picosecond fiber amplifier*. Opt. Express, **20** (5), pages 4850–4855 (Feb 2012). doi:10.1364/OE.20.004850.

[13] van der Geer, S. and M. de Loos. *General Particle Tracer User's Manual version 2.80*. Pulsar Physics (2007).

[14] Gulliford, C., *et al.* *Demonstration of Low Emittance in the Cornell Energy Recovery Linac Injector Prototype*. Preprint arXiv:1304.2708 [physics.acc-ph] (2013).

[15] *Advanced Photon Source Upgrade Project Preliminary Design Report.*

[16] Balewski, K., *et al. PETRA III UPGRADE.* In *Proceedings of IPAC2011 THPC020 p. 2948* (2011).

[17] Bazarov, I. V., *et al. Numerical Comparison of DC and SRF Photoguns For High Brightness Electron Beams.* Nucl. Instr. and Meth. A (2011). Submitted.

[18] Slade, P. G. *The vacuum interrupter: theory, design, and application.* CRC Press (2008).

[19] Furuta, F., *et al. Reduction of field emission dark current for high-field gradient electron gun by using a molybdenum cathode and titanium anode.* Nucl. Instr. and Meth. A, **538** (1-3), pages 33–44 (2005).

[20] Bazarov, I. V., *et al. Benchmarking of 3D space charge codes using direct phase space measurements from photoemission high voltage dc gun.* Phys. Rev. ST AB, **11** (100703) (2008).

[21] Bazarov, I. V., B. M. Dunham, and C. K. Sinclair. *Maximum Acheivable Beam Brightness from Photoinjectors.* Phys. Rev. Lett., **102** (104801) (2009).

[22] Breidenbach, M., *et al. An Inverted-Geometry, High-Voltage Polarized Electron-Gun with UHV Load Lock.* Nucl. Instr. and Meth. A, **350** (1-2), pages 1–7 (1994).

[23] van den Putte, M. J. J., *et al. The Polarized electron source at NIKHEF.* volume 421, pages 260–269. Urbana, IL, USA (1998).

[24] Yamamoto, M., *et al. 200 keV Polarized Electron Source for Linear Collider.* In *Proceedings of the XXI International Linac Conference*, pages 680–682. Gyeongju, Korea (2002).

[25] Schneider, W. J., *et al. A load-locked Gun for the Jefferson Lab Polarized Injector.* In *Proceedings of the 1999 PArticle Accelerator Conference*, pages 1991–1993. New York, New York (1999).

[26] Kaiser, K. (2010). Kaiser Systems, Inc., Private Communication.

[27] Fremerey, J. K. *Residual gas: Traditional understanding and new experimental results.* In *Proceedings of the 14th International Vacuum Congress (IVC-14)*, page 197. Birmingham, UK (1999).

[28] Temnykh, I. A. and C. K. Sinclair (2009). Unpublished.

[29] Alley, R., *et al. The Stanford linear accelerator polarized electron source.* Nucl. Instr. and Meth. A, **365** (1), pages 1 – 27 (1995). ISSN 0168-9002. doi:DOI:10.1016/0168-9002(95)00450-5.

[30] Baptiste, K. *et al. Status of the LBNL normal-conducting CW VHF photoinjector.* In *Proceedings of PAC09.* Vancouver, BC, Canada (2009).

[31] (2011). Private communication with B. Carlsten (LANL).

[32] Haimson, J. *Recent Advances in High Voltage Electron Beam Injectors*. Nuclear Science, IEEE Transactions on, **22** (3), pages 1354 –1357 (june 1975). ISSN 0018-9499. doi: 10.1109/TNS.1975.4327885.

[33] Park, C. D., *et al. Reduction in hydrogen outgassing from stainless steels by a medium-temperature heat treatment*. Journal of Vacuum Science & Technology A: Vacuum, Surfaces, and Films, **26** (5), pages 1166–1171 (2008). doi:10.1116/1.2956625.

[34] Moore, B. C. *Thin-walled vacuum chambers of austenitic stainless steel*. Journal of Vacuum Science & Technology A: Vacuum, Surfaces, and Films, **19** (1), pages 228–231 (2001). doi:10.1116/1.1333083.

[35] Nemanič, V. and J. Šetina. *Experiments with a thin-walled stainless-steel vacuum chamber*. The 46th international symposium of the american vacuum society, **18** (4), pages 1789–1793 (2000). doi:10.1116/1.582425.

[36] Redhead, P. A., J. P. Hobson, and E. V. Kornelsen. *The physical basis of ultrahigh vacuum*. American Institute of Physics, New York (1993).

[37] Dunham, B. M. Private Communication.

[38] Luo, Y., D. A. Slater, and R. M. Osgood. *Low-damage processing of CdTe(100) surfaces using atomic hydrogen*. Applied Physics Letters, **67**, pages 55–57 (1995).

[39] Okada, Y. and J. James S. Harris. *Basic analysis of atomic-scale growth mechanisms for molecular beam epitaxy of GaAs using atomic hydrogen as a surfactant*. Journal of Vacuum Science & Technology B: Microelectronics and Nanometer Structures, **14** (3), pages 1725–1728 (1996). doi:10.1116/1.588547.

[40] Yu, Z., *et al. Defect reduction in ZnSe grown by molecular beam epitaxy on GaAs substrates cleaned using atomic hydrogen*. Applied Physics Letters, **69** (1), pages 82–84 (1996). doi:10.1063/1.118127.

[41] Bazarov, I. V., *et al. Efficient temporal shaping of electron distribution for high-brightness photoemission electron guns*. Phys. Rev. ST AB, **11** (4) (2008).

[42] Karkare, S. and I. Bazarov. *Effect of nano-scale surface roughness on transverse energy spread from GaAs photocathodes*. Applied Physics Letters, **98** (2011).

[43] *Accelerators for America's Future* (June 2010). http://www.acceleratorsamerica.org/.

[44] *Workshop on Photocathodes for RF Guns* (March 2011). http://photocathodes2011.eurofel.eu/.

[45] Liu, Z., *et al. Narrow cone emission from negative electron affinity photocathodes*. Journal of Vacuum Science Technology B: Microelectronics and Nanometer Structures, **23** (6), page 2758 (2005). doi:10.1116/1.2101726.

[46] Springer, R. W. *Los Alamos National Laboratory.* Private Communication.

[47] Ouzounov, D., *et al. The Laser System for teh ERL Electron Source at Cornell University.* In *The twenty-second Particle Accelerator Conference, PAC'07*, pages 530–532. Albuquerque, New Mexico, USA (2007).

[48] PriTel, Inc., Naperville, IL 60567.

[49] Veshcherevich, V. and S. Belomestnykh. *Bunchner Academy for ERL.* In *Proceedings of the 2003 Particle Accelerator Conference*, pages 1198–1200. Portland, USA (2003).

[50] Shemelin, V., *et al. Dipole-mode-free and kick-free 2-cell cavity for the SC ERL injector.* In *Proceedings of the 2003 Particle Accelerator Conference*, pages 2059–2061. Portland, USA (2003).

[51] Geng, R. L., *et al. Fabrication and performance of superconducting RF cavities for the Cornell ERL injector.* In *Proceedings of the 2007 Particle Accelerator Conference*, pages 2340–2342. Albuquerque, NM (2007).

[52] Belomestnykh, S., *et al. CW RF systems of the Cornell ERL Injector.* In *Proceedings of the XXIV Linear Accelerator Conference*, pages 857–859. Victoria, BC, Canada (2008).

[53] Dwersteg, B., *et al. TESLA RF Power Couplers Development at DESY.* In *Proceedings of the 10th Workshop on RF Superconductivity*, pages 443–447. Tsukuba, Japan (2001).

[54] Belomestnykh, S., *et al. High Power Testing RF System Components for the Cornell ERL Injector.* In *Tenth European Particle Accelerator Conference, EPAC06*, pages 472–474. Edinburgh, Scotland (2006).

[55] Veshcherevich, V., *et al. Design of High Power Input Coupler for Cornell ERL Injector Cavities.* In *Proceedings of the 12th International Workshop on RF Superconductivity*, pages 590–592. Ithaca, NY (2005).

[56] Belomestnykh, S., *et al. Development of High Power RF Power Delivery System for 1300 MHz Superconducting Cavities of Cornell ERL Injector.* In *Proceedings of XXII International Linear Accelerator Conference*, pages 694–696. Luebeck, Germany (2004).

[57] Liepe, M., *et al. Design of the CW Cornell ERL injector cryomodule.* In *21st Particle Accelerator Conference (PAC 05)*, page 4290 (2005).

[58] Aune, B., *et al. Superconducting TESLA cavities.* Phys. Rev. ST Accel. Beams, **3** (9), page 092001 (Sep 2000). doi:10.1103/PhysRevSTAB.3.092001.

[59] Akai, K., *et al. RF systems for the KEK B-Factory.* Nucl. Instr. and Meth. A, **499** (1), pages 45 – 65 (2003). ISSN 0168-9002. doi:DOI:10.1016/S0168-9002(02)01773-4.

[60] Geng, R., *et al. Progress of 2-Cell Cavity Fabrication for Cornell ERL Injector.* In *Particle Accelerator Conference, 2005. PAC 2005. Proceedings of the*, pages 4248 – 4250 (May 2005). doi:10.1109/PAC.2005.1591780.

[61] Sobenin, N., *et al. Thermal Calculations of Input Coupler for Cornell ERL Cavities*. In *Proceedings of the XIX Russian Particle Accelerator Conference*, pages 307–309. Dubna, Russia (2004).

[62] Veshcherevich, V., *et al. High Power Tests of Input Couplers for Cornell ERL Injector*. In *Proceedings of the 13th Workshop on RF Superconductivity*, pages 517–519. Beijing, China (2007).

[63] Liepe, M. and R. Wolf. *Wake Fields in the Cornell ERL Injector*. In *the 2009 International Workshop of RF Superconductivity*. Berlin, Germany (2009).

[64] Liepe, M., *et al. High-current ERL Injector*. In *Proceedings of the 2009 International Workshop of RF Superconductivity*. Berlin, Germany (2009).

[65] Liepe, M. *et al. A new Digital Control System for CESR-c and the Cornell ERL*. In *SRF03* (2003).

[66] Chojnacki, E. P., *et al. Design and Fabrication of the Cornell ERL Injector Cryomodule*. In *Eleventh European Particle Accelerator Conference, EPAĆ08*, page 844. EPAC08, Genoa, Italy (2008).

[67] Amuneal Manufacturing Corp. Technical report, Philadelphia, PA, USA, Amumetal 4k (A4K) (2010). http://www.amuneal.com/magnetic-shielding/idea-share/whats-new-cryogenic-shielding.

[68] Burning, J. and Fabricating (2010). Warren, MI, USA, http://www.jjburning.com/.

2.4 Linac

2.4.1 Introduction

The main Linac of the Cornell Energy Recovery Linac (ERL) comprises 64 cryomodules each containing 6 superconducting cavities and a superferric quadrupole and steering-corrector package. Section 1.3 explains the need for employment of superconducting cavities. The Linac occupies 700 m of underground tunnel and serves to accelerate the beam from injection energy, 15 MeV, to 5 GeV and decelerate again to approximately the injection energy after passing through the x-ray-producing insertion devices as depicted in Fig. 2.1.2 (ERL Extension of CESR). The superconducting cavity units of the cryomodules and the cryogenic shields are maintained at temperature by a helium cryogenic plant located above the tunnel. Each cavity is individually driven by an RF power source with amplitude and phase controlled by low-level RF circuitry adjacent to the cryomodules. The supporting utilities and cryogenics are described in Chapter 4.

State of the art of superconducting RF

Accelerator facilities utilizing superconducting cavities with elliptical shape are becoming prevalent around the world. As new machines continue to push the limits of low emittance and higher-duty cycle, the large iris and low loss of superconducting cavities enable the realization of beam-performance goals. The cavity-performance parameters of other superconducting RF-based facilities are listed in Tab. 2.4.1. The FLASH facility is the most relevant to the Cornell ERL design as it is the product of many years of SRF cavity and cryomodule development now known as the TESLA Technology Collaboration (TTC), and is the basis for this ERL Linac design. This technology is the precursor of the European XFEL facility [1] and it is also the basis for development of the International Linear Collider (ILC) [2]. The result of the many years of TTC development is a cryomodule configuration known as TTF-III that accomplishes reliable performance of the numerous components, a minimal cryogenic heat load, ease of fabrication, and minimization of cost. A photograph of a TTF-III cryomodule in the FLASH tunnel at DESY is shown in Fig. 2.4.1.

Advances in SRF-cavity performance are occurring continuously, as evidenced by the proposed facilities' parameters, which have been obtained in developmental tests, as mentioned in Tab. 2.4.1. The parameters of the Cornell ERL resulted from an optimization encompassing the full machine as described in §2.4.2 below.

Principles governing the baseline design

The ERL Linac design is based on TTF-III technology with modifications for continuous wave (CW) operation. This builds upon the considerable development work performed for this Linac technology over the past 15 years. TTF-III technology is at the forefront of SRF Linac performance in regard to cavity gradient, quality factor Q, power coupled to the beam, cavity tuning, minimal cryogenic heat load, industrial fabrication, and operational reliability. This technology is characterized by module-vacuum vessels joined end-to-end with large lengths of the Linac sharing a common insulation vacuum. For the baseline design, the ERL Linac will have a north and a south section; the north will have 35 modules and is 344 m long, and the

Table 2.4.1: Accelerator facilities utilizing superconducting RF elliptical cavities.

Facility	Type	Frequency (GHz)	Temperature (K)	Cavity Type	Q at Operational Gradient	Operational Gradient (MV/m)
FLASH	e^- Linac	1.3	1.8	9-cell	1×10^{10}	23
JLAB	e^- Linac	1.497	2.1	5-cell	5×10^9	7.5
Cornell	Test cryomodule	1.3	1.8	7-cell	3×10^{10}	16
SNS	p^+ Linac	0.805		6-cell	5×10^9	8-12
CESR	e^--storage ring	0.5	4.5	1-cell	1×10^9	5-8
KEK-B	e^--storage ring	0.5	4.5	1-cell	2×10^9	4-7
LEP-II	e^+-e^--stor. ring	0.35	4.5	4-cell	3.2×10^9	6
LHC	p^+-p^--stor. ring	0.4	4.5	4-cell	2×10^9	5
		Proposed or under construction				
XFEL	e^- Linac	1.3	2.0	9-cell	1×10^{10}	23.6
Cornell ERL	e^- Linac	1.3	1.8	7-cell	2×10^{10}	16
JLAB upgrade	e^- Linac	1.497	2.1	7-cell	6×10^9	17.5
ILC	e^- Linac	1.3	2.0	9-cell	1×10^{10}	31.5

south will have 29 modules and is 285 m long. Placement of an insulation-vacuum break in each of the long Linac sections is under study.

The modifications to the TTF-III technology for CW operation and energy recovery have significant operational differences. From a facility point of view, because the resistive power dissipated in the SRF cavities is absorbed by the refrigeration system at 1.8 K, having CW cavity operation makes the refrigeration system a major utility component. This favors relatively low-cavity gradient as cryogenic power per unit length scales as the square of the gradient. Another consideration that favors lower gradient is that field emission and consequent radiation produced within a given cavity scale exponentially with cavity gradient. This not only adds to the cryogenic load but will also produce a significant radiation level in CW operation. A lower cavity gradient will lessen field emission, and thus shielding requirements.

Achieving as high a cavity Q as possible at a given temperature has a direct benefit of reducing the size of cryoplant. There are three components needing control for highest Q: the BCS component with exponential temperature dependence; the temperature-independent residual resistance, which depends on the surface processing; and the trapped magnetic flux component, which depends on the effectiveness of the magnetic shielding. The latter requires the magnetic shielding in the cryomodule to reduce the background magnetic fields at the cavities to $< 2\,\mathrm{mG}$ to ensure that residual RF losses due to flux pinning are negligible. This will be accomplished by using a demagnetized carbon-steel-vacuum vessel, a mu-metal lining of the vacuum vessel at 293 K, and a shield around each cavity using material formulated for optimal magnetic performance at 1.8 K. With cavity Q dominated by BCS resistance, selection of the cavity temperature then becomes an optimization of refrigeration power and scaling of the BCS resistance with temperature, which favors a cavity temperature of 1.8 K [3].

Reliability and uninterrupted run time of the ERL light source is a performance goal for the

Figure 2.4.1: A photograph of a TTF-III cryomodule in the FLASH tunnel at DESY.

machine. With the Linac total of 384 SRF cavities, the trip rate per cavity needs to be below once per several years to accomplish a machine trip rate of less than once per day. A modest cavity gradient will play a major role in making this feasible, since it has been demonstrated at all of the facilities listed in Table 2.4.1 that operation of SRF cavities is extremely reliable if the cavity gradient and input RF power are not pushed to the limits. The input RF power to each cavity is low due to the energy recovery, typically 2 kW average and 5 kW peak power, so trips due to RF couplers should occur at a very low rate.

The RF-source architecture is likewise designed for reliable machine operation; there will be a dedicated source for each cavity. With this configuration, the loss of one RF source translates to the loss of only one cavity. Having a dedicated source per cavity also allows the flexibility to tune for the best performance of each cavity, which in conjunction with gradient and RF power overhead, will be utilized to compensate for a tripped cavity to provide uninterrupted machine operation. The challenge to the RF system will be in the form of the high loaded quality factor Q_{ext} of the input couplers. This will place tight constraints on maintaining the RF field phase and amplitude in both absolute terms along the length of the Linac and in local terms due to microphonic perturbations of individual cavities. The RF feedback system will be capable of compensating for microphonic perturbations at the expense of increased average

forward power, as demonstrated in the ERL-injector prototype at Cornell. An important developmental task will be to show that the fast-piezo component of the cavity tuner can be used to mechanically compensate for microphonics, and thus lower the Linac RF-power budget.

The short bunch length of 0.6 mm ($\approx 2\,\mathrm{ps} \cdot c$) and high average beam current of 100 mA CW in both the accelerating and decelerating beams in the ERL demands heavy damping of the higher order modes (HOMs) in the cavities. The loaded Q's of such modes and their shunt impedance place direct limits on the beam-breakup (BBU) limited-beam current. The average HOM power is expected to be 200 W per cavity, assuming no resonant excitation of any particular mode. Most of the power will be in the frequency range of 1-10 GHz, but the short bunch length will contain HOM spectral content up to the 100 GHz range. The HOM damping scheme must have strong coupling over this broad bandwidth and be able to dissipate the average power. Beamline-HOM loads have been chosen in the baseline design to accomplish these requirements. The beamline loads will operate at 100K to minimize the cryoplant load, and thus necessitate thermal gradients along the beamline between cavities by way of cooled intercepts. Operation of the ERL-injector prototype at Cornell has given important insight as to the requirements of the RF-absorbing material in the beamline loads, and new robust materials have been developed as a result. The alternate use of waveguide and loop-HOM couplers are the subjects of ongoing investigations [4–6], and while they have the benefit of transporting the HOM power to external-room temperature loads, it is still to be determined if they will have the requisite bandwidth and power capability, and how the structural complexity will compare to beamline loads. Another consequence of the short bunch length and high HOM frequencies is that the design of the mechanical contour of the beamline must have careful consideration of any features with dimensions of $\sim 0.6\,\mathrm{mm}$ or larger, such as flange gaskets and RF pickups, to avoid excitation of high frequency modes and consequent heating.

Another departure from TTF-III technology necessitated by ERL CW operation is the much higher consumption of 1.8 K superfluid helium per cavity and its return gas load. At the cavity level, the helium vessel must have a large aperture to the superfluid reservoir to allow conduction of the nominal 12 W heat flow per cavity. At the module level, standard TTF-III technology incorporates a single superfluid-helium manifold joined between modules to run the entire length of a Linac section, with a feed from one end of the Linac. For the ERL, this configuration would present too much flow restriction; consequently the baseline concept has a larger helium source manifold, and a JT valve supplying a superfluid reservoir per module. The needed design is being developed. As the ERL developmental projects proceed and the design matures, there will also likely be advances in aspects of TTF technology from the ILC and XFEL programs, including cost reductions and industrialization. Cornell has close communication and collaboration with these projects and will share in such benefits as a long-standing member of the TTC. Cornell is also serving as a major partner in the Daresbury ERL demonstration project, providing the 7-cell SRF cavities and technical consultation [7]. Other collaborations are forming for ERL development work, such as microphonic compensation with the Helmholtz Zentrum Berlin (HZB) and RF-absorber material development for HOM loads with the Ningbo Institute of Material Technology and Engineering (NIMTE) in China, the Spheric and Coorstech Companies and Alfred University in the United States.

In the sections that follow, the details of many of the ERL-Linac cryomodule components

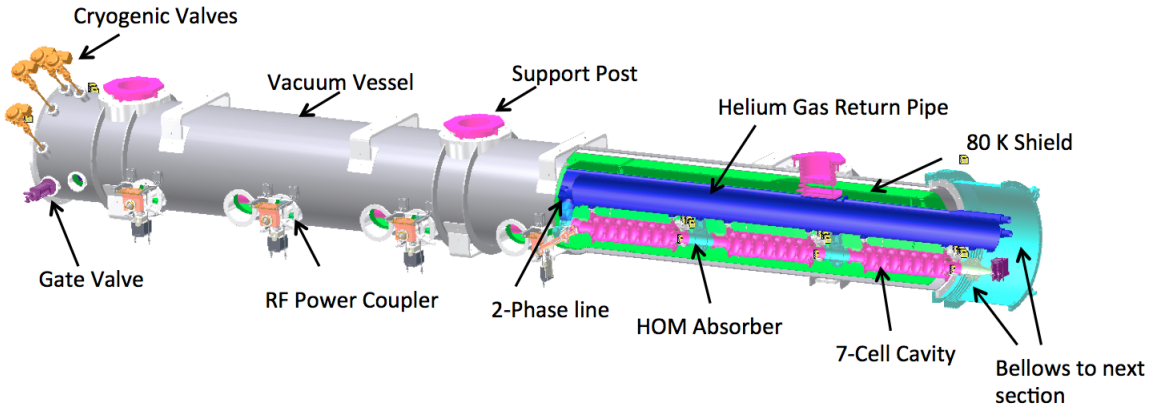

Figure 2.4.2: Cross section of the ERL main Linac cryomodule.

will be described. These features were heavily influenced by experience with the injector-cryomodule prototype (see §2.3.6). A cut-away CAD model of the Linac cryomodule is shown in Fig. 2.4.2, which includes only its main features. The design incorporates six 7-cell SRF cavities, beamline HOM loads, coax-RF couplers, one quadrupole, one set of X-Y steering coils, and gate valves at each end. This cryomodule is 9.82 m long. As a point of reference, Tab. 2.4.2 lists the beamline components of the cryomodule and their lengths.

2.4.2 Cavity

The superconducting cavities in the main Linac of the ERL significantly influence the performance, cost and reliability of the accelerator in several ways. The design of the cavity must be optimized according to the ERL specific requirements.

The optimization of the main Linac cavity design is driven by the three primary objectives:

- The cavities must be able to support beam currents up to the design value of $2 \times 100\,\mathrm{mA}$, and strong suppression of Higher-Order-Modes (HOM) in the main Linac is therefore essential. In addition, fluctuations in the HOM frequencies from cavity to cavity are desirable to reduce coherent effects and thereby increase the BBU threshold current.

- A large value of R/Q for the fundamental mode (at 1.3 GHz) is highly desirable to minimize the dynamic cryogenic load by the accelerating RF field in the cavities.

- The performance of the cavity design must be robust under small shape imperfections, which are always present due to finite fabrication tolerances.

Linked to the cavity design are the operating parameters of the cavity. Most of these can be chosen and optimized freely (within certain boundaries). The intrinsic quality factor Q_0 of the cavity is not a free parameter, and it is crucial to assume a realistic value for it, since it determines the size of the cryogenic refrigerator required. The following sections discuss the ERL main Linac cavities and their baseline operating parameters in detail. Subsequent sections present the RF and mechanical design of the main Linac cavities in detail, including the choice

Table 2.4.2: Beamline components and lengths of the Linac cryomodule.

	Component	Length (m)
	Gate Valve	0.0750
	Taper	0.0500
Repeat 6 times	HOM Absorber	0.0600
	110mm Cu beam tube	0.0476
	110mm Nb beam tube	0.2150
	Cavity active length	0.8061
	110mm Nb beam tube	0.2150
	110mm Cu beam tube	0.0476
	HOM Absorber	0.0600
	Taper	0.0500
	BPM	0.0750
	Quadrupole	0.4500
	X-Y Steering Coils	0.1500
	Gate Valve	0.0750
	Intermodule flex	0.4885
	Module Length	9.8213
	Fill Factor	0.49

of cavity flanges, the LHe vessel design, and the inner magnetic shielding of the cavity. The final sections briefly cover the fabrication of the cavities and their surface preparation.

Frequency choice

The choice of frequency f_0 of the accelerating mode of the main Linac cavity is determined by several factors. These include heat-load considerations, HOMs and the resulting beam breakup current, availability of RF-power sources, as well as the maximum bunch repetition and the minimum bunch charge at given beam current.

The cryogenic losses of a cavity can be separated into static and dynamic losses. It is desirable to minimize these losses since they are the main driver of an ERL's operation cost. For a given length of a multi-cell cavity, the surface area scales with $1/f_0$. The static heat load per length therefore, tends to scale also with $1/f_0$ (assuming that wall thicknesses are unchanged). The surface resistance of the superconductor scales as f_0^2 at higher temperatures where the BCS resistance dominates, and becomes approximately frequency independent at lower temperatures where the residual resistance dominates. Accordingly, the intrinsic quality factor $Q_0 = G/R_\mathrm{S}$ scales with $1/f_0^2$ at higher temperatures and is independent of frequency at lower temperatures. For the same accelerating gradient and the same active cavity length, the stored energy U in the cavity per length L scales with $1/f_0^2$ (i.e., with the volume of the cavity per length). The dynamic power dissipated in the walls of a cavity is given by

$$\frac{P_\mathrm{diss}}{L} = \frac{2\pi f_0 U}{Q_0 L}\,. \tag{2.4.1}$$

Accordingly the dissipated power per active cavity length scales linearly with frequency at higher temperatures and with $1/f_0$ at lower temperatures.

State-of-the-art multi-cell cavities show residual surface resistances of 5 to 10 nΩ. Taking this into account as well as the frequency and temperature dependences of the BCS surface resistance and the efficiency dependence of the refrigerator on operating temperature, one finds that an operating temperature of 1.8 K reduces the AC cooling power at all frequencies between 500 and 1500 MHz. At this temperature, residual resistance dominates over the BCS resistance, favoring the higher frequencies [8, 9]. In addition, the risk of surface contamination and field emission increase with surface areas, also favoring the higher frequencies.

In regard to the BBU threshold, one notes that for large return times, and for ERLs with many cavities, the threshold current does not strongly depend on the return time. It is then true that there is a reciprocal relation between threshold current and the HOM frequency f, assuming that R/Q and Q of a given mode remains unchanged, which is the case if the number of cells per cavity is unchanged. Decreasing the fundamental frequency from 1.3 GHz to 650 MHz would therefore increase the threshold current by a factor of 2. This strategy of increasing the threshold current has several problems. First, as discussed above, it would significantly increase the AC power required to cool the SRF cavities. Second, to obtain the same average current, the bunch charge would have to be larger, which strengthens space-charge forces and therefore increases the emittance of the electron beam thereby decreasing the spectral brightness of x-ray beams, which is the ultimate quality factor of an ERL design.

The Cornell ERL main Linac is based on 1.3 GHz SRF cavities. This frequency minimizes operating costs, supports operation at the design beam current of 100 mA, as shown in the following sections, and allows the ERL main Linac to make use of the extensive technology developed for the International-Linear-Collider and the XFEL, which are also based on 1.3 GHz superconducting RF.

Cavity operating parameters: Q_0, $E_{\rm acc}$, and $Q_{\rm ext}$

The three main cavity operating parameters are the intrinsic quality Q_0 factor of the SRF cavity (which also depends on the operating temperature T), the operating accelerating field gradient $E_{\rm acc}$, and the external quality factor $Q_{\rm ext}$. All three parameters strongly impact the ERL main Linac design and cost. While the intrinsic quality factor is determined by the cavity preparation, the operating temperature and the magnetic shielding in the cryomodule, the other two parameters can be chosen freely (within limits).

Intrinsic Q_0 and operating temperature

The dynamic power dissipated in the walls of a single cavity by the accelerating RF field during operation is given by

$$P_{\rm cavity} = \frac{V_{\rm acc}^2}{2\frac{R}{Q}Q_0}\,, \tag{2.4.2}$$

where $V_{\rm acc}$ is the accelerating cavity voltage, and (R/Q) is the ratio of cavity shunt impedance to cavity intrinsic quality factor, which is a shape dependent factor. The total dynamic cavity

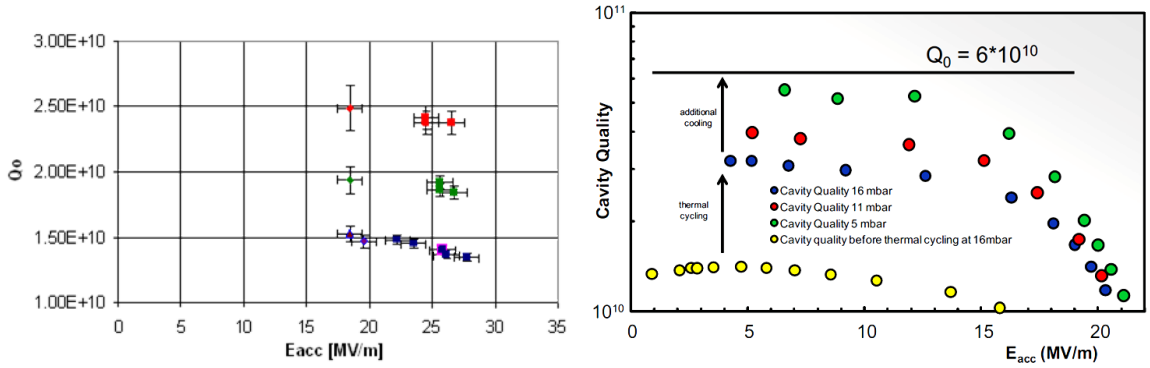

Figure 2.4.3: State-of-the-art performance of fully equipped 9-cell SRF cavities. Left: Average performance of eight 9-cell cavities in a FLASH cryomodule at DESY at different operating temperatures (red: 1.6K, green: 1.8K, blue: 2K). Right: Performance of a 9-cell cavity in a horizontal test cryomodule at different temperatures (16 mbar corresponds to 1.8K) [8, 9].

power in the ERL main Linac is then

$$P_{\text{total}} = \frac{V_{\text{total}} E_{\text{acc}}}{2\frac{R/Q}{L_{\text{cav}}} Q_0}\,, \tag{2.4.3}$$

where L_{cav} is the active length of the cavity. In case of the ERL, the total accelerating voltage of the main Linac is $V_{\text{total}} = 5\,\text{GV}$, resulting in a significant total power dissipated at the operating temperature of the cavities of the order of several kW. It is obvious that the intrinsic quality factor has dramatic impact on the size of the cryogenic refrigerator and on the capital and operating cost of the ERL. The intrinsic quality factor depends on the so-called geometry factor G of the cavity (determined by its cell shape) and the surface resistance R_{s} of the superconducting material used for the cavity walls: $Q_0 = G/R_{\text{s}}$. As noted above, state-of-the-art multi-cell cavities now exhibit residual resistances of 5 to 10 nΩ. At 1.8 K this results in Q_0 of 2×10^{10} to 4×10^{10}.

Fully equipped state-of-the-art multi-cell cavities, installed in cryomodules, have achieved quality factors of 2×10^{10} to 3×10^{10} at medium field gradients of about 15 MV/m (see Fig. 2.4.3). It should be noted that the graph on the left side of Fig. 2.4.3 shows the average performance of all eight 9-cell cavities installed in one cryomodule in the FLASH accelerator. Based on these proof-of-principle measurements, an average quality factor of 2×10^{10} at the operating field gradient is assumed for the ERL main Linac at an operating temperature of 1.8 K. This corresponds to the requirement that the residual surface resistance has to be 10 nΩ or less.

Very high intrinsic quality factors have also been achieved during the first cryomodule test of the Cornell ERL main linac cavity. The cavity received a bulk buffer-chemical polish (BCP) of 150 μm, was heat treated at 800 C for two hours, received a final 10 μm BCP, two eight-hour high pressure rinses, and then was baked under vacuum at 120 C for 48 hours. The cavity was installed in a one-cavity Horizontal Test Cryomodule (HTC) for a first horizontal cryomodule test of the cavity. In order to understand the details on preserving high cavity

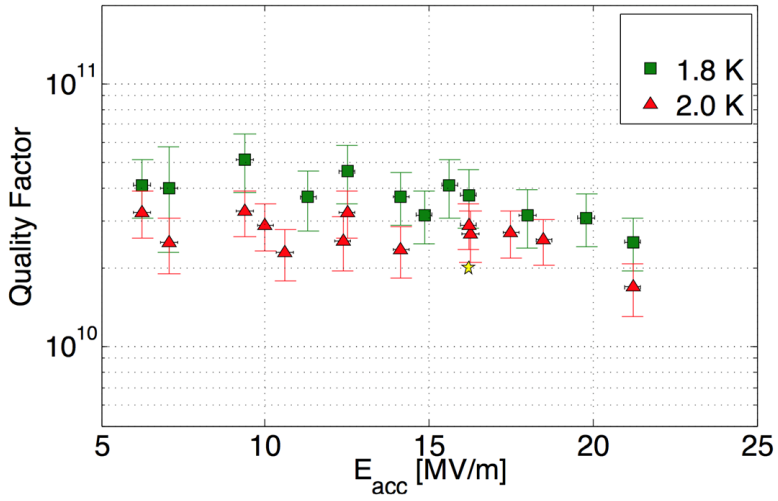

Figure 2.4.4: Intrinsic quality factor vs accelerating field curve at 1.6 K and 1.8 K for the prototype Cornell ERL main linac cavity installed in a test cryomodule. This cavity is fully equipped with power couplers and higher order mode dampers [11].

Q's under different operational configurations, a three step approach was chosen. During the first cryomodule test of the cavity, measurements were done using only a small probe coupler. The performance of the cavity installed in the test module significantly exceeded the 2×10^{10} specification, reaching quality factors at $E_{\mathrm{acc}} = 16.2\,\mathrm{MV/m}$ of $Q_0 = 3 \times 10^{10}$ at 1.8 K and $Q_0 = 4 \times 10^{10}$ at 1.6 K. At lower fields, the quality factor even reached $Q_0 = 6 \times 10^{10}$ at 1.6 K [10]. In a second setup (HTC-2), the final power couplers were mounted and the cavity was re-measured, resulting in only minor changes of the Q-factor. In a third and now final step, the HOM absorbers were mounted reflecting exactly the geometric and EM design of the full linac cavity setup proposed within this report. The performance of the cavity in this full setup is given in Fig. 2.4.4, clearly indicating the performance above specifications. During dismounting of HTC-2 and mounting of HTC-3 the cavity was chemically reprocessed. For details and references to the different treatment and testing steps see [10].

Accelerating gradient

The optimal accelerating field gradient in the cavities of the main Linac is set by considerations of cost of the main Linac (construction and operation cost), the increase in cavity trip rate and electron field emission at higher field gradients. The approach taken is to find the gradient region at which cost is minimized, and then to select a field gradient at the lower end of that region to maximize accelerator availability and to minimize any potential risks from electron field emission. The detailed cost model used for optimization includes the construction costs of the main Linac cryomodules of the RF system including RF power sources, of the cryogenic refrigerator, and of the tunnel length occupied by the main Linac. The total energy gain in the main Linac of a 100 mA beam is fixed at 5 GeV, while the accelerating field gradient in the cavities (and thereby the number of cavities) is varied to yield costs. The main conclusion from

these studies is that the region of minimal cost is quite broad. The model used here shows that the construction costs are the same within 5 % for medium field gradients between 14.5 MV/m and 28 MV/m, with the actual minimum at 18 MV/m. The broad region of minimal cost is a result of the fact that the length of the main Linac and the number of cavities decrease linearly with gradient, but the total dynamic heat load of the cavities in continuous operation and the total RF power required for operating the cavities increase linearly with gradient. Cost studies for other SRF projects have resulted in the same conclusion that medium field gradients in the 15 to 20 MV/m range are optimal for CW Linac [12]. Selecting an accelerating field gradient at the lower end of the 14.5 MV/m to 28 MV/m optimal region is highly advisable for several reasons:

- The size of the 1.8 K cryogenic refrigerator increases linearly with gradient (neglecting static heat loads at 1.8 K, which are small compared to the dynamic cavity load), and so does the AC power and the operating cost of the cryogenic plant. At present, refrigeration plants up to about 5 kW at 1.8 to 2 K are in operation (e.g., CEBAF, LHC).

- The operating cost strongly increases with field gradient, since the total dynamic heat load in the cavities and the total RF power required for operating the cavities increase linearly with gradient.

- The risk of electron field emission increases exponentially with field gradient. Measurements at the FLASH Linac at DESY have shown that detectable field emission in state-of-the-art cavities starts at gradients of $\sim$ 15 to 20 MV/m, and increases by an order of magnitude every 3 to 5 MV/m [13]. Field emission generates captured dark current, reduces the quality factors of the SRF cavities, and generates radiation (x-ray and neutron) in the tunnel. All of these effects are highly undesirable and staying near or below the onset of field emission is therefore advisable.

- Accelerating field gradients in the 15 to 20 MV/m range are nowadays achieved routinely with yields near 100 %. Gradient specifications in this medium field range can significantly simplify the surface treatment of the cavities. Standard chemical etching with BCP (HF, HNO_3 and H_3PO_4, usually in a ratio of 1:1:1 or 1:1:2) is sufficient to yield gradients in this range. Treatment of the cavity surface by the more complex method of electropolishing is only required if it would routinely result in lower residual resistances. This is a topic of ongoing SRF cavity research at numerous laboratories around the globe.

These considerations have led to a baseline specification of the accelerating field gradient in the cavities of the ERL main Linac of 16.2 MV/m, which is at the lower end of the 14.5 MV/m to 28 MV/m optimal cost region. The corresponding cavity dynamic heat load at 1.8 K is $\sim 4\,\mathrm{kW}$.

Cavity external Q_{ext}

In the main Linac of an ERL, the optimal loaded Q_{ext} of the SRF cavities is set by the microphonics level. 'Microphonics' refers to the detuning of an RF cavity by external sources like ground vibrations or LHe bath pressure fluctuations. These vibration sources can couple

Table 2.4.3: Measured microphonic levels measured in SRF Linacs [14].

machine	σ (Hz)	6σ (Hz)	Comments
CEBAF	2.5 (average)	15 (average)	significant fluctuation between cavities
ELBE	1 (average)	6 (average)	
SNS	1 to 6	6 to 36	significant fluctuation between cavities
TJNAF FEL	0.6 to 1.3	3.6 to 7.8	center cavities more quiet
TTF	2 to 7 (pulsed)	12 to 42 (pulsed)	significant fluctuation between cavities

to the cavity via multiple paths. It is useful to distinguish between random noise and defined frequency vibrations. When a vibration source frequency lines up with a mechanical resonance of a cavity, particularly strong microphonics can occur.

Maintaining low cavity microphonic levels is of great importance for an ERL. The main Linac cavities have virtually zero beam loading (the energy transfer from the decelerated beam to the RF-cavity fields compensates the energy transfer from the RF fields to the accelerated beam), and so for efficient cavity operation they should be operated at a very high loaded quality factor Q_{ext}. The optimal Q_{ext} is solely determined by the ratio of the fundamental mode frequency f_0 and the typical detuning Δf

$$Q_{\text{ext,optimal}} = \frac{f_0}{2\Delta f}\,. \tag{2.4.4}$$

The required RF power is directly proportional to the detuning. In designing an ERL, it is therefore extremely important to have a good estimate of the peak cavity detuning when determining the required RF peak power. If one underestimates the peak detuning, and thus the installed RF power is not sufficient, the RF source will run against its maximum output power, and so the cavity is likely to trip every time the cavity detuning exceeds the estimated peak detuning.

Most existing $v_{\text{p}} \approx c$ superconducting RF accelerators have significant beam loading. Because of the resulting relatively high fundamental mode bandwidth (typically between 100 Hz and a few 1 kHz), microphonics is of lesser concern in such machines. Accordingly only limited effort has been made in the past in measuring microphonics, understanding its sources, and improving the mechanical design of the cavities and cryostat to minimize microphonics. Table 2.4.3 summarizes measured rms microphonics levels for different superconducting machines. The peak cavity detuning is estimated as 6σ. In all cases significant fluctuation in microphonics has been found from cavity to cavity, even within the same cryomodule. Table 2.4.3 shows that proofs of principle for low microphonics SRF cryomodules exist, with a peak detuning below 10 Hz appearing feasible if care is taken during the cryomodule design to minimize excitation of cavity vibrations. To be conservative, our parameters assume a peak detuning of 25 Hz.

Assuming 10 Hz as typical peak detuning of the SRF cavities in the ERL main Linac results in a baseline loaded quality factor of 6.5×10^7 and a typical RF-peak power of $\sim 2\,\text{kW}$ per cavity. For some individual cavities and in some rare events, larger cavity detunings should be expected. To prevent cavity trips and beam loss in these cases, 5 kW of RF power will

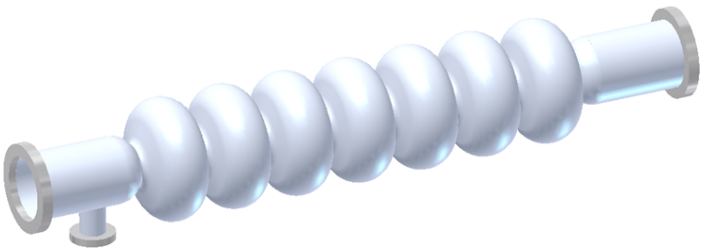

Figure 2.4.5: CAD model of the 7-cell ERL main Linac cavity.

be installed per cavity in the ERL main Linac, allowing maximal detuning during these rare events of up to 25 Hz.

Passive and active means will be used to reduce microphonics in the main Linac cavities below the levels listed in Tab. 2.4.3. As discussed in the following sections in greater detail, the mechanical design of the cavities and of the cryomodule will include microphonics considerations. Besides designing the cryomodule for minimal microphonics, a further reduction in microphonics amplitude could potentially be achieved with active control schemes, making use of a fast frequency tuner. Initial studies have shown promising results [15].

The baseline ERL cavity

This section discusses the RF and mechanical design of the baseline main Linac superconducting RF cavity. The baseline cavity is a standing-wave 7-cell structure of solid niobium with a fundamental mode frequency of 1.3 GHz (see Fig. 2.4.5). Power is coupled into the cavity via one coaxial RF input power coupler located at an end-beam tube. Large diameter beam tubes ensure propagation of all monopole and dipole HOMs to beam tube RF absorbers located between the individual cavities to ensure strong suppression of HOMs and thereby support operation of beam currents up to 100 mA. The cells of the cavity are surrounded by a LHe tank to immerse the cavity into 1.8 K LHe. Each cavity is further equipped with a frequency tuning system (slow tuner driven by a stepping motor and fast tuner driven by piezoelectric crystals), and a field pick-up probe to monitor the cavity-RF fields. Table 2.4.4 summarizes the main parameters of the main Linac cavity. The following subsections give more details on the cavity design.

RF design

This section discusses details of the RF design of the shape of main Linac cavity.

Design philosophy The shape of a multi-cell SRF cavity is defined by a large number of parameters, which can be adjusted according to the design goals of the specific accelerator. In the case of the ERL, the cavity design needs to fulfill the following requirements:

- The RF design should reduce dynamic losses by the fundamental mode as far as possible while still satisfying the other design goals.

Table 2.4.4: ERL main Linac cavity design parameters. Note that R/Q is always in the circuit definition.

Parameter	Value
Type of accelerating structure	Standing wave
Accelerating mode	$TM_{0,1,0}$ π
Fundamental frequency	1.3 GHz
Design gradient	16.2 MV/m
Intrinsic quality factor	$> 2 \times 10^{10}$
Loaded quality factor	6.5×10^7
Cavity half bandwidth at $Q_L = 6.5 \times 10^7$	10 Hz
Operating temperature	1.8 K
Number of cells	7
Active length	0.81 m
Cell-to-cell coupling (fundamental mode)	2.2%
Iris diameter center cell / end cells	36 mm / 36 mm
Beam tube diameter	110 mm
Geometry factor (fundamental mode)	270.7 Ω
R/Q (fundamental mode)	387 Ω
E_{peak}/E_{acc} (fundamental mode)	2.06
H_{peak}/E_{acc} (fundamental mode)	41.96 Oe/(MV/m)
$\Delta f/\Delta L$	350 Hz/ μm
Lorentz-force detuning constant	1 Hz / $(MeV/m)^2$
Cavity total longitudinal loss factor for $\sigma = 0.6$ mm	14.7 V/pc
Cavity longitudinal loss factor for $\sigma = 0.6$ mm, non-fundamental	13.1 V/pC
Cavity transverse loss factor for $\sigma = 0.6$ mm	13.7 V/pC/m

- The RF design needs to support operation of the ERL at a 100 mA accelerating beam current.
- The performance of the RF design needs to be stable under small shape imperfections, which are unavoidable in the fabrication process of deep drawing and welding.
- The ratio of peak electric surface field to accelerating field E_{pk}/E_{acc} shall not exceed 2.1 to reduce the risk of field emission (the ratio of electric fields in the ILC cavity is 2.0).
- The cell shape shall be non-reentrant. This simplifies cavity cleaning and surface treatment.
- Transverse kick fields in the coupler region shall be minimized to avoid emittance growth.

The RF design of the cavity is complicated by the fact that there are a large number of free parameters in the cavity shape and that there are different objectives for the design, which are partly contradictory because optimization for minimal losses and for maximal HOM damping

Table 2.4.5: Comparison of figures of merit and geometries for center cells before and after re-optimization to increase the width of HOM passbands. Cryogenic losses are slightly increased. The geometry factor and $E_{\rm pk}/E_{\rm acc}$ are for the fundamental mode. Key: Equ.=Equator, Horiz.= Horizontal, Vert.=Vertical. The last four dimensions are half-axes of ellipses, measured in cm.

	$(R/Q)G$	$E_{\rm pk}/E_{\rm acc}$	Wall angle	Iris radius	Equ. horiz.	Equ. vert.	Iris horiz.	Iris. vert.
Before	15576 Ω	2.00	85	3.5	4.399	3.506	1.253	2.095
After	14837 Ω	2.06	77	3.598	4.135	3.557	1.235	2.114

lead to different shapes of the cells. In designing the ERL main Linac cavity, the following approach has been taken to reduce the number of free parameters in each step by breaking the design work down into several steps, each focusing on a specific design objective:

- The center cells of the multi-cell main Linac cavity are identical and have been optimized initially to minimize dynamic wall losses by the RF field while keeping $E_{\rm pk}/E_{\rm acc} < 2.1$.
- The end cells were optimized to reduce the strength of the strongest dipole HOMs to increase the beam break-up (BBU) current above the design goal of 100 mA.
- The design was then evaluated for robustness under small shape imperfections and the shape of the center and end cells was iterated slightly to achieve sufficient robustness.
- The maximum number of cells was found by adding additional center cells to the multi-cell cavity design, and the BBU performance of the resulting cavity was simulated.
- The loss factor of the final cavity shape was computed and the input coupler region at one of the two end beam tubes was designed.

Center cell design The center cells of the ERL main Linac cavity are identical and have been optimized initially to minimize dynamic losses while keeping $E_{\rm pk}/E_{\rm acc} < 2.1$. The shape of the cell was optimized for different iris radii between 30 and 43 mm (see Fig. 2.4.6 using a computerized optimization routine and the electromagnetic eigenmode code CLANS [16]. In each case, the shape dependent factor GR/Q was maximized to minimize the dynamic wall losses of the accelerating mode at a given field gradient. The usual basic cell shape consisting of two elliptical sections connected by a tangential line was used to ensure avoidance of multipacting in the cells.

Reducing the iris radius reduces the dynamic heat load by the RF field in the cavity, but increases the magnitude of the loss factor of the cavity. An increase in loss factors means an increase in average HOM power excited by the electron beam. Further, reduction of the radius reduces the cell to cell coupling and thus coupling of the HOM power to the beamline loads and the robustness of the design against small manufacturing errors. As discussed in [17], the parameter set resulting from the indicated compromises are presented in Tables 2.4.5 and 2.4.6.

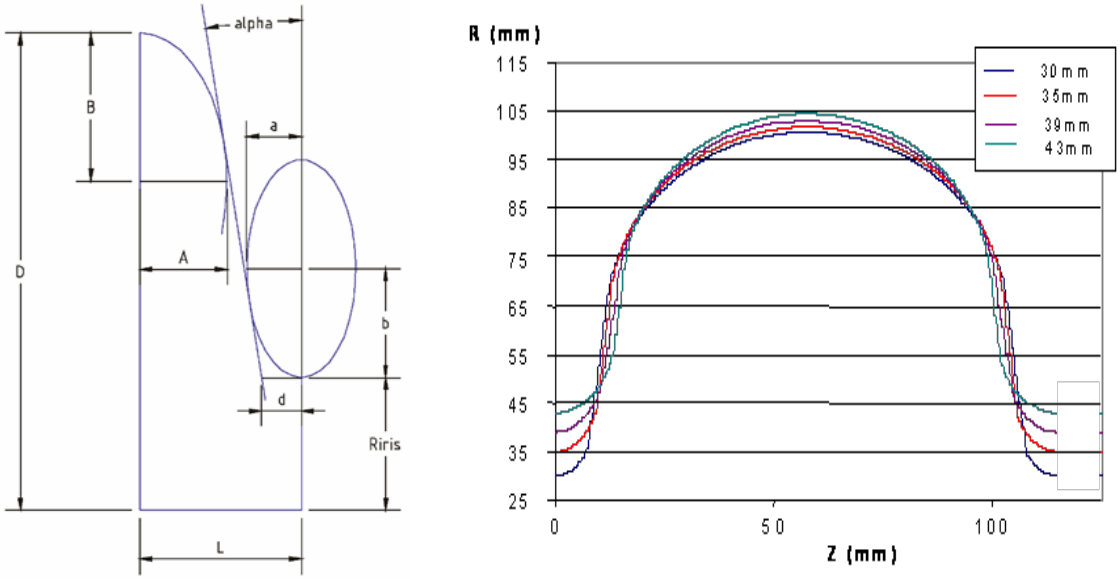

Figure 2.4.6: Left: Basic cell shape consisting out of two elliptical arc sections connected by a tangential straight line. Right: Center cell shaped for different iris radii optimized to minimize cryogenic losses (via maximizing GR/Q for the accelerating mode). The angle alpha of the tangential line is kept above 8° to ensure non-reentrant cell shapes.

End cell design and HOM performance The ERL is specified to run accelerating currents of 100 mA through the main Linac. This current is limited by higher-order-modes in the cavity that are excited by the beam and can cause beam instability. In a 1-turn ERL, the threshold current $I_{\rm th}$, through an isolated cavity with a single HOM, has been modeled as

$$I_{\rm th} = -\frac{\omega_\lambda}{e\left(\frac{R}{Q}\right)_\lambda Q_\lambda}\frac{1}{T_{12}\sin(\omega_\lambda t_{\rm r})}\,, \tag{2.4.5}$$

where ω_λ is the HOM frequency, Q_λ is the quality factor of the mode, R/Q is in units of Ω/cm^2 (in circuit definition), t_r is the bunch return time, and the transport matrix element T_{12} describes how a transverse momentum is transported to a transverse displacement after one turn [18]. Equation 2.4.5 suggests that the parameter $(R/Q)Q/\omega$ should be used as a

Table 2.4.6: Frequency width of the first 6 dipole passbands. Note that bands 3 and 6 were widened significantly while the other bands had their widths decreased only slightly.

Dipole band	~ 1.8 GHz	~ 1.9 GHz	~ 2.5 GHz	~ 2.7 GHz	~ 3.1 GHz	~ 3.4 GHz
Before	192 MHz	95 MHz	31 MHz	277 MHz	55 MHz	10 MHz
After	188 MHz	73 MHz	107 MHz	227 MHz	47 MHz	20 MHz

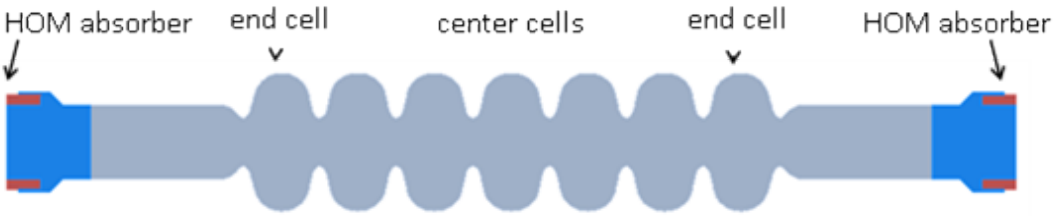

Figure 2.4.7: Shape of the main Linac cavity with HOM absorber sections at the beam tube ends.

figure of merit in the cavity design when optimizing it for maximal BBU threshold current. However, the ERL main Linac will have a large number of cavities, and coherent effects will influence I_{th} through the Linac. This coherent effect will depend on the variation of the HOM frequencies from cavity to cavity and on the quality factor of a given type of mode. Lower quality factors will result in wider HOM-resonance curves and therefore in more overlapping of the modes in different cavities, more coherence, and a lower threshold current. Thus, a new BBU figure of merit parameter was determined for an ERL Linac with a large number of cavities by running BBU simulations and varying the parameters of a given HOM in the cavities. The conclusion of the BBU runs is that

$$I_{\mathrm{th}} \propto \frac{\omega_\lambda}{\left(\frac{R}{Q}\right)_\lambda \sqrt{Q_\lambda}} \tag{2.4.6}$$

for an ERL Linac with a large number of cavities and for $10^2 < Q < 10^6$.

Accordingly, the end-cells of the ERL main Linac have been optimized with the goal to minimize the maximum value $(R/Q)_\lambda \sqrt{Q_\lambda}/f$ of any dipole HOM of the cavity. The end cells were optimized by varying 5 free parameters per end cell. The dipole mode fields and their damping were calculated with the 2D finite element codes CLANS2 [19] for HOM frequencies up to 10 GHz. The 2D-cavity model used is shown in Fig. 2.4.7, and includes the cavity itself, and half of an HOM absorber at either end (the center of an HOM absorber is the symmetry plane for a string of main Linac cavities). This model therefore simulates the Q in a string of cavities. The model includes the dielectric losses by the selected RF absorbing material in the HOM absorbers ($\epsilon' = 30$; $\epsilon'' = 20$; $\mu' = 1$; $\mu'' = 0$). Particle tracking was then used to compute the final threshold current through an ERL composed of these cavities. The blue curve in Fig. 2.4.8 shows that as the relative cavity-to-cavity HOM frequency spread increases, so does the threshold beam current. In practice, the frequency spread will be the result of slight variation in cavity shapes in the cavity fabrication process. This is shown as the red curve in Fig. 2.4.8.

Typical fabrication tolerances of ± 0.25 mm to ± 0.5 mm result in a cavity-to-cavity frequency spread σ_f/f of about 1×10^{-3} to 3×10^{-3}. At this frequency spread, particle tracking for the optimized 7-cell cavity predicts a BBU threshold current of about 300 mA to 500 mA, several times the 100 mA requirement for the accelerating beam of the ERL. If needed, the BBU threshold can be increased considerably by intentional means. An ensemble of cavity designs giving an approximately uniform frequency spread to the important HOM dipole bands will be created for the manufacture of the ERL cavities.

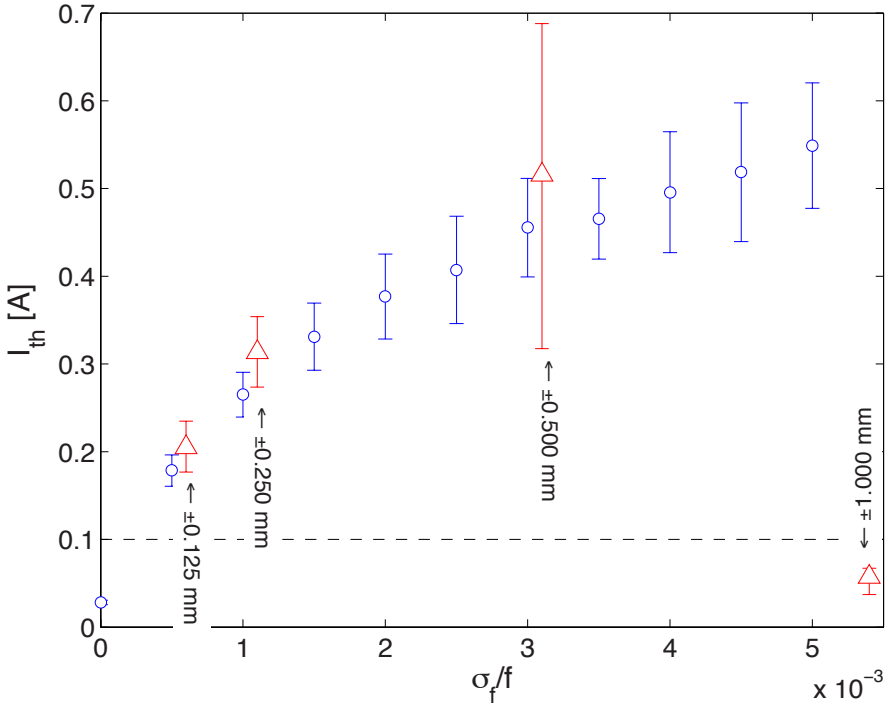

Figure 2.4.8: Average beam breakup current versus relative frequency spread for simulated ERLs. The blue circles mark the threshold current through an ERL with every cavity having the same nominal HOM frequency, Q, and R/Q values of the worst higher-order modes as a function of relative cavity-to-cavity frequency spread. The red triangles denote the average threshold current for ERLs generated from realistically shaped cavities, having different frequencies, Qs and R/Qs from shape imperfections, and no artificial cavity-to-cavity frequency spread. The lower (upper) error bars mark the threshold current that 90% (10%) of the simulated ERLs achieve. For small values, as machining tolerances loosen, the frequencies of cavity HOMs are spread over a larger range, contributing to larger threshold currents. When the machining errors are more than 0.5 mm, the underlying properties of the optimized cavity geometry are lost, and the threshold current plummets. In all cases except the 1 mm variation size, simulated ERLs well exceed the design specification of 100 mA current, denoted by the dashed horizontal line.

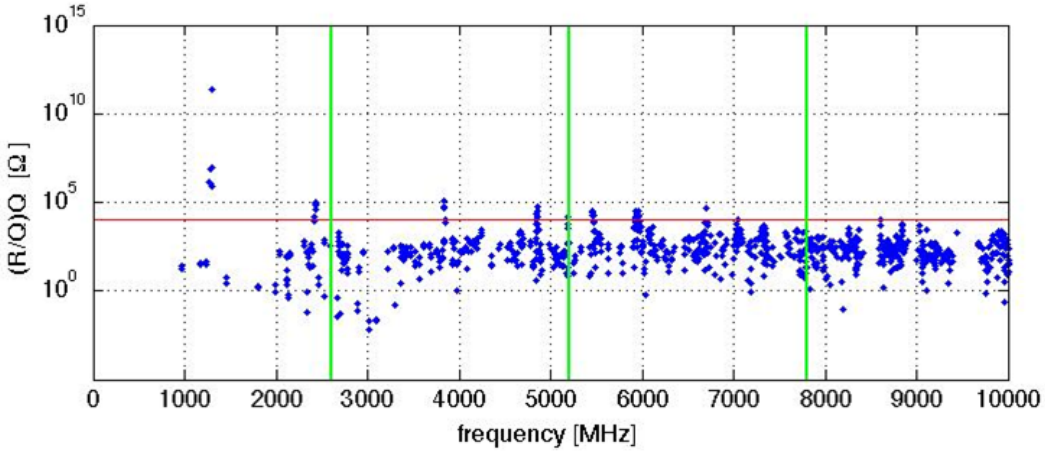

Figure 2.4.9: Monopole modes strength $(R/Q)Q$ for all monopole modes in the optimized 7-cell cavity up to 10 GHz. Green lines indicate the beam harmonics. The red line shows the $(R/Q)Q = 1000\,\Omega$ limit for modes within $\Delta f = 10^{-3} \cdot f$ of these harmonics. Modes with $(R/Q)Q > 1000\,\Omega$ that are not close the the green lines are benign.

All monopole modes up to 10 GHz have been calculated for the Linac cavity shape to ensure that modes that might be driven resonantly are sufficiently damped. The HOM power transferred to a mode by the beam in case of resonant excitation is given by

$$P = 2\left(\frac{R}{Q}\right) QI^2\,, \tag{2.4.7}$$

where Q is the quality factor of the mode and I is the average beam current (0.2 A for the combined accelerated and decelerated beam in the main Linac). Requiring that the maximum HOM power in case of resonant excitation is below 400 W per cavity then gives $(R/Q)Q < 10^4$ for any mode that could be excited resonantly, i.e. which has a frequency within $\Delta f = 10^{-3} \times f$ of a beam harmonic at $f = N \times 2.6\,\mathrm{GHz}$. Calculation shows that all monopole modes near the first 3 beam harmonics are sufficiently damped in the 7-cell ERL main Linac cavity. These results are shown in Fig. 2.4.9.

Short range wakefields The longitudinal loss factor $k_{||}$ of a cavity determines the average power transferred from the beam to electromagnetic fields (wakefields) excited by the beam,

$$P_{\mathrm{average}} = k_{||} qI\,, \tag{2.4.8}$$

where q is the bunch charge and I is the average beam current. The longitudinal loss factor and the wake potential of the 7-cell ERL main Linac cavity have been calculated for a bunch length of $\sigma = 0.6\,\mathrm{mm}$ yielding $k_{||} = 14.7\,\mathrm{V/pC}$, where the fundamental mode contributes 1.6 V/pC and the HOMs contribute 13.1 V/pC. Note that the main Linac cavities are one of the main contributors to the total impedance of the ERL and thereby make a significant contribution to the final intra-bunch energy spread . The average HOM power excited by the

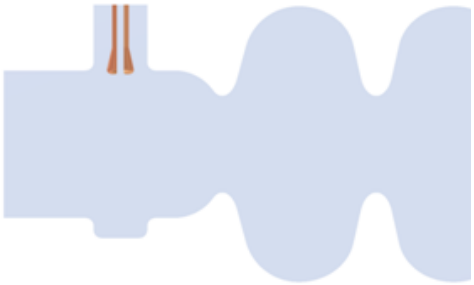

Figure 2.4.10: Input coupler port of the ERL main Linac cavity with $Q_{\text{ext}} = 6.5 \times 10^7$ and symmetrizing stub at the opposite site of the beam tube.

beam in a main Linac cavity is then about 200 W. Individual cavities will have smaller or larger power values, depending on their actual HOM frequencies (which will vary from cavity to cavity as a result of small cavity-shape imperfections), which will change the number of modes excited resonantly by the bunch train.

Input coupler port and transverse coupler kicks The position of the 40 mm input coupler port on one of the cavity end-beam tubes was found such that the tip of the inner conductor of the coax input coupler protrudes 2.7 mm inside of the beam tube wall at an external Q of 6.5×10^7 (see Fig. 2.4.10). Non-zero transverse fields can be present in the input coupler region even on the beam axis since the coupler port breaks the axial symmetry. Such transverse coupler fields are highly undesirable, since they will cause emittance growth of the beam passing the ERL main Linac. One way of reducing the emittance growth is adding a small symmetrizing stub across from the coupler as illustrated in Fig. 2.4.10. The stub is used to minimize the asymmetry in the beam pipe, causing the transverse fields in the coupler region. The method reduces amplitudes of the off-axis fields and thus reduces the magnitude of the coupler kick with weak dependence on the depth of the stub once it is over 10 mm deep [20]. Our preliminary design therefore uses 20 mm depth.

Mechanical design

This section gives an overview of the mechanical design of the Cornell ERL main Linac cavity, including its LHe vessel and inner magnetic shield.

Mechanical modes The cavity cells will be fabricated out of 3-mm thick Niobium sheets for mechanical strength, with stiffening rings between the individual cells. The optimal position of these stiffening rings will be found by mechanical simulations with ANSYS. The objectives of these optimizations are (1) to increase the resonance frequencies of mechanical vibration modes of the cavity to reduce cavity vibration excitation by external sources, and (2) to decrease the frequency shift of the accelerating mode by fluctuations in the LHe bath pressure surrounding the cavity. The power density of the ground vibration spectrum decreases with frequency so high mechanical resonance frequencies of the cavities are desirable to reduce driven vibrations. Figure 2.4.11 shows the lowest frequency mechanical vibration modes of

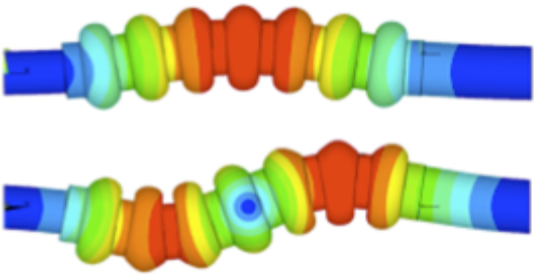

Stif. ring	$0.7*r_{eq}$	$0.65*r_{eq}$	$0.4*r_{eq}$	no ring
mode	freq / Hz	freq / Hz	freq / Hz	freq / Hz
1	131.03	115.15	85.34	54.62
2	131.04	115.15	85.33	54.62
3	315.52	268.39	191.3	133.34
4	315.52	268.39	191.3	133.34

Figure 2.4.11: Mechanical vibration modes of the main Linac 7-cell cavity for different radial positions of the stiffening between the individual cells. r_{eq} is the cell equator radius.

the main Linac cavity structure for different radial positions of the stiffening rings between the cells. As expected, the frequencies of the modes increase with the radial position of the stiffening rings. An upper limit for the radial position is given by the requirement that the cavity needs to remain tunable in length by the frequency tuner, and by the second objective that the sensitivity to LHe pressure changes should be minimized.

As the example in Fig. 2.4.11 shows, the radial position of the stiffening rings also changes the sensitivity of the cavity frequency to fluctuations in the pressure of the liquid helium surrounding the cavity cells. Optimizing the position of the rings allows minimizing this contribution to the cavity microphonics.

The beam tubes of the main Linac cavity will be fabricated out of 1.5 mm thick, low-RRR niobium to reduce static heat loads from the HOM absorbers located between the cavities at 100 K to the 1.8 K cavities.

Cavity flanges Different types of flanges have been used on superconducting cavities in the past, including niobium flanges with indium wires, ConFlat-flanges, and aluminum diamond shaped gaskets with NbTi flanges. The main objective of these flanges is to provide a clean, highly reliable connection to the next element in the beamline. However, in high current accelerators like the ERL, it is also crucial that the impedance of the flange design be as small as possible to eliminate potential heating issues, since they are inside the cryomodule vacuum and therefore cooled only via conduction through the beam-pipe.

KEK has developed a zero-gap (zero-impedance) flange design, which uses a copper gasket compressed between two small, flat surface rings with 90° edges [21] (see Fig. 2.4.12). NbTi versions of such a zero-gap flange design will be considered for use in the ERL main Linac for the cavity flanges. An R&D program has been started to verify the high reliability of this flange design found in previous studies [22]. In parallel, a new flange design will be studied which is a hybrid of the KEK zero-gap [21], a DESY diamond seal [22] and a taper seal flange [23]. This configuration shown in Fig. 2.4.13 may allow for the reliability of the DESY diamond seal with low compression force and elastic spring as well as the minimal wall perturbation of the KEK zero-gap.

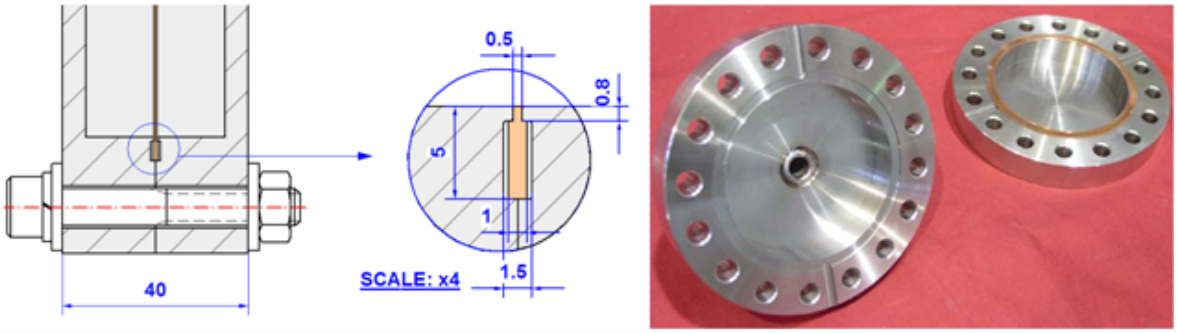

Figure 2.4.12: Zero-gap KEK flange design [23].

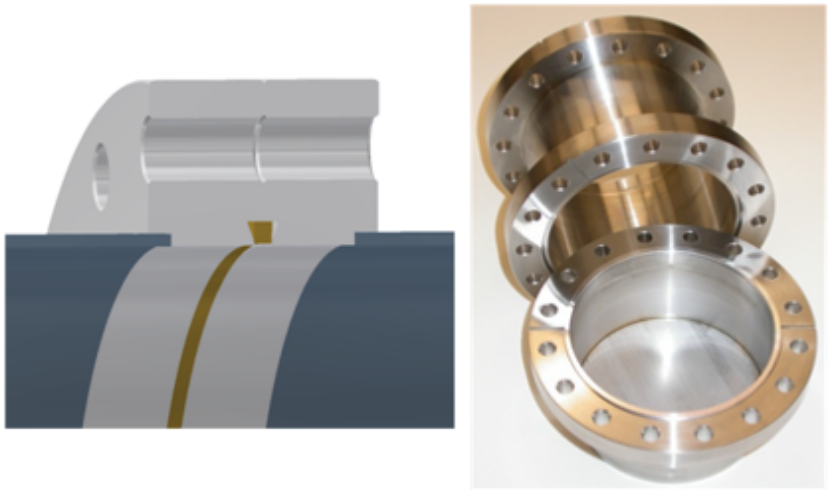

Figure 2.4.13: Vacuum flange hybrid of the KEK zero-gap, a DESY diamond seal and a taper seal flange.

LHe vessel The cavity cells are welded into a cylindrical titanium vessel, which holds the superfluid helium needed for cooling the cavities to 1.8 K. The tank further serves as part of the cavity-frequency tuning system, including a short bellow section to allow the length of the cavity to be adjusted, and is used to support the cavity in the cryomodule. Titanium has a thermal contraction which is almost identical to that of niobium, thereby minimizing any buildup of mechanical stresses during cool-down of the cavity from room temperature to 1.8 K. A stainless steel vessel would have a 2 times larger thermal contraction than the niobium cavity and would result in intolerable stresses in the cavity, resulting in plastic deformation unless the tuning mechanism is operated during cool-down. Titanium has the additional advantage that it can be welded directly to the Nb/Nb-Ti conical vessel end plates on the cavities using either TIG welding or electron-beam welding.

The heat flux (power per cross-sectional area) through superfluid helium in the LHe vessel needs to be less than the limiting heat flux of $\sim 1.5\,\mathrm{W/cm^2}$, at which the temperature of the bath at the heat source would reach the lambda point, and the helium would cease to be superfluid. The smallest cross-sectional areas of the helium in the tank surrounding the cavity

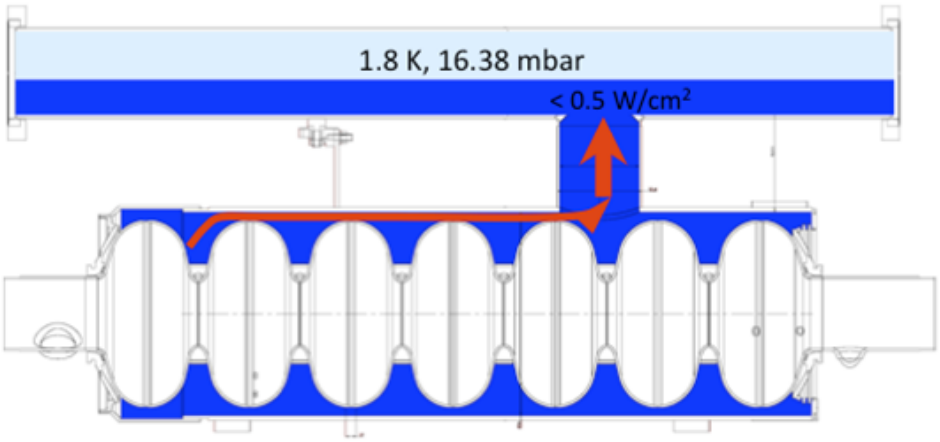

Figure 2.4.14: Heat flow in the LHe vessel and the chimney connecting the tank to the two phase line. The heat flow in the superfluid helium is below 0.5 W/cm^2 everywhere.

are at the cell equators (see Fig. 2.4.14). The diameter of the LHe vessel has been chosen such that the heat flux in these areas stays well below 1.5 W/cm^2 at the chosen operating parameters.

During initial cool-down, the LHe vessels of the cavities can be filled via a warm-up - cool-down pipe connected to the bottom of the LHe tanks. A chimney of sufficiently large diameter ($> 20\,\mathrm{cm}^2$) connects each LHe tank to the two-phase He pipe in the cryomodules as shown in Fig. 2.4.14.

The cavity-helium tank structure is a mechanical structure with many eigenmodes driven by external vibration sources and pressure fluctuations the LHe bath. The mechanical design of this structure is optimized to avoid low-frequency mechanical resonances and resonances at multiples of the 60 Hz line frequency to minimize cavity microphonics. Measurements at the Cornell ERL injector cryomodule have shown that the dominating source of microphonics is due to fast fluctuations in the LHe pressure [24]. The stiffness of the cavity-helium tank structure is therefore designed to minimize the frequency shift of the cavity with changes in LHe pressure.

Inner magnetic shield It has been shown that a DC residual magnetic flux present at the cavity will be trapped when the cavity is cooled through the transition temperature. This results in a residual resistance of about 0.35 nΩ per mG of trapped flux at 1.3 GHz [25]. The earth's field must be adequately shielded to achieve high Q_0 factors. The residual DC-magnetic field at the cavity locations needs to be much less than 30 mG to achieve residual resistances below 10 nΩ and intrinsic quality factors above 2×10^{10} at 1.8 K. In the ERL, this will be achieved by three layers of shielding of the Earth's magnetic field: an outer vacuum vessel made out of carbon-steel, an outer magnetic shield at room temperature lining the inside of the vacuum vessel, and an inner magnetic shield around the LHe vessels of the cavities. The inner shield will be made out of A4K, [26], which has a high permeability at cryogenic temperatures, and will be heat treated for operation at 2 K. The shielding design goal is < 2 mG.

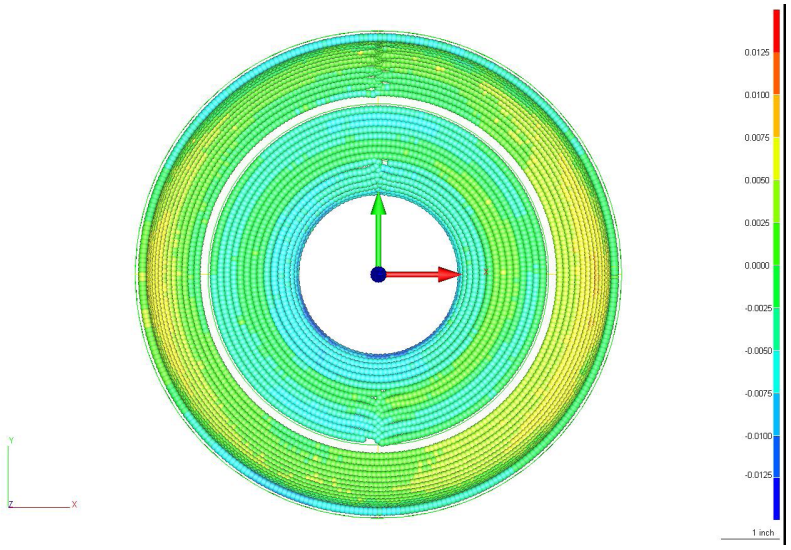

Figure 2.4.15: Overall accuracy of the cavity cup shape, measured with a coordinate-measuring machine. The deviation from the ideal shape is well below 200 μm, being better than required by the BBU limit estimated above.

Table 2.4.7: Summarized target frequencies for all cavity production steps.

Production Step	Frequency (MHz)
Cavity designed shape in vacuum	1299.655
Cavity designed shape in air	1299.234
Cavity nominal desired freq as built	1298.985
Air, 20C, 150 μm BCP	1297.425
Vacuum, 20 C	1297.884
Vacuum, 2 K	1299.700
Vacuum, 2 K, tuned 300 kHz (stretched)	1300.000

Cavity fabrication

The ERL main Linac cavities will be fabricated from high-purity (RRR $>$ 300) bulk niobium. RRR 300 Niobium has become the standard in SRF cavity fabrication, with higher RRR values often produced by post-purifying the cavity at around 1400° C. This improves the thermal conductivity of the material, which in turn safeguards against quenches due to normal-conducting defects. An eddy-current scan or newer techniques based on SQUID scans of the delivered sheets will be used to detect such defects in the niobium before it is used for cavity production. The half cells for the cavities are deep-drawn and then electron-beam welded to fabricate the full 7-cell cavity. As shape variations play an important role in determining the BBU limit, a careful analysis of all pressed cups is essential. Our data on 7 prototyped cavity showed the maximum deviation being less than 200 μm. Figure 2.4.15 shows a typical measurement, taken with a coordinate-measuring machine (CMM).

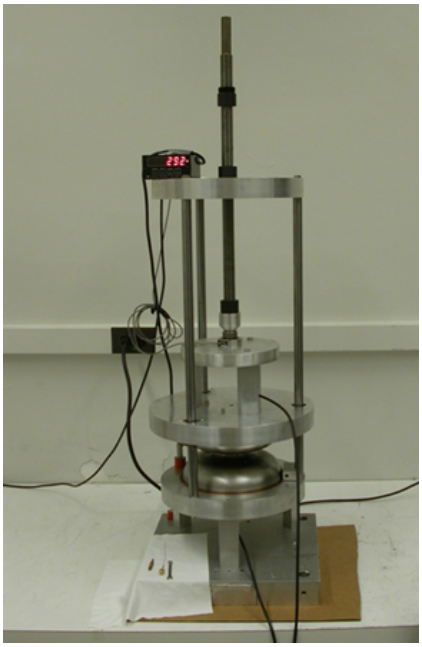

Figure 2.4.16: RF measurement set-up to determine the dumbbell trimming. This individual trimming process ensures a proper compensation of the small shape variations, leading to an almost perfect cavity after all fabrication steps

After pressing the cups, two of them are welded at the iris to form dumbbells. These dumbbells have excessive length at the equator and trimmed individually to account weld shrinkage, chemical etching, and cooling to 1.8 K. Table 2.4.7 summarizes the different frequencies targeted during the production steps, ensuring that the cavity will have the correct frequency at its operating temperature. The trimming length for the dumbbells is determined by an RF measurement, shown in Fig. 2.4.16.

After trimming the dumbbells, the full cavity is welded together. The beam-tube sections are of extruded, low RRR-niobium tubes, with NbTi flanges (ratio 45/55 by weight) electron-beam welded to them.

The field flatness of a cavity fabricated in that manner is shown in Fig. 2.4.17. Even though the field flatness (as a result of the dumbbell trimming) is pretty good, the whole cavity is tuned to field flatness after the chemistry process again. The apparatus to do this is also shown in Fig. 2.4.17. The procedure described above is suitable for a large series production have been developed and transferred to industry before [27].

Cavity treatment

Numerous techniques for cavity surface preparation exist [28]. These include an initial degrease, chemical etching with BCP (HF, HNO_3 and H_3PO_4, usually in a ratio of 1:1:1 or 1:1:2) or electropolishing, followed by high-pressure water rinsing, and heat treatments at 600 to 1400° C for hydrogen degassing or post purification, respectively. These steps may have to be repeated several times. A final treatment often includes in-situ baking at around 120° C

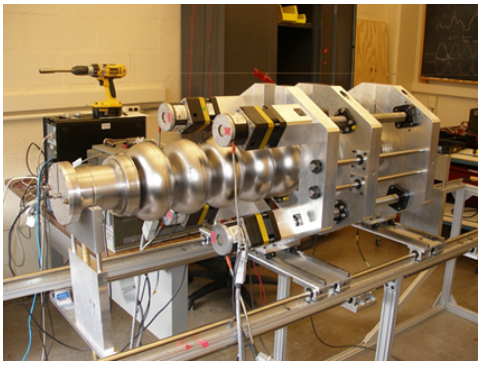

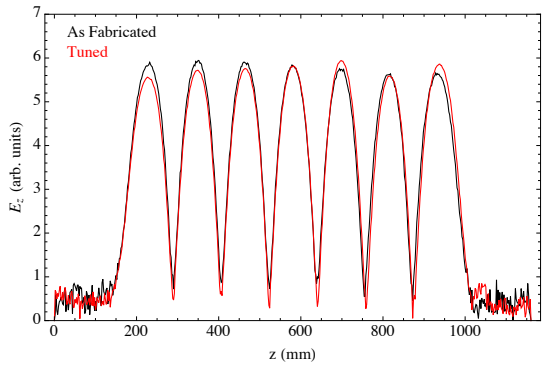

Figure 2.4.17: Left: This setup is used to tune each cavity to a flat field. It slightly pushes or pulls on the irises, while the field flatness is measured with a bead-pull.
Right: Measured field flatness of a cavity as welded and after field flatness tuning, measured with a bead-pull set-up.

for 48 hours, which has been shown to improve the BCS losses and often removes the so-called "high-field Q-slope" that frequently limits the cavity performance [29].

It is desirable to simplify the treatment of the ERL main Linac cavities as much as possible while still meeting the performance specifications. Chemical etching with BCP has been shown to reliably yield accelerating gradients of 20 to 25 MV/m in multi-cell cavities [30]. Following fabrication of the cavity, a "damage layer" of 100 to 200 μm will be removed from the inner cavity surface in several steps by BCP to achieve good RF performance. This removal is taken into account in the cavity design. The acid is cooled below 15° C during the process to minimize hydrogen migration into the niobium. After high pressure rinsing with ultra-pure water and drying in a class 10 clean room, the cavities will be annealed at 800° C in an ultra-high-vacuum furnace to out-gas hydrogen and relieve mechanical stress built up during the cavity-fabrication process. This heating step is followed by tuning the individual cavity cells for field homogeneity of the accelerating mode and a second, light BCP ($\sim$ 10 μm). In the final step the cavities will be high pressure rinsed again, evacuated and heated at 120° C for 48 hours to minimize the BCS surface resistance. The performance of the cavities will be verified in an RF vertical acceptance test in a superfluid helium bath cryostat.

Current research indicates that electropolishing might result in higher intrinsic quality factors at medium field gradients [31] and thereby compensate for the added cost and complexity of electropolishing. If future research confirms this, one or both of the BCP steps in the ERL cavity preparation might be replaced by electropolishing.

2.4.3 Tuner

The function of the tuner is to stretch or compress the SRF cavity along its beam axis to adjust the frequency of the accelerating π-mode at 1.3 GHz. This adjustment is needed to synchronize the resonant frequencies of all 384 cavities in the Linac to the master oscillator.

As part of the tuner-cavity mechanical system, the cavity's cylindrical helium tank will incorporate a short bellows section to minimize the tank's longitudinal mechanical stiffness,

leaving only the stiffness of the niobium cavity cells for the tuner to act upon. The tuner is attached to the helium tank with attachment points that span the tank's bellows. Thus nearly all of the tuner components must operate at the helium tank temperature of 1.8 K.

Two different operating regimes are required of the tuner. First, a slow time-scale response of the order 1 Hz with a coarse-cavity tuning range of ~ 600 kHz is needed to adjust the cavity frequency due to influences such as:

- contractions upon cooldown to 1.8 K
- variations in helium bath pressure
- manufacturing irregularities
- de-tuning a problematic cavity to minimize beam interaction.

Slow tuning is typically accomplished by a stepping motor with gearing and levers to provide the requisite force along the cavity axis. The slow portion of the tuner is utilized after cavity cooldown to adjust the frequency operating point, and exercised rarely thereafter until warmup. The cavity must be parked in a specific state of compression by the slow tuner prior to cooldown from 293 K to 1.8 K so that the differential thermal contraction between the tuner and the cavity does not plastically deform the cavity. The same requirement for the parked condition applies during warm-up.

The second tuning regime is a fast time-scale response of the order of 1 kHz with a fine cavity tuning range of ~ 1 kHz. The fast tuning is needed to adjust the cavity frequency due to influences such as:

- Lorentz force detuning during cavity field ramp up
- correction of microphonic perturbations of the cavity
- feedback control within the low-level RF system to adjust beam-transit phase,

Fast tuning is accomplished by sandwiching piezo-electric ceramic stacks between the slow tuning mechanical linkages and their cavity attachment locations. The actuated piezo force/displacement then adds in series to the slow-tuning mechanism to result in a superposition of the forces upon the cavity. The piezos must be rated for an adequate blocking force and elongation given a reasonable actuation voltage in the cryomodule vacuum insulation environment. The piezo actuation voltage should be less than 1000 V at maximum displacement for reliable wiring within the vacuum vessel. Listed in Tab. 2.4.8 are the performance parameters required for both the fast and slow components of the ERL Linac SRF cavity tuner.

Design of the main Linac cavity tuner

Several proven options are available for the cavity-tuner design. The choice for the baseline tuner was between adaptations of the Saclay I tuner [32–34] and the INFN-blade tuner [35], related to earlier work at DESY. Both designs have performed well in SRF cavity tests at various facilities and have experienced several generations of optimization, but both designs

Table 2.4.8: ERL Linac cavity tuner performance specifications.

Parameter	Value
Cavity elongation tuning	350 Hz/μm
Cavity spring constant	4.63×10^6 N/m
Cavity force tuning	289 Hz/N
Cavity lowest mechanical resonance	91 Hz
Slow tuner response bandwidth	1 Hz
Slow tuner cavity frequency range	600 kHz
Slow tuner dimensional range	368 μm
Fast tuner response bandwidth	1 kHz
Fast tuner cavity frequency range	1.5 kHz
Fast tuner dimensional range	0.9 μm
Minimum piezo blocking force	2073 N
Maximum piezo voltage	1000 V
Minimum tuner spring constant	6×10^9 N/m
Minimum tuner mechanical resonance	1000 Hz
Tuner operating temperature	1.8 K

require modest modifications for the ERL Linac application. The Saclay I tuner was chosen for the ERL Linac due to the following features that are advantageous to CW, high Q_{ext} cavity operation:

- lower group delay in its tuning response, resulting in lower phase lag for microphonic compensation [36, 37]
- more compact, making integration of the magnetic shield simpler
- mechanically simpler, reducing manufacturing and assembly cost
- greater reliability statistics given its use in the FLASH facility

Also, since the Saclay tuner will be used in the XFEL facility presently under construction, a foundation of production testing and industrial experience will be established.

An illustration and photograph of the Saclay I tuner is shown in Fig. 2.4.18. The modifications to the tuner in Figure Fig. 2.4.18 will be to increase the bore diameter to fit over a larger diameter beam tube of the 7-cell cavity and to select a piezo stack matched to the tuning forces of the cavity.

2.4.4 HOM load

The Higher Order Mode (HOM) loads in the cryomodule are intimately linked to the SRF cavity design and mitigation of the beam breakup instability (BBU) as described in §2.4.2. The average HOM power is expected to be 200 W per cavity. Most of the power will be in the frequency range 1-10 GHz, but the short ERL bunch length will allow HOM spectral content up to the 100 GHz range. The HOM damping scheme must then have strong coupling over

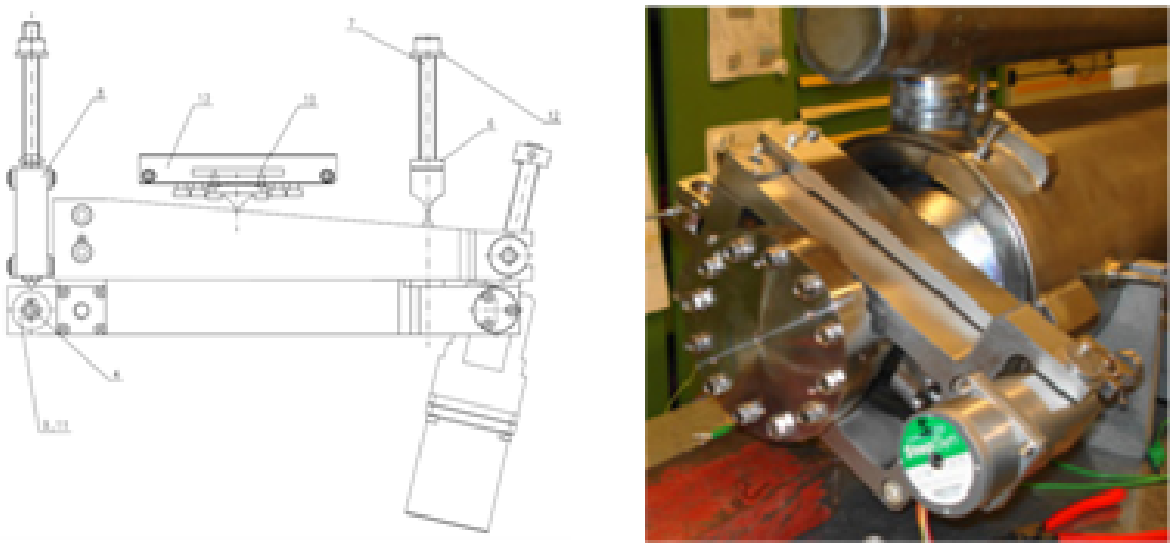

Figure 2.4.18: Illustration and photograph of the a Saclay I tuner.

this broad bandwidth and be able to dissipate the high average power. Among the options for an HOM damping configuration are:

- beamline loads where the RF absorber is a lining of the beampipe
- loop-coupled antenna located in side apertures on the beampipe that absorb HOM power at 2–5 K or transport RF in coax to remote loads
- waveguide loads coupled transversely to the beampipe that transport the RF to remote loads
- button-type pickups located in small apertures on the beampipe that transport RF in coax to remote loads.

The beamline loads are conceptually straightforward, where HOMs propagate as TE or TM modes in the circular beampipe and are heavily damped at the absorber. This provides broadband damping with only modest dependence on the RF absorber properties and no need for careful geometrical tuning of coupling structures. To avoid an undue load on the refrigeration plant from the expected 200 W of HOM power, the RF absorber is maintained at 100 K and thus necessitates thermal gradients along the beamline between cavities. The thermal gradient is defined by a 5 K intercept between the 1.8 K cavity and the 100 K HOM absorber, where selection of the 100 K temperature was a result of an optimization process to minimize the total cryogenic load of the full module as described in §2.4.8 below.

The challenge with beamline loads is that since the RF absorber resides on the beamline, only tens of centimeters from the SRF cavity, in addition to RF absorption it must also be: high vacuum compatible, have finite DC conductivity to drain static charge, be able to withstand significant radiation, have no particulate generation, and have the requisite thermo-mechanical properties to operate at cryogenic temperatures as configured in an HOM- load assembly.

Such beamline loads have performed well at room temperature as part of the CESR-B [38] and KEK-B [39] cryomodules for over a decade. A cryogenic version of a beamline load was installed in the ERL injector prototype cryomodule [40] and valuable insight was gained from the cold tests and beam operation. In the HOM prototypes, it was discovered that all three types of RF absorbing materials have their DC conductivity drop at cryogenic temperatures, and can thus accumulate considerable static charge and deflect low energy beams [41]. Also, thermal expansion differences between the RF absorbers and their heat sinks can result in long-term fatigue than can eventually cause solder bonds to delaminate. This insight has guided development of a next-generation beamline load that resolves these issues as described in §2.4.4 below. A cryogenic version of a beamline load has also been developed for the XFEL cryomodule [1] and has been shown to perform well in that application, although its power limit of about 100 W may not be sufficient for the ERL Linac.

Loop-coupled HOM loads are prevalent on several SRF cavity designs, such as XFEL, ILC, and SNS [42, 43]. In these pulsed-beam applications, the average absorbed HOM power is only a few watts. Much larger powers were absorbed in the HERA electron ring with 50 mA beam current. There have nevertheless been challenges revealed with loop couplers in operating machines, such as with antenna overheating, multipactor, and mis-tuning due to fabrication variations [44] [45]. The button-type HOM couplers are still at the conceptual and modeling stage of their development, and it is expected that they will face bandwidth, power, and tuning challenges analogous to those of the loop couplers. A challenge with the modeling and analysis of loop and button-HOM damping is that they have non-axisymmetric geometries and require 3D-simulation tools. The meshing and computational demands then become time consuming and can restrict the number of modes and accuracy of the analysis, raising the concern that a BBU susceptible HOM could be missed, especially with component fabrication variations [46].

Waveguide-HOM couplers have been successfully used at JLAB for many years at lower powers, typically around 10 W [47].

The use of waveguide-HOM coupling is the subject of ongoing investigations [5], and while they could have the benefit of transporting the HOM power to external room-temperature loads, it is still to be determined if they will have the requisite damping bandwidth, and how the full structural complexity will compare to that of beamline loads.

Beamline-HOM loads have been chosen for the baseline Cornell ERL main Linac design to best accomplish the damping requirements that are critical to mitigating BBU. Details of their design are presented in the following sections.

ERL main linac HOM load

A CAD model of the ERL main Linac beamline HOM load is shown in Fig. 2.4.19. The load has an RF absorber as a unitary cylinder brazed into a tungsten-heat sink, stainless-steel bellows for flexibility of flange alignment and cavity length variations. There will be 5 K intercepts at the transition between the bellow and the end-group section, the later will be copper plated to avoid excessive RF heating. The HOM load will be mounted to the Helium Gas Return Pipe (HGRP) as well.

RF-absorbing materials that have the requisite properties are in advanced development and full scale samples are in hand. They are based on SiC or AlN with embed carbon nanotubes or graphite. A key is to have a sufficient fractional loading of carbon so as to exceed the

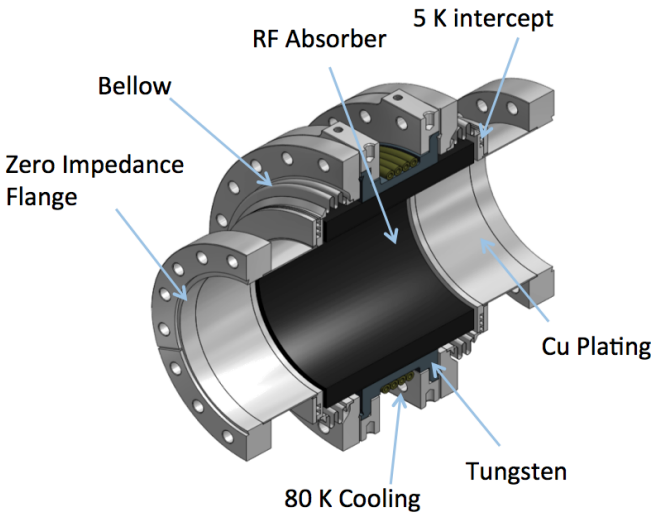

Figure 2.4.19: CAD model cross section of the ERL main Linac beamline HOM load.

percolation threshold in the material and establish a DC conductivity that is nearly independent of temperature. This will also provide a satisfactory broadband dielectric loss tangent of $\delta = 0.2 - 0.6$. Plots of measured RF and DC electrical properties of a carbon- loaded RF absorbing ceramic are shown in Fig. 2.4.20. This material appears to satisfy all of the electrical and particulate requirements of a beamline HOM load absorber [48]. First in situ tests show adequate RF absorption, while the DC conductivity may slightly differ from batch to batch.

For the HTC program, two prototype HOM absorbers have been fabricated (see Fig. 2.4.21 showing the HOM absorber installed under the HGRP and connected to the cavity). Based on this prototype experience some optimization is currently underway. This is mainly dedicated to get reliable batch to batch material properties and to accommodate for the rather low CTE of the material. As a cost saving measure, the material can be shrink-fitted to Titanium which we successfully proved on a sample cylinder.

2.4.5 Input coupler

The fundamental RF-input coupler has two main functions: i) efficient transfer of power from an RF power source to the accelerating mode of a beam-loaded RF cavity, i.e., a passive impedance matching network, and ii) providing an RF-transparent barrier between a gas-filled transmission line, coaxial or waveguide, and the ultra-high vacuum of the beamline RF cavity, which necessitates the use of at least one ceramic RF window.

Several CW and pulsed RF-power couplers have been developed at different laboratories around the world for superconducting cavities, both rectangular waveguide and coaxial configurations [49]. Since the ERL superconducting Linac cryomodule is based on TTF technology, early on in the project we decided [50] to use coaxial couplers derived from the TTF-III design [51, 52]. This input coupler has the following important features:

- Low static heat leak

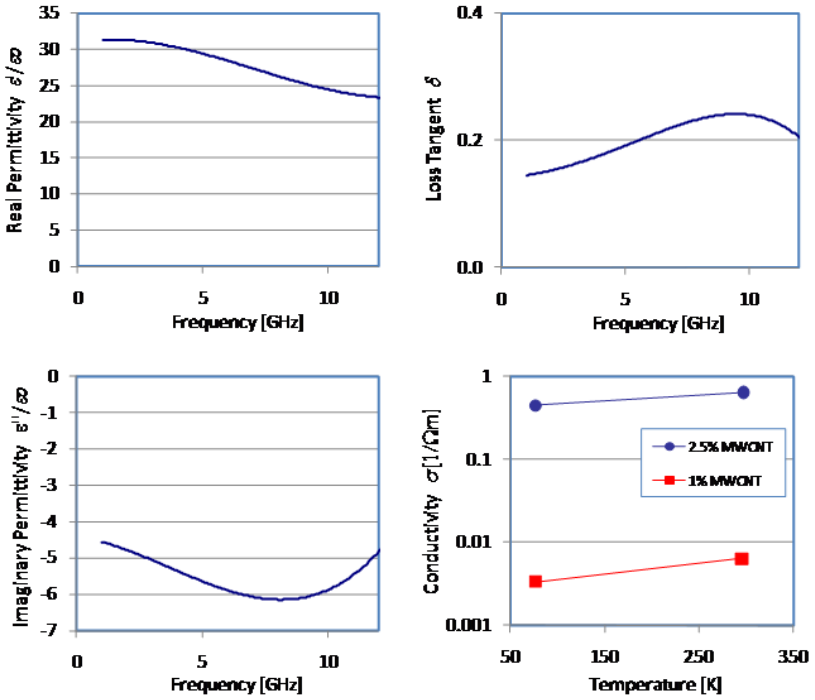

Figure 2.4.20: Measured RF and DC electrical properties of a carbon-loaded RF absorbing ceramic.

- Two ceramic windows - one warm and one cold - allowing sealing of the SRF cavity input coupler port during an early assembly stage in a clean room, thus reducing the risk of cavity contamination
- Coupling to the cavity adjustable over one order of magnitude by varying the axial position of the inner-conductor antenna
- Bellows accommodating lateral movement of the cavity in a cryomodule by up to 15 mm during cool-down from room temperature to 2 K

The TTF-III coupler was designed for a pulsed superconducting Linac application. Hence not all of the features of the TTF-III design are relevant for the ERL main Linac, which operates CW with 2/5 kW CW average/peak power. Further, there are features specific to CW operation that must be added to the TTF-III design. A wealth of experience in designing, fabricating, testing, and successfully commissioning CW RF couplers has been gained for the prototype-ERL injector, described in §2.3.6. Here we describe a conceptual design for the ERL main Linac RF coupler.

ERL main Linac coupler design

The input couplers for Cornell Energy Recovery Linac must deliver up to 5 kW CW RF power to the main Linac cavities, though under nominal conditions they will operate with 2 kW

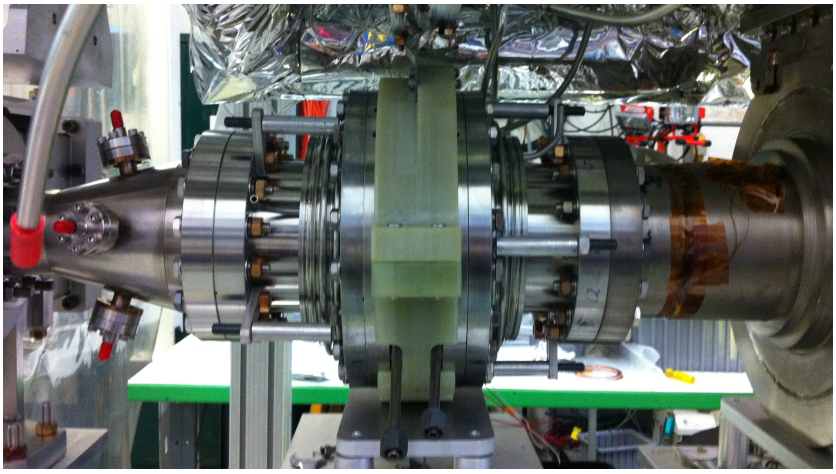

Figure 2.4.21: HOM absorber installed under the HGRP within the HTC cold mass

average and 5 kW peak power. The 5 kW peak power is required for transient modulation to compensate for cavity detuning due to microphonic perturbations. Due to the principles of energy recovery in a superconducting cavity, the couplers will operate under conditions with full reflection for the great majority of the time and thus require active cooling of the inner conductor as in the ERL injector input couplers. To make the design more economical, the couplers will provide fixed coupling to the cavities with $Q_{\text{ext}} = 2 \times 10^7$ Coupling adjustability can be achieved using three-stub tuners in the feed-transmission line to have a range of $2 \times 10^7 - 1 \times 10^8$, with the nominal operational $Q_{\text{ext}} = 6.5 \times 10^7$.

The design of the ERL main Linac coupler takes into account experience gained from the ERL injector couplers [53]. The proposed main Linac coupler is shown in Fig. 2.4.22 and Fig. 2.4.23 [54]. This design utilizes a rectangular-waveguide-feed transmission line, though it is possible that a coaxial-feed line could be implemented to reduce space if it is compatible with the design of the full RF-power delivery system. As with the TTF-III and ERL-injector couplers, the ERL main Linac coupler consists of three sub-assemblies: the cold and warm coaxial sub-assemblies, and the waveguide. The two coaxial portions of the coupler and their ceramic windows are the same size as those in the TTF-III coupler. The cold portion of the coupler with the protruding antenna attaches to the SRF-cavity coupler-port flange, which will be at a temperature slightly above 2 K. A copper thermal intercept held at 5 K is located on the coupler outer conductor a few cm from the cavity flange to minimize the heat load to the 1.8 K-cavity helium vessel. An 8" ConFlat flange then joins the cold coupler to the warm coupler. The warm coupler has two bellows sections on both the inner and outer conductors for flexible compliance, as will be described in the next paragraph. The warm coupler has a copper thermal intercept held at 100 K located on the outer conductor a few cm from the vacuum vessel flange to minimize the heat load to the 5 K system. The vacuum vessel flange resides at 293 K, beyond which is a vacuum pumping port on the outer conductor for the warm portion of the coupler, an instrumentation port, and then the coax-rectangular waveguide transition. All coaxial components, with the exception of the inner-conductor antenna portion and the thermal intercepts, are made of stainless steel with copper plating on surfaces carrying RF

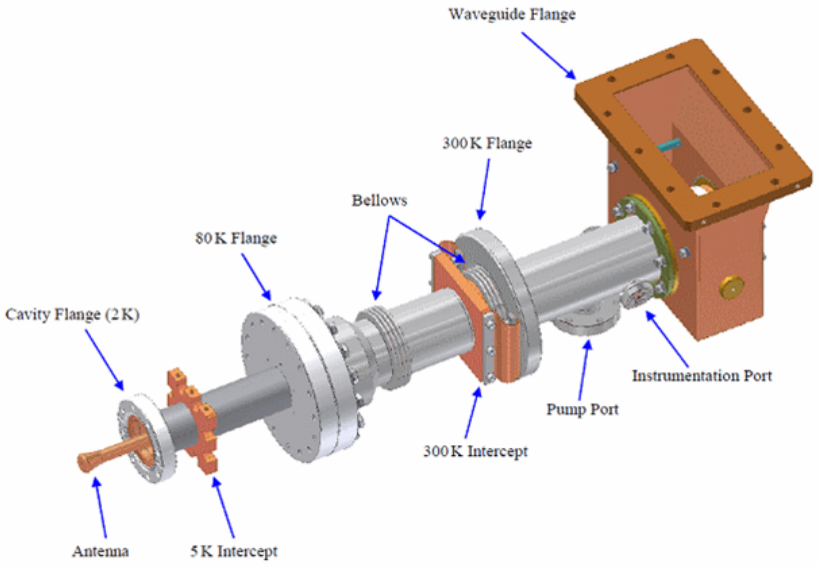

Figure 2.4.22: CAD model of the fully assembled ERL Linac input coupler.

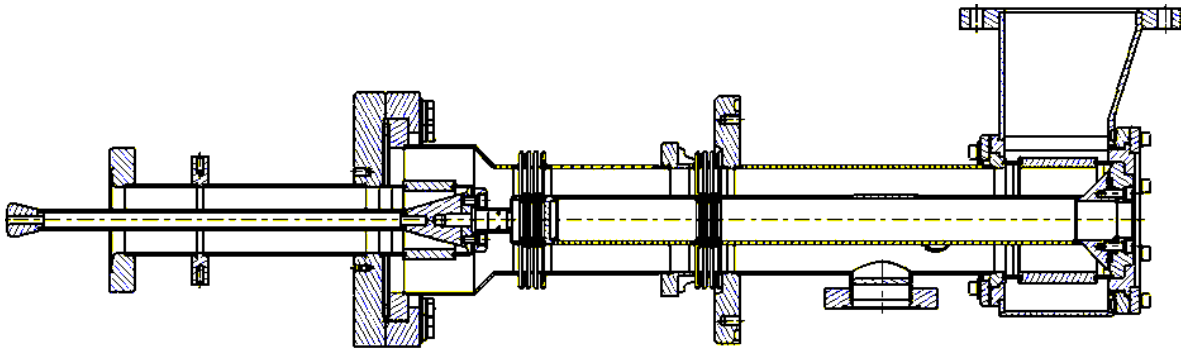

Figure 2.4.23: Section view of the ERL Linac input coupler.

currents.

Similar to the TTF-III couplers, the ERL Linac couplers must accommodate lateral movement of the cavities during cool-down of up to 10 mm, since one end of the coupler is attached to the moving cavity and the other end is attached to the fixed vacuum vessel port. For the TTF-III couplers, bellows on the inner and outer conductors of the warm assembly and on the outer conductor of the cold assembly provide some flexibility. This arrangement, however, causes the antenna to skew. If the lateral movement is large enough, the antenna can touch the outer conductor of the cavity coupler port. Besides shorting the coax coupler, the scratching of the surfaces will generate copious particulate and significantly degrade the SRF-cavity performance. For the ERL Linac coupler, this problem is overcome by placing two sets of bellows only on the warm portion of the coupler, on both the inner conductor and on the outer conductor, as shown in Fig. 2.4.24. In this way, high flexibility is achieved while keeping the cold antenna fixed relative to the cavity coupler port.

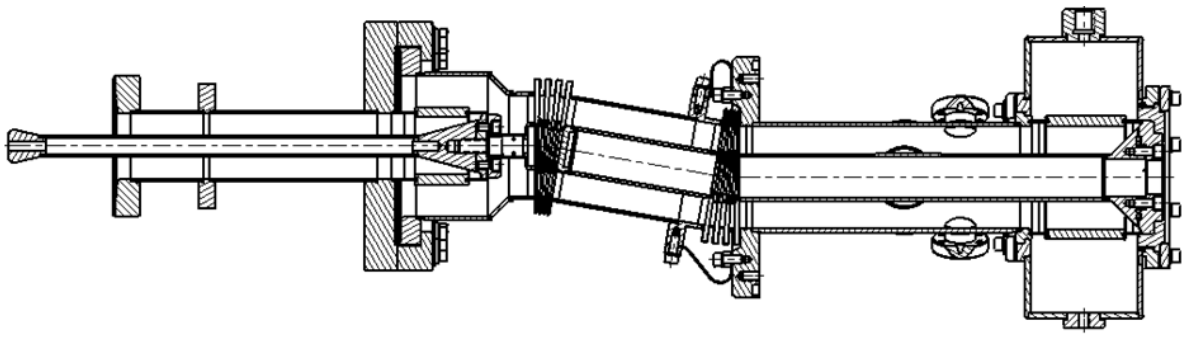

Figure 2.4.24: The ERL Linac input coupler is mechanically flexible, yet maintains alignment of the cavity antenna.

Table 2.4.9: Heat loads of the ERL main Linac input coupler.

	Static Heat Load	Dynamic Load at 2 kW CW
2 K	0.03 W	0.15 W
5 K	1.55 W	1.94 W
80 K	2.26 W	9.33 W

The static and dynamic heat loads of the ERL main Linac input coupler are listed in Tab. 2.4.9. The elimination of a thin-walled bellows on the cold sub-assembly to maintain a fixed antenna alignment slightly increases the static heat load to the 5K thermal intercept. However, this contribution to the total refrigeration load of a Linac cryomodule is a small percentage, as summarized in §2.4.8.

The ERL main Linac input coupler has been modeled for multipactor susceptibility using the code Mutipac2.1 [55]. The results showed no evidence of mutipacting in the ERL RF coupler.

2.4.6 Superconducting quadrupole and dipoles

Each Linac cryomodule contains one quadrupole with adjacent horizontal and vertical steering coils.

Quadrupole design

A iron yoke magnet design has been selected for the quadrupole since the relatively low gradient can be realized with a conventional iron-based design using superconducting coils, allowing the quadrupole to utilize the 1.8 K liquid helium available in the cryomodule. A CAD model of the yoke and coils is shown in Fig. 2.4.25, with the coils also shown separately for clarity. The pole pieces have a hyperbolic shape with a 70 mm bore and the coils lie flat except at the ends. The coils for this type of lens are single layered and can be manufactured with minimal effort [56]. Numerical simulations of the quadrupole were performed with MERMAID and take into account the real properties of the yoke material (Steel 1010). A detailed parameter

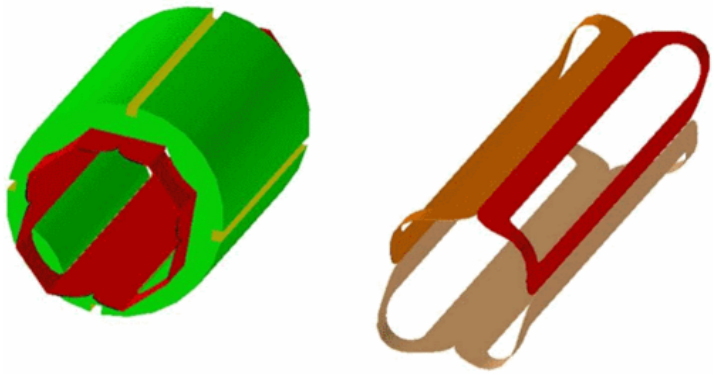

Figure 2.4.25: Isometric view of the quadrupole lens cold mass (at the left) and the set of four coils without the iron (at the right).

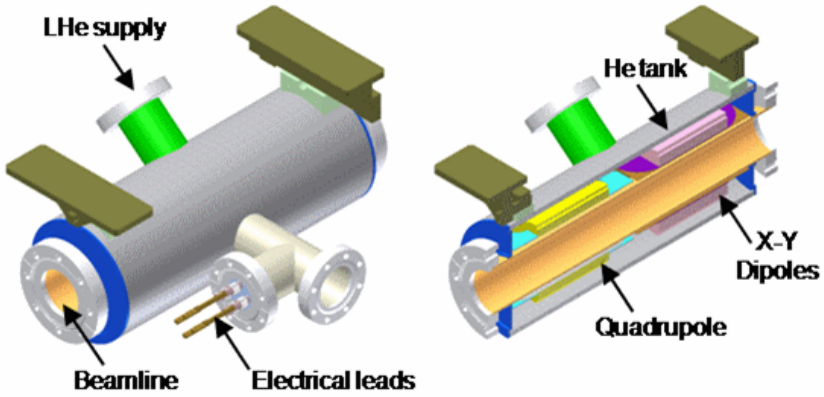

Figure 2.4.26: The superconducting quadrupole and dipole lenses in their helium vessel with the HTS leads.

list of the quadrupole is given in Tab. 2.4.10. A CAD model of the full quadrupole and dipole package is shown in Fig. 2.4.26. The length of the assembly is $\sim 350\,\text{mm}$.

The stray magnetic field from the magnet package must be carefully minimized inside of the cryomodule to maintain a high SRF cavity Q_0. The typical background magnetic field inside of the module vacuum vessel will be about 25 mG, and additional shielding intimate to the SRF cavity will reduce this to $< 2\,\text{mG}$ at the cavity walls. The amplitude of the unshielded quadrupole magnetic field along the beamline at a 1 cm radius is shown in Fig. 2.4.27. The field drops off rapidly, where at a distance of 15 cm from the edge of the yoke it is $< 3.7 \times 10^{-5}$ of its value at the center of the quadrupole, corresponding to a maximum unshielded stray field of $\sim 65\,\text{mG}$. Cryogenic magnetic shielding will also be wrapped around the magnet package to ensure that the stray field is negligible.

Table 2.4.10: Parameters of the ERL main Linac superconducting quadrupole magnet.

Winding type	Flat coils
Iron yoke inner diameter	70 mm
Iron yoke outer diameter	107 mm
Maximal current	110 A
Maximal gradient	19.4 T/m
Linac module current range	$0.75 - 49\,\mathrm{A}$
Linac module gradient range	$0.13 - 8.6\,\mathrm{T/m}$
Magnetic length	125.6 mm
Number of turns	86/pole
Wire diameter (bare/insulated)	0.33/0.41 mm
Copper to superconductor ratio	2:1.66
RRR	> 100
Filament diameter	$20\,\mu$m
Twist pitch	25.4 mm
Iron yoke length	100 mm
Coil length	137 mm
Stored magnetic energy at max current 100 A	45 J
Self inductance	0.009 H
Integrated gradient at current 100 A	2.21 T
Integrated b6/b2 at current 100 A, at 30 mm	1.8×10^{-3}
Integrated b10/b2 at current 100 A, at 30 mm	2.7×10^{-3}
Coil peak field	0.76 T
Gradient at 2.5 A	0.00437 T/m
Saturation at nominal current 100 A (integrated)	0.17%

Dipole design

For the dipole corrector, a single-layer coil is chosen similar to that for the quadrupole. However, the dipole coil is placed inside of the iron yoke as this gives minimal stray fields outside of the corrector, as seen in Fig. 2.4.28 and Fig. 2.4.29. Again, numerical simulations of the dipole were performed with MERMAID and take into account the real properties of the yoke material (Steel 1010). A detailed parameter list of the dipole is given in Tab. 2.4.11. The stray magnetic field from the dipole does not decay as rapidly as for the quadrupole field, as seen in Fig. 2.4.29. The stray dipole field is still quite low, however, and the dipole will be located downstream of the quadrupole, away from the SRF cavity closest to the magnet package, so that it is adjacent to the gate valves, as shown in Fig. 2.4.2.

Installation in the cryomodule

The magnet package body will reside at the 1.8 K temperature of the helium vessel. The four HTS current leads coming out of the assembly will have a 5 K heat sink and then a 100 K heat sink at the module thermal shield. The four leads will be wired as:

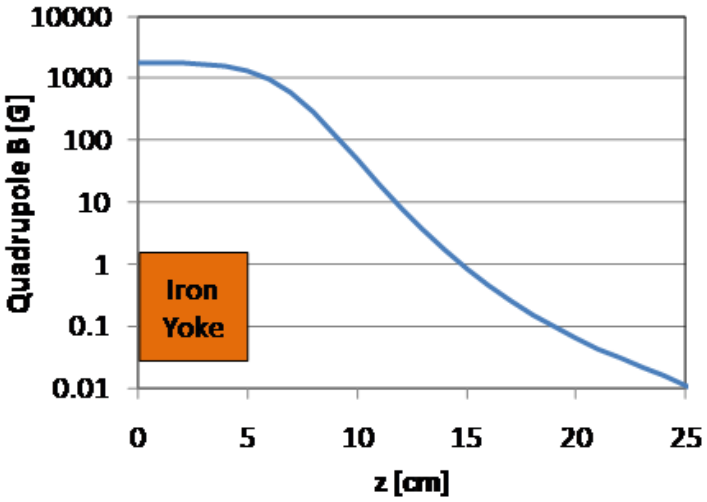

Figure 2.4.27: Unshielded quadrupole field dependence along the beamline at a 1 cm radius. The iron yoke ends at 5 cm.

1. Quadrupole supply
2. X-dipole supply
3. Y-dipole supply
4. Common return

The typical heat leak for a 200 A, 150 mm long HTS lead between 77 K to 4.2 K is 20 mW. So the total heat leak to 1.8 K could reach $0.08 - 0.1\,\mathrm{W}$/package. The HTS leads will also be wrapped by magnetic shielding to reduce their stray-magnetic fields. From this analysis, the heat load of the entire magnet system is negligible compared to the dynamic load of the cavities.

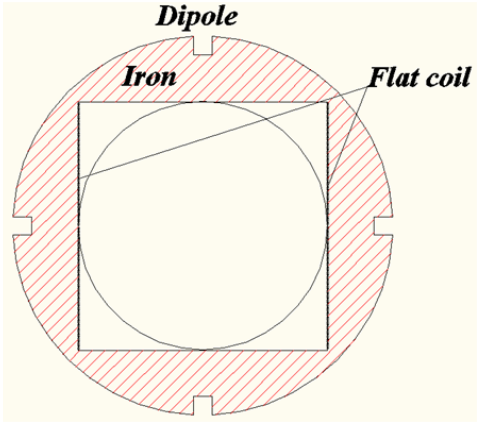

Figure 2.4.28: The dipole corrector superconducting coils and iron yoke.

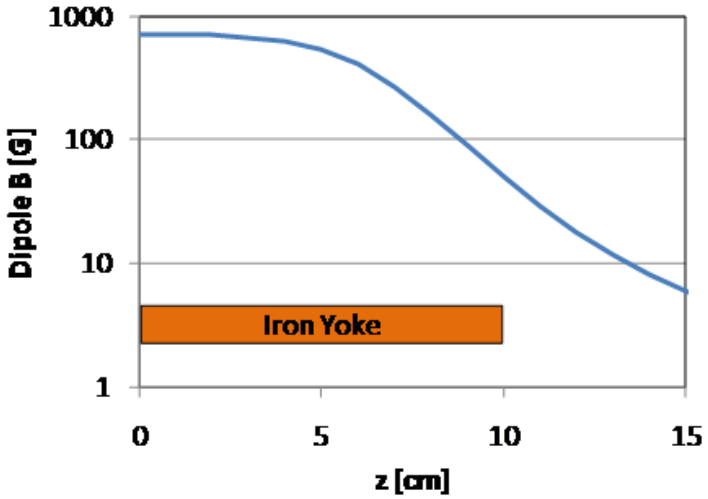

Figure 2.4.29: Unshielded dipole field dependence along the beam axis. The iron yoke ends at 10 cm.

2.4.7 Cryomodule beam position monitor

A beam position monitor (BPM) will be included in every main Linac cryomodule and will be located adjacent to the magnet package. The BPM will be held at a temperature of about 5 K. Under consideration are both a button-style BPM similar to that developed for the XFEL at DESY [57] and a compact design as used in CESR-TA. Both types are shown in Fig. 2.4.30.

2.4.8 Cryomodule

The ERL Linac cryomodule design is based on TTF-III technology with modifications for CW operation. In this technology scheme, the cryomodule units that are about 10 m long are connected by bellows with no intervening warm breaks, and all connected units share a common insulation vacuum. The cryogen transfer lines are internal to the module vacuum vessel and are connected between units in situ by welding together flexible joints. The beamline is also connected in situ between units under a portable clean room.

The ERL Linac cryomodule (shown in Fig. 2.4.2) is based on the TTF-III module structure. All of the cavity-helium vessels are pumped to 1.8 K (16 mbar) through a common 30 cm inside diameter Gas Return Pipe (HGRP), which also serves as the mechanical support from which the beamline components are suspended. To minimize the heat load to the refrigeration plant, all of the 1.8 K cryomodule components are surrounded by 5 K intercepts to minimize the heat leak to 1.8 K, and the 5 K intercepts are likewise surrounded by 100 K intercepts, which absorb the heat load from the 293 K vacuum vessel. The HGRP is suspended from composite support posts that are constructed from low-thermal conductivity G-10 fiberglass. The composite posts have integral metal stiffening disks and rings that also serve as thermal intercepts at 5 K and 100 K between the 1.8 K face that attaches to the HGRP and the 293 K face that attaches to the vacuum vessel bosses that support the cold mass. There are stainless steel manifolds of smaller diameter than the HGRP running the length of the modules that

Table 2.4.11: Parameters of the ERL main Linac superconducting dipole magnets.

Winding type	Flat coil
Yoke aperture square side	70 mm
Yoke outer diameter	107 mm
Maximal current	22 A
Maximal field	0.071 T
Typical current	11 A
Typical field	0.03 T
Magnetic length	138 mm
Number of turns	88
Wire diameter (bare/insulated)	0.33/0.41 mm
Copper to superconductor ratio	2:1.66
RRR	> 100
Filament diameter	20 m
Twist pitch	25.4 mm
Iron yoke length	100 mm
Coil length	170 mm
Stored magnetic energy at nominal current 20 A	1.4 J
Self inductance	0.007 H
Integrated b1 at nominal current 20 A	0.935 Tcm
Integrated b3/b1 at nominal current 20 A, at 30 mm	3.2×10^{-3}
Integrated b5/b1 at nominal current 20 A, at 30 mm	1.7×10^{-3}
Coil peak field	0.6 T
Saturation at nominal current 20 A (integrated)	0.1 %

transport the supply of liquid helium and the supply and return of 5 K and 100 K helium gas for the thermal intercepts. Jumper tubes with 5 mm inner diameter are connected between the 5 K and 100 K supply and return manifolds to the various thermal intercepts within a module. A shell of 6 mm thick, grade 1100 aluminum sheet surrounds the beamline and the HGRP and is linked to the 100 K manifold to serve as a thermal radiation shield between the 293 K vacuum vessel and the cold mass. The aluminum 100 K shield has apertures through which the RF couplers pass and also has panels with instrumentation feedthroughs. The 100 K shield is mechanically suspended from one of the integral metal stiffeners in the composite support posts. Multi-layer insulation is wrapped around the exterior of the 100 K shield as well as all of the 1.8 K and 5 K cold mass components.

As the full ERL main Linac is assembled in the tunnel, cryomodule units are brought into place, the beamlines are aligned, and a flexible joint connected under a portable clean room then mates the beamline module-to-module. The cryogenic manifolds are welded together with short bellows sections as well as the HGRP. A short section of 100 K shield is inserted between modules to maintain its continuity and a flexible sleeve adapter then joins the adjacent vacuum vessels.

The magnetic shielding in the cryomodule must keep the field in the region of the cavities to $< 2\,\mathrm{mG}$ to have negligible residual wall loss and provide a good safety margin for the goal of

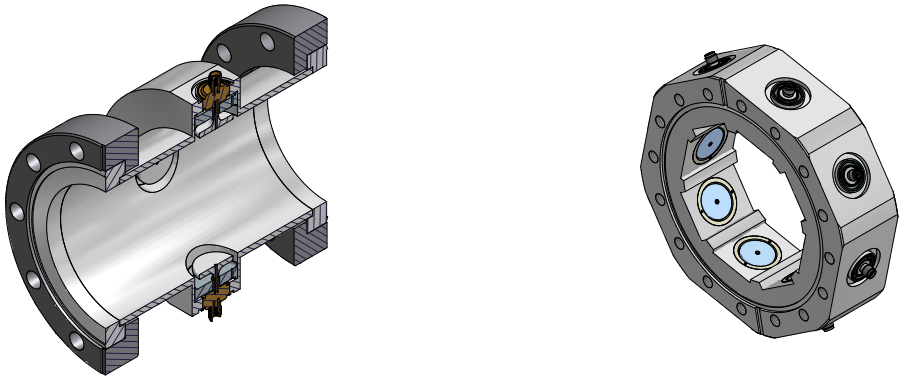

(a) Similar to XFEL

(b) Compact CESR-TA

Figure 2.4.30: Linac BPM designs.

cavity $Q_0 = 2 \times 10^{10}$. Such a low field is accomplished by de-gaussing the carbon steel vacuum vessel, lining it with co-netic mu-metal shielding that will be at 293 K, and then wrapping each cavity's 1.8 K helium vessel with a magnetic shield that is formulated to have maximal shielding at low temperatures around 4 K [58].

ERL Linac modifications to TTF-III technology

The CW, high current operation of the ERL Linac necessitates several changes to standard TTF technology which has evolved for low-duty factor operation. Additional changes unrelated to CW operation have been implemented here as a result of experience gained from fabrication and operation of TTF modules. Most of these changes were also implemented in the ERL injector prototype cryomodule, as described in §2.3.6, and have proven to be successful [59]. Briefly, the main differences between the ERL Linac cryomodule and the TTF-III module are:

- Implement beamline HOM loads for strong broadband damping of HOMs generated by the high current and short bunches.
- Use a high average power coax RF input coupler per cavity, with lateral flexibility for cool down and fixed coupling. Detailed modeling and appropriate cooling for the prototype ERL injector have shown that overheating can be avoided.
- Do not include a 5 K shield
- Increase the diameter of the cavity helium vessel port to 10 cm for the high CW heat load
- Include a JT valve in each cryomodule for the high CW heat load.
- Increase the diameter of the 2-phase 2K He pipe to 10 cm for the high CW gas load.
- Use precision fixed surfaces between the beamline components and the HGRP for easy "self" alignment of the beamline

- Use rails mounted on the inside of the vacuum vessel and rollers on the composite support posts to insert the cold mass into the vacuum vessel, as opposed to the "Big Bertha" handler
- Cooling of thermal intercepts is provided by small "jumper" tubes with flowing He gas, such as to the HOM loads and the RF couplers, as opposed to copper straps
- Locate access ports in the vacuum vessel to allow the tuner stepper motor to be accessible for replacement while the string is in cryomodule

Cryomodule beamline components and lengths

The ERL Linac cryomodule length is chosen as a balance between beam optics considerations and keeping the unit physically manageable. The maximum module length for transport on a standard flat-bed truck is about 16 m or 52 ft. To maximize the Linac's active acceleration fill factor, it is desirable to place quadrupoles as sparsely as possible. Beam optics simulations show that the maximum quadrupole spacing is about one doublet every twelve 7-cell cavities. This would give a cryomodule length of about 19 m, which is too long. The fill factor can be maintained while shortening the module length by having six cavities with one quadrupole and one set of horizontal and vertical corrector coils per module. Thus the quadrupole doublet is accomplished in every two modules with a manageable module length of 9.82 m or 32.2 ft. Listed in Tab. 2.4.12 are the ERL main Linac cryomodule beamline components, their individual lengths, and the total length of the module.

Cryomodule components and assembly

Cryomodule assembly starts with the beamline and proceeds as a layered growth out to the vacuum vessel and warm coupler attachment. The specific choices for the configuration of many of the components also impacts the configuration of other components. For example, the choice between using a blade tuner vs. a Saclay tuner dictates the type of bellows and support flanges on the cavity helium vessel, as well as the permalloy magnetic shield around the helium vessel. Similarly, the choice of the required power rating of the coupler significantly alters not only the complexity of the coupler, but also the details of the vacuum vessel coupler ports, such as their dimensional and alignment error tolerance, which is a cost driver. Described in the following is the assembly sequence of the baseline choices for the principle cryomodule components, along with descriptions of the components not discussed in previous sections.

Beamline string assembly

The beamline consisting of the cavities, HOM loads, cold couplers, quadrupole, steering coils, beam position monitor, tapers, and gate valves (Tab. 2.4.12) is assembled in a class 100 or better clean room. All components are flushed with filtered water or alcohol and individually receive a mild vacuum bake at 120° C for 24 hours. The components are mounted on an assembly fixture one by one in the clean room. Each added component is aligned to the other components with the only critical alignment being the azimuthal position about the beam axis. This azimuthal alignment is needed so that the flat precision mounting surface at their tops

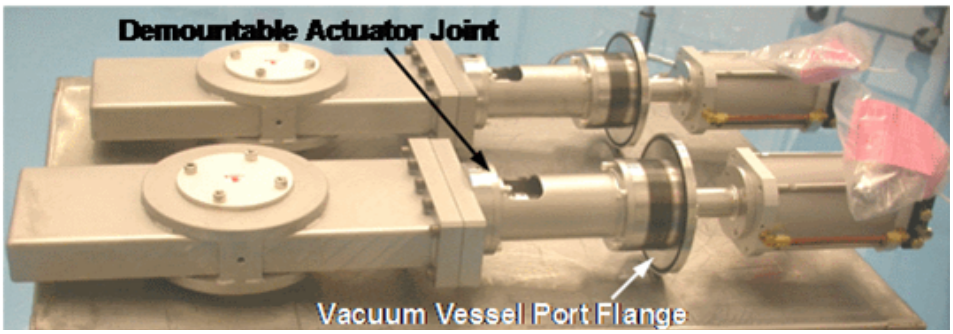

Figure 2.4.31: Cryogenic and RF rated pneumatic gate valves for the beamline.

will mate to the planar-precision surfaces on the HGRP. This alignment can be accomplished with a simple accurate spirit level. Any longitudinal spacing or planar shift errors of the mounting surfaces is accommodated by the flex in the HOM load bellows. The component mating vacuum flanges are then bolted together. A photograph of the assembled ERL injector prototype beamline string in the clean room is shown in Fig. 2.3.34. After all components are attached, the string is vacuum leak tested while still in the clean room so that only filtered particulate-free air will pass through any potential leak. The pumping and purging during the leak test is performed at a slow rate of 1-2 Torr/minute through the viscous flow range of 760 Torr to 1 Torr to minimize propagation of any particulate contamination throughout the beamline.

A beamline component not described in previous sections is the gate valve. To maintain the cleanliness of the beamline, the gate valves at each end of the string must be closed after the vacuum-leak test in the cleanroom and rarely opened again until the cryomodule is installed in its final tunnel location. A cryogenic-rated gate valve is available from VAT, which also has an "RF aperture" to provide RF shielding in the open position for accelerator beamline service. A photograph of this valve is shown in Fig. 2.4.31. This valve was also designed to have a demountable pneumatic actuator that includes a vacuum vessel flange. With this feature, the cold mass can be inserted into the vacuum vessel without the actuator, then have the actuator attached through a vacuum vessel port with the controls and pneumatic connections available exterior to the vacuum vessel. The Linac interlock control system can then seal off any cryomodule in the event of a vacuum trip. A photograph of the valve installed in the ERL-injector prototype vacuum vessel is shown in Fig. 2.4.32. The addition of a pneumatic actuator differs from the gate valves used in TTF modules where the valve is only manually operated, is inaccessible from the vacuum vessel exterior, and is opened just prior to sealing the vacuum vessel joint between modules with no possible automated interlock closure.

Cold mass assembly fixture and HGRP attachment

As a parallel operation to the beamline string assembly in a clean room, the cold mass assembly fixture can be set up in a high-bay area with overhead crane access. The composite support posts are attached to the HGRP and the HGRP is hung from the assembly fixture by the composite posts. The 2-phase pipe is then mounted aside the HGRP using G-10 standoffs and its exhaust is welded into the HGRP. A photograph of the ERL Injector HGRP hung from

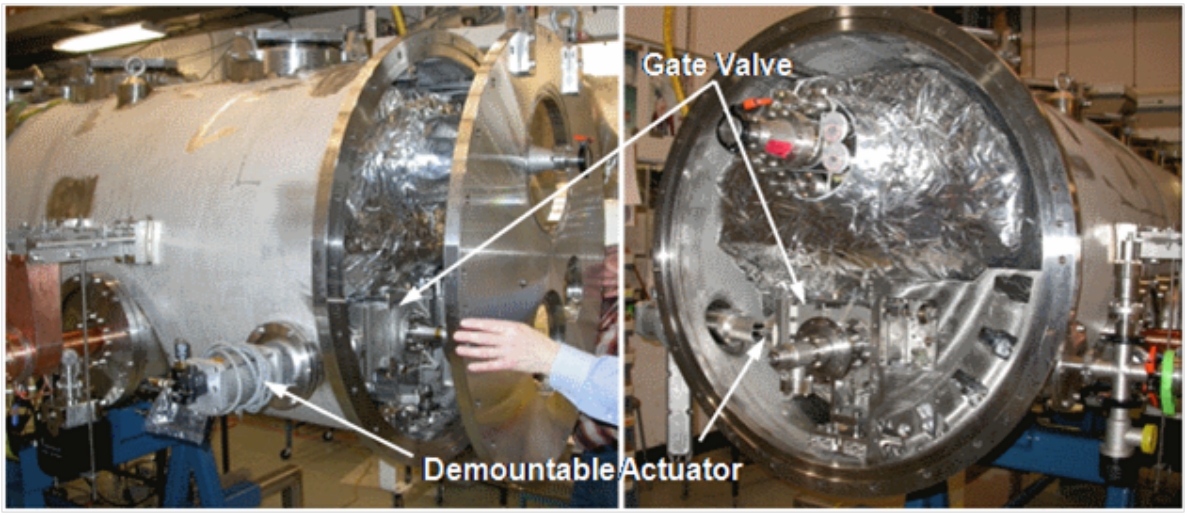

Figure 2.4.32: Cryogenic-rated pneumatic gate valve installed in the ERL Injector vacuum vessel.

the cold mass assembly fixture by the composite posts is shown in Fig. 2.4.33.

The choice of the number of composite posts supporting the HGRP and the HGRP wall thickness were determined by analyses of the static deformation of the titanium HGRP due to the estimated 4082 kg (9000 lb) weight of the cold mass and by the desire to lessen the relative motion of beamline components due to thermal contraction. The result was a decision to employ four posts per cryomodule with two sections to the HGRP. A schedule 80 pipe section was selected for the HGRP. With these choices the resulting static deflection is computed to be 0.07 mm with peak stress of 17 MPa providing a large safety factor compared to the 275 MPa yield published for Grade 2 Ti.

Beamline string attachment to HGRP

After the beamline string passes the vacuum leak test, it is removed from the clean room and positioned underneath the cold mass assembly fixture. The string is raised and the precision mounting surfaces on the string and the HGRP are brought together with integral alignment pins and keys being engaged. The mating surfaces are then bolted together. String attachment to the HGRP in this manner proved to be quick and easy for the ERL injector, the entire procedure taking about 1 hour. Shown in Fig. 2.4.34 is the injector beamline hung from the HGRP.

Cavity magnetic shielding and tuner

After the beamline is hung from the HGRP, the helium tanks of the cavities are wrapped with magnetic shielding. This shielding will reside at 1.8 K. Consequently, this magnetic shielding layer is fabricated from A4K [58], which retains its shielding properties at cryogenic temperatures.

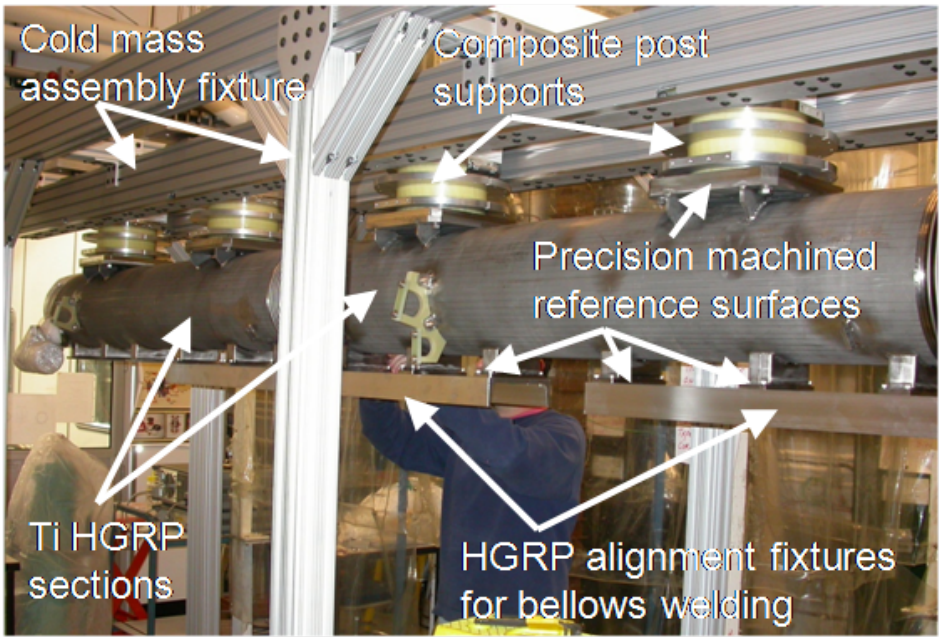

Figure 2.4.33: HGRP and 2-phase pipe hung from the cold mass assembly fixture by the composite posts for the ERL Injector.

The cavity tuners are attached after the magnetic shielding. The stepping motors of the tuners have to be wrapped in a copper sleeve that is tied to 5 K line to prevent the motor heat from propagating to the helium vessel. The stepping motors are also wrapped with A4K shielding since they can have stray fields of a few hundred milliGauss in close proximity to access apertures in the cavity shield. Part of the tuner attachment process is pre-bias of the tuner force on the cavity. This bias is required to compensate for stresses developed during cooldown due to CTE differences between the cavity materials and the tuner materials. Without the pre-bias force, it is possible that the cavity could plastically deform, the piezos could crack, or the piezos could become loose, depending on the specific configuration of the tuner. A good measure of the bias force is the frequency of the cavity at room temperature. The tuner is initially attached with the cavity in its relaxed position. Then Belleville washers in the piezo support mechanism are compressed with adjustment nuts until the cavity is at its target biased warm frequency. Note that the beamline cold couplers have protective caps placed on them in the clean room, and the caps include a spring-loaded RF contact from the coupler center conductor to an SMA header on the cap. This allows the cavity frequency to be monitored during the tuner bias operation. A photograph of the tuner bias operation for the ERL injector is shown in Fig. 2.4.35.

Liquid He, 5 K gas manifolds and thermal intercepts

Several cryogen manifolds run the length of the cryomodule and are welded to those of the next module during module installation in the Linac tunnel. These manifolds include a liquid helium supply to the JT valve required per module, a liquid helium supply to the "warm-

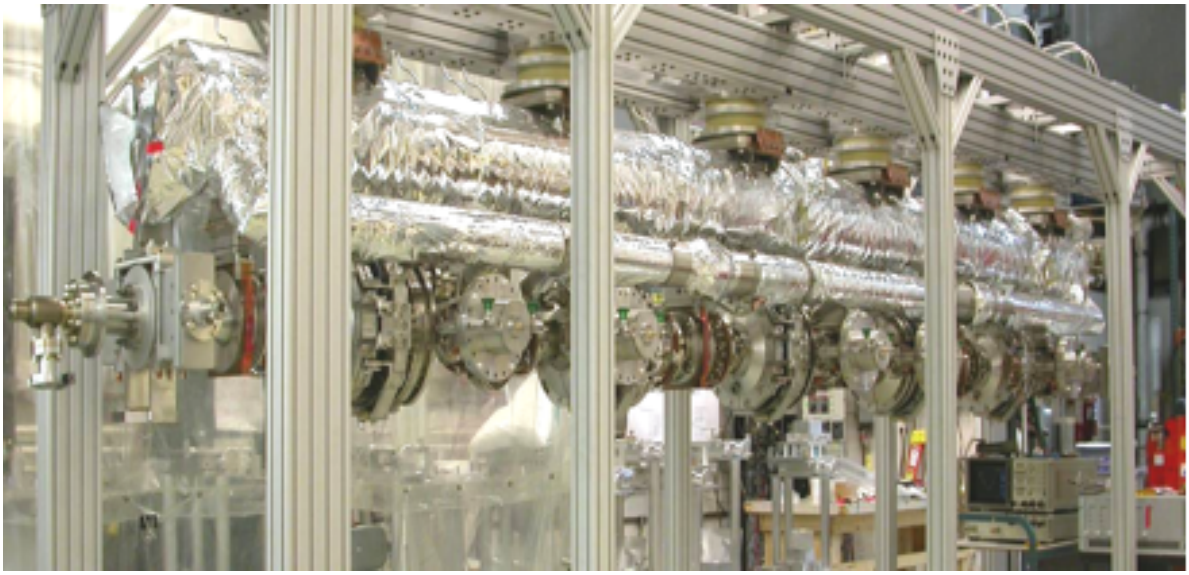

Figure 2.4.34: Beamline string hung from the HGRP for the ERL Injector.

up/cool-down" ports located at the bottoms of the helium vessels needed for convective flow, the supply and return of 5 K helium gas, and the supply and return of 100 K helium gas. A JT valve is required per module due to the high cavity heat load and helium mass flow for CW operation.

The liquid helium and 5 K gas manifolds are mounted close to the HGRP using G-10 standoffs, thus keeping similar temperatures in close proximity to each other with low thermal conductivity connections between them. These manifolds are the next components mounted on the cold mass. Jumper tubes from the liquid helium manifolds are then routed to the JT valve and the helium vessel fill ports. The 5 K gas supply and return manifolds must then be routed to thermal intercepts on the HOM loads and RF couplers by way of jumper tubes having 3-5 mm ID. In standard TTF technology, the connections between the manifolds and thermal intercepts are accomplished by copper straps. For the ERL Linac, both the 5 K and 100 K heat loads are large enough to require gas flow from the manifolds to the intercepts through jumper tubes. If high RRR copper or aluminum straps were used as heat sinks, the cross-sectional area would be tens of cm^2 and consume too much space, as well as not being sufficiently flexible. Flexible straps made of "tough pitch" copper attached between the 5 K manifold and the composite support post 5 K rings provide sufficient thermal conductance for this intercept.

100 K manifolds and thermal shield

The 100 K manifolds are mounted farther outboard of the 5 K manifolds, one of which is integral to the 100 K shield. The material of the 100 K thermal radiation shield is grade 1100 aluminum, chosen for its high thermal conductivity and light weight. The shield is fabricated from standard flat panels that are cut and formed to shape. The top portion of the shield is attached to the 100 K ring of the composite support post and is $\frac{1}{4}$" thick to support the

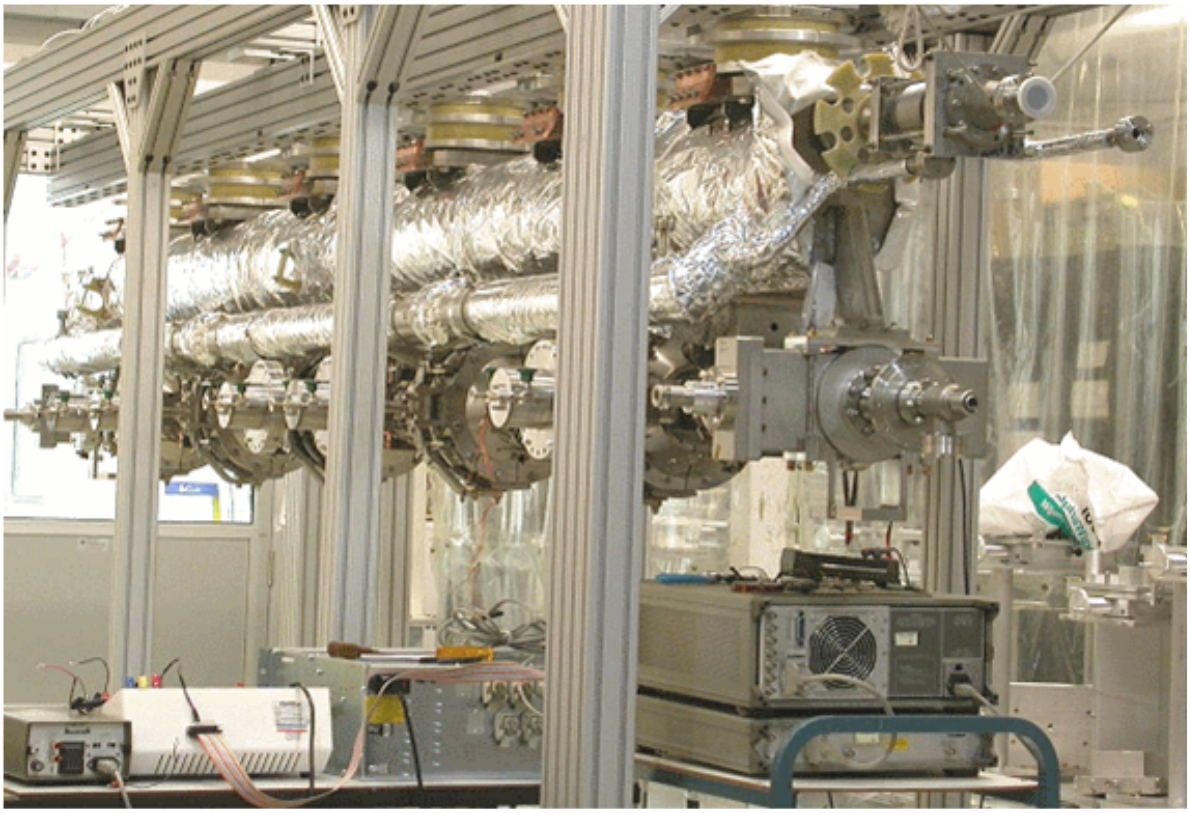

Figure 2.4.35: The tuner pre-bias operation for the ERL Injector.

weight of the cryogen manifolds and the lower portion of the shield, as shown in Fig. 2.4.36, at this stage of cold-mass assembly. A thermal model of the 100 K shield with an integral 100K manifold with heat loads from radiation, the composite post, and feedthroughs shows that the shield resides at less than 2 K above the manifold gas temperature [60].

Table 2.4.12: ERL main Linac cryomodule beamline components, their individual lengths, and the total length of the module.

	Component	Length (m)	Length (in)
	Gate valve	0.0750	2.953
	Taper	0.0500	1.9
Repeat 3 times	Large Cu beam tube	0.0794	3.125
	Large beam tube HOM absorber	0.0600	2.362
	Large Cu beam tube	0.0794	3.125
	Large Nb beam tube	0.1864	7.338
	Large beam tube transition	0.0307	1.211
	Cavity active #1	0.8059	31.729
	Small Nb beam tube	0.1495	5.885
	Small Cu beam tube	0.0794	3.125
	Small beam tube HOM absorber	0.0600	2.362
	Small Cu beam tube	0.0794	3.125
	Small Nb beam tube	0.1495	5.885
	Cavity active #2	0.8059	31.729
	Large beam tube transition	0.0307	1.211
	Large Nb beam tube	0.1864	7.338
	Large Cu beam tube	0.0794	3.125
	Large beam tube HOM absorber	0.0600	2.362
	Large Cu beam tube	0.0794	3.125
	Taper	0.0500	1.969
	BPM	0.0750	17.717
	Steering Coils	0.1500	5.906
	Quadrupole	0.4500	2.953
	Gate valve	0.0750	2.953
	Intermodule flex	0.3297	12.981
	Module Length	9.8213	386.667 (= 32.22 ft)

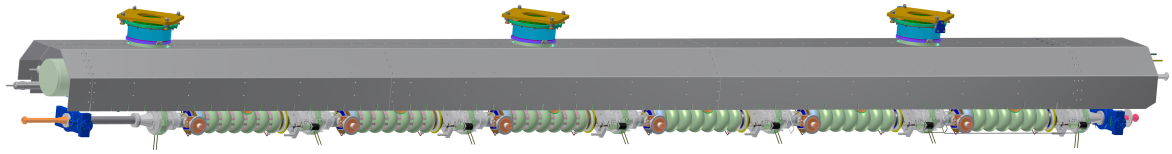

Figure 2.4.36: CAD model of the top portion of the 100K shield attached to the cold mass.

Figure 2.4.37: Photograph of the completed ERL Injector 100 K shield being wrapped with MLI.

After the cryogen manifolds and intercept jumpers are connected to the cold mass, low-thermal conductivity coax cable is routed from the cavity RF field probes, as well as the cabling from temperature sensors, helium level sticks, and other instrumentation. The lower half of the 100K shield is attached and the instrumentation cabling is thermally anchored to an instrumentation feed-through panel in the shield. The 100K shield is then wrapped with 30 layers of Multi Layer Insulation (MLI) and the cold mass is ready for insertion into the vacuum vessel. A photograph of the completed ERL injector 100K shield being wrapped with MLI is shown in Fig. 2.4.37.

Vacuum vessel and magnetic shield

The vacuum vessel must support the weight of the cold mass, withstand the atmospheric pressure differential, have ports for RF couplers and instrumentation, ports for gate valve actuators, mounts for support in the Linac tunnel, lifting points for transport, and end flanges to accommodate the bellows sleeve that link the cryomodules. The locations of the ports on the vacuum vessel are dictated by the cold-mass components. The vacuum vessel supports have some freedom of location, though vessel deformation under loading must not exceed acceptable limits. The maximum deformation of the top ports that bear the load of the cold mass by way of the composite posts was modeled and found to be 0.13 mm.

The majority of the material of the vacuum vessel will be carbon steel, with the vacuum

flanges that will have o-ring seals made of stainless steel to ensure that there will be no oxidation of the seal surfaces. The interior of the vacuum vessel will be burnished and painted with low vapor pressure vacuum compatible polyurethane paint. The exterior will likewise be burnished and painted with a marine paint.

Since carbon steel is a magnetic material, the vessel will be de-gaussed and care taken to not re-magnetize the vessel. Bench tests of carbon steel tubes show that local magnetization of the tube by permanent magnets can result in remnant magnetic fields in the interior of a few Gauss. The steel can be easily de-magnetized by intimate coils carrying 5300 Amp-turns, such that the remnant magnetic fields in the interior are reduced to about 250 mG. Further lining the interior of the vessel with Co-Netic mu-metal shielding then reduces the remnant magnetic fields in the interior to about 5 mG. However, the interior field could rise to the 25 mG level if the steel vessel is re-magnetized with permanent magnets. At the SRF cavity, these background magnetic fields are further attenuated by the cryogenic A4K magnetic shield [58] that will surround each SRF cavity. The cavity shield will reduce the magnetic field at the cavity to levels of $< 2\,\mathrm{mG}$, which then contributes negligible residual resistance to the SRF cavity surface.

The bellows section that mates adjacent cryomodule vacuum vessels will differ from the TTF-III bellows section since the ERL Linac will utilize at least one pneumatic gate valve per module. The pneumatic gate valves will allow any module to be isolated upon an interlock trip, and the pneumatic actuator will be connected through a port on the bellows section.

Cryomodule and cavity alignment

The prototype ERL injector cryomodule serves as the basis for the design of the cryomodule and cavity alignment system for the main Linac elements. Perhaps the most challenging element of the assembly procedure is the alignment of the quadrupole magnets to the needed tolerance ($< 500\ \mu$m) lateral displacement with respect to the beam axis). Reference of the magnetic center of the quadrupoles to a reference point on the outside of the cryomodule when the magnet is cold will be essential for the successful operation of the ERL. The reproducibility of this translation will be one of the components of the study of the prototype Linac cryomodule. It will determine whether or not externally adjustable mounts for the quadruapoles will be required to be able to use beam based alignment techniques to align the quadrupoles to the required tolerance. The tolerances for the location of the accelerating cavities in the cryomodules are given in Tab. 2.1.6.

The assembly of the cryomodules will be carried out in clean rooms using fixtures and techniques very similar to the ones used for the assembly of the ERL injector cryomodule and the FLASH cryomodules and planned for the XFEL cryomodules. The finished ERL cryomodules will be transported in the tunnel in a manner similar to the transport of the LHC cryomodules with a tape or wire guided vehicle to their location and then translated onto their supports. A guided vehicle sized for the tunnel and beam line height can have a vertical lift capability of up to 25 cm with lateral push and pull sufficient to place and remove the cryomodules.

The interconnection and leak testing of the connected cryomodules will be carried out in a manner very similar to that used for the FLASH cryomodules and planned for the XFEL. Connection of the cryomodules to the cryogen supply lines and the warm transitions needed

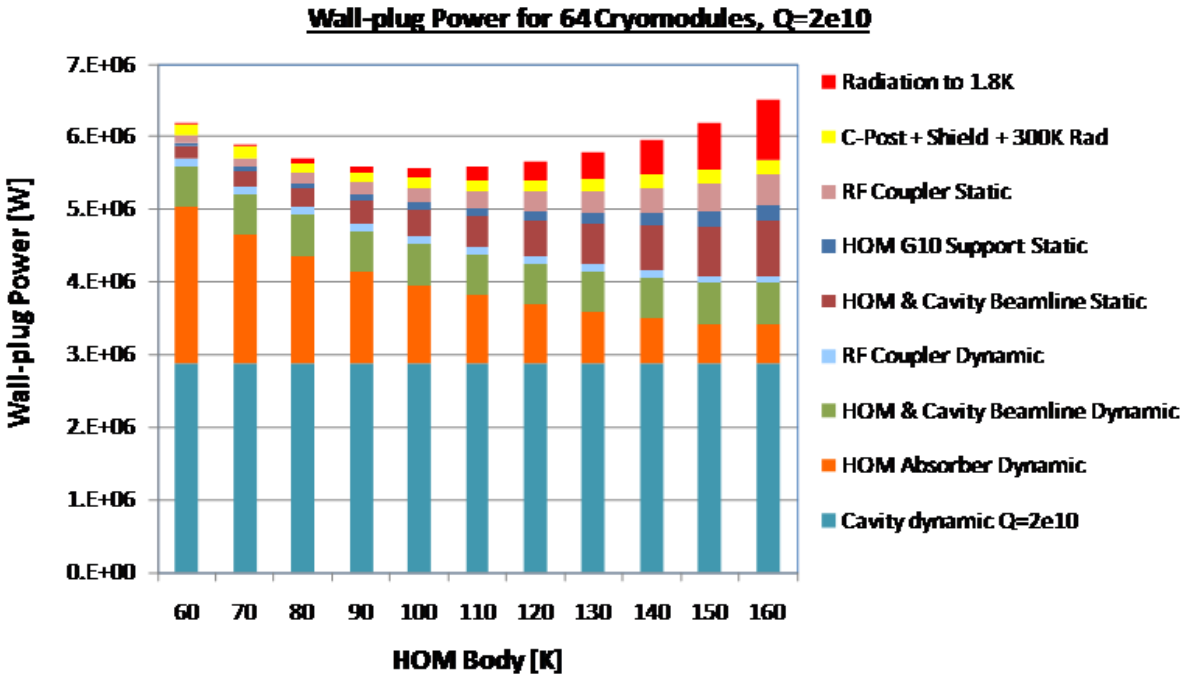

Figure 2.4.38: Wall-plug refrigeration power for a 64-module ERL main Linac with the SRF cavities having $Q_0 = 2 \times 10^{10}$ as a function of the intermediate intercept temperature.

to connect to other accelerator components will also be modeled after the ones planned for the XFEL.

Linac cryomodule heat loads

Having determined that the optimum cavity-operating temperature is 1.8 K, the optimal intermediate temperatures and corresponding heat loads are next to be determined. An important consideration arising from the configuration of the cavities is that the cavity beamtubes protruding from the cavity helium vessel must be superconducting. Considering the convenience of using helium gas just above boiling temperature, we choose 5 K as the next higher intermediate temperature. The thermal radiation shields and the HOM absorbers will need to be at some intermediate temperature between 5 K and 293 K. Detailed modeling shows a broad optimum at 100 K, as shown in Fig. 2.4.38. The models include analysis of the cold components and their material properties vs temperature as well as the Coefficients of Performance of refrigeration vs temperature derived from reports of manufacturers.

The distribution of wall-plug refrigeration power among cryomodule components for the 100 K intermediate temperature case is shown as a pie chart in Fig. 2.4.39. The SRF cavity dynamic load is about 52% of the total refrigeration load, with the dynamic HOM load being the next largest. The thermal gradient along the beamline due to the HOM loads being held at 100 K contributes the most to the static heat load. Table 2.4.13 lists the heat loads and wall-plug power per cryomodule and for the full Linac at the 100 K optimum.

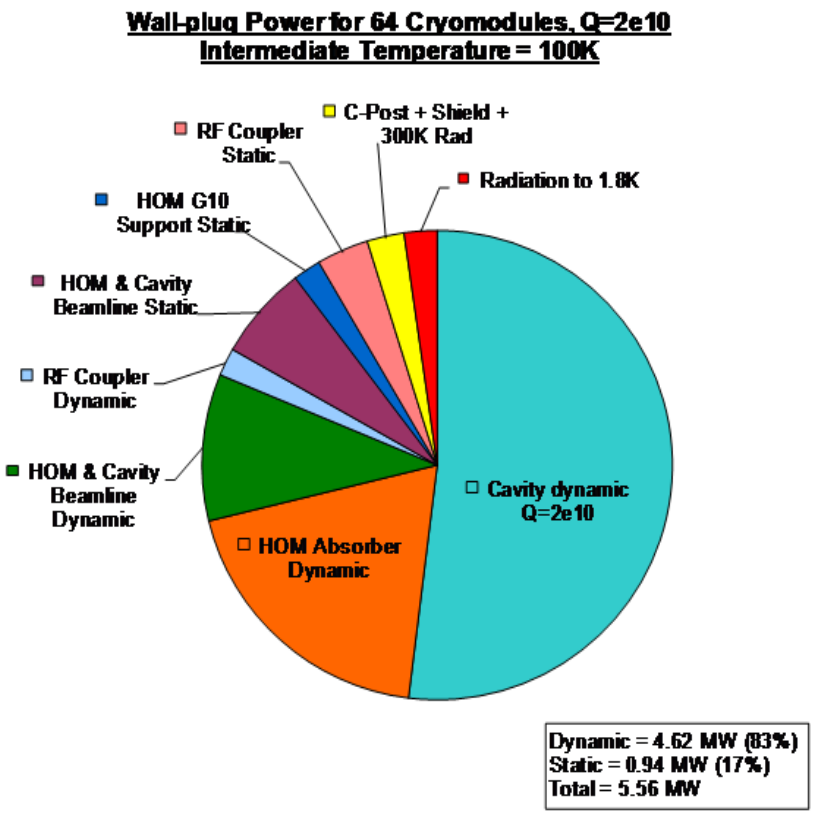

Figure 2.4.39: Distribution of wall-plug refrigeration power for the 64-module main Linac with a 100 K intermediate temperature.

As noted in the section on the cryogenic system and utilities, two helium refrigeration companies were asked to make studies of refrigerators that could handle the estimated thermal loads then estimated. In their studies, they utilized available suites of compressors and expanders with some practical compromises for control systems. The reports are available as references [61] [62]. The calculated operating electric powers using the available compressors and expanders are reported in the utilities section with a safety factor of 1.5 included.

To validate the predicted ERL heat loads listed in Tab. 2.4.13, Tab. 2.4.14 shows the predicted and typical measured static heat loads for the late-model FLASH TTF-III cryomodules [63]. The measured static load to 2 K is about 25% higher than predicted, but the other measured static loads are very close to the predicted values. These measured heat loads would be accommodated by a cryoplant that had a 50% capacity safety factor.

Cryomodule vacuum system

During operation the cryopumping of the accelerating cavities dominates all other pumping in the cryomodules. The challenge is to develop a pump down strategy that minimizes the risk of contamination of the accelerating cavities. A single piece of dust (even in μm size) will lead to field emission lowering Q_0 and a possibie quench of the cavity. A slow pump down sequence

Table 2.4.13: Heat loads and wall-plug power per cryomodule and for the full Linac with the SRF cavities having $Q_0 = 2 \times 10^{10}$.

	ERL Linac	
Per Module	Heat Load	Wall plug
1.8 Static (W)	7.28	5,240
1.8 Dynamic (W)	68.99	49,692
1.8 Total (W)	76.26	54,932
5 K Static (W)	45.16	8,882
5 K Dynamic (W)	25.65	5,045
5 K Total (W)	70.82	13,928
100 K Static (W)	50.09	598
100 K Dynamic (W)	1455.50	17,369
100 K Total (W)	1509.41	17,966
Module wall plug (W)		86,826
# modules	64	
Linac wall plug (W)		5.56×10^6
Safety factor	1.5	
Linac wall plug $\times$ safety factor (W)		8.34×10^6

Table 2.4.14: Predicted and typical measured static heat loads for late-model FLASH TTF-III cryomodules.

Per Module	FLASH Predicted	FLASH Measured
2K Static (W)	2.80	3.5
4.5K Static (W)	13.90	13
70K Static (W)	76.80	78

minimizes this risk. After the clean assembly of the cavity string in the cryomodule, the beam line will be pumped down and closed off by the beam line gate valves at either end of the cryomodule. The beam line will remain under vacuum during transport to the final location of the cryomodule. Cold cathode ion gauges will be used to monitor the beam line vacuum at all times. Leak testing will be carried out at each stage of the cryostat assembly following the procedures that were developed during the ICM assembly. These procedures were very similar to the one followed for the assembly of the FLASH cryomodules and the ones proposed for the XFEL cryomodules.

After placement of the cryo-modules in the Linac tunnel, interconnection vacuum beampipes will be installed to complete the Linac beamline vacuum. Each interconnection includes stainless steel beampipes, a flexible bellows (with proper RF-shielding or absorbers), a vacuum pumping port and gauge port. As the interconnections are enclosed in the Linac insulation vacuum walls, extensions are added to the pump/gauge port(s) to allow access to the port(s). Proper RF screens must be incorporated in the vacuum pump/gauge ports to minimize HOM heating at the screens. All components used on the interconnection (including ion pumps

and vacuum gauges) must be cleaned in a Class 100 clean room to remove particulates, and properly bagged for transportation to the site. A portable clean room capable achieving Class 100 will be set up to enclose the entire interconnection during the installation process.

The insulation vacuum will be maintained after initial pump down by the cryopumping of the outer surface of cavity helium vessels. There will be a pump port closed off by a suitable valve to allow this pump down. There will also be suitable ports to allow monitoring of the insulation vacuum along with appropriate gauges to continuously record the condition of the insulation vacuum. In case of sudden accidental release of cryogens inside the cryostat module, it will be equipped with safety blowoff ports that will require 10 psi overpressure to release.

Cryomodule instrumentation

Instrumentation for the cryomodule needs to be sufficient to correctly monitor the operation of the cryomodule. Since it will replicated 64 times for the full Linac, care needs to be take to avoid unnecessary monitoring. The required monitors would include helium level sensor for the JT/2-phase-pipe, temperature sensors in a number of locations with different types of sensors depending on the requirements, helium pressure sensors, and low level rf probes for accelerating gradient control. In addition there will be the tuner stepper and piezo drives, heaters and cavity alignment sensor if experience with the prototype cryomodule currently under construction indicates that this will be needed. As with other aspects of the main Linac cryomodules, the final design of the instrumentation package will be guided by the experience from the ICM, FLASH, and the planning for the XFEL.

2.4.9 Manufacturing plan

The Cornell ERL program is presently in the development phase to prove out the performance of key components of the facility. A great deal of insight has already been gained from the ERL injector and other prototypes at Cornell. A prototype main Linac cryomodule will be designed and fabricated in the next two years. Following this, a final cryomodule design will be completed that is compatible with all of the contiguous infrastructure of the ERL facility. The highlights of the development phase of the main Linac are described in the next section, followed by a description of the production phase.

Main Linac prototype cryomodule

As part of the Cornell ERL development program, prototypes will be fabricated and tested for the main Linac SRF cavity, RF coupler, HOM loads, and cavity tuner. After establishing satisfactory performance of the prototypes, production versions will be fabricated to complete one full Linac cryomodule. In parallel, the rest of the Linac cryomodule will be designed and a full prototype fabricated. There are several logistical options available that will allow the 10 m long prototype cryomodule to be assembled at Cornell with minimal modification to the existing facilities.

Testing of the prototype Linac cryomodule will include the following high-level tasks of increasing complexity:

- Cryogenic test of cooldown, cavity alignment, and heat leaks

- RF test of the cavity field, Q, and microphonics.

The first test of cooldown can easily be accomplished with existing Cornell facilities. The RF test would require a modest RF source and radiation shielding around the test area due to field emission from the cavities. A beam test of dressed, prototype cavities (i.e. cavities with HOM absorbers), coupler and field probes attached, will be beam tested at high beam current using the prototype injector to measure the cryogenic consequences of high current running on HOM absorber heating and search for trapped modes that could engender BBU in the full linac.

Main Linac 64-module production

The pace for production of the 64 cryomodules for the ERL main Linac is targeted to be 2 cryomodules per month, requiring about 2.7 years to complete the full Linac, with 1-2 more months added to produce spare cryomodules. The production pace is determined by the size of the test and assembly facility (for comparison refer to [64]). Since this facility is comprised of costly components, such as a clean room and refrigeration plant, and would likely have a one-time use, it is unlikely that an industrial partner would invest in such a facility without a longer term use. It is possible that such facilities that will be required by other laboratories for cryomodule production programs could be utilized if they have no commitments in the ERL production time frame.

An example layout of a cryomodule production facility is shown in Fig. 2.4.40, which is sized to produce 2 cryomodules per month. The facility includes:

- Clean room with HPR-cavity rinse, vacuum and gas feeds, equipment lock air showers, and 2 beamline string assembly areas
- High bay assembly area to accommodate 3 modules, overhead crane access, an adjacent overhead door to allow flatbed truck entry for loading and unloading
- Cryomodule test area with radiation shielding
- Cavity chemistry etch area
- Cavity 120° C vacuum bake area
- Cavity vacuum furnace for H_2 de-gassing (800° C) or purification (1400° C)
- Cavity tuning equipment
- Cavity vertical test pits with radiation shielding
- Cavity helium vessel Ti welding area
- De-ionized water production and storage
- Liquid helium refrigeration plant including an LN_2 tank for cavity vertical test and module tests

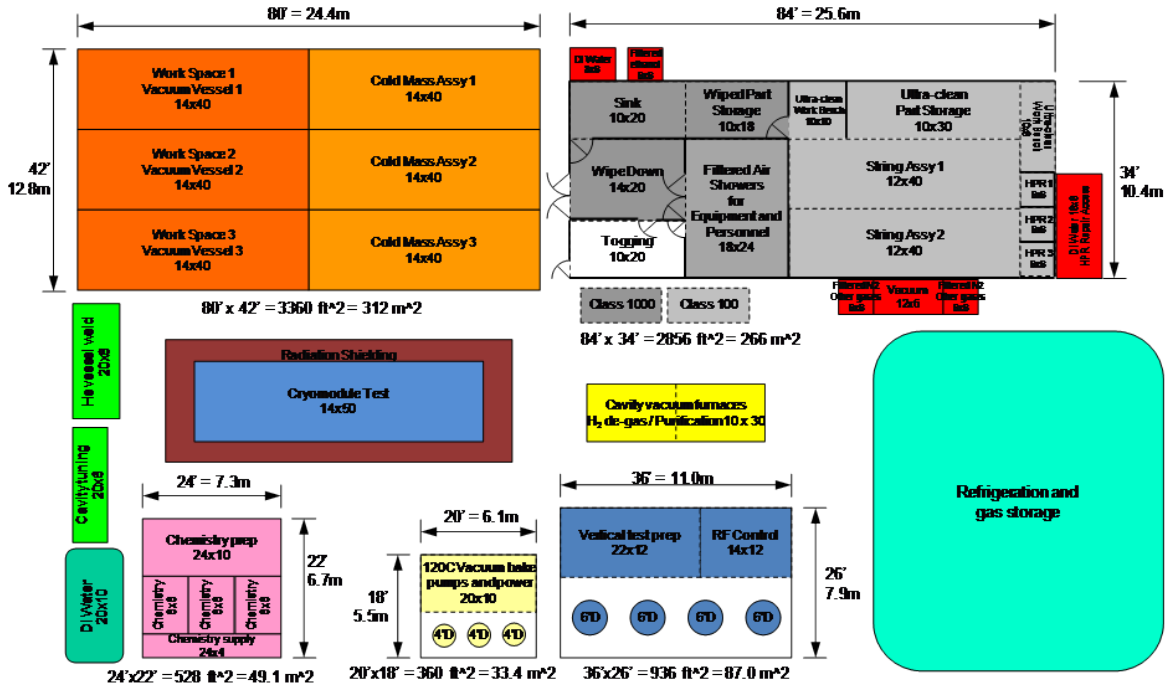

Figure 2.4.40: Block diagram of the space required for typical cryomodule production tasks to assemble two cryomodules per month.

The utilities for the production facility would include considerable AC power for the refrigeration plant and vacuum furnaces, a chilled water supply, and N_2 gas distribution from the LN_2 tank boil-off. It is possible that this facility could be erected in the existing Wilson Lab using existing portable shielding and the existing refrigeration plant.

2.4.10 Tunnel Filling

General Considerations

The tunnel is driven in two sections as shown in the overall layout Fig. 2.1.2. As discussed earlier, this affords the opportunity to compensate for wake-driven energy spread and other transit time manipulations. For both economy and proximity of the low-level RF electronics to the cavities being controlled, the electronics and high power amplifiers are placed as close to the cryomodules as shown in Fig. 2.4.41.

There is expected to be significant radiation in the Linac tunnels because of field emission in the cavities, and the magnitude of this can be estimated from experience at FLASH [65]. Accordingly the electronics racks will be shielded by 6-inch thick panels of heavy concrete as shown in Fig. 2.4.41. The intention is to have the panels on sliders so that they can be moved easily for access to the electronics behind.

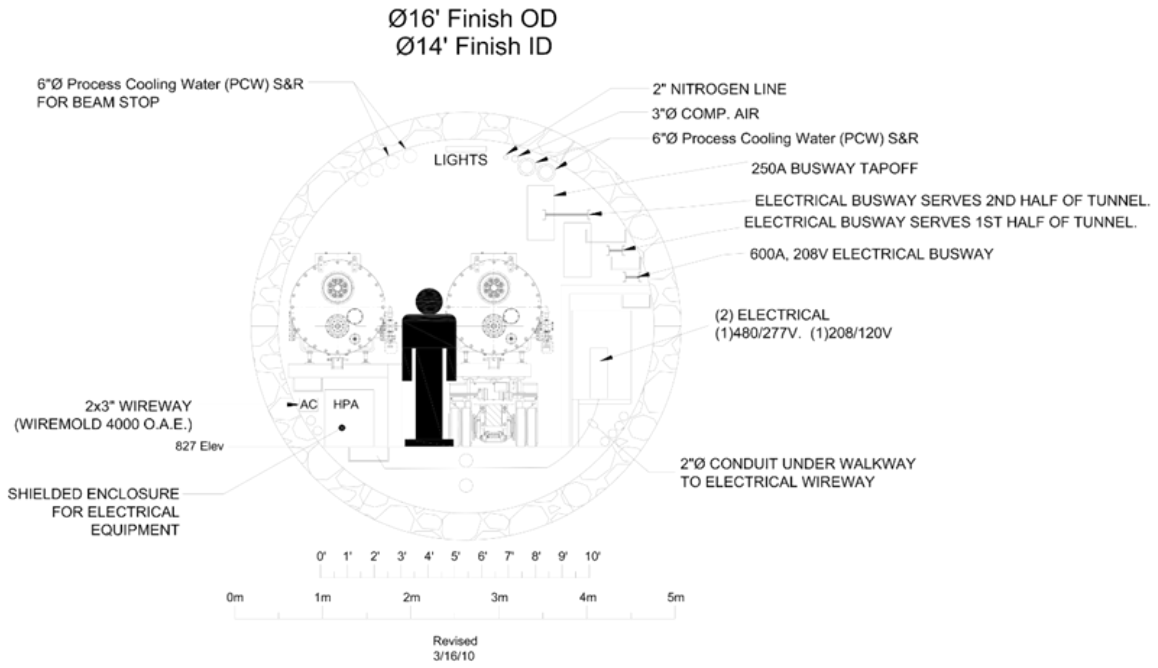

Figure 2.4.41: Tunnel cross-section showing safety provision for persons passing, equipment placement, shielding and utility pipes and ducts.

Utility considerations

Tunnel equipment requires water and forced air for cooling as well as electric power, clean nitrogen for venting, and compressed air for the activation of valves. The quantities are found in the utility tables in §4.4. A tentative disposition of the supply pipes and cables together with equipment placement is shown in Fig. 2.4.41.

Safety considerations

A primary determinant of the tunnel size is the requirement that a person can pass safely between the cryomodules in place and a cryomodule being transported in the tunnel for installation or removal as shown in Fig. 2.4.41. Ventilation by air at a velocity of 400 fpm is provided when the tunnel is occupied to sweep away helium spills, and fire barriers are provided to separate the tunnel from the x-ray halls. Proposals to achieve these safety objectives can be found in the architectural and conventional engineering report of the Arup company [66]. Helium safety matters are presented in §4.6.

References

[1] *The European X-Ray Free-Electron Laser Technical Design Report (XFEL), DESY 2006-097.* Technical report. ISBN 978-3-935702-17-1 http://www.xfel.eu/documents/technical_documents/.

[2] *International Linear Collider Reference Design Report, ILC-REPORT-2007-001.* Technical report.

[3] Petersen, B. *Some aspects of the layout and optimization for the cryogenic supply of superconducting linacs.* Nucl. Instr. and Meth. A, **557** (1), pages 280 – 286 (2006). ISSN 0168-9002. doi:DOI:10.1016/j.nima.2005.10.084. Energy Recovering Linacs 2005 - Proceedings of the 32nd Advanced ICFA Beam Dynamics Workshop on Energy Recovering Linacs.

[4] Rimmer, R. *Higher-order mode calculations, predictions and overview of damping schemes for energy recovering linacs.* Nucl. Instr. and Meth. A, **557** (1), pages 259 – 267 (2006). ISSN 0168-9002. doi:DOI:10.1016/j.nima.2005.10.080. Energy Recovering Linacs 2005 - Proceedings of the 32nd Advanced ICFA Beam Dynamics Workshop on Energy Recovering Linacs.

[5] Marhauser, F., *et al. HOM Survey of the First CEBAF Upgrade Style Cavity Pair.* In *The 23rd Particle Accelerator Conference*, pages 2123–2125. Vancouver, British Columbia, Canada (2009).

[6] Hammons, L. and H. Hahn. *HOM Absorber Development for BNL ERL Cryomodules.* In *The International Workshop on Energy Recovery Linacs, ERL09*. Ithaca, NY, USA (2009). http://accelconf.web.cern.ch/accelconf/ERL2009/html/author.htm.

[7] McIntosh, P. A., *et al. Assembly Preparations for the International ERL Cryomodule at Daresbury Laboratory.* In *14th International Conference on RF Superconductivity (SRF 2009)*, pages 864–868. Berlin, Germany (2009). http://accelconf.web.cern.ch/AccelConf/SRF2009/papers/thppo098.pdf.

[8] Liepe, M. and J. Knobloch. *Superconducting RF for energy-recovery linacs.* Nuclear Instruments and Methods in Physics Research Section A: Accelerators, Spectrometers, Detectors and Associated Equipment, **557** (1), pages 354 – 369 (2006). ISSN 0168-9002. doi:DOI:10.1016/j.nima.2005.10.099. Energy Recovering Linacs 2005 - Proceedings of the 32nd Advanced ICFA Beam Dynamics Workshop on Energy Recovering Linacs.

[9] Kugeler, O. *et al. Manipulating the intrinsic quality factor by thermal cycling and magnetic fields.* In *14th International Conference on RF Superconductivity (SRF 2009)*, pages 352–354. Berlin, Germany (2009). http://accelconf.web.cern.ch/AccelConf/SRF2009/papers/tuppo053.pdf.

[10] Valles, N., *et al. Testing of the Main-Linac Prototype CAvity in a Horizontal Test Cryomodule for the Cornell ERL.* In *Proccedings to 3rd International Particle Accelerator Concerence IPAC12* (2012). http://accelconf.web.cern.ch/accelconf/IPAC2012/papers/weppc075.pdf.

[11] Valles, N., *et al. Cornell ERL Main Linac 7-cell Cavity Performance in Horizontal Test Cryomodule Qualifications, WEPWO068.* In *Proccedings to 4rd International Particle Accelerator Concerence IPAC13* (2013).

[12] Kraemer, D., E. Jaeschke, and E. Eberhardt. *The BESSY Soft X-ray Free Electron Lasers.* Technical report, BESSY, Berlin (2004). ISBN 3-9809534-0-8.

[13] Mukherjee, B. *Measurement of Critical Radiation Levels at FLASH and their Relevance to XFEL.* FLASH seminar (May 29, 2007). http://flash.desy.de/sites/site_vuvfel/content/e870/e2179/infoboxContent2180/Flash-Seminar-290507.pdf.

[14] Liepe, M. and J. Knobloch. *Superconducting RF for energy-recovery linacs.* Nucl. Instr. and Meth. A, **557**, pages 354–369 (2005).

[15] Liepe, M. *et al. Status of the Cornell ERL Injector Cryomodule.* In *25th International Linear Accelerator Conference (LINAC10).* Tsukuba, Japan (2010). http://www.lns.cornell.edu/~liepe/webpage/docs/TU303.pdf.

[16] Myakishev, D. G. and V. P. Yakovlev. *The new possibilities of SuperLANS code for evaluation of axisymmetric cavities.* In *1995 Particle Accelerator Conference (PAC95)*, pages 2348–2350. Dallas, Texas, USA (1995). http://accelconf.web.cern.ch/AccelConf/p95/ARTICLES/MPC/MPC17.PDF.

[17] Valles, N. and M. Liepe. *Seven-Cell Cavity Optimization for Cornell's Energy Recovery Linac.* In *2009 International Workshop of RF Superconductivity (SRF2009)*, pages 538–542. Berlin, Germany (2009). http://accelconf.web.cern.ch/AccelConf/SRF2009/papers/thppo008.pdf.

[18] Hoffstaetter, G. and I. Bazarov. *Beam-Breakup Instability Theory for Energy Recovery Linacs.* Phys. Rev. ST-AB, **7**, page 054401 (2004). ISSN 0168-9002. doi:DOI:10.1103/PhysRevSTAB.7.054401.

[19] Myakishev, D. *CLANS2-A Code for Calculation of Multipole Modes in Axisymmetric Cavities with Absorber Ferites.* In *1999 Particle Accelerator Conference (PAC1999)*, pages 2775–2777. New York, NV, USA (1999). http://accelconf.web.cern.ch/AccelConf/p99/PAPERS/THA76.PDF.

[20] Buckley, B. and G. H. Hoffstaetter. *Transverse emittance dilution due to coupler kicks in linear accelerators.* Phys. Rev. ST Accel. Beams, **10** (11), page 111002 (Nov 2007). doi:10.1103/PhysRevSTAB.10.111002.

[21] Matsumoto, H., *et al. Experience with a Zero Impedance Vacuum Flange at He Super-Leak Temperature for the ILC.* In *The tenth European Particle Accelerator Conference, EPAC'06*, pages 753–755. Edinburgh, Scotland (2006).

[22] Zapfe-Duren, K., *et al. A New Flange Design for the Superconducting Cavities for TESLA.* In *The Eighth Workshop on RF Superconductivity*, pages 457–462. Abano Terme (Padova), Italy (1997).

[23] Kurokouchi, S., S. Morita, and M. Okabe. *Characteristics of a taper-seal type gasket for the Conflat ®; sealing system.* Journal of Vacuum Science Technology A: Vacuum, Surfaces, and Films, **19** (6), pages 2963 –2967 (November 2001). ISSN 0734-2101. doi: 10.1116/1.1415359.

[24] Conway, Z. and M. Liepe. *Electromagnetic and Mechanical Properties of the Cornell ERL Injector Cryomodule.* In *2009 Particle Accelerator Conference (PAC09)*, pages 915–917. Vancouver, Canada (2009). http://accelconf.web.cern.ch/AccelConf/PAC2009/papers/tu5pfp042.pdf.

[25] Padamsee, H. *RF Superconductivity for Accelerators.* John Wiley and Sons, Inc (1998).

[26] Amuneal Manufacturing Corp., Philadelphia, PA http://www.amuneal.com/.

[27] Singer, W. *et al. Preparation Phase for the 1.3 GHz Cavity Production of the European XFEL.* In *2010 International Particle Accelerator Conference (IPAC10)*, pages 3633–3635. Kyoto, Japan (2010). http://accelconf.web.cern.ch/AccelConf/IPAC10/papers/thoara02.pdf.

[28] Kneisel, P. *SRF cavity technology.* In *International Accelerator School for Linear Colliders 19-27 May 2006.* Sokendai, Hayama, Japan (2006). http://linearcollider.org/files/ilc_school/Lecture_11_Peter_Kneisel.ppt.

[29] Ciovati, G. *Effect of low-temperature baking on the radio-frequency properties of niobium superconducting cavities for particle accelerators.* Journal of Applied Physics, **96** (3), pages 1591 – 1600 (2004). ISSN 0021-8979. doi:DOI:10.1063/1.1767295.

[30] Weise, H. *Superconducting EF Structures - Test Facilities and Results.* In *2003 Particle Accelerator Conference (PAC03)*, pages 673–677. Portland, Oregon (2003). http://accelconf.web.cern.ch/Accelconf/p03/PAPERS/ROPC007.PDF.

[31] Valles, N. *et al. Exploring the Maximum Superheating Fields on Niobium.* In *14th International Conference on RF Superconductivity (SRF 2009)*, pages 406–410. Berlin, Germany (2009). http://accelconf.web.cern.ch/AccelConf/SRF2009/papers/tuppo072.pdf.

[32] Bosland, P. and B. Wu. *Mechanical study of the Saclay piezo tuner PTS (Piezo Tuning System).* Technical Report CARE-Note-2005-004-SRF, DAPNIA - CEA Saclay (2005). http://jra-srf.desy.de/sites/site_jra-srf/content/e86/e123/e125/e429/infoboxContent432/note-2005-004-SRF.pdf.

[33] Liepe, M., W.D.-Moeller, and S. Simrock. *Dynamic Lorentz Force Compensation with a Fast Piezoelectric Tuner.* In *The 2001 Particle Accelerator Conference (PAC 2001)*, pages 1704–1706. Chicago, Illinois, USA (2001).

[34] Bosotti, A., *et al. A fully automated device for checking XFEL piezo-tuner installation.* In *14th International Conference on RF Superconductivity (SRF 2009)*, pages 693–697. Berlin, Germany (2009). http://accelconf.web.cern.ch/AccelConf/srf2009/papers/thppo049.pdf.

[35] Pagani, C., *et al. ILC Coaxial Blade Tuner*. In *The tenth European Particle Accelerator Conference, EPAC'06*, pages 466–468. Edinburgh, Scotland (2006). http://accelconf.web.cern.ch/AccelConf/e06/PAPERS/MOPCH171.PDF.

[36] Neumann, A., *et al. Microphonics in CW TESLA Cavities and their Compensation with Fast Tuners*. In *12th International Conference on RF Superconductivity (SRF 2007)*, pages 377–383. Beijing, China (2007).

[37] Kugeler, O. *Cavity Tuners*. In *The International Workshop on Energy Recovery Linacs, ERL09*. Ithaca, NY, USA (2009). http://accelconf.web.cern.ch/accelconf/ERL2009/html/author.htm.

[38] Chojnacki, E. and W. J. Alton. *Beamline RF Load Development at Cornell*. In *1999 Particle Accelerator Conference*, pages 845–847. New York, USA (1999). http://accelconf.web.cern.ch/AccelConf/p99/PAPERS/MOP77.PDF.

[39] Tajima, T., *et al. HOM Absorbers of Superconducting Cavities for KEKB*. In *European Particle Accelerator Conference, EPAC'96*, pages 2127–2129. Barcelona, Spain (1996). http://accelconf.web.cern.ch/AccelConf/e96/PAPERS/WEPL/WEP061L.PDF.

[40] Shemelin, V., M. Liepe, and H. Padamsee. *Characterization of ferrites at low temperature and high frequency*. Nucl. Instr. and Meth. A, **557** (1), pages 268 – 271 (2006). ISSN 0168-9002. doi:DOI:10.1016/j.nima.2005.10.081. Energy Recovering Linacs 2005 - Proceedings of the 32nd Advanced ICFA Beam Dynamics Workshop on Energy Recovering Linacs.

[41] Chojnacki, E., *et al. DC Conductivity of RF Absorbing Materials*. In *14th International Conference on RF Superconductivity (SRF 2009)*, pages 643 –647. Berlin, Germany (2009). http://accelconf.web.cern.ch/AccelConf/srf2009/papers/thppo035.pdf.

[42] Sekutowicz, J. *Higher Order Mode Coupler for TESLA*. In *The Sixth Workshop on RF Superconductivity*, pages 426–439. Virginia, USA (1993). http://accelconf.web.cern.ch/AccelConf/SRF93/papers/srf93g04.pdf.

[43] Watanabe, K., *et al. New HOM coupler design for ILC superconducting cavity*. Nucl. Instr. and Meth. A, **595** (2), pages 299 – 311 (2008). ISSN 0168-9002. doi:DOI:10.1016/j.nima.2008.06.048.

[44] Kneisel, P. *et al. Testing of HOM Coupler Designs on a Single Cell Niobium Cavity*. In *2005 Particle Accelerator Conference*, pages 4012–4014. Knoxville, Tennessee (2005). http://epaper.kek.jp/p05/PAPERS/TPPT077.PDF.

[45] Kim, S. *et al. Study on Fault Sccenarios of Coaxial Type HOM Couplers in SRF Cavities*. In *2006 Linear Accelerator Conference (LINAC06)*, pages 770–772. Knoxville, Tennessee (2006). http://accelconf.web.cern.ch/accelconf/l06/PAPERS/THP081.PDF.

[46] Kazimi, R., *et al. Observation and Mitigation of Multipass BBU in CEBAF*. In *The eleventh European Particle Accelerator Conference, EPAC'08*, pages 2722–2724. Genoa, Italy (2008). http://accelconf.web.cern.ch/AccelConf/e08/papers/wepp087.pdf.

[47] Campisi, I. *et al. CEBAF Cryomodules: Test Results and Status.* IEEE Transactions on Magnetics, **27** (2), pages 2300–2303 (1991). ISSN 0018-9464. doi:DOI:10.1109/20.133677.

[48] Huang, Q., *et al. Carbon Nanotube RF Absorbing Materials.* In *14th International Conference on RF Superconductivity (SRF 2009)*, pages 648–651. Berlin, Germany (2009). http://accelconf.web.cern.ch/AccelConf/srf2009/papers/thppo036.pdf.

[49] Belomestnykh, S. *Overview of input power coupler developments, pulsed and CW.* In *The 13th Workshop on RF Superconductivity*, pages 419–423. Beijing, China (2007).

[50] Belomestnykh, S., *et al. High average power fundamental input couplers for the Cornell University ERL: requirements, design challenges and first ideas.* Technical Report Cornell LEPP Report ERL 02-8 (2002).

[51] Moeller, W.-D. *High power coupler for the TESLA Test Facility.* In *9th Workshop on RF Superconductivity*, pages 577–581. Santa Fe, NM,USA (1999). For the TESLA Collaboration.

[52] Dwersteg, B., *et al. TESLA RF Power Couplers Development at DESY.* In *Proceedings of the 10th Workshop on RF Superconductivity*, pages 443–447. Tsukuba, Japan (2001).

[53] Veshcherevich, V., *et al. High power tests of input couplers for Cornell ERL injector.* In *The 13th Workshop on RF Superconductivity*, pages 517–519. Beijing, China (2007).

[54] Veshcherevich, V. and S. Belomestnykh. *Input coupler for main linac of Cornell ERL.* In *The 14th International Conference on RF Superconductivity*, pages 534–545. Berlin, Germany (2009).

[55] Yla-Oijala, P. *Electron multipacting in TESLA Cavities and Input Couplers.* Particle Accelerators, **63**, pages 105–137 (1999). http://cdsweb.cern.ch/record/1120324/files/p105.pdf.

[56] A. Mikhailichenko and T. Moore. *Simple Procedure for Superconducting Coil Winding.* In *The 2001 Particle Accelerator Conference (PAC 2001)*, pages 3645–3647. Chicago, IL (2001).

[57] Lorenz, R. *et al. Measurement of the Beam Position in the TESLA Test Facility.* In *1996 Linear Accelerator Conference (LINAC96)*, pages 527–529. Geneva, Switzerland (1996). http://accelconf.web.cern.ch/accelconf/l96/PAPERS/TUP76.PDF.

[58] Amuneal Manufacturing Corp. Technical report, Philadelphia, PA, USA, Amumetal 4k (A4K) (2010). http://www.amuneal.com/magnetic-shielding/idea-share/whats-new-cryogenic-shielding.

[59] Chojnacki, E., *et al. Design and Fabrication of the Cornell ERL Injector Cryomodule.* In *The eleventh European Particle Accelerator Conference, EPAC'08*, pages 844–846. Genoa, Italy (2008). http://accelconf.web.cern.ch/AccelConf/e08/papers/mopp123.pdf.

[60] Chojnacki, E., *et al.* *Cryogenic Heat Load of the Cornell ERL Main Linac Cryomodule.* In *The 14th International Conference on RF Superconductivity*, pages 638–642. Berlin, Germany (2009). http://accelconf.web.cern.ch/AccelConf/SRF2009/papers/thppo034.pdf.

[61] *Cryogenic Plant Study and Budgetary Estimate for ERL Facility, Proposal, November 2006.* Proposal submitted to CLASSE by Linde Kryotechnik, AG. Report is on file at Cornell.

[62] *Helium Refrigeration system for the ERL Cornell Project – Technical Proposal, December,.* Technical report, Air Liquid (2006). Proposal submitted to CLASSE, Modified May, 2010.

[63] Peterson, T. *An Overview of the International Linear Collider (ILC) Cryogenic System.* Cryogenic Operations Workshop at SLAC (May 09, 2006). http://www.slac.stanford.edu/econf/C0605091/present/PETERSON.PDF.

[64] Napoly, O. *XFel Module Assembly at CEA-Saclay.* Fermilab Accelerator Seminar (February 17, 2009). http://beamdocs.fnal.gov/AD-public/DocDB/ShowDocument?docid=3311.

[65] R.J. Hernandez Pinto, M. V., M. Otto. *Radiation Measurements in the FLASH Tunnel in Summer 2006.* Technical report, DESY, Hamburg (2006). DESY Technical Note 2006-04.

[66] ARUP. *Energy Recovery Project Definition Design, Volume I Report.* Technical report (2010).

2.5 RF Systems

2.5.1 Introduction

RF system requirements

The ERL main Linac superconducting cavities operate in a regime with zero beam loading (in the absence of errors) as the decelerated re-circulating beam cancels the beam loading of the accelerated beam. This essential feature of an ERL allows one to operate these cavities at a high external quality factor, ideally equal to the cavity intrinsic quality factor, to minimize the RF power requirements. However, taking into account such factors as the cavity detuning due to environmental noise (microphonics) and the accelerator return loop path length fluctuations, significantly increases the RF power demand [1]. Other factors, such as the power required to compensate for beam loss in the return loops or additional power required during the beam ramp-up, contribute significantly less to the overall power budget and are not considered here.

To analyze the effects under consideration, it is convenient to use a formula for the RF generator power from [2]. In a slightly modified form, taking into account that the beam now consists of two beams – accelerating and decelerating – and neglecting beam losses and second order terms, the formula for the RF power P_{forw} required to maintain a given accelerating voltage V_{acc} in the ERL cavities is

$$P_{forw} = \frac{V_{acc}^2}{4 \cdot R/Q \cdot Q_L} \cdot \frac{\beta + 1}{\beta} \left\{ 1 + \left(2Q_L \cdot \frac{\Delta\omega}{\omega_c} + \frac{I_b R/Q \cdot Q_L}{V_{acc}} \cdot \Delta\phi \right)^2 \right\} \tag{2.5.1}$$

$$Q_L = \frac{Q_0}{\beta + 1} = Q_{ext} \frac{\beta}{\beta + 1} \tag{2.5.2}$$

where R/Q is the ratio of cavity shunt impedance R to its intrinsic quality factor Q_0, Q_L is the loaded quality factor, and Q_{ext} is the external quality factor of the input power coupler. β is the coupling coefficient, I_b is the accelerating beam current, $\Delta\omega = \omega_c - \omega$ the peak cavity detuning caused by microphonics, and $\Delta\phi$ is the decelerating beam phase error due to fluctuations in the return loop path.

Considering only the effect of microphonic noise:

$$P_{frow} = \frac{V_{acc}^2}{4 \cdot R/Q \cdot Q_L} \cdot \frac{\beta + 1}{\beta} \left\{ 1 + \left(2Q_L \cdot \frac{\Delta\omega}{\omega_c} \right)^2 \right\} \tag{2.5.3}$$

From this equation, the maximum power is determined by the peak cavity detuning, and for each value of peak detuning, there is an optimal external quality factor that minimizes the required RF power as illustrated in Fig. 2.5.1.

Experience at several laboratories [3] indicates that achieving peak microphonics detuning of less than 10 Hz is possible. On the other hand, the same experience and the measurements on the ERL injector prototype [4] have shown significant cavity-to-cavity and cryomodule-to-cryomodule spread in this noise level. Based on these facts, typical peak detuning due to microphonics is assumed to be 10 Hz. Allowing for the variation of detuning from cavity to cavity, the maximum peak detuning is taken as 20 Hz. The optimal value of the external

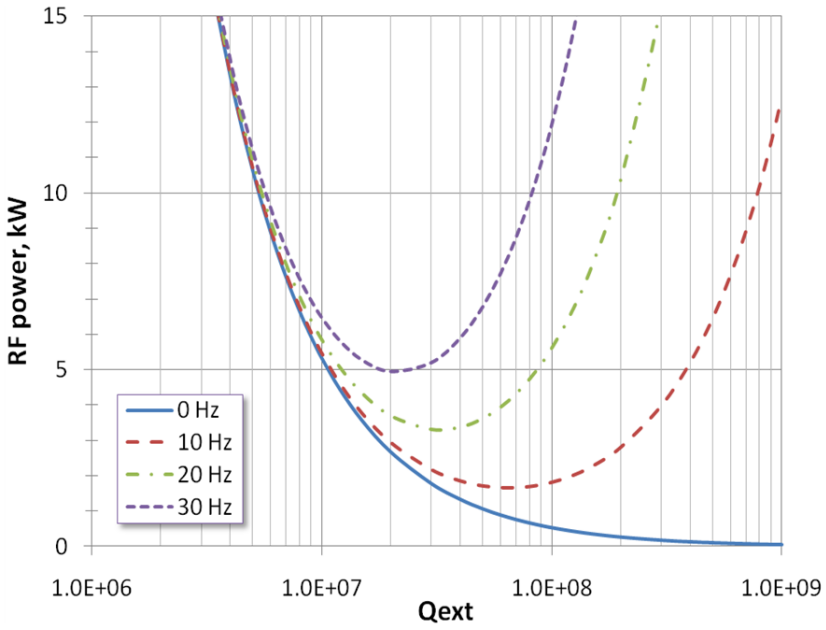

Figure 2.5.1: Required RF power to maintain an accelerating gradient of 16.2 MV/m in a 7-cell main Linac cavity as function of the coupler external quality factor for different peak microphonic detuning (no re-circulating beam phase errors).

quality factor of 6.5×10^7 was chosen for the typical peak detuning. For this Q_{ext} and maximum detuning of 20 Hz, the required peak power is 4.12 kW and the average power is 1.22 kW.

Next consider the effect of a small phase error $\Delta\phi$ of the re-circulating beam. While a DC component of this error or a slow phase drift can be exactly cancelled by the appropriate cavity detuning, fast fluctuations would require additional RF power to counteract. To keep the required peak RF power below 5 kW, the peak $\Delta\phi$ should be less than 0.1°. Cavity field amplitude and phase stability requirements are derived following the analysis presented in [1]. Table 2.5.1 summarizes main requirements to the Linac RF system.

State of the art

All existing RF systems for L-band CW SRF Linacs – CEBAF and the FEL at Jefferson Laboratory, ALICE at the Daresbury Laboratory, ELBE at HZDR (Dresden-Rossendorf) – employ a simple scheme with one cavity per High Power RF Amplifier (HPA). This scheme provides better cavity field amplitude and phase control, more operational flexibility, and better RF system efficiency. It was also in part dictated by available RF power sources.

Three types of high CW RF power generating devices are available from industry: klystrons, inductive output tubes (IOTs), and solid state amplifiers. Their applications in accelerators are summarized in [5–7]. Klystrons have traditionally been used in the past and they are still the technology of choice at higher power levels. However, they are highly non-linear devices if operated close to saturation and their efficiency drops very quickly at reduced output power. It is worth noting that the largest presently operating CW superconducting Linac RF system

Table 2.5.1: Main requirements to the Linac RF system

Operating frequency	1.3 GHz
Number of 7-cell cavities	384
Accelerating gradient	16.2 MV/m
Accelerating voltage per cavity	13.1 MV
R/Q (circuit definition)	400 Ω
Q_{ext}	6.5×10^7
Peak detuning due to microphonics	20 Hz
Typical detuning due to microphonics	10 Hz
Peak RF power per cavity	5 kW
Average RF power per cavity	< 2 kW
Amplitude stability	1×10^{-4} rms
Phase stability	0.05° rms

in the world, CEBAF, uses 1497 MHz klystrons. The CEBAF klystrons operate very reliably with an average lifetime of 165,000 hours [8]. Analysis for the CEBAF 12 GeV Upgrade RF showed no overall cost savings for IOT-based amplifiers over klystron-based ones [9] and the klystron technology has been chosen for the upgrade RF system.

IOTs currently have practically replaced klystrons in the TV broadcast industry and are also offered in L-band by several manufacturers. The main advantages of IOTs over klystrons are higher efficiency ($> 60\%$ at maximum output power), the absence of saturation, higher linearity (but not at low power levels), smaller size, and lower cost per tube. The disadvantages are lower gain, non-linear behavior at low power levels, and limited output power. While no large-scale installations of L-band IOTs exist and no long-term reliability data are available, several tubes are in service around the world. These tubes are at the Cornell ERL injector prototype, ALICE (Daresbury Laboratory), ELBE (HZDR, Dresden-Rossendorf), HoBiCaT (HZB), and the ERL prototype (KEK). The latest available statistics from industry (one manufacturer) on broadcast IOTs is from 2007. At that time, the mean time before failure (MTBF) was reaching 42,230 hours with some tubes having maximum operating hours of more than 70,000 hours. The statistics were for 343 tube positions and are expected to improve over time as many of the originally installed tubes were still operational and hence not included in the calculations.

Following recent advances in high-power transistor technology, solid-state amplifiers are being adopted for high-power RF systems in accelerators. In the past, the efficiency of solid-state amplifiers was much worse than that of the other two technologies, but recently manufacturers have begun to specify typical RF efficiencies up to 50% with an overall system efficiency (including DC power supplies) of 42% [10]. This is approaching that of IOT and klystron-based amplifier systems. A prototype 10 kW solid-state amplifier was recently installed and commissioned at HZDR (Dresden-Rossendorf) [11]. The advantages of solid-state amplifiers are low power supply voltage, graceful degradation, and easier maintenance due to their modular design. It is important to note, that due to their modular design, a single, output-power-transistor failure does not cause complete system failure and only reduces the available output power.

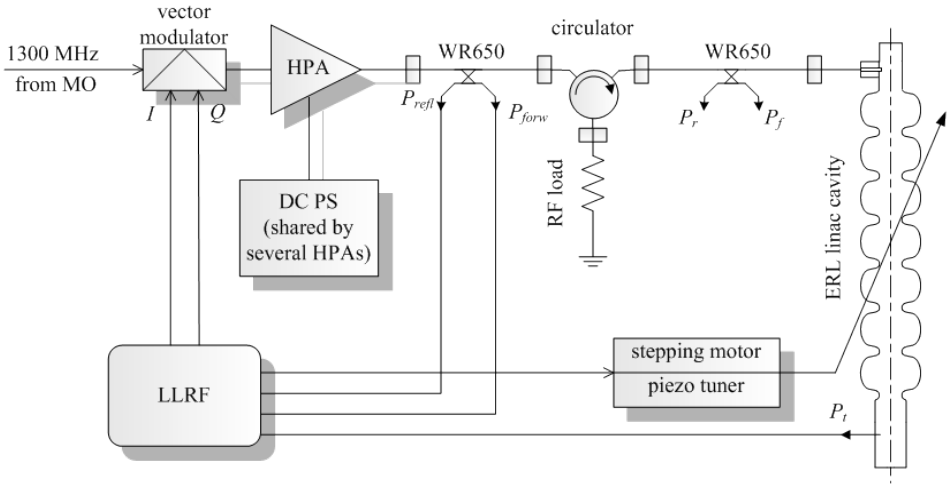

Figure 2.5.2: Block diagram of an RF channel for the ERL main Linac.

Table 2.5.2: Main specifications for the ERL Linac RF HPA.

Frequency	1.3 GHz
Peak output RF power	$\geq$ 5 kW
Average output RF power	$\geq$ 2 kW
Bandwidth at 1 dB points (min.)	$\pm$1.5 MHz
Bandwidth at 3 dB points (min.)	$\pm$2.5 MHz
RF phase pushing (0.03 kW to 5 kW output power)	$< 7°$
Gain change (0.03 kW to 5 kW output power)	$<$ 3 dB
RF output amplitude ripple (0.03 kW to 5 kW output power)	$<$ 0.2% rms
RF output phase ripple (0.03 kW to 5 kW output power)	$< 0.5°$ rms
Efficiency at 5 kW	$\geq$ 50%
Efficiency at 2 kW	$\geq$ 40%

2.5.2 Architecture of the main Linac RF

The ERL main Linac RF system consists of 64 RF stations (35 in the north Linac and 29 in the south Linac) with one station per cryomodule. One station is comprised of six independent RF channels (one per cavity), each including a HPA, Low Level RF (LLRF) controls, interlocks and monitoring electronics, and a waveguide or rigid coaxial transmission line connecting the HPA to the cavity fundamental power coupler. A three-stub tuner can be inserted in the transmission line for Q_{ext} adjustment if necessary. One or more DC power supplies are shared by the station's HPAs. All components of the RF stations will be installed in the Linac tunnel in radiation-shielded enclosures. Figure 2.5.2 shows a basic block diagram for one RF channel.

2.5.3 High-power RF: Choice of the RF technology and Phase 1b efforts

The Linac RF HPAs will be located in the Linac tunnel at the SRF cryomodules. To satisfy the requirements outlined in §2.5.1 and the limited space in the tunnel, the HPA must be a compact, modular, highly efficient, linear, high-gain amplifier. Such an amplifier should meet the specifications listed in Table 2.5.2. The solid-state technology was chosen for the baseline design due to its advantages particularly with regards to linearity, complexity, size and cost. We are therefore in the process of testing a 5 kW, 1.3 GHz solid state amplifier. However, issues regarding reliability and radiation hardness require further investigation before a final decision is made. These issues will be explored during Phase 1b. A prototype unit will be ordered from industry, thoroughly tested off line and then used in a main Linac cryomodule high-power test. Based on the test results, a final decision will be made on which technology to choose for HPA.

2.5.4 Low level RF

Master oscillator and reference signal distribution

The 1.3 GHz reference signal required for cavity regulation is generated by the master oscillator. In the simplest case, the master oscillator uses an RF oscillator with a resonant frequency of 1.3 GHz [12], which is phase-locked to a quartz oscillator and/or a rubidium transition to provide sufficient long-term stability. The required timing stability of the master oscillator depends strongly on the ERL operation mode. In the 100 mA operation mode with its 2 ps (rms) long bunches, a timing stability of 200 fs is required corresponding to $1/10^{\text{th}}$ of the bunch duration. Master oscillators operating at 1.3 GHz offering a better frequency stability than this already exist, for example at FLASH [13].

The required distribution length for the 1.3 GHz signals is around 500 m, which would still barely be possible via coaxial cables in terms of cable losses. Alternatively, a lower frequency could be distributed, allowing for lower transport losses, and the 1.3 GHz signals would then be generated by phase locking local 1.3 GHz oscillators to this distributed signal. Both of these schemes could deliver long-term stability in the picosecond range, which might be sufficient for the 2 p*s* bunch mode of the ERL, especially, if beam-based feedback loops are used to compensate for cable drifts.

The short-pulse operation mode with its sub-100 fs bunches will require significantly improved stability, which can be achieved with the optical synchronization schemes as discussed in the beam diagnostics and controls section.

Low level RF system

The objectives of the LLRF control system are to stabilize the accelerating fields in the main Linac cavities, and to provide excellent operability, availability, and maintainability. The design of the LLRF system is driven by the following requirements:

- A compact, cost-effective design is essential, since all of the LLRF electronics will be placed in the main Linac tunnel, and space is limited.

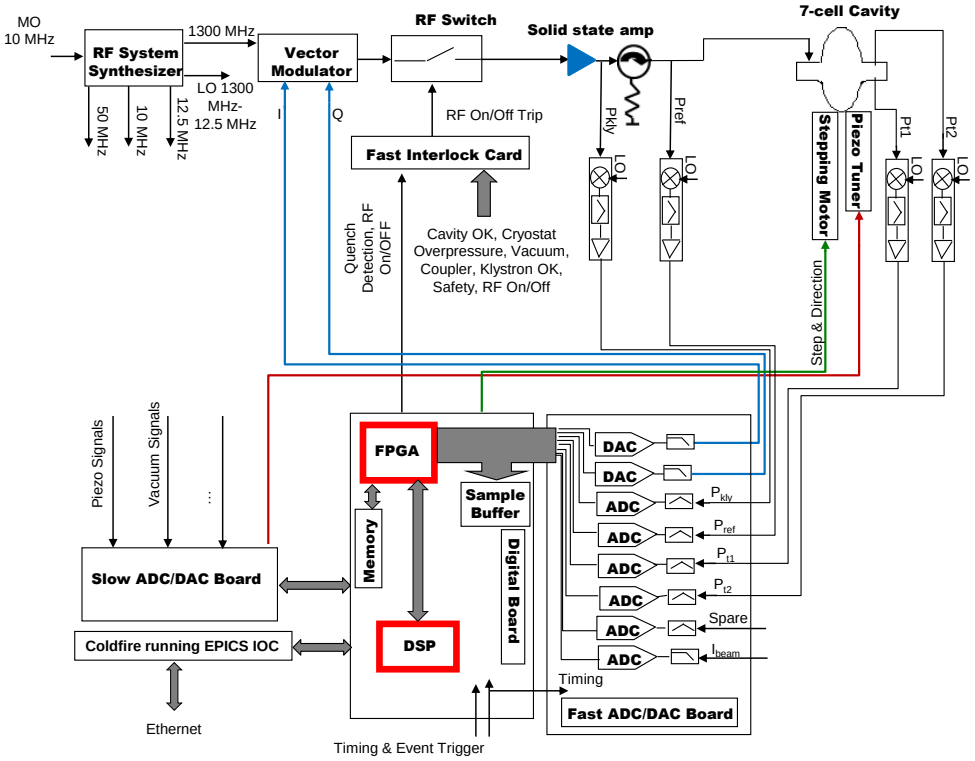

Figure 2.5.3: Block diagram of the main Linac LLRF system for a single cavity. Shown are both the RF hardware (RF synthesizer, vector modulator, solid state amplifier, down-converters) and the digital hardware (fast ADC/DAC board, main digital processor board, slow ADC/DAC board, EPICS IOC processor board). A fast, analog interlock provides protection in addition to the digital trip detection.

- The LLRF electronics will be in a radiation producing environment (x-rays and neutrons).
- No direct access to the electronics will be available during operation of the accelerator.
- The RF fields in the cavities need to be stabilized to $\sigma_A/A = 10^{-4}$ in relative amplitude and $\sigma_p = 0.05^\circ$ in phase.
- Efficient main Linac cavity operation requires operating at high loaded-quality factors of 6.5×10^7 and above.

These requirements resulted in the design described below. Figure 2.5.3 shows the block diagram of the main Linac LLRF system. Operation at very high-loaded quality factors requires operating each cavity from an individual RF power source. Accordingly, there will be an individual LLRF system for each main Linac cavity. A digital LLRF system will be used since it allows running the complex feedback and feed forward loops while providing easy integration of diagnostics and data logging. All RF signals (forward power, reflected

power, and the cavity field probe signal) will be down-converted to an intermediate frequency and then 4 times oversampled by analog-to-digital converters (ADC) to give a complex phasor representing the amplitudes and relative phases of the RF signals. Very fast digital components like Field-Programmable Gate Arrays (FPGAs) will be used to achieve very low feedback loop latency $< 1\,\mu$s, allowing high feedback gains of several thousand to achieve sufficient field stability in the presence of the strong field perturbations mentioned above. The large phase perturbations by cavity microphonics make an in-phase quadrature (IQ) field feedback controller the preferred choice over of a traditional amplitude and phase controller. A digital filter will be used to avoid feedback loop instabilities caused by the $6/7\ \pi$ TM010 mode. The fast feedback loops stabilizing the RF cavity field will be accompanied by feedback and feedforward loops controlling the cavity frequency. These slower loops will compensate the change in cavity frequency due to the Lorentz force detuning when the field amplitude is changed (for example during turn-on of the cavity fields), and partly compensate the cavity detuning by microphonics. Sophisticated trip detection and a state machine will provide protection, exception handling, automated calibrations, cavity turn-on and trip recovery.

The RF and digital hardware for a single cavity will be packaged into a compact LLRF unit in order to minimize the impact on accelerator operation. Problems of a failed unit can be diagnosed and repaired off-line, and the impact on the availability of the accelerator minimized. The radiation environment will be addressed in several ways . Radiation shielding will be used to reduce x-rays and neutrons to an acceptable level at the LLRF electronics. Estimates of the expected radiation level in the ERL main Linac tunnel have shown that this is achievable with modest radiation shielding. In addition, where required, radiation-hard electronic components will be used. Single-event upsets by neutrons will be diagnosed by running two identical copies of the digital control loops in parallel. If a bit in one of the loops is changed by a neutron, the results of the two control loops will disagree. A re-flash of the digital components on that given cavity unit will then be used to repair such single event upsets.

The digital IQ LLRF system built for the Cornell ERL injector serves as a prototype for the LLRF system of the main Linac [14]. Figure 2.5.4 shows the digital processor board of this system together with a block diagram of its digital components. The prototype LLRF system has all the functionallity needed for the main Linac and meets the performance specifications given above. The final version will have a more compact form factor and will employ a hardware platform with very high reliability, e.g. a modified version of the MicroTCA platform. The prototype LLRF system has been tested extensively with the low-loaded quality factor cavities in the Cornell ERL injector, as well as with very high quality factor cavities both with and without ERL like beam operation. Figure 2.5.5 , Fig. 2.5.6 and Fig. 2.5.7 show some highlights from these LLRF tests.

In a proof of principle experiment, Cornell's digital LLRF system has been connected to one of the 7-cell cavities in the TJNAF ERL-FEL. After an initial test at the standard loaded quality factor of $Q_L = 2 \times 10^7$, the loaded Q_L was increased to a record value of 1.2×10^8. Excellent field stability was achieved with full 5 mA beam current in energy recovery mode(see Fig. 2.5.5) Less than 500 W of driving RF power was required for operation at a gradient of 12.3 MV/m. No dependence of the field stability on beam current (0 to 5.5 mA) and off-crest angle (between -40° and $+40^\circ$) was found. Even at this high loaded Q ,the cavity operated very reliably over several hours without any trips. Piezo tuner based frequency control proved to be very effective in keeping the cavity on resonance during cavity field ramp-up. The Lorentz

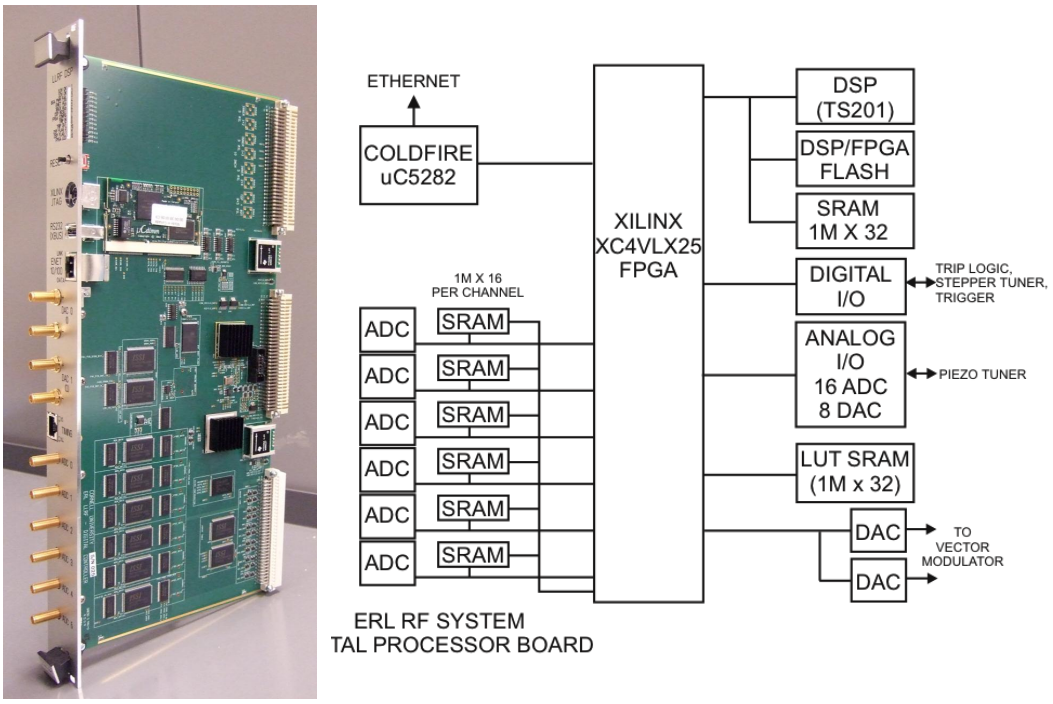

Figure 2.5.4: Digital LLRF system developed for the Cornell ERL injector prototype. Left: Main processor board. Right: Block diagram of the digital boards with the XILINX FPGA and a TigerSHARC DSP. The system uses six 16-bit ADCs running at 50 MHz and two fast 16 bit DACs as analog outputs for field control.

force detuning of the cavity was compensated effectively by the piezo tuner, and allowed ramp-up to high gradients in less than 1 s reliably even at $Q_L = 1.2 \times 10^8$ (see Fig. 2.5.5). This is desirable for fast trip recovery in a large ERL. This described test demonstrates that no fundamental limit prohibits cavity operation at a loaded Q of up to 10^8, and that very high field stability can be achieved at the same time.

In a second test of Cornell's digital LLRF system with a high-loaded Q cavity, the LLRF system was connected to a 9-cell ILC type cavity at the Helmholtz-Zentrum Berlin. The cavity was operated at three different loaded Q values of 5×10^7, 1×10^8, and 2×10^8. In all three cases, excellent field stability in amplitude and phase was achieved by running with proportional feedback gains of several thousand to compensate for the strong field perturbations caused by cavity microphonics ($\sim$ 6 Hz rms, $\sim$ 30 Hz peak) (see Fig. 2.5.6). Feedback control of microphonics cavity detuning has been demonstrated successfully at the Cornell ERL injector cryomodule. The frequency tuners of the 2-cell injector cavities are equipped with fast piezo-electric actuators for fast-frequency tuning. First steps have been taken to explore the potential and robustness of microphonics compensation using these fast tuners in a feedback loop. For robustness, a proportional-integral-derivative (PID) frequency feedback loop was implemented

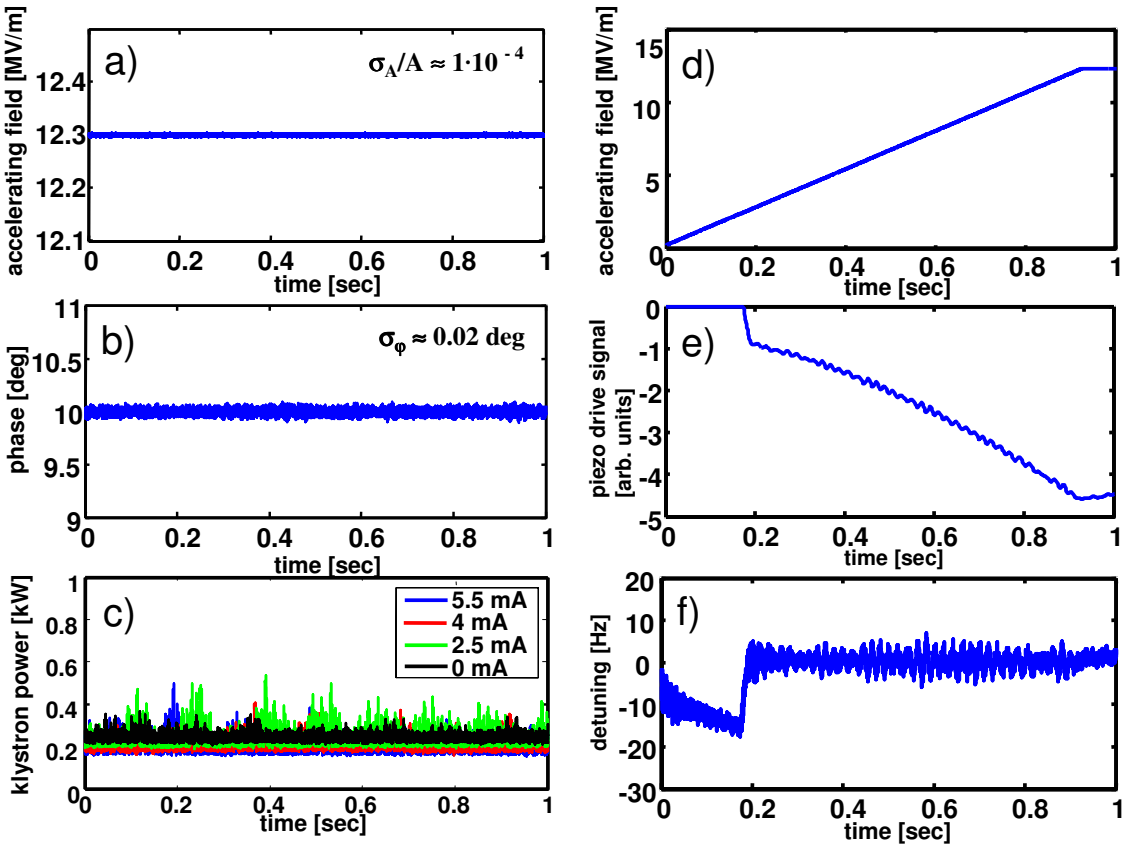

Figure 2.5.5: Results from a test of Cornell's LLRF system at the TJNAF FEL-ERL operating a 7-cell cavity with a high loaded quality factor Q_L of 1.2×10^8. (a-c) CW operation. The field stability is exceeding the Cornell ERL main Linac specifications. (d-e) Cavity filling with piezo tuner based Lorentz-force detuning compensation [15]

with a simple digital filter in the LLRF system. Optimizing the gains and the digital filter provided a 70% reduction in the rms microphonics level (see Fig. 2.5.7).

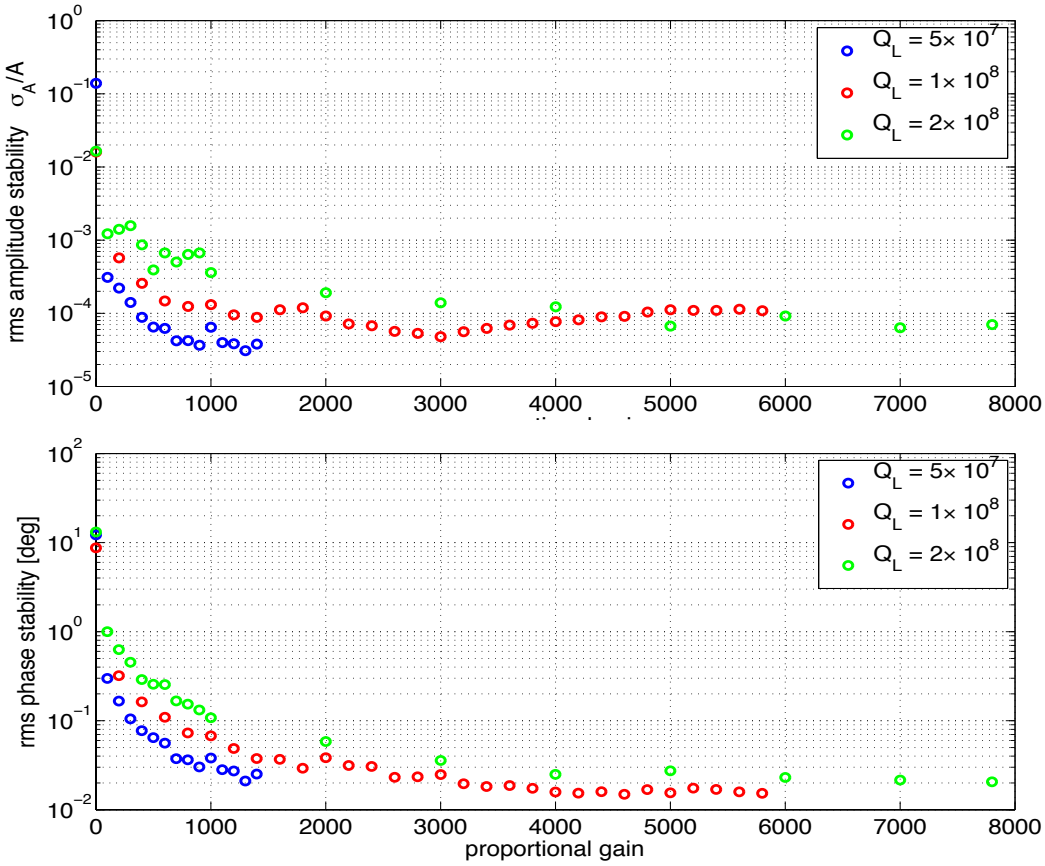

Figure 2.5.6: Amplitude and phase stability as function of proportional gain at different loaded Q_L values of 5×10^7, 1×10^8, and 2×10^8. The RF field in the 9-cell ILC cavity at the Helmholtz-Zentrum Berlin is stabilized by Cornell's digital LLRF system.

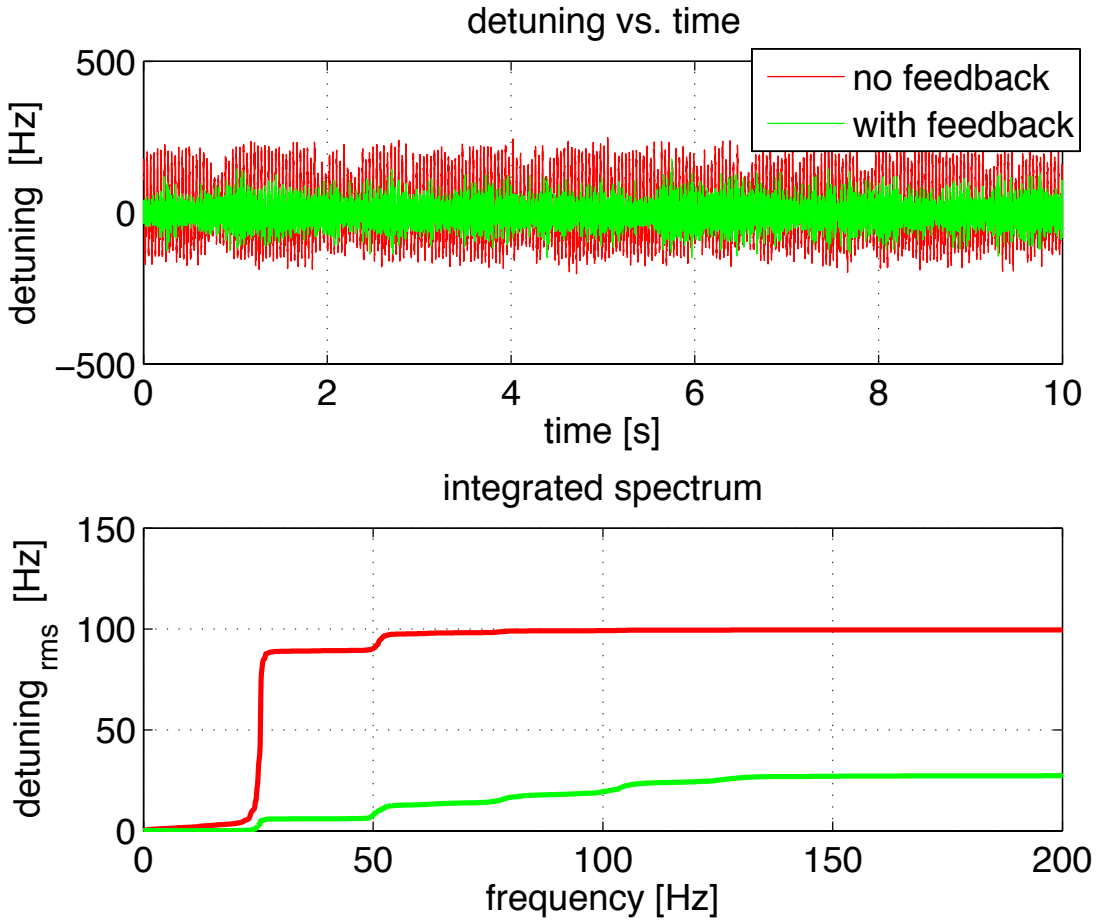

Figure 2.5.7: Microphonics compensation by a fast piezo-electric tuner in feedback mode at the Cornell SRF injector cryomodule. Top: Detuning vs. time with and without compensation. Bottom: Integrated micro- phonics spectrum for the two detuning cased shown above. The feedback loop reduced the microphonics level by $\sim 70\%$.

References

[1] Liepe, M. and S. Belomestnykh. *RF parameter and field stability requirements for the Cornell ERL prototype*. In *Proceedings of the 2003 Particle Accelerator Conference*, pages 1329–1331. Portland, USA (2003).

[2] Wilson, P. B. *High Energy Electron Linacs: Application to StorageRing RF Systems and Linear Colliders*. Technical Report SLAC-PUB-2884, SLAC (1982). http://www.slac.stanford.edu/cgi-wrap/getdoc/slac-pub-2884.pdf.

[3] Liepe, M. and J. Knobloch. *Superconducting RF for energy-recovery linacs*. Nucl. Instr. and Meth. A, **557** (1), pages 354 – 369 (2006). ISSN 0168-9002. doi:DOI:10.1016/j.nima.2005.10.099. Energy Recovering Linacs 2005 - Proceedings of the 32nd Advanced ICFA Beam Dynamics Workshop on Energy Recovering Linacs.

[4] Conway, Z. and M. Liepe. *Electromagnetic and Mechanical Properties of the Cornell ERL Injector Cryomodule*. In *the 23rd Particle Accelerator Conference*, pages 915–917. Vancouver, British Columbia, Canada (2009).

[5] Belomestnykh, S. *RF systems for CW SRF linacs*. In *The XXIV Linear Accelerator Conference*. Vancouver, British Columbia, Canada (2008).

[6] Bohlen, H. and T. Grant. *Vacuum Electron Device Limitations for High-Power RF Sources*. CWRF2008 Workshop on High Power RF (2008). http://cwrf08.web.cern.ch/cwrf08/.

[7] Caplot, M., *et al. New generations of RF amplifiers: from gridded tubes to dual technology solutions*. CWRF2008 Workshop on High Power RF (2008). http://cwrf08.web.cern.ch/cwrf08/.

[8] Walker, R. and R. Nelson. *Operating Experience and Reliability Update on the 5 kW CW Klystrons at Jefferson Lab*. CWRF2008 Workshop on High Power RF (2008). http://cwrf08.web.cern.ch/cwrf08/.

[9] Hovater, C. *CEBAF Energy Upgrade Low Level RF (LLRF) Activities*. Seminar at Cornell University (2006).

[10] *Preliminary datasheet of BLA10000CW 1300 MHz amplifier* (2010). Bruker BioSpin, private communications.

[11] (2010). Private communications with H. Buettig (HZDR Rossendorf) and P. Dupire (Bruker BioSpin).

[12] Stockwell, P., *et al. A Low Phase Noise 1.3 GHz Dielectric Resonator Oscillator*. http://psi.com.au/media/pdfs/FSC2006%20-%201-3%20GHz%20Dielectric%20Oscillators.pdf.

[13] Simrock, S., *et al. Performance of the new master oscillator and phase reference system at FLASH*. In *the twenty-second Particle Accelerator Conference*, pages 188–190. Albuquerque, New Mexico, USA (2007).

[14] Liepe, M. In *Proceedings of the 2003 Particle Accelerator Conference*. Portland, Oregon, USA (2003).

[15] Liepe, M. In *the 2005 Particle Accelerator Conference*. Knoxville, TN, USA (2005).

2.6 Electron transport lines

Overview

The electron transport lines consist of all of the electron beamline segments that are neither part of the Linacs nor part of the injector. Ideally they transport the beam without increasing the emittance. They comprise systems of dipoles, quadrupoles and sextupoles that steer and focus the beams onto the design orbit passing through the insertion devices (IDs), which stimulate the beams to radiate in the x-ray region of the spectrum. Instrumentation is provided to measure the beam properties and position with respect to the design orbit. The electron beamline portions presented in this chapter are shown schematically in Fig. 2.6.1.

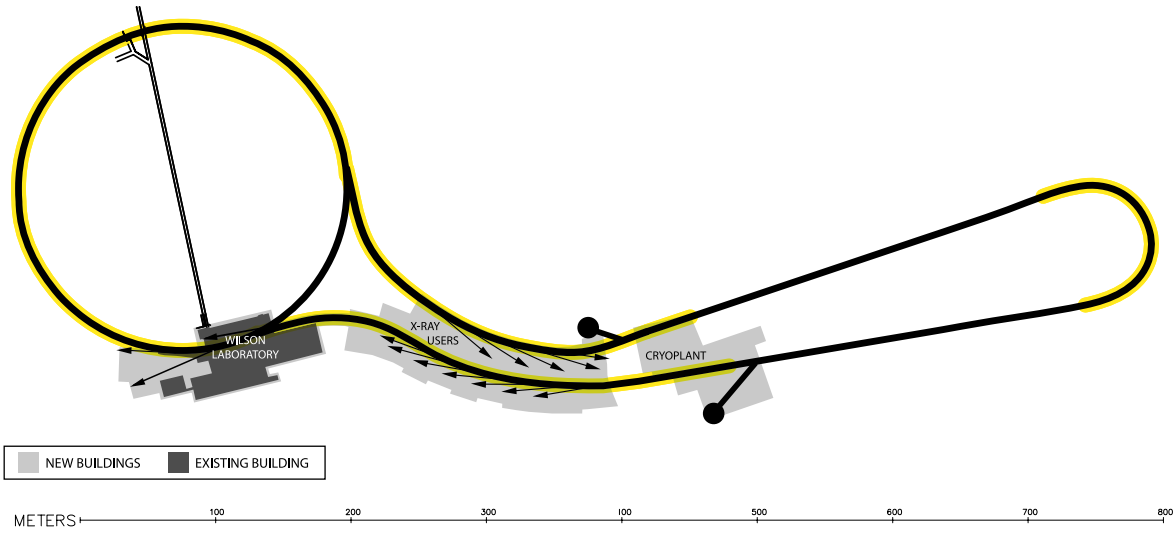

Figure 2.6.1: The yellow highlighting color indicates the portion of the electron trajectory discussed in this chapter

State of the art

Magnet quality apertures large enough for storage-ring service routinely reach one part in 10^4 compared to the ideal field at a radius large compared to the beam size. Residual gas pressures in the nanotorr regime are common at power depositions of several kW per meter. These qualities are adequate for the ERL. In component and beam-positional stability, the Swiss Light Source (SLS) currently holds the record for achieved vertical emittance in storage rings of < 3 pmrad in the vertical. The girders can be aligned to 50 to 100 μm. Using beam-based alignment, the rms orbit deviations from quadrupole centers can be held to about 10 μm [1]. At the LCLS, the orbit stability is measured at 3 μm rms with alignment of the undulator sections after beam-based alignment at under 10 μm [2].

ERL transport line parameters

The nomenclature used for the various transport line segments is shown below in Fig. 2.6.2 Numbers of components of various kinds needed in these segments are given in Tab. 2.6.1. A typical optical cell with component location is shown schematically in Fig. 2.6.3

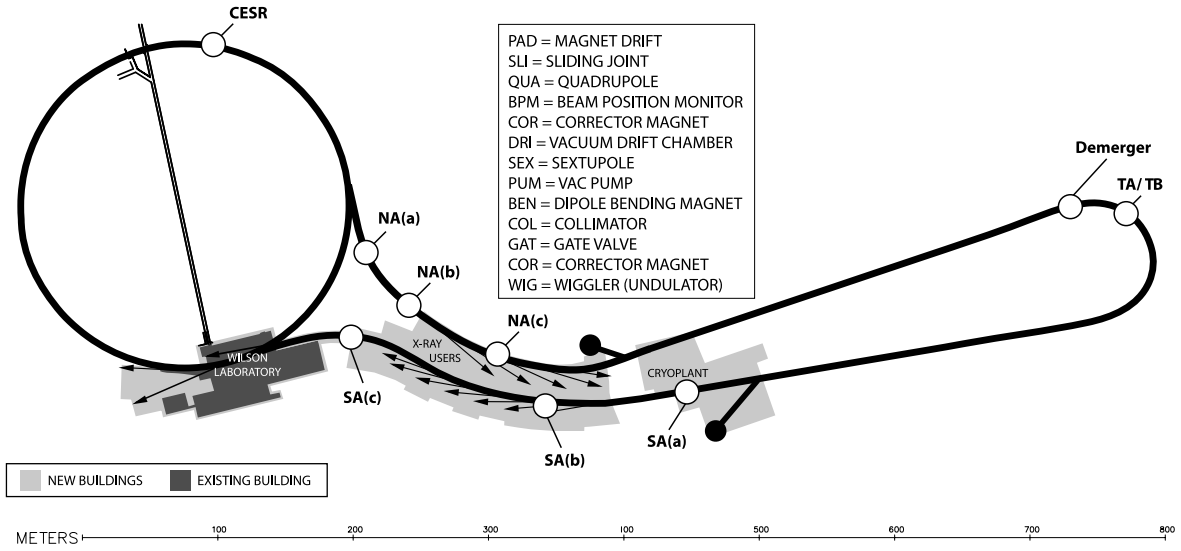

Figure 2.6.2: Segments of the electron-transport line

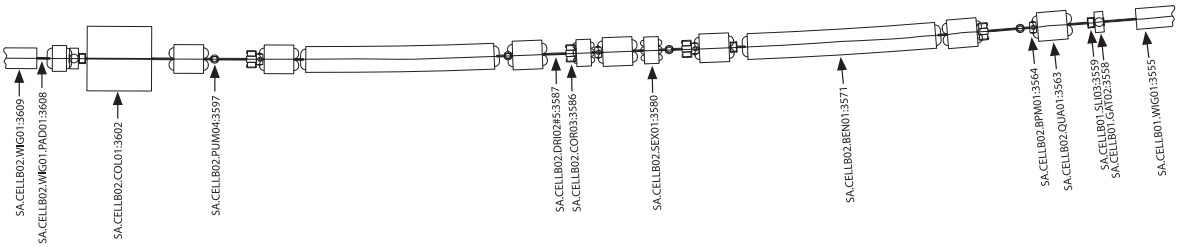

Figure 2.6.3: Typical cell schematic in south arc, undulator at right proceeding to next undulator at left. Note protective collimator and short bend immediately upstream of left hand undulator.

2.6.1 Magnet

Dipoles

The optics demands of an ERL are quite different from a storage ring since first- and second-order dispersion and time of flight terms must be carefully controlled at all points. These constraints combined with those of the terrain and existing infrastructure, plus other specialized needs, result in a large variety of dipole magnets in the design. The optics are arranged in achromatic cells comprising several dipoles and quadrupoles. In order to keep the beam orbit

Table 2.6.1: Some parameters of the transport line segments.

Quantity	TA	TB	SA	CESR	NA
Energy (GeV)	2.8	2.2	5.0	5.0	5.0
Length (m)	159.3	142.9	410.4	768	291.3
Dipoles (35 mm gap)	18	18	50	exist	29
Quadrupoles (bore 43 mm)	37	37	115	exist	63
Sextuples (bore 51 mm)	7	7	19	exist	16
10 m vacuum chambers	16	15	32	exist	24
Flanges	32	30	64	exist	48
Metal gate valves	3	3	20	exist	12
Tapers	1	1	20	exist	10
Beam Position Monitors	37	17	115	exist	63
Pump ports	47	41	58	exist	53
Lumped pumps	47	41	58	exist	53
Distributed pumps	$\approx$ 320m	$\approx$ 300m	$\approx$ 640m	exist	$\approx$ 480m
Vent ports	3	3	20	exist	12
Gauge ports	6	6	40	exist	24
RGA ports	3	3	20	exist	12
Sliding joints	19	17	51	exist	25
Ion clearing electrodes	16	16	41	42	28

Table 2.6.2: Dipole parameters by type.

Type	Quantity	Field (T)	Arc Length (m)	Radius (m)
1	4	0.467	4.000	35.7
2	6	0.443	3.870	37.6
3	6	0.351	3.802	47.5
4	16	0.578	3.000	15.8
5	14	0.479	3.000	15.8
6	4	0.292	2.955	57.1
7	12	0.312	2.937	53.5
8	8	0.425	2.925	39.3
9	2	0.312	2.923	53.5
10	2	0.319	2.920	23.7
11	4	0.331	2.822	50.4
12	12	0.253	2.807	65.9
13	2	0.602	1.995	15.2
14	2	0.300	1.000	25.3
15	4	0.443	0.500	37.6
16	1	0.136	0.489	122.4
17	14	0.028	0.300	600.0
18	1	0.057	0.249	294.1
19	1	0.136	0.245	122.4
20	2	0.070	0.250	238.1

within 10% of its transverse size, the dipole field strength within each achromat must track one another within 10^{-7}, whereas if all of the dipole fields in each achromat vary together the tolerance is a more reasonable 10^{-4}. In order to achieve this, and minimize the number of high-precision power supplies needed, the lengths of the dipoles have been adjusted to allow powering of all strong dipoles in each section of the ERL from a single power source. The fields and lengths of the individual dipoles are given in Tab. 2.6.2. In view of the need to avoid unnecessary halo, the field quality of the dipoles is stated as departure from the ideal dipole field by no more than ± 1 part in 10^4 within the 12.7 mm radius of the beam pipe. Subsequent simulations may ease this requirement. In considering the coil cross section, the cost of power over five years must be balanced with the cost of materials for construction. For that reason, we lean toward copper coils. The stated power supply requirements reflect a relatively low-current density in the coils. A concept cross section is shown in Fig. 2.6.4. The 14–600 m bend-radius magnets are provided to keep upstream-generated radiation from propagating down the x-ray beam lines into the hutches.

Quadrupole magnets

The field quality of the quadrupoles is specified for the ERL optics to be such that the field at 12.7 mm off-center is to be within 2 parts in 10^4 of the field of an ideal quadrupole at that radius. It is expected that the cores of these magnets will be manufactured using lamination

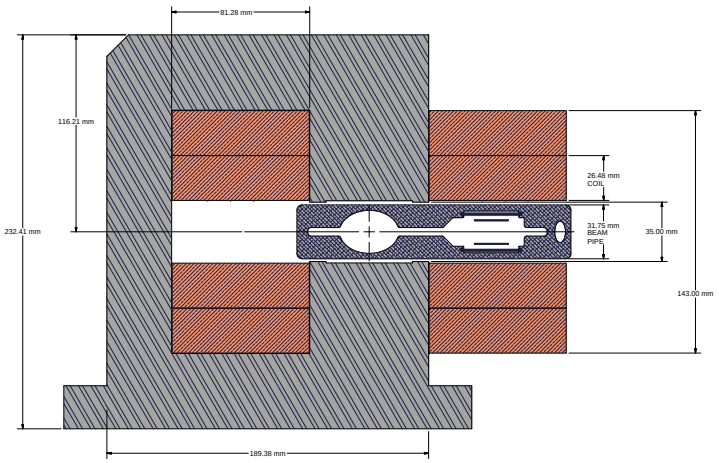

Figure 2.6.4: Concept design of a dipole using lamination technology

technology and that copper will be used for the coils to minimize the power usage. Figure 2.6.5 shows a cross-section. Table 2.6.3 gives the distribution of quadrupole strengths used in the optics design. The bore of the quadrupoles are 43 mm with an effective length of 0.5 m.

Sextupole magnets

Sextupole magnets are used to adjust the lattice parameters as described in §2.1. Figure 2.6.6 shows a cross-section of the 51 mm bore sextupoles having an effective length of 250 mm. Table 2.6.4 displays the strength distribution.

H and V steering magnets will be capable of +/- 0.4 mrad and will be installed in pairs occupying the same longitudinal space, in emulation of the current design contemplated for NSLSII [3]. The scheme is depicted in Fig. 2.6.7. There will be 150 of these in the warm parts of the machine, and 64 superferric pairs in the Linacs.

Magnet supports

In order to provide solid, low-thermal, low-vibration expansion mountings for the magnet strings comprising the ERL confinement system, a plinth wall is proposed. Figure 2.6.8 and Fig. 2.6.9 show the concept for the quadruple − sextupole pairs and dipoles separately.

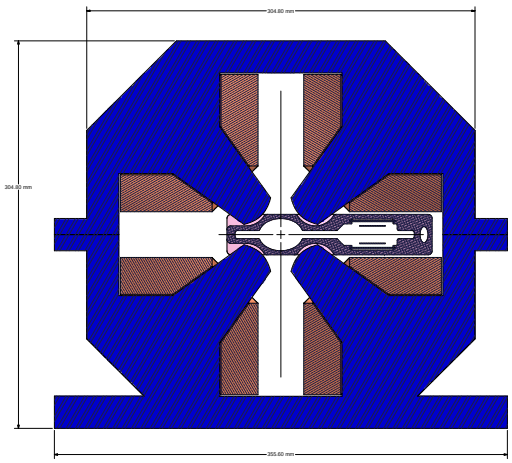

Figure 2.6.5: Quadrupole lamination cross section showing cut-outs for poles in vacuum chamber.

Table 2.6.3: Quad strengths – All quadrupoles are normal conducting with the exception of the Linac lenses which are superferric.

Strength (T/m)	Linac A&B	TA	SA	CESR	NA	TB
0.0 − 5.0	70	3	19	exist	8	5
5.0 −10.0	0	34	10	exist	10	28
10.0 −15.0	0	0	39	exist	22	4
15.0−20.0	0	0	7	exist	18	0
20.0 −25.0	0	0	22	exist	4	0
25.0−30.0	0	0	11	exist	1	0
30.0−35.0	0	0	7	exist	0	0
> 35	0	0	0	0	0	0

Table 2.6.4: Sextupole strength distribution.

Strength (T/m^2)	TA	SA	CESR	NA	TB
0−100	7	0	exist	16	7
100− 200	0	4	exist	0	0
200 − 300	0	1	exist	0	0
300 − 400	0	14	exist	0	0

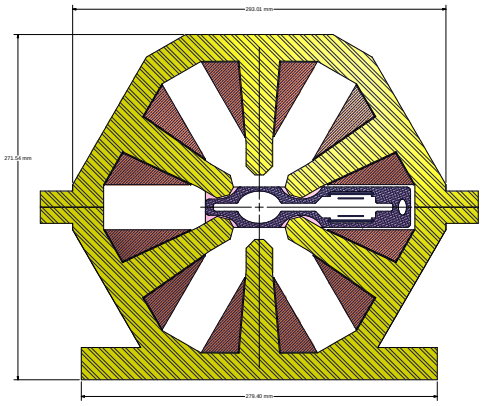

Figure 2.6.6: Sextupole lamination cross section showing pole cutout in vacuum chamber at sextupole location.

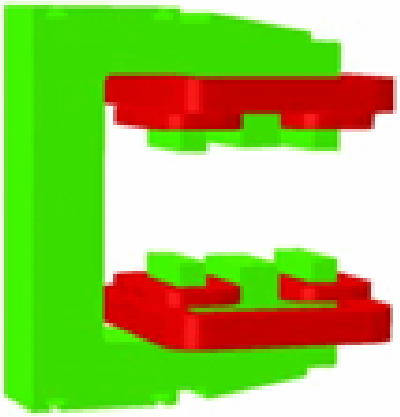

Figure 2.6.7: 3D depiction of the NSLS2 156 mm combined correction magnet that can be emulated in the ERL.

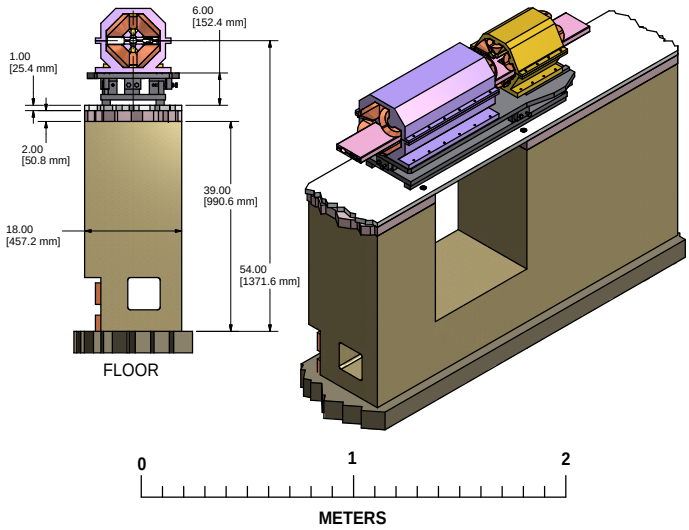

Figure 2.6.8: Quadrupole-sextupole combination mounted on the plinth wall with fine-position adjusting mount.

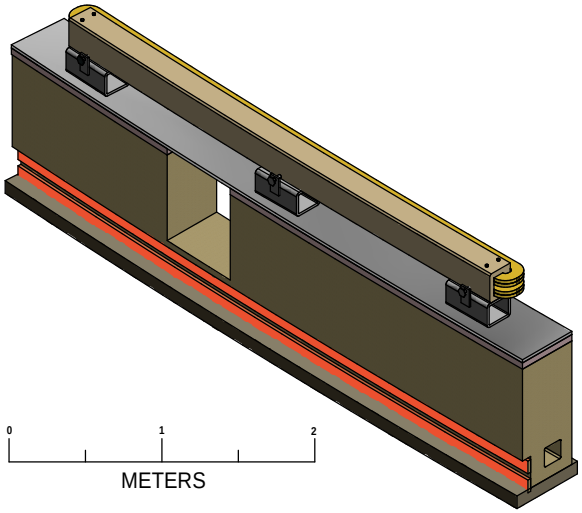

Figure 2.6.9: : Dipole mounted on the plinth wall.

Magnet power supplies

General requirements for all power supplies are listed in Tab. 2.6.5. The stability requirements shall be met for any combination of ±5% line-voltage change (both long and short term) and $\pm 5^oC$ change in ambient air temperature or $\pm 2^oC$ change in cooling water input temperature (long term). All power supplies dissipating more than 200 W must be water cooled. The control interface shall be capable of updating set point and readback of current at greater than 5 Hz rate. Power supplies and other electronics will be located in racks outside the shielding wall but as close to the magnets, vacuum equipment, and instrumentation as possible.

Table 2.6.5: Magnet power supply general parameters

Parameter	Conditions	Tolerance
Input Voltage	See tables below 60 Hz	±10 %
Power factor at load	At or above 50% rated power	$> 90\%$
Control resolution	See individual descriptions	18 or 16 bit
Output voltage ripple & noise		$< 0.2\%$ rms
Transient recovery	±5% line voltage transient	0.2% within 100 ms
Output current stability (see above)	1s− 24 hr referred to full scale	Dipole $\pm 2.5 \times 10^{-5}$; Quad $\pm 5 \times 10^{-5}$ 6-pole $\pm 1.0 \times 10^{-4}$; Corr. $\pm 2.5 \times 10^{-5}$
Cooling water	Operating	30 ± 5°C. 100 psi max

Dipole power supplies

Five large dipole-power supplies will be required − one for each section of the ERL. Two smaller supplies will be used for strings of short (30 cm) dipoles in each of the arc sections. All require high quality regulation with 18-bit control and provision for monitoring at a similar resolution. Output voltage and currents are shown in Tab. 2.6.6

Table 2.6.6: Dipole power supply parameters

Quantity	Output Voltage (V)	Output Current (A)	Input Voltage (V)
2	300	750	480 −3 phase
3	200	750	480 −3 phase
2	80	20	208−1 or −3 phase

Quadrupole power supplies

Each quadruple requires an independently adjustable current. Most quadrupoles' requirements are satisfied by 1.5 kW power supplies with a smaller number between 1.5 and 5 kW as shown in Tab. 2.6.7 High quality regulation with 18 bit resolution for control and monitoring is needed.

Table 2.6.7: Quadrupole power supply parameters

Quantity	Output Voltage (V)	Output Current (A)	Input Voltage (V)
211	15	100	208 −1 phase
45	25	200	208 −3 phase

Sextupole power supplies

Each sextupole requires an independently adjustable current with power supply parameters in Tab. 2.6.8.

Table 2.6.8: Sextupole power supply parameters

Quantity	Output Voltage (V)	Output Current (A)	Input Voltage (V)
49	30	50	208−1 phase

Dipole corrector power supplies

Each dipole corrector (steerer) requires independently adjustable bipolar current. These supplies are designed to regulate well around zero current and cross-over sign without significant transients. Requirements are given in Tab. 2.6.9

Table 2.6.9: Corrector power supply parameters

Quantity	Output Voltage (V)	Output Current (A)	Input Voltage (V)
290	±30	±50	208 −1 phase

2.6.2 Insertion devices

Currently the Delta undulator is the primary candidate for the insertion devices (see Tab. 2.6.10 for a list of parameters), which include 3 of 25 m length and 11 of 5 m length in the plan as shown in layout diagram Fig. 2.6.10.

2.6.3 Vacuum chambers, pumps and instrumentation

The vacuum chamber, pumping and vacuum instrumentation as well as BPM and ion clearing electrode concepts are dealt with in §2.2. A rough shape of the chamber is indicated by figures of magnet cross sections in the previous paragraphs.

2.6.4 Collimators

Intra-beam scattering (IBS) results in a halo of electrons about the core of the electron beam which, if neglected would result in unacceptable radiation in the insertion devices of small

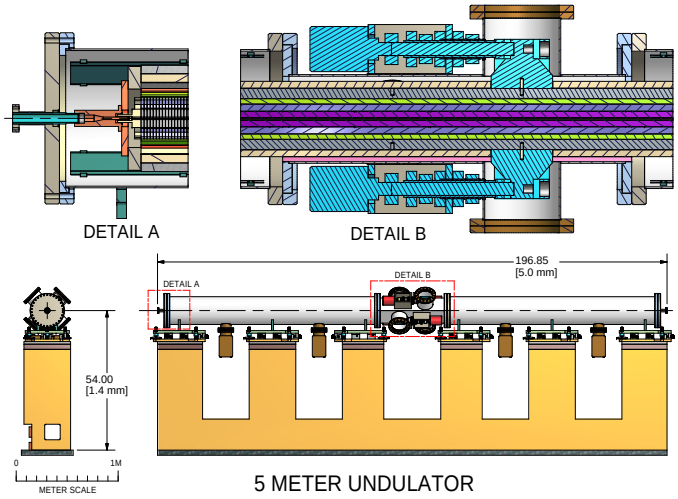

Figure 2.6.10: Delta undulator 5 m length supported by the plinth wall.

Table 2.6.10: Undulator parameters

Unit Length	5 m
Period	20 mm
Material	NdFeB
Gap/Bore	5 mm
Peak Field	0.91 T helical
	1.296 T planar

(5 mm) aperture. Protective collimators are thus necessary to assure that the consequent radiation can be dealt with by the personnel shielding. In the x-ray halls, the Touschek and Intra Beam Scattering (IBS) losses at the collimators are typically one to a few pA. In other areas, the IBS losses are more substantial and need a different collimator type. Concepts for the two types of collimators are discussed in the vacuum chapter, §2.2.4.

2.6.5 Extraction beamline (EX)

Purpose

It will be advantageous to have a low repetition rate, low emittance beam of variable current for studying matters relevant to the physics of the ERL and various FEL schemes. Seeding schemes, XFEL-O, and other studies will arise as accelerator science advances.

Injection

The bunches for the extracted beamline could come from the dedicated operation of the primary injector up to a bunch charge of ≈ 200 pC or somewhat higher. If higher charges or simultaneous operation with x-ray running are required, then a second injector will be needed. Space for such an injector is available. A repetition rate of up to 10 kHz with 1 nC per bunch is envisioned.

Layout

Figure 2.6.11 shows the layout of the EX section beginning just downstream of the beam stop. The fast kicker discussed in §2.1.12 produces a 1 mrad bend, initiating the extraction process. A bunch compressor and transport optics deliver the extracted beam to the shielded area shown in the figure, terminating in a beam stop capable of 5 kW dissipation. The part of the EX section downstream of the bunch compressor is shielded by a special heavy concrete enclosure.

2.6.6 CESR

As discussed in §2.1.8, the baseline design is to use a portion of the existing CESR lattice with all its ancillary hardware as part of the return arc. While the IBS generated in CESR is relatively large and the emittance growth per unit length greater than in other parts of the transport, both are acceptable. The emittance of the beam in the north arc after the CESR portion of the transport is degraded by only a factor of two. As a later upgrade, the CESR arc can be modified for reduced IBS losses and smaller emittance growth.

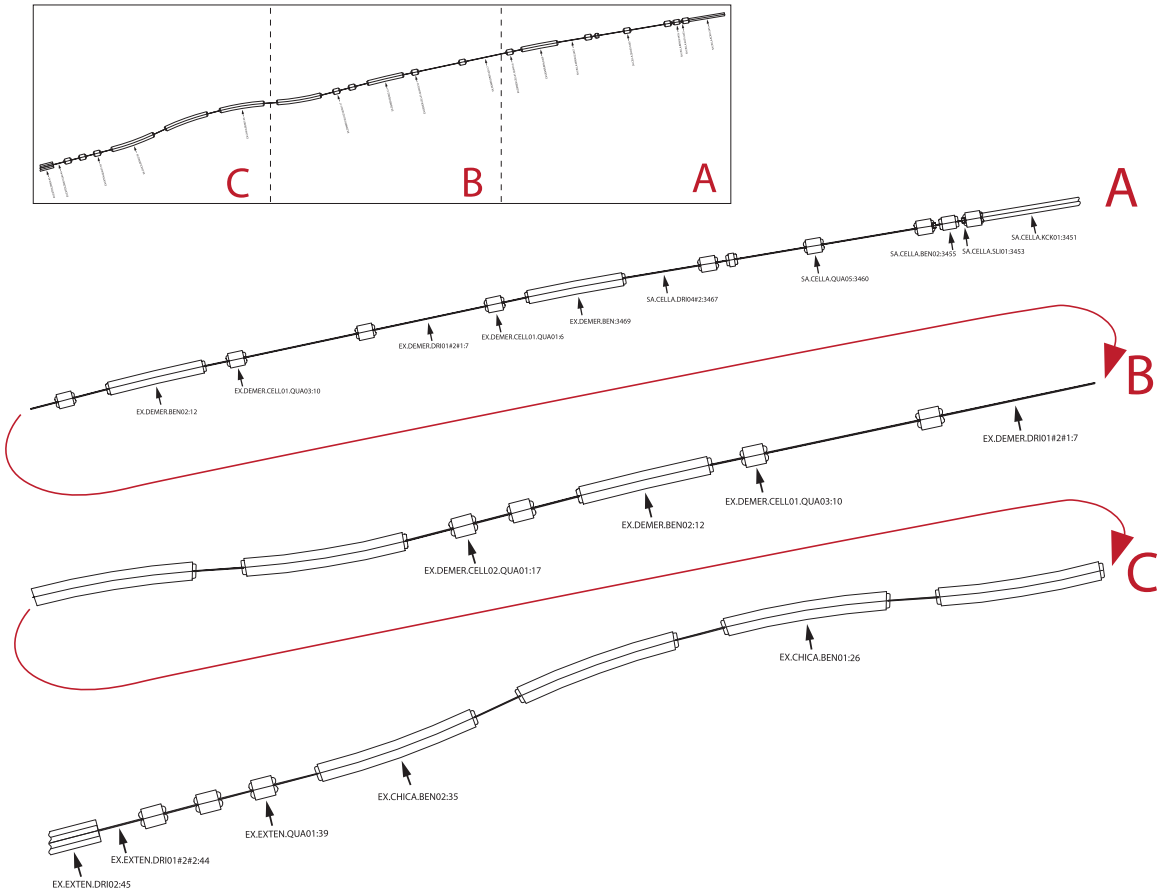

Figure 2.6.11: Layout of the EX beamline beginning just downstream of the stop for the decelerated beam.

References

[1] Boege, M. *et al. Ultra-low vertical emittance at the SLS.* In *The 23rd Particle Accelerator Conference*, pages 2279–2281. Vancouver, British Columbia, Canada (2009).

[2] Emma, P. *First lasing of the LCLS X-ray FEL at 1.5 Angstrom.* In *The 23rd Particle Accelerator Conference*, pages 3115–3119. Vancouver, British Columbia, Canada (2009).

[3] Danby, G. *et al. Design and measurement of the NSLS II correctors.* In *The 23rd Particle Accelerator Conference*, pages 148–150. Vancouver, British Columbia, Canada (2009).

2.7 Insertion devices

2.7.1 Introduction

The Cornell ERL is designed for up to 14 x-ray beamlines with undulator magnets used as radiation sources. The type of the undulator magnet for each beamline is based on the beam line purpose. Tab. 2.7.1 lists x-ray beamlines according to function with the required photon energy range and space available for the various IDs.

The unique properties of the ERL x-ray beams are determined by a high-quality electron beam passing through its insertion devices comprising periodic arrays of magnets or wire coils that 'wiggle' the beam, and in the process, produce the optimal hard and soft coherent x-ray beams for experimentation at the ERL facility.

Third-generation synchrotron radiation facilities have brought ID technology to a high state of optimization for storage-ring use. These developments form a solid base of principles and practices that can be advanced even further for ERL applications. The advancements involve optimizations to cover various photon energy ranges, taking advantage of the very small ERL source size, divergence, polarization control of the emitted x-rays, and ease of tunability. The ERL machine gives ID designers new freedom in its magnetics due to the interesting new machine properties. Since the ERL is not a storage ring, no extra horizontal aperture is required for injection and thus the ID magnets may be close to the electron beam. Small bore devices with an inner diameter of 5 mm or smaller are now practical.

The electron beam energy is high enough at 5 GeV and the emittance and energy spread are small enough to make small-period IDs perform exceptionally well. Undulators with small gaps (and therefore small periods down to about twice the gap dimension) become feasible. More periods per ID unit length mean more flux and spectral brightness per unit length.

In addition, the lattice and layout of the ERL can accommodate long ID lengths compared to standard storage-ring ID straights. The ERL's very low energy spread of $\Delta E/E$ of 2×10^{-4} means that constructive interference can be maintained even in 1000-period long devices. This is important not only for maintaining a very high average x-ray flux on the x-ray beamline, but may permit monochromator-less beamlines, thus removing all the optical issues of associated coherence preservation through the optics.

A further feature is the practical use of the higher harmonics of the x-ray spectrum for high-photon energy experiments (up to 80–100 keV), a scheme that is well-developed by the current third generation storage-ring sources.

There are, of course, concerns and optimizations for any technology that breaks new territory. Some of the design concerns for ERL insertion devices (as well as for many existing IDs) are:

- Cost per meter of the segment IDs
- Predicted reliability over a 10 year period
- Overall complexity of mechanics and magnetics
- Radiation damage resistance of undulator technology
- rms phase errors (in degrees) from period to period down the length of the device

Table 2.7.1: The 14 ID beamlines at Cornell's ERL. The beamlines are optimized for x-ray use in the indicated energy ranges. The purposes of the beamlines are indicated and range from coherent diffraction to several kinds of nanoprobes.

beamline	application	mode	ID length	E (keV)	BL length
Coherent diffraction and XPCS	Microscopy and dynamics at nm	Hi-Coh	25 m	5-25	80 m
Nanoscope, Nanoprobe	TXM/STXM with high NA	Hi-Coh	5 m	5-25	75 m
Soft x-ray	Microscope for biomaterials, XMCD nanomagnetic imaging, ARPES	Hi-Coh	5 m	0.1 - 5	75 m
Nanoprobe	General, 1 nm beam	Hi-Coh	5 m	1-10	80 m
Protein Crystallography I	High throughput, microfocus	Hi-flux	5 m	5-25	40 m
Protein Crystallography II	Wide range tunability	Hi-flux	5 m	5-25	40 m
Inelastic x-ray Scattering	1 meV resolution	Hi-flux	25 m	5-25	80 m
Femtosecond timing	Charge density waves	Ultra-fast	25 m	2-25	80 m
Materials Science I	High pressure science	Hi-flux	5 m	5-100	75 m
Materials Science II	General material science	Hi-flux	5 m	5-25	45 m
Resonant Scattering	x-ray science	Hi-flux	5 m	5-25	80 m
SAX I, XPCS, grazing incidence	Mesoscopic science	Hi-flux	5 m	5-25	80 m
SAX II	Mesoscope science	Hi-flux	5 m	5-25	80 m
Diagnostics	Beamsize and position measurements	All modes	5 m	5-25	40 m

- Ability to correct phase errors when observed
- Metrology to determine field qualities and errors from Hall probe, scanning wires, etc.
- Metrology to verify what has been produced and if the magnetic field qualities change over years of use
- Amount of development needed for prototypes and production versions
- What is the practical limit to useful harmonic number?
- How quickly (in hours or days) does it take to remove the device after a damage incident and replace it with a spare?

- Vacuum qualities - Does it take a lot of conditioning to get it ready to work in the ERL?
- How quickly (in minutes or seconds) will it take to tune from circular to linear polarization?
- How reproducible will the magnetic fields be after a change from linear to circular polarization and back to linear again? (or for any other mechanical or temperature change)
- How can the trajectory be tuned so that the integral of B*dL over the device length is low enough not to disturb the ERL electron optics?
- How will beam image currents and HOMs be dealt with?
- Will separate quadrupoles and collimators be periodically needed along the 25 m ID magnetic length device? What are the magnetic field tolerances needed for a 1000-pole undulator to have a relative line width equal to 1 divided by the number of periods? What are the operating and maintenance costs predicted to be over the life of the ID?

The ERL insertion device group is investigating insertion devices based on pure permanent technology as well superconducting technology. The state of progress in each of these areas is discussed in the next two sections.

2.7.2 Permanent magnet insertion devices

General remarks

ERL insertion devices based on permanent magnets (PM) are being designed to take advantage of unique ERL operational characteristics. In contrast to storage rings, an ERL does not require additional space around electron beams for newly injected particles. Thus, the beam aperture size (and the ID gap) can be significantly reduced and made round. This feature alone allows placement of magnetic material very close to the beam axis as well as permitting a symmetrical magnetic structure around the electron beam. The consequence of a smaller gap is a stronger magnetic field. The opportunity for a magnetic structure with 4-fold symmetry simplifies construction and magnetic field tuning. Both of these features are incorporated into the Delta undulator design.

The Delta design may also be useful for Free Electron Laser (FEL) applications. Although ERL and FEL machines use the same type of electron beam and their operations are similar, the ID requirements are quite different for each application. Early FEL undulators were generally not adjustable in their magnetic field value and the x-ray energy was adjusted by varying the energy of electron beam. This is not practical with an ERL facility where it is important to provide x-rays with various energies for several experimental stations working simultaneously and to dynamically tune the photon energy as the experiment progresses. Another significant difference between FEL and ERL machines is that the average beam current in the Cornell ERL is planned to be two orders of magnitude larger than at an XFEL such as the LCLS and consequently the beam-generated heat load inside the ID is much higher.

Two candidates for permanent magnet ID designs that can be used at an ERL are considered. The prime candidate is of an innovative ‘Delta’ type. A second plan is to adapt a more conservative in-vacuum planar-type undulator approach.

State of the art

At present, the brightest x-ray beams are generated by planar undulators based on permanent magnet (PM) technology. Advanced types of PM undulators developed recently are listed below.

In-vacuum undulators (IVU)

The first in-vacuum undulator was constructed and put into operation at KEK (Japan) in 1991 [1]. IVUs have magnet arrays enclosed in a vacuum vessel. The enclosure eliminates the need for the vacuum beam pipe inside the ID and allows reduction of the undulator gap down to a size of a few millimeters. Smaller gaps allow for a stronger magnetic field, which in turn can be translated into a device with more poles per unit length and, as a consequence, can produce more x-ray flux and higher x-ray brightness than larger gap devices. Presently the IVU technology is well established. In-vacuum undulators are considered standard devices at ESRF [2], [3] and other laboratories. The IVU operating at NSLS beamline X25 has the smallest gap of 3.3 mm [4].

Cryogenic permanent magnet undulators

Cryogenic Permanent Magnet Undulators (CPMU) have evolved directly from the IVU type. In [5], the authors propose to utilize a $\sim 20\%$ increase in the remnant field strength of NdFeB PM material as well as significant increases in the intrinsic coercivity at cryogenic temperatures of $\sim$ 150 K. The latter characteristic is critical for the magnet to resist radiation damage coming from the nearby electron beam. A CPMU prototype was developed, constructed, [6] and installed in a storage ring at ESRF. First operational experiences and performance studies are described in [7]. The main operational concerns are the temperature gradients across the magnetic material arising from the beam-induced heat load and the impact of the undulator structure on the local beam vacuum. The temperature gradient across the magnet material causes a variation of the magnetic field strength, which may reduce the undulator performance. Vacuum degradation may result in production of bremsstrahlung radiation in the ID, which will be sent down the x-ray beamline. So far this undulator design has demonstrated reasonable performance.

General requirements for ERL IDs

Peak field and K-parameter requirement

The required x-ray energy range for the typical undulator in Tab. 2.7.1 extends from 5 to 25 keV with middle energy of around 15 keV. To provide reasonable photon flux in this range, the synchrotron radiation critical energy should be not less than 15 keV. Using an expression from reference [8], see p. 184:

$$\epsilon_c = 0.655\,\mathrm{keV}\left(\frac{E}{\mathrm{GeV}}\right)^2\left(\frac{B}{\mathrm{T}}\right) \tag{2.7.1}$$

and assuming a 5 GeV beam energy, one finds that the peak field should be 0.9 T or higher.

The maximum value of the undulator parameter K, ($K = 0.934 \cdot (B/\ \mathrm{T}) \cdot (\lambda/\,\mathrm{cm})$, where B is the peak field, and λ is the undulator period), can be derived from the requirement that the 1st and 3rd undulator radiation harmonics should overlap. The expression for photon energy in a planar undulator, see [8] p. 188, for the i^{th} harmonics is:

$$\epsilon_n = 9.49\,\mathrm{keV} \cdot i \cdot \left(\frac{E}{\mathrm{GeV}}\right)^2 \frac{1}{(1+\frac{1}{2}K^2)} \left(\frac{\lambda_\mathrm{p}}{\mathrm{mm}}\right)^{-1} \tag{2.7.2}$$

where λ_p is the undulator period length.

Knowing that at $K = 0.5$ the 1st harmonic photon flux will drop by 50% (see Table 1 in [8] p. 190) one can find that, to satisfy the 1st and 3rd harmonics overlap condition, the undulator parameter K should equal 2.25.

Optical phase errors (phase shaking)

According to [9], reduction of the photon flux of i^{th} undulator harmonics due to undulator phase errors can be estimated as:

$$\frac{dF_n}{F_n} \approx -i^2\,\theta^2 \tag{2.7.3}$$

where $\frac{dF_n}{F_n}$ is the normalized flux reduction and θ is the rms phase error. For a reduction $\frac{dF_n}{F_n} \sim 10\%$ and $i = 5$ (the maximum harmonic number planned for use), an rms phase error of 3.70° or less is required.

Orbit walk-off

Using the criterion that the orbit walk-off should not exceed 10% of the beam size inside the undulator, the walk-off error should be less than 1 μm. The actual tolerable walk-off error for each undulator will vary with the emittace produced by the specific operating mode and the chosen beta function.

PM radiation damage and ID life-time estimation

The radiation damage dose rate to the ID can be estimated assuming that the major source of radiation damage is only due to high energy electrons scattered from the residual gas inside of the ID. Starting from the small-angle Coulomb scattering cross-section

$$\frac{d\sigma}{d\Omega} = \frac{4\,Z^2}{\gamma^2}\,r_e^2 \frac{1}{(\theta^2+\theta_{\mathrm{min}}^2)^2} \tag{2.7.4}$$

where Z is the atomic number, γ the relativistic factor, and r_e the classical electron radius, the flux rate of high energy electrons through a cylindrical surface of radius a per unit length as a function of residual gas density n_{gas} , beam current I_e and distance s from the undulator upstream end:

$$F(s) = \frac{I_e}{e}\,n_{\mathrm{gas}}\,\frac{4\,Z^2}{\gamma^2}\,r_e^2\,\frac{s^2}{a^2} \tag{2.7.5}$$

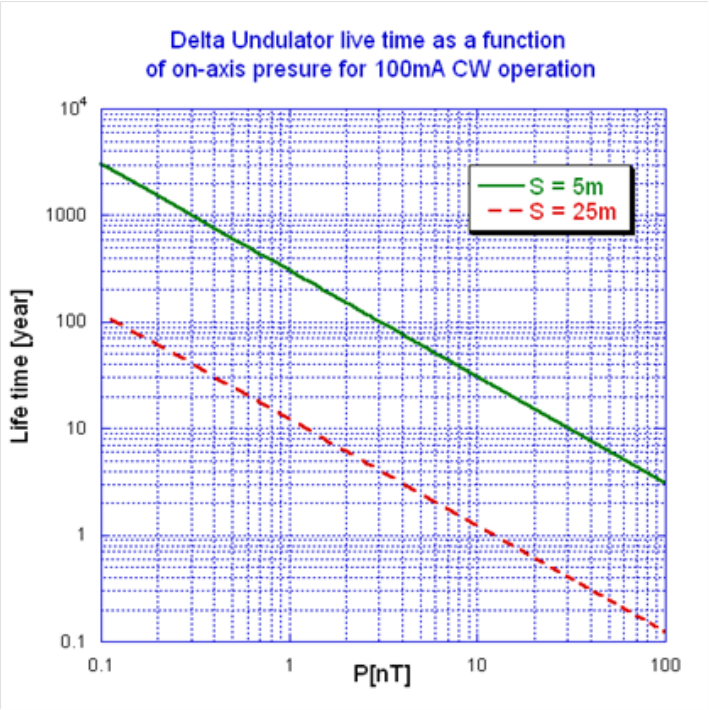

Figure 2.7.1: Estimated ID lifetime as function of on-axis pressure.

Assuming that residual gas content is similar to air, i.e. Z=7.5 (This is the worst possible scenario. In practice, in the absence of vacuum leaks, the content of residual gas is dominated by hydrogen with Z=1), 5 mm bore, 5 GeV beam energy and that all scattered electrons deposit energy into $\sim$ 5 mm layer around bore, the estimated rate of the dose accumulation is:

$$\dot{D}\left(\frac{\text{rad}}{\text{s}}\right) = 8.2 \times 10^{-5} \cdot \left(\frac{I_e}{\text{A}}\right) \cdot \left(\frac{P}{\text{nT}}\right) \cdot \left(\frac{s}{\text{m}}\right)^2 \tag{2.7.6}$$

Following [10], the estimated dose causing a 1% PM demagnetization at the downstream end of the PM undulators is 2 Mrad. Using this dose as a criterion, the dependence of the ID lifetime on the on-axis vacuum is shown in Fig. 2.7.1 It should be noted that although this estimate is made for a round bore ID like the Delta undulator, it can be applied to IDs with flat poles after small corrections.

Other general remarks

The undulator gap size is planned to be 5 mm. The choice is driven by the following arguments. The smaller gap results in a stronger magnetic field, which can be translated to a device with a shorter period, many more poles, and consequently a higher photon flux. However, the small gap will limit the access for magnetic field measurement, increase beam heat load and increase the risk of radiation damage due to beam losses. A 5 mm gap seems to be a reasonable compromise. The undulator period is dictated by the requirement of fundamental and third undulator harmonics overlap. For a 5 GeV beam energy, a 5 mm gap and NdFeB 40SH

magnetic material to provide harmonic overlap for $K = 2.25$, the undulator period should be $\sim$ 19 mm for a Delta and $\sim$ 24 mm for a PPM structure.

The choice of undulator length depends on many factors, including parameters of the magnetic measurement facility, and transportation capability. Shorter sections will be easier to build, tune, and transport. However, with longer sections available, the ID space can be used more efficiently. Both 2.5 m and 5 m lengths are under consideration at the present time. An in-vacuum configuration is a natural choice for 5 mm gap IDs. This type of undulator is well established. Operation at low temperature is preferable but not critical. As mentioned in the 'state of the art' section, ID operation at $\sim$ 120 K would increase PM intrinsic coercivity (H_{ci}) and increase the remnant field (B_r) by $\sim$ 10%. The first factor increases the resistance to radiation-induced demagnetization; the second would result in higher peak undulator field. In addition, lowering the magnet temperature would significantly reduce its out-gassing rate. This type of operation is presently under evaluation.

2.7.3 'Delta' undulator

The delta undulator was designed in anticipation of a new era of synchrotron radiation sources based on energy recovery Linac techniques [11]). The device is called a 'delta' undulator based upon the shape of its PM blocks, and makes optimum use of the unique conditions expected in the ERL. In comparison with conventional undulator magnets, it has:

- Full x-ray polarization control. It may generate various states of linearly polarized x-rays as well as left and right circular polarized x-rays with photon flux much higher than existing Apple–II type devices
- The delta design has 40% stronger magnetic field in linear and approximately two times stronger fields in circular polarization modes. These advantages translate into higher x-ray flux
- The undulator is very compact. The tested prototype was enclosed in a 25.4 cm diameter cylindrical vacuum vessel.

These advantages were achieved through a number of unconventional approaches. Among them is control of the magnetic field strength via longitudinal motion of the magnet arrays. The moving mechanism is also used for x-ray polarization control. The compactness is achieved using a recently developed permanent magnet soldering technique for fastening PM blocks.

Concept

Four identical magnet arrays assembled on base plates are symmetrically placed around the beam axis as illustrated on Fig. 2.7.2. One pair of magnet arrays generates vertical magnetic fields; another set of magnets generates the horizontal fields. Field strength is controlled by an adjustable phase (AP) scheme [12] where the peak field is controlled by moving the magnetic arrays relative to each other in the longitudinal (electron beam) direction. The same motion is used to control the polarization. To provide longitudinal displacement for the field strength and polarization control, magnet arrays are mounted on miniature rails attached to the thick plates, forming a rigid frame. In the linear polarization mode, the array pairs generating

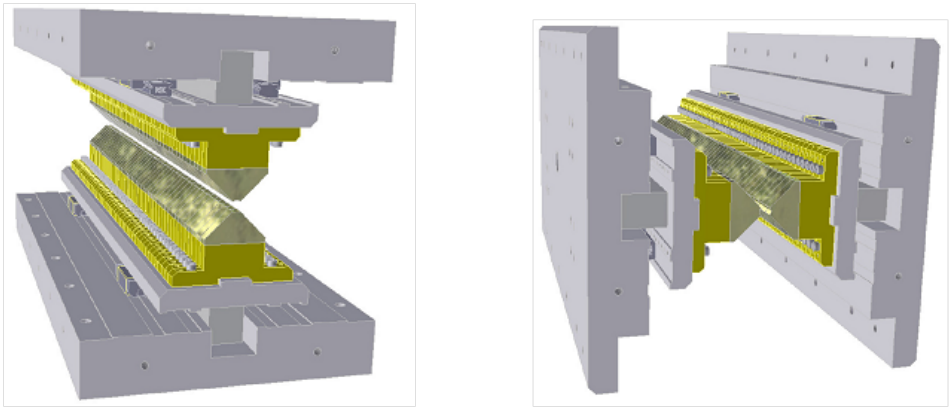

Figure 2.7.2: Two pairs of magnet arrays forming a Delta undulator structure. The left side shows arrays that generate the vertical field and the right side the horizontal.

vertical and horizontal magnetic fields are in phase. The resulting fields are planar and $\sqrt{2}$ stronger than those from a single pair. In the helical mode, the pairs are shifted relative to each other by 1/4 of a period or by 90^o, so the resulting field is helical. To change the field strength, two arrays forming the pair should be shifted longitudinally in opposite directions.

This arrangement can be considered as a combination of two independent AP undulators. It can also be viewed as a kind of Apple–III structure as mentioned in [13]. The Delta structure has similarities with the undulators described in[14] and [15] as well.

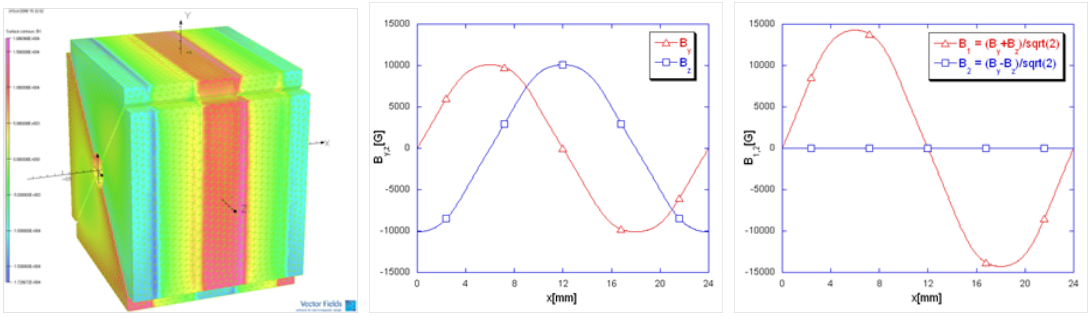

Figure 2.7.3: 3D model used in magnetic field modeling (left) and magnetic field components on beam axis for helical mode (middle) and planar mode (right) for 24 mm period.

Magnetic field properties

An example of 3D magnetic modeling is shown in Fig. 2.7.3 (left plot). The model has 5 mm diameter bore, 0.5 mm wide slits between magnetic arrays, and a NdFeB 40SH PM material with $B_r = 1.26$ T. The two other plots show magnetic field components along the beam axis for the helical and planer modes calculated for a 24 mm period. The peak field is 1.05 T in the helical mode (middle plot), when the horizontal field phase is shifted by 1/4 of a period

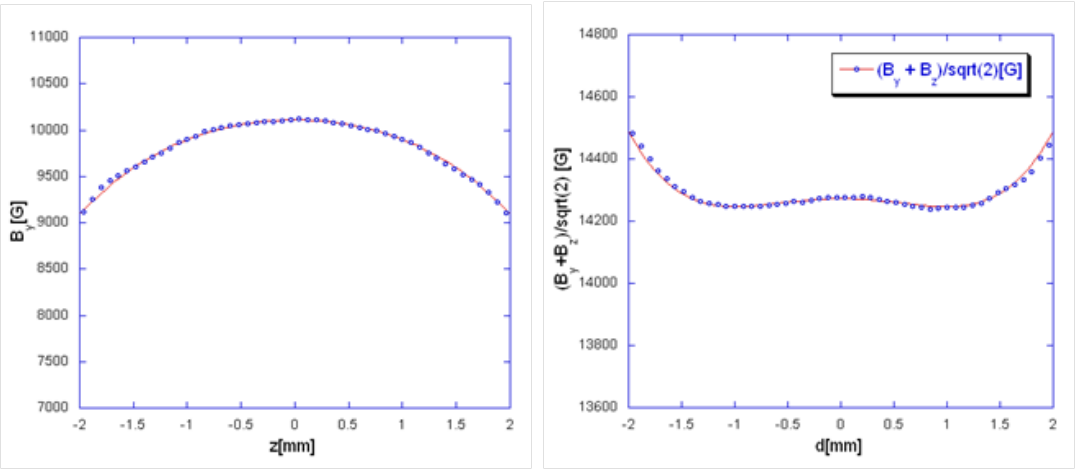

Figure 2.7.4: Field roll-off in helical (left) and planar (right) modes.

(90^o) relative to the vertical set of magnets. The calculated peak field is 1.43 T in the planar mode when both vertical and horizontal fields add in phase.

The field variation across the bore (roll-off) is calculated in Fig. 2.7.4. In the helical mode (left plot), the variation of the ±1 mm region around the central axis can be approximated by $dB/B \approx -0.02\, d^2/\,\mathrm{mm}^2$ where d is the distance from the axis. In planar mode, the field roll-off can be approximated as $dB/B \approx -0.0037\, d^2/\,\mathrm{mm}^2$. These variational formulas predict that 100 μm of misalignment of the undulator magnets relative to the beam axis (or beam trajectory relative undulator axis) will cause a $\sim\ 2 \times 10^{-4}$ variation of undulator K parameter in helical mode and 0.3×10^{-4} in planar mode. Both these variations due to magnet misalignments are acceptable.

Dependence of the peak field and undulator K parameter on the period for a 5 mm bore is depicted in Fig. 2.7.5 (left). The data indicate that fundamental and third-order undulator harmonics will be overlapping at a 19 mm period ($K = 2.25$ criteria). The plot on the right side of Fig. 2.7.5 compares a Delta undulator peak field as a function of a gap to period ratio with other PPM undulator magnet designs. The data for comparison were taken from [16]. The advantage of the Delta structure is evident in the considerably higher peak fields in both the planar and helical modes.

Mechanical design and beam heating load

Mechanical properties of the Delta undulator structure were analyzed in [11] and tested in [17]. It was found that the undulator components experience the highest stress in the planar mode. The left plot in Fig. 2.7.6 depicts results of an ANSYS stress analysis made for the tested prototype model of an undulator frame operated in a planar mode. The illustration on the right side of Fig. 2.7.6 shows the simulated effect of a heat load generated by the beam image current [11]. The temperature rise of the top of the magnets should not exceed 0.20°C at a maximum of 28 W/m of ERL beam-induced heat–loading relative cooling elements attached to the underside of the magnet arrays.

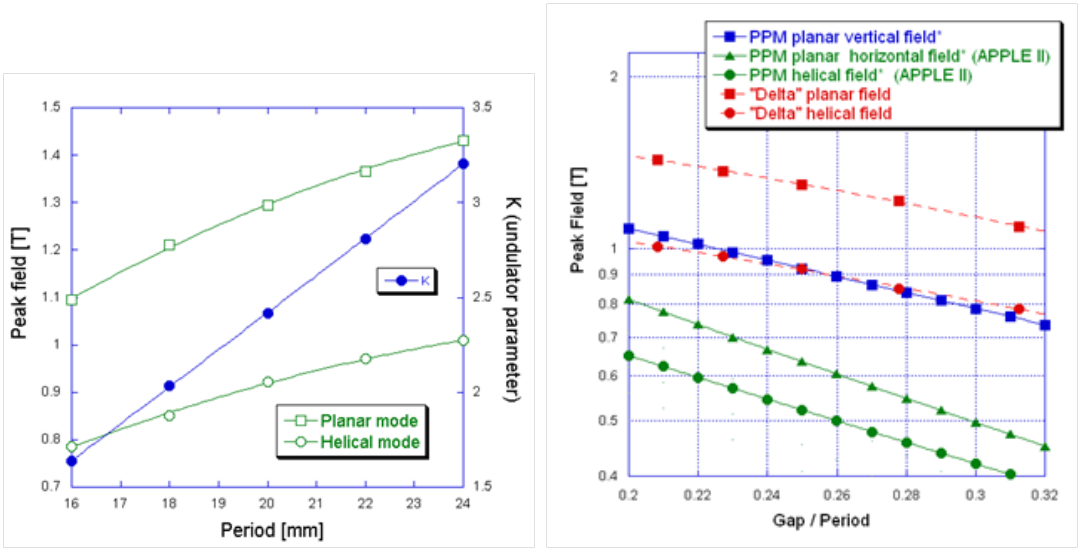

Figure 2.7.5: Left plot – peak field in planar and helical modes and undulator parameter K as a function of period. Right plot – peak field as function of gap over period ratio for 'Delta' and others PPM undulators.

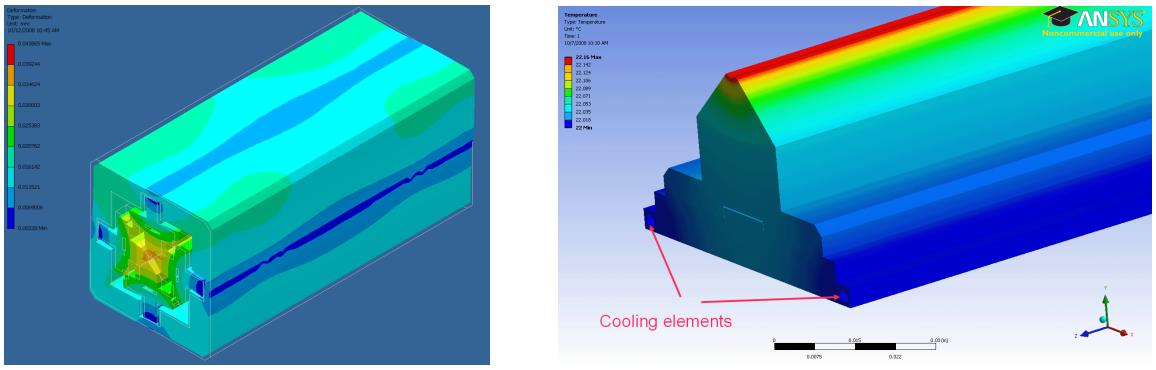

(a) Frame deformation

(b) Heat load

Figure 2.7.6: (a) Undulator frame deformation in the planar mode ranging from 3 μm to 44 μm, and (b) results of heat load analysis holding the device at 22°C with a maximum increase of 0.16°C.

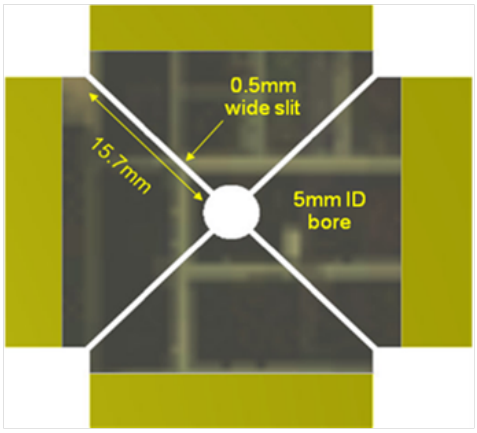

Figure 2.7.7: Delta undulator structure cross-section with ventilation channels dimensions.

On-axis vacuum considerations

The on-axis vacuum can be estimated in the following way. Fig. 2.7.7 depicts the Delta undulator cross section with its important dimensions.

The on-axis region is connected to the well-pumped outer volume by four channels of 0.5 mm width and 15.7 mm long length. A total molecular conductance (C) for four channels can be determined by using data in [18]. For the given geometry, the data imply $C \sim 0.278$ L/s per cm of structure length. The Ni–plated, PM-blocks out-gassing rate has been studied in [19]. An out-gassing rate (R) of less than 4×10^{-12} Torr/L/sec/cm^2 was observed after 48 hours of 120 C baking. The pressure differential between the central on-axis region and outside can be estimated as:

$$dP = \frac{AR}{C} = \frac{3.1415 \cdot 0.05 \cdot (4 \times 10^{-12})}{0.278} = 2.26 \times 10^{-11} \text{ Torr} = 0.022 \text{ nTorr} \qquad (2.7.7)$$

This pressure difference is acceptable.

Prototyping results

To verify basic principles of the design, a 30 cm long prototype model was built and tested. The two pictures on Fig. 2.7.8 illustrate the model. The left picture shows the undulator cross section with the Delta shape PM blocks forming a round bore installed in a box–like frame. The picture to the right shows three of four magnet arrays installed during assembly.

Magnetic field properties

Each magnet array was tuned individually to have optical phase errors of 3 degrees rms or less prior to final assembly. After the assembly was complete, the magnetic field was measured with the special setup described in [17]. Fig. 2.7.9 and Fig. 2.7.10 show the field components, the resultant calculated beam trajectory, and the on-axis X–ray spectra calculated for the field. Figure 2.7.9 presents this data for both helical modes. Figure 2.7.10 shows this information for a planar mode. Both helical model modes demonstrated a 0.91 T peak field (90% of the

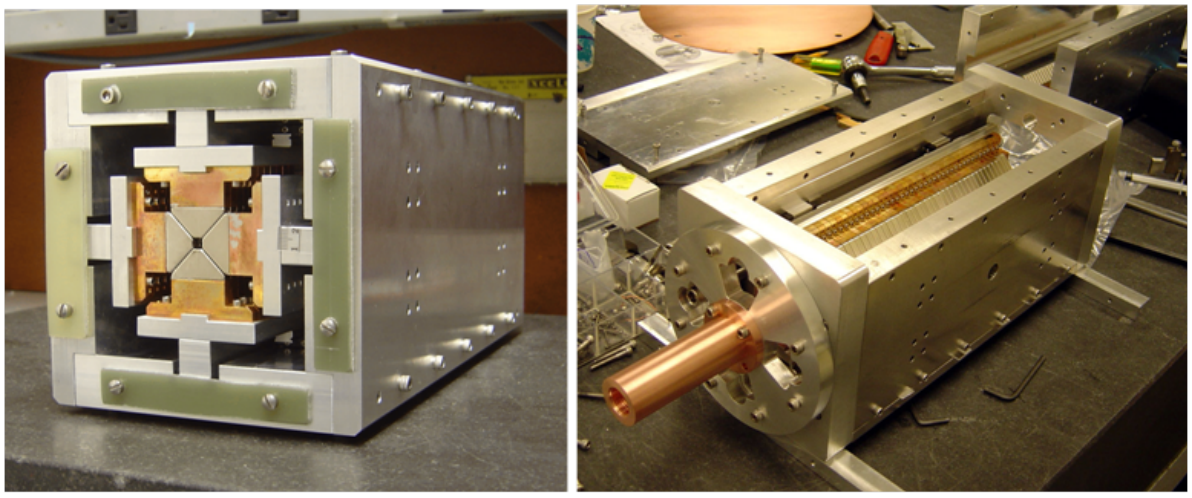

Figure 2.7.8: Delta undulator model in assembly process.

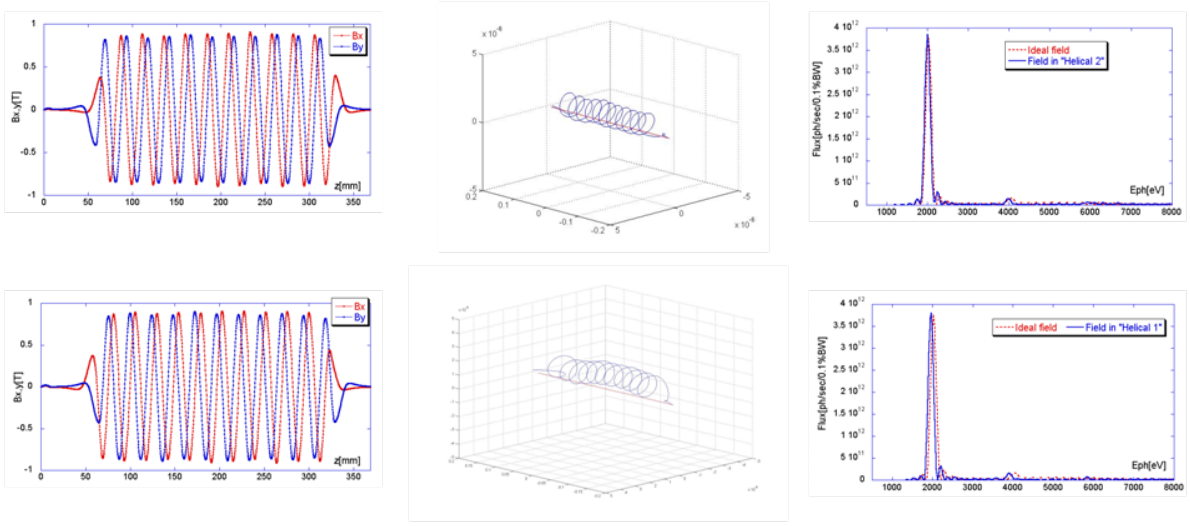

Figure 2.7.9: Left plots show vertical and horizontal field components measured in both helical modes corresponding to left and right x-ray polarizations. Central plots are 3D trajectories calculated for 5 GeV beam using measured magnetic field. Right plots are on-axis x-ray photon spectra calculated for measured and ideal fields.

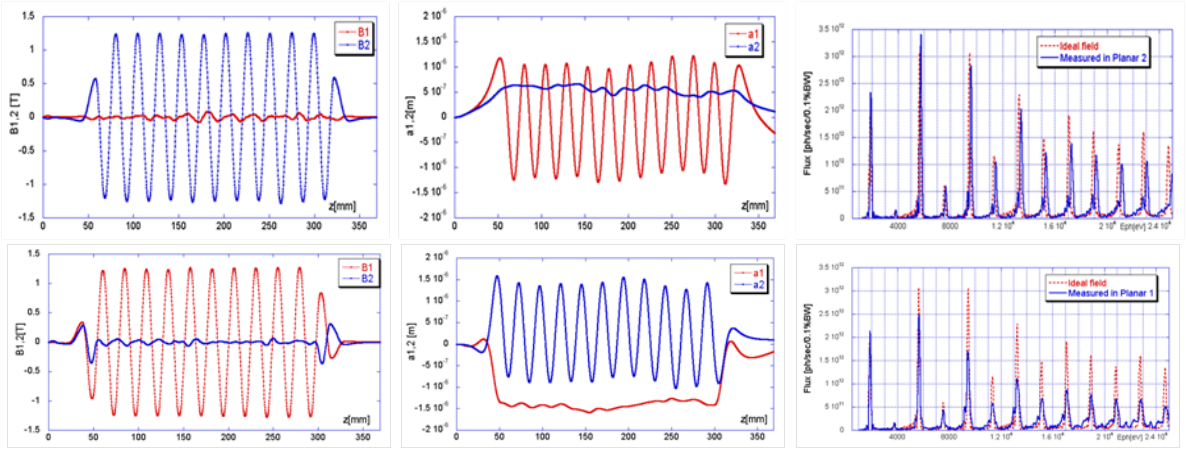

Figure 2.7.10: Measured magnetic field components (left), and predicted trajectories (center), and on-axis x-ray spectrum (right) in planar modes.

design). The negligible difference between x-ray spectra calculated for the measured and ideal fields indicated good field quality at this stage of development.

A peak field of 1.28 T was measured in a planar mode (89% of the design). The difference in spectra calculated for ideal and measured field (10% and 40% at 5^{th} harmonics) is probably due to a small shift of the magnet arrays in the transfer direction caused by a strong attractive magnetic force between adjoining arrays. This problem will be addressed and fixed in the next version of the device.

Vacuum properties

The magnet arrays were attached to the frame plates, enclosed in a vacuum vessel and pumped down in order to evaluate vacuum properties. The measured pressure was 4 nTorr after 100 hrs baking at 90 C with the very modest pumping speed of an 8 liters/sec. RGA spectral analysis indicated that 90% of the residual gas was H_2. Magnetic field measurement after the baking indicated no noticeable change in the magnetic field.

Beam test at the Accelerator Test Facility in BNL

The model undulator was tested with beam at the Accelerator Test Facility in Brookhaven National Laboratory at the end of 2009 ([20]). See Fig. 2.7.11.

Optical radiation was generated and observed on the fundamental undulator frequency from the device working in both helical and planar modes. The experimental results are compared with predictions in Fig. 2.7.12.

Data marked with circles on the left plot in Fig. 2.7.12 shows the measured dependence of the radiation intensity at a 5300 nm wavelength with electron beam energy and the Delta undulator in a planar mode. The dashed line represents the model calculation under an assumption of a 1.28 T peak undulator field. The sharp rise in intensity at a 55 MeV beam energy (due to the fundamental mode) is in agreement with observation.

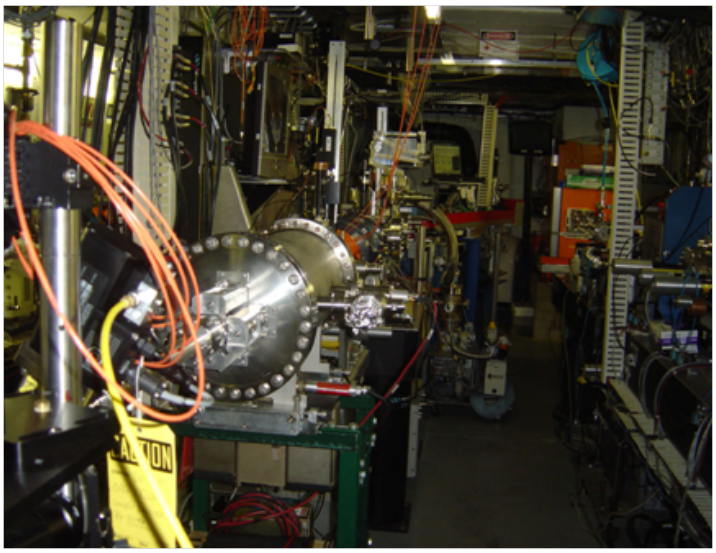

Figure 2.7.11: Delta undulator model installed in ATF beam line #2.

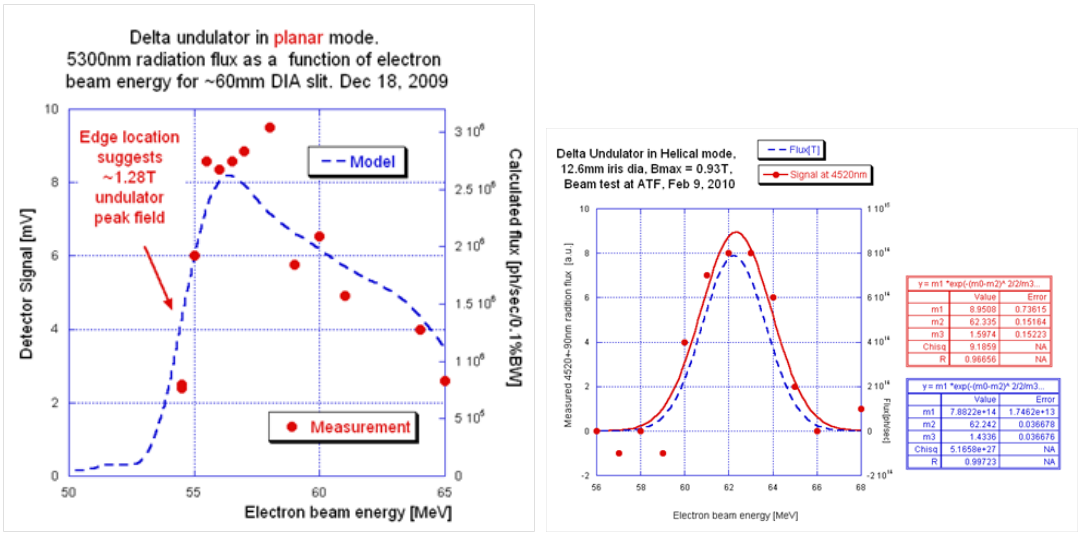

Figure 2.7.12: Radiation intensity measured at 5300 nm as a function of electron beam energy (left plot) with the Delta undulator in the planar mode. Radiation intensity at 4500 nm wavelength (right plot) as a function of electron beam energy for the Delta undulator model in the helical mode.

The plot on the right side of Fig. 2.7.12 depicts experimental data and the model prediction for the Delta undulator operating in a helical mode producing 4520 nm radiation. The observed peak location of 62.3 MeV was calculated to be caused by a 0.93 T undulator peak field. This peak field value was measured with a Hall probe after the beam test was concluded and was in good agreement with the 0.93 T calculated value.

Planar undulator

Planar undulators are considered as a back-up plan for the Delta design. They have been in use in storage-ring and FEL facilities for a long time, are well understood, and using these is a conservative approach.

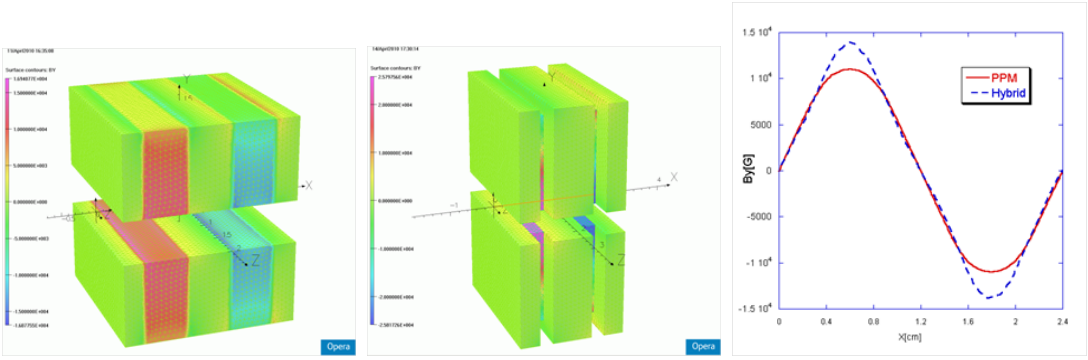

Figure 2.7.13: 3D models and field profile: PPM (left), Hybrid (center), magnetic field (right)

Magnetic structure modeling

Pure permanent magnet (PPM) structures were analyzed for the magnetic field formed by rectangular PM blocks magnetized in different directions. Hybrid structures can be made where magnetic blocks are combined with vanadium permendur poles. See Fig. 2.7.13. The left plot shows a PPM-type structure; the center plot is for a hybrid-type structure. All modeling results were obtained from the magnetic calculation code Opera–3D.

For equal gaps and periods, the hybrid structure demonstrated an approximately 20% higher magnetic field than a PPM structure. Although the hybrid structure has better field performance, its overall advantage is not obvious. It also has a stronger demagnetizing field, which elevates the risk of radiation damage and may limit the maximum temperature used during vacuum baking. The hybrid structure shows saturation effects in its poles, thus increasing its difficulties during operation and tuning. In addition, it requires more PM material and creates more mechanical stress.

Supporting structures

The AP scheme ([12]) can be used for the PPM case. Magnet arrays can be mounted inside a solid frame as depicted in Fig. 2.7.14 (left) on miniature rails that provide longitudinal motion. Mechanical drivers will be placed outside the vessel and mechanically coupled to the magnetic

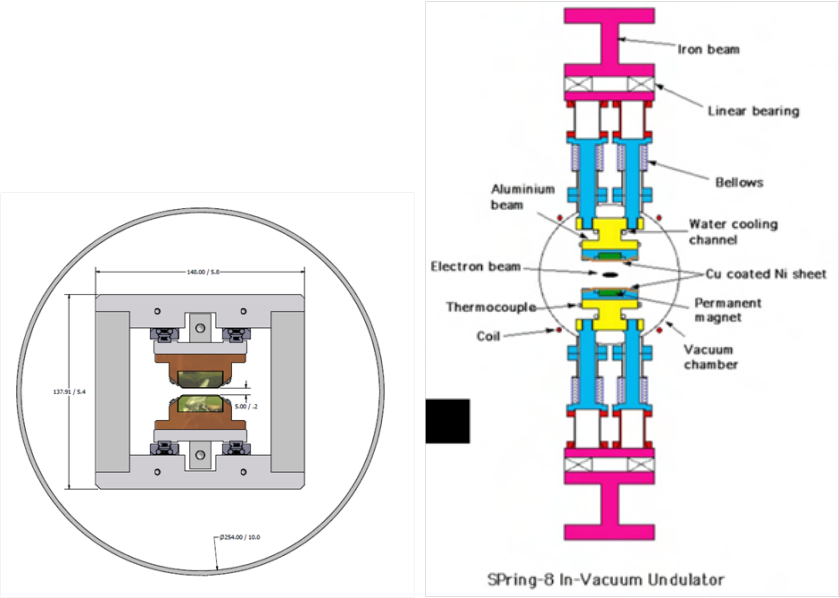

Figure 2.7.14: Supporting structures for PPM (left plot) and hybrid in–vacuum undulators (right). Vacuum chambers in both cases have similar dimensions.

arrays. Drivers should move arrays by at least 6 mm (1/4 undulator period) in both directions or more. The stress due to magnetic forces will be applied to the frame and driver components but not to the vacuum vessel. The initial analysis indicates the feasibility of such a scheme.

In the case of the hybrid-type magnetic structure, the magnetic field is controlled by a gap adjustment, a situation, Figure 2.7.14 (right), that requires a very large C–shaped supporting frame similar to the ones used at ESRF, SPring–8, and other laboratories. Thus the hybrid scheme is more expensive and takes up more space in comparison with the AP scheme. Taking all factors into account, the conclusion is that the PPM structure with the AP field control is preferable.

30-cm long Delta-undulator prototype summary and next steps

The novel Delta undulator technology is now in an advanced stage of prototyping. A 30 cm long in–vacuum prototype has successfully passed through early design stages including a first Linac beam test at the Accelerator Test Facility (ATF) facility at BNL.

The next step is to complete the engineering and fabrication work needed to scale the Delta design to a longer segment length. Segment lengths of 2.5 to 5 m are under consideration at the present time. The next round of development must also show how ERL beam image currents and HOMs will be satisfactorily dealt with on the curved inner surfaces next to the electron beam and how needed mechanical tolerances of the magnetic arrays can be held over distances greater than a meter in length.

2.7.4 Superconducting undulators

Undulators based on superconducting technology provide an alternative to PM technology for making insertion devices for the ERL. Insertion devices with superconducting (SC) windings of short period and small gap are known for producing some of the highest magnetic fields and thus could offer an opportunity for reaching the highest photon fluxes at energies of 100 keV or more. This is why these devices are under investigation by the ERL ID group.

Insertion devices with superconducting (SC) windings are well behaved under radiation exposure, as seen from their operation at the TEVATRON, LHC, CESR-B and Vepp2 damping ring [21]. We have considerable design, construction, and operational experience with SC wigglers installed at CESR [22, 23] and with undulators fabricated and tested at Cornell, [24] including a 4 m long device fabricated for an ILC positron source [25].

More recently, a SC workshop on undulators was held at Argonne National Laboratory, September 20–21, 2010 as a satellite workshop to SRI2010. Novel concept and fabrication ideas for SC undulators and wigglers were presented there for hard x-ray production [26]. Table 2.7.2 indicates the potential for an SC ID designed to produce higher field then a permanent magnet Delta ID, for the same gap and period. The change from helical to planar mode is accomplished by changing the current in the windings.

For the SC ID, rms phase error depends on accuracy in positioning SC wires. We estimate that a precision of 0.2 mm is feasible, leading to phase errors of less than 3°. The SC undulator uses two windings, of opposite helicity, to generate elliptical, circular and linearly polarized x-rays; a third winding of the same period but shifted by a half period can change the orientation of linear polarization. A K factor from 0 to 1.5 is possible with no mechanical motion for undulator periods of 15 to 25 mm and apertures of 5 to 8 mm. The early concept [27] has been applied to recent 3D magnetic designs using the MERMAID code [28]. Figure 2.7.15 shows a prototype SC double winding configuration undulator with the current directions indicated.

As was noted at the SC undulator workshop at Argonne, SC undulator research and development is being actively pursued at several locations around the world and advances can be expected; indeed, more research and development will be required for SC IDs to realize their ultimate promise.

For the purposes of this design study, it is sufficient to note that the permanent magnet undulators described in this document are already in an advanced state of development and are already on a path to achieve the x-ray beam characteristics specified for the ERL applications.

Table 2.7.2: Comparison between Delta and SC undulators. 5 mm clear bore diameter.

	$B_{\max}$ (T) in helical mode		$B_{\max}$ (T) in planar mode	
Period (mm)	Delta	SC	Delta	SC
24	1.0117	1.097	1.431	2.194
22	0.9686	1.058	1.37	2.194
20	0.9162	1.009	1.296	2.018
18	0.8533	0.9497	1.207	1.899
16	0.7787	0.8679	1.101	1.736

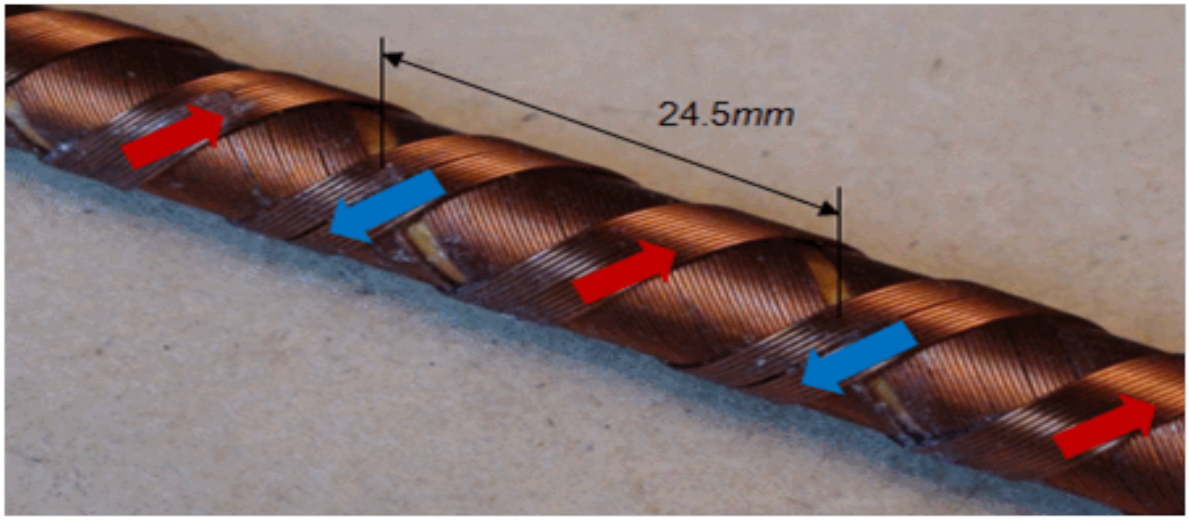

Figure 2.7.15: Coils wound over copper tube with six wire strands together in flat SC cable [26]. Period 24.5 mm. Outer diameter is 10 mm, inner diameter clear for beam is 8 mm. Direction of current in corresponding coil is shown by arrow

Obviously, if SC IDs develop to the point of practical utilization by the time of construction of an ERL facility, then they will be considered in the context of available undulators at that time. For now, the ERL ID group is continuing research and development on permanent magnet undulators specific to ERLs. SC undulator technology is making rapid progress, and could be included in the baseline design when construction of the ERL begins.

References

[1] Yamamoto, S., *et al. Construction of an in-vacuum type undulator for production of undulator x rays in the 5–25 keV region.* Review of Scientific Instruments, **63** (1), pages 400–403 (1992).

[2] Chavanne, J., *et al. In-Vacuum Undulators at ESRF.* In *The 2003 Particle Accelerator Conference*, pages 253–255. Portland, Oregon USA (2003).

[3] Hara, T., *et al. In-vacuum undulators of SPring-8.* Journal of Synchrotron Radiation, **5**, pages 403–405 (1998).

[4] Rakowsky, G., *et al. NSLS in-vacuum undulators and mini-beta straights.* In *The 2001 Particle Accelerator Conference (PAC 2001)*, pages 2453–2455. Chicago, Illinois,USA (2001).

[5] Hara, T., *et al. Cryogenic permanent magnet undulators.* Phys. Rev. ST Accel. Beams, **7** (5), page 050702 (May 2004). doi:10.1103/PhysRevSTAB.7.050702.

[6] Kitegi, C., *et al. Development of a Cryogenic Permanent Magnet In-Vacuum Undulator at the ESRF.* In *The tenth European Particle Accelerator Conference, EPAC'06*, pages 3559–3561. Edinburgh, Scotland (2006).

[7] Chavanne, J., *et al. First operational experience with a cryogenic permanent magnet undulator at the ESRF.* In *The 23rd Particle Accelerator Conference*, pages 2414–2416. Vancouver, British Columbia, Canada (2009).

[8] Chao, A. W. and M. Tigner. *Handbook of Accelerator Physics and Engineering (3rd printing)* (2006).

[9] Walker, R. *Interference effects in undulator and wiggler radiation sources.* Nucl. Instr. and Meth. A, **335** (1-2), pages 328 – 337 (1993). ISSN 0168-9002. doi:DOI:10.1016/0168-9002(93)90288-S.

[10] Temnykh, A. B. *Measurement of NdFeB permanent magnets demagnetization induced by high energy electron radiation.* Nucl. Instr. and Meth. A, **587** (1), pages 13 – 19 (2008). ISSN 0168-9002. doi:DOI:10.1016/j.nima.2008.01.002.

[11] Temnykh, A. B. *Delta undulator for Cornell energy recovery linac.* Phys. Rev. ST Accel. Beams, **11** (12), page 120702 (Dec 2008). doi:10.1103/PhysRevSTAB.11.120702.

[12] Carr, R. *Adjustable phase insertion devices as X-ray sources.* Nucl. Instr. and Meth. A, **306** (1-2), pages 391 – 396 (1991). ISSN 0168-9002. doi:DOI:10.1016/0168-9002(91)90346-R.

[13] Bahrdt, J., *et al. Undulators for the BESSY Soft-X-Ray FEL.* pages 610–613 (2004).

[14] Onuki, H. *Elliptically polarized synchrotron radiation source with crossed and retarded magnetic fields.* Nucl. Instr. and Meth. A, **246** (1-3), pages 94 – 98 (1986). ISSN 0168-9002. doi:DOI:10.1016/0168-9002(86)90053-7.

[15] Volby, P. *Helical Undulator For Producing Circularly Polarized Photons," Workshop on new kinds of positron sources for linear collider.* Published as slac-r-502, SLAC (1997). 1997 Proceedings of the Workshop on New Kinds of Positron Sources for Linear Colliders SLAC: http://www.slac.stanford.edu/cgi-wrap/getdoc/nkpslc97-015.pdf.

[16] Elleaume, P., J. Chavanne, and B. Faatz. *Design considerations for a 1 Å SASE undulator.* Nucl. Instr. and Meth. A, **455** (3), pages 503 – 523 (2000). ISSN 0168-9002. doi:DOI: 10.1016/S0168-9002(00)00544-1.

[17] Temnykh, A. *Evaluation of Magnetic and Mechanical Properties of Delta Undulator Model.* Technical Report CBN-09-01, , Cornell University, LEPP (2009). http://www.lns.cornell.edu/public/CBN/2009/CBN09-1/CBN_09-01.pdf.

[18] O'Hanlon, J. F. *A Users Guide to Vacuum Technology.* Second edition.

[19] Li, Y. *ADC In-Vacuum Undulator Magnet Material Out-gassing Test Report* (2008).

[20] Temnykh, A., *et al. Delta undulator model: Magnetic field and beam test results.* Nucl. Instr. and Meth. A, **In Press, Corrected Proof**, pages – (2010). ISSN 0168-9002. doi:DOI:10.1016/j.nima.2010.11.011.

[21] Anashin, V. V. *Superconducting Spiral Undulator for Measuring the Radiation Polarization Colliding Beams in the Vepp-2m Electron Positron Storage Ring.* Instruments and Experimental Techniques, **29 (6)**, pages 1267–1271 (1986).

[22] Mikhailichenko, A. *Wiggler for CESR operation at 2-GeV.* Technical Report CBN-04-07, Cornell University (May 2001).

[23] Rice, D., *et al. Production and testing considerations for CESR-c wiggler magnets.* In *the 2003 Particle Accelerator Conference*, volume 1, pages 167–169. Portland, OR (2003).

[24] Mikhailichenko, A. *Test of Short Period SC Undulator.* In *The eleventh European Particle Accelerator Conference, EPAC'08*, pages 595–597. Genoa, Italy (2008).

[25] Clarke, J., *et al. Construction of a full scale superconducting undulator module for the international linear collider position sources.* In *The eleventh European Particle Accelerator Conference, EPAC'08*, pages 709–711. Genoa, Italy (2008).

[26] Mikhailichenko, A. *SC Undulator and SC wiggler for the Cornell ERL.* In *16th Pan-American Synchrotron Radiation Instrumentation Conference.* Argonne National Laboratory, USA (2010).

[27] Alferov, D. F., Y. A. Bashmakov, and E. G. Bessonov. *Device for Obtaining Polarized Electromagnetic Radiation.* Zhurnal Tekhnicheskoi Fiziki. Authors Certificate No 538508, USSR.

[28] MERMAID- MEsh Routine for MAgnet Interactive Design. Sim Limited, 630058, Novosibirsk, P.O. Box 160, Russia.

2.8 Beam Stops

2.8.1 Introduction

Three very different beam stops are required for the ERL. These are the primary beam stop, tune-up stops, and moderate power stops for high-energy beams. While these latter two stops are relatively conventional, the primary beam stop has challenging performance requirements. In the sections below, the technical issues and design details for each of these three types of beam stops are described, and where relevant, comparisons to other similar beam stops are included.

The primary beam stop must intercept the full beam current at the end of the energy recovery process, and safely dissipate the beam power as waste heat. The design beam current is 100 mA, and for the present purposes, the maximum beam energy at the beam stop is 15 MeV, leading to a beam power of 1.5 MW. The range of 15 MeV electrons is less than $8\,\mathrm{g/cm^2}$ in practical beam stop materials, and thus the beam power is deposited over a very small depth. The natural beam spot size is quite small, even after energy recovery. The effective area of the beam then needs to be expanded to more than $1\,\mathrm{m^2}$ where it intercepts the surface of the stop, to reduce the power density in the stop material to a level that can be safely handled. This expansion can be accomplished by several techniques, such as strongly defocusing the beam, rastering the beam over a larger area, or intercepting the stop surface at a shallow angle. All of these methods will be employed for the primary stop.

Several tune-up stops will be installed at yet to be established key locations around the beam path. These small stops will normally occupy a 'fail-safe' position out of the beam path. The active part of the stop is within the accelerator vacuum system, and is moved in and out of the beam through a bellows isolated mechanism. The stops are remotely inserted when it is necessary to set up a beam following a shutdown, or check various accelerator parameters such as linear optics or cavity phasing. These stops are capable of continuously dissipating only 10 kW of beam power, corresponding to 2 μA of average current at the full 5 GeV beam energy. Thus, only a very low duty-factor beam or a very small bunch charge at full-duty factor can be used. These beam conditions will be reliably and automatically established before a tune-up stop can be placed in the beam path. As the tune-up stops are used a relatively small fraction of the time, and are low power, only very modest shielding will be required. They will be cooled by the water systems in the accelerator tunnel. The tune-up stops are not technically demanding, and similar stops have been used at other laboratories.

Finally, the ERL facility will be used to deliver high-energy beams for accelerator-physics studies. For example, one might deliver a CW train of high-charge bunches at a relatively low-repetition rate for investigation of various FEL ideas. For these beams, the average beam current would be relatively low – of order 10 μA – and energy recovery would be unnecessary. Rather, the electron beam would be stopped at high energy. While the average beam power is relatively low in these cases – of order 50 kW – the stop must be quite different, since high-energy electrons penetrate a considerable thickness of matter and shower multiplication significantly increases the local power deposition. Such stops have been developed at other laboratories, and the technical issues are well understood.

2.8.2 State of the Art

CEBAF at Jefferson National Laboratory has the following installations: a 45 kW, 67 MeV injector tune-up stop; two 110 kW all-metal high-energy tune-up stops; and two 1 MW, 5 GeV primary stops [1].

2.8.3 The Primary Beam Stop

The primary beam stop must dissipate up to 1.5 MW of beam power generated by a 100 mA average current, 10- to 15 MeV electron beam. The range of 15 MeV electrons in matter is short – less than 8 g/cm^2 in suitable stop materials. In addition, the natural beam spot size is quite small – much less than 1 cm^2. Such an electron beam striking any material would very rapidly destroy it. Thus it is necessary to greatly expand the beam size where it intercepts the stop surface to produce power densities low enough to be safely and reliably dissipated. Clearly the stop material must have a reasonably high-thermal conductivity, to limit the maximum temperature at the uncooled entrance face of the stop. As there is no significant shower multiplication from 15 MeV electrons, the surface of the stop, which is furthest from the cooling water, will have the highest temperature.

The only practical choice for the primary stop material is aluminum. Aluminum offers the very significant advantages of a high-photoneutron threshold (13.3 MeV) and relatively low-residual radioactivity comprised primarily of short-lived isotopes. The relatively low-residual radioactivity of aluminum is a significant consideration for the ultimate disposal of a decommissioned beam stop. The aluminum used will be an alloy, and the various alloying elements have lower photo-neutron thresholds. These elements will be responsible for a fraction of the residual radioactivity of a 15 MeV aluminum stop. Copper has a significantly lower photo-neutron threshold, and much higher residual radioactivity of longer-lived isotopes. Beryllium would be exceptionally expensive, and has a very low photoneutron threshold. Carbon, as pyrolytic graphite, is mechanically difficult, and has an extremely anisotropic thermal conductivity.

The stop must remain fully functional during several decades of operation at very high average power. With an aluminum stop, it is especially critical to control the water chemistry to avoid corrosion. Therefore, heat will be removed from the primary beam stop with a closed circuit de-ionized (DI) water circulation system, which will be continuously powered. The only acceptable metals in this system are aluminum and stainless steel. The water chemistry will be carefully monitored at all times to assure proper pH, resistivity, and the absence of harmful ions.

It is very desirable to minimize the deposition of beam power directly in the cooling water, to minimize hydrogen production through radiolysis [2]. At the same time, it is desirable to locate the cooling water as close as practical to the interior surface of the stop to minimize thermal effects. These realities lead directly to the use of a stop shaped like an ogive (pointed arch) of revolution, similar to a high-power klystron collector. Even with an optimum thickness stop wall, there will be enough radiolysis in the cooling water to require monitoring the hydrogen level in the closed cooling circuit. It is anticipated that the modest quantities of hydrogen generated can be vented to the atmosphere, with no need for hydrogen recombination systems. Were hydrogen recombination to prove necessary, reliable hydrogen recombination systems were developed for the high-power beam stops at SLAC, and were duplicated, with improved

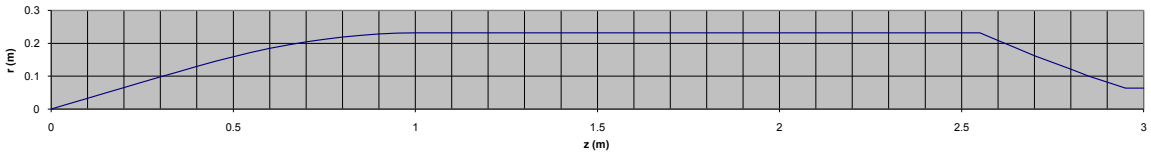

Figure 2.8.1: The inner surface profile of the Phase 1a beam stop

instrumentation, for the high-power stops at Jefferson Lab [1, 2]. The 15 MeV beam energy is far too low to produce either tritium or ^{7}Be through spallation of oxygen, so there will be no direct long-lived radioactivity in the DI water circuit. Heat will be removed from the closed DI water circuit with a water-to-water heat exchanger. The pumps, deionization and filtration equipment, surge tank, hydrogen-venting scheme, and water-to-water heat exchanger will be located remote from the stop itself, to allow servicing and to eliminate any potential for radiation damage. All plumbing and piping in the closed-circuit system will be of either aluminum or stainless steel [3].

The primary stop will be a powerful source of prompt, low-energy gamma radiation as well as a modest flux of low-energy neutrons. The primary radiation shielding for the stop will result from locating it in a small-diameter underground tunnel spur deep underground. Detailed calculations of the total radiation from the stop are being made with the code MCNP [4]. These calculations are being used to design the shielding of the stop tunnel, and to determine if additional shielding is required around the stop to prevent groundwater activation [5]. A similar ogive-shaped aluminum beam stop, capable of dissipating 575 kW maximum average beam power between 5 and 15.75 MeV, has been constructed for the Phase 1a ERL program. This stop is operated in an open room, and thus requires substantial local shielding. This shielding was also designed with the aid of MCNP. A detailed comparison of the measured effectiveness of this shielding with the MCNP calculations, for both neutrons and gammas, will be conducted during Phase 1a prototype-injector beam operations.

If the stop were to be operated in normal air, significant quantities of nitric acid would be produced by radiolysis of nitrogen, leading to the production of nitric oxide, which oxidizes to form nitrogen dioxide, which, with water, forms nitric acid. As a consequence, the stop tunnel will be sealed and purged with a dry, inert gas such as argon, to eliminate the possibility of nitric acid formation. This solution has proven very effective with the two high-average power (1 MW) beam stops routinely operated at Jefferson Laboratory.

Although it is very desirable to isolate the stop from the accelerator vacuum system, this is simply not possible. For example, even in a beryllium window, the power deposition from the dE/dx losses of a 100 mA average current beam is 30 kW per mm of window thickness (the window thickness is irrelevant for cooling considerations). It is certainly not practical, and likely not possible, to remove such a large amount of heat from a thin window in vacuum. Thus, the beam stop will of necessity be within the accelerator vacuum system. A differential vacuum pumping system will be used to isolate the high-gas load from the stop when operating at high average beam power from the much lower pressure in the beam line from the accelerator. A similar differential pumping system has been constructed for the Phase 1a program, and measurement of its effectiveness is being used to design the differential pump system for the

Figure 2.8.2: The completed Phase 1a beam stop before installation of its shielding.

primary stop. Finally, a reasonably fast-acting, RF shielded gate valve will be located well upstream of the beam stop, to provide protection to the accelerator in the event of a stop failure. This is very important as the superconducting Linac is relatively close to the primary beam stop.

Examples of ogive-shaped beam stops for high average power, low-energy beams are the stop for the Phase 1a program and for the 100 mA, 6.7 MeV proton beam of the Low Energy Demonstration Accelerator (LEDA) [6, 7]. In addition, ogive-shaped collectors operating in the MW power range have been used with high-power klystrons for a very long time. Although this technology would seem to be well developed and suitable for high-power electron beam stops up to beam energies where the electron range becomes too large, dissipation of such high powers must be approached with caution, as seemingly small errors can result in severe damage to the stop. For example, all three of the 1.9 MW ogive-shaped collectors of the high power klystrons for the LEDA accelerator suffered severe damage during initial operation and had to be rebuilt [8]. Furthermore, the higher energy of the ERL beam compared to a klystron beam translates into a physically larger system than for a klystron collector. The primary beam stop will require careful tests during fabrication and assembly (e.g. rigid material certifications; x-ray, dye penetrant, and sonic inspection of welds; etc.) to assure the final stop will perform and survive as needed.

The profile of the inner surface of the stop built for the Phase 1a project is shown in Fig. 2.8.1. The 3-meter-long stop was assembled from three shorter segments by electron beam welding. A photograph of the completed stop is shown in Fig. 2.8.2. Water cooling channels are machined in the outer surface of the stop body, which is mounted inside an aluminum jacket. To reduce thermal stresses, the stop body is free to move longitudinally within the jacket. GEANT was used to calculate the power deposition in the stop body, and ANSYS calculations then determined the temperatures throughout the stop, the thermal stresses, etc. The results of some of these calculations are given in Fig. 2.8.3. Beam on-off cycles are sudden, and result in rapid temperature changes, which in turn may lead to eventual

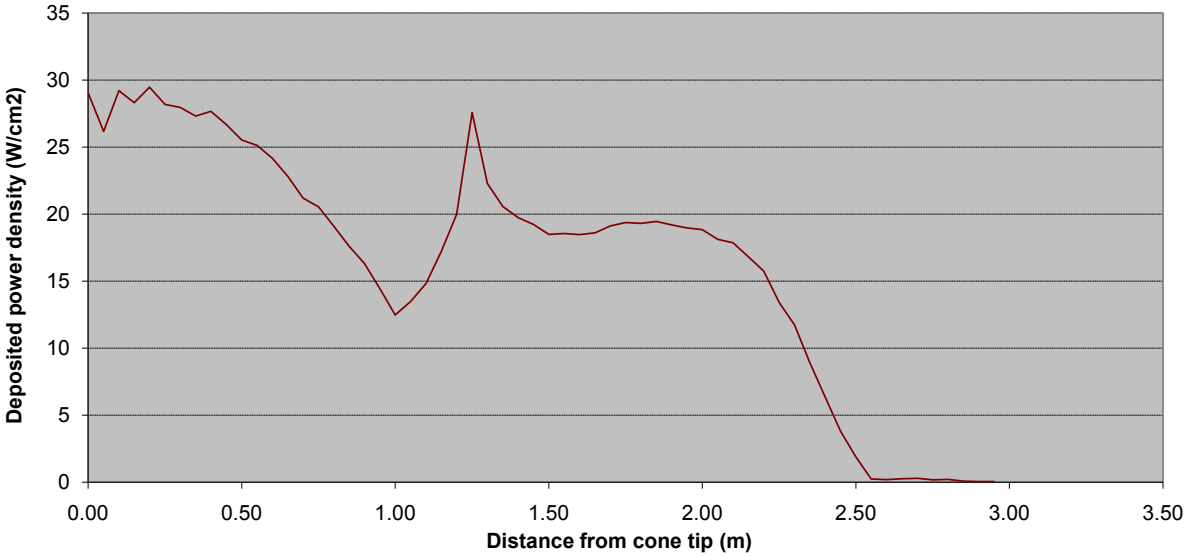

Figure 2.8.3: Energy deposition for 600 kW beam power at optimized condition

fatigue failure. The water flow was chosen to limit the maximum temperature differentials in the stop, leading to a very large number of temperature cycles before the onset of fatigue failure. For the design of a 60 gpm water flow, the flow velocity is only 1.71 m/sec. Erosion of water channels will therefore not be a problem.

The Phase 1a stop has a peak power density, as calculated with GEANT4, of 30 W/cm^2 with 600 kW of incident beam power. This gives a maximum heat flux in the water cooling channels of 60 W/cm^2. To reduce the peak-power density in the full-power primary stop, one must enlarge the stop surface area. If one were to retain the conservative 30 W/cm^2 value, the stop would need to be enlarged by the square root of 3, or 1.73, in both radius and length, leading to a 5.2-m-long stop of 46 cm radius. We anticipate that the final primary stop will be larger than the Phase 1a stop, but likely not by the full factor of 1.73. The size of available electron beam welding machines will also limit the maximum dimensions to be less than this. The factor by which the Phase 1a stop will be enlarged will be based on measurements made on that stop, and on further calculations. As with the Phase 1a stop, GEANT is being used to model the energy deposition in the stop, and ANSYS is being to study the equilibrium temperatures and the thermal stresses. The thermal stresses will be kept below a level that would pose a risk of fatigue failure over the stop anticipated operating life.

Two active devices are used to enlarge the beam area at the stop surface – a quadrupole that strongly over-focus the beam, and three deflector magnets arranged as a sextupole powered by three-phase, 60 Hz AC that move the beam spot in a circular path at 60 Hz. If either of these devices failed, the stop would rapidly overheat, quite possibly to the point of damaging, or even melting the stop surface, particularly if there were a transition from nucleate to film boiling at the water-metal interface. Redundant hardwired interlocks will assure that each of the beam focusing and rasterring magnets is properly powered. On any interlock failure, the beam will be aborted. Similar interlocks will be provided on the cooling water flow, pressure differential, and temperature. Field strengths, cooling requirements, and sweep amplitudes of

the said system for this design are based on experiences with the successful Phase 1a dump.

It is important that the beam is not only properly enlarged, but that it is also correctly positioned in the stop. A quadrant detector at the entrance to the stop will assure the correct beam size and position at the stop entrance, while upstream BPMs will assure the correct entrance angle. Each element of the quadrant detector will cover close to 90 degrees of azimuthal angle, and will intercept a very small fraction of the beam. The elements must be water-cooled, protected from RF heating, and the ceramics providing electrical isolation shielded from the possibility of charging from stray scattered electrons. Basically, each element is a low-efficiency Faraday cup, and thus must be thick enough to assure beam electrons are stopped. Interlocks on the amplitude of the DC and 60 Hz left-right and up-down difference signals assure that the quadrupole over-focusing and raster amplitude are correctly set, and that the beam centroid is properly centered on the stop.

The design of the high-power Phase 1a stop was independently reviewed by an outside expert [9]. This review concluded that the stop design was conservative at 500 kW, and likely acceptable at 600 kW. A number of areas that must be investigated during the design of the 1.5 MW primary stop were presented.

2.8.4 Tune-up Stops

For a variety of beam setup activities, such as cavity phasing or establishing the linear beam optics, it is desirable to use low-average power beam, and to not have to transport this beam around the entire machine. These tune-up stops need to dissipate only a low average power – on the order of up to 10 kW – corresponding to 2 μA average current at 5 GeV. This current may be comprised of a 1.3 GHz train of 0.8 fC bunches, or of bursts of higher charge bunches at a greatly reduced duty factor, as required for the particular task at hand.

The tune-up stops are quite simple. For example, a copper cylinder 3.8 cm in diameter and 15 cm long, brazed into a stainless-steel water jacket and cooled on its external surface, is quite adequate. The active section of the stop is completely within the accelerator vacuum system. The stop is mounted on a bellows mechanism and inserted into the beam line by a spring-loaded air cylinder. The 'fail safe' position of the stop, provided by the spring loading, is out of the beam line. Redundant radiation-hard interlock switches assure that when the stop is not in the 'out' position, the average beam current cannot exceed 2 μA. Special precautions will assure that HOMs will not be excited in the stop chamber when the stop is in its out position.

As the tune-up stops never operate at high power, and are used only infrequently, they do not require extensive shielding. Local lead and iron shielding of modest thickness is all that is required. Cooling water is provided by the magnet cooling water.

A system of tune-up stops very similar to those required for the ERL has been implemented at Jefferson Lab, for setting up beam in the CEBAF accelerator. We anticipate that the ERL tune-up stop system can be very largely copied from the Jefferson Lab system.

2.8.5 Moderate Power Stops

For various accelerator physics studies, it may be desirable to deliver high-charge bunches in a relatively low-repetition rate train, with a correspondingly low-average current on the order of

10 μA. In this case, energy recovery is unnecessary and would involve costly additional beam transport. Thus, beam stops for these low currents of high-energy beam are required. These stops are very different than those above, as the electrons penetrate much farther into the material, shower multiplication produces energy deposition much higher than the dE/dx from individual beam electrons, and the gamma and neutron radiation produced is much harder and more intense.

For average beam powers on the order of 50 kW at high energy, it is practical to design stops in which the entire beam energy is dissipated in metal. With nearly all the beam power absorbed in metal, the issues of radio-activation and radiolysis in the cooling water are minimal. Such stops were developed at Jefferson Lab with power-handling capability of 100 kW or more [1] which can be adopted for these accelerator physics studies.

2.8.6 Summary

Solutions are presented for each of the three different types of beam stops required for the ERL. With 1.5 MW of low-energy electrons, the primary stop is the most challenging. Three examples of stops already constructed – the Phase 1a stop for 600 kW, 15 MeV electrons, the LEDA 1.9 MW klystron collectors, and the LEDA stops for 670 kW, 6.7 MeV protons – demonstrate that good technical solutions exist. Extensive calculations, comparison with the performance of the Phase 1a stop, and attention to design details and cooling system characteristics will assure that the device will operate satisfactorily at full power for several decades.

Tune-up stops, required for beam setup activities, are technically not demanding, and have been implemented elsewhere. We will simply copy what has already been done.

Full-energy, low-average current, all metal stops will be developed as required for specialized beam uses. An all-metal stop meeting many of these requirements has been demonstrated at Jefferson Lab, and this technology can be extended to higher beam power and current if required.

References

[1] Wiseman, M., *et al. High power electron beam dumps at CEBAF.* In *Proceedings of the 1997 Particle Accelerator Conference 3*, pages 3761–3763. Vancouver, B.C., Canada (1997).

[2] Walz, D. R., *et al. Beam Dumps, Energy Slits and Collimators at SLAC–Their Final Versions and First Performance Data.* IEEE Transactions on Nuclear Science, **14** (3), pages 923–927 (1967).

[3] Dortwegt, R. *Low-conductivity water systems for accelerators.* In *Proceedings of the 2003 Particle Accelerator Conference 1*, pages 630–634. Portland, USA (2003).

[4] Hendricks, J., *et al. MCNPX 26F Extensions.* Los Alamos National Laboratory (2008).

[5] Kostroun, V. *Groundwater and Soil Activation by the ERL 1.5 MW Electron Collector.* Technical Report ERL-RN-10-001, CLASSE (2010).

[6] Hagan, T. H. V., *et al. Design of an ogive-shaped beamstop.* In *Proceedings of the XIX International Linac Conference*, pages 618–620. Chicago, IL, USA (1998).

[7] Rybarcyk, L. J., *et al. LEDA beam operations milestone and observed beam transmission characteristics.* In *Proceedings of the XX International Linac Conference*, pages 584–586. Monterey, CA (2000).

[8] Rees, D., W. Roybal, and J. B. III. *Collector failures on 350-MHz 1.2-MW CW klystrons at the low-energy demonstration accelerator (LEDA).* In *Proceedings of the XX International Linac Conference 2*, pages 998–1000. Monterey, CA (2000).

[9] Walz, D. (2010). Personal communication.

Table 2.9.1: ERL flight distances and flight times

Location (Time of Flight)	Distance from Gun (m)	Time-of-Flight from Gun (μs)
Injector ($T_{\rm I}$)	20.61	0.069
Linac A [first pass] ($T_{\rm LA1}$)	364.34	1.215
Turn-Around A ($T_{\rm A}$)	523.64	1.747
Linac B [first pass] ($T_{\rm LB1}$)	808.44	2.697
S, N, & CESR Arcs ($T_{\rm CESR}$)	2050.95	6.841
Linac A [second pass] ($T_{\rm LA2}$)	2394.67	7.988
Turn-Around B ($T_{\rm B}$)	2552.04	8.513
Linac B [second pass] ($T_{\rm LB2}$)	2837.84	9.466
Beam Stop ($T_{\rm STOP}$)	2846.09	9.494
		Time-of-Flight from Injector (μs)
Re-circulation ($T_{\rm RECIRC}$)		6.773

2.9 Start-up Procedures

An ERL requires a start-up plan that is different from those employed for either Linacs or storage rings. The laser-driven photo-cathode has some limitations on bunch patterns that can be produced; the injector's optics are strongly influenced by space charge and beam loading of the injector RF cavities. This implies that during final setup procedures the charges of the bunches should be close to the design operating level, and since the SRF cavities in the two main Linacs have high loaded Q's, beam loading of the cavities will produce a significant energy slew across a long bunch train when operating in a non-energy-recovery mode. When energy recovery is first initiated, the timing and pattern of bunches must be controlled accurately to avoid additional energy variations from bunch-to-bunch or train-to-train. Some of the instrumentation requires special bunch patterns to function correctly. Finally, during the current ramp-up mode, the beam loading of the main Linac cavities limits the rate at which charge may be added to beam.

Figure 2.9.1 is a schematic layout for the ERL complex and includes a simplified illustration of the trajectory of an electron bunch within the ERL. The bunch begins at a time T_0 in the injector, passing through the merger before reaching Linac A at time ($T_{\rm I}$), and then completing one pass through Linac A ($T_{\rm LA1}$), Turn-Around A ($T_{\rm TA}$), Linac B ($T_{\rm LB1}$) and the CESR Arc (and south and north arcs) before returning to the entrance to Linac A at time ($T_{\rm CESR}$). At this location in the circuit a high-energy beam stop is placed for use when the bunch is not undergoing energy recovery. In the energy-recovery mode, the bunch will continue through Linac A ($T_{\rm LA2}$), Turn-Around B ($T_{\rm TB}$), Linac B ($T_{\rm LB2}$), and the Beam Stop ($T_{\rm STOP}$). There is also an intermediate energy beam stop placed after the turn-around arcs to allow for the adjustment of the turn-around arcs before injecting the beam into Linac B. The time the beam takes to recirculate, i.e. go through Linac A, Turn-Around A, Linac B, the South and North Arcs and CESR, returning to the entrance for Linac A, is $T_{\rm RECIRC} = T_{\rm CESR} - T_{\rm I}$, and for the current design this is approximately 6.8 microseconds. The detailed times are given in Tab. 2.9.1.

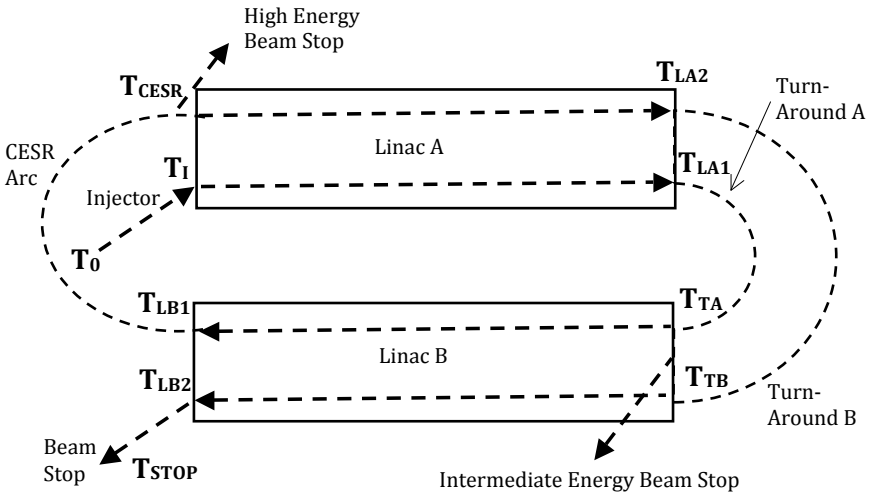

Figure 2.9.1: Functional block diagram of a bunch's traversal of the ERL.

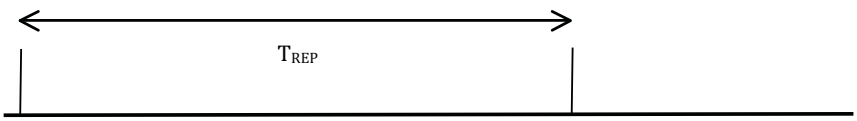

Figure 2.9.2: Bunch pattern during the first-turn-steering mode of operations.

First turn steering

Because space charge and beam loading effects in the injector are important, its tuning will be done with the design bunch charge of 77 pC. The first turn steering of a single bunch from the injector through the rest of the ERL will be accomplished by using the BPM system and screens that can be inserted into the accelerator aperture. With a $4 \times 60\,\mathrm{Hz}$ repetition rate beam (see Fig. 2.9.2), the high energy beam stop will need to be capable of an average beam power of $5\,\mathrm{GeV} \cdot 77\,\mathrm{pC} \cdot 240\,\mathrm{Hz} = 100\,\mathrm{W}$. The intermediate energy beam stop at one half the beam energy could receive one half of the beam power (50 W). The actual power levels will be determined by the dark current and the limited extinction ratio of the laser that will have to be determined experimentally. During this process, as the train of bunches passes by beam position monitor (BPM) detectors for the first time, the timing of the detection of the signal will be established for each BPM processor. When it is completed, this mode of operation will have seen the adjustment of the Linac phasing, the centering of the trajectory to within several millimeters of the final trajectory and the first correction of the optics in the complete accelerator except for Turn-Around B.

First turn accelerator setup

In order to complete the beam trajectory through the ERL, bunches with the proper delay of their arrival time will pass through Linac-A on the decelerating phase, Turn-Around B,

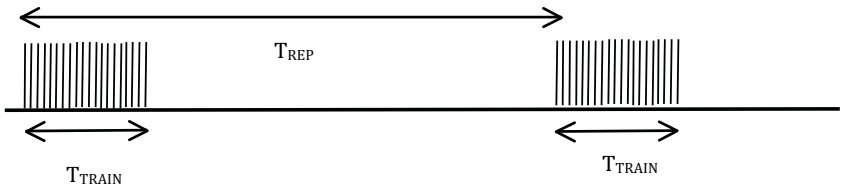

Figure 2.9.3: Bunch pattern during the first-turn-accelerator-setup mode of operations.

up to the Intermediate-Energy beam stop. After orbit and basic optics corrections through Linac-B, the beam's arrival time will be adjusted to the decelerating phase and transported to the beam stop. After the beam has been tracked up to the final beam stop and the timing for the BPM processing has been confirmed, more precise position measurements and corrections will be undertaken by both single trajectory and average trajectory acquisitions. As shown in Fig. 2.9.3, the beam is modulated to be a train of 77 pC bunches spaced at 1.3 GHz of duration T_{TRAIN} (e.g. approximately 100 ns), long enough for the BPM system and other diagnostics to function more accurately to give the average train parameters, and short enough for beam loading of the Linac sections ($\delta p/p = 2 \times 10^{-5}$ per bunch) to not produce a very large energy spread across the train. The repetition period for the trains is T_{REP}, which is again harmonic with T_{RECIRC} and is capable of being locked to low harmonics of the AC line frequency. The envelope of each train's current should have reasonably flat amplitudes for many tens of nanoseconds during the time-slice used for the beam measurements. In this mode, the offsets of the BPMs with respect to the quadrupole centers would be determined and dispersion free trajectory corrections would be applied. Then the focusing optics can be measured using response matrix techniques and corrections may be applied to bring the optics into agreement with the accelerator's design model.

Low power energy recovery

Utilizing the bunch pattern shown in Fig. 2.9.3, the timing of the bunches recirculating back through the Linacs, can now be refined. This will be accomplished by comparing the phase transients in Linac-A and Linac-B in the time just before the accelerating-pass and after the decelerating-pass of the bunch train, or by minimizing the required forward power to the cavities. The beam transport efficiency must also be taken into account before using this to adjust the path-length delay for the proper energy recovery arrival time.

Energy recovery accelerator setup

After taking the train of bunches through the entire circuit of the ERL, a second train of bunches is added with a delay of T_{RECIRC} (Fig. 2.9.4) Since there will be energy recovery in Linac-A and -B from the first train of bunches, the beam loading of the RF cavities will be compensated and the energy of each of the bunches in the second train will be nearly the same throughout the train. Assuming that the energies of Linac-A and Linac-B are increased slightly to account for the beam loading of the first train, then more precise orbit, optics, and time-of-flight corrections can be applied by measuring the beam parameters of the energy-

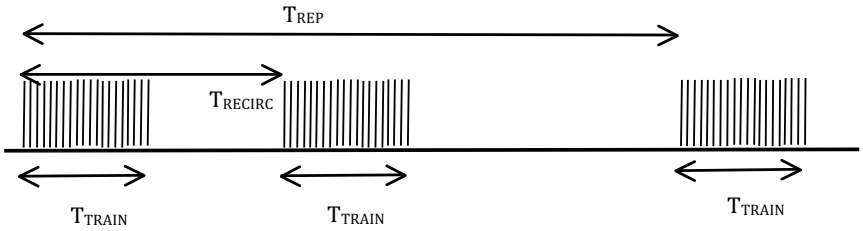

Figure 2.9.4: ERL bunch pattern for the Energy recovery accelerator setup-mode.

recovered part of the bunch train. At this point the position feedback loops can be placed in operation.

Current ramp-up

Having established the parameters for the ERL with a train of bunches operating with energy recovery, the ERL will be poised to ramp up the current to full CW operation. This will be accomplished by adding a trailing train spaced by T_{RECIRC} after each of the set of bunch trains already in operation. To reduce beam loading of the Linac RF cavities, additional trailing trains will be added in time intervals equal to approximately the Linac RF cavity filling time ($\sim 16\,\mathrm{ms}$). So the time it will take to add trains (spaced by T_{RECIRC}) to fill in the gap between repeated trains, T_{REP}, will be $T_{\mathrm{REP}}^2/T_{\mathrm{RECIRC}} = (16\,\mathrm{ms})^2/6.77\,\mu\mathrm{s} = 37\,\mathrm{s}$. At this point there will be a continuous set of trains of length T_{TRAIN} spaced by T_{RECIRC} and the energy of all bunches will be the same since the Linac RF cavity beam loading will be compensated by the second pass of each train through the Linac cavities.

The final step of the current ramp-mode will be to fill in the gap $T_{\mathrm{RECIRC}} - T_{\mathrm{TRAIN}}$ between trains. Assuming that an additional set of bunches of duration T_{INC} will be added every T_{REP}, this step will take a time of $T_{\mathrm{RECIRC}}/T_{\mathrm{INC}} \cdot T_{\mathrm{REP}} = 6.77\,\mu\mathrm{s}/40\,\mathrm{ns} \cdot 16\,\mathrm{ms} = 2.7\,\mathrm{s}$.

In normal operation when the ERL begins to ramp its current after the accelerator parameters have already been established, the only difference from the preceding procedure will be to begin with the beam having the train spacing used in the Energy Recovery Accelerator Setup-mode (Fig. 2.9.4). After a pause to make certain all feedback loops are operating correctly, the current will be ramped in the two steps described in the preceding paragraphs of this section. These two steps for incrementing the current will take approximately 40 seconds to complete.

Laser considerations

In order to execute the startup procedure described in the preceding sections, the laser must be capable of producing light pulses for bunches having the required time structures. This is accomplished by hardware for two distinct laser-pulse timing patterns. During the ERL Injector Phase 1-A tests, beams with the same time structures as these bunch patterns have been in routine use. The first of these laser setups generated trains of bunches with a 50 MHz repetition rate and could be gated for various numbers of bunches in the trains. To generate the single bunches needed for the first-turn-steering mode of operation (Fig. 2.9.2), the laser

will be gated to generate for a train having only one bunch. The second of the laser setups created trains of 1.3 GHz spaced bunches of various lengths, routinely operating with train lengths up to hundreds of microseconds long at a 60 Hz repetition rate. In the Phase 1-A laser system configuration, the Pockels cell modulator driver was not capable of operating at a 160 kHz repetition rate and smoothly transitioning to full duty cycle for the bunches. We are in the process of designing a gating scheme, which is capable of the parameters required for the bunch patterns specified above.

Beam loss considerations

In addition to using the intermediate and high-energy beam stops upstream of the Linacs, to minimize the damage and radiation from beam particles lost during the establishment of initial conditions for the first operation of the ERL, the train of bunches will be operated in a 'single shot' mode. In this mode the BPM and other beam instrumentation systems would record the beam's trajectory, RF phase transients, radiation loss location, and accelerator parameter corrections before injecting any subsequent train of bunches.

As part of the first tune up of the ERL beam, the beam abort system will need to be commissioned before continuing with first turn accelerator setup in order to protect sensitive components when the beam operates at the higher repetition rate.

ERL BPM system specifications

There are five different modes of operation of the ERL needed to take conditions from injecting the first beam through routine day-to-day operations. The beam position monitors will be located next to quadrupoles at locations that are optimum for Singular Value Decomposition (SVD) based beam orbit correction schemes. In the Linac and parts of the turn-around arcs there will be both the accelerating and the decelerating beams and it will be necessary to measure the position of each beam independently.

1. **First turn trajectory**
   - Objective: To transport a low-power beam from the injector to the high-energy stop immediately before a return to Linac-A for deceleration in order to measure and roughly correct the trajectory and optics. The high-energy beam power is limited to 100 W plus the dark current and laser extinction.
   - Bunching pattern: Single 77 pC bunch at a 240 Hz repetition rate.
   - Goal for BPM resolution:

     ± 1 mm at 240 Hz readout

     $\pm 100\,\mu$m at 2.5 Hz readout

2. **First turn accelerator setup**
   - Objective: To transport a low power beam from the injector to the high-energy stop immediately before the return to Linac-A for deceleration in order to measure and to begin to refine the trajectory and optics and to start setting up the slow orbit feedback. The high-energy beam power is limited to 100 W.

- Bunching pattern: Single 77 pC bunch at a 240 Hz repetition rate.
- Goal for BPM resolution:

  $\pm 100\,\mu$m at 240 Hz readout

  $\pm 10\,\mu$m at 2.5 Hz readout

3. **Low-power energy recovery**
   - Objective: To transport a low-power beam (< 100 W) from the injector to the final beam stop after deceleration in Linac-B in order to measure and roughly correct the trajectory and optics. The low beam power is to allow for the beam being lost before reaching the beam stop.
   - Bunching pattern: Single 77 pC bunch at a 240 Hz repetition rate.
   - Goal for BPM resolution:

     ± 1 mm at 240 Hz readout

     $\pm 100\,\mu$m at 2.5 Hz readout

4. **Energy recovery accelerator setup**
   - Objective: To transport a low power beam from the injector to the final beam stop after deceleration in Linac-B in order to measure and to continue to refine the trajectory and optics and to start setting up the slow orbit feedback in the return loop.
   - Bunching pattern: Multiple trains of 77 pC bunches (duration ~ 100 ns) with a $6.7\,\mu$s spacing operating at a 240 Hz repetition rate.
   - Goal for BPM resolution:

     $\pm 100\,\mu$m at 240 Hz readout

     $\pm 10\,\mu$m at 2.5 Hz readout

5. **Current ramp-up**
   - Objective: To transport a beam of increasing power, from the injector to the final beam stop after being decelerated in Linac-B in order begin energy recovery. The beam is in a train of bunches in a pulse of duration from 80 ns to continuous, operating at a 240 Hz repetition rate. As the average beam current is increased the trajectory and optics and slow orbit feedback are further corrected.
   - Bunching pattern: 77 pC bunches spaced at 1.3 GHz in trains of duration increasing from 80 ns to continuous, operating with a 240 Hz repetition rate
   - Goal for BPM resolution:

     $\pm 100\,\mu$m at 240 Hz readout

     $\pm 10\,\mu$m at 2.5 Hz at all times for slow orbit observations / feedback

     $\pm 0.3\,\mu$m at 1 kHz after reaching continuous beam current operation for slow orbit feedback

2.10 Beam Diagnostics and Control

2.10.1 Introduction

The end product of the ERL is the x-ray beam produced in the undulators, and the task of the beam diagnostics and control system is to stabilize the ERL beam to the needed accuracy. The most stringent beam requirements are for the beam in the 25 m long undulator with:

- $\sigma_x = 0.3\,\mu$m (horizontal beam position jitter)
- $\sigma_y = 0.3\,\mu$m (vertical beam position jitter)
- $\delta E/E = 2 \times 10^{-4}$ (beam energy spread)
- $\sigma_{x,y,\mathrm{rms}} = 0.3\,\mu$m (beam size variation)
- $\sigma_z = c \times 20\,$fs (bunch length variation)
- $\sigma_t = 20\,$fs (arrival-time variation)

While these tolerances are tight, they are not beyond the state of the art in presently operating storage rings and FELs. As much as possible, existing designs for the various beam diagnostics and control systems will be used in the ERL. Therefore none of the proposed systems should need an extensive research and development program to achieve their parameters.

The ERL's main distinction is the presence of two beams in the Linac structures that need to be individually diagnosed and controlled. The fact that the two beams generate a 2.6 GHz signal in the beam position monitors, in addition to the 1.3 GHz signal can be used to determine the positions of the two beams separately.

The following sections describe the components of the beam diagnostics and control system. The ERL has five different operating modes and the system must accommodate each of these modes. The first section describes the start-up procedure, and is followed by the beam position monitoring system. The various feedback systems are then described, and the likely seismic environment at the ERL completes this chapter.

2.10.2 Beam position measurement system

The conceptual design for the beam position monitor (BPM) system is based on experience from the use of three generations of BPM processors, capable of bunch-by-bunch and turn-by-turn position measurements in CESR and a simple adaptation of these processors for CW use with the ERL prototype injector. The basic block diagram for the beam position monitor system is shown in Fig. 2.10.1. A vacuum chamber with either four striplines or four button pickups is the element employed as the beam position detector where approximately 90 % of the BPMs will be button detectors and the remainder will be more sensitive stripline detectors. Since the beam has a 1.3 GHz CW repetition frequency f_0, there will be a 1.3 GHz band pass filter with 50 MHz bandwidth for each of the signals. This will produce a 1.3 GHz signal averaged over about 26 bunches. Each filtered signal will then be down converted to 12.5 MHz and fed into one of the four input ports of the BPM electronics. The input analog board will have the ability to change its gain over a range of nearly 200. The signal will be sampled

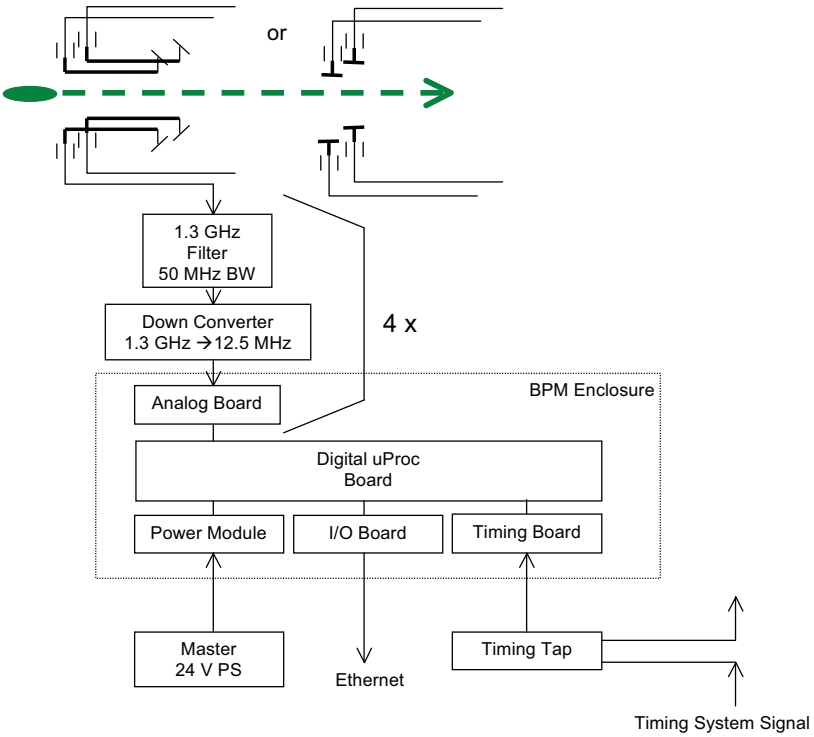

Figure 2.10.1: Block diagram of a beam position monitoring system.

at 50 MHz and an I/Q (amplitude and phase) measurement is performed. From the relative amplitudes of the 4 BPM signals the beam's position will be inferred.

The Digital Signal Processor (DSP) will provide average position results, timing error correction and other diagnostic information at various update rates ranging from 10 Hz to 10 kHz. The expectation is that the control system will be able to access this information at about a 10 Hz rate. As with the current CESR BPM system, the proposed BPM system will have the ability to acquire trajectory data triggered at 80 ns increments in a variety of timing patterns. The control of its timing system will be very flexible and will permit triggering of the trajectory data acquisitions locked to triggers of other instrumentation.

The position sensitivity for a stripline composed of four equally spaced strips around the circumference of a beam pipe of radius R is determined by the relative signals on each stripline. Using a beam displaced in the same plane as two diametrically oppositely spaced strips, the sensitivity can be estimated from the ratio of the difference voltage V_Δ and the sum voltage V_Σ from the strips to be proportional to the 'measured' x position,

$$x_\mathrm{m} = \frac{R}{2}\frac{V_\Delta}{V_\Sigma}\,.$$

The ratio of the difference over sum of 0.1 % would correspond to a 'measured' x position of 6.3 μm for the proposed stripline parameters for the ERL.

Table 2.10.1: Comparison of the expected resolution of stripline and button BPM detectors under various beam conditions. TN: thermal noise.

Operation Mode	Measurement Bandwidth	Stripline BPM Resolution (μm)	Button BPM Resolution (μm)
CW operation or	12.5 MHz	1.9	6.5
current ramp-up mode	10 kHz	0.17	0.58
1.3 GHz, 77 pC beam	10 Hz	0.005	0.018
	12.5 MHz (TN)	0.43	6.3
first turn trajectory mode,	240 Hz	17	160
240 Hz, 77 pC single bunch	240 Hz (TN)	11	160
first turn trajectory mode	12.5 MHz	2.7	25
240 Hz, 19 pC single bunch	10 kHz	0.23	2.2
	10 Hz	0.007	0.07
	12.5 MHz (TN)	1.7	25
first turn accelerator setup &			
low power energy recovery /	240 Hz	1.9	6.5
energy recovery accelerator setup	240 Hz (TN)	0.43	6.3
1.3 GHz, 77 pC, 240 Hz rep. rate,			
100 ns train duration			

Noise level and BPM resolution

The expected rms thermal noise voltage $V_{\rm n}$ is 3.2 mV for each of the BPM signals for the proposed stripline or button BPM system. After adding the two contributions in quadrature and including the fact that the automatic gain software will typically have the ADCs operating from 40-80 % of full scale, the noise level and resolution expected places a range for the position resolution of $1.4 - 2.5\,\mu$m for normal 1.3 GHz operation for the sampling of a single 12.5 MHz period. When averaging is employed, the average resolution will become $0.17\,\mu$m with a 10 kHz update rate or 5 nm with a 10 Hz update rate. Table 2.10.1 summarizes the expected resolution for the different modes of ERL operation.

System configuration for locations with two beams

In certain sections of the accelerator such as Linac A and B both the accelerating and decelerating beams will be present simultaneously. Measuring beam positions in these regions will raise some interesting challenges. The approach that has been adopted here uses the fact that the two beams will be equally spaced in time and thus produce a 2.6 GHz signal in addition to the normal 1.3 GHz signal. The relative amplitudes of these two frequency components are related to the charges in the accelerating and decelerating beams, q_A and q_D respectively, and the displacements of each beam, (Δx_A, Δy_A) and (Δx_D, Δy_D). The individual beam position information can then be extracted from the amplitudes and phases of the two frequency components.

2.10.3 Transverse beam stabilization

After accelerating the electron bunches to high energy, it is most important to deliver stable x-ray beams to the users. To avoid diluting the advantages of the low emittance beam, the position of the x-ray beam needs to be stable to better than 10 % of the x-ray beam size at the experiment, $\sigma_{\mathrm{x,x-ray}}$ and $\sigma_{\mathrm{y,x-ray}}$. The projection of the x-rays from the source point implies that the positional deviations (Δx, Δy) and angular deviations ($\Delta x'$, $\Delta y'$) of the electron beam's centroid at the source point must be held to 10 % of the standard deviations of its positional (σ_x, σ_y) and angular ($\sigma_{x'}$, $\sigma_{y'}$) distributions. If the electron beam has been stabilized against multi-pass beam breakup, then the next most serious effect will be centroid motion e.g. due to the variations from the laser driver, vibrations of the positions, or slow drifts in fields of accelerator elements and energy variations of the Linac RF accelerating fields. Feedback to precisely control the beam's trajectory through the ERL will be employed to counteract these deleterious effects.

To place a scale for the desired position stability, there are two cases to consider. The first is when the 77 pC bunches have a geometric emittance of 30 pm. In a region within the undulators where β_x and β_y are approximately 2.5 m, $\sigma_{x,y} = 8.4\,\mu$m and $\sigma_{x',y'} = 3.5\,\mu$rad, making the implied stability for $\Delta_{x,y} = 0.8\,\mu$m and for $\Delta_{x',y'} = 0.35\,\mu$rad. The second case is for the 19 pC high-coherence bunches, having the lower emittances of 8 pm. In the undulators with similar optics and beta functions, the beam sizes are $\sigma_{x,y} = 4.5\,\mu$m and $\sigma_{x',y'} = 1.8\,\mu$rad, and the stability requirements thus become $\Delta x, y = 0.4\,\mu$m, and $\Delta x', y' = 0.18\,\mu$rad. As an example if the beta-functions at the steering magnets were in a range from 5 m to 50 m, then the typical deflections to produce the minimum change just equal to $\Delta x, y = 0.4\,\mu$m and for $\Delta x', y' = 0.18\,\mu$rad would be in the range of $0.4\,\mu$rad to $4\,\mu$rad. With maximum steering strengths of ± 0.4 mrad for the ERL's corrector magnets, if these magnets are employed for feedback, they will need to be able to be set to less than $\pm 3 \times 10^{-4}$ of full scale.

Slow orbit feedback

The slow trajectory feedback is designed to correct the highest bandwidth position errors that are possible using the standard lower bandwidth steering correctors. If the slow position feedback system is configured using conventional laminated dipole magnets surrounding an aluminum beam pipe, the zero of the lead-lag compensation of the feedback loop should be set at the pole of the power supply and magnet transfer function, which should be at the eddy current frequency for the magnet laminations and is of the order of 60-100 Hz. This determines the frequency for the zero, leaving the next lowest pole at the beam pipe's eddy current roll-off frequency, which is 360 Hz for aluminum. This then becomes the unity gain frequency for the position feedback loop for a conventional single pole frequency roll-off, implying that the position feedback loop's bandwidth would be approximately 360 Hz.

If the source of the vibration's coupling to the beam occurs some distance away from particularly sensitive accelerator elements (e.g. the undulators) two or more position feedback clusters can be employed to suppress the motion of the beam due to the vibrations, and their effects would roughly multiply. Ultimately a detailed simulation study of slow trajectory will be undertaken to confirm this final feedback solution. In order to fully utilize the capability of the position feedback systems to stabilize the undulator beams, it will be necessary to have

steering power supplies with sufficient resolution (and this might require a second trim-steering winding and power supply for the correctors) and to have an accurate method of establishing the location of the BPMs relative to the x-ray experiment. The BPM locations may need to be determined either inertially or with a dynamical (e.g. laser-based) readout.

Lastly, there is one additional facet to the implementation of slow-position feedback for the ERL. It is likely that slow-trajectory feedback clusters will be enabled throughout the ERL in relatively few locations along the beamline because there may be no significant differential vibrational excitations of the beam and the feedback can, therefore, be disabled in that region. If this is the case, then the regions not enabled will still be susceptible to possible longer-term drifts in magnet fields, magnet supports, or stray fields. A solution to these long-term sources for trajectory drifts will be to have the control system execute a slow feedback loop (less than 1 Hz), which measures the beam's position throughout the entire trajectory, and make small changes to corrector magnets to restore the beam to a reference trajectory.

Fast orbit feedback

The preceding section described the slow-position feedback utilizing conventional steering magnets arranged in localized clusters with the BPMs from that region. As was shown above, this will give a slow feedback loop having an open loop gain with a single pole roll-off and a unity gain frequency of approximately 360 Hz. To anticipate the possibility of sources for beam motion at higher frequencies, wider bandwidth feedback is envisioned. Examples of possible higher frequency sources for beam motion are 1) oscillations in the Gun HV PS, 2) changes in beam loading of the RF accelerator cavities due to small photo-emission variations of the gun, caused by intensity variations of the laser, or 3) residual trajectory errors after the RF cavities' energy feedback loops have corrected phasing errors of the Linac's accelerating voltage.

The bandwidth of the general slow-trajectory feedback scheme proposed in the two preceding sections is limited by two separate effects: the eddy currents in the steering magnet's laminations and eddy currents in the vacuum chambers. Ferrite magnets acting on the beam through coated ceramic vacuum chambers or stripline kickers can overcome this. Installing a set of these deflection elements in both the horizontal and vertical planes along with BPMs in a similar clustered configuration as described for the slow trajectory feedback will allow a fast trajectory feedback loop with a bandwidth exceeding 100 kHz.

Control of beam position in the injector

The diagnostics in the injector will be comprised of devices that can be categorized into two classes: the diagnostics suitable for CW high average current beam and interceptive diagnostics usable with a low-power tune-up beam. The CW diagnostics will provide the necessary information on the beam centroids (two transverse positions, time of arrival and energy), bunch charge, and beam current, whereas the interceptive diagnostics will allow measurements of the second moments of the beam distributions as well as the phase space density maps of the pulsed beam containing the full bunch charge. Two additional types of devices will be used to monitor parameters of the full power beams. A THz spectrometer using the radiation from the dipole magnet in the merger will provide estimates of the longitudinal form-factor of the bunch and the flying wire will provide beam profile measurements under the

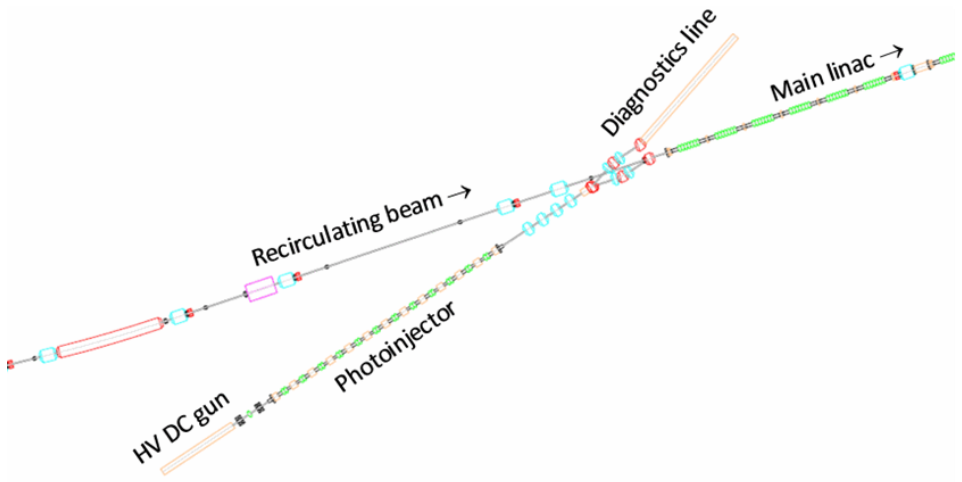

Figure 2.10.2: The location of the diagnostics beamline used for tune up of the injector at its full charge per bunch.

conditions of the full average current operation. The flying wire (20 micron diameter carbon filament moving transversely through the beam once with up to 20 m/s speed), although not non-interceptive in its nature, will minimally perturb the high-current beam and will be used occasionally during the machine setup stage at sufficiently high average current ($> 10\,\mathrm{mA}$).

Since the beam in the injector is space-charge dominated even at the design energy of about 15 MeV, it will be necessary to characterize the phase space prior to the injection into the main Linac. In the low-energy range of the injector, by far the most reliable method of assessing the transverse phase space density is through beam collimation by precision slits in order to convert the beamlet from space charge to emittance-dominated regime for subsequent probing to determine its intrinsic divergence. In order to characterize the beam under the conditions identical to those of the actual operation, a diagnostics line will be introduced symmetrically mirroring the main Linac arrangement (see Fig. 2.10.2). The first merger dipole can be used to switch the beam into the diagnostics line, which contains beam profile monitors, emittance measurement system, and longitudinal phase space characterization capability. These will all be suitable for full bunch charge characterization at a much reduced duty factor (the average beam current is less than 100 uA to limit the total beam power to about 1 kW).

2.10.4 Beam position and arrival time monitors

The primary diagnostics for monitoring the beam position and arrival time will be stripline BPMs, successfully deployed during Phase 1a photoinjector development stage. The photoinjector is equipped with 10 BPMs. The resolution of a 100 Hz data stream for beam position is on the order of a few microns for nominal bunch charge operation, which is more than adequate for photoinjector needs. Additionally, all BPMs report arrival time phases relative to the 1.3 GHz reference signal with a 0.1° accuracy under typical operation conditions. Beam orbit and phases will be compared to the online model, which will be incorporated into the

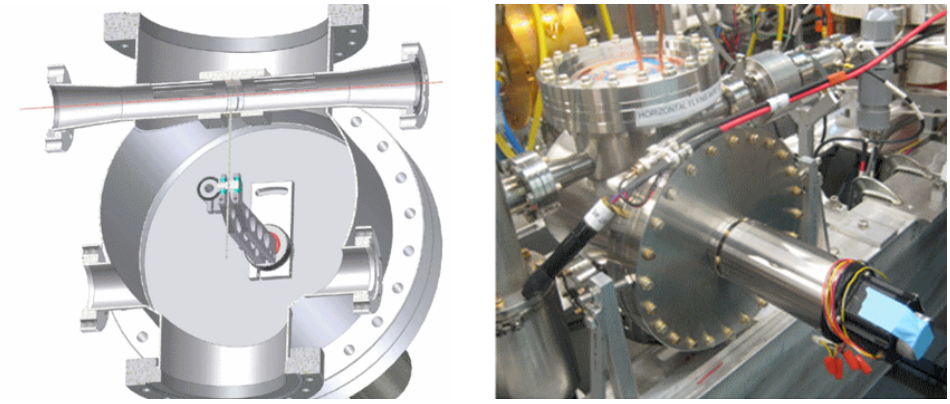

Figure 2.10.3: The cross-section of the flying wire profile monitor (left) and installation of the device in the Cornell ERL injector prototype (right).

control system.

2.10.5 Beam size

View screens with resolution of about 30 μm will be used to obtain the beam profile for the pulsed train tune up beam. Two different materials will be used to cover several orders of magnitude in beam current: BeO that is sensitive to sub-nano-Ampere average currents, and less sensitive CVD diamond screens that can take up to 1 μA of beam current. Each screen station will be equipped with both high- and low-sensitivity screens and interfaced to a 12-bit video camera serving the profile information to the control system. RF shielded assemblies will be employed throughout when the screens are retracted to minimize perturbations due to wakefields on the beam and heating effects.

Determining the transverse profile of the full average current beam is a challenging task. The MW level average power of the beam precludes interceptive techniques, while the low energy of the injector limits the usefulness of non-interceptive techniques analyzing the synchrotron radiation due to its rather long wavelength well outside the visible optical range. Possible approaches involve reduction of the 100 % duty factor beam with a very fast kicker into a dedicated diagnostics beamline equipped with a suite of interceptive diagnostics or the use of specialized diagnostics capable of withstanding the full MW power of the beam. A flying wire profile monitor (see Fig. 2.10.3) has been developed within the framework of the Phase 1a development work that allows the characterization of the full 100 mA average current beam. The system consists of a 20 μm carbon filament traversing the electron beam with a speed of up to 20 m/s. The filament causes scattering of a very small fraction of the electrons inside the bunch train with these electrons being lost on the beam pipe several meters downstream of the device and thus providing a signal proportional to the local density of the beam as intercepted by the filament. This diagnostics is intended for occasional use, primarily during the high average current beam setup. Further evaluation of this diagnostics approach is underway within the Phase 1b effort.

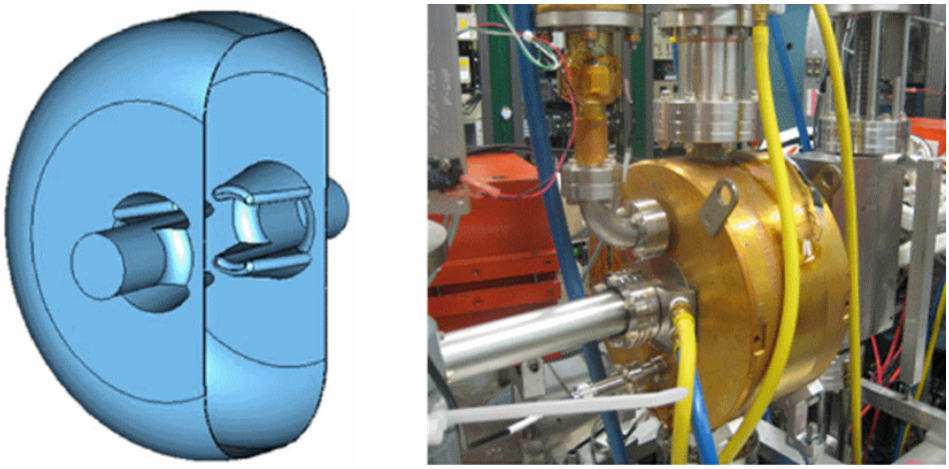

Figure 2.10.4: RF deflecting cavity used for temporal profile measurements in the injector. RF geometry (left) and installed device in the injector beamline (right).

Bunch length

A RF deflecting cavity (see Fig. 2.10.4) operating in $TM_{1,1,0}$-like mode at 1.3 GHz will be the primary diagnostics for the bunch length measurements [1]. The deflector is operated in pulsed mode consistent with the tune-up beam structure and low power requirement of the view screens downstream of the cavity used to register the streaked beam image. When not in use, the deflector will be detuned to avoid adverse effects on the beam. For better resolution, collimating slits can be used upstream of the cavity to increase the measurement resolution. Time resolution of about 100 fs has been demonstrated with the device in the Cornell ERL injector prototype. Additional collimation in the horizontal plane prior to the dipole magnets of the merger creating the dispersion allows direct mapping of the longitudinal phase space while simultaneously measuring the bunch length and the energy spread of transversely selected beam slice.

A THz spectrometer [2] picking up the radiation from the merger dipole will allow the characterization of the longitudinal profile form-factor for the full power beam in the bunch length region of interest (1-3 ps) . The spectrometer has been fully developed in the Phase 1a injector, and operational experience will be obtained within Phase 1b injector prototype operation.

Energy spread and fluctuations

Energy spread measurements will be carried out in the dispersive section of the merger. A beam dispersion of 0.3 m coupled with a collimated beam size of less than 100 μm (FWHM) will allow for a relative energy resolution of less than 10^{-3} for a given transverse slice as selected by the precision collimator. Likewise, energy fluctuations of less than 10^{-4} will be measurable with the BPMs located in the merger section.

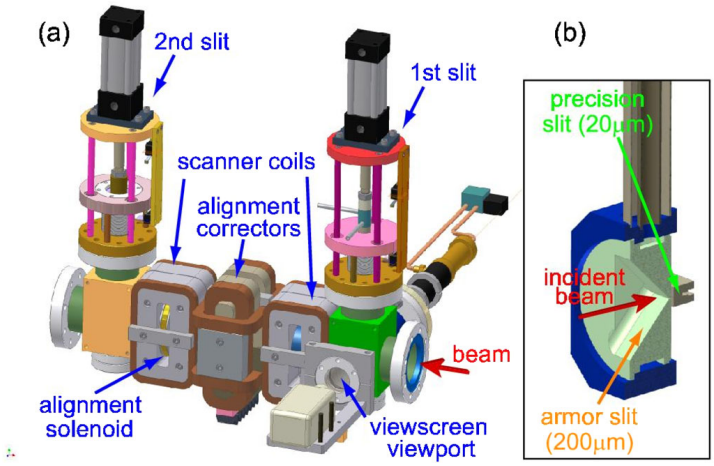

Figure 2.10.5: (a) Emittance measurement system as used downstream of the DC gun. The 15 MeV version of the device (not shown) is similar with the difference of a larger separation between the two slits (1.5 m). (b) details of one of the slits showing water cooled armor slit (80 μm opening for the 15 MeV version) protecting the precision slit.

Emittance

The emittance measurement system (see Fig. 2.10.5) will be comprised of precision slits (20 μm opening) and magnetic beam scanners. The signal is detected on a Faraday cup downstream of the second slit assembly. Avoiding mechanically moving parts will enable fast data acquisition at a several kHz rate, allowing detailed transverse phase space maps to be obtained in a matter of several seconds. A pair of the precision slits (both horizontal and vertical plane) will be located in the diagnostics beamline downstream of the merger, and the other set of retractable precision slits will be placed upstream of the deflecting cavity in the straight section following the injector cryomodule. Furthermore, each of the precision slits will be equipped with a special armor slit that dramatically reduces the beam power incident on the precision slit, thus, allowing the use of this diagnostics with about 1 kW of beam power or about 100 μA of average current. The resolution of the normalized emittance using this approach is better than 0.1 mm-mrad rms normalized [3].

Current measurement

A fast current measurement at a MHz rate is achieved using signals from a dedicated stripline BPM pickup. This fast signal will be used with the low-level RF control to compensate for the beam loading as well as with a dedicated feedback loop to stabilize the intensity of the laser. Slower precision measurements of the beam current will be accomplished using a DC current transformer having a noise level of a couple of μA over 1 s integration time.

Beam loss and halo measurement

A water-cooled movable copper edge will be used to determine the stray particle (halo) distribution both through detection of bremsstrahlung and direct current measurement from the isolated copper edge serving as a Faraday cup. A system to monitor beam scraping is planned that employes sensitive lock-in amplification capable of detecting nano-Ampere-level beam-current losses in the photoinjector. It will be similar to the one developed for the CEBAF accelerator [4].

Control of beam position for two beams in the ERL Linac

Having both an accelerated beam and a decelerated beam in the ERL Linacs will present special challenges for the beam position feedback. Since the steering corrector magnets planned for installation in the cryostat will be superconducting, it is not possible for these magnets to have sufficient bandwidth to develop trajectory feedback to stabilize ground vibrations, so this will require a different approach. The first step will be to measure the positions of each beam and then correct the trajectories of each beam separately by: 1) placing the trajectory of both beams on the axis of the Linac as nearly as possible, while accounting for the difference in energy of the beams; 2) putting more emphasis on the correction of the accelerated beam; and 3) adjusting the beams' incident trajectories before the merging of the two beams to reduce the differential orbit errors. One solution for the beam trajectory feedback in the Linacs will be to use fast and slow feedback clusters for each beam independently before their mergers upstream of both Linac-A and Linac-B and then to rely on slow orbit correction within the Linacs to reduce long-term trajectory drifts.

Control of beam parameters in undulators

The trajectory feedback cluster will in principle be capable of maintaining the beam's position and angle at both a source point within an undulator and at the end of the feedback cluster. Within the undulator regions of the accelerator, there are some outstanding design issues, which will need to be addressed. The first is that the spacing between adjacent undulators is relatively short; there is not a large phase advance and not many locations for BPMs or steering correctors. Between each undulator, it will be sufficient to utilize a pair of BPMs and a pair of horizontal and vertical steering correctors in a modified feedback configuration to stabilize any error induced upstream of the source point of the downstream undulator. However, it would be advisable for the redundancy of the position measurements to have at least three BPMs. Likewise, if the final optics design permitted a third horizontal and vertical corrector, spaced with a significant phase advance from the other two, these steerings could be viewed effectively as a backup set of correctors if one of the other two were to fail in service. In this proposed feedback implementation for the undulator regions, there will be one (or possibly two) position feedback clusters with the full set of BPMs and steerings upstream of the first of the south or north arc undulators. This feedback will stabilize the beam before it arrives at the first undulator. Between each of the next pairs of undulators, there will be the modified feedback configurations, which will be able to correct displacement and angle errors for each of the undulator source points.

The next question is: How will the beam stabilization be undertaken? One scheme is to separately stabilize the electron beam, using the ERL steering correctors, and the x-ray beam, using moveable gratings. However, if there is correlated motion remaining from the electron beam feedback, the x-ray beam feedback will need to correct this also. Another possibility is to take x-ray and electron beam position signals and connect them into a feedback matrix in the cluster feedback processor with appropriate weights and have them act on the electron beam's position to keep the x-ray beam on target. These two possibilities raise a significant concern in the ability to distinguish the core of the undulator beam from the much broader $1/\gamma$ fan of radiation. One approach would be to distinguish energy from power, perhaps by the use of a filter or by energy sensitive florescence that could be imaged with high resolution during the set-up procedures. Another possibility for the x-ray beamlines would be to establish either an inertial system as reference or perhaps a laser system as a reference for the BPMs. Determining which of these two viable solutions along with the appropriate instrumentation will be an important part of the final design optimization of the ERL.

2.10.6 Beam arrival time and experiment synchronization

Bunch arrival time measurements will be required at several locations within the accelerator in order to monitor and control the proper functioning of the energy recovery process as well as to provide a timing reference to the experimenters. The required resolution of these monitors depends strongly on the ERL operation mode. The design goal will be for a bunch arrival-time monitor resolution of about $1/10^{\text{th}}$ of the bunch duration, which corresponds to 200 fs (rms) for the 100 mA operation mode with its 2 ps (rms) long bunches, and 10 fs (rms) for the short bunch mode, which delivers bunches of less than 100 fs rms duration. This resolution should be achieved in a measurement bandwidth of at least 1 MHz so that these monitors can be utilized in fast control loops to stabilize the bunch arrival time. Ideally, the monitors will be capable of measuring the arrival times of single bunches, since this would allow for the study of high frequency noise contributions. This can be helpful to further improve the machine stability as well as to understand fast beam instabilities.

The resolution of the beam arrival-time measurement resolution will be degraded by two contributions: the distribution of the time-reference signal to the locations in the accelerator where the measurements take place; and the resolution limit of the beam arrival-time detection itself. The easiest approach for the arrival-time detection would be a scheme in which a beam-induced RF signal is mixed against a reference RF signal that will allow for resolutions of better than 50 fs. If very high frequencies are used for the phase detection process, even sub-10 fs resolution is feasible (see, e.g., [5]). The main difficulty with such a scheme is, however, the stable distribution of the reference RF signal within the accelerator. Even with very tight RF cable temperature control and with specially selected cable types with low thermal coefficients, the timing from the reference signals can easily drift by several picoseconds when cable lengths reach many hundred meters. As a result, an active way of measuring and controlling the travel times through the cables would be required.

An alternative approach of distributing the timing signals is to use the optical signal from a laser as a timing reference and to distribute this signal via optical fibers. The advantage of such a scheme is the fact that optical timing detectors allow for much better resolution than is achievable with RF technology. At the Sub-Picosecond Pulse Source (SPPS), the

timing reference of a laser was used to synchronize two color pump-probe experiments at an accelerator-driven light source for the first time. The electron bunch arrival time was measured with pulses from a Ti:Sapphire laser using electro-optical methods. The same laser was used as the pump source of the experiments. The time stamps derived from these arrival-time measurements reduced the arrival time jitter in the post-analysis to around 60 fs [6].

X-ray free-electron lasers that are capable of producing light pulses much shorter than 10 fs [7, 8] have initiated research on optical synchronization schemes that can deliver sub-10 fs precision. Two different approaches currently exist. In the first, the fiber length is stabilized based on an interferometric scheme that uses the narrowband optical frequency of a continuous-wave laser [9]. RF signals can be distributed over this stabilized link by RF modulation of the amplitude of the laser signal. At the end of the fiber link, the RF signal is extracted from the laser signal and can be used for synchronization purposes. In the second scheme, a mode-locked laser is used as a time reference and the optical fibers by which the signals are transmitted are stabilized based on optical cross-correlation between pulses from the laser and those reflected back at the end of the fiber link [10]. In this approach, the laser pulses from the fiber links can be utilized to drive an electro-optical detection scheme without the need for any additional intermediate systems, that might degrade the timing stability. This allows for measurements of the bunch arrival time with respect to the reference laser with a resolution of better than 10 fs [11]. This is currently the best reported resolution for an arrival-time measurement with respect to a remotely located time reference. The ERL design will use a similar scheme to provide an arrival-time resolution of 10 fs that will be required for the experimental program.

Optical timing reference and femtosecond stable distribution of reference signals

Passively mode-locked, femtosecond lasers capable of producing laser pulses trains with a timing jitter of only a few femtoseconds at frequencies above a few kHz (see, e.g., [12, 13]) exist and are now commercially available (see, e.g., [14]). Laser-timing changes occurring at lower frequencies can be corrected for with piezo-electric transducers used to lock the laser repetition frequency to a long-term stable, low-noise RF reference frequency. In order to simplify the dispersion compensation of optical fibers, a laser with an Erbium-doped gain medium is used.

For the ERL the laser pulse train will be transmitted via an optical fiber to the remote location in the accelerator. Figure 2.10.6 shows the schematic setup to stabilize the travel time of the optical pulses through the fiber. At the end of the fiber-link, part of the laser power will be reflected by a Faraday rotating mirror. In an optical cross-correlator, changes of the travel-time through the fiber will be determined by measuring the timing between the returning pulses and those directly from the laser. Variations of the travel-time will then be compensated for by a piezo-electric fiber stretcher in combination with a motorized optical delay-stage.

Femtosecond resolution bunch arrival-time monitors

Figure 2.10.7 below illustrates the principle of the electro-optical bunch arrival-time monitor (BAM). The beam will induce a fast transient signal in a broadband beam pick-up, which will

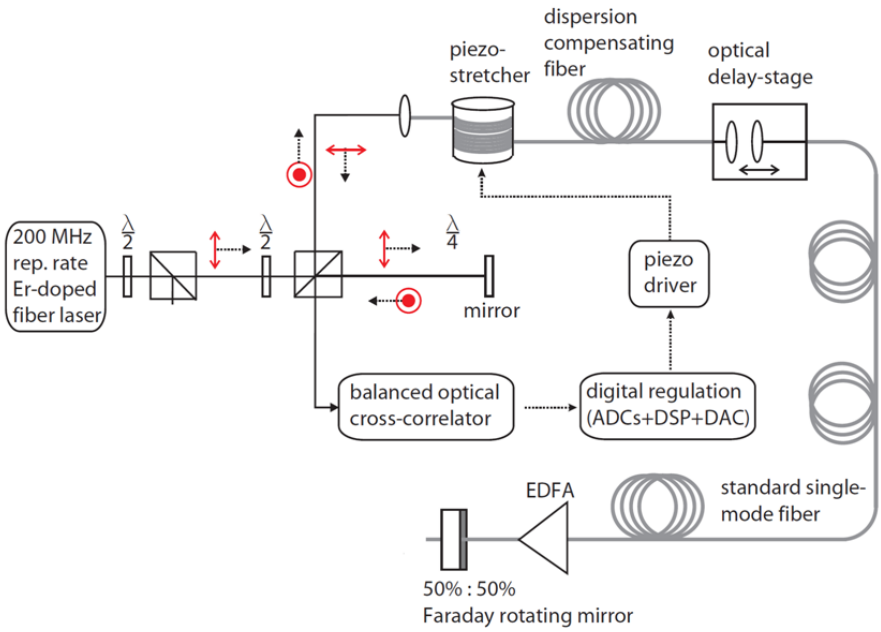

Figure 2.10.6: Schematic setup to stabilize the travel time of light pulses through an optical fiber with femtosecond precision (from [12]).

be used as the input of a Mach-Zehnder type electro-optical amplitude modulator (EOM). The timing of the reference laser will be adjusted in such a way that one pulse arrives at the time of the zero-crossing of the electrical signal when it passes the EOM. Electron bunch arrival time variations will shift the time of this zero-crossing and therefore lead to a different modulation voltage seen by the laser pulses and thus to varying laser-pulse energies after the EOM. By detecting the energy of individual laser pulses, the bunch arrival time can be deduced.

In order to reduce the dependence of the detection scheme on the electron bunch charge as well as to increase the dynamic range, a slow feedback loop with an optical delay line as an actuator will be used to keep the laser pulse near the zero-crossing of the transient signal even when the bunch arrival time changes. By this means, the dynamic range for slow beam arrival time changes will be limited only by the range of the delay line which can be many hundred picoseconds (around 360 ps in [12]). The dynamic range for fast timing changes will be limited to around 3 to 4 ps. This range can be extended by adding a second EOM that is driven by a strongly attenuated RF signal (see Fig. 2.10.8).

In the ERL, two new difficulties arise compared to the FLASH system [11, 12] that will require further research. The first one is the lower bunch charge of the ERL (77 pC or 25 pC), depending on the operation mode, which will be 10 to 30 times lower than in [11]. In order to maintain the same single bunch resolution, a modified beam pick-up will be required. If an arrival-time resolution of 10 fs is not required on a bunch-by-bunch basis but only in a bandwidth of 1 MHz, this will relax the required single bunch resolution by a factor of 36 since the results for many bunches can be averaged.

The second difficulty originates from the high repetition rate of the ERL. Ringing of the beam pick-up signal longer than the bunch spacing of 770 ps can degrade the measurement

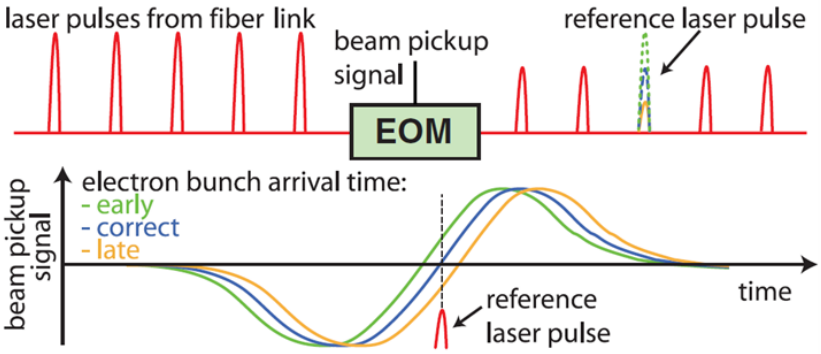

Figure 2.10.7: Principle of the electro-optical bunch arrival-time monitor (BAM). The amplitude of the reference lasers pulse train is modulated inside of an electro-optical modulator (EOM) driven by the signal of a fast beam pick-up. The electron bunch arrival time is then deduced from the laser amplitude (from [11]).

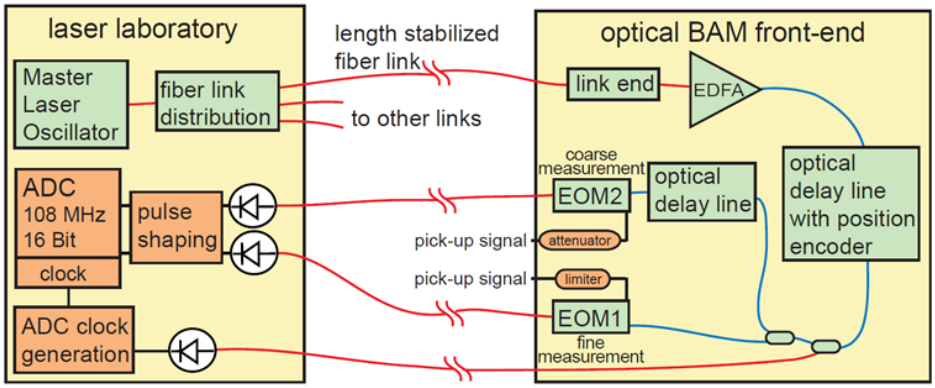

Figure 2.10.8: Schematic setup of the electro-optical detection scheme of the bunch arrival-time monitor (BAM) as it was used in first prototypes at FLASH (see [12]).

resolution. Even more important is the fact that due to the electron bunch rate, all laser pulses will be modulated in their pulse energies. This eliminates the possibility of normalizing the energy of a laser pulse modulated by the beam to that of a preceding, unmodulated pulse as used in [11, 12]. This normalization acts like a high pass filter and eliminates the influence of laser power variations as well as of ground currents in the beam pipe. A possible solution to account for laser amplitude variations would be to split the laser signal before it enters the EOMs and to measure the pulse energies of the unmodulated pulses separately. The influence of ground currents in the beam pipe can be reduced by high pass filtering the beam pick-up signal.

These issues will be resolved as part of the on-going ERL research and development program.

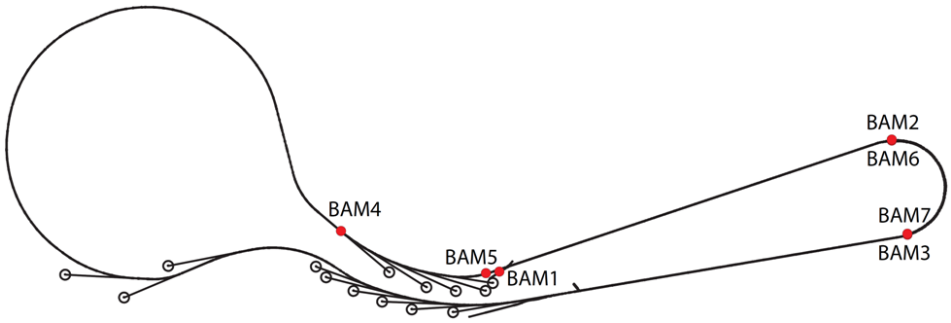

Figure 2.10.9: Important locations for the bunch arrival-time monitors (BAMs) along the ERL.

Placement of bunch arrival-time monitors and bunch arrival-time control

The most important locations at which bunch arrival-time monitors (BAMs) are required are illustrated in Fig. 2.10.9. The locations are chosen such that no arrival-time measurements take place at locations in which the accelerating and decelerating beam are superimposed.

BAM1 will measure the injection time into Linac A and BAM3 will measure the injection time into Linac B for the accelerating beam. BAM4 will be located close to the experimental beam lines in the north arc to provide the arrival-time of the compressed electron bunches to the experiments. BAM5 and BAM7 will measure the injection time for the decelerating beam into both Linacs.

The combination of two adjacent BAMs can be used for high resolution time-of-flight measurements for the accelerator section between both BAMs. By modulating the beam energy, also the R_{56} transport matrix element can be determined with high resolution using

$$R_{56} = \Delta t \cdot c \cdot \frac{E}{\Delta E} \,,$$

where c is the speed of light, E the beam energy, and ΔE the beam energy modulation.

BAM2 provides redundant information to BAM1 but it is placed after the injection merger so that the residual R_{56} element of the merger can be measured. BAM6 can isolate time-of-flight / R_{56} element changes in the turnaround.

Femtosecond stable synchronization of lasers for experiments

Experimental lasers (and also the injector laser) can be synchronized to the optical time reference laser by means of (two-color) optical cross-correlation. Potentially, such schemes will allow synchronizing both lasers to sub-fsec levels [15].

RF reference signals for cavity regulation

For ERL operating modes that do not longitudinally compress the electron bunches, the beam will be accelerated on the crest of the sinusoidal RF cavity field. This will result in a relaxed phase stability requirement for the cavity fields. For the case that the timing changes of all cavities are statistically independent, the beam energy spread will not be affected by RF phase

fluctuations. Systematic drifts of all RF cavity phases by ±0.5 deg will only lead to an increase in the beam energy spread of around 20 %.

The demands on the phase stability will be significantly increased for the cases in which the electron bunches are longitudinally compressed. One of the most sensitive parameters affected by the variation of the cavity RF phases is the bunch arrival time. A phase variation of the combined field of all cavities by 0.005 deg will lead to an arrival-time shift of 10 fs, which is the required arrival-time stability in the bunch compression modes. In the case of statistically independent phase fluctuations of all 384 cavities, this leads to a phase stability requirement of around 0.1 deg (or a corresponding RF timing variation of $\sim 200\,\mathrm{fs}$) for each cavity. Over longer time periods, this stability requirement reaches the limit of what has been achieved with conventional RF based timing systems. With optical timing systems, significantly better stability has been achieved [9, 16]; however, these systems have a limited number of end points and the performance may degrade with the number of end points needed for the ERL. The total cost for such a large optical synchronization system may also be high. Further research and development will provide the needed information for the decision as to the optimal path for providing the needed cavity regulation.

Beam arrival time and bunch compression stabilization

It may be possible to significantly reduce the requirements on the RF reference signal stability by using beam-based methods to measure the bunch compression as well as the bunch arrival-time. This information could then be used to perform correction of the phases and field amplitudes of several adjacent cavities [11]. Possible monitors that could be used in such a longitudinal feedback system would be BAMs or BPMs in a dispersive section for beam energy measurements and bunch compression monitors (BCM). These would provide measurements of the beam phase.

The feedback can then either act only on the superconducting cavities in the main Linacs, or could also act in addition on dedicated normal-conducting feedback cavities. The second approach provides the possibility of operating at a much larger feedback bandwidth compared to the superconducting cavities because of their much shorter filling time. Estimates of the required power and accelerating gradient for these normal conducting cavities are underway.

2.10.7 Longitudinal beam profile measurement

Electro-optical systems, transverse deflecting cavities, and the measurement of beam-induced diffraction radiation will be used to measure the longitudinal beam profile in the ERL.

Electro-optical schemes

Various electro-optical schemes have been developed for measurements of the longitudinal bunch profile [6, 17–19]. Because of the reduced complexity of the methods described in [17] and [19], one of these two schemes will be used in the ERL.

Figure 2.10.10 shows the operation of the 'spectral decoding' scheme [17]. A broadband laser pulse is linearly chirped and sent through an electro-optically active crystal in the beam pipe, where it co-propagates with an electron bunch. The coulomb field of the electron beam leads to a polarization rotation of the laser pulse inside of the electro-optical crystal. After

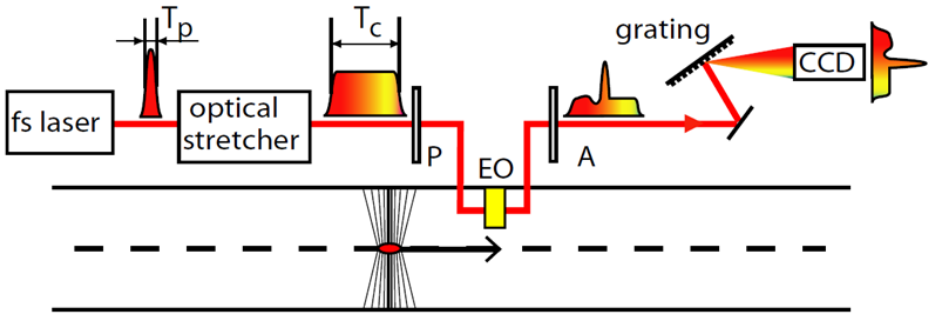

Figure 2.10.10: A typical layout for an electro-optical system for measuring the longitudinal beam profile [20]

a polarizer, these polarization changes are converted into an intensity modulation, which is measured with a spectrometer. By this, the longitudinal shape of the coulomb field can be determined and thus the longitudinal bunch shape. The resolution of this method is limited to around 100 fs, mainly due to phonon resonances inside of the electro-optical crystals as well as due to the generation of intensity sidebands after the final polarizer.

A second scheme [19] uses a similar setup, but in contrast to the first scheme, a very narrowband laser pulse (or even a CW laser) is used. The polarization rotation induced by the electron bunch inside of the electro-optical crystal leads to spectral sidebands, which again are measured with a spectrometer. While the first method measures the temporal beam profile, this method determined the frequency spectrum of the electron bunch and potentially, much shorter structures than 100 fs can be measured.

Both schemes have the advantage that they are non-destructive and that they would work at full beam current in the ERL. The effect of a high-current beam on the properties of the crystal might be a potential problem. This will be studied as part of the ongoing ERL research and development program.

Transverse deflecting structures

Transverse deflecting structures (TDS) currently provide the best longitudinal bunch shape resolution. The typical setup is shown in Fig. 2.10.11. Inside of the structure, the electron beam receives a time-dependent kick, which is measured with a beam profile monitor. The time resolution can be better than 20 fs [21, 22] and in combination with a dispersive section the longitudinal phase space distribution can also be determined from the temporal beam profile. By combining this with quadrupole scan techniques, the slice emittance along the beam bunch can also be measured.

The pulsed deflecting RF field in the TDS would require pulsed operation of the ERL and will be used mainly as an instrument for tuning and understanding the beam transfer through the accelerator. In combination with a very fast kicker and a septum magnet, an online measurement of the longitudinal phase space might be feasible in special cases.

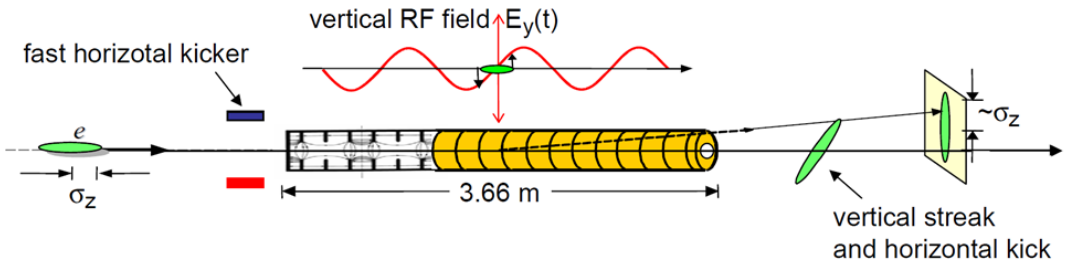

Figure 2.10.11: Typical transverse deflecting structure system for measuring the longitudinal bunch shape.

Diffraction radiation based monitors

Diffraction radiation, which is emitted when the electron bunches traverse a metallic slit or pin-hole, can also provide a tool for monitoring changes in the longitudinal bunch profile. In the simplest case, the integrated intensity of the emitted THz radiation is measured. Bunch length variations change the longitudinal form factor and thus the radiation intensity. The simplicity of this scheme make this bunch compression monitor ideally suited for a beam-based feedback system [11].

Even more information about the bunch shape can be determined by analyzing the THz radiation with a spectrometer [23].

This approach could provide a cost-effective method for providing continuous measurements for a beam-based feedback system. The concern is the possible effect on the beam emittance due to possible HOM generation by the structure. Simulations will be carried out to understand the importance of this possible effect.

2.10.8 Diagnostics in the main Linac

Multiple monitor emittance diagnostics

A multiple monitor emittance measurement system will be installed after the main Linac and before the beam enters the undulator sections. The system will verify the emittance minimization scheme used in the injector. It is important to do the measurements at this location since the emittance measurements after the injection merger take place at an energy of 15 MeV and space-charge effects within the first acceleration module of the main Linac can cause the beam emittance to change.

The system will also be used to study the potential beam emittance degradation due to beam transport through the two main Linacs and the first turn-around loop. Possible sources for emittance degradation are incoherent and coherent synchrotron radiation as well as ion accumulation effects. Simulations predict that all of these effects have limited impact on the beam emittance; however, ions trapped within the beam pipe can defocus the beam and therefore modify the Twiss parameters compared to the design parameters. This would lead to a beta-beat within the undulator sections and thus to increased x-ray beam sizes at the experimental stations.

A multi monitor emittance measurement system equipped with viewscreens as well as with

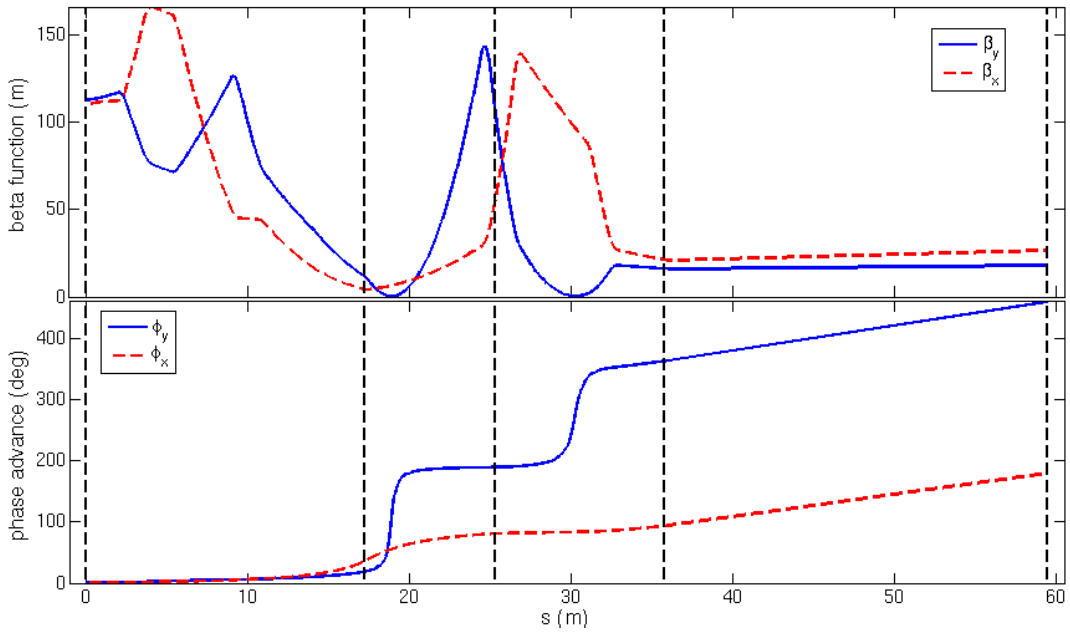

Figure 2.10.12: Beta functions and phase advance in the south-arc section of the ERL. The dashed lines indicate the locations at which beam profile monitors should be located for measurements of the beam emittance and Twiss parameters.

high-speed wire scanners will provide beam size measurements for low- as well as for high-beam currents. By optimizing the monitor placement as well as the beam optics, the beam phase space ellipses can be determined from the measured beam sizes, giving the transverse beam emittances as well as the Twiss parameters.

Due to the ultra-low beam emittance and the resulting small spot sizes, beam size measurements at full beam energy are challenging. To achieve reasonable beam size measurements with the limited resolution provided by state-of-the-art Optical Transition Radiation (OTR) viewscreens and wire scanners, large beta functions at the locations of the monitors are preferable. The calculations to determine the beam emittance as well as the beam Twiss parameters, however, also require a more or less homogeneous coverage of a 180 degree phase advance in both transverse planes. Elsewhere, this can be performed by appropriately positioning three screens in a drift space in which the beta-functions have a waist [24] or by using four beam size monitors within a FODO lattice [25].

In order to save space and still allow for accurate measurements, an optimized configuration that uses five monitors distributed within the south-arc section right after the main Linac has been studied. Figure 2.10.12 shows the placement of the monitors and the corresponding design lattice functions. The fifth monitor is located after the first undulator in order to provide higher resolution in the horizontal plane without modifying the existing beam optics.

The resolution for the beam emittance measurement as well as for the Twiss parameters was analyzed using methods described in [26]. A beam size resolution given by the rms of a 5 μm rms monitor resolution and 10 % of the beam size at the monitor location was assumed. For the layout shown in Fig. 2.10.12 this resulted in an emittance uncertainty of around 20 %

in the vertical plane and 25 % in the horizontal plane assuming a normalized beam emittance of 0.3 mm-mrad in both planes.

X-ray based online beam size monitoring

X-ray based beam size monitors will be used to observe emittance or beam optics variations during operation. A variety of high resolution methods exist (see, e.g., [27–30]), which have been extensively studied at third-generation light sources. Amongst those methods are pin-hole and pin-hole array x-ray monitors, as well as observation of the vertically polarized optical synchroton radiation at PSI in Switzerland. Beam size resolutions of better than 2 μm have be achieved.

When the beam Twiss parameters are known, a single beam size measurement in a section with no dispersion is sufficient to measure the beam emittance. In the presence of horizontal dispersion, two measurements are required. These systems will be installed in both turnaround arcs, as well as in the CESR ring. The required beam Twiss parameters will be provided by initial measurements with the emittance measurement systems in the injector as well as in the south arc.

Beam current measurements

The beam current signal along the accelerator will be provided by the BPM system. At several locations, a high dynamic-range bunch-charge monitor, based on the signal of a stripline pick-up and a logarithmic power detection will be used. A DC transformer will be used for the absolute beam current measurement.

Energy spread measurements

Wire scanners and screens in the dispersive section in the two turnarounds, as well as inside CESR, will be used for the energy spread measurements. In a section with a horizontal dispersion of 0.5 m, which can be generated at several locations, beam size monitors with a 5 μm resolution will provide an energy resolution of $\delta E/E = 10^{-5}$ for a sufficiently small horizontal beta function. This is more than sufficient to measure and verify the design energy spread of 2×10^{-4} for the entire beam and will also - albeit limited in resolution - allow for measurements of the slice energy spread. By having both wire scanners and screens, the energy spread will be studied at low- as well as at high-beam currents.

Beam loss measurements

The requirements for the beam loss monitoring systems for the ERL are challenging. The conventional technique of simply measuring the beam current at two different locations in the machine and taking the difference of the two measurements to find the loss is not possible with current technology. In the insertion device region, the losses have to be limited to 1 pA out of 100 mA and 1 nA for the rest of the machine and would require a part in 10^{11} and 10^{8} sensitivity respectively. To achieve the needed sensitivity, the radiation from the lost beam particles must be measured locally.

Ionization chambers are the most robust devices to measure radiation loss but have limited sensitivity [31]. PIN diodes provide more sensitivity but may be prone to radiation damage in the higher radiation areas [32]. Cherenkov counters consisting of a radiator viewed by a photomultiplier [33] can be fairly robust in terms of radiation damage and have better sensitivity than PIN diodes. The most sensitive detectors are bulk sciintillators [34] viewed by photomultipliers but the bulk scintillators are subject to radiation damage in varying degrees depending on the scintillating material.

The final design for the ERL beam loss monitoring system will be a combination of all of these techniques tailored to the requirements for each of the regions of the machine.

2.10.9 Seismic Environment

Data on the motion of the quadrupoles in CESR have been obtained under a variety of conditions. A geotechnical consultant, Terrascience Systems, Ltd., has taken extensive measurements in and around two test borings near the turn-around ends of the main Linacs. Data from the LIGO site at Hanford Washington have also been analyzed especially with respect to vehicle traffic on a nearby highway.

The conclusions from the LIGO studies [35] are that:

1. The largest semi-continuous off-site seismic signal in the 1 to 50 Hz band is produced by traffic on the surrounding roads.

2. Seismic motion from trucks can be greater than 10 nm at the nearest stations. Motions from cars are usually less than 1 nm.

3. Experiments with site vehicles suggest that the seismic frequency is given by the velocity and axle-spacing of the vehicle (see Fig. 2.10.13).

4. Signal propagation velocities are in the range of $450 \pm 25\,\mathrm{m/s}$.

5. Tamper signals travel at about $300\,\mathrm{m/s}$ at 10 Hz and about 75 m/s at 50 Hz.

6. Q of the vibration produced by several trucks in the 4.4 to 6 Hz range was ~ 70.

7. Typical amplification by the building structure is a factor of 2 to 3.

The results from the Terrasciences Systems tests [36] indicate that the geotechnical conditions at the ERL site have eigen-frequency peak responses in the 4 to 6 Hz region. This is in the middle of the spectrum generated by typical truck traffic. Their measurements for one-hour periods during the tests are given in Fig. 2.10.14.

To convert these velocity spectra to amplitude spectra in order to compare with the LIGO results requires multiplying by $1/f^2$. The distance to Route 366 from the test site is about 100 m and it is about 20 m from Judd Falls Road.

Vibration amplitude measurements using a sensitive accelerometer (Wilcoxon Model No. 731A/P31 with a bandwidth of 0.1 to 450 Hz) of the CESR tunnel floor and of a typical quadrupole magnet frame in the CESR ring are given in Fig. 2.10.15. The cross-tunnel trace is the quietest place in CESR in terms of seismic noise.

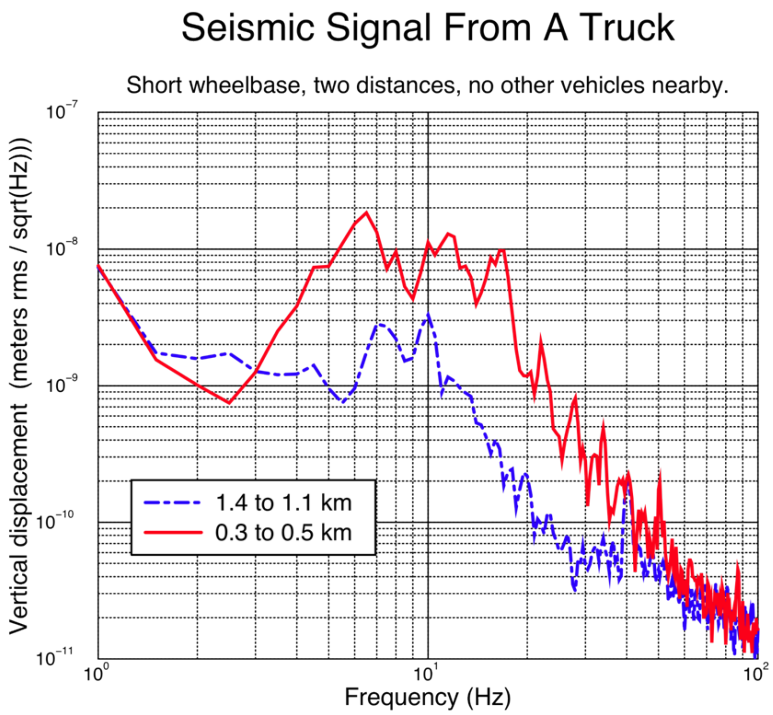

Figure 2.10.13: Seismic signal from a truck on the highway near LIGO site at Hanford Washington. Signal measured in test pits near the LIGO interferometer.

These vibration spectra can form the basis for determining the necessary isolation of sensitive machine components to meet the stringent ERL beam stability requirements. In most cases only modest improvement will be needed. For the undulator region, beam based-feedback can be used to provide the needed stability of the x-ray beams. The engineering requirements for this feedback are easily met with current technology.

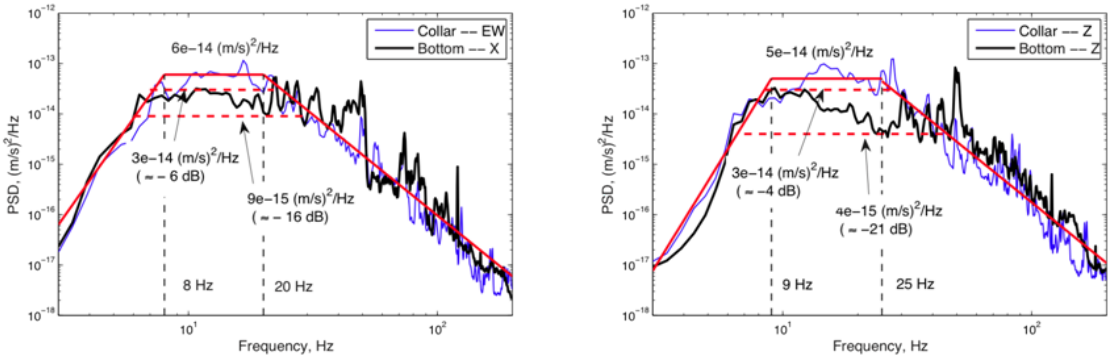

Figure 2.10.14: Velocity spectra measured by Terrasciences Systems near the proposed ERL site.

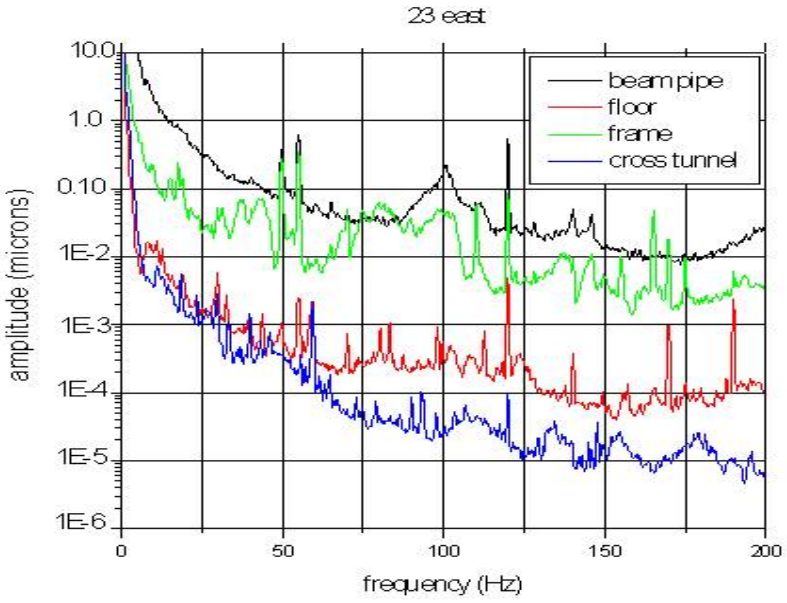

Figure 2.10.15: Results from vibration amplitude measurements in various locations in the CESR storage ring. The trace labeled frame is the frame that holds the quadrupole at this location. Cross tunnel is the floor of the diametric tunnel.

References

[1] Belomestnykh, S. *et al. Deflecting cavity for beam diagnostics at Cornell ERL injector.* Nucl. Instr. and Meth. A, **614**, pages 179–183 (2010).

[2] Schneider, G., *et al. Comparison of electron bunch asymmetry as measured by energy analysis and coherent transition radiation.* Phys. Rev. E, **56** (4), pages R3780–R3783 (Oct 1997). doi:10.1103/PhysRevE.56.R3780.

[3] Bazarov, I. V., *et al. Benchmarking of 3D space charge codes using direct phase space measurements from photoemission high voltage dc gun.* Phys. Rev. ST AB, **11** (100703) (2008).

[4] Allison, T., *et al. The CEBAF Beam Scraping Monitor.* In *Proceedings of the PAC 2001 Conference, Chicago, USA*, page 2389 (2001).

[5] Andersson, A. and J. P. H. Sladen. *First Tests of a Precision Beam Phase Measurement System in CTF3.* In *Proceedings of the PAC 2007 Conference, Albuquerque, USA* (2007).

[6] Cavalieri, A. L., *et al. Clocking Femtosecond X Rays.* Phys. Rev. Lett., **94** (11), page 114801 (Mar 2005). doi:10.1103/PhysRevLett.94.114801.

[7] *Operation of a free-electron laser from the extreme ultraviolet to the water window.* Nature Photonics, **1**, pages 336 – 342 (June 2007).

[8] Ding, Y. *et al. Measurements and Simulations of Ultra-Low Emittance and Ultra-Short Electron Beams in the Linac Coherent Light Source.* Technical Report SLAC-PUB-13525, SLAC (2009).

[9] Wilcox, R., *et al. Stable transmission of radio frequency signals on fiber links using interferometric delay sensing.* Opt. Lett., **34**, pages 3050–3052 (2009).

[10] Kim, J., *et al. Long-term femtosecond timing link stabilization using a single-crystal balanced cross correlator.* Opt. Lett., **32**, pages 1044–1046 (2007).

[11] Löhl, F., *et al. Electron Bunch Timing with Femtosecond Precision in a Superconducting Free-Electron Laser.* Phys. Rev. Lett., **104** (14), page 144801 (Apr 2010). doi:10.1103/PhysRevLett.104.144801.

[12] Löhl, F. *Optical Synchronization of a Free-Electron Laser with Femtosecond Precision.* Ph.D. thesis, University of Hamburg (2009).

[13] *Attosecond-resolution timing jitter characterization of free-running mode-locked lasers.* Opt. Lett., **32**, pages 3519–3521 (2007).

[14] Onefive GmbH. *Ultra low timing jitter performance & characterization of Origami femtosecond laser series.* White Paper P/N 09-001, Onefive GmbH (2009).

[15] *Attosecond active synchronization of passively mode-locked lasers using balanced cross-correlation.* Opt. Lett., **28**, pages 947–949 (2003).

[16] *Drift-free femtosecond timing synchronization of remote optical and microwave sources.* Nat. Photon, **2**, pages 733–736 (2008).

[17] Wilke, I., *et al. Single-Shot Electron-Beam Bunch Length Measurements.* Phys. Rev. Lett., **88** (12), page 124801 (Mar 2002). doi:10.1103/PhysRevLett.88.124801.

[18] Berden, G., *et al. Electro-Optic Technique with Improved Time Resolution for Real-Time, Nondestructive, Single-Shot Measurements of Femtosecond Electron Bunch Profiles.* Phys. Rev. Lett., **93** (11), page 114802 (Sep 2004). doi:10.1103/PhysRevLett.93.114802.

[19] Jamison, S. P., *et al. Upconversion of a relativistic Coulomb field terahertz pulse to the near infrared.* Appl. Phys. Lett., **96**, page 231114 (2010).

[20] Steffen, B. *Electro-optic methods for longitudinal bunch diagnostics at FLASH.* Ph.D. thesis, University of Hamburg (2007).

[21] Brachmann, A. *et al. Femtosecond Operation of the LCLS for user experiments.* In *Proceedings of the IPAC10 Conference, Kyoto, Japan* (2010).

[22] Röhrs, M., *et al. Time-resolved electron beam phase space tomography at a soft x-ray free-electron laser.* Phys. Rev. ST Accel. Beams, **12** (5), page 050704 (May 2009). doi: 10.1103/PhysRevSTAB.12.050704.

[23] Delsim-Hashemi, H. *Infrared single shot diagnostics for the longitudinal profile of the electron bunches at FLASH.* Ph.D. thesis, University of Hamburg (2008).

[24] Akre, R., *et al. Commissioning the Linac Coherent Light Source injector.* Phys. Rev. ST Accel. Beams, **11** (3), page 030703 (Mar 2008). doi:10.1103/PhysRevSTAB.11.030703.

[25] Löhl, F., *et al. Measurements of the transverse emittance at the FLASH injector at DESY.* Phys. Rev. ST Accel. Beams, **9** (9), page 092802 (Sep 2006). doi:10.1103/PhysRevSTAB. 9.092802.

[26] Löhl, F. *Measurements of the transverse emittance at the VUV-FEL.* Master's thesis, University of Hamburg (2005).

[27] Hofmann, A. *Electron and proton beam diagnostics with synchrotron radiation.* IEEE Transaction on Nuclear Science, **NS-28** (1981).

[28] Hofmann, A. and F. Meot. *Optical Resolution of Beam Cross-Section Measurements by means of Synchrotron Radiation.* Nucl. Inst. Meth., **203**, pages 483–493 (1982).

[29] *The geometry and optics of synchrotron radiation.* Particle Accelerators, **5**, page 199 (1973).

[30] Peatman, W. B. and K. Holldack. *Diagnostic front end for BESSY II.* J. Synchrotron Rad., **5**, page 639 (1998).

[31] Stockner, M. *et al. Classification of the LHC BLM Ionization Chamber.* In *Proceedings of DIPAC 2007 Conference, Venice, Italy* (2007).

[32] Juexina, L. *et al. Design of the Beam Loss Monitoring System in Strong Prompt Radiation Field.* Nucl. Instr. And Meth. A, **579**, pages 465–467 (2007).

[33] Gorodetzky, P. *et al. Quartz Fiber Calorimetry.* Nucl. Instr. And Meth. A, **361**, pages 161–179 (1995).

[34] Zorn, C. *A Pedestrian's Guide to Radiation Damage in Plastic Scintillators.* **32**, pages 377–383 (1993).

[35] Schofield, R. *Talk to LIGO Collaboration.*

[36] Zaicenco, A. Technical report, Terrascience Systems Ltd. (2010).

2.11 Control system integration

2.11.1 Introduction

This section describes preliminary plans for the integrated control system of the Cornell ERL. Starting with requirements, it reviews the control systems used at recent accelerators and outlines the proposed three-layer architecture (see Fig. 2.11.1).

It describes the need for a Data Acquisition System (DAQ) in a control system to provide a high level of throughput, data organization, and synchronization. A justification is made for following the designs of the DESY FLASH and European XFEL control systems, based on their integrated DAQ systems, many other advantages and their similarities to the Cornell ERL. The three control system layers – Front-End, Service, and Application or Client layers – are described, with their associated major components. Controls for x-ray beamlines and the cryoplant are also described, along with a discussion of reliability, availability and maintainability. The section closes with a description of IT utilities, computing and network infrastructures.

Requirements

Cornell ERL parameters relevant to controls The key control system parameters and functional requirements are summarized in tables Tab. 2.11.1 and Tab. 2.11.2.

State of the art

Three-tier model In the current standard model, an accelerator control system consists of a distributed network of computers connected via a communication protocol which is layered over Ethernet TCP/IP protocol. The system is realized in three tiers or layers: a front-end layer, a middle service layer, and an application or client layer (see the block diagram in Fig. 2.11.1).

The front-end layer handles access to all equipment controllers and sensors, hiding proprietary field or network buses from upper layers. The ubiquitous, critical timing and event system is in this layer. The service layer allows for efficient and centralized data acquisition and buffering of accelerator information. The service layer decouples the front-end systems from the client application layer by making device and accelerator-wide abstraction possible as well as providing utility services such as directory, alarm notification, and data archiving services. The client application is responsible for presentation of the machine state to the operator and also provides an environment for developing programmed control applications.

Recent and under-construction accelerators The implementation of the tiered model varies by site. EPICS (Experimental Physics and Industrial Control System) [1] is widely employed at accelerators world-wide but is rooted in an older two-tier paradigm and is often supplemented with additional components to create a system resembling the three-tier model. For example, at SNS (Spallation Neutron Source) EPICS is supplemented with a Java based application and service programming framework called XAL [2]. The XAL framework provides a modern object-oriented development environment that facilitates the creation of sophisticated Client and Service layer applications including the integration of on-line modeling. XAL has also been

Table 2.11.1: Parameters relevant for controls

Type	Quantity	Comment
Bunch repetition rate	1.3	GHz
Beams in Linac	2	Simultaneous
Linac RF stations	384	
Injector RF stations	12	
Dipole circuits	7	require $\pm 2 \times 10^{-5}$ stability
Quadrupoles	252	$\pm 5 \times 10^{-5}$
Sextupoles	49	$\pm 1 \times 10^{-4}$
Steering coils	145	$\pm 2 \times 10^{-5}$ bipolar, normal conducting, for global orbit correction
Steering coils	$\sim$ 40 ea	$\leq$ 250 Hz, for fast feedback
Superferric steering coils	136	$\pm 2 \times 10^{-5}$ bipolar
Vacion pump	200	Read status + current (log)
NEG pump	$\sim$ 200	Monitor during activation
Ion gauges	$\sim$ 40	Status and pressure (log)
Gate valves	$\sim$ 40	Monitor status
BPM	252	Read out and record
Ion clearing electrodes	$\sim$150	Status and voltage
Thermocouples	$\sim$1000	Read and record
Cryoplant	$<$ 1000	Control + monitor points
Utilities (water cooling system)	$\sim$ 100	Pressure, temp, flows
Network max exten	$\sim$1	km from backbone switch

Table 2.11.2: Key functional requirements for controls

Acquire and present data from $\sim 10,000$ dynamic data points
Manage $\sim 100,000$ configuration parameters
Automated management of $\sim$ 400 SRF cavities
Precise frequency reference and event timing distribution systems
Precise orbit control and feedback based on hundreds of BPMs and steering elements
Orbit control to $<$ 1.0 micron at insertion devices
Physical extent approximately one kilometer
Incorporate high-rate data streams providing information about the transient behavior
Maintain a historic record of accelerator configuration and data
Centralized monitoring and management of all infrastructure and equipment
Secure, remote access

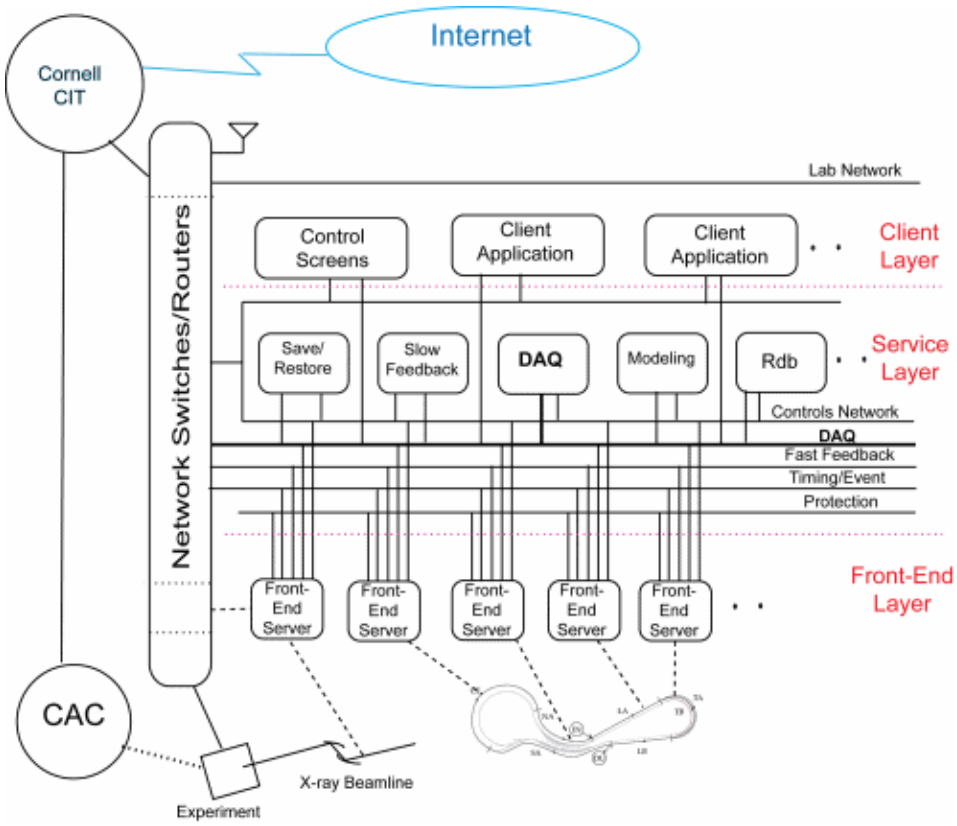

Figure 2.11.1: Overall Diagram of Proposed Three Layer Cornell ERL Control System

adapted for use with the EPICS based controls at LCLS (Linac Coherent Light Source)[3]. Rooted in work at the ALS (Advanced Light Source) the Matlab Middle Layer Toolkit (MMLT) [4, 5] extends EPICS with a Matlab based framework for the realization of client and service layer programs, including an interface to accelerator simulation tools in addition to traditional control functions. The MMLT is used with EPICS at a number of accelerators around the world. An example of a non-EPICS based realization of the standard control system model is DOOCS (Distributed Object-Oriented Control System [6]) developed at DESY beginning in the late 1990s. In this case, an entirely object-orientated approach to software development was adopted from the start and DOOCS has proven well suited to the realization of the three-tier model with the same core software functioning effectively at all three levels.

DAQ concept At DESY, DOOCS has been extended to include an integrated Data Acquisition System (DAQ). Previous control system implementations have been primarily geared to monitoring and control at low rates, typically up to approximately 10 Hz. A modern accelerator has many devices capable of generating data at rates that are orders of magnitude greater than this. While in previous control systems these devices were handled on an ad hoc basis, the DAQ system at DESY sets out an integrated approach to dealing with such devices. The DESY DAQ system [7, 8] seeks to regularize, centralize and synchronize the collection of data from high throughput devices. The DAQ system is implemented as a middle layer service thereby simplifying the task of creating control applications.

2.11.2 Cornell ERL control system architecture

Need for a DAQ in the Cornell ERL Control System The Cornell ERL will contain a number of subsystems capable of generating high rate data streams. Beam Position Monitors (BPMs), Beam Size Monitors (BSMs), Beam Loss Monitors (BLMs), Low Level RF (LLRF), and Machine Protection System (MPS), are examples of such systems. While a statistical representation of their streams (average, rms, etc.) is sometimes adequate, the analysis of beam dynamics and events, such as RF Cavity quenches or beam losses, requires the ability to capture and analyze the associated signal transients. Successful ERL operation will depend on the efficient capture and handling of these disparate data streams. A DAQ system is an infrastructure for doing just this. It requires Front-End hardware capable of streaming high-rate data in a way that is uniform across subsystems. It requires a network infrastructure capable of transporting the data with high throughput, and it requires a middle layer service capable of collecting and synchronizing the data while simplifying its presentation to accelerator physicists and client layer control applications. By making a DAQ system part of the control system plan from the beginning, one can ensure that due consideration to its requirements is given in the design of instrumentation, infrastructure, and software.

Choice of the European XFEL control system as a design model for the Cornell ERL The FLASH project at DESY operates a very successful DAQ system. The next generation of this DAQ system is currently under development to serve the European XFEL project. The XFEL control system [9], with its DAQ, serves as an excellent model for the ERL control system. The design of the Cornell ERL control system will follow closely the XFEL control system to enable re-use of hardware and software developed for the XFEL. Additionally, Cornell has a

long standing relationship to DESY, including a role in the original creation of the FLASH DAQ system, which increases confidence in being able to successfully model ERL controls on the XFEL system.

DOOCS and EPICS software frameworks As mentioned earlier, the XFEL control system is built on DOOCS. At the same time, the ability to communicate with EPICS servers is included in DOOCS. Currently in operation is a control system for the Cornell ERL injector prototype which is based mainly on EPICS and includes DOOCS servers, affording the opportunity to understand the issues related to the use of both systems together. The ERL control system will include both EPICS and DOOCS components in a configuration yet to be determined.

Data transport The three tiers of the Cornell ERL Control System will be tied together via a data transport protocol which is layered over TCP/IP. The data transport protocol provided in EPICS is called Channel Access. It has demonstrated reliable, efficient communication with EPICS front-end servers (IOCs) with which it is well integrated. It is less suited for implementing communication between middle layer services and client applications. Work is currently under way on a next generation of EPICS, EPICS4 [10], and a new version of Channel Access [11]. Data transport in EPICS4 will offer greater flexibility for interlayer communication. The Cornell ERL control system designers will follow developments in this area very closely. The DOOCS control system software offers a simple and flexible data transport model. This model is based on a data object that has built-in network visibility. From the application programmer viewpoint one simply uses these network visible objects in place of local objects.

This approach has proven to be a powerful solution for both implementing layered services and supplying high-rate data acquisition at DESY. Work is ongoing at DESY towards further development of the high performance data transport in DOOCS. DOOCS is under study to better assess the feasibility of implementing ERL controls using DOOCS based software. It is preferred to have a single data transport protocol providing inter-communication between all tiers. This protocol must also be suited to implementing the high data rate DAQ component of the control system. ERL control system software choices will seek to take advantage of existing software solutions which best provide data transport suited to the range of control systems functions.

Front-end layer

The front-end layer provides monitoring and control connections to the diverse collection of accelerator hardware while presenting a standard interface to the control layers above it. There are a number of proven solutions for this layer, including EPICS and DOOCS, and both of these will have roles in the control system we are planning. EPICS will used this for illustration.

An EPICS Front-End server or Input Output Controller (IOC) runs on either a common off-the-shelf (COTS) computer or an embedded processor, communicating with the target hardware via the protocol of the target, and making the target hardware visible to the control system. For intelligent devices, real-time control is often realized by the devices themselves with EPICS providing only management and monitoring functions. For devices with less

demanding requirements, real-time control can be provided by the EPICS IOC. The intelligent devices and IOCs are interconnected via the network infrastructure, configured to manage traffic and ensure reliability.

The hardware at the lowest level of the control system is dominated by serial and network connected devices with embedded intelligence. Examples of such devices include:

- Programmable Logic Controllers (PLCs) for general purpose inputs and outputs as well as for equipment and personnel protection.
- Low-Level RF (LLRF) digital controllers (one per RF cavity)
- RF power tubes
- Beam Position Monitor processors (one per BPM)
- Magnet Power Supplies
- Vacuum pump controllers and gauges.

For the most demanding instances of control hardware a hardware framework based on emerging ATCA and uTCA standards is envisioned [12]. This hardware, an outgrowth of the telecom industry, represents a forward looking replacement for VME and PCI crates and enables COTS-based solutions for demanding high-bandwidth instrumentation and control hardware.

Front-End servers run independently of the upper control layers but rely on upper layers for configuration, accumulation, and archiving of data. EPICS, with its mature suite of software tools and wide range of supported devices, facilitates the development of accelerator subsystems prior to the development of the upper control systems layers and prior to the integration of subsystem controls into the global control system.

Timing and event system The timing and event system is distributed to all parts of the ERL and, with the exception of RF phase control, is the basis for synchronizing all aspects of ERL behavior. The master timing generator is synchronized to the RF Master Oscillator and through a combination of fiber optic and coax cabling, distributes a reference timing signal to front-end equipment, which is stabilized to 10 ps. Incorporated into the hardware infrastructure, clock and timing relays in the front-end equipment utilize the distributed reference to provide sufficient timing precision to control all critical sequences in the functioning of the ERL. A second synchronization signal is planned for distribution to allow local phase-locked loops in subsystems to establish and maintain synchrony.

Event triggers are generated and distributed locally to initiate actions that are time sensitive. Event triggers have 10 ps precision, based on the master RF clock, and include a timestamp with sufficient number of bits to uniquely identify each RF clock frequency cycle. Event triggers can be programmed and generated for any purpose that is needed. Timestamps are also generated locally for asynchronous events and are included with every element of data that is collected by the DAQ system. These timestamps are central to reconstructing sequences of events, for instance, in the case of a post-mortem dump resulting from a fault signaled by the MPS.

Low-level RF system Each cavity has a dedicated Low-Level RF controller that implements high-speed controls loops implemented in firmware. A connection to the Timing System provides event triggers. There is an embedded front-end server as well as an additional DAQ interface to support capture of transient records as discussed in §2.5)

RF power controls A PLC provides monitoring and supervision for RF power devices. The PLC is connected to the control system through a front-end server but provides greater determinacy than network dependent supervision could provide, as described in §2.5.

Other sub-systems Beam Position and Beam Size Monitors have a dedicated signal processor capable of providing high rate data to DAQ and Orbit Feedback systems. A connection to the timing system provides event triggers. There is an embedded front-end server as well an additional DAQ interface, as explained in §2.10. Laser front-end controls are both PLC-based where required for equipment protection and front-end server based. Controlled hardware includes motors related to optics adjustments as well as laser beam characterization instruments.

Magnet power supplies are controlled through PLCs connected to front-end servers, as well as directly from front-end servers. Magnet power supplies that are part of the Orbit Feedback system additionally have connections to the Timing System to receive event triggers.

Vacuum pumps and instrumentation are low bandwidth devices connected to the control system through PLCs connected to front-end servers as well as directly to front-end servers. The Machine Protection System is implemented in dedicated hardware to achieve the required response time and reliability. However the system can be configured and monitored via front-end controls. It also provides data to the DAQ system as discussed in §2.12 . The Personnel Protection System will be implemented in dedicated hardware to achieve the required reliability and be entirely independent of the ERL Control System except for a gateway to allow monitoring, alarm handling, logging, and archiving.

Utilities and infrastructure Monitoring and supervision of utilities and infrastructure will be integrated into the ERL Control System. Many utilities systems, e.g. HVAC, have their own local controls supplied by their manufacturer and are required for autonomous operation and maintenance. In these cases the ERL Control System will have primarily a monitoring role, but with carefully defined control function to provide global precision environmental feedback and stabilization. There will be thorough logging capabilities that will be remotely accessible by technical staff with maintenance responsibilities.

Service layer

Data acquisition system (DAQ) For ERL feedback, monitoring and automation, the DAQ systems will provide access to data from across the ERL physical layout. These different systems and monitors will have different characteristic times of interest and thus differing data rates. However, data from these systems must be synchronized across subsystems and to the beam for analysis of transients, beam loss and commissioning diagnostics. The DAQ will centrally aggregate the data from its distributed sources, provide universal timestamps, synchronize the data to events, and make the data available to analysis programs and feedback

devices. The DAQ architecture and design will closely follow that of the European XFEL DAQ [9].

Data may often be represented by statistical measurements delivered at low rates. Hundreds of kBytes of data can provide a snapshot of the machine state, and such data delivered at 10 Hz rate is sufficient for many aspects of machine operation. Transient events, however, whether unexpected, experimental, or diagnostic, may generate in excess of a GByte of data per event. Efficient operation of the accelerator requires the rapid capture and presentation of data from such events. We estimate the DAQ system will need to handle peak data rates in excess of a GByte per second. The synchronization of data from such events will, in some cases, require time stamping of data with sub-nanosecond resolution.

Archiving Data from the accelerator will be archived to RAID disks for immediate accessibility. The data will be characterized for a reduction process in a central database. This reduction characterization will typically take the following form: after one month, reduce every ten samples of a particular parameter to their average. As the data age, they will be moved to other storage systems. The retrieval of data from various sources for a client will be handled in the service layer, and the source will be transparent to the client.

Feedback and monitoring Many accelerator systems will need continual monitoring loops; some of which will need actions performed (feedback) based on the monitoring information. The rates for these loops will vary and in large part the response time desired will dictate how the loops are implemented. The faster loops ($> 30\,\mathrm{Hz}$) will be implemented in front-end hardware (FPGAs) or front-end servers, either DOOCS or EPICS based. This placement is dictated by reducing data transfer latency and overhead. Moderate speed feedback and monitoring loops (between 1 and $30\,\mathrm{Hz}$) can be added at the DAQ level. Implementing at the DAQ level offers the benefits of its synchronization, shared memory and distributed input capability. Slower loops may be implemented in the DAQ or other service layer code. At all levels, code for PID type control will be available which can be used in most of the feedback cases. Other algorithms will be implemented as needed.

Automation Automation services involve having a series of tasks completed in a specific order or based on states of accelerator hardware or subsystems. These automated events can be user- or machine-triggered. User-initiated automation will be implemented with well established sequencer software based on State Notation Language (SNL). Machine-initiated automation will be based in hardware (FPGAs, PLCs), in servers (EPICS or DOOCS), or in Finite State Machines (FSMs). Automation requiring machine synchronization can be implemented in the DAQ.

Modeling An accelerator model service will be provided in the service layer. This service will be able to provide accelerator model information to applications and other services. The model can be generated from current machine conditions as an online model, from archived machine conditions, or from accelerator physics applications. The model can then be used for analysis or to test changes to the machine in a predictive mode.

Alarm handling service A large accelerator is a capable of generating many simultaneous alarms of different severity and exhibiting various degrees of interrelatedness. Providing a hierarchical, filtered view of the accelerator alarm state is critical to efficient accelerator operation and appropriate alarm response. Alarm conditions in the front-end layer are collected by the service layer alarm handler. The alarm handler applies filters to alarm sets and provides for notification to client layer applications as well as supporting subscription to e-mail, text and voice notification. Alarm configuration is centralized. We plan to use relational databases and web technologies such as Java Message Service which are well suited to implementing an alarm handler middle layer service [13].

Save and restore service The Save and Restore Service provides for capturing all settings associated with a particular machine state and for returning to that state upon demand. In addition to servicing the client layer it provides a web interface for management and comparison of saved machine states.

Web services An electronic logbook will be provided for creating, editing and viewing operational and experimental notes. The logbook capabilities include:

- Secure viewability on- and off-site
- Robust accessibility during critical machine failures
- Automatic acceptance of entries created by client and service layer software
- Capability of alerting groups of people to entries in their area of expertise
- Attachments of images and other supporting documentation

Several free open-source electronic logbook options are available which either meet all these requirements as is, or can do so with minor modification. A selection for deployment will be made at a later time. Important experience is being gained through development of the electronic log for the ERL prototype injector.

The control system will also provide support for comprehensive web-based monitoring as well as various message services (e-mail, text, voice) for alarm, event notification, and other operational needs.

Relational data base Storage in a database is needed for accelerator monitored data and input configuration data. The monitored data needs to be archived and intelligently filtered for permanent storage. This data must remain accessible to client applications continually and the interface to both the archived data and the latest dynamic data read from the accelerator should be seamless. Client applications will need complicated and varied data from the accelerator, so the database must have robust and adaptable querying capability.

The synchronization of the control system configuration with the actual state of the accelerator facility is a critical and difficult-to-achieve goal. It is important that configuration data be kept up to date across all systems and services, so ideally this configuration data should have a single point of entry from which the data is then propagated to all relevant systems. An accelerator configuration database will include among its capabilities the automated generation of software configuration files.

Client layer

There are many applications in the client layer, the most important examples of which are described in the following paragraphs. The control screen environment for operations and monitoring must meet the following criteria:

- A rich group of screen building block components should be available
- It should be easily extensible with new tools, code, and plug-ins
- There should be an easily accessible central location for screens so that keeping distributed screens up to date will be straightforward.

We are evaluating the jDDD[14] screen tool-set and display program, as used at DESY, as it meets all of these requirements. jDDD also offers the further advantages of including built-in Java Web Start capability and Subversion repository support. EPICS also provides a similar set of tools for generating controls screens.

A client application that connects to the alarm service will make alarm information widely available and viewable. The control and acknowledgment capability will have appropriate access control.

There will be a save-restore client that will provide an interface to the save-restore service. This client will allow full and partial saving and restoring of acceleration sections. The user will be able to compare saved conditions to each other and to the current machine state, as well as view a history of changes loaded into the accelerator.

A channel browser client will provide users with the ability to search for and obtain information about control system channels. A tool to plot various control system channels in real-time and in combination with archived data will be available. The same or another tool will be used for viewing historical data and to examine beam transient or loss data.

It is important for students, users, scientists and staff to develop analytic and experimental programs that interface to the control system quickly and efficiently. The control system at the ERL should leverage their existing knowledge base as much as possible. To that end, control system interfaces to commonly used programming languages and tools will be provided. C/C++ and Java will provide the backbone of application programming languages. Matlab and LabView will provide interactive experimental environments. In addition, Matlab and Python/Jython will provide scripting support.

The control system will permit remote (off-facility) access, under extremely limited and controlled circumstances, through fully authenticated, secure connections. Remote users will have control permissions which vary with user, accelerator state and instance.

Capture of post-mortem information in the event of a fault is handled as a standard capability of the DAQ system. The MPS trigger, and any other error conditions that needs to be configured become event triggers for the DAQ, and the entire array of ERL information flowing into the DAQ prior to the trigger is automatically captured and stored for analysis. Software for convenient analysis of these dumps will be written.

X-ray beamline and experiment

Control requirements X-ray experiments require exquisite precision and stability to exploit the full potential of the ERL. Micron-sized x-ray pulses with psec timing are needed with stability requirements that are one tenth of these parameters. This requires similar stability in all dimensions of the electron beam and of the undulator where the x-rays are generated. In addition the experiments require considerable flexibility on the part of the ERL, to change undulator gaps and phases as needed, without compromising the stability of beam alignment or operating conditions for any of the other experiments. Also, the x-ray beamline and experiment controls have to function autonomously from the accelerator controls when their shutter is closed, with complete freedom to set up, align and test beamline and experiment equipment.

X-ray beamline control approach and control requirements The beamline controls are not separate from the ERL controls in that they share the same network, computing technology, controls center, and development staff. They will be logically distinct, as implemented in the controls software, with a carefully defined gateway between the two sides. This has been implemented successfully at light sources such as the ALS [15]. As the experiment calls for changes to undulator settings (e.g. gap and phase) across the gateway, previously defined feed forward and feedback mechanisms fully compensate the ERL orbit parameters to negate the effect. Precision beam stabilization may be required across the ERL to x-ray beamline divide, but in most cases stabilization of the electron beam alone should be sufficient as the electron beam instrumentation provides greater accuracy than the x-ray instrumentation.

X-ray experiment data acquisition and computation needs In the new era of pixel detectors, the potential for data rates from x-ray experiments is enormous. At full rate, not only would network and storage capacities be exceeded, but processing all the data off-line or after the experiment finished would be entirely impractical. Clearly, methods of drastically reducing the data from these detectors, in real time, will be developed before operations begin. With this assumption, in this PDDR, we are leaving to the experimental collaborations the responsibility of data acquisition, on-line data reduction, storage, processing and analysis of x-ray experiment data. At the same time there will be on-site capacity for low data rate experiments, and particularly, for experiments that choose to move reasonable amounts of data (e.g. Gbytes to a few Tbytes) in real time to off-site locations. Cornell affiliated experiment collaborations may choose to process data at the Cornell Center for Advanced Computing (CAC), and for this, we will have 10Gbit network connectivity to address their needs. Most other experiments are expected to provide their own local data acquisition, processing and storage capabilities, transporting their resulting data for further analysis at home institutions via portable storage devices. This is entirely practical with current data storage technology.

Cryoplant controls

The cryoplant will be delivered with its own autonomous turn-key control system, located within the cryoplant itself. It will be created by the cryoplant manufacturer and will be sufficient for its independent commissioning and operational function. In addition to autonomous operation from a cryoplant control center, there will be a gateway between it and the ac-

celerator control system, which will allow monitoring, logging, archiving, and remote control functions for the cryoplant by the ERL control system, including routine operation from the ERL control room. The gateway will also pass information regarding changes in operational status, load requirements and alarm conditions. Timing requirements and data rates are modest and soft control over network will provide sufficient performance.

Although consideration will be given to compatibility between the two control systems, cryoplant controls will be primarily the responsibility of the plant manufacturer. The requirements given to the manufacturer will be carefully specified to ensure desired operational performance under conditions existing at this site, including recovery from power irregularities, and the need for remote operation from the ERL control room. In this we will be guided by the wide experience at our sister laboratories through close consultation with their experts.

Reliability, availability, and maintainability

The necessary high availability of the Cornell ERL will require the design of the control system to address issues of reliability and maintainability in multiple dimensions. A prerequisite of a high availability system is reliable hardware components, thus control hardware will make use of commercial components with demonstrated reliability. Reliability will be enhanced through redundancy when appropriate for critical systems.

When control system failures do occur it is essential that the time required to identify and recover be minimized. To this end extensive hardware status monitoring will be essential for all systems. The control system will provide for automatic and manual remote switchover to spare systems as appropriate. Recovery related disturbances will be reduced through the use of systems which support hot-swap of components.

Controls software contributes to availability in multiple ways. First, the software itself must be reliable, a goal that can be approached through modern design methodology as embodied in object oriented languages. The software must be verified on test stands and have defined release and bug tracking systems. Software changes will be documented by a version control system. Software developers will be provided with a modern integrated development environment to facilitate code development and management of code changes.

Coordination of hardware and software to achieve high availability requires a dedicated infrastructure of a relationship database and organizational procedures which insure that the database continually reflects the state of the accelerator, its equipment and current configuration. The Alarm Handler Service will facilitate rapid identification and recovery of failures. The accelerator database will help reduce failures related to configuration conflicts and errors while facilitating failure recovery and preventive maintenance.

Software and firmware management

The control system will necessarily consist of a wide variety of programs, services and codes, which will have a complicated inter-dependence such that changes made in one may require changes in many of the others. Management of the software and firmware will include use of a central-version control repository such as Subversion (SVN). SVN allows for development branches that can be tested before moving changes into a production version. SVN also provides the means to distribute source code remotely to facilitate code collaboration offsite.

Use of an integrated development environment (IDE) will be encouraged for rapid development and integration of resources and application programmable interfaces (APIs). Many modern IDEs, such as Eclipse and Netbeans, include the capability to edit, build, test and profile large-scale projects. They also support version control software and conflict resolution. The IDE can provide a useful platform for fast, collaborative, and coordinated code development.

2.11.3 Computing infrastructure

Computing technology is changing so rapidly that plans for computing infrastructure can be based only on what one could build today, while making extrapolations into the future for storage capacity, processor speed, and network performance. When it comes to construction, what is actually built will be based on the best technologies available at the time and incorporate best practices learned from other facilities.

The CLASSE laboratory computing facility provides the IT infrastructure for the Cornell ERL project. Although staffed and managed independently from the rest of the university, it exists within the context of the broader Cornell University IT structure, using Cornell's backbone network for connection to the Internet and taking advantage of university provided services, such as e-mail and scheduling. Although there will be computing and data storage facilities for scientific analysis on-site, the bulk of data processing and analysis for x-ray experiments will be the responsibility of those doing the experiments and is expected to be handled off-site.

Physical infrastructure and basic services The main computing facility consists of a server room in Wilson Laboratory. This is the network hub and location of central ERL Control System servers. Equipment that does not need to be located directly on site can be located in the Physical Sciences Building and Newman Laboratory located across campus. Cornell will provide high-speed network connectivity to the Center for Advanced Computing (CAC) located approximately a kilometer from Wilson Lab., as needed, for experimental data analysis.

The CLASSE laboratory computing facility will provide central support for all the basic services required for laboratory IT such as: system administration, workstation hardware/software support, file storage, backup, and Web services.

Compute clusters, CAC, and storage Although not intended for data analysis of x-ray experiments, there will be compute clusters to meet the computational needs of CLASSE and the Cornell ERL. For computation critical to ERL operations, such as on-line modeling, a computer cluster will be located on site, but for non-critical computations such as simulations, there will be one or more compute clusters in the Physical Sciences Building with a batch queuing system for efficient shared use.

Beyond locally available facilities, the CAC can provide high-performance computing systems and data storage to this project as well as other researchers at Cornell and their collaborators. It also has high speed network connectivity to the TeraGrid, National LambdaRail, Internet2 and the New York State Grid.

Networks The ERL Control System requires extensive network segmentation and throughput. Centrally located core switches, with level three routing, are planned for network parti-

tioning and connectivity of the backbone network. These switches isolate major traffic flows and separate the control system network from general purpose laboratory network functions for high availability control operation.

The backbone network is based on 10 Gbit, or faster, Ethernet, with 10Gbit trunk fibers radiating out from backbone switches to local front-end switches which connect 1Gbit Ethernet to equipment shelves and individual pieces of equipment. Multiple trunks are used where needed to provide adequate throughput and latency, separating types of traffic where appropriate. The Ethernet network is modular enough to permit easily implemented network hardware upgrade over time as new traffic patterns and potential bottlenecks surface.

The Cornell ERL will have wired and wireless network deployed throughout the entire facility, for general purpose and maintenance purposes. Segmentation into appropriate subnets can provide protection of the control system as well as remote maintenance of control system and ERL components. In experimental areas separate wired and wireless network access will be provided for the needs of outside users while maintaining isolation from the ERL Control System and laboratory staff networks.

Access and security The overall strategy for access and security is to provide robust authentication for everyone within the facility and to establish appropriate authorization for access based on users' roles and needs. Routers and firewalls will provide separation of the controls network from the general laboratory network and from outside the laboratory. At the same time, they will selectively allow expert remote access from the outside and expert access to remote resourcesacross the boundary, as needed, in a carefully restricted and monitored fashion. Intrusion detection, monitoring, and logging will be deployed to maintain the security and integrity of the controls network. Registration of visitors will permit appropriate restricted access.

References

[1] EPICS main Web site: http://www.aps.anl.gov/epics/.

[2] Galambos, J., *et al. XAL Application Programming Framework*. In *9th International Conference On Accelerator And Large Experimental Physics Control Systems (ICALEPCS 2003)*, pages 332–336. Gyeongju, Korea (2003).

[3] Dalesio, L. B. *NSLS II Control System*. In *11th International Conference On Accelerator And Large Experimental Physics Control Systems (ICALEPCS 2007)*, pages 253–255. Knoxville, Tennessee, USA (2007).

[4] Portman, G., J. Corbett, and A. Terebilo. *An accelerator control middle layer using MATLAB*. In *Particle Accelerator Conference (PAC 2005)*, pages 4009–4011. Knoxville, Tennessee, USA (2005).

[5] Corbett, J., A. Terebilo, and G. Portmann. *Accelerator Control Middle Layer*. In *The twentieth biennial Particle Accelerator Conference (PAC 2003)*, pages 2369–2371. Portland, Oregon, USA (2003).

[6] Grygiel, G., O. Hensler, and K. Rehlich. *DOOC: A Distributed Object Oriented Control Sustem on PC's and Workstations*. In *International Conference On Accelerator And Large Experimental Physics Control Systems (ICALEPCS 97)*. Beijing, China (1997). See also http://tesla.desy.de/doocs/.

[7] Agababyan, A., *et al. Data Acquisition System for a VUV-FEL Linac*. In *The 5th International Workshop on Personal Computers and Particle Accelerator Controls, PCaPAC 2005*. Hayama, Japan (2005).

[8] Agababyan, A., *et al. The Data Acquisition System (DAQ) of the FLASH Facility*. In *11th International Conference On Accelerator And Large Experimental Physics Control Systems (ICALEPCS 2007)*, pages 564–566. Knoxville, Tennessee, USA (2007).

[9] XFEL Control System, see please: http://xfel.desy.de/tdr/tdr/.

[10] http://epics-pvdata.sourceforge.net/.

[11] Žagar, K., *et al. Evolution of the EPICS Channel Access Protocol*. In *12th International Conference On Accelerator And Large Experimental Physics Control Systems (ICALEPCS 2009)*, pages 40–42. Kobe Japan (2009).

[12] Larsen, R. S. *Advances in Developing Next-Generation Electronics Standards for Physics*. Slac-pub (2009).

[13] Kasemir, K. *SNS Alarm System (BEAST); EPICS Meeting in NFRI, Daejeon, Korea* (2009). http://www.aps.anl.gov/epics/meetings/2009-07/index.html.

[14] Sombrowski, E., *et al. JDDD: A JAVA DOOCS Data Display for the XFEL*. pages 43–45 (2007).

[15] Steier, C., *et al. Operational experience integrating slow and fast orbit feedbacks at the ALS.* In *The ninth European Particle Accelerator Conference, EPAC'04,*, pages 2786–2788. Lucerne, Switzerland (2004).

2.12 Machine Protection

Overview

Both the electron and x-ray beams in the ERL have great power densities. Protection of the electron and x-ray beamline components will require great care. The electron beam transit time through the ERL is about 6.7 μs. The per pass stored energy in the beam is about 3.3 kJ, enough to do significant damage to machine components if deposited therein via accidental beam loss. Such loss can be due to a failure of the control system or to failure of any one of the many beamline components. In addition, there is continuous loss of beam particles due to intra-beam scattering, and this requires that the undulator permanent magnets be protected from the scattered electrons. Thus the machine protection system (MPS) requires both passive and active components. The passive system consists of protective collimators located upstream of each undulator as described in §2.6 and §2.1.17. The active protection system includes interlocks and fast failure detection using several different kinds of devices as well as means for removing the beam in a time comparable to the ERL transit time and depositing the beam energy harmlessly into a beam stop designed for that purpose. Similarly, there must be an x-ray beamline component protection system to avoid overheating and damage by a suitable system of interlocks and monitors.

Other important protection systems, not directly connected with the beams, are not included here. Examples would be internal heating in electronic and magnetic components and power supplies, water pumps, and ventilation equipment.

State of the art

Several electron accelerators with greater stored energy and multi-microsecond beam times have successful machine protection systems, e.g. the B-Factories with ampere level circulating beams and higher beam energies than the ERL, plus the large synchrotron radiation machines, SPring-8, ESRF, APS and PETRA III, and NSLS-II ([1], under construction). Thus we have several examples of machine protection systems in existence to emulate. For some perspective we give here the circulating electron beam power density of several of these machines, normalized to the same value of $\beta_{h/v} \sim 10\,\mathrm{m}$:

ERL (target) : $5.3 \cdot 10^{11}\,\mathrm{W/mm^2}$;

KEK-B: $8.9 \cdot 10^{10}\,\mathrm{W/mm^2}$;

SPring-8 : $1.7 \cdot 10^{11}\,\mathrm{W/mm^2}$;

NSLS-II (target): $7.5 \cdot 10^{11}\,\mathrm{W/mm^2}$.

The ERL target values are comparable to those already achieved in the B-factories and synchrotron radiation storage rings, and almost identical with the NSLS-II target values. What makes ERL different is the rather small horizontal aperture of 5 mm (round) at the IDs. As the brightness of the x-ray beam reflects that of the electron beam, the ERL will require and benefit from systems similar to those designed and developed for SPring-8 and NSLS-II. Triggering times at circular machines tend to be rather long (for example $\sim 22\,\mu$s for PEP-II),

partly due to their large circumference, the wait time for an abort gap, and electronics delay times. Once triggered, the abort kickers turn on in less than 1 μs (see [2]).

MPS performance parameters

Relevant performance targets for the electron beam can be found in §2.1. As the electron transit time is about 6.7 μs, it will be important to trigger the beam extraction system in a time shorter than this. The layout of the Cornell ERL electron beamline consists of long, nearly parallel sections that are relatively close together, which should allow triggering of the extraction kickers and laser beam stop quickly if the electronics and logic are properly designed. Extensive simulations will be required to optimize the protection system design for minimum response time.

2.12.1 Equipment to be protected

Vacuum chambers and interconnections

Vacuum chambers have to be protected from overheating by synchrotron radiation and the direct electron beam, as well as from excess HOM deposition caused by hardware failure, e.g. in an expansion joint. Each sliding joint and any irregularities in the vacuum chamber will have an attached thermocouple, with readout connected to the interlock system.

Undulators

Even the best grade NdFeB permanent magnet material has a radiation sensitivity of about 1×10^4 Gy for less than 1% demagnetization as discussed in §2.7. Thus it is necessary to prevent the undulators from exposure to synchrotron radiation and direct electron beam loss. To this end, each undulator is protected by a heavy collimator as described in §2.1.17.

X-ray mirrors and lenses

Potential damage to mirror elements as well as thermal distortion that would affect the x-ray beam coherence is of great concern. Protection will require that coolant flow interlocks and temperature sensors be used extensively.

Accelerating cavities

Very low energy deposition in the SRF cavities is essential to their proper operation. If the beam is aborted by the machine protection system, excessive beam loss in the cavities has to be avoided, and the RF system turned off in a controlled fashion so that the RF field in the cavities does not become too large. Field and phase monitoring and beam loss monitors will trigger the beam extraction and removal of RF power drive as appropriate.

Injector complex

The injector system will utilize a protection system similar to the one already implemented on the Phase 1a injector currently in operation.

Main beam stop

Up to 1.5 MW of electron beam power are expeted to be deposited. It will utilize a protection system similar to the one already implemented on the Phase 1a injector currently in operation. This system also monitors H_2 buildup in the cooling water.

2.12.2 Interlocks

It is important to abort the beam in response to any faulty condition, and to prevent beam turn-on if the system is not ready. The interlocks will also abort the beam if any sub-system fails during operation. At the highest level, a master interlock system will ensure that all of the sub-system chains are ready. Sub-systems consist of sensors attached to equipment, vacuum, pressure, cooling flow and temperature sensors, voltage, current, cavity field level and phase value monitors (one at each cavity) to name a few. All of these and more will have to be included in the overall interlock chain.

2.12.3 Triggering of fast beam extraction

A number and variety of monitors will provide trigger signals for fast beam abort (FBA) to avoid damage to beamline components (both x-ray and electron). In addition to stopping the beam, the laser beam illuminating the photocathode is turned off at the same time.

Interlock unready

If any subsystem interlock fails during beam operation, or for some reason is not in its ready state, the FBA has to be activated. This system will be redundant so that if one of the elements fails, the beam can be aborted safely.

Fast change in cavity field or phase

The LLRF, system will be used to monitor cavity behavior, and check for any failures or quenches.

Electron beam loss

Fast-beam loss monitors positioned along the entire electron beam path will monitor any abnormal losses. Currenlty, 200 monitors are planned, one approximately every 10 meters. The monitors will be located at positions where beam losses are most likely to occur, e.g. at the collimators that protecting the undulators. As the expected losses due to IBS will vary markedly along the ERL, the FBA trigger thresholds will have to be set individually. Further, the thresholds will need to be conditional, and recognize beam ramp-up, initial tuning, and other circumstances. A useful guide to such systems can be found in a thesis that describes the FLASH machine protection system ([3]. Wide dynamic range beam loss monitor detectors have been developed at accelerator laboratories and by industry ([4])

Radiation level

Radiation levels in the user areas must be kept below 'public at large' levels as discussed in §4.6. While the shielding provided by the ratchet wall enclosure is intended to be conservatively designed, it will be necessary to monitor and control the radiation levels in user areas. A level in excess of the allowed maximum value will result in a FBA with a location indication of the recorded excess.

Orbit deviation

A significant deviation from the saved orbit can be used to trigger the FBA using the BPM system.

Gun spark

If there is a high voltage discharge at the gun, the beam will necessarily be interrupted at the injector, and result in unsatisfactory acceleration and beam energy recovery conditions. Thus a gun spark will be detected and used to trigger the FBA.

Laser Failure

Similarly, a failure involving laser timing or light intensity or of the beam current regulating feedback that controls laser intensity will result in unsatisfactory acceleration and energy recovery conditions and will trigger the FBA.

Other trigger signals

Additional channels will be provided as experience dictates and operating conditions encountered in practice will occur.

2.12.4 Fast beam extraction system

As mentioned above, the challenge of stopping a high energy, high power density beam has been dealt with at other laboratories, and gives confidence that this can be done reliably. Many details have to be worked out prior to a preliminary engineering design. Nevertheless one can form a general idea of what the system will look like for planning and costing purposes. In what follows, we present such a concept, based on a specially designed 'collimator' that functions as beam stop and fast kicker to drive the beam into the "collimator". To be conservative at this stage of planning, we foresee up to four in-line beam absorbing collimators as indicated in Fig. 2.12.1. Details can be found in [5]

Collimator

Schematically, a beam stop-collimator is shown in Fig. 2.12.2. In this case, D is taken as 7 cm, and the separation of kicker and stop, L is adjusted by matching to the optics. . A conservative choice of 10 mrad is used for the kicker estimate. In Fig. 2.12.3 a conceptual sketch of an actual collimator-stop is shown.

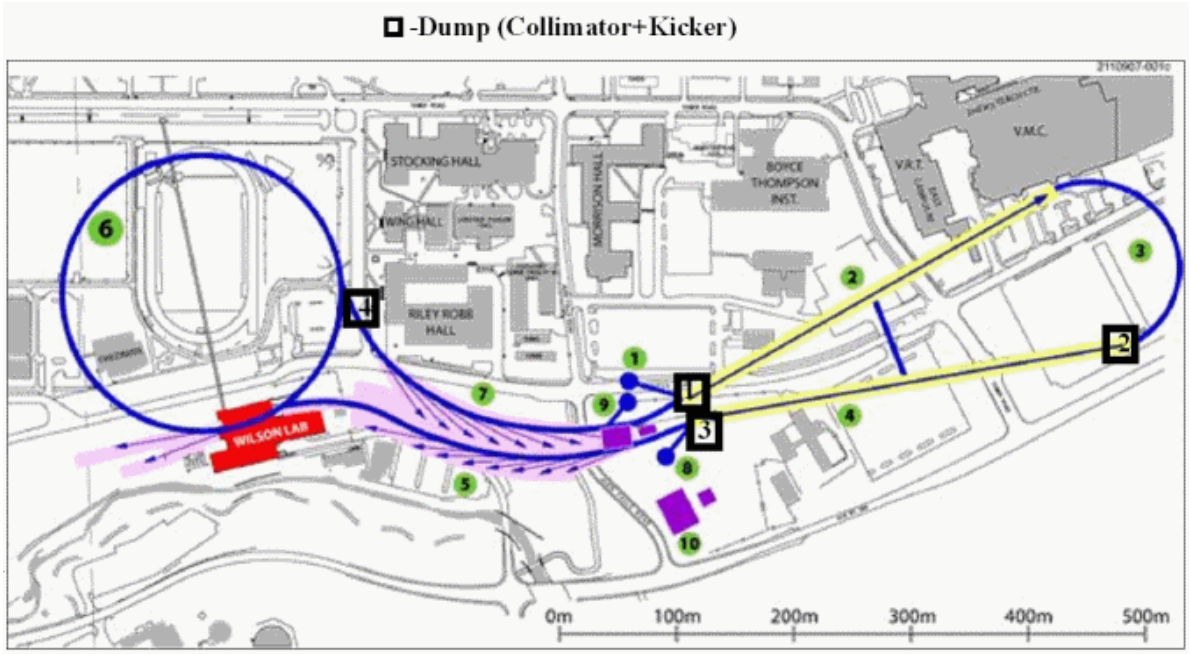

Figure 2.12.1: Schematic layout with potential locations for the beam absorbing collimator and kicker combinations

Various schemes for fast-kicker magnets have been successfully produced in the past. One scheme, based on a high-resistivity, metalized, ceramic tube vacuum chamber is shown in Fig. 2.12.4. Using available materials, it seems practical to make a system with a 10 ns risetime and a pulse length approaching 8 μs using six, 10 cm long kicker units each pulsed at 30 kV, 2.5 kA [6]. The driving pulse can be provided by a standard pulse-forming network discharged by a thyratron. Figure 2.12.5 shows an arrangement of four of the six kicker magnets arranged in series. The assembly could be less than 1 m long.

2.12.5 Next design steps

To understand the full consequences of the various component and sub-system failures, and how to detect them, a simulation model will be used. Adding IBS physics to the simulation will permit an evaluation of the dynamic range and variety of threshold settings that will be needed for the beam loss monitors and readout electronics. Adding detector properties and discriminator electronics with logic and signal paths will permit a design that minimizes the time from trigger event detection to FBA [7].

Before the design is finished, it will be important to integrate the equipment protection system and personnel protection system designs, particularly in the injector region, due to its critical nature, and in the user areas to assure that maximum protection is afforded to the users and general public at the laboratory.

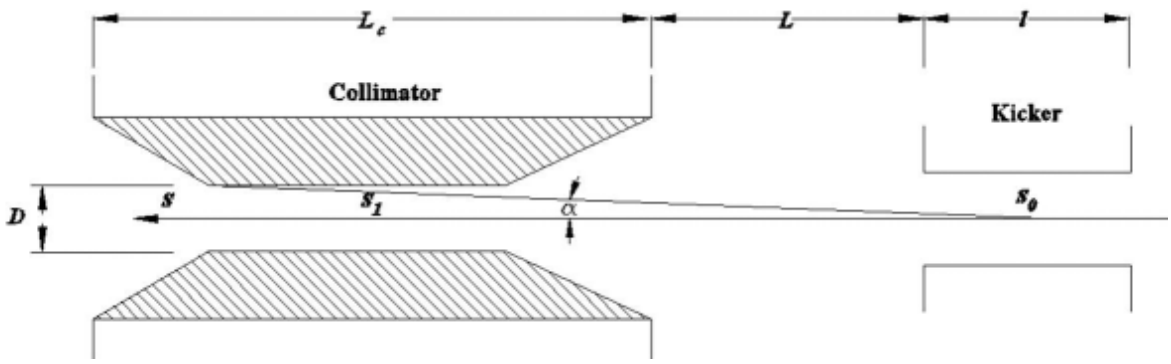

Figure 2.12.2: Principle of a beam absorber based on a fast kicker followed by a specially designed collimator.

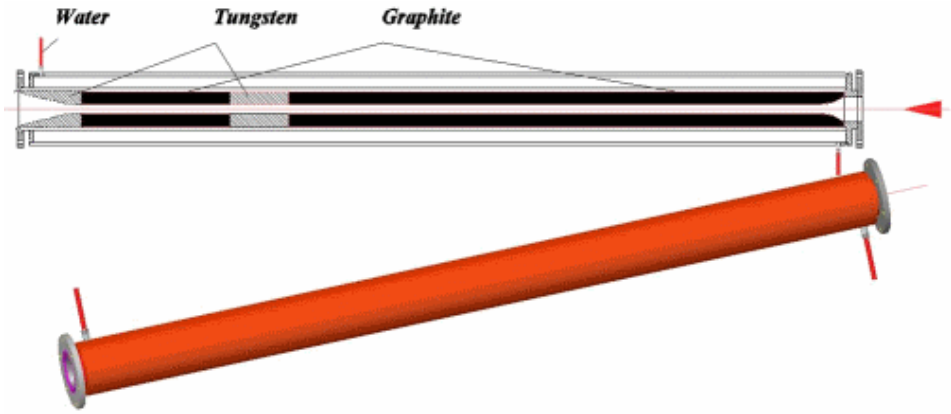

Figure 2.12.3: Beam collimator-stop based on pyrolitic graphite with additional collimation for safety and a water chamber to remove the absorbed hea.t

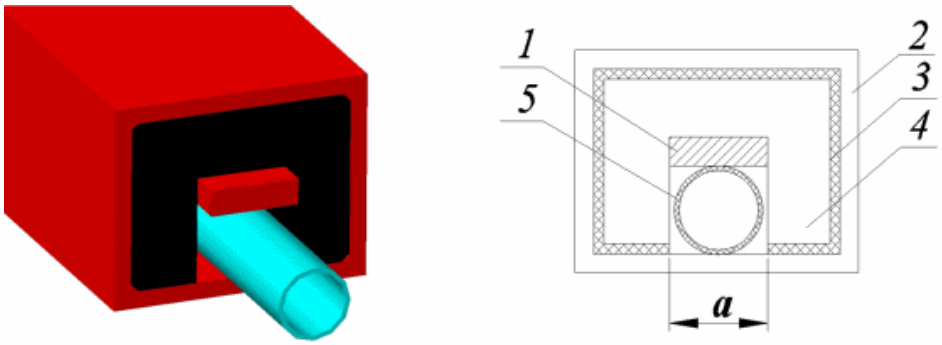

Figure 2.12.4: Crosssection of a kicker magnet: 1) central electrode; 2) enclosure; 3) insulation; 4) laminated iron or ferrite; 5) ceramic chamber.

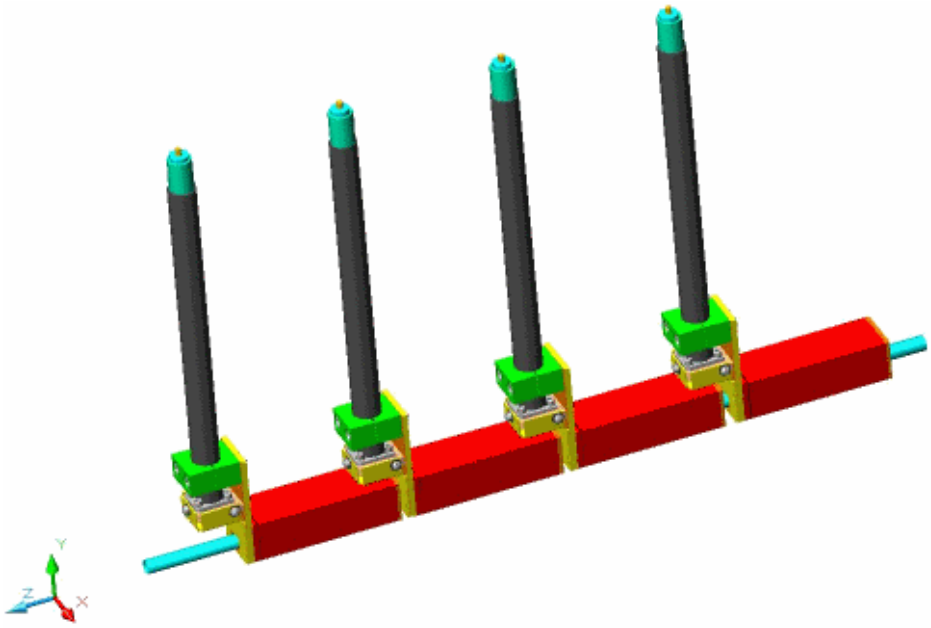

Figure 2.12.5: A series of kickers (each about 10 cm in length) with a common ceramic vacuum tube passing through. Four of six are shown.

References

[1] *NSLS-II Preliminary Design Report*. Technical report, Brookhaven National Laboratory (2007). http://www.bnl.gov/nsls2/project/PDR/.

[2] de Lamare, J. *The Abort Kicker System for the PEP-II Storage Rings at SLAC*. Technical Report SLAC-PUB-10011, SLAC (2003). http://www.slac.stanford.edu/cgi-wrap/getdoc/slac-pub-10011.pdf.

[3] Froelich, L. *Machine Protection for FLASH and the European XFEL*. Technical Report TESLA-FEL 2009-03, DESY (2009). http://flash.desy.de/sites/site_vuvfel/content/e403/e1642/e2410/e2411/infoboxContent51201/DESY-THESIS-2009-012_TESLA-FEL_2009-03.pdf.

[4] Fisher, A. *Instrumentation and Diagnostics for PEP-II*. Technical Report SLA- PUB-7835, SLAC (1998). http://slac.stanford.edu/pubs/slacpubs/7750/slac-pub-7835.pdf.

[5] A.Mikhailichenko. *Physical foundations for design of high energy beam absorbers*. Technical Report CBN-08-8, Cornell University (2008). http://www.lns.cornell.edu/public/CBN/2008/CBN08-8/CBN08-8.pdf.

[6] Mikhailichenko, A. *Fast Kicker*. Technical Report CBN-09-3, Cornell University (2009).

[7] Mikhailichenko, A. *Kicker and Dump Systems for ERL*. Technical report, Cornell (2009). http://www.lns.cornell.edu/public/CBN/2009/CBN09-5/CBN_09-05.pdf.

2.13 IT utilities

2.13.1 Overview

Information technology is so fluid that we can only describe here what we would plan for IT utilities if we were building the ERL now. Extrapolation of storage capacity, CPU performance, and network speed can be taken into account, but accurate detailed plans are impossible at this point. What will actually be installed, as the ERL is constructed, will be based on the best technology available at the time and incorporate best practices gleaned from other accelerator facilities.

The CLASSE laboratory computing facility will provide the IT infrastructure for the ERL project. Although staffed and managed independently from the rest of the university, it exists within the context of the broader Cornell University IT structure. It uses Cornell's backbone network for connection to the Internet and university provided services, such as e-mail and scheduling. It is subject to university IT policies regarding network security, data stewardship, and other matters. The computing facility provides core services including those required for desktop support, network access, and data storage. The computing and network resources of the ERL Control System, described in §2.11, are an operationally autonomous part within the computing facility. Although there will be computing and data storage facilities for scientific analysis on site, the data processing and analysis of X-ray experiment data will be the responsibility of those doing an experiment and is expected to be addressed offsite. The Cornell Center for Advanced Computing (CAC) would be the natural facility for extensive experimental data analysis for scientists based at Cornell.

Physical infrastructure

The main computing facility consists of a server room in Wilson Laboratory. This is the network hub for distribution throughout the laboratory and connection to the campus network and the Internet. Adequate UPS power and $n + 1$ redundant cooling will be provided for the major server, storage, and network equipment of the laboratory and control system. As space is restricted at Wilson, equipment that does not need to be located directly on site, such as off-line computer clusters and backup storage, can be located across campus in the CLASSE server room in the Physical Sciences Building. The core superconducting RF (SRF) research and engineering facilities are also across campus in Newman Laboratory and will have computing equipment and a network connection via fiber-optic cable to Wilson Lab. Dedicated high-speed network connectivity can be provided between Wilson Lab. and the CAC, located approximately a kilometer away, as needed for experimental data analysis.

Basic services

The CLASSE laboratory computing facility will provide central support for all the basic IT services required for the laboratory. These include:

- Workstation hardware and software support
- System administration

- Centrally served file storage for individuals
- File system backup
- Software application licensing and support
- Videoconferencing support
- Collaboration tools
- Web services and support
- Service and issue tracking
- Business system support

The university's central IT organization, Cornell Information Technologies (CIT) provides basic services for CLASSE, and the ERL, including:

- E-mail
- Scheduling
- Software licensing for some applications
- Backbone Internet connectivity
- Network security services (e.g. intrusion monitoring)

Computer clusters

Although not intended for data analysis of ERL experiments, there will be one or more computer clusters to meet the computational needs of CLASSE and the ERL. For computation critical to ERL operations, including simulation and on-line modeling, a computer cluster will be located on site in Wilson Lab. For non-critical or more extensive computations, there will be a computer cluster located in the Physical Sciences Building with a batch queuing system for efficient shared use.

University research computing facility

For computations beyond the capacity of the laboratory facility, CAC provides high-performance computing systems, data storage, and applications to researchers at Cornell and their collaborators. The CAC serves faculty researchers from dozens of disciplines and is a natural choice for Cornell-affiliated ERL users with significant computing requirements. CAC staff has extensive expertise in HPC systems, storage, database systems, data analysis, and visualization. CAC network connectivity includes TeraGrid, National Lambda Rail, Internet2, and New York State Grid. As a core facility of Cornell University, CAC receives funding from Cornell and its supporters, including the National Science Foundation. CAC's financial model is designed to recover the cost of operation, upgrade, and replacement of the equipment used.

Storage

Extensive storage capability is available to meet ERL requirements. RAID-based disk storage on a storage area network can be extended to the Petabyte scale as needed for simulations, machine physics data, ERL control system archives, and experimental data if required. Long-term storage on tape is also available.

Network

The ERL control system necessitates heavy use of network segmentation and throughput. Centrally located core switches with level-three routing capability provide the basic partitioning and connectivity of the backbone network. These isolate major traffic flows and separate the control system network from general purpose laboratory network functions for uninterrupted control operation.

The backbone network is based on 10 Gbit Ethernet technology, with 10 Gbit trunk fibers radiating out from central switches to local front-end switches connecting 1 Gbit Ethernet to equipment shelves and isolated pieces of equipment. Multiple trunks are used where needed to provide adequate throughput/latency, separating types of traffic where appropriate. The Ethernet network is modular enough to permit easily implemented adaptation over time to traffic patterns and potential bottlenecks. The ERL will have wired and wireless network access deployed throughout the entire facility, for general purpose and maintenance purposes. Segmentation into appropriate subnets will provide protection for the control system as well as remote management of control system and ERL components. In experimental areas, separate wired and wireless network access will be available for the needs of outside users while maintaining suitable isolation from other laboratory networks.

Access and security

The overall plan for access and security is to provide robust authentication for everyone within the facility and to establish appropriate authorization for access based on users' roles and needs. Routers and a central firewall will isolate and protect the ERL controls network from the general laboratory network and from the Internet. At the same time, they will selectively allow expert entry from the outside and access to remote resources across the boundary, as needed, in a carefully restricted and monitored fashion. Logging, intrusion detection and careful monitoring will be deployed to maintain security of all laboratory subnets, with special attention to the controls network. Special provisions on a separate network will be made for outside experiment staff and visitors to have access appropriate to their needs without undue restrictions.

2.13.2 Electronic document management system

CLASSE currently uses Invenio, from CERN, running on a local server, against a local backend MySQL database, for its general document EDMS needs. We plan to expand and maintain this to meet the document needs of ERL design, construction, and operations. CLASSE uses Autodesk Inventor for mechanical drawings with Vault as a repository.

Business systems IT facilities

Since CLASSE is a unit of Cornell University, the CLASSE Business Center, responsible for ERL business systems, operates within the broader context of Cornell's central IT systems. Besides local workstations, all business IT facilities are supplied and supported by Cornell University.

Relational data base

A relational database facility (currently MySQL) will be provided by the laboratory to meet the database needs of the control system, business center, as well as the miscellaneous requirements of running a scientific laboratory, such as documentation, record keeping, parts inventories, and personnel information. Appropriate provisions will be made for replication, backup, segmentation, performance, availability, and isolation, as needed.

2.13.3 ERL control system needs

The computing and network needs of the ERL control system are described in §2.11. Although logically within the context of the CLASSE laboratory computing facility, the ERL-controls-IT infrastructure will be largely autonomous, such that controls-T availability will not be affected by interruptions of service, planned or unplanned, of the laboratory facility or the university. Because they are so critical to the ERL, laboratory utilities such as power and cooling will be monitored and, where appropriate, controlled, as part of the ERL control system.

2.13.4 Beamline experiment IT needs

In the new era of pixel detectors, the potential for data rates from X-ray experiments is enormous. At full rate, not only would network and storage capacities be exceeded, but processing all the data off-line or after the experiment finished would be impractical. Clearly, methods of drastically reducing the data from these detectors must be developed in the intervening years before the ERL is operational. It is now too early in this process to make realistic plans for needed IT resources. With this assumption, the experimental collaborations must have primary responsibility for data acquisition, on-line data reduction, storage, processing, and analysis of X-ray experiment data. At the same time, there will be on-site capacity for experiments with low to modest data rates and for experiments that choose to move reasonable amounts of data (e.g. Gbytes to a few Tbytes) in real time to off-site locations. Cornell-affiliated experiment collaborations may choose to process data at the CAC, and for this, we will have 10 Gbit network connectivity to address their needs. Most other experiments are expected to provide their own local data acquisition, processing, and storage capabilities, transporting their resulting data for further analysis at home institutions via portable storage devices.

2.14 System availability

2.14.1 Introduction

Providing stable beams to scientists with a high level of availability is a primary design consideration for the ERL. Cornell's ERL team is involved in the operation of the CHESS light source with state of the art availability, and there has therefore been a commitment to this goal from the start. This began in the early design stages and will be maintained throughout the life of the experimental program.

Presented below is an outline of major components of the work to be done throughout the design and engineering phases. One has to anticipate that with new technologies it will take significant time to understand the main impediments to highly reliable operation. During the preparation for construction, this topic will be worked out in detail.

Establishment of reliability standards begins with a top-down analysis to define reliability goals for individual subsystems. Within each subsystem, reliability in terms of Mean Time Between Failure (MTBF) as well as maintainability in terms of Mean Time To Repair (MTTR), are considered from early concept through final design and implementation. Evaluation of component failure rates is done by using manufacturer data or by using well-established methods such as MIL-STD-756b or MIL-HDBK-217.

Availability may, of course, be increased by improving fault tolerance through redundant components or subsystems, by demanding conservatively rated power components, by specifying high reliability (such as rad-hard) components, and by testing extensively and by commissioning components. These all have costs that must be evaluated for efficacy [1].

During operation, aggressive maintenance programs, control of cooling water chemistry, electrical transient suppression, reduction of thermal cycling, and other preventative measures will increase MTBF.

In estimating facility availability, it will be assumed that the 'infant failures' stage is over and that any persistent failures related to design or manufacturing shortcomings have been corrected.

2.14.2 Availability accounting

The overall availability of beams for users is the product of the average availability of each of the systems that are critical for operation. A first approach to a full picture of the individual components would be to divide equally the allotment of non-available time among the systems. However, in this case some systems would find it impossible to meet their goals while others would do so easily. Thus an allotment reflecting practical realities is needed.

Availability is determined by two main components: 1) reliability, or mean time between failures (MTBF); and 2) time to fix and restore to service. This second component has three parts: 1) time to diagnose and localize the problem; 2) time to repair; and 3) time to restore the accelerator to service. For convenience these will all be grouped under the mean time to repair (MTTR). Availability is defined by:

$$\text{Availability} = \frac{\text{MTBF}}{\text{MTBF} + \text{MTTR}}. \tag{2.14.1}$$

When a downtime in any subsystem will result in a down-time of the facility, then the facility availability will be the product of all of the subsystems availabilities. A reasonable allocation of subsystem availabilities may be determined by taking into account several features of each subsystem, including:

- Number of units
- Complexity of each unit
- Stressful conditions
- Self-diagnostic capabilities
- Time to replace/repair
- Redundancy

As detailed, reliability calculations provide better data, so the subsystem allocations can be adjusted appropriately. For example, a detailed analysis of expected availability of the International Linear Collider has been carried out using a MATLAB program [2].

Special considerations

Beyond the normal mechanical and electronic failures, several special conditions need to be considered in the ERL.

Momentary interruptions Cavity breakdown and similar transient phenomena can cause momentary loss of beam. While the mean time between such events will be significantly less than 'hard' failures, recovery will be generally fast and beam restored quickly (current ramp time). In addition, the effect of unexpected interruptions to data flow in experiments must be included in net availability calculations.

Ionizing and neutron radiation Over extended periods of time, radiation will degrade components. Most construction materials are reasonably rad-hard in the environment expected for an ERL. The exception is the permanent magnets in the insertion devices (ID), where a demagnetizing effect similar to heating close to the Curie temperature is seen. Here careful analysis of the radiation distribution, characterization of materials, and control of abnormal beam conditions must be carried out to extend the wiggler lifetime.

Electronics are particularly sensitive to radiation – both ionizing and neutron. To a greater extent than with the ID magnets, careful design, placement, and shielding must be done to assure satisfactory reliability. The primary source of lost electrons will be intrabeam scattering. With careful optics design, most of the scattered particles can be transported to localized collimators, minimizing the radiation along most of the beam path. Clearly the areas around these collimators must be avoided when placing electronics. In the ratchet wall areas, the electronics can be placed outside of the primary shielding wall. Assessment of beam losses, shielding, and sensitivity of electronic components (including integrated dose and single-event upset effects) will be given high priority as the ERL design evolves.

A third effect from radiation is that of personnel protection. In addition to carefully design shielding, at least two layers of active protection will be required to assure compliance with regulatory guidelines under any operating or fault conditions of the facility. This protection can be a reliability issue if not well designed and robust against false trips.

Fault tolerance

Fault tolerance can take several forms. Redundant components will reduce MTTR. Paralleled, hot-swappable components can reduce the loss of beam time by allowing continuous operation even with failure of an active component. Can the ERL run without a cryomodule with only minor retuning? What kind of failures can be tolerated until the next scheduled access?

Re-establishing operations

Once a failure preventing beam operation has occurred, a three-step recovery process begins:

1. Fault diagnosis – Where is the failure and what component must be replaced or repaired? Extensive monitoring and diagnostics, including 'intelligent' programs can reduce this component of the recovery

2. Replacement of the failed component(s) – Accessibility and swapability will be emphasized in the design stages to speed replacement of failed components. Lock-out systems will be designed to minimize overhead in access to power components.

3. Recovery of beam – Effects from temperature cycling and hysteresis will be minimized by designing bus work to allow access with the magnets energized. If a magnet shutdown is required, compensating methods will be employed to minimize the time needed for temperature stabilization after the repair. Computer control of the shutdown and startup processes will be used to save time and reduce human error.

2.14.3 Beam stability

Slow degradation in the performance of components – feedback systems timing, mechanical parts affecting vibration levels, tunnel motion – or the presence of electrical noise can affect beam stability and other conditions affecting availability of beams suitable for carrying out experiments. In addition to good design practices, appropriate instrumentation to detect and isolate sources of beam instability will be essential.

References

[1] Bellomo, P., A. Donaldson, and D. MacNair. *B-Factory Intermediate DC Magnet Power Systems Reliability Modeling and Results.* In *The 2001 Particle Accelerator Conference (PAC 2001)*, pages 3684–3686. Chicago, Illinois, USA (2001).

[2] Himel, T., *et al. Availability and Reliability Issues for ILC.* In *The twenty-second Particle Accelerator Conference, PAC'07*, pages 1966–1969. Albuquerque, New Mexico, USA (2007).